UNIVERSITÉ DE GENÈVE

Archive ouverte UNIGE
https://archive-ouverte.unige.ch

Thèse 2024

Open Access

This version of the publication is provided by the author(s) and made available in accordance with the copyright holder(s).

Characterizing dust depletion and the properties of dust in galaxies throughout cosmic time

Konstantopoulou, Christina

How to cite

KONSTANTOPOULOU, Christina. Characterizing dust depletion and the properties of dust in galaxies throughout cosmic time. Doctoral Thesis, 2024. doi: 10.13097/archive-ouverte/unige:182284

This publication URL: https://archive-ouverte.unige.ch/unige:182284
Publication DOI: 10.13097/archive-ouverte/unige:182284

© This document is protected by copyright. Please refer to copyright holder(s) for terms of use.

UNIVERSITÉ DE GENÈVE
Département d'Astronomie
Centre de Recherche Astrophysique de Lyon

FACULTÉ DES SCIENCES
Professeur Annalisa De Cia
Dr. Jens-Kristian Krogager

Characterizing dust depletion and the properties of dust in galaxies throughout cosmic time

THÈSE

**présentée à la Faculté des Sciences de l'Université de Genève
pour obtenir le grade de Docteur ès sciences,
mention Astronomie et Astrophysique**

par

Christina KONSTANTOPOULOU

de

Amaliada (Grèce)

Thèse N^{O} 5863

GENÈVE
Observatoire Astronomique de l'Université de Genève
2024

UNIVERSITÉ DE GENÈVE

FACULTÉ DES SCIENCES

DOCTORAT ÈS SCIENCES, MENTION ASTRONOMIE ET ASTROPHYSIQUE

Thèse de Madame Christina KONSTANTOPOULOU

intitulée :

«Characterizing Dust Depletion and the Properties of Dust in Galaxies Throughout Cosmic Time»

La Faculté des sciences, sur le préavis de

Madame A. DE CIA, professeure assistante et directrice de thèse
Département d'Astronomie

Monsieur P. OESCH, professeur associé et codirecteur de thèse
Département d'Astronomie

Monsieur J.-K. KROGAGER, docteur et codirecteur de thèse
Centre de Recherche Astrophysique, University de Lyon, Lyon, France et
Franco-Chilean Laboratory for Astronomy, University of Chile, Chile

Madame M. DESSAUGES, docteure
Département d'Astronomie

Madame V. D'ODORICO, docteure
Astronomical Observatory of Trieste, Trieste, Italy

Madame F. KEMPER, professeure
Institut of Space Sciences, Barcelona, Spain

autorise l'impression de la présente thèse, sans exprimer d'opinion sur les propositions qui y sont énoncées.

Genève, le 20 novembre 2024

Thèse - 5863 -

Le Décanat

N.B. - La thèse doit porter la déclaration précédente et remplir les conditions énumérées dans les "Informations relatives aux thèses de doctorat à l'Université de Genève".

To my grandmother.

ABSTRACT

Cosmic dust plays a crucial role in the evolution of galaxies. It absorbs and re-radiates the light from stars and galaxies, altering the light that we observe. Half of the metals in the interstellar medium (ISM) of galaxies are incorporated into dust. Acting as a coolant, cosmic dust is necessary for the formation of stars and is a catalyst for the production of molecules. Therefore, cosmic dust affects the overall chemical enrichment of the ISM. One of the most effective ways to study the chemical composition of the ISM is through absorption-line spectroscopy. This powerful method allows us to probe the gas-phase abundances of various metals and determine how much of these metals are locked up in dust grains, a phenomenon called dust depletion. By characterizing dust depletion across different galactic environments, we can gain valuable insights into the origin, composition, and evolution of cosmic dust. Understanding dust depletion enables a more in depth study of the ISM chemical properties, with broader implications on galaxy evolution.

My PhD has primarily focused on characterizing dust depletion across a wide range of galactic environments, from the Milky Way to distant galaxies, and investigating the properties of cosmic dust. I collected ISM metal column density measurements from the literature and complemented these with new column density measurements of titanium and nickel, which I performed using Voigt-profile fitting, on 70 damped Lyman-α absorbers (DLAs) towards quasars (QSOs). This allowed me to characterize the dust depletion of 18 metals, using the relative abundances of metals, in the Milky Way, the Magellanic Clouds, DLAs towards QSOs and towards gamma-ray bursts (GRBs). The results of this work have strong implications on the origin of cosmic dust and the dust production mechanisms. Motivated by these findings, I conducted a follow-up study to investigate further the dust properties in these samples. We developed a novel method to determine the dust-to-metal (DTM) and dust-to-gas (DTG) ratios, dust composition, and extinction using dust depletion. These results have strong implications on the dust and metal content of different galaxies up to $z = 6.3$. My contribution to the dust depletion scheme, has impacted several other studies on the dust and metal content of galaxies, including the investigation of chemical diversity of gas in distant galaxies, the dust and metal content in the environment of GRB afterglows and the characterization of α-element enhancement in local and distant galaxies. Finally, we developed a novel method to characterize dust depletion, using observed correlations between the relative abundances of 17 metals in diverse galactic environments. This unified method offers a new approach in the characterization of dust depletion, which supersedes the previous schemes and is valuable for understanding the chemical evolution of galaxies across cosmic time.

The continued study of cosmic dust and dust depletion will bring us closer to a comprehensive understanding of galaxy evolution. By refining our methods for dust depletion, and by applying these to even more distant and diverse galaxies, we can unveil the processes that shape the chemical makeup of the universe over cosmic time.

RÉSUMÉ

La poussière cosmique joue un rôle crucial dans l'évolution des galaxies. Elle absorbe et réémet la lumière des étoiles et des galaxies, modifiant ainsi la lumière que nous observons. La moitié des métaux présents dans le milieu interstellaire (MIS) des galaxies sont incorporés dans la poussière. Jouant un rôle important dans le refroidissement du gaz, la poussière cosmique est nécessaire à la formation des étoiles et sert de catalyseur pour la production de molécules. Par conséquent, la poussière cosmique affecte l'enrichissement chimique global du MIS. L'un des moyens les plus efficaces d'étudier la composition chimique du MIS est l'analyse spectroscopique des raies d'absorption. Cette méthode puissante nous permet de sonder les abondances de divers métaux de la phase gazeuse et de déterminer la quantité de ces métaux enfermés dans les grains de poussière, un phénomène appelé déplétion dans la poussière. En caractérisant la déplétion des métaux dans la poussière à travers différents environnements galactiques, nous pouvons obtenir des informations précieuses sur l'origine, la composition et l'évolution des poussières cosmiques. La compréhension de la déplétion dans la poussière permet une étude plus approfondie des propriétés chimiques du MIS, et plus généralement, des processus régissant la formation et l'évolution des galaxies.

Mon doctorat s'est principalement concentré sur la caractérisation de la déplétion des métaux par la poussière dans un large éventail d'environnements galactiques, de la Voie lactée aux galaxies lointaines, et sur l'étude des propriétés de la poussière cosmique. J'ai rassemblé des mesures de densité de colonne de métaux du MIS provenant de la littérature et je les ai complétées par de nouvelles mesures de densité de colonne de titane et de nickel, que j'ai effectuées par ajustement de profils de Voigt, sur 70 absorbeurs Lyman-α amortis (DLAs) vers des quasars (QSOs). Cela m'a permis de caractériser le phénomène de la déplétion dans la poussière pour 18 métaux, en utilisant les abondances relatives des métaux, dans la Voie Lactée, les Nuages de Magellan, les DLAs le long de la ligne de visée de quasars et les sursauts gamma (GRBs). Les résultats de ce travail ont de fortes implications sur l'origine de la poussière cosmique et les mécanismes de production de la poussière. Motivée par ces résultats, j'ai mené une étude de suivi pour étudier plus en détail les propriétés de la poussière dans ces échantillons. Nous avons développé une nouvelle méthode pour déterminer les rapports poussière-métal (DTM) et poussière-gaz (DTG), la composition de la poussière et l'extinction en utilisant la déplétion dans la poussière. Ces résultats ont de fortes implications sur le contenu en poussières et en métaux de différentes galaxies jusqu'à $z = 6.3$. Ma contribution au phénomène de la déplétion des poussières a eu un impact sur plusieurs autres études sur le contenu en poussières et en métaux des galaxies, y compris l'étude de la diversité chimique du gaz dans les galaxies lointaines, le contenu en poussières et en métaux dans l'environnement des rémanences de GRB et la caractérisation de l'enrichissement en éléments α dans les galaxies locales et lointaines. Enfin, nous avons développé une nouvelle méthode pour

caractériser la déplétion de la poussière en métaux, en utilisant les corrélations observées entre les abondances relatives de 17 métaux dans divers environnements galactiques. Cette méthode unifiée offre une nouvelle approche dans la caractérisation de la déplétion dans les poussières, qui supplante les méthodes précédentes et est précieuse pour comprendre l'évolution chimique des galaxies au cours de l'histoire de l'Univers.

L'étude continue de la poussière cosmique et de la déplétion dans la poussière nous rapprochera d'une compréhension globale de l'évolution des galaxies. En affinant nos méthodes de la déplétion dans poussières et en les appliquant à des galaxies encore plus éloignées et plus diverses, nous pourrons dévoiler les processus qui façonnent la composition chimique de l'univers au cours du temps cosmique.

ACKNOWLEDGMENTS

First and foremost, I would like to thank my PhD supervisors Annalisa De Cia and Jens-Kristian Krogager (JK). There are no simple ways to express my gratitude for giving me the opportunity to go through my PhD in such an exciting, encouraging and fun way. I have been lucky to have experienced outstanding guidance, motivation and support in every aspect of my PhD journey. Thank you for allowing me to grow scientifically and personally during these four years. You are both amazing people and scientists and I feel honored to have worked and learned from you. Thank you so much for everything!

Annalisa your endless enthusiasm has always inspired me, thank you for always being so kind and thoughtful. From a peculiar start in Geneva during the pandemic, to the visits in Munich, you have tirelessly provided me with enormous support in my endeavours, during these past four years. You taught me exactly what being a researcher is all about. You made this journey not only productive but fun and meaningful. Thank you for introducing me to the ESO headquarters in Munich, a place that contributed to so many groundbreaking and fascinating discoveries that greatly inspired me and motivated me to go on. Thank you for giving me the opportunity to travel around the world, to places I never imagined visiting during my PhD: Japan, Chile and all over Europe, raising awareness to the world about how metals are missing and our passion about astronomy.

JK thank you for your always well-thought insights and helping me tackle complexity with calm. Thank you for introducing me to the 4MOST consortium. I look forward for the exciting new discoveries. Thank you for teaching me VoigtFit so patiently. I genually enjoyed fitting those 70 DLAs during that first summer of my PhD - because of your guidance things seemed so much easier and simpler than they really are.

Special thanks to my PhD sibling, Tanita. Thank you for the constant support. It was an absolute pleasure to share this journey with you. Thank you for the encouragement and reminding me my motivation at difficult times. I think we helped each other to keep our spirits up. Sharing all the trips to Munich made things much better and being away from home much easier. All the fun times at the Observatory, at the bars, our first Oktoberfest, our amazing trip to Patagonia, our Southernmost breakfast, our Southernmost beer, admiring glaciers, the girl and the iceberg, finding pumas, guanacos, exchanging currencies and collecting stamps! Thank you for sharing these experiences with me. I can safely say that this PhD journey would not have been the same without you.

Cédric Ledoux thank you so much for welcoming me at ESO in Chile. Thank you for your guidance, scientific advice and discussions, which made all my projects immensely better. I always admired your wisdom and your ways of thinking. I feel honored to have worked with you.

Annalisa and Cédric thank you for allowing me to make one of my dreams come true, to visit Paranal Observatory, observe with the Very Large Telescope, admire the Southern sky and even visit the Extremely Large Telescope construction site. This trip was undoubtedly

one of the highlights of my PhD and I will never forget the trip itself and the people that made it possible.

Μαμά και Μπαμπά σας ευχαριστώ για όλα. Τίποτα από όλα αυτά δεν θα ήταν δυνατά χωρίς εσάς. Πάντα ήσασταν το μεγαλύτερό μου στύριγμα σε ότι κάνω. Σας ευχαριστώ για όλα.

Thank you Angelica for welcoming me in Geneva. Moving to a new country to start my PhD in the middle of the pandemic, knowing noone, and not being able to go out is not easy. Having you made things much easier and we managed to have so much fun together despite the difficulties.

So many thanks go to the amazing friends I made in Geneva - Racha, Hans, Kris, Kevin, Alex, Malinka, Benedetto, Joana, Elena, Cyrus. Thank you so much for the unforgettable times we had together. Racha, Hans and Kris thank you for the endless support throughout these past 2,5 years. You are so special to me and I am so happy to have met you. Thank you for always being there for me at all times, for the countless fun times, the dinners, the parties, the festivals, the talks, the PhD jokes. I promise I will clean all your houses now that I have a PhD in dust. Special thanks to Racha for always being there for me, for the emotional, psychological support and endless patience. Thank you Kris for all the jokes and laughs - I think we finish each other's sandwiches. My deepest gratitude goes to my boyfriend Hans. Your constant support means the world to me, you brighten my days and fill them with love and joy. Thank you for being so patient and loving during this period of me writing this thesis and preparing for my defense.

While attending conferences, workshops, seminars and summer schools, I had the pleasure to meet incredible people that made these events unforgettable. Many thanks especially to Andrea, Eric and Céline for the memorable times during the conferences. I have to say that these conferences would not have been the same without you Andrea. I am glad we became friends and thank you for the support and all the interesting conversations. Also you are the best guide in Florence. Grazie mille e Coca Cola con la cannuccia corta! p.s I'm sorry I delayed your paper while updating my coefficients, I hope you can forgive the queen.

I also want to thank the Observatory community for the support and fun times throughout this journey, especially Alberto, Rui, Sophie, Guido, Damien, Anna, Romain, Casper, Khaled, Mara, Andrea. Tanita, Casper and Khaled I am so grateful for our hilarious trip to Pisa. I learned so much about this unfortunate construction, had the best afternoon with aperol spritz and non-stop laughter. I will never forget it. Unfortunately my research on the tower of Pisa is not included in this thesis, as I envisioned, but the Pisa tower is definitely in the acknowledgments. Finally I would like to thank my former professors and continuous mentors and colleagues already since my Master's in Copenhagen, Johan, Lise, Anja, Darach, Kasper. You are wonderful researchers and people, you have guided me and inspired me throughout my academic path.

CONTENTS

1 Introduction **3**
- 1.1 Galaxy formation and evolution - the baryon cycle . . . 3
- 1.2 The interstellar medium of galaxies . . . 6
- 1.3 Cosmic probes . . . 7
- 1.4 The role of cosmic dust in galaxies . . . 10
  - 1.4.1 Dust extinction . . . 13
  - 1.4.2 Dust depletion . . . 14
  - 1.4.3 Dust production and destruction . . . 17
  - 1.4.4 Dust composition . . . 21
- 1.5 Thesis goals and structure . . . 23

2 Absorption-line spectroscopy **25**
- 2.1 Spectroscopy with VLT/UVES and HST/STIS . . . 27
- 2.2 The absorption line profile . . . 28
- 2.3 The Voigt profile . . . 29
- 2.4 Voigt-profile fitting - VoigtFit . . . 30
  - 2.4.1 Setup and parameter file . . . 30
  - 2.4.2 Continuum normalization and component definition . . . 30
  - 2.4.3 Mask definition . . . 31
  - 2.4.4 Column densities . . . 31
- 2.5 Gas-phase metal abundances . . . 35
- 2.6 Gas-phase metallicity . . . 36
- 2.7 Stellar nucleosynthesis . . . 36

3 Dust depletion of metals from local to distant galaxies I: Peculiar nucleosynthesis effects and grain growth in the ISM **39**
- 3.1 Abstract . . . 40
- 3.2 Introduction . . . 41
- 3.3 Samples . . . 43
  - 3.3.1 QSO- and GRB-DLAs . . . 44
  - 3.3.2 Milky Way and the Magellanic Clouds . . . 45
- 3.4 Methods and results . . . 45
  - 3.4.1 New column density measurements. Voigt-profile fitting . . . 45
  - 3.4.2 Estimating the dust depletions . . . 46
  - 3.4.3 Corrections for α-element enhancement and Mn underabundance . . . 48
  - 3.4.4 Dust-depletion sequences . . . 49
  - 3.4.5 Titanium depletion . . . 50
  - 3.4.6 Nickel depletion . . . 55

3.5 Discussion . . . 56
3.5.1 Chromium . . . 57
3.5.2 Ionization of sulfur . . . 57
3.5.3 Nucloesynthesis as the cause of the deviations observed in the Magellanic Clouds . . . 58
3.6 Summary and conclusions . . . 61
3.A Statistical analysis for Mn and the α-elements . . . 62
3.B Elements with limited coverage . . . 62
3.C Velocity profiles of the new Ni and Ti DLA measurements . . . 64
3.D Column densities of all the samples . . . 95
3.E Updated column densities and coefficients for phosphorus . . . 101
4 Dust depletion from local to distant galaxies II: Cosmic dust-to-metal ratio and dust composition 107
4.1 Abstract . . . 108
4.2 Introduction . . . 109
4.3 Data Samples . . . 110
4.4 Methods and results . . . 111
4.4.1 Dust depletion measurements . . . 111
4.4.2 Dust-to-metal and dust-to-gas mass ratios . . . 111
4.4.3 Dust composition . . . 113
4.4.4 Dust extinction A_V from depletion . . . 113
4.5 Discussion . . . 119
4.5.1 DTM, DTG, and the origin of dust . . . 119
4.5.2 Cosmic metallicity evolution of the neutral gas - Comparison between QSO- and GRB-DLAs . . . 122
4.5.3 Dust composition . . . 123
4.5.4 Dust extinction from depletion compared to extinction from SED . . . 126
4.6 Conclusions . . . 132
4.A Additional figures . . . 133
4.B Dust properties of the data sample . . . 140
5 DUNE: Dust depletion UNified method across cosmic time and Environments 147
5.1 Abstract . . . 148
5.2 Introduction . . . 149
5.3 Samples . . . 151
5.4 Methods and results . . . 152
5.4.1 Stage 1: Designing DUNE . . . 152
5.4.2 Correlations among dust tracers . . . 153
5.4.3 Overall strength of depletion: Δ . . . 154
5.4.4 Indirect reference dust tracers . . . 157
5.4.5 Dust depletion of individual elements . . . 158
5.5 Stage 2: Application of the method . . . 161

5.5.1 Abundance patterns when H is known . . . 161
5.5.2 Metal patterns when H is unknown . . . 161
5.5.3 Relative metal patterns . . . 163
5.6 Discussion . . . 163
5.6.1 Strengths and limitations . . . 163
5.6.2 Comparison with previous methods . . . 164
5.6.3 Coefficients for mixed groups . . . 165
5.6.4 Krypton . . . 165
5.6.5 Carbon and oxygen . . . 169
5.6.6 Sulfur depletion in the diffuse ISM . . . 171
5.6.7 Variations of the dust depletion with interstellar conditions . . . 172
5.7 Summary and conclusions . . . 173
5.A Testing our methodology without Zn . . . 174
5.B Additional figures . . . 176
5.C Additional tables . . . 182
6 A hunt for close projected quasar pairs **189**
6.1 Target selection . . . 190
6.2 Observations with the Nordic Optical Telescope . . . 190
6.3 Data reduction . . . 193
6.4 Results . . . 194
6.4.1 Spectroscopic confirmation of quasar pairs . . . 194
6.4.2 Dust extinction . . . 195
6.4.3 Efficiency of astrometric selection in identifying QSO pairs . . . 199
6.4.4 The special configuration of a close projected pair of QSOs . . . 200
6.5 Conclusions . . . 201
7 Conclusions and Future Perspectives **203**
7.1 Summary and Conclusions . . . 203
7.2 Open questions and future perspectives . . . 208
A List of publications **213**
B Additional Voigt-profile fits **217**
C QSO pairs spectra **241**
D Other Contributions **249**

Bibliography **261**

1

INTRODUCTION

"I took the stars from my eyes,
and then I made a map,
and knew that somehow I could find my way back."
∼ Cosmic Love by Florence & the Machine ∼

1.1 GALAXY FORMATION AND EVOLUTION - THE BARYON CYCLE

The evolution of galaxies is one of the most intriguing processes in astrophysics, marking the transformation of amorphous structures in the early Universe to the rich and diverse galaxies we observe today. This journey begins shortly after the Big Bang, with the appearance of initial density fluctuations in the nearly uniform cosmic matter distribution (Peebles, 1980). The matter within galaxies consists of dark matter and baryonic matter. We now know that most of the mass in galaxies is primarily in the form of dark matter (about 85 %, Ostriker and Steinhardt, 2003; Planck Collaboration et al., 2016), which is not visible. Instead, it is the baryonic matter that makes galaxies visible. Small gravitationally bound clumps of dark matter start to form under the effects of gravity on these fluctuations (White and Rees, 1978; Springel, Frenk, and White, 2006). It is inside these dark matter halos that baryonic matter, consisting of protons, electrons and neutrons, begins to cool down and condense. The cooling and condensation processes allow the gas to collapse under its own gravity and start forming the first stars, which cluster together and form the first irregular protogalaxies. In the early stages of galaxy formation, the baryonic mass is primarily contained in the gas of the *interstellar medium* (ISM) of a galaxy, rather than in stars (White and Rees, 1978).

Galaxy evolution is a complex and dynamic process that spans billions of years. Over time, the newly formed protogalaxies begin to merge and interact, progressively form larger and more complex structures (Mo, van den Bosch, and White, 2010). These interactions can result in the formation of spiral galaxies, like the Milky Way, consisting of a rotating disk of stars, gas, and dust, and a central bulge. In spiral galaxies, star formation activity takes place in their spiral arms, fueled by the accumulation of gas and dust. Some galaxies might evolve into elliptical galaxies through major mergers, having a more spheroidal shape with little to no ongoing star formation (Mo, van den Bosch, and White, 2010). During

a galaxy's evolution, they experience bursts of extreme star formation activity, evolving in what we call starburst galaxies. Other galaxies, can develop to more irregular forms with no particular shape, evolving to irregular galaxies, which contain large amounts of gas and dust, experiencing intense star formation. Mergers and interactions can shape the morphological diversity among galaxies, and their chemical evolution is governed by the life cycles of gas and stars. The ongoing process of star formation and gas dynamics shapes the growth and chemical evolution of galaxies over time.

Galaxies start to evolve chemically as their stars synthesize heavier elements, or metals, through nuclear fusion, a process known as stellar nucleosynthesis. Within stars, hydrogen is fused into helium and progressively into heavier elements, such as carbon, oxygen, and iron. Therefore, the evolution of these stars is very important in understanding the chemical evolution of galaxies (Tinsley, 1980; Matteucci, 2012; Kobayashi, Karakas, and Lugaro, 2020). When stars exhaust their nuclear fuel they end their lives through various mechanisms depending on their mass. Low and intermediate mass stars, with masses lower than 8 $M_{\odot}$, at the end of their evolution shed their outer layer through stellar winds (Karakas, 2017). Massive stars end their lives via violent supernova (SN) explosions (Arnett, 1996). Through these mechanisms, some of the metals that are synthesized through nuclear fusion in stars are expelled into the ISM. The presence of metals in the ISM chemically enriches it and cools down the gas supporting subsequent generations of star formation and assist the formation of galactic structures, such as disks and bulges (Fall and Efstathiou, 1980). The circumgalactic medium (CGM), contains a significant part of a galaxy's baryons, possibly more than half, depending on their mass and metallicity (Tumlinson, Peeples, and Werk, 2017; Péroux and Howk, 2020). The CGM is often diffuse gas extending at large distances from the visible galaxy (~ 300 kpc) and plays a crucial role in the continuous circulation of baryonic matter within and around galaxies, the so called *baryon cycle*.

The baryon cycle in galaxies includes the accretion of gas onto the disks of galaxies, the formation of stars from gas clouds, the evolution of these stars until their eventual death, and, subsequently the return of baryonic matter to the ISM. In order to form stars and to maintain star formation, galaxies have to continuously replenish their ISM by accreting gas from their surrounding halos, with significant contribution from the intergalactic medium (IGM) (Fox and Davé, 2017; Zabl et al., 2019). The accreted gas is expected to fuel the formation of new stars and is expected to be metal-poor, because it is thought to originate from the CGM/IGM that have not undergone significant metal enrichment.

As the newly formed stars evolve, they return the baryonic matter, including newly synthesized metals, back to the ISM through stellar winds, supernovae (SNe) and active galactic nuclei (AGN). Feedback mechanisms, such as outflows and galactic winds, driven by star formation and AGN, can then eject from the galaxy some of the enriched gas of its ISM. As a result, the outflowing gas is metal enriched (Péroux and Howk, 2020; Cameron et al., 2021; Wendt et al., 2021). Additionally, ram pressure can further strip away some gas from the ISM, contributing to the enrichment of the CGM and IGM with metals (Domainko et al., 2006). Part of the outflowing gas falls back into the ISM, in the form of galactic fountains, a process that may depend on the mass of the galaxy (Oppenheimer and Davé, 2008; Marasco et al., 2022).

The CGM therefore acts as a reservoir that supplies new material to sustain star formation and re-distributes newly formed metals (Tumlinson, Peeples, and Werk, 2017). It contains both metal-poor infalling gas, which fuels new star formation, and metal-rich outflowing gas. This outflowing gas could enrich the CGM in metals that would later mix and may re-accrete, effectively recycling the metals within the galaxy. A schematic view of the baryonic cycle is shown in Fig. 1.1, illustrating how gas is exchanged between the ISM, CGM and IGM.

Although challenging, the study of the baryon cycle is essential for understanding galaxy evolution, because it encodes the complex interactions between star formation, gas accretion and feedback mechanisms that regulate the circulation of metals and eventually the growth and evolution of galaxies. Investigating the chemical evolution of galaxies provides a detailed understanding of how elements are being synthesized in stars and stellar mergers/explosions, and recycled via the baryon cycle within galaxies over time. Therefore, the investigation of the abundances of different metals within galaxies, offers a comprehensive view of the life cycle of galaxies, from their formation in the early Universe to their complex evolutionary pathways.

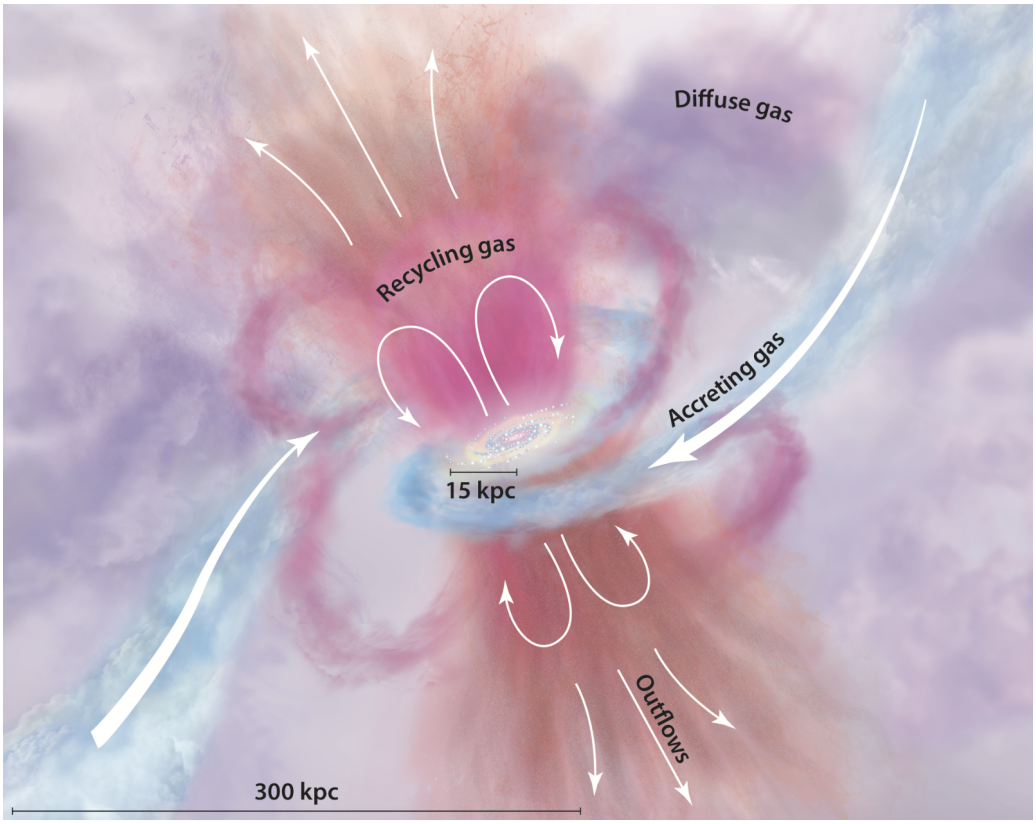


Figure 1.1: A cartoon view of the CGM from Tumlinson, Peeples, and Werk (2017). Metal-poor gas, depicted in blue, is inflowing from the IGM and accreted through the CGM onto the galaxy. The metal-enriched material (orange, pink) is expelled from the galaxy in the form of outflows, part of which falls back onto into the ISM as galactic fountains. The surrounding medium in varying tones of purple represents the mixed diffuse gas filling the CGM.

1.2 THE INTERSTELLAR MEDIUM OF GALAXIES

Between the stars of a galaxy lies the material from which they are made of and to which they return some of the heavy elements that they produce during nuclear burning or SN explosions. This matter between the stars in a galaxy is called the *interstellar medium* (ISM) and its baryonic matter consists of gas (in ionized, atomic, and molecular form) and dust (Draine, 2011). Additionally to the baryonic matter, the ISM consists of cosmic rays, magnetic fields, electromagnetic radiation, gravitational fields and dark matter. The ISM is one of the most important components of galaxies, playing a critical role in their lifecycle, since the ISM is responsible for the formation of stars and the dynamics and evolution of galaxies. The ISM is complex and consists of several distinct phases, which are defined based mainly on the ionization state of the gas and on its temperature, as well as its density and volume filling (e.g., Draine, 2011). These phases consist of:

- The *hot ionized medium* (HIM): is collisionally ionized gas, which has been heated at extremely high temperatures ($T \gtrsim 10^{5.5}$K)[1] by supernova explosions and has low density ($n_H \sim 0.004\,cm^{-3}$). In this phase hydrogen is fully ionized (HII), while other highly ionized metals, such as OVI, CIV and NVIII, are commonly found in this phase.
- The *warm ionized medium* (WIM): is ionized gas by ultraviolet photons, for example from hot, young stars. The photoionized regions are preserved by stellar radiation and can form regions of ionized gas called HII regions. The WIM has typical temperatures of $T \sim 10^4$ K and density in the range of $n_H \sim 0.3$ - $10^4\,cm^{-3}$. Hydrogen is partially ionized, while other ionized metals, such as SiII, OII and NII are typically found in this phase.
- The *warm neutral medium* (WNM): is neutral gas mainly found inside and around galaxies, occupying about $\sim 40\,\%$ of its volume. It is heated to temperatures $T \sim 10^{3.7}$ K, is at densities $n_H \sim 0.6\,cm^{-3}$ and can act as a reservoir for the cooler phases of the ISM, providing material that can eventually cool and condense to form stars. Hydrogen is neutral (HI) and ions such as FeII, SiII, OI and MgII are typically found in this phase.
- The *cold neutral medium* (CNM): is dense atomic gas, often in the form of HI clouds with temperatures $T \sim 10^2$ K and densities $n_H \sim 30\,cm^{-3}$. Hydrogen is neutral (HI) and ions such as CI, NaI, and FeI are typically found in this phase.
- The *diffuse molecular gas*: in this phase molecular hydrogen (H_2) and other molecules are distributed in the diffuse gas. This phase exists alongside other components of the ISM, such as atomic hydrogen HI and has a temperature of $T \sim 50$ K. The diffuse molecular gas exhibits sufficiently large densities ($n_H \sim 100\,cm^{-3}$) and column densities, allowing for an abundance of H_2 molecules within the cloud interior, thanks to the self-shielding ability of H_2 molecules. In this phase we can find molecules such as CO and OH.

1 The numbers presented in the phases of the ISM are representative and inferred from the Milky Way. Other galaxies, especially in the early universe, may look different.

- The *dense molecular gas*: consists of gravitationally dense molecular clouds with high densities $n_H \gtrsim 10^3$ cm^{-3} and low temperatures T $\sim$ 10 - 50 K. These dark clouds have large visual extinction $A_V \gtrsim 3$ mag due to their large amounts of dust. This is the phase where star formation occurs. Dense molecular clouds, such as giant molecular clouds (GMCs), are the birthplaces of stars and planetary systems. Hydrogen is molecular (H_2) and other molecules, such as CO and HCO+ can be found in this phase.

The significance of the ISM in galaxy evolution and formation is profound, because it provides the raw material for star formation, and this conversion of gas into stars regulates the stellar population and the evolution of galaxies. Through processes such as SN explosions and stellar winds, the ISM plays a crucial role in feedback mechanisms that regulate the recycling of matter and metals in particular. These processes within the ISM affect the birth of new stars and planetary systems, and subsequently the growth and evolution of galaxies.

The local ISM composition is overall similar to Solar and the Sun is primarily composed of hydrogen (H) (about 71 % by mass) and helium (He) (about 27 % by mass) from the Big Bang. Only approximately ∼1 % of metals are found in the ISM gas-phase (Lodders, 2003; Asplund, Amarsi, and Grevesse, 2021). These heavy elements are produced in stars and ejected into the ISM by strong stellar winds and supernovae explosions (Nomoto, Thielemann, and Yokoi, 1984). Metals are critical for cooling the ISM and start the process of star formation by getting recycled into new stars (Schneider et al., 2011), thus, the ISM affects the chemical composition of future generations of stars. Therefore, understanding the ISM is essential for unraveling the complex interplay between stars, gas and metals within their galactic environment, shedding light on how galaxies form, evolve, and sustain themselves over cosmic timescales.

The work presented in this thesis focuses on the warm neutral medium inside and around galaxies, which we probe using absorption-line spectroscopy. The method of absorption-line spectroscopy will be discussed in Chapter 2.

1.3 COSMIC PROBES

As discussed in the previous sections, the gas in and around galaxies provides critical insights into their chemical composition, and by extension, their evolution. Understanding the role and properties of the ISM is therefore crucial for a comprehensive study of galaxy evolution. The ISM of different galaxies can be probed in great detail using bright background sources, such as quasars - quasi-stellar objects (QSOs) and towards gamma-ray bursts (GRBs) in the distant Universe, and stars in the local Universe, observed through absorption-line spectroscopy. This powerful method allows for the determination of the column densities of various ions in the gas phase (e.g., FeII, ZnII, SiII, OI, MgII), from which the metal abundances in the ISM of the galaxy can be derived (e.g., Wolfe et al., 1995; Savage and Sembach, 1996; Prochaska and Wolfe, 1999). A gas-phase metal abundance is defined as $[X/H] = \log \frac{N(X)}{N(H)} - \log \frac{N(X)_\odot}{N(H)_\odot}$, where N(X) is the column density of an element X, N(H) the H column density and $N(X)_\odot$, $N(H)_\odot$ their equivalent solar values. The

methodology used in this thesis to obtain column densities, which are essential for the determination of metal abundances, is described in Chapter 2.

QSOs were initially discovered as radio sources exhibiting a star-like appearance in their optical counterpart, hence they were called quasi-stellar radio sources (Schmidt, 1963; Greenstein and Schmidt, 1964). They are point-like, intrinsically very luminous and are very distant and bright objects in the Universe, making them excellent cosmological probes. They are powered by the accretion of gas onto black holes. When material, such as gas and dust falls towards a black hole, it spirals around and towards the black hole due to loss of angular momentum. This leads to the formation of an accretion disk, creating friction and heating up the material that falls in. The gas becomes hot and highly ionized, and part of it is expelled away from the disk in the form of a relativistic jet along the QSO's rotational axis (Blandford and Znajek, 1977). These very strong energy outputs of QSOs span a wide range of wavelengths, including X-rays, radio and optical wavelengths. Their optical spectra are characterized by strong, broad emission lines, produced intrinsically by moderately dense gas, which is accreting onto the black hole. Due to their great cosmological importance, large catalogs of QSOs have been built (e.g., York et al., 2000; Richards et al., 2009; O'Meara et al., 2015; Lyke et al., 2020), thanks to extensive surveys, such as the Sloan Digital Sky Survey (SDSS, Schneider et al., 2002), the Keck Observatory Database of Ionized Absorption toward Quasars (KODIAQ) survey and the "Quasars and their absorption lines: a legacy survey of the high-redshift Universe with VLT/X-shooter" (XQ-100 López et al., 2016). The total number of spectroscopically confirmed QSOs is 907,144 according to the compilation by Flesch (2023) up to 30 June 2023. This catalogue also includes 66,026 QSO candidates with 99% probability of being QSOs. Due to their extreme luminosity and cosmological distance, QSOs are excellent probes of the ISM of distant galaxies. As the light from QSOs travels through space, it passes through the gas and dust present in intervening galaxies, causing absorption lines in the spectrum of the QSO. By analyzing these absorption lines one can obtain a detailed view of the chemical composition of the ISM in these distant galaxies.

GRBs, like QSOs, are powerful tools for probing the distant universe. They were discovered serendipitously in 1969 and confirmed to be at cosmological distances by van Paradijs et al. (1997), hence their extragalactic origin. GRBs are the most energetic explosions known in the Universe, with durations ranging from milliseconds to several minutes, and have stellar origin. The GRB progenitors depend on the type of GRB. Most classifications of GRBs distinguish two main classes, long and short GRBs, with different origins for each. Long GRBs are typically associated with the collapse of massive stars (collapsars) that result to a black hole and are quite often accompanied by a SN explosion. This connection has been detected in a number of cases, such as the SN associated with GRB 030329 (e.g., Hjorth et al., 2003). On the other hand, short GRBs are believed to arise from the merger of binary neutron stars or from the merger of a neutron star with a stellar-mass black hole. For example, the short burst GRB 170817A, related to a gravitational wave event detected by LIGO/Virgo confirmed its origin to be from a neutron star merger (Abbott et al., 2017). The jets created by long GRBs interact with the surrounding circumstellar medium. This interaction produces the GRB afterglows, which can be observed across a broad range of wavelengths, from X-rays to radio frequences. Optical afterglows of GRBs can be extremely

bright, up to a factor of 10^8 more bright that their host galaxies (Racusin et al., 2008; Bloom et al., 2009), giving opportunity for detailed spectroscopic observations of the afterglow. Observations of GRB afterglows are valuable for the study of the chemical enrichment in the ISM of galaxies (e.g., Vreeswijk et al., 2004; Sparre et al., 2014; Wiseman et al., 2017; Bolmer et al., 2019; Saccardi et al., 2023; Heintz et al., 2023). The spectra of the afterglow carry the imprint of material within the host galaxy itself, providing insights into the metal and dust content of the gas surrounding the GRB. Additionally, the light from the GRB afterglow can go through intervening material along the line of sight, causing absorption lines in the GRB afterglow spectrum. This allows for the study of the metals and dust content in the gas of other galaxies along the line of sight (e.g., Jakobsson et al., 2004).

Damped Lyman-α absorbers (DLAs, defined by N(HI) $\geq 2 \times 10^{20}$ cm^{-2}) are observed in absorption towards QSOs and GRBs and are associated with gas inside and around galaxies. Due to the large amounts of neutral hydrogen in the gas of DLAs, the gas is self-shielded against ionization (e.g., Viegas, 1995; Wolfe, Gawiser, and Prochaska, 2005). This means that ionization corrections are negligible when determining metal abundances, as will be discussed in Chapter 2. DLAs are characterized by a strong and broad Lyman-α absorption feature. The DLA gas is causing absorption lines of multiple species in the spectrum of the QSO/GRB, which exhibits intrinsic emission lines. In QSO spectra, DLAs normally occur because of intervening galaxies at lower redshift, which absorb the light of the QSO along the line of sight. In the case of GRBs, DLAs are normally assumed to be located in the host galaxy of the GRB, so the absorption features are at the same redshift as the intrinsic emission lines of the GRB. This is an important distinction, because the Ly-α emission and absorption sometimes overlay in GRB spectra. DLAs are often used to study the abundances of several elements in a wide range of galactic environments and physical conditions, and can be studied regardless of the luminosity of the absorbing galaxy. They are the largest cosmic reservoir of HI (e.g., Wolfe et al., 1995; Noterdaeme et al., 2009), and carry the majority of metals in the high redshift Universe, especially at $z > 3$ (Péroux and Howk, 2020). They specifically probe the neutral gas within and around galaxies of a wide range of masses, including low-mass galaxies, which are the most common (e.g., Fontana et al., 2004), and low-metallicity galaxies. Therefore, DLAs offer a unique way for studying metal abundances in distant galaxies and contribute significantly to our understanding of galaxy evolution.

GRB sightlines pierce directly the inner parts of star-forming galaxies, because they are associated with the death of massive stars. These stars are typically located in dense star-forming regions of the galaxies, which are usually in the more central parts of the galaxies. As a result, GRB sightlines provide a direct probe of the dense, metal-rich environments in which stars form. On the other hand, the sightlines towards QSOs are more randomly distribute and are more likely to probe the ISM at larger impact parameters (e.g., Prochaska et al., 2007; Fynbo et al., 2008). This difference in the location of GRB and QSO sightlines offer the opportunity to study the gas in and around galaxies from different perspectives. An illustration of the typical impact parameters and different lines of sights piercing a galaxy is shown in Fig. 1.2.

In the local Universe, one can use stars as bright background sources to study the ISM that lies between the observer and the star. Most commonly, bright type-O and type-B stars

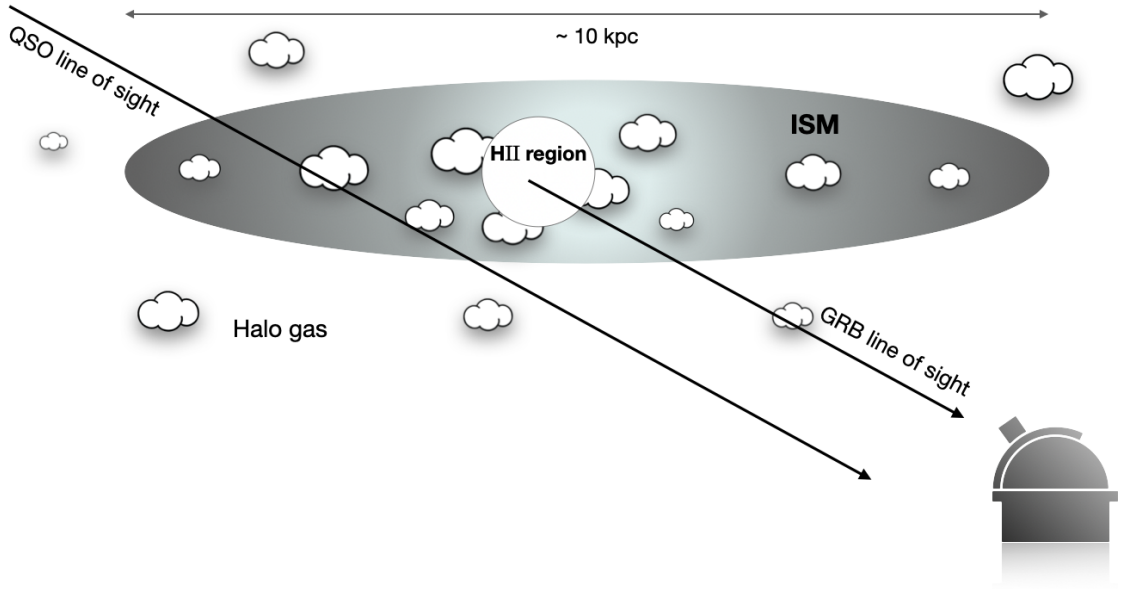


Figure 1.2: A cartoon illustration of the likely differences between QSO-DLA and GRB-DLA lines of sight (following Prochaska et al., 2007). QSO-DLAs lines of sight pierce randomly the foreground galaxy, preferentially intersecting outer regions of the ISM of galaxies. On the other hand, GRB-DLAs originate in the most central parts of their host galaxies, piercing the central parts of the star-forming HII regions of their host galaxy. The radial extent of the galactic disk is of the order of $\sim$10 kpc

are observed in the Milky Way or in the Small and Large Magellanic Clouds (Jenkins, 2009; De Cia et al., 2021; Roman-Duval et al., 2021; Ritchey et al., 2023b). These stars are hot, massive and excellent sources to study the ISM, due to the relatively fewer intrinsic features in their spectra. This simplicity in the spectra of OB stars allows for a clear distinction between stellar and ISM features. Additionally, the stars are typically selected to have rotational velocities that are high enough (e.g., 50 km s^{-1}) to broaden their spectral lines, further enhancing the separation between stellar and ISM features. This makes it easier to clearly identify and study the features of the ISM.

1.4 THE ROLE OF COSMIC DUST IN GALAXIES

The first compelling evidence for the presence of material dimming starlight as it passes through space was given by the Swiss-American astronomer Robert Julius Trumpler in 1930 (Trumpler, 1930). Trumpler (1930) determined the distances of open star clusters from the magnitudes of the stars observed at the Lick Observatory. The results of his work showed that the most distant clusters appeared to have smaller apparent sizes, experiencing some kind of absorption of starlight, and therefore appearing fainter than expected. He attributed this to *interstellar dust*, present within the Galaxy and resulting in absorption and scattering of starlight proportionally to distance. This means that the

brightness of more distant clusters was extinguished more than that of nearby clusters. The identification of interstellar dust as a cause of starlight absorption was later also concluded by Stebbins, Huffer, and Whitford (1939).

Interstellar dust consists of very small, solid particles composed mostly of elements such as hydrogen, carbon, silicon, oxygen, magnesium and iron. The size of dust grains is variable but it ranges between a few nanometers to micrometers in radius (Mathis, Rumpl, and Nordsieck, 1977; Weingartner and Draine, 2001). Its composition for the most part is assumed to be silicates, iron and carbonaceous materials, such as graphite or amorphous carbon, and it will be discussed in more detail in Section 1.4.4. Despite their small size, dust grains represent a crucial component of the ISM and have a profound influence on galaxies.

Over time, many different studies have been dedicated to shedding light on the properties of dust and its effect on galaxies. Dust is fundamentally important regulating several physical and chemical processes of galaxies, and therefore has significant impact on their evolution. Dust acts as a key catalyst for star formation (Draine, 2003; McKinnon et al., 2018; Li, Narayanan, and Davé, 2019), cooling interstellar gas clouds, which is essential for the collapse and formation of new stars (Draine, 2003; Li, Narayanan, and Davé, 2019). Moreover, dust grains provide surfaces for chemical reactions, including the formation of molecular hydrogen (H_2), which is critical for star formation (Hollenbach and Salpeter, 1971; Hollenbach and McKee, 1979). The distribution and properties of dust within galaxies affect their observed morphology and color, altering the way we see galaxies when they are observed. Dust can obscure starlight and make parts of the galaxy appear darker. Additionally, about 50% of metals in the ISM of the Milky Way are in form of dust (Draine, 2003). Finally, around 30%-50% of the light in the Universe is re-radiated by dust grains in the infrared, altering the light that we observe (Bernstein, Freedman, and Madore, 2002; Draine, 2003). Understanding dust properties and distribution is therefore crucial for accurate measurements of galaxy luminosity and mass, as well as for studying the physical and chemical conditions of the ISM (Galliano, Galametz, and Jones, 2018). Therefore, characterizing the dust properties is of fundamental importance to our understanding of galaxy formation and evolution.

Over the decades, our understanding of interstellar dust has improved significantly, thanks to several studies that aimed at unveiling the properties of dust and its impact on galactic environments. Through these efforts, different observational techniques have also been developed to effectively determine in detail the properties of dust. Dust absorbs and scatters ultraviolet (UV) and optical light and subsequently re-emits it in the infrared (IR), which makes IR observations especially useful in the study of dust. Studying dust in the IR allows for the detection of thermal emissions from dust grains that are not visible in the optical spectrum. The identification of specific characteristics in the dust emission spectrum and modeling of these features can give some insights as to whether the particular silicates are in an amorphous or crystalline state, which gives important clues about the physical conditions in which dust formation and destruction occurs (e.g., Molster and Kemper, 2005; Kemper, Markwick, and Woods, 2011). The Infrared Astronomical Satellite (IRAS), launched in 1983 started mapping the dust in the Milky Way and other galaxies in the IR. Subsequent missions, like the Spitzer Space Telescope and the Herschel Space Observatory,

provided detailed IR observations, revealing the composition and distribution of dust with higher resolution (e.g., Werner et al., 2004; Kirk et al., 2009; Pilbratt et al., 2010; Knight et al., 2021). The Atacama Large Millimeter/submillimeter Array (ALMA) has further advanced the study of cosmic dust by offering unprecedented sensitivity and resolution in the millimeter and submillimeter wavelengths, allowing for detailed studies of dust in emission in the cold ISM of both nearby and distant galaxies (ALMA Partnership et al., 2015). The Gaia mission, has undoubtedly revolutionized our understanding of the dust distribution in the Milky Way, by enabling detailed three-dimensional maps of interstellar dust. This can be achieved by observing stars in various wavelengths, mainly in the optical, recording their precise positions, distances and colors, and detecting the reddening effects of intervening dust (Gaia Collaboration et al., 2021). A Gaia map of the the Milky Way's extinction caused by interstellar dust is shown in Fig. 1.3. Another technique to study dust is polarimetry, which reveals the orientation and alignment of dust grains with magnetic fields, providing insights into the structure and dynamics of the ISM (ALMA Partnership et al., 2015; Planck Collaboration et al., 2016), but it can also be studied in the X-rays (e.g., Rogantini et al., 2020; Psaradaki et al., 2024). In addition, dust has extensively been studied in the optical and UV. Using spectroscopic observations one can study dust extinction (see Section 1.4.1) and from the metal absorption lines (see Chapter 2), one can investigate the chemical abundances in dust and composition of dust grains (e.g., Field, 1974; Savage and Sembach, 1996; Phillips, Gondhalekar, and Pettini, 1982; Savaglio, Fall, and Fiore, 2003; Jenkins, 2009; De Cia et al., 2016; Roman-Duval et al., 2021; Konstantopoulou et al., 2022, 2024) (see Chapters 3,4).

Finally, complementing these observational techniques, numerous models have been developed to understand the formation, evolution, and impact of dust in galaxies. Models such as those by Mattsson et al. (2014), Feldmann (2015), Popping, Somerville, and Galametz (2017), and Triani et al. (2020) help interpret the observations and provide insights into the properties of dust. A synergy between observational data and theoretical models is essential for a comprehensive understanding of the properties and role of cosmic dust in galactic environments.

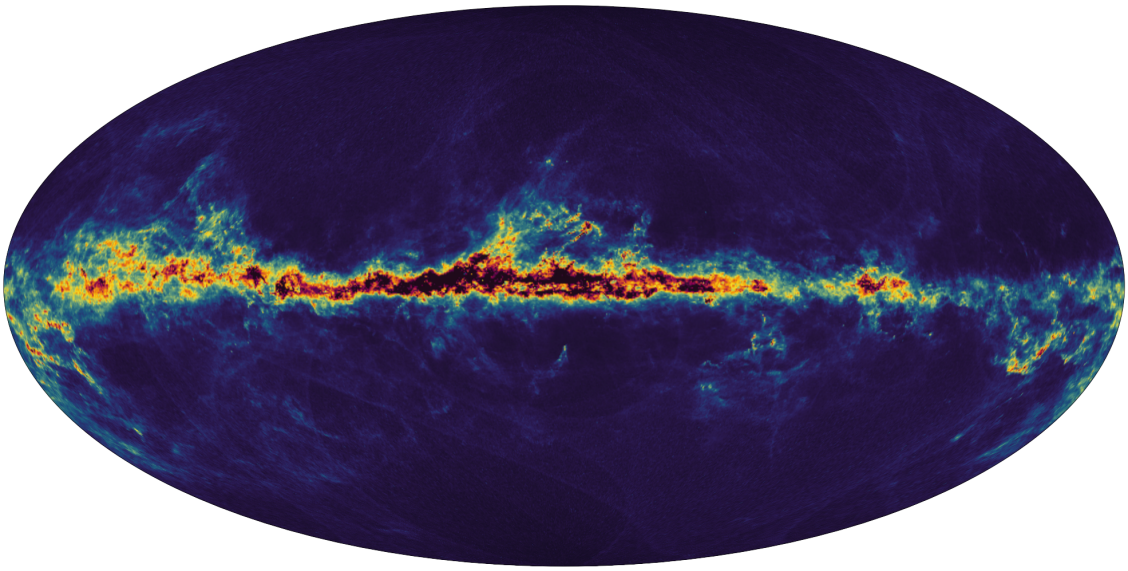


Figure 1.3: Gaia map of the interstellar dust in the Milky Way. This is a dust extinction (A_V) map, showing the absorption of light by interstellar dust. The dark regions in the center of the Galactic plane in black are the regions with a lot of interstellar dust fading to the yellow as the amount of dust decreases. The dark blue regions above and below the Galactic plane are regions where there is little dust. Created by T.E.Dharmawardena, Gaia group @MPIA. Credit: ESA/Gaia/DPAC

1.4.1 *Dust extinction*

Dust extinction is the absorption of light due to the presence of dust in the line of sight from the bright source to the observer. Due to the wavelength dependence of dust extinction, i.e. dust absorbs more efficiently at shorter wavelengths than at longer wavelengths, the emitted light from the background source appears overall fainter and redder than it would be if there was no dust along the line of sight. Because dust extinction can obscure and alter the intrinsic properties of the observed sources, it is essential to account for this effect. The amount of extinction as a function of wavelength, A_λ is the extinction curve, which varies depending on the dust composition, grain size and metallicity along the line of sight. The difference in extinction between B and V bands, $E(B-V)$ = A_B - A_V, is called color excess or reddening. The color excess is linked to the visual extinction (A_V) through the the ratio of total to selective extinction, $R_V = A_V / E(B-V)$, which is indicative of the average dust grain size distribution. The average value of R_V for the Milky Way is $R_V = 3.1$ (e.g., Cardelli, Clayton, and Mathis, 1989).

Different galaxies exhibit distinct extinction curves due to differences in their dust properties, such as grain size distribution and composition. The Milky Way has a well-studied extinction curve, which is characterized by a prominent bump at 2175 Å (Draine, 1989; Pei, 1992). This feature is often attributed to the presence of polycyclic aromatic hydrocarbons (PAHs, Draine, 2003) and generally carbonaceous dust grains are believed to produce this type of extinction (e.g., Fitzpatrick and Massa, 1986; Gordon et al., 2003;

Valencic, Clayton, and Gordon, 2004; Gordon et al., 2023; Lin, Yang, and Li, 2023). The LMC exinction curve shows a less pronounced 2175 Å feature than in the Milky Way, while the SMC exhibits mostly no 2175 Å feature, indicating a lack of PAHs. However, there are some exceptions SMC extinction curves with a 2175 Å feature e.g., Gordon and Clayton, 1998a; Gordon et al., 2003; Welty and Crowther, 2010.

Extinction curves at high redshifts vary, and are generally more difficult to constrain than in local galaxies, except for GRB afterglows. GRB afterglows can be simply fit by a (broken) power law. This make it easier to detect and model the effects of dust extinction. Extinction curves for GRB afterglows, which are typically featureless, are often SMC-like (Schady et al., 2007) and do not show a 2175 Å feature, although there are also some exceptions showing the 2175 Å feature (Elíasdóttir et al., 2009; Zafar et al., 2012; Heintz et al., 2019b).

The extinction curves of QSOs are generally challenging to constrain because QSOs, being powered by gas accretion around supermassive black holes, are highly variable and bright. Nevertheless, there has been efforts to constrain QSO extinction curves and are often found to resemble that of the SMC with a lack of a 2175 Å feature (Fynbo et al., 2011; Krogager et al., 2016) or LMC-like with a 2175 Å feature (e.g., Geier et al., 2019). However, there are QSOs with a Milky Way-like extinction curve and a 2175 Å feature present (Zhang et al., 2022; Fynbo et al., 2023).

1.4.2 *Dust depletion*

Early works on interstellar abundances already established that the gas-phase abundances of several metals are significantly lower, relative to hydrogen, than their solar values (e.g., Field, 1974; Phillips, Gondhalekar, and Pettini, 1982). These abundance deficiencies of certain elements correlate with their condensation temperatures, suggesting that they have condensed into dust grains (Savage and Mathis, 1979). The relation between gas-phase abundances with the condensation temperature of different elements in shown in Fig. 1.4. It is clear that the gas-phase abundances of the different metals is often lower than their solar values, an effect increasingly significant at higher condensation temperatures.

It is now well established that a significant fraction of metals is missing from the gas-phase of the ISM because they are instead incorporated into dust grains, a phenomenon called *dust depletion* (Field, 1974; Phillips, Gondhalekar, and Pettini, 1982; Savage and Sembach, 1996; Savaglio, Fall, and Fiore, 2003; Jenkins, 2009; De Cia et al., 2016; Roman-Duval et al., 2021). In total, about 50 % of the metals in the Milky Way's ISM are locked into dust grains. Dust depletion is differential, meaning that some elements have a higher affinity to get locked in dust grains than others (Jenkins, 2009). Metals that have high condensation temperatures, meaning that they condense into solid grains at relatively high temperatures, have a higher tendency to be incorporated into dust grains and are called refractory, while metals with lower condensation temperatures, are called volatile and are less easily incorporated into dust grains (Field, 1974; Savage and Sembach, 1996; Jenkins, 2009). This effect can be quite significant for some elements, e.g., 90-99% of Fe is missing from the gas-phase of the Milky Way (Jenkins, 2009). Dust depletion affects the amount of metal abundances that are observed in the ISM and thus it is important to characterize it.

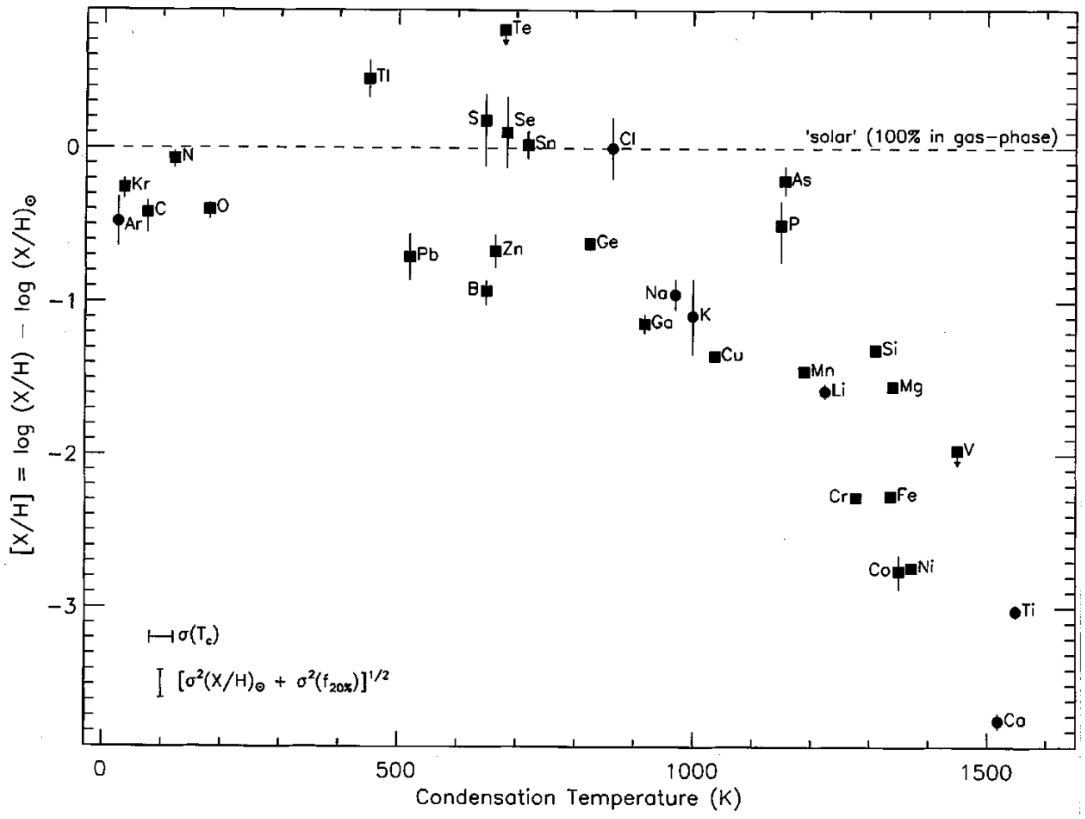


Figure 1.4: Gas-phase metal abundances [X/H] with respect to their condensation temperatures T_c for the cool diffuse interstellar cloud toward ζ Oph from Savage and Sembach (1996). The condensation temperature here corresponds to the temperature at which 50% of the element X is removed from the gas-phase. The dashed line shows the solar abundance, where 100% of the metals are in the gas-phase.

Savage and Sembach (1996) used observations of 13 absorbing systems and found that metals tend to be more heavily depleted in denser and cooler environments, like in the disk of the Galaxy, rather in the more diffuse halo. This study established how different metals exhibit varying depletion tendencies based on their condensation temperatures and chemical affinities to form dust, consistent with the findings of Field (1974). Additionally, Savage and Sembach (1996) identified distinct depletion patterns in the Milky Way's ISM, with similarities showing in four different types of clouds, those in the cool disk, warm disk, warm halo and in a combination of disk and halo.

While previous studies have focused on just a few lines of sight in the Milky Way to study dust depletion, Jenkins (2009) significantly expanded this by examining 243 lines of sight in the Milky Way and identified tight correlations among the observed abundances of 17 metals. These correlations can be explained by an increasing amount of dust depletion in the ISM, which can be described by a depletion strength F_* for each line of sight. There is a continuous distribution of the overall strength of dust depletion, from the least to the most dusty systems in the Milky Way. The trends between observed metal abundances

and the depletion strength F_* are referred to as depletion sequences and they are linear, with varying slopes from one element to another. The steeper the slopes the larger the tendency of an element to deplete into dust. Jenkins (2009) created a unified scheme of dust depletions of several metals across several lines of sight in the Milky Way.

Given that dust is observed at significant amounts at all redshifts, including at high-z and low metallicity environments, dust depletion is expected to be effective also at high-z absorption systems. The works by Prochaska et al. (2001), Vladilo (2002), Ledoux, Bergeron, and Petitjean (2002), and Noterdaeme et al. (2008) studied dust depletion at high-z, by focusing on QSO-DLA systems. These studies significantly contributed to our understanding of dust depletion. It is important to note that previous studies used gas-phase abundances of metals to study dust depletion, assuming that the intrinsic abundances should be solar. The study of dust depletion at high-z is harder, because it is not possible to observe (and assume) the metallicity of individual stars. By using instead relative abundances of metals to characterize dust depletion, one does not need to make assumptions on the metallicity. Several works made important contributions in this field, such as De Cia et al. (2016) who extended the study of dust depletion to a wider range of environments, including the Milky Way as well as high-z and low-metallicity systems. By studying the relative abundances of metals (i.e. the ratios of the column densities of various metals), they characterized dust depletion in 70 QSO-DLAs and over a dozen of Milky Way systems. They identified empirical correlations between each relative abundance and the amount of dust, which is quantified with [Zn/Fe], which is a tracer of dust. The use of relative abundances of metals allows for the study of dust depletion in different galactic environments with various metallicities and conditions.

De Cia (2018) included the SMC and LMC in the study of dust depletion based on the relative abundances, and found that the same dust depletion sequences are valid also for these environments and that the Magellanic Clouds have depletion strengths mostly in between the Milky Way and DLAs. Roman-Duval et al. (2021) studied dust depletion in the Magellanic Clouds, using the method developed by Jenkins (2009) and later compared to QSO-DLAs (Roman-Duval et al., 2022b) using the method developed by De Cia et al. (2016). Roman-Duval et al. (2021) found that dust depletion is stronger in the Magellanic Clouds than in DLAs, which is consistent with previous works (De Cia, 2018). Also, they found variations in the dust depletion patterns across different regions within the Large Magellanic Cloud by analyzing dust-to-gas ratios and metal abundances.

While these studies have significantly contributed to our understanding of dust depletion, most of them primarily focused on specific galactic environments and have relied on underlying assumptions in their methodology. A comprehensive understanding of how metals deplete into dust grains from the gas-phase, via dust grain growth in the ISM, and the return to the gas-phase, via dust destruction, is critical to understand the chemical enrichment of the universe over cosmic time. My work aims to expand the study of dust depletion to a wider range of galactic environments and creating new methodologies that have less assumptions, and thus refining the dust depletion schemes. A detailed study of dust depletion and its characterization across a wide range of galactic environments is presented throughout this thesis and more specifically in Chapters 3,4 and 5.

1.4.3 *Dust production and destruction*

The three main dust production mechanisms are considered to be condensation in SN ejecta (Dunne et al., 2003; Indebetouw et al., 2014; Matsuura et al., 2015), dust condensation in the envelopes of AGB stars (Ferrarotti and Gail, 2006; Gail et al., 2009), and grain growth in the ISM (Draine, 2003; Jenkins, 2009; Mattsson, Andersen, and Munkhammar, 2012; Dwek, 2016; De Cia et al., 2016). While all three mechanisms can produce dust, the types of dust and the methods of production may differ depending on the mechanism.

Supernovae: Stars with masses $M_* > 8\,M_\odot$ end their lives exploding as core-collapse SNe. As SN ejecta expand and cool down, they become sites of dust formation. The direct observations of dust formation in core-collapse SNe, after the explosion of SN 1987A (Danziger et al., 1989; Moseley et al., 1989; Matsuura et al., 2017), have motivated theoretical studies of dust formation and destruction in SNe (e.g., Nozawa et al., 2007, 2011; Slavin et al., 2020). A single core collapse SN is predicted to produce dust masses in ranges between 0.03 $M_\odot$ and $\sim$ 1 - 2 $M_\odot$ (Bianchi and Schneider, 2007; Sarangi and Cherchneff, 2015; Brooker et al., 2022), depending on the mass and the rotation of the stellar progenitor. Figure 1.5 shows the SN produced dust masses days after the explosion (Schneider and Maiolino, 2024). Lower-mass (13 - 15 $M_\odot$) and rotating progenitors produce dust more efficiently, because rotational mixing can lead to more metal-enriched ejecta. More massive progenitors ($\geq$ 20 $M_\odot$) often experience strong stellar winds that cause mass loss of the ejecta, reducing the production of dust mass. During explosions of even more massive progenitors ($\sim$ 30 $M_\odot$), strong feedback processes can significantly reduce the produced dust mass because of destruction of dust grains. It has been theorized that the lack of newly formed dust in the ejecta of the most massive progenitors, could be due to a much hostile physical conditions in the ejecta and on destructive effects of the reverse shock (Nozawa et al., 2011). In these unfavorable conditions, the dust observed from IR emission in the remnants of the most massive progenitors should all come from pre-existing circumstellar dust heated by the explosion of the blast wave.

Not all newly formed dust in SN ejecta will be able to survive the explosion shock and be released to the ISM. During the expansion of the SN ejecta, a forward shock is released into the ISM. This shock heats and compresses the surrounding ISM gas, creating a hostile environment for the dust grains, whose survival is compromised by sputtering due to collisions with the gas particles (Draine and Salpeter, 1979; Nozawa, Kozasa, and Habe, 2006). Following the forward shock, a reverse shock is released into the ejecta. This reverse shock, generated by the interaction between the expanding SN blast wave and the ISM, can cause significant dust destruction, depending on the grain compositions and sizes. Larger grains are generally more resistant to destruction and have a higher probability of surviving the reverse shock (Kirchschlager et al., 2023). Moreover, the survival rate depends on the density of the surrounding ISM, with predictions that about 2 - 20 % of the initial dust mass survives the reverse shock on timescales of about 4 - 8 $\times$ 10^4 yr after the SN explosion (Bianchi and Schneider, 2007; Slavin et al., 2020).

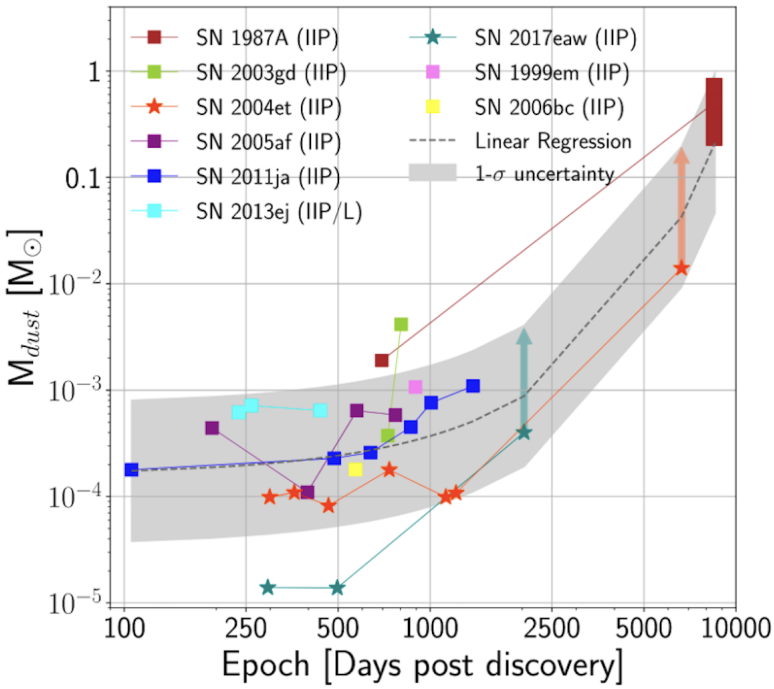


Figure 1.5: Dust masses produced by SNe IIP as a function of post-explosion time from Schneider and Maiolino (2024). Dust masses are based on mid-infrared observations, including recent JWST detections of SN 2004et and SN 2017eaw (Shahbandeh et al., 2023).

AGB stars: Other sources of dust production include low and intermediate mass evolved stars ($0.8\,M_{\odot} \leq M_{*} \leq 8\,M_{\odot}$) during the end of their lives in the Asymptotic Giant Branch (AGB) phase. Typically, stars take several billion years, depending on their initial mass, to evolve from the main sequence to the AGB phase. There they are expected to spend approximately 1 to 10 million years. During this phase, these stars experience strong mass loss and thermal pulses. The sites of dust production in AGB stars are the cool, dense atmospheres during their thermally pulsating phase. Stars lose mass at high rates through stellar winds, developing optically thick circumstellar dust shells, as solid particles condense in the outflowing gas. The large mass loss rates observed in AGB stars, result from a combination of atmospheric levitation by pulsation-induced shock waves and radiative acceleration of dust grains which form in the atmospheres (Höfner and Olofsson, 2018). It is assumed that dust grains grow on some kind of seed nuclei, such as small TiO_2 seeds, that are formed before dust condensation begins (Gail and Sedlmayr, 1998; Ferrarotti and Gail, 2006).

Dust grains produced by AGB stars can also be destroyed, mainly through thermal evaporation and chemical sputtering (Ferrarotti and Gail, 2006). During thermal evaporation, grains are heated to very high temperatures, which can cause their sublimation, especially in the proximity of the star. During chemical sputtering, gas-phase species of the ISM can react with the dust grains and chemically erode them. For example, H can react with C or Si atoms in the grains and remove them, leading to gradual destruction of the grains. While a large number of models have attempted to explain dust from AGB stars, the major limitation is that they assume a stationary, spherically symmetric wind (e.g., Ferrarotti

and Gail, 2006). This approximation is not fully consistent, as shown by high-resolution millimeter and optical observations by Montargès et al. (2023). On the other hand, while it is difficult to infer stellar parameters from observations, several millimeter, infrared and optical observations have been performed to characterize dust in AGB envelopes (e.g., Matsuura, Woods, and Owen, 2013; Ventura et al., 2018; Montargès et al., 2023).

Grain growth in the ISM: Finally, dust grains can form in the ISM, by accretion of gas-phase elements. Grain growth in the ISM is a generally slow process. The timescales for significant grain growth in the diffuse ISM are estimated to be $\sim 10^8 - 10^9$ yrs (Draine, 2003). In contrast, in molecular clouds, where densities are higher and the environment is highly turbulent, grain growth can occur much faster and more efficiently, with timescales ranging from $\sim 10^5 - 10^7$ yrs (O'Donnell and Mathis, 1997; Mattsson, 2020). In fact, most of the destruction occurs in the diffuse ISM and grain growth is most efficient in denser environment, such as molecular clouds. Draine and Salpeter (1979), Jones et al. (1994), and Jones, Tielens, and Hollenbach (1996) estimate the grain lifetime to be $\sim 10^8$ yrs, with C-dust having a longer lifetime than the silicate grains. Efficient grain growth in the ISM is necessary to explain the large amount of Fe missing from the gas-phase, as observed in several studies (Savage and Sembach, 1996; Jenkins and Tripp, 2006; De Cia et al., 2016; Roman-Duval et al., 2021).

Dust at high-z: Observations reveal the presence of large dust masses at high-z (e.g., Santini et al., 2010; Riechers et al., 2013; Mattsson et al., 2015; Watson et al., 2015; Laporte et al., 2017; Shao et al., 2019; Leśniewska and Michałowski, 2019). Dust formation sources, such as SNe and AGB stars have been proposed to explain the observations, but they both face limitations.

AGB stars are unlikely to produce the large dust masses that are observed at high-z. While AGB stars can significantly contribute to the dust budget in the local Universe, the timescales required to reach their dust production phase are too long to explain such rapid dust formation that is observed at high-z. In fact, AGB stars can live up to 10^8 - 10^9 yrs, comparable to the age of the Universe at $z \geq 6$ (Morgan and Edmunds, 2003). The amount of dust observed at these redshifts and beyond cannot be explained solely by AGB stars. However, their contribution cannot be neglected at shorter timescales ($\sim$500 Myr, Valiante et al., 2009). The time that is required for the low- and intermediate-mass stars to evolve to AGB stars is much longer than the short timescales of the early Universe, making them unlikely sources of dust production at high-z.

SNe are capable of producing significant amounts of dust on much shorter timescales. However, they are also highly efficient in destroying dust, due to the strong shocks caused by the SNe explosions. Some studies suggest that the destruction rate is so high that SNe alone cannot explain the observed dust masses at high-z (e.g., Santini et al., 2010; Mattsson et al., 2015; Leśniewska and Michałowski, 2019).

Grain growth in the ISM has emerged as a viable alternative to explain the large dust masses observed at high-z. While grain growth in the ISM is generally a slow process, the presence of turbulence can significantly increase the efficiency of dust production (Mattsson et al., 2019). This allows for faster grain growth that could potentially explain the large amounts of dust in the early Universe.

Estimating the timescales for dust production is not trivial, as it depends on various factors, including the physical conditions in the ISM. However the complexity of the ISM is not modeled in detail, and often models need to make simplified assumptions. Figure 1.6 shows the evolution of dust mass fractions with time for the three main sources of dust production, SNe, AGB stars and grain growth in the ISM, for different dust species. This dust model by Zhukovska, Gail, and Trieloff (2008) indicates that grain growth in molecular clouds dominates the dust mass fraction in the ISM.

Ultimately, the exact ways in which dust is formed and eventually destroyed are still unknown in a certain degree. Thus characterizing the dust properties with scaling relations is important for enhancing our understanding of galaxy evolution. These relations include the dust-to-metal ratio (DTM), which is the fraction of metals in dust grains, and the dust-to-gas ratio (DTG), which is the fraction of interstellar mass in dust compared to the total mass of the gas.

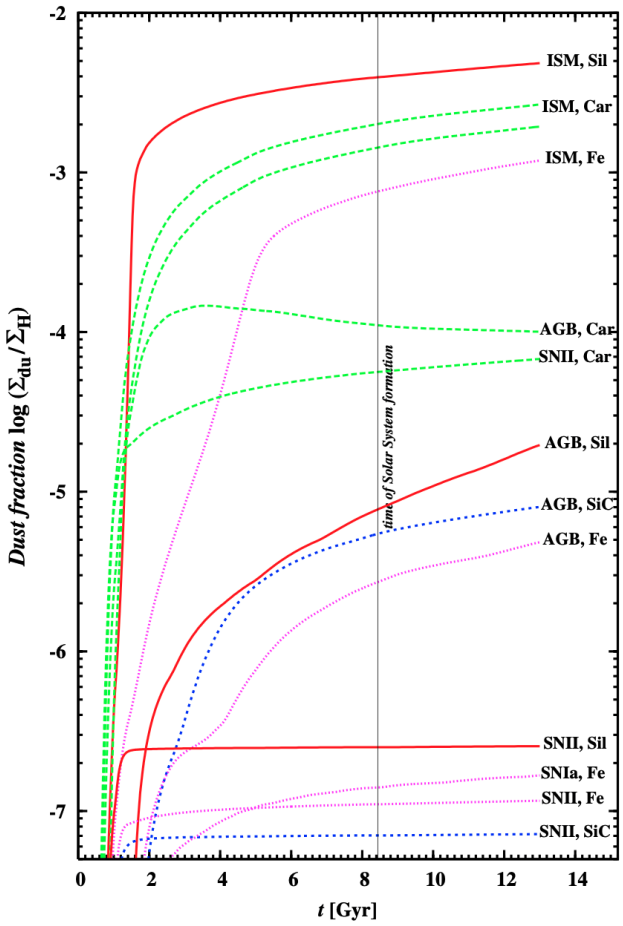


Figure 1.6: Evolution of dust mass fraction in the ISM with time, as modeled by (Zhukovska, Gail, and Trieloff, 2008), for the three main sources of dust. Different linestyles represent different dust species. The vertical solid line at t = 8.2 Gyr shows the time of the Solar System formation.

1.4.4 *Dust composition*

The composition of dust grains depends on the conditions at the time of their formation, such as the mass and metallicity of the progenitor star, the elemental composition of the stellar atmospheres of AGB stars as well as the physical conditions in the ISM, such as temperature, density, metallicity or turbulence. Understanding the types of dust grains and how they are formed is crucial for gaining insights into the chemical evolution of galaxies. Several different techniques are used to determine the chemical composition of dust, including the study of dust features at long wavelengths (e.g., Draine, 2003), the study of optical extinction curves and features (Cardelli, Clayton, and Mathis, 1989; Fitzpatrick and Massa, 1990; Pei, 1992), and observations of metal abundances (with respect to H) or relative abundances of metals (with respect to other metals). Regardless of the technique used, it is generally accepted that the main dust species that make up dust grains are silicates, which comprise mainly olivine ($Mg_{2x}Fe_{2(1-x)}SiO_4$) and pyroxene ($Mg_xFe_{1-x}SiO_3$), Fe-rich and C-rich dust (Pei, 1992; Draine, 2003; Draine and Li, 2007).

The composition of the dust grains produced by SNe depends on the stellar progenitor's mass, metallicity and rotation. Various theoretical models (e.g., Bianchi and Schneider, 2007; Sarangi and Cherchneff, 2015) predict several grain species, including different types of silicates, such as enstatite ($MgSiO_3$, which is an Fe-free pyroxene $Mg_xFe_{1-x}SiO_3$), forsterite (Mg_2SiO_4, which is an Fe-free olivine $Mg_{2x}Fe_{2(1-x)}SiO_4$), silicon dioxide (SiO_2), pure silicon (Si) and silicon carbide (SiC), as well as carbon grains (C), metallic iron (Fe), iron sulfide (FeS), iron oxyde (FeO), magnetite (Fe_3O_4), pure magnesium (Mg) and magnesia (MgO). Non-rotational models for a 15 $M_\odot$ progenitor predict the formation of larger amount of carbon grains than silicates, while all rotating progenitors should produce more silicates due to more metal-enriched ejecta caused by rotational mixing. While SNe Type Ia are major Fe producers, dust associated with the ejecta of SNe Type Ia has not been observed to date, despite extensive searches (e.g., Blair et al., 2007; Gomez et al., 2012; Williams et al., 2013).

The grain composition of the dust produced by AGB stars depends on the elemental composition of the stellar atmospheres. The main dust species that is predicted to be produced by AGB stars include carbon dust (C-dust), silicates, which comprises forsterite (Mg_2SiO_4), fayalite (Fe_2SiO_4), enstatite ($MgSiO_3$), silicon dioxide (SiO_2) and ferrosilite ($FeSiO_3$), and other types such as iron dust, and silicon carbide (SiC) (Zhukovska, Gail, and Trieloff, 2008; Ventura et al., 2018). However, AGB stars are not expected to produce significant amounts of Fe-rich dust and it has never been observed in AGB stars, although it is abundantly observed in dust grains in the ISM.

The dust grains in the warm neutral ISM are formed through accretion of gas-phase elements onto pre-existing seeds. The primary components of dust grains produced through grain growth in the ISM includes basic silicates, such as olivine ($Mg_{2x}Fe_{2(1-x)}SiO_4$) and pyroxene ($Mg_xFe_{1-x}SiO_3$), C-rich dust, and Fe-rich dust. The Fe-rich dust could be in the form of metallic Fe (Fe), iron oxides, such as wüstite (FeO), magnetite (Fe_3O_4), iron sulfite (FeS) and pyrite (FeS_2) (Mattsson et al., 2019; Roman-Duval et al., 2022b). The dust composition in the ISM is still a matter of debate. Several studies, generally agree on the major candidates of dust composition, even though they have differences in their assumptions

and detailed results, despite using different methods to derive the dust composition, such as dust depletion (Jenkins, 2014; De Cia et al., 2016; Roman-Duval et al., 2022a), modeling (Mattsson et al., 2014; Feldmann, 2015; Mattsson, 2020) and in situ measurements (Mann, 2010; Sterken et al., 2015). The main components that make up the dust grains are silicates, which is mainly olivine and pyroxene as well as C-dust and Fe-dust. For the silicates an olivine-pyroxene mixture is often proposed (Draine, 2003; Kemper, Vriend, and Tielens, 2004; Mattsson et al., 2019).

Figure 1.7 shows the primary types of dust formed by different production mechanisms, as modeled by Zhukovska, Gail, and Trieloff (2008), which are also summarized in Table 1.1. The observations of relative abundances of metals can quantify the amount of metals in the gas-phase and in the dust grains of the ISM. This approach can be used to infer the dust composition and is presented in Chapter 4.

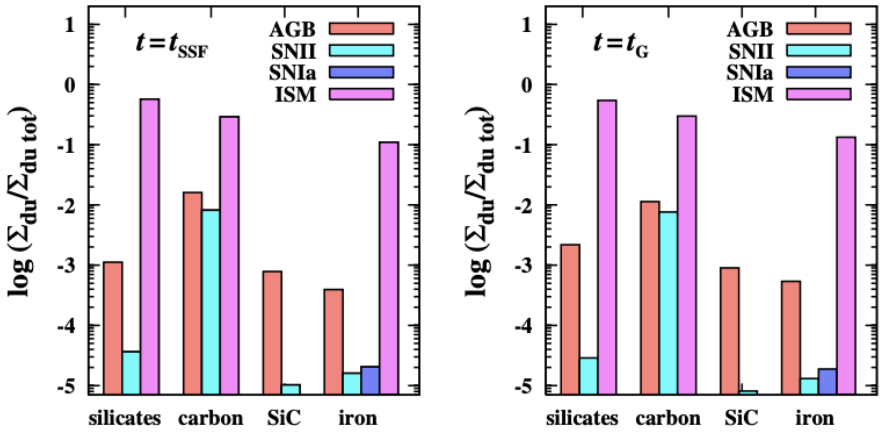


Figure 1.7: Composition of interstellar dust grains formed by different production mechanisms. The dust production mechanisms shown are SNe Type II, SNe Type Ia, AGB stars and ISM grain growth, and for different dust species (silicates, carbon dust, SiC and iron dust), as modeled by Zhukovska, Gail, and Trieloff (2008). Left: At the instant of Solar System formation (t=t_{SSF}). Right: At the present Solar neighbourhood (t=t_G).

Table 1.1: Most prominent dust species produced by different production mechanisms

Mechanism	Silicates	Fe-dust	C-dust	SiC
Core-collapse SNe	✓	✓	✓	✓
SNe Type Ia	—	(✓)	—	—
AGB stars	✓	(✓)	✓	✓
ISM	✓	✓	✓	—

Notes: The dust species in the parenthesis are modeling expectations (e.g., Ferrarotti and Gail, 2006; Nozawa et al., 2011; Slavin, Dwek, and Jones, 2015; Ventura et al., 2018) and not direct observations.

1.5 THESIS GOALS AND STRUCTURE

My work has mainly focused on exploring of the properties of cosmic dust, through the investigation of the gas-phase abundances in the ISM of a broad range of galactic environments, from the Milky Way to distant galaxies. I have specifically aimed at characterizing the effect of dust depletion in different galaxies. Dust plays a significant role in galaxies, influencing star formation, affecting the appearance of galaxies and alters the light that we observe. The study of the depletion of metals into dust grains - dust depletion - provides us insights about the distribution of metals in different galaxies, gives us clues about the origin of dust and the chemical enrichment of the gas in and around galaxies across cosmic time. Therefore, characterizing dust depletion provides insights about the chemical evolution of galaxies. During my PhD, I mainly focused on the following:

- To characterize the dust depletion of several metals (18 in total) in a large sample of local and distant galaxies, including titanium - a key element previously missing from the pre-existing depletion schemes. Characterizing dust depletion for several metals and for different environments is essential for completing and solidifying these dust depletion schemes, which, in turn, enhances our ability to infer accurate metallicities and comprehend dust composition.
- Increase the sample and diversity of dust depletion study and refine the dust depletion coefficients, which are valuable for studies that take into account dust.
- Investigate the metal and dust content both in local and distant galaxies through understanding the galactic scaling relations that apply to dust, including the relation between metallicity and dust content – traced through the dust-to-gas ratio (DTG) and dust-to-metals ratio (DTM), as well as the dust composition of different galaxies.
- To reconcile the two pre-existing main dust depletion schemes, the one developed by De Cia et al. (2016) for different environments (Milky Way, Magellanic Clouds, DLAs), and the one developed for the Milky Way by Jenkins (2009), and create a new unified method to characterize dust depletion in diverse galactic environments.

My thesis is structured as follows:

In Chapter 2, I present the methodology that I followed for the determination of column density measurements using absorption-line spectroscopy, a powerful technique for the characterization of the chemical enrichment of the ISM.

In Chapter 3, I present my work, published by Konstantopoulou et al. (2022), on characterizing dust depletion of 18 elements, in total, including new Ti and Ni column density measurements conducted on a sample of 70 QSO-DLAs. In this project, I expanded the samples and characterized dust depletion from local to distant galaxies (Milky Way, Magellanic Clouds, QSO- and GRB-DLAs), refining and expanding the dust depletion coefficients that are used in dust studies.

In Chapter 4, I present my work, published by Konstantopoulou et al. (2024), on investigating the properties of metals and dust in different galactic environments (Milky

Way, Magellanic Clouds, QSO- and GRB-DLAs). I detail the derivation of the DTM and DTG ratios, the dust composition in terms of mass, the cosmic metallicity evolution of the neutral gas and the determination of the dust extinction using dust depletion. This project was enabled due to the wide collection of available data and the dust depletion estimates of Konstantopoulou et al. (2022)

In Chapter 5, I present the development of a new method to characterize dust depletion using observed correlations of relative abundances of metals, that serve as dust tracers, in diverse galactic environments. I detail the designing of the method, the estimates on the overall strength of depletion per line of sight and depletion of individual elements, refining once again their coefficients. In addition, I present guidelines on the different applications of the method to observations. This work is re-submitted to A&A after positive referee report.

In Chapter 6, I present my work on a side project on close projected pair QSOs. I present the observations, data reduction and analysis of the color-unbiased sample of selected candidate QSO pairs. In this project, I spectroscopically confirmed 22 pair QSOs, with projected separations < 10 arcsec. I explored the Gaia-assisted QSO target selection and its capabilities for discovering QSOs that have been missed by other large surveys.

Finally, in Chapter 7, I conclude and present future perspectives in the studies of dust depletion, the metal enrichment of gas in galaxies and further remaining open questions.

2

ABSORPTION-LINE SPECTROSCOPY

"We sail through endless skies,
Stars shine like eyes,
The black night sighs."
∼ Planet Caravan by Black Sabbath ∼

Absorption-line spectroscopy has proven to be a powerful tool for the study of the chemical composition of the gas in galaxies (Savage and Sembach, 1996; Prochaska and Wolfe, 1999). By observing bright background sources, such as stars in local galaxies, or QSOs and GRBs in distant galaxies, one can infer in great detail the chemistry and kinematics of their gas. Figure 2.1 shows an example of absorption line spectroscopy from Péroux and Howk (2020). As the light from these bright sources travels towards the observer, it passes through the intervening gas between the source and the observer. A schematic view of this can be seen in the top of Fig. 2.1. The gas absorbs at specific wavelengths that correspond to the electronic transitions in the elements that are present in the gas and are imprinted in the spectrum of the source that is being observed. The bottom of Fig. 2.1 shows an example of a QSO spectrum with multiple absorption metal lines in its spectrum, as well as neutral hydrogen HI absorption (Ly-α). By analyzing the absorption lines imprinted on the spectrum of the background source, one can determine important information, like the metal (relative) abundances and velocity of the gas. These can be used to infer the kinematics and the chemical enrichment of the ISM both in local and distant galaxies.

In the local Universe, one can use UV and optical absorption-line spectroscopy towards bright background OB stars or SNe, to measure column densities of a plethora of metals (e.g., OI, CII, AlII, SiII, TiII, CrII, FeII, CoII, NiII, ZnII). These column densities are then used to obtain metal abundances, providing us with important information about the chemical composition of the ISM in local galaxies, such as the Milky Way, the LMC and the SMC (Field, 1974; York et al., 1983; Savage and Sembach, 1996; Jenkins, 2009; Jenkins and Wallerstein, 2017; Roman-Duval et al., 2021; De Cia et al., 2021). In the distant Universe, individual stars within a galaxy are too faint to distinguish, however QSOs and GRBs are very bright and often outshine the light from the galaxy itself (see Chapter 1). This makes them relatively easy to observe with large telescopes, such as the Very Large Telescope (VLT). By observing damped Lyman-α absorbers (DLAs, as described in Section 1.3) and GRBs one can obtain a wide range of column density measurements (e.g., OI, MgII, PII,

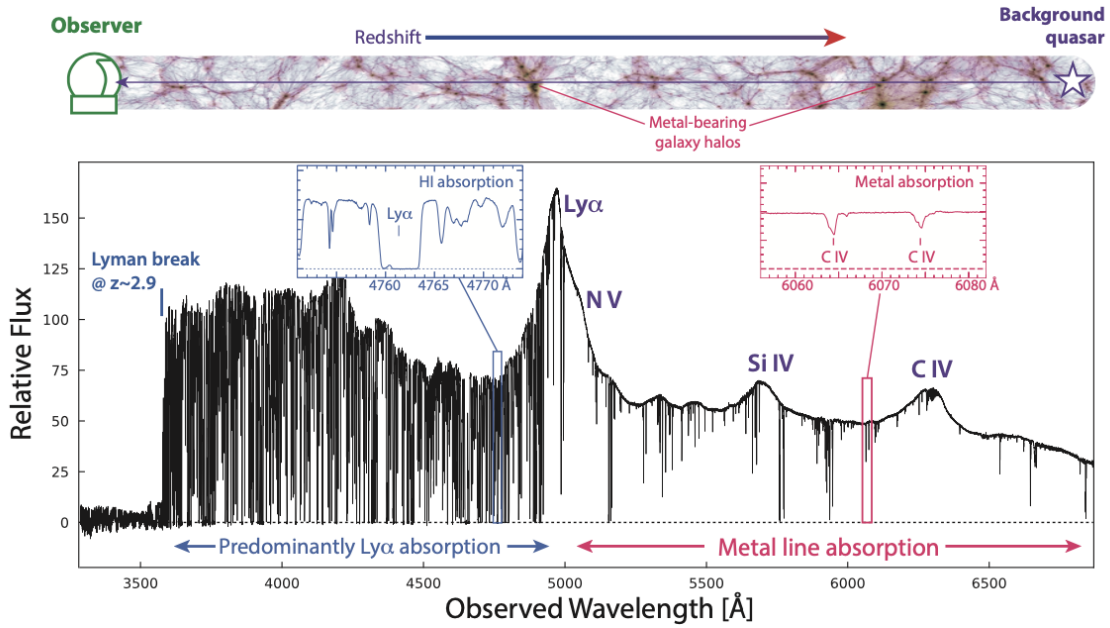


Figure 2.1: An example of absorption line spectroscopy towards a background quasar from (Péroux and Howk, 2020). (Top:) schematic view of the configuration. The light from the background QSO pierces through metal-bearing galaxy halos, imprinting metal absorption lines in the spectrum of the QSO. (Bottom:) A high-resolution QSO spectrum at $z_{em} = 3.0932$ observed with UVES/VLT (D'Odorico et al., 2016). Intrinsic metal lines emitted from the QSO itself can be seen in the spectrum (marked in purple), as well as metal absorption lines and Ly-α absorption. The insets show absorption from an intervening absorber at $z = 2.9$.

SiII, TiII, CrII, FeII, CoII, NiII, ZnII), from which the metal abundances in the ISM of distant galaxies can be inferred (Prochaska and Wolfe, 1999; Ledoux, Bergeron, and Petitjean, 2002; Vladilo, 2002; Prochaska et al., 2007; Petitjean, Ledoux, and Srianand, 2008; Kulkarni et al., 2015; De Cia et al., 2018; Bolmer et al., 2019; Heintz et al., 2019a,b; Saccardi et al., 2023; Heintz et al., 2023).

2.1 SPECTROSCOPY WITH VLT/UVES AND HST/STIS

A large amount of data used in this thesis are obtained using the Ultraviolet and Visual Echelle Spectrograph (UVES) on the Very Large Telescope (VLT), as well as the Space Telescope Imaging Spectrograph (STIS) on the Hubble Space Telescope (HST).

UVES is a high-resolution optical spectrograph mounted at the Nasmyth B focus of the Unit Telescope 2 (UT2) of the VLT. It is a two-arm cross-dispersed echelle spectrograph with high efficiency. The light beam entering the telescope is split into two arms (UV to Blue and Visual to Red) within the instrument. A dichroic beam splitter allows for a parallel operation of the two arms or can be operated seperately. The spectrograph covers a wavelength range 300 - 500 nm (in the Blue arm) and 420 - 1100 nm (in the red arm). The spectral resolution for a 1-arcsec slit is about R $\sim$ 40,000, while the maximum resolution that can be reached, using a narrower slit, is about R $\sim$ 80,000 in the blue and R $\sim$ 110,000 in the red (Dekker et al., 2000). The magnitude limits are 17-18 mag (in the blue arm) and 18-19 mag (in the red arm). These characteristics make UVES particularly suitable for absorption line studies of the ISM, as it offers high spectral resolution, which is essential for accurate abundance determinations of the narrow metal lines in the ISM using spectra of high redshift QSOs (e.g., Prochaska and Wolfe, 1999; D'Odorico et al., 2004; Ledoux et al., 2006; Fox et al., 2007; De Cia et al., 2016). It also offers broad wavelength coverage, which is important for a broad coverage and identification of several metal absorption lines. With this information in hand, the chemical composition of the ISM can be determined in great detail. In this thesis, spectra of QSO-DLAs obtained at high spectral resolution (R = 35,000-58,000) using UVES (blue and red spectroscopic arms) have been used.

The Space Telescope Imaging Spectrograph (STIS) is a versatile imaging spectrograph installed on the Hubble Space Telescope (HST). Due to the small apertures or slits used and advanced optics of STIS, it provides spatially resolved spectroscopy from 1150 to 10,300 Å at low to medium spectral resolution and high spatial resolution echelle spectroscopy in the UV. With spatially resolved spectroscopy several spectra from different locations within the field of view can be obtained, making it possible to analyze spectra of different regions separately. The high spatial resolution of STIS makes it possible to distinguish between closely separated objects, resolving fine details in the observed object. The echelle gratings are available only in the UV and are designed to maximize the spectral coverage in single observations of point sources. For echelle spectroscopy STIS can achieve medium to high resolution (R $\sim$ 30,000-114,000). In this thesis, spectra of stars obtained using the high-resolution echelle spectrograph in the UV have been used, particularly, the STIS Near-UV echelle setting E230M with resolving power R $\sim$ 30,000. This STIS mode allows for precise measurements of the chemical abundances in the ISM of the Milky Way and

nearby galaxies (e.g., Roman-Duval et al., 2021; De Cia et al., 2021; Ritchey et al., 2023b), providing a detailed overview of the chemical composition of the ISM.

In this work I have analyzed, using Voigt-profile fitting, 70 QSO-DLAs observed with VLT/UVES (Konstantopoulou et al., 2022) and two OB stars observed with HST/STIS (De Cia et al., 2021). The Voigt-profile fitting analysis will be discussed in Section 2.4.

2.2 THE ABSORPTION LINE PROFILE

The analysis of absorption lines in spectra can offer an incredible amount of information about the atoms and ions present in the absorbing gas. This information is obtained by modeling the absorption lines using specific line profiles, which are described by atomic physics and the properties of the gas from which the line originates, for example its density and temperature. The radiative transfer equation, describing the variation of the specific intensity I_ν as it interacts with matter, is given by

$$I_\nu = I_\nu(0)e^{-\tau_\nu} \tag{2.1}$$

where I_ν is the specific intensity after absorption, $I_\nu(0)$ is the specific intensity before absorption and τ_ν the optical depth, which is a measure of the transparency of the medium and is given by

$$\tau_\nu(s) = \int_0^s n\sigma_\nu \, ds = N\sigma_\nu \tag{2.2}$$

where n is the number density over a path s, σ_ν the absorption cross section and N is the column density of the gas.

The line profile, $\Phi(\nu)$, as a function of frequency from the line center, is determined by the physical properties of the gas, including temperature, turbulence as well as the intrinsic quantum properties of the transition, such as the damping constant (or lifetime of the transition). The intrinsic strength of the absorption line, called the oscillator strength or f-value, is determined by the probability that a transition between energetic levels will occur. The absorption line profile is determined by the *natural broadening* and the *Doppler thermal broadening*. The natural broadening in the line profile is a result of quantum mechanical effects - due to the quantum mechanical uncertainty in energy levels, and results in the Lorentzian profile (Rybicki and Lightman, 1979), which represents the intrinsic profile of the line. This does not take into account the thermal motion of the gas. On the other hand, the Doppler thermal broadening is a result of thermal motion, and along with instrumental broadening and turbulent motions in the gas result in the Gaussian (or Doppler) profile. The Doppler broadening parameter, or *b-value*, describes the velocities of the gas particles. The b-value can then be expressed as

$$b = \sqrt{v_{th}^2 + v_{turb}^2} \tag{2.3}$$

including broadening from both thermal v_{th} and turbulent v_{turb} velocities.

2.3 THE VOIGT PROFILE

A substantial part of this thesis is based on measurements done using Voigt-profile fitting. Voigt profiles are the most advanced way to describe an absorption system, because it combines both Gaussian and Lorentzian distributions to account for the complex broadening effects that occur in spectral lines. This convolution allow Voigt-profiles to distinguish and deblend individual components from a complex line profile. This enables the study of individual gas clouds (e.g., Ramburuth-Hurt et al., 2023), which although can be performed, with larger uncertainty at lower resolution, it becomes more accurate with high spectral resolution. Considering the above, the overall absorption line can be described as a convolution between Lorentzian and Gaussian (or Doppler) profile by the Voigt profile as

$$\phi(\nu) = \frac{\Gamma}{\pi^2} \int_{-\infty}^{\infty} \frac{1}{b\sqrt{\pi}} \frac{e^{-(v/b)^2}}{\left[\nu - \nu_0 \left(1 + \frac{v}{c}\right)\right]^2 + \left(\frac{\Gamma}{4\pi}\right)^2} dv \tag{2.4}$$

where Γ is the half-width at half-maximum of the Lorentzian distribution, b is a parameter that determines the width of the Gaussian distribution, v is the variable of integration over the Gaussian distribution, ν_0 is the central frequency of the Lorentzian distribution and c is the speed of light.

The absorption profile can be very complex, due to the presence of multiple absorbing clouds in the same line of sight. The overall resulting absorbing profile can be caused by several narrow components. Each individual line-profile component can be characterized by three parameters: its velocity position v, broadening b-value, and column density N. The velocity components of all transitions from the same ion are expected to be the same. Additionally, ions that coexist in the same medium are subject to the same kinematics and therefore their line profiles should be similar and can be fit simultaneously. However, the velocity component structure is not the same for all ions, because the broadening depends on the thermal and turbulent broadening which behave differently with the mass of the absorbing species. *Saturation* and *contamination* can complicate further the process of absorption-line fitting. Saturation occurs when the absorption lines become so strong that all of the flux at the line's core wavelength is absorbed. In these cases, the absorption line flattens out in the core of the line, and the flux reaches zero (or close to it), making it challenging to measure the true column density of the line. Contamination occurs when the absorption line has contributions from additional factors, such as telluric absorption, absorption lines from other sources, noise or instrumental artifacts, causing the distortion of the true line profile. This is particularly problematic in regions of the spectrum where multiple elements have absorption features close to each other, leading to blended lines that complicate the analysis. In the context of DLAs, contamination is often caused by the Lyman-α forest, where numerous hydrogen absorption lines from gas at lower redshifts overlap with the lines of interest, making it challenging to distinguish between them. To circumvent contamination, it is important to observe multiple transitions of the same ion, which allows to disentangle the true line-profile and for a more accurate determination of the column density. The total column density of the resulting absorption-line profile can be calculated by summing the column densities of each individual component. The column density derivation will be discussed in Section 2.4.4.

2.4 VOIGT-PROFILE FITTING - VOIGTFIT

To fit Voigt-profiles in the absorption lines of some of the spectra used in this thesis, I have used the software VoigtFit[1],[2] (Krogager, 2018), which decomposes the line profiles into their individual velocity components, fitting different transitions of several ions and of different elements simultaneously. The software is run interactively and for each spectrum separately, in total for 70 QSO-DLAs obtained with UVES on the VLT as part of the fitting process done for Konstantopoulou et al. (2022), two OB stars obtained with VLT/UVES and two HST/STIS spectra of OB stars. Most of the UVES spectra are presented in Konstantopoulou et al. (2022) and featured in Chapter 3, while the rest are shown in the Appendix B. The latter are spectra that lack a detection of ZnII, which was one of the requirements for the sample selection in Konstantopoulou et al. (2022), as described in Chapter 3. The measurements on the OB stars obtained with STIS and UVES are used in De Cia et al. (2021) as a cross-check of the results with an independent method.

2.4.1 *Setup and parameter file*

A parameter file (input file) is used for each spectrum, that contains all the important information required for VoigtFit to run. In the parameter file, first I load the data, define the spectral resolution of each spectrum, as well as the redshift z and the continuum normalization method. Then I specify the selected transitions to fit (e.g., FeII λ2260, NiII λ1741, etc.) and the transitions to be masked interactively, if needed.

2.4.2 *Continuum normalization and component definition*

The continuum normalization is done automatically by VoigtFit, once the average continuum level is defined in an interactive window as shown in the top panel of Fig. 2.2. For the continuum normalization, I choose 1st order Chebyshev polynomials, because the continuum is relatively flat. The fitting procedure is run interactively, using a reference ion, usually FeII or SiII if FeII is saturated or too contaminated. Saturated lines are not considered during Voigt-profile fitting, as they cannot be used reliably for column density measurements. After that, the location of the components are interactively defined on the reference ion, as shown in the middle panel of Fig. 2.2, and are later copied in the rest of the ions. Each individual component determines the redshifts and provides an initial estimate of the optical depth from the depth of the absorption profile. The interactive component definition is repeated several times for different lines of the same ion, incorporating all identified components.

1 https://github.com/jkrogager/VoigtFit
2 https://voigtfit.readthedocs.io/en/latest/

2.4.3 *Mask definition*

In the last step, I define the contaminated regions, again in an interactive window, as shown in the bottom panel of Fig. 2.2. Contaminated regions are distinguished from absorption related to the given system, by assessing whether the features are only present in one transition or in multiple transitions. Absorption features that are physical are expected to be present in multiple transitions of the same ion, indicating that they are associated with the system. On the other hand, contaminated regions are typically present in one transition of the ion. Contaminated regions can compromise the continuum fitting and the resulting fit, thus anything that does not belong to the continuum or the line itself that is fitted, is masked out and excluded from the fitting process. Clearly saturated lines are removed from the fit. This process is typically repeated several times until the fit has converged and the best-fit parameters for each components of the fitted ions is returned and saved by the software. Figure 2.3 shows an example of Voigt-profile fitting on the UVES spectrum of the QSO-DLA system towards Q 2348-011b.

2.4.4 *Column densities*

A column density is a measure of the number of particles (atoms or ions) that are present in a given column of gas along the line of sight. The column densities of different ions in the absorption lines of the spectra, or the number of atoms and ions present along the line of sight, are an output of VoigtFit, after the fit has converged. The software measures the column densities of individual components ($\log N_i$), as well as the the total column density along the line of sight ($\log N_{tot}$), which is the sum of the column densities of the individual components and can be expressed as

$$\log N_{\rm tot} = \log \left(\sum_i 10^{\log N_i} \right) \tag{2.5}$$

In cases where there is no clear detection of an ion, the software can be set to determine a 3σ upper limit on the column density. Using as reference a well defined line profile (such as FeII or SiII), VoigtFit can estimate the upper limit within 99% of the optical depth of the reference line profile.

Using VoigtFit I obtained new column density measurements of TiII and NiII, which are published in Konstantopoulou et al. (2022), but some of the TiII and NiII column densities are not included in Konstantopoulou et al. (2022) due to the lack of detection in ZnII. Those extra column density measurements or limits in case of no detection of Ti and Ni, are shown in Table 3.3

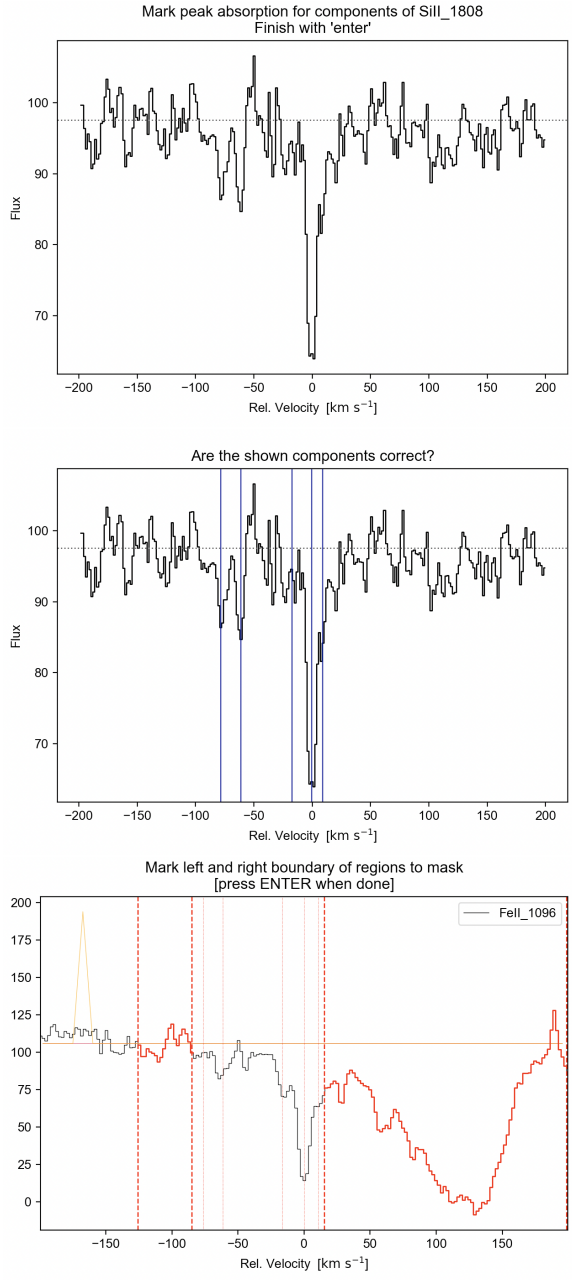


Figure 2.2: Example of the fitting process on the spectrum of the QSO-DLA towards Q 2348-011b. Top panel: The average continuum level has been defined on the reference transition SiII λ1808. Middle panel: The location of the components has been chosen. Bottom panel: The contaminated regions on FeII λ1096 have been manually selected in order to be masked out by VoigtFit.

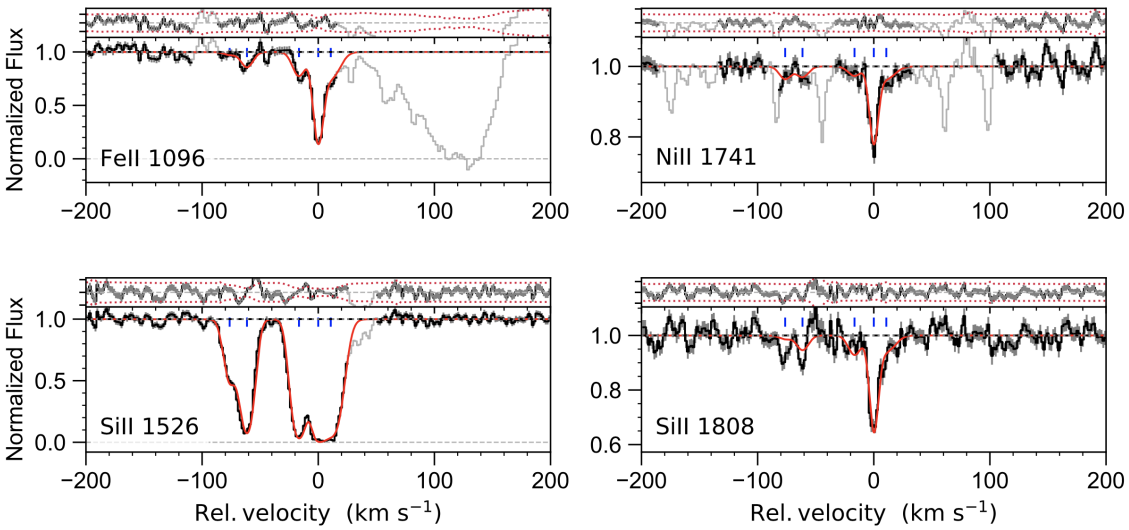


Figure 2.3: Velocity profiles of selected transition lines (FeII λ1096, NiII λ1741, SiII λ1526, SiII λ1808) from the QSO-DLA system at z_{abs} = 2.61473 towards Q 2348-011b. The spectrum is shown in black and the fit in red lines. Masked regions are shown in gray. The top sub-panels show the residuals, and the blue tick marks show the individual velocity components.

Table 2.1: New UVES QSO-DLA Ti and Ni measurements or limits

QSO	z_{abs}	log N(FeII)	log N(NiII)	log N(TiII)
Q0102-190b	2.92648	13.80±0.01	<13.05	<12.38
Q0112+030	2.42299	14.85±0.01	13.57±0.06	12.48±0.16
Q0112-306a	2.41844	13.41±0.03	...	<12.28
Q0112-306b	2.70163	14.78±0.01	13.65±0.014	...
Q0336-017	3.06209	14.74±0.03	13.42±0.05	<12.51
Q0450-131	2.06658	14.23±0.01	13.34±0.04	12.65±0.09
Q0913+072	2.61843	13.07±0.02	<12.41	<12.02
Q1036-229	2.77779	14.61±0.02	13.72±0.02	<12.16
Q1108-077b	3.60767	13.86±0.02	<12.35	<12.25
Q1210+175	1.89177	14.77±0.03	13.67±0.02	12.31±0.03
Q1232+082	2.33771	14.37±0.02	13.30±0.03	12.43±0.09
Q1337+113a	2.50792	13.41±0.02	<12.85	<12.55
Q1337+113b	2.79584	14.33±0.01	13.20±0.06	<12.63
Q1340-136	3.11835	13.92±0.01	12.89±0.05	...
Q1409+095	2.45593	13.72±0.03	<12.62	<12.88
Q1451+123a	2.25466	14.41±0.02	13.60±0.05	<12.97
Q1451+123c	3.17112	13.27±0.04	13.31±0.06	<13.11
Q2059-360a	2.50734	13.49±0.01	<12.78	<12.29
Q2059-360b	3.08261	14.48±0.01	13.02±0.06	<12.43
Q2206-199b	2.07622	13.34±0.01	12.24±0.09	<11.59
Q2231-002	2.06615	14.73±0.01	13.61±0.02	...
Q2332-094b	3.05722	14.37±0.01	13.19±0.11	<12.51
Q2343+125	2.43123	14.50±0.01	13.36±0.03	<11.97
Q2348-011a	2.42695	14.77±0.01	13.74±0.02	<12.52
Q2348-011b	2.61473	14.57±0.03	13.34±0.05	...

Notes: Upper limits are given at the 3σ confidence level. The redshifts are taken from De Cia et al. (2016).

2.5 GAS-PHASE METAL ABUNDANCES

The measurements of column densities can be used to estimate the gas-phase metal abundances in gas clouds. Metal abundances can give valuable information about the chemical composition and chemical enrichment processes in gas clouds. The abundance of an element X is defined as

$$[X/\mathrm{H}] = \log \frac{\mathrm{N(X)}}{\mathrm{N(H)}} - \log \frac{\mathrm{N(X)}_\odot}{\mathrm{N(H)}_\odot} \tag{2.6}$$

where N(X) is the column density of element X (expressed in surface density in atoms per cm^{-2}), $\log N(X)_\odot$ is the solar abundance of element X, with $\log N(H)_\odot = 12$ (e.g., Asplund et al., 2009; Asplund, Amarsi, and Grevesse, 2021). When probing the neutral gas of the ISM, X and H are in their dominant ionization states. For example, in the warm neutral medium FeII, MgII, SiII, ZnII, TiII, NiII, SII, CrII, PII and OI are dominant. N(H) is the total column density of hydrogen, which is defined as $N(\mathrm{H}) = N(\mathrm{HI}) + 2\,N(\mathrm{H_2})$. In the Milky Way, H_2 is always included to total column density of H, while in distant galaxies, such as in QSO-DLAs and GRB-DLAs, H_2 is not typically measured and is considered negligible in the calculation of the total hydrogen column density (e.g., Ledoux, Bergeron, and Petitjean, 2002; Noterdaeme et al., 2008; Bolmer et al., 2019).

Different processes shape the observed gas-phase metal abundances in the ISM of galaxies. Those include the overall metallicity, the presence of dust, ionization and stellar nucleosynthesis. To accurately obtain gas-phase metal abundances, it is essential to take into account ionization effects, when the HI column density is low. For high HI column densities ($N(\mathrm{HI})_\odot \gtrsim 10^{20}\,\mathrm{cm}^{-2}$), ionization corrections are generally not needed because the gas is sufficiently shielded against photo-ionization and thus remains neutral as HI (Viegas, 1995). Under these conditions, most elements predominantly exist in their dominant ionization state (e.g., MgII, SiII, FeII, TiII). It is estimated that up to 8% of the gas in the warm neutral medium is ionized (e.g., Jenkins, 2013). In this thesis, only lines of sight with high HI column densities ($N(\mathrm{HI})_\odot \gtrsim 10^{20}\,\mathrm{cm}^{-2}$) are used, such that no ionization corrections are required for the derivation of metal abundances.

While metallicity variations can affect the observed metal abundances [X/H], they have no effect on the observed relative abundances [X/Y]. The relative abundance of an element X with respect to Y is defined as

$$[X/Y] = \log\, N(X) - \log\, N(Y) - \log\, N(X)_\odot + \log\, N(Y)_\odot \tag{2.7}$$

where N(X) is the column density of element X (surface density in atoms per cm^{-2}) and $\log N(X)_\odot$ is the solar abundance of element X (e.g., Asplund et al., 2009; Asplund, Amarsi, and Grevesse, 2021). Relative abundances are independent from the ISM metallicity. Because different metals have a different tendency to deplete into dust grains, the relative abundances can carry important information about dust depletion. Relative abundances will be widely used in this thesis.

2.6 GAS-PHASE METALLICITY

Most metal abundances relative to hydrogen are not good proxies of the overall metallicity of the ISM in different galaxies. This is because the determination of metallicity is complicated by other effects in the ISM, such as dust depletion, nucleosynthesis effects and possibly, ionization. To obtain an accurate and reliable measure of the metallicity, one has to account for the total amount of metals in the ISM. While the measured column densities estimate the amount of metals in the gas-phase of the ISM, they do not account for the amount of metals in the dust grains. Large amounts of metals are removed from the gas-phase of the ISM, because they are locked into dust grains, an effect called dust depletion (Field, 1974; Savage and Sembach, 1996; Savaglio, Fall, and Fiore, 2003; Jenkins, 2009; De Cia et al., 2016; Roman-Duval et al., 2021). This is affecting the accurate determination of the gas-phase metallicity, and thus, it is important to characterize dust depletion for a comprehensive study of the ISM. The effect of dust depletion has been presented briefly in Section 1.4.2 and its characterization is presented in detail in Chapter 3.

In the Milky Way De Cia et al. (2021) find that the metallicity of the ISM is not homogeneous, but rather there are large variations observed, while Ritchey et al. (2023b) find that the metallicity of the Milky Way ISM is rather homogeneous. A potential reason for the discrepancy between De Cia et al. (2021) and Ritchey et al. (2023b) is the inclusion or not of the volatile elements in the analysis. De Cia et al. (2021) base their analysis mostly on the observations of refractory and mildly-refractory metals, while the analysis by Ritchey et al. (2023b) is based mostly on volatile elements. In the Magellanic Clouds, De Cia et al. (2024) find that the neutral ISM gas is fairly well mixed in terms of metallicity, with only a few exceptions of lines of sight with lower metallicities. This clearly demonstrates the importance of dust depletion corrections for the metallicity determinations in the Milky Way and other galaxies.

2.7 STELLAR NUCLEOSYNTHESIS

The metal abundances and metallicity in the ISM of galaxies are a direct result of stellar nucleosynthesis. However, our determination of the metal abundances can be affected by differences in nucleosynthesis. Specifically, stellar nucleosynthesis can result in an overabundance or underabundance of specific elements, such as α-element enhancement and Mn underabundance. In this section I discuss the effects of stellar nucleosynthesis in the neutral gas of the ISM.

Different elements are produced by different nucleosynthetic processes in stellar phenomena, depending on the mass of the stars and the type of supernovae. Metals are synthesized inside stars and then are ejected when these stars end their lives, depending on the kind of star or SN. The next generation of stars forms from gas clouds enriched with heavy elements by previous stellar generations. The α-elements, such as O, Mg, Si, S, Ti, are primarily produced as part of stellar nucleosynthesis in massive stars, which end their lives in supernova explosions (e.g., Timmes, Lauroesch, and Truran, 1995; Kobayashi et al., 2006; Kobayashi, Karakas, and Lugaro, 2020). Among the elements that are synthesized during

the quiescent burning stages in such massive stars, in the range of 8 to $\sim$130,$M_{\odot}$, are O and Mg, as they burn lighter elements into heavier ones during their lifetime. On the other hand, elements such as Si and Ti are produced mostly in the explosive nucleosynthesis that occurs in core-collapse SNe. The fusion of α particles (He nuclei) under these harsh conditions is accompanied by the ejection of a large amount of α-elements and a smaller amount of Fe-peak elements into the ISM (Nomoto et al., 2006). On the other hand, the Fe-group elements, Cr, Mn, Fe, Ni, Co, Cu, including Zn, are produced by Type Ia supernovae (SNe Ia) (Nomoto et al., 1997). The delayed enrichment of Fe from SNe Ia, which occurs on a longer timescale than core-collapse SNe, results in an observed overabundance of the α-elements with respect to Fe ([α/Fe]). Figure 2.4 shows the the evolution of heavy element abundance ratios [X/Fe] for different elements X with respect to [Fe/H], as measured from stellar atmospheres. Here [Fe/H] is the metallicity and is not the same as the [Fe/H] that is measured in the ISM gas, which is also dominated by dust depletion effects. The overabundance of α-elements is seen at low values of the metallicity [Fe/H]. As Type Ia SNe begin to explode, they produce large amounts of Fe-peak elements, which reduce the [α/Fe] ratio, resulting in a linear decrease until [α/Fe] $\sim$ 0.

Nucleosynthesis effects, such as α-element enhancement and Mn underabundance can impact the determination of the relative abundances of metals [X/Y], which are used in this thesis to study the dust in the ISM gas. To accurately isolate and study the effects of dust using relative abundances, it is important to account and correct for these nucleosynthesis effects. To characterize the depletion of metals in dust, I accounted for α-element enhancement and Mn underabundance when determining relative abundances that included α-elements and Mn in [X/Y], as will be described in Section 3.4.3. On the other hand, when both X, Y in [X/Y] are either α-elements or are both non-α-elements, the relative abundance [X/Y] will not be affected by nucleosynthesis effects and one can avoid applying corrections for it, as will be discussed in Section 5.4.1.

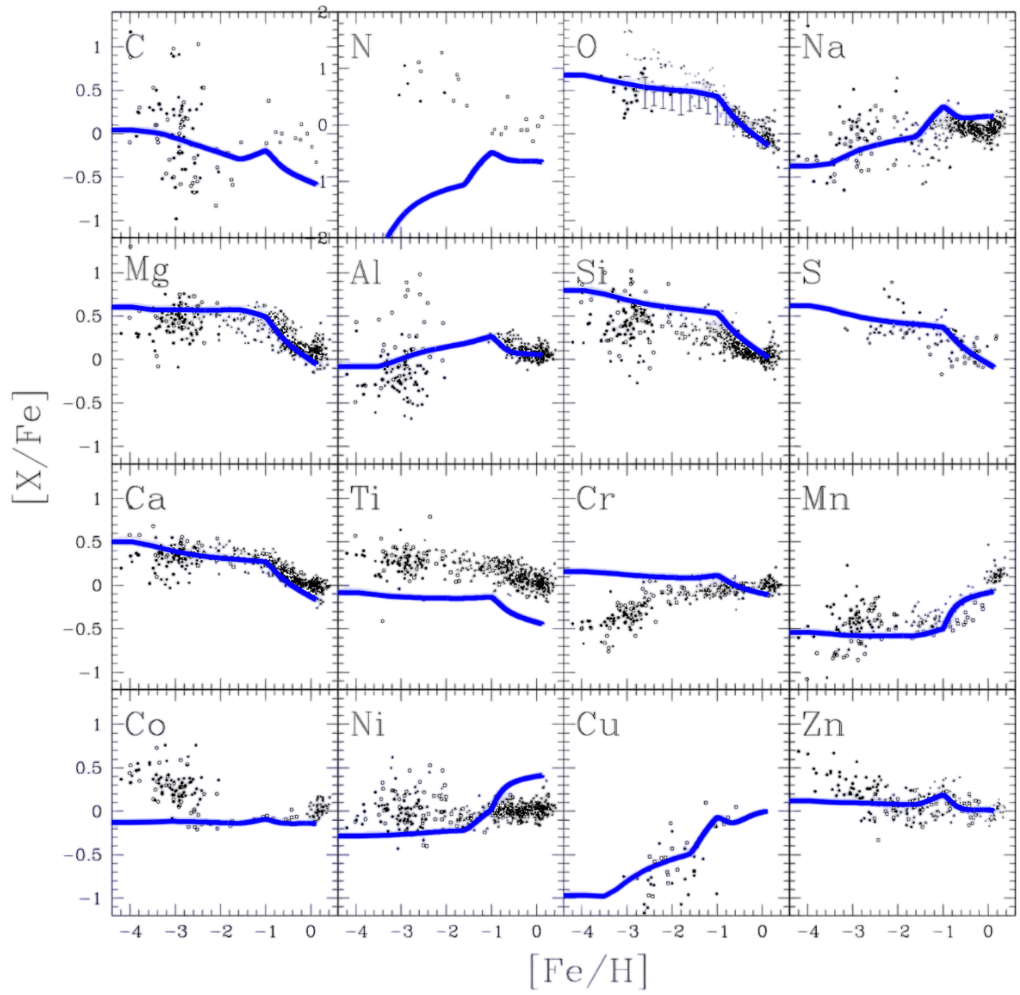


Figure 2.4: The shapes of the nucleosynthetic curves of different elements. The black points are observational data from Edvardsson et al. (1993), Ryan, Norris, and Beers (1996), Bensby, Feltzing, and Lundström (2003), Gratton et al. (2003), Cayrel et al. (2004), Gehren et al. (2004), and Honda et al. (2004) and the blue solid line is the chemical evolution model by Nomoto et al. (2006). Figure taken from Nomoto et al. (2006).

3

DUST DEPLETION FROM LOCAL TO DISTANT GALAXIES I: PECULIAR NUCLEOSYNTHESIS EFFECTS AND GRAIN GROWTH IN THE ISM

"All we are is dust in the wind."
∼ Dust in the wind by Kansas ∼

In the previous Chapters, I have defined the framework of this thesis and methodology to derive gas-phase metal abundances. Because dust depletion can significantly affect the determination of gas-phase metal abundances, it is crucial to understand its effect and characterize it. In addition, dust depletion can give unique insights into the properties of cosmic dust. Therefore, I have dedicated significant amount of work on the characterization of dust depletion. Previously, dust depletion was characterized either concentrating on a smaller range of galactic environments, for example in the Milky Way (Jenkins, 2009), in the Milky Way and QSO-DLAs (De Cia et al., 2016) or in the Magellanic Clouds (Roman-Duval et al., 2021), or with a inclusion of a smaller amount of elements (e.g., De Cia et al., 2016). Some of these works were based on the assumption of a constant metallicity (e.g., Jenkins, 2009), yielding important insights about dust depletion in specific galaxies, but restricting the expansion to different galactic environments. Other studies focused on the relative abundances of metals (e.g., De Cia et al., 2016) offering a more flexible approach and allowing the application of the method to distant galaxies.

In the current Chapter, I present the results of my work on characterizing dust depletion in local and distant galaxies, which is published in A&A (Konstantopoulou et al., 2022). This work builds upon the methodology of De Cia et al. (2016) expanding this approach to 18 metals and combining several galactic environments, providing a more comprehensive analysis of dust depletion. I compiled a large amount of literature measurements of column densities and, using the methodology described in Chapter 2, I measured new column densities for Ti and Ni in a sample of 70 QSO-DLAs. Using these measurements I characterized the dust depletion of 18 metals and in different galactic environments (the Milky Way, the Magellanic Clouds, QSO- and GRB-DLAs). The results of this work, have strong implications on the origin of cosmic dust and highlight the importance of grain growth in the ISM, as a dominant mechanism for dust production. Additionally, in Section 3.E, we have updated the column densities of P for the Milky Way sample of (Konstantopoulou et al., 2022), using newer oscillator strengths, and its coefficients. Overall, in this work,

I refined and expanded the dust depletion coefficients for several elements, which were estimated by including a wide range of galactic environments.

This Chapter contains the following article with title:

"Dust depletion from local to distant galaxies I: Peculiar nucleosynthesis effects and grain growth in the ISM"

Authors: Christina Konstantopoulou, Annalisa De Cia, Jens-Kristian Krogager, Cédric Ledoux, Pasquier Noterdaeme, Johan P. U. Fynbo, Kasper E. Heintz, Darach Watson, Anja C. Andersen, Tanita Ramburuth-Hurt and Iris Jermann

The paper is published in Astronomy&Astrophysics, Volume 666, Issue A12, June 2022 A&A, 666, A12 (2022) and is presented unmodified below.

3.1 ABSTRACT

Large fractions of metals are missing from the observable gas-phase in the interstellar medium (ISM) because they are incorporated into dust grains. This phenomenon is called dust depletion. It is important to study the depletion of metals into dust grains in the ISM to investigate the origin and evolution of metals and cosmic dust. We characterize the dust depletion of several metals from the Milky Way to distant galaxies. We collected measurements of ISM metal column densities from absorption-line spectroscopy in the literature, and in addition, we determined Ti and Ni column densities from a sample of 70 damped Lyman-α absorbers (DLAs) toward quasars that were observed at high spectral resolution with the Very Large Telescope (VLT) Ultraviolet and Visual Echelle Spectrograph (UVES). We used relative ISM abundances to estimate the dust depletion of 18 metals (C, P, O, Cl, Kr, S, Ge, Mg, Si, Cu, Co, Mn, Cr, Ni, Al, Ti, Zn, and Fe) for different environments (the Milky Way, the Magellanic Clouds, and DLAs toward quasars and towards gamma-ray bursts). We observed overall linear relations between the depletion of each metal and the overall strength of the dust depletion, which we traced with the observed [Zn/Fe]. The slope of these dust depletion sequences correlates with the condensation temperature of the various elements, that is, the more refractory elements show steeper depletion sequences. In the neutral ISM of the Magellanic Clouds, small deviations from linearity are observed as an overabundance of the α-elements Ti, Mg, S, and an underabundance of Mn, including for metal-rich systems. The Ti, Mg, and Mn deviations completely disappear when we assume that all systems in our sample of OB stars observed toward the Magellanic Clouds have an α-element enhancement and Mn underabundance, regardless of their metallicity. This may imply that the Magellanic Clouds have recently been enriched in α-elements,

potentially through recent bursts of star formation. We also observe an S overabundance in all local galaxies, which is an effect of ionization due to the contribution of their HII regions to the measured SII column densities. The observed strong correlations of the depletion sequences of the metals all the way from low-metallicity quasi-stellar object DLAs to the Milky Way suggest that cosmic dust has a common origin, regardless of the star formation history, which, in contrast, varies significantly between these different galaxies. This supports the importance of grain growth in the ISM as a significant process of dust production.

3.2 INTRODUCTION

Interstellar dust plays an important role in various physical and chemical processes that contribute to galactic evolution (Dwek, 1998; Draine, 2011). However, the composition and origin of dust grains in distant galaxies are not yet well understood. The properties of dust have been studied more extensively in the Milky Way and in the Small Magellanic Cloud (SMC) and the Large Magellanic Cloud (LMC) (Fitzpatrick and Massa, 1986; Pei, 1992; Gordon et al., 2003). Characterizing dust at high redshift is more challenging, but crucial for improving our understanding of the early Universe (Watson et al., 2015). Recent observational constrains on the dust properties at early stages of chemical evolution are fundamental for complementing existing models of dust production and evolution (Calura, Pipino, and Matteucci, 2008; Zhukovska, Gail, and Trieloff, 2008; Arrigoni et al., 2010; Triani et al., 2020).

Absorption-line spectroscopy has proven to be the most powerful tool of the various observational techniques for determining the composition of the interstellar medium (ISM) of a galaxy (Prochaska and Wolfe, 1999; Savage and Sembach, 1996). It provides measurements of the column densities of different ions in the gas phase, from which the chemical abundances in the ISM of a galaxy can be determined. However, part of the metals are incorporated into dust grains. This effect is called dust depletion. It alters the relative abundances of the gas phase and challenges a comprehensive study of the ISM (Field, 1974; Savage and Sembach, 1996; Savaglio, Fall, and Fiore, 2003; Jenkins, 2009; De Cia et al., 2016; Roman-Duval et al., 2021). It is therefore crucial to have a thorough understanding of the depletion of metals from the Local Group to high redshifts to be able to enhance our knowledge about the origin of cosmic dust and its composition (Mattsson et al., 2019).

In the Local Group, UV and optical absorption-line spectroscopy toward background stars can provide a detailed insight into the metal abundances of the elements in the ISM (Field, 1974; York et al., 1983; Savage and Sembach, 1996; Jenkins and Wallerstein, 2017; Roman-Duval et al., 2021). For distant galaxies, damped Lyman-α absorbers (DLAs, defined by $\log \mathrm{N(HI)} \geq 20.3$ cm^{-2}, e.g., Wolfe, Gawiser, and Prochaska 2005) toward bright background sources such as quasars (quasi-stellar objects, QSOs) and gamma-ray bursts (GRBs) are studied in absorption. DLAs predominantly trace galaxies at the low-mass end of the distribution (Ledoux et al., 2006; Christensen et al., 2014), and studying them contributes to our understanding of dust depletion, nucleosynthesis, metallicity, and molecular content across cosmic time (Prochaska and Wolfe, 1999; Ledoux, Bergeron, and

Petitjean, 2002; Vladilo, 2002; Prochaska et al., 2007; Petitjean, Ledoux, and Srianand, 2008; Kulkarni et al., 2015; De Cia, 2018; Bolmer et al., 2019; Heintz et al., 2019a,b). DLAs remain the best means for estimating elemental abundances in distant galaxies, allowing access to the study of elements in a wide range of environments and physical conditions, regardless of the luminosity of the absorbing galaxy.

Damped Lyman-α absorbers are the largest reservoirs of HI in the Universe and carry the majority of metals at high-z (Péroux and Howk, 2020). Among the elements that can be observed in absorption, singly ionized titanium (TiII) is unique. While Ti is an α-element, it is also highly refractory and thus heavily depleted into dust grains, much more even than iron (e.g., Jenkins, 2009; Ledoux, Bergeron, and Petitjean, 2002). These particular properties mean that Ti can be a tracer of dust, but also a tracer of α-element enhancement. Titanium is dominant in HI-dominated gas, with negligible contribution from ionized HII gas because its ionization potential is almost equal to that of neutral hydrogen (Viegas, 1995). Most of the Ti in the Galactic ISM appears to be depleted into dust grains (Jenkins, 2009), but much less is known about Ti depletion in lower-metallicity systems, such as those found among QSO-DLAs. By constraining Ti at high redshifts, we can better understand the chemistry of the gas and the properties of dust in these galaxies.

Jenkins (2009) used abundances of several elements in Milky Way stars to estimate the overall dust depletion in each line of sight. However, the main assumption of this method is that the metallicity of the gas is solar. This assumption cannot be made for DLAs because the gas metallicity in these systems can vary and can be significantly lower (Pettini et al., 1994). In addition, De Cia et al. (2021) showed that the ISM metallicity in galaxies is not necessarily uniform. Instead, De Cia et al. (2016) characterized the dust depletion of several metals in QSO-DLAs and the Milky Way without any assumption on the gas metallicity. We expand this study and add more elements to the current dust depletion scheme. We study the depletion properties of C, P, O, Cl, Kr, S, Ge, Mg, Si, Cu, Co, Mn, Cr, Ni, Al, Ti, Zn, and Fe using the De Cia et al. (2016) formalism, which is based on the observations of relative abundances, in different environments, from the Local Group to distant galaxies. In Section 2 we present the samples that we used for our analysis. In Section 3 we describe the method for estimating the dust depletions. We discuss our results in Section 4, and we finally summarize and conclude in Section 5.

Throughout the paper we use a linear unit for the column densities N in terms of ions cm^{-2}. We refer to relative abundances of elements X and Y as $[X/Y] \equiv \log\frac{N(X)}{N(Y)} - \log\frac{N(X)_\odot}{N(Y)_\odot}$, where reference solar abundances are reported in Table 3.1. We report $1\,\sigma$ and $3\,\sigma$ significance levels for the errors and limits, respectively.

Table 3.1: Solar abundances.

Element	$12 + \log(X/H)_\odot$ [a]	Source [b]
C	8.43	s
P	5.42	a
O	8.69	s
Cl	5.23	m
Kr	3.12	t
S	7.135	a
Zn	4.61	m
Ge	3.60	a
Mg	7.54	a
Si	7.51	m
Cu	4.25	m
Co	4.91	a
Mn	5.47	m
Cr	5.63	a
Ni	6.20	a
Fe	7.46	a
Al	6.43	a
Ti	4.90	m

Notes:[a] Reference solar abundances are adopted from Asplund, Amarsi, and Grevesse (2021). [b]Photospheric (s), meteoritic (m), or average (a) abundances are used based on the recommendations from Lodders, Palme, and Gail (2009).

3.3 SAMPLES

The full sample in this work consists of new column density measurements of QSO-DLAs as well as literature measurements of column densities in the neutral ISM in different galaxies: the Milky Way, the Magellanic Clouds, and QSO- and GRB-DLAs. We used the QSO-DLA sample of De Cia et al. (2016) to make new measurements of Ti and Ni column densities, whenever possible. We only considered systems observed with high spectral resolution (R = 35 000-58 000) when measuring Ti and Ni column densities. For the Milky Way, we used ISM abundances from Jenkins (2009), De Cia et al. (2021), Welty and Crowther (2010), and Phillips, Gondhalekar, and Pettini (1982). For the LMC, we used Roman-Duval et al. (2021), and for the SMC, we used Welty and Crowther (2010), Tchernyshyov et al. (2015), Jenkins and Wallerstein (2017), the abundances of QSO-DLAs were taken from Berg et al. (2015), De Cia (2018), and those for DLAs toward GRBs from Bolmer et al. (2019).

Our sample probes gas in different regions of galaxies spanning a diversity of galaxy types and properties. GRB-DLAs select gas-rich galaxies, such as QSO-DLAs, but with active star formation and preferentially piercing through inner parts of these galaxies, while QSO-DLAs can be more peripheral (e.g., Prochaska et al., 2007; Fynbo et al., 2008). The Milky Way and Magellanic Cloud samples are also observations through the inner parts

of galaxies. The Magellanic Clouds are in a different phase of their star formation history, with recent bursts of star formation (Harris and Zaritsky, 2009; Indu and Subramaniam, 2011; Crowther et al., 2016; Joshi and Panchal, 2019; Bestenlehner et al., 2020; Hasselquist et al., 2021), probably due to the proximity to the Milky Way and close encounters between the two Magellanic Clouds.

We collected measurements of 18 elements (C, P, O, Cl, Kr, S, Ge, Mg, Si, Cu, Co, Mn, Cr, Ni, Al, Ti, Zn, and Fe) from all the samples in order to characterize the dust depletion by estimating the relative abundances (De Cia et al., 2016; Jenkins and Wallerstein, 2017) of these elements. Different literature samples use different values for the oscillator strengths of the different ions. We homogenized them by correcting the column densities to the newest possible oscillator strengths for all the samples. We adopted the oscillator strengths from Cashman et al. (2017) for KrI, MgII, SiII, CuII, CoII, MnII, CrII, AlII, and TiII, those from Boissé and Bergeron (2019) for NiII, those from Kisielius et al. (2015) for ZnII, those from Kisielius et al. (2014) for SII, and those from Kurucz (2017) for P. When there was no recent change to the oscillator strength, the value from Morton (2003) was used for the other metals.

3.3.1 *QSO- and GRB-DLAs*

The QSO-DLA sample is a compilation of new column density measurements and literature measurements (De Cia, 2018; Noterdaeme et al., 2010; Ma et al., 2015; Fynbo et al., 2017; Noterdaeme et al., 2017). The new QSO-DLA column density measurements were made using a large sample of 70 QSO-DLAs observed at high spectral resolution with the Very Large Telescope (VLT) Ultraviolet and Visual Echelle Spectrograph (UVES) from De Cia et al. (2016). The procedure that we followed is described in Section 3.4.1. Additionally, we used the constrained preexisting measurements of these QSO-DLAs to study the depletion of O, S, Si, Mg, Mn, and Cr. The literature sample includes one large QSO-DLA and one GRB-DLA sample. The main QSO-DLA sample was published in De Cia (2018). This contains a QSO-DLA sample observed with UVES from De Cia et al. (2016), a large QSO-DLA sample from Berg et al. (2015), and a few metal-rich QSO-DLAs from Ma et al. (2015), Fynbo et al. (2017), Noterdaeme et al. (2010) and Noterdaeme et al. (2017). The Berg et al. (2015) catalog includes 395 QSO-DLAs, 44 of which are selected from the Herbert-Fort et al. (2006) catalog as metal-rich systems, and the rest are a literature compilation of column densities of all QSO-DLAs published between 1994 and 2014, with medium- or high- resolution requirement ($R > 10\,000$). In the full QSO-DLA sample, 237 systems have both Zn and Fe constrained measurements.

Finally, we use a sample of 22 GRB-DLAs at redshifts $z > 2$ observed with VLT/X-Shooter with medium resolution ($R \sim 10\,000$) from Bolmer et al. (2019), 9 of which have both Zn and Fe constrained measurements. Our final QSO-DLA sample consists of 139 systems, of which 15 literature and 13 new measurements were used to constrain the Ti depletion, 73 literature and 23 new measurements were used to constrain the Ni depletion, and the rest of the systems were used for the other elements.

3.3.2 *Milky Way and the Magellanic Clouds*

We included a sample of ISM metal column densities from the Milky Way, the LMC, and the SMC. The Milky Way sample includes a compilation of elemental abundances from 243 lines of sight in the Milky Way (Jenkins, 2009), 25 bright O and B stars observed with the Hubble Space Telescope (HST) Space Telescope Imaging Spectrograph (STIS) with a resolving power of R $\sim$ 30 000 (De Cia et al., 2021) and Al measurements from Phillips, Gondhalekar, and Pettini (1982). The SMC sample is composed of elemental abundances toward 19 lines of sight from Welty and Crowther (2010), Tchernyshyov et al. (2015), Jenkins and Wallerstein (2017). The LMC sample counts 32 abundances of massive stars observed with HST/STIS from Roman-Duval et al. (2021). Of these, 39 galactic, 16 SMC, and 31 LMC lines of sight have Zn and Fe constrained measurements.

Table 3.2: Number of Ti and Ni measurements for the Milky Way, QSO-DLAs, the LMC, SMC, and GRB-DLAs. References: ($\star$) This work; (1) Berg et al. (2015) ;(2) Jenkins (2009); (3) De Cia et al. (2021); (4) Welty and Crowther (2010); (5) Tchernyshyov et al. (2015); (6) Jenkins and Wallerstein (2017); (7) Roman-Duval et al. (2021); (8) Bolmer et al. (2019).

Environments	Ti	Ni	References
Milky Way	31	23	(2), (3)
DLAs	28	98	($\star$), (1)
LMC	10	29	(7)
SMC	13	12	(4), (5), (6)
GRBs	1	8	(8)

3.4 METHODS AND RESULTS

3.4.1 *New column density measurements. Voigt-profile fitting*

We determined the column densities of Ti and Ni in QSO-DLA spectra from UVES/VLT using the Voigt-profile fit method, which decomposes the line profiles into their individual velocity components and fits all transitions simultaneously. Using the Python package VoigtFit[1] (Krogager, 2018), we modeled TiII (λ1910 , λ3067 , λ3073 , λ3230 , λ3242 , and λ3384) and NiII lines (λ1317 , λ1370 , and λ1741) when they were covered by the UVES spectra. To better constrain the fit, we also modeled transitions of FeII, SiII, and CrII. In some cases, we included ZnII, SII, MnII, MgII, and PII. All the velocity profiles of the modeled transitions are shown in Appendix 3.C.

We adopted the individual velocity components, namely the redshift z and the broadening parameter b, that are listed in Table F.1 of De Cia et al. (2016), using FeII as reference. We visually inspected the FeII lines, and when they appeared to be saturated, we used SiII instead. For Q0347-383, Q0528-250a, Q0528-250b, Q0551-366, Q0841+129c, Q2138-444b,

1 https://github.com/jkrogager/VoigtFit

and Q2231-002, we added additional components that we identify in the line profile. In addition to TiII and NiII, we measured ZnII using the transitions λ2026 and λ2062 for Q0102-190a and Q0841+129a, respectively. The contaminating features were masked out, and the continuum level was automatically placed using Chebyshev polynomials. Contaminated lines can bias the continuum placement and the resulting fit. When needed, the interactive masking was repeated until the fit was reasonable. Due to the high column density of neutral hydrogen in QSO-DLAs, which shields metals against higher ionizations, no ionization corrections are needed to derive the metal abundances. We adopted the newest oscillator strengths from Cashman et al. (2017) for TiII, those from Boissé and Bergeron (2019) for NiII, and those from Kisielius et al. (2015) for ZnII. For FeII, there is no recent change to the oscillator strength, and therefore the value from Morton (2003) was used.

When TiII or NiII were not detected, we estimated the 3σ upper limits because the lines are not strongly contaminated. We used the line profile of a well-constrained transition (FeII or SiII) as reference. The reference was used to determine the limits of the line profile containing 99% of the optical depth, within which the upper limit was calculated.

For some ions (in systems Q0405-443c, Q1117-134, and Q1223+178), the fit did not converge properly although there was a detection. To constrain the fit in these cases, we fixed the line profile using redshift z and b-values from a fit of another previously well-constrained ion (e.g., FeII or SiII).

The total number of Ti and Ni measurements from all the samples that we used are summarized in Table 3.2. The total column densities as well as the upper limits are reported in Table 3.3. Out of the 70 QSO-DLAs that were studied, we were able to obtain a constrained measurement of TiII from only 13 systems, and 18 limits were estimated. NiII was measured in 23 systems, and 7 limits were estimated. Combining these with the QSO-DLA literature sample, we have 28 Ti and 98 Ni constrained measurements in total.

The velocity profiles of all the modeled TiII and NiII transitions are shown in Appendix 3.C. The total column densities were used to characterize the depletion of Ti and Ni with the relative method. They are reported in Table 3.7.

3.4.2 *Estimating the dust depletions*

Metals are missing from the observable gas-phase and are instead depleted into dust grains. The depletion of an element X, δ_x, is defined as

$$\delta_X = [X/H]_{\rm gas} - [X/H]_{\rm tot}, \tag{3.1}$$

where $[X/H]_{\rm gas}$ are the observed gas-phase abundances, and $[X/H]_{\rm tot}$ are the total (gas + dust) abundances. De Cia et al. (2016) showed that the depletion of an element X can be purely estimated from some relative abundances. In general, the relative abundance of an element X with respect to another element Y ([X/Y]) is more sensitive to the depletion of X if Y is a volatile element. Thus, the depletion of X can be derived from the observed [X/Zn] after correcting for the mild depletion of Zn, which we discuss below. The depletion of various metals X correlates with the overall strength of the depletion, or dust tracer, for

Table 3.3: New UVES QSO-DLA Ti and Ni measurements

QSO	z_{abs}	log N(FeII)	log N(ZnII)	log N(NiII)	log N(TiII)
Q0010-002	2.02484	15.18±0.04	12.09±0.04	13.69±0.03	<12.38
Q0058-292	2.67142	14.75±0.02	12.14±0.02	13.55±0.08	12.30±0.11
Q0100+130	2.30903	15.05±0.02	12.34±0.01	...	12.72±0.11
Q0102-190a	2.36966	14.44±0.02	11.61±0.08	13.16±0.07	12.20±0.12
Q0216+080a	1.76873	14.47±0.02	11.87±0.06	<13.08	<12.22
Q0347-383	3.02485	14.35±0.02	12.13±0.05	<13.70	<11.92
Q0405-443a	1.91267	15.16±0.02	12.34±0.03	13.87±0.01	12.48±0.02
Q0405-443b	2.55000	15.05±0.01	12.36±0.04	13.76±0.01	<12.22
Q0405-443c	2.59466	15.08±0.02	12.50±0.01	13.80±0.01	12.55±0.05
Q0458-020	2.03956	15.33±0.05	13.05±0.02	14.06±0.03	<12.72
Q0528-250a	2.14105	14.78±0.02	12.19±0.03	13.65±0.01	12.62±0.07
Q0528-250b	2.81111	15.48±0.01	13.01±0.01	14.29±0.01	12.76±0.06
Q0551-366	1.96221	15.05±0.03	12.92±0.03	14.09±0.01	<12.56
Q0841+129a	1.86384	14.89±0.04	11.94±0.11	13.60±0.02	12.38±0.05
Q0841+129b	2.37452	14.72±0.02	12.03±0.02	13.55±0.01	<13.06
Q0841+129c	2.47622	14.48±0.02	11.77±0.03	13.30±0.02	<11.94
Q1111-152	3.26552	14.82±0.02	12.22±0.09	13.56±0.01	...
Q1117-134	3.35046	14.82±0.03	12.11±0.05	<13.53	12.49±0.05
Q1157+014	1.94349	15.47±0.01	12.93±0.01	14.19±0.01	12.99±0.01
Q1209+093	2.58437	15.36±0.02	12.96±0.02	14.16±0.04	<12.60
Q1223+178	2.46607	15.21±0.01	12.34±0.02	13.86±0.05	12.73±0.06
Q1331+170	1.77635	14.62±0.02	12.44±0.03	13.41±0.02	<11.95
Q1409+095a	2.01881	14.34±0.02	11.60±0.13	13.15±0.08	<12.88
Q1444+014	2.08679	13.99±0.03	12.02±0.06	<12.81	<12.43
Q1451+123a	2.25466	14.42±0.05	11.85±0.11	<13.60	<12.97
Q2116-358	1.99615	14.72±0.05	12.33±0.08	13.61±0.02	<12.43
Q2138-444a	2.38279	14.54±0.01	12.02±0.08	<12.90	<12.64
Q2138-444b	2.85234	14.63±0.02	11.81±0.02	13.33±0.02	<11.83
Q2206-199a	1.92061	15.34±0.01	12.70±0.01	14.16±0.02	12.86±0.02
Q2243-605	2.33062	14.95±0.01	12.38±0.02	13.83±0.02	12.64±0.03
Q2332-094a	2.28749	14.23±0.03	12.31±0.02	13.25±0.04	...
Q2343+125	2.43123	14.51±0.02	12.05±0.02	13.36±0.03	<11.97
Q2359-022a	2.09510	14.47±0.01	12.38±0.08	<13.59	<12.51

Notes: Upper limits are given at the 3σ confidence level. The redshifts and the column densities for Fe and Zn are taken from De Cia et al. (2016), except for Q0102-190a and Q0841+129a, for which we made new Zn measurements.

instance, [Zn/Fe]. These correlations are referred to as depletion sequences (De Cia et al., 2016).

To derive the depletion of X from the observed [X/Zn], we assumed a depletion of Zn, $\delta_{\rm Zn}$ = -0.27 $\times$ [Zn/Fe], as derived from the Milky Way and QSO-DLAs by De Cia et al. (2016). We also corrected for α-element enhancement and Mn underabundance, which is

further discussed in the next section. Taking these assumptions into account, δ_X was then derived as

$$\delta_X = [\mathrm{X/Zn}] + \delta_{Zn} - \alpha_X, \tag{3.2}$$

where α_X is the intrinsic $[\mathrm{X/Fe}]_{\mathrm{nucl}}$ due to stellar nucleosynthesis, for example, α-element enhancement or Mn underabundance.

A good dust tracer can be any relative abundance of two elements ([X/Y]) that have very different refractory properties (i.e., they deplete very differently), but follow each other in nucleosynthesis. In this paper, we use [Zn/Fe] as a dust tracer (but other relative abundances, e.g., [Si/Ti] or [O/Si], can be used). [Zn/Fe] is the ratio of two elements with very different degrees of incorporation into dust grains, with Zn being a volatile element and Fe a refractory element. [Zn/Fe] is also called the depletion factor and is often used as a tracer of the overall dust depletion in QSO-DLAs (Noterdaeme et al., 2008). Zn and Fe trace each other (Timmes, Lauroesch, and Truran, 1995) in the metallicity range considered here (-2 $\leq$ [M/H] $\leq$ 0). Stellar measurements show that [Zn/Fe] $\sim$ 0 in the metallicity range -2 $\leq$ [M/H] $\leq$ 0 (e.g., Saito et al., 2009; Barbuy et al., 2015), which is appropriate for most QSO-DLAs (De Cia, 2018). Outside this metallicity range, [Zn/Fe] appears to be supersolar in metal-poor halo stars (Primas et al., 2000; Nissen et al., 2004, 2007) and subsolar in the bulge (Barbuy et al., 2015). Moreover, [Zn/Fe] correlates well with [Si/Ti] (see Fig. A.1. of De Cia et al., 2016). Si and Ti follow each other nucleosynthetically, and if Zn did not trace Fe, then we would see a deviation from the linear relation, but this is not observed. More details about the reliability of [Zn/Fe] as a dust tracer can be found in De Cia (2018).

3.4.3 *Corrections for α-element enhancement and Mn underabundance*

The depletion δ_X is by definition a negative value (eq. 3.1). Figure 3.1 shows the observed gas-phase relative abundances [X/Zn] against [Zn/Fe] before any dust or α-element enhancement corrections. Fig. 3.1 shows that at the offsets of [X/Zn] with [Zn/Fe] = 0 for some elements, [X/Zn] is positive. This is due to an enhancement of the α-elements observed in the gas phase as a result of the chemical enrichment of the ISM by supernovae. Core-collapse supernovae produce large amounts of α-elements, such as O, Si, S, Mg, and Ti, with only a smaller production of Fe-peak elements (Nomoto et al., 2006). This results in an observed overabundance of the α-elements with respect to Fe ([α/Fe]). On the other hand, type Ia supernovae mostly produce the Fe-peak elements and a smaller amount of α-elements, leading to a linear decrease of [α/Fe] until [α/Fe] $\sim$ 0. Mn is mostly produced by type Ia supernovae, leading to a Mn underabundance compared to Fe before the contribution of SNe Ia becomes strong (Nomoto et al., 1997). We refer to these effects as nucleosynthesis effects because they are the product of explosive nucleosynthesis in stars that enrich the ISM with metals.

We applied corrections to account for effects such as α-element enhancement and Mn underabundance. To do this, we adopted the shapes of the nucleosynthetic curves from De Cia et al. (2016) (see their Fig. 7). In particular, we assumed that at lower metallicities and low [Zn/Fe], there is an α-element enhancement and Mn underabundance ($\alpha_{\mathrm{X},0}$), while

at higher metallicities and at high [Zn/Fe], there is a plateau at $\alpha_{X,0}$ = 0.05. In between, $\alpha_{X,0}$ decreases linearly with [Zn/Fe]. The shapes of the curves are consistent with the nucleosynthetic patterns observed in the Galaxy (see Lambert 1987, McWilliam 1997, for O, Si, Mg, and S in galactic stars and in Wheeler, Sneden, and Truran 1989, Mishenina et al. 2015 and Battistini and Bensby 2015 for Mn). The values of $\alpha_{X,0}$ are obtained by the intercepts of the relative abundances [X/Zn] at [Zn/Fe] = 0. They are $\alpha_{O,0}$ = 0.38 $\pm$ 0.10, $\alpha_{S,0}$ = 0.25 $\pm$ 0.03, $\alpha_{Si,0}$ = 0.26 $\pm$ 0.03, $\alpha_{Mg,0}$ = 0.30 $\pm$ 0.04, and $\alpha_{Mn,0}$ = -0.39 $\pm$ 0.03. For Ti, we used $\alpha_{Ti,0}$ = 0.29 $\pm$ 0.08, estimated by McWilliam (1997) for the Galaxy, which is identical to the intercept of [Ti/Zn] with [Zn/Fe] = 0 that we measure, $\alpha_{Ti,0}$ = 0.29 $\pm$ 0.03.

While the plateau and the overall shape of the α-element enhancement and Mn underabundance distribution with metallicity is rather well constrained, the position of the knee (the metallicity at which $\alpha_{X,0}$ starts to decrease) is unknown for QSO-DLAs, and we may expect it at lower metallicities (de Boer et al., 2014) because we expect QSO-DLA galaxies to have lower stellar masses overall (Christensen et al., 2014; Krogager et al., 2017). For the LMC, the α-element knee is poorly constrained and might be at similar metallicities as in the Milky Way or at [M/H] $\sim$ -1.5 dex (de Boer et al., 2014). For the Magellanic Clouds and for QSO-DLAs, we assumed the middle point (at [Fe/H = -1.3]) of the knee position range estimated by de Boer et al. (2014) (see their Fig. 3). The approximate assumption of the position of the α-element knee for these environments can be improved with future observations. Nevertheless, the exact positioning of the α-element knee has a very small effect on the α-element correction and therefore does virtually not affect our results. In addition, we explored the possibility of a different assumption for the Magellanic Clouds, a constant distribution of α-element enhancement (and Mn underabundance), as we discuss in Section 3.5.3.

Using these assumptions on the effects of α-element enhancement and Mn underabundance, we derived the depletions using eq. 3.2. Corrections for these effects were taken into account for the derivations of the depletions, but contribute very little ($\leq$ 0.4 dex) compared to the strong dust depletion effects on the gas-phase metal abundances, which can reach up to 3 dex for highly depleted metals such as Ti (Jenkins, 2009).

3.4.4 *Dust-depletion sequences*

We followed the method of De Cia et al. (2016) to characterize the depletion of several elements in different environments (QSO-DLAs, GRB-DLAs, Milky Way, LMC, and SMC) using a literature compilation that includes systems with Zn and Fe constrained measurements. In their method, De Cia et al. (2016) use the relative abundance of an element X with respect to a lightly depleted element, such as Zn, P, or S, to estimate the dust depletion of element X (δ_X). The depletion of X correlates linearly with the dust tracer (e.g., [Zn/Fe]), and thus the dust depletion can then be expressed by a simple linear relation. We characterize the dust depletion of P, S, Si, Mg, Mn, and Cr in the above environments and further focus on the dust depletion of Ti and Ni, which have not been characterized before with this method and for which we provide new column density measurements. We extend our study to additionally characterize the dust depletion of O, C, Cl, Kr, Ge, Cu, Co, and Al for the Milky Way and QSO-DLAs, but only a few measurements are available at low levels of

depletion (QSO-DLAs), and only two LMC measurements are added to the O depletion sequence.

We fit the dust depletion sequences as derived from the observed relative abundances and after correcting for the depletion of Zn and for α-element enhancement or Mn underabundance with a linear least-squares approximation that took the errors on both x-axis ([Zn/Fe]) and y-axis (δ_X) ($\sigma_{[Zn/Fe]}$ and σ_{δ_X}) into account. We used the Python package `scipy.odr`, which performs orthogonal distance regression to the data and determines the parameters that minimize the sum of the squared error for each data point. It uses the ODRPACK library (Boggs et al., 1992), which implements a modified trust-region Levenberg-Marquardt-type algorithm to estimate the function parameters. The dust depletion can be represented by linear fits to the data as

$$\delta_X = A2_X + B2_X \times [\mathrm{Zn/Fe}], \tag{3.3}$$

where the $A2_X$ and $B2_X$ coefficients for all the elements are reported in Table 3.4. These are given for two different assumptions on the nucleosynthetic curves of the Magellanic Clouds, one with the knee at [Fe/H] = -1.3, and one assuming a constant over- or underabundance plateau. Although the differences are small, we recommend that the second assumption coefficients are used.

Figure 3.2 shows the depletion sequences of the larger coverage elements (P, S, Si, Mg, Mn, and Cr). We discuss the elements with limited coverage in Appendix 3.B. For Ti, Ni, P, S, Si, Mg, Mn, and Cr, we performed fits to the individual environments, but also to all the data merged together. We also fit the relative abundances of element X with respect to Zn against [Zn/Fe]. The coefficients $A1_X$ and $B1_X$ were derived from the linear fit of the observed sequences of relative abundances,

$$[\mathrm{X/Y}] = A1_X + B1_X \times [\mathrm{Zn/Fe}]. \tag{3.4}$$

The best merged fit is shown with solid red lines in Fig. 3.4, from which we derived the coefficients $A1_X$, $B1_X$, $A2_X$, and $B2_X$. We report the coefficients $A2_X$ and $B2_X$ for the merged fit and the individual environments, the intrinsic scatter σ_{δ_X} of the data, estimated as the standard deviation of the x and y-component residuals for each data point, and the statistical properties of the fits to the individual sample and the merged data in Tables 3.5 and 3.6.

3.4.5 *Titanium depletion*

In this and the next section, we focus on titanium and nickel, for which we characterize the depletion based on the technique of relative abundances for the first time. We used a relatively large dataset that included our new measurements.

The depletion of Ti was derived from the observed relative abundances of [Ti/Zn] and [Zn/Fe] (Fig. 3.4) in 28 QSO-DLAs, one GRB-DLA, ten LMC, 13 SMC, and 31 Milky Way systems. Only one constrained measurement of Ti is available for GRB-DLAs, which was included in the merged fit, but the individual fit was not performed for this group. The linear regression fits to the Ti depletions in the different environments and the merged fit are shown in Fig. 3.4.

Table 3.4: Coefficients $A2_X$ and $B2_X$ resulting from the linear merged fit $\delta_X = A2_X + B2_X \times [Zn/Fe]$ of the depletion sequences shown in Figures 3.4, 3.2, 3.8, the degrees of freedom ν, and the Pearson correlation coefficients r. Exception are Zn and Fe, which are taken from De Cia et al. (2016). [a] r = -1 by construction. The coefficients are given for two assumptions on the knee position for the Magellanic Clouds. We recommend that the one with constant α_X is used.

X	SMC/LMC knee at [Fe/H] = -1.3			Constant α_X			ν
	$A2_x$	$B2_x$	r	$A2_x$	$B2_x$	r	
C	0.00	-0.10±0.10	-0.10	0.00	-0.10±0.10	-0.10	3
P	0.03±0.05	-0.21±0.08	-0.46	0.03±0.05	-0.21±0.08	-0.46	43
O	0.00±0.00	-0.20±0.05	-0.31	0.00±0.00	-0.20±0.05	-0.50	22
Cl	0.00	-0.12±0.09	-0.80	0.00	-0.12±0.09	-0.80	6
Kr	0.00	-0.04±0.09	-0.53	0.00	-0.04±0.09	-0.53	3
S	0.01±0.02	-0.48±0.04	-0.68	0.01±0.02	-0.48±0.04	-0.68	99
Zn	0.00±0.01	-0.27±0.03	-1.00[a]	0.00±0.01	-0.27±0.03	-1.00[a]	...
Ge	0.00	-0.40±0.04	-0.91	0.00	-0.40±0.04	-0.91	1
Mg	0.01±0.03	-0.60±0.04	-0.86	0.01±0.03	-0.66±0.04	-0.91	69
Si	-0.04±0.02	-0.72±0.03	-0.87	-0.04±0.02	-0.75±0.03	-0.88	151
Cu	0.00	-0.73±0.04	-0.87	0.00	-0.73±0.04	-0.87	4
Co	0.00	-0.89±0.19	-0.87	0.00	-0.89±0.19	-0.87	6
Mn	0.07±0.02	-1.06±0.03	-0.96	0.07±0.02	-1.03±0.03	-0.96	93
Cr	0.12±0.01	-1.30±0.01	-0.98	0.12±0.01	-1.30±0.01	-0.98	192
Ni	0.07±0.02	-1.31±0.03	-0.96	0.07±0.02	-1.31±0.03	-0.96	168
Fe	-0.01±0.03	-1.26±0.04	-1.00[a]	-0.01±0.03	-1.26±0.04	-1.00[a]	...
Al	0.00	-1.66±0.35	-0.69	0.00	-1.66±0.35	-0.69	7
Ti	-0.06±0.03	-1.64±0.04	-0.97	-0.07±0.03	-1.67±0.04	-0.97	81

Table 3.5: Orthogonal distance regression results of the fits for the depletion of Ti in the different environments. The columns list the χ^2, the reduced χ^2_ν, the degrees of freedom ν, the ${\chi_\nu}^2$ difference between the fit to the individual samples, and the merged fit to the individual sample ($\Delta{\chi_\nu}^2$), the Pearson correlation coefficients r, the p - value, and intrinsic scatter σ_{δ_X}.

Ti	$A2_X$	$B2_X$	χ^2	χ^2_ν	ν	$\Delta\chi^2_\nu$	r	p - value	$\sigma_{\delta_{Ti}}$
Milky Way	0.02±0.30	-1.73±0.22	57.84	2.00	29	0.07	-0.81	4.13e-08	0.12
QSO-DLAs	-0.17±0.07	-1.36±0.19	61.24	2.36	26	0.16	-0.87	2.32e-09	0.13
LMC	-0.53±0.12	-1.01±0.13	2.83	0.35	8	0.96	-0.97	3.00e-06	0.05
SMC	-0.35±0.04	-1.11±0.06	0.79	0.07	11	0.86	-0.99	2.90e-10	0.02
GRB-DLAs	-	-	-	-	-	-	-	-	-
Merged fit	-0.06±0.03	-1.64±0.04	164.49	2.03	81	-	-0.97	$\ll$	0.13

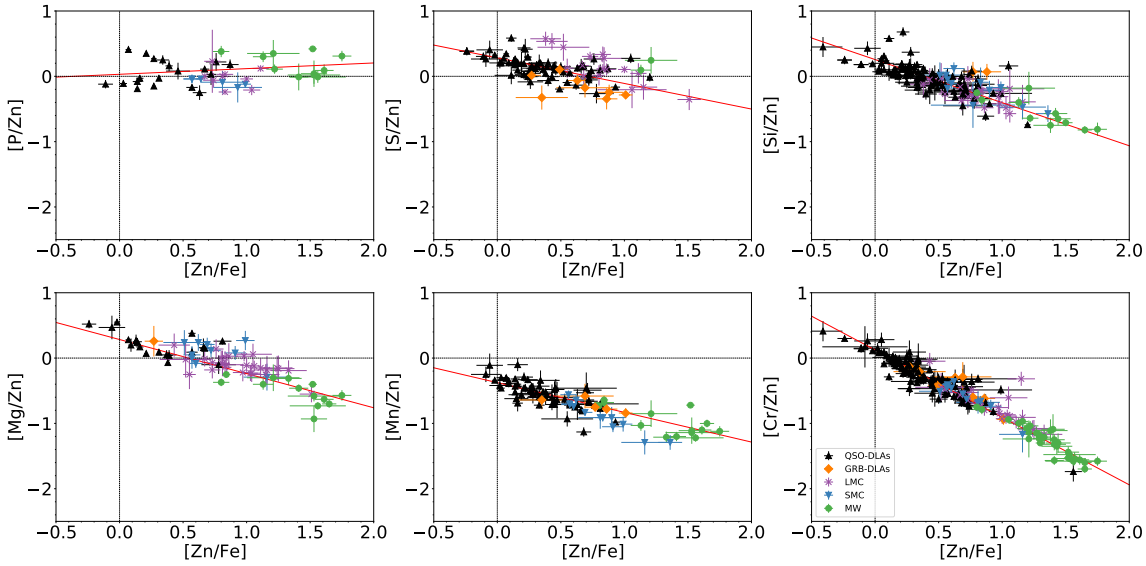


Figure 3.1: Relative abundances of element X with respect to Zn against [Zn/Fe]. The black triangles show QSO-DLAs, the green dots show the Milky Way, the purple stars show the LMC, the blue triangles show the SMC, and the orange diamonds show the GRB-DLAs. The red line shows the linear fit to the data.The slope becomes steeper for elements that are more strongly depleted into dust grains.

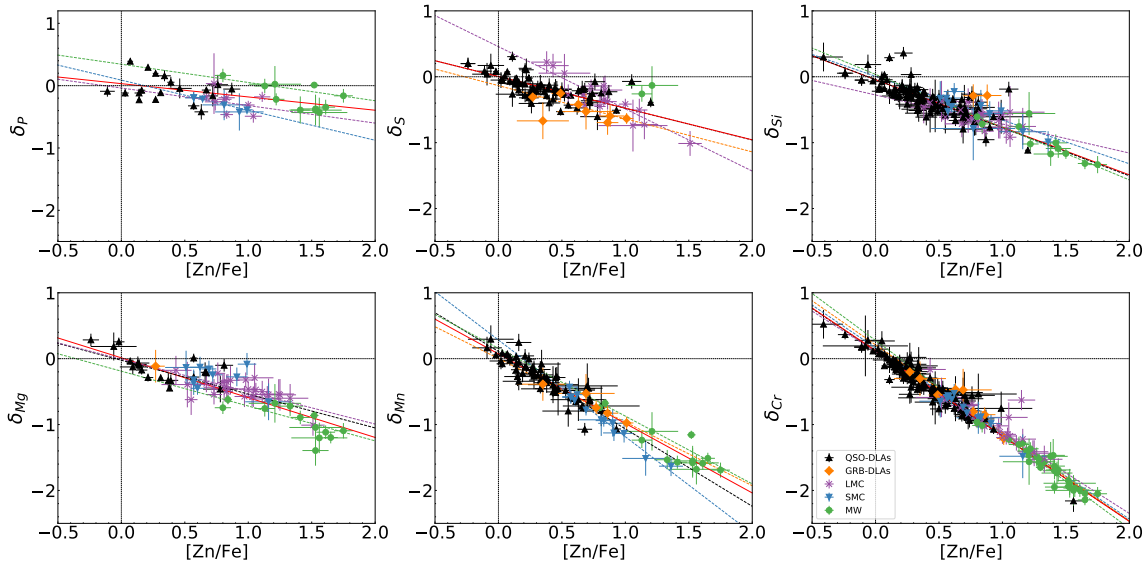


Figure 3.2: Dust depletion of element X (δ_X) against [Zn/Fe]. The black triangles show QSO-DLAs, the green dots show the Milky Way, the purple stars show the LMC, the blue triangles show the SMC, and the orange diamonds show the GRB-DLAs. The red line shows the linear fit to the data. The slope becomes steeper for elements that are more strongly depleted into dust grains.

To evaluate the goodness of the fits, we estimated the χ^2, the reduced χ^2_ν, the Pearson correlation coefficients r, the p-value for each fit, and the difference between the individual

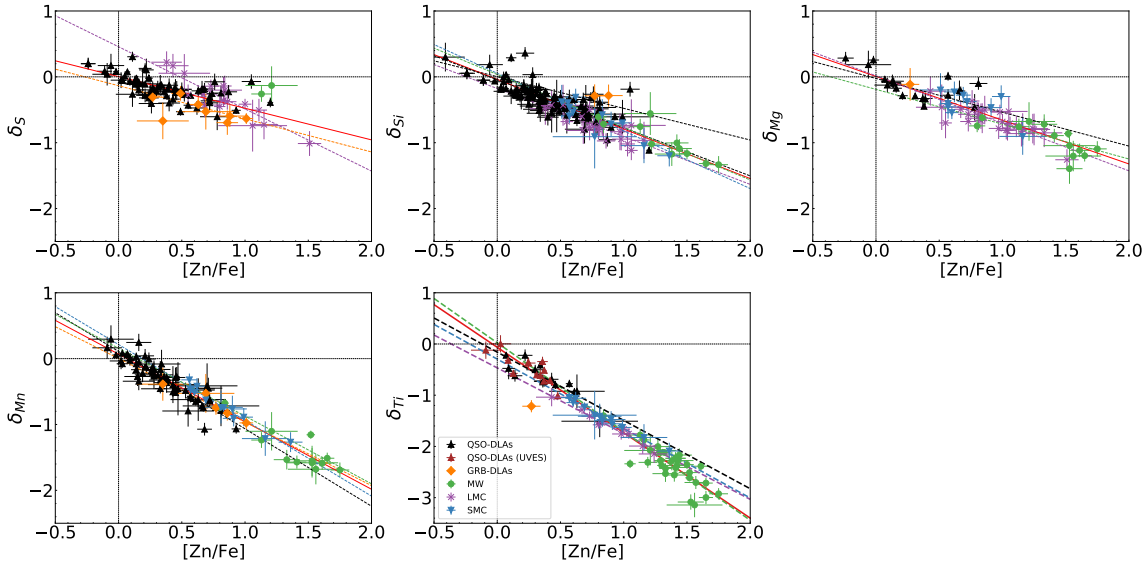


Figure 3.3: Same as Fig. 3.2 for the α-elements and Mn after assuming a constant overabundance for the α-elements and an underabundance plateau for Mn in the Magellanic Clouds.

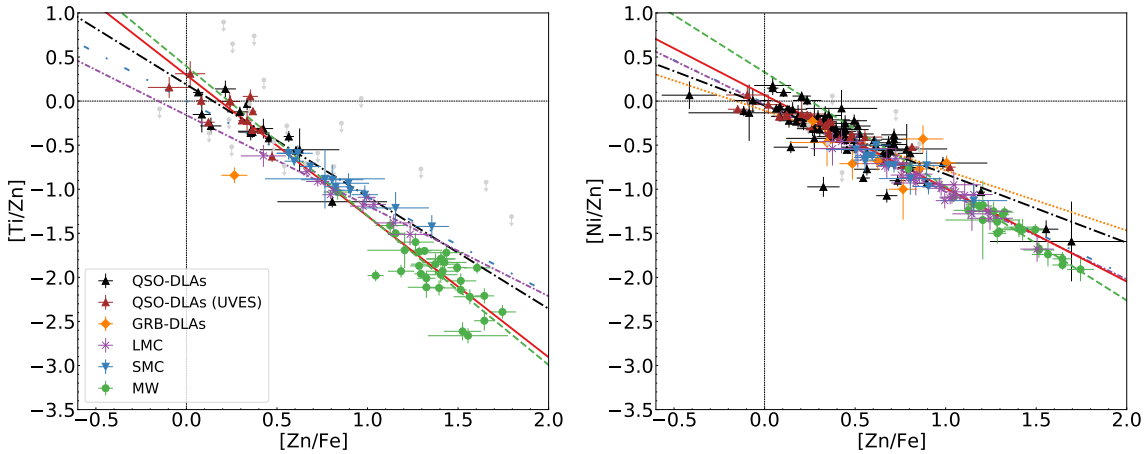


Table 3.6: Same as Table 3.5, but for Ni.

Ni	A2$_X$	B2$_X$	χ^2	χ^2_ν	ν	$\Delta\chi^2_\nu$	r	p - value	$\sigma_{\delta_{Ni}}$
Milky Way	0.33±0.12	-1.57±0.09	10.16	0.48	21	0.59	-0.97	2.09e-14	0.03
QSO-DLAs	-0.01±0.02	-1.12±0.04	279.04	2.91	96	0.60	-0.90	$\ll$	0.11
LMC	-0.05±0.05	-1.26±0.05	4.31	0.16	27	0.25	-0.98	1.07e-19	0.03
SMC	-0.07±0.10	-1.21±0.16	1.93	0.19	10	0.18	-0.94	4.53e-06	0.04
GRB-DLAs	-0.15±0.15	-0.90±0.20	6.50	1.08	6	0.80	-0.71	5.00e-02	0.10
Merged fit	0.07±0.02	-1.31±0.03	328.53	1.96	168	-	-0.96	$\ll$	0.10

datasets and the merged fit ($\Delta\chi^2_\nu$). This is reported in Table 3.5 and further discussed in Appendix 3.A.

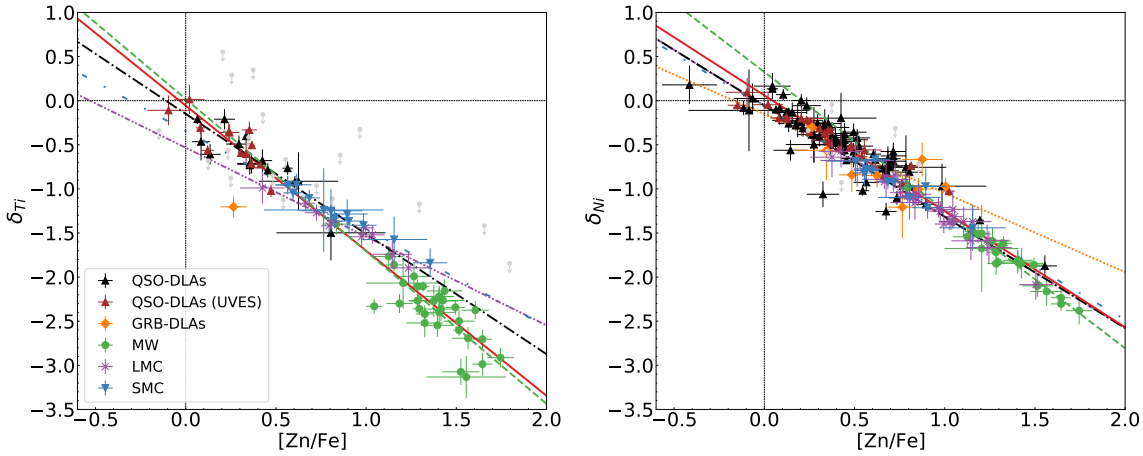


Figure 3.4: Relative abundances of Ti and Ni with respect to Zn against [Zn/Fe] (top). Dust depletion of Ti and Ni against [Zn/Fe] and the linear fits for the QSO-DLAs (black triangles and black dashdotted line) for the Milky Way (green points and dashed green line), for the LMC (purple stars and dash-dot-dotted purple densely line), for the SMC (blue triangles and dash-dotted blue line), and for the GRB-DLAs (orange diamonds and dotted orange line; bottom). The 3σ upper limits are shown with gray arrows. The solid red line shows the linear fit to the merged data.

The strongest titanium depletion can be observed for the Milky Way, where 90 to $\sim$ 99.9% of titanium is depleted into dust. $\delta_{\rm Ti}$ lies between $\sim$ -1.4 and -3.1 dex, which is similar to the Ti depletion that Jenkins (2009) estimated for the Milky Way ISM using fewer data. They estimated the depletion with an independent method ($\sim$ -1.1 to -3.2 dex). This is an important comparison because the depletion of Ti is so strong that it dominates other potential effects that may affect different methods in different ways, such as α-element enhancement, ionization, or the metallicity of the ISM. In particular, the consistency of our estimates of the strongest depletion of Ti in the Milky Way with those of Jenkins (2009) confirms that our assumption on the depletion of Zn (to estimate $\delta_{\rm Ti}$ from [Ti/Zn]) is in the correct range. The titanium depletion in QSO-DLAs is considerably weaker and ranges from about 0.003 to -1.5 dex. QSO-DLAs can probe systems with low metallicity and dust content, and in turn, very low dust depletions, all the way down to zero for dust-free QSO-DLAs. Even for the most refractory elements such as Ti, dust depletion can be zero. In the Magellanic Clouds, the range is in between that of the Milky Way and the QSO-DLAs, ranging from about -1 to -1.9 dex for the LMC and -1 to -1.8 dex for the much smaller sample of the SMC.

The best merged-fit coefficients for Ti are $A2_{\rm Ti}$ = -0.07 $\pm$ 0.03 and $B2_{\rm Ti}$ = -1.67 $\pm$ 0.04. Wiseman et al. (2017) made an approximate estimate on the coefficients of Ti and Ni based only on Milky Way data and are also consistent with our results (private communication). Other studies also find that the strong Ti depletion is most relevant in higher-metallicity environments (e.g., Jenkins, 2009; Welty and Crowther, 2010). This is consistent with our results because Ti depletion appears to be stronger in the Milky Way and decreases with decreasing metallicity (Magellanic Clouds and DLAs). Increasing depletion with increasing metallicity is also typically the case for the other metals. We observe, however, a potential

departure of the Ti depletion from linearity in the medium range of metallicities, in the Magellanic Clouds, which is discussed in Sect. 3.5.3.

GRB120327A slightly deviates from the linear fit of the depletion sequence with a low Ti content ($\log$ N(TiII) = 12.69 $\pm$ 0.08) (see the orange diamond in Fig. 3.4). This might be due to dust depletion, ionization, nucleosynthesis, or a measurement problem, such as line contamination. A low Ti abundance might be caused by dust depletion, but the effect would be less prominent than what we observe and would be observed for the other metals as well. However, all other metals (Zn, S, Cr, Ni, and Fe) for this system fit the expected depletion pattern well. TiII has a low-ionization potential, making it more sensitive to ionization than the other ions (e.g., FeII or SiII). There is no evidence for ionization for the DLA toward GRB120327A, which has a very high HI column density ($\log$ N(HI) = 22.07 from Bolmer et al. 2019), so that HI is expected to be quite efficient at shielding metals. Nucleosynthesis effects are also ruled out because we observe an underabundance, in contrast to an overabundance that we would expect from α-element enhancement. Finally, this does not appear to be a measurement problem (because of the way in which the Ti column density was measured) because the Ti line profile was well modeled by Bolmer et al. (2019), but was only based on one transition, which is the weak λ1910 TiII line.

3.4.6 *Nickel depletion*

We used measurements of Ni from 98 QSO-DLAs, eight GRB-DLAs, 23 Milky Way, 29 LMC and 12 SMC targets to characterize the depletion of Ni. The depletions of Ni for the different environments are shown in the right panels of Fig. 3.4, and the goodness-of-fit parameters are reported in Table 3.6.

Within the Milky Way, about 90% to 99% of Ni is depleted into solid dust grains, similarly to Fe. The highest depletion is observed for the Milky Way, where it ranges from about -1 to -2.4 dex. The depletion in the LMC ranges from -0.6 to -2 dex. Finally, for the QSO-DLAs, it is 0.2 to -1.9 dex, for the SMC, it is -0.7 to -1.4 dex, and for GRB-DLAs, it is -0.3 to -1.2.

The correlation between $\delta_{\rm Ni}$ and [Zn/Fe] is tight in all the environments (QSO-DLAs, GRB-DLAs, Milky Way, and LMC) when they are merged, but also individually. The strong linear relation is reflected in the r value of the merged fit (r = -0.96), as well as the high statistical significance ($p \ll 10^{-1}$) and the relatively small intrinsic scatter of $\sigma_{\delta_{\rm Ni}}$ = 0.10.

The best merged-fit coefficients for Ni are $A2_{\rm Ni}$ = 0.07 $\pm$ 0.02 and $B2_{\rm Ni}$ = -1.31 $\pm$ 0.03. Jones, Stark, and Ellis (2018) also based their work on the observations of relative abundances to estimate the depletion of Ni, but in sub-DLA absorption systems, with measurements tabulated by Quiret et al. (2016). They reported a depletion sequence that is characterized by $A2_{\rm Ni}$ = -0.03 $\pm$ 0.06 and $B2_{\rm Ni}$ = -1.19 $\pm$ 0.11, but with a relatively large intrinsic scatter $\sigma_{\delta_{\rm Ni}}$ = 0.18.

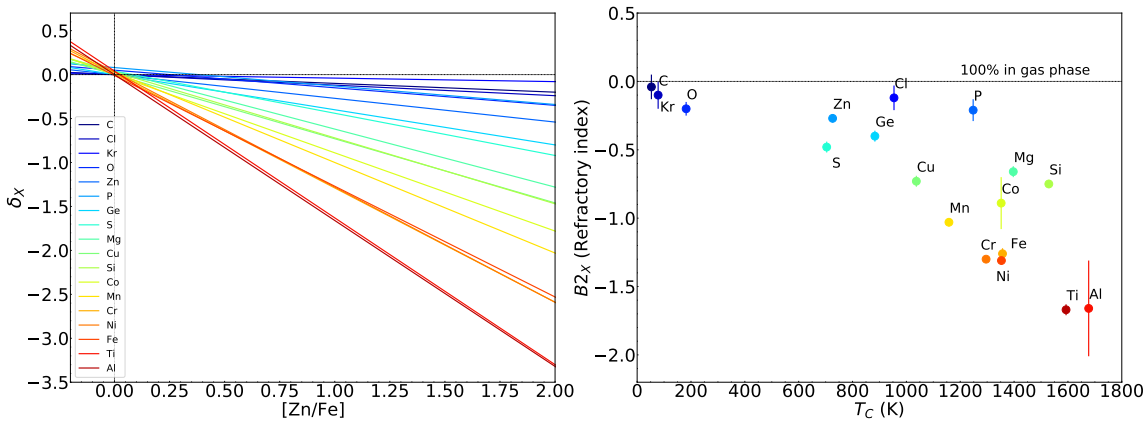


Figure 3.5: Merged fits of the dust depletion (δ_X) as a function of [Zn/Fe] for all the elements (left). The elements are sorted by depletion strength. The slopes of the fits of the depletion sequences $B2_X$ (or refractory index) as a function of the respective element condensation temperature T_c (right). The dust depletion relation with $B2_X$ is described by $\delta_X = A2_X + B2_X \times$ [Zn/Fe]. The condensation temperatures T_c are compiled by Lodders (2003). Elements with higher condensation temperatures are more strongly depleted into dust.

3.5 DISCUSSION

The sequences of the dust depletion for the majority of the elements from low-metallicity QSO-DLAs to the the Milky Way are linear. We note that while there is a dependence on [X/Zn] and [Zn/Fe] because both ratios have Zn in common, the same linear correlations are also found when [X/Si] and [X/P] is used instead of [X/Zn] (see De Cia et al., 2016). The slopes of these linear relations depend on the condensation temperature of the elements X. Thus, these relations are a result of dust depletion and not a dependence on the x-y axes.

The linear fits of the depletion sequences to all the available data of each element from all the environments (Milky Way, Magellanic Clouds, and QSO- and GRB-DLAs) we considered are presented in the left panel of Fig. 3.5. The fits become steeper for elements that are more strongly depleted into dust grains (refractory elements). In addition, the slope of the depletion sequences, $B2_X$, or refractory index, which is a measure of how strongly depleted an element is, decreases with the condensation temperature (Field, 1974; Savage and Sembach, 1996; Jenkins, 2009; Mattsson, Andersen, and Munkhammar, 2012; Tchernyshyov et al., 2015; De Cia et al., 2016). This relation can be observed in the right panel of Fig. 3.5, where the condensation temperatures T_c are compiled by Lodders (2003). The slope dependence on the refractory properties of metals confirms that the cause of the observed linear correlation is indeed dust depletion.

3.5.1 *Chromium*

Figure 3.1 shows that the zero intercept (at [Zn/Fe] = 0) of the Cr depletion sequence is not exactly zero, but instead it is higher by ~ 0.13 dex $\pm$ 0.01. This may suggest that chromium might partly be affected by an α-element enhancement.

Chromium belongs to the iron-group elements, and like half of the iron-group elements, it is mainly produced by type Ia supernovae (SNe Ia) (Nomoto et al., 1997; Travaglio et al., 2004; Kobayashi and Nomoto, 2009; Kobayashi, Karakas, and Lugaro, 2020). However, Cr is also a product of the α process, synthesized in the incomplete Si-burning regions of SN II during explosive nucleosynthesis (Kobayashi et al., 2006; Nomoto et al., 2006). Nomoto et al. (2006) showed that Cr can be copiously produced by core-collapse supernovae, with [X/Fe] ~ 0.1 for progenitor masses up to 20 $M_\odot$. Thus, core-collapse supernovae, which produce the α-elements, produce a significant amount of Cr after radioactive decay, leading to a small Cr overproduction. This would explain a small α-element enhancement, but it would not reach the enhancement of the α-elements (O, S, Si, and Mg). At no depletion ([Zn/Fe = 0]) we do observe [Si/Zn] $\sim$ [S/Zn] $\sim$ [Mg/Zn] $\sim$ [Ti/Zn] ~ 0.3 dex and [O/Zn] ~ 0.50 dex (which excludes a large α-element enhancement amplitude for Zn), but instead, we observe [Cr/Zn] ~ 0.13 dex $\pm$ 0.01. Prochaska and Wolfe (2002) reported a slight overabundance of Cr at low levels of [Zn/Fe], and Dessauges-Zavadsky et al. (2006) also reported an overabundance of Cr by ~ 0.13 dex, as well as an overabundance of the α-elements, consistent with our results. We did not take this small overabundance into account when we corrected for nucleosynthesis effects because Cr is not typically considered an α-element.

The highly depleted QSO-DLA point at [Zn/Fe] = 1.555 of the Cr depletion sequence shown in Fig. 3.2 is J1211+0833. The host galaxy of this system is found to be a chemically enriched, evolved, massive, and star-forming disk-like galaxy (Ma et al., 2018). This system is so chemically enriched that it has left the low-metallicity QSO-DLA regime and lies in the high-metallicity range of the Milky Way. It still follows the Cr dust depletion sequence, however. This further supports our results that the depletion sequences are consistent for all the environments.

3.5.2 *Ionization of sulfur*

Fig. 3.1 shows that SII column densities are higher when they are observed toward stellar sources (MW, SMC, and LMC) than in measurements toward background QSOs or GRBs. This difference between measurements of SII column densities in local and distant galaxies is clearly explained by ionization effects.

The ionization potential of SII is the highest (23.4 eV) of the elements considered in this work and is not easily ionized. This means that SII can be found in both HI and HII regions, while other elements are easily ionized to their double-ionized state in the HII regions, therefore they do not contribute to what we measure in the neutral ISM. This SII in the HII regions can add to what we consider to be present in the foreground HI gas. At the same time, the SII transitions are quite strong, which virtually prevents measurements of SII in lines of sight with large amounts of N(HI). Therefore SII is determined only in lines of sight

with low N(HI), which makes the contribution from the HII region of the star relatively important. Overall, DLA gas probes only the neutral phase, while the absorbers toward HII regions, for instance, in the Milky Way or the Magelanic Clouds, have an increased contribution from SII of the HII regions. The case of S is further discussed in Jenkins (2009), Jenkins and Wallerstein (2017).

3.5.3 *Nucleosynthesis as the cause of the deviations observed in the Magellanic Clouds*

Figures 3.4 and 3.2 show a potential bending of the dust depletion sequences for Ti, Mg, S, and Mn in the Magellanic Clouds. In particular, Ti, S, and Mg have a shallower and Mn a steeper slope in the Magellanic Clouds than in the Milky Way. This potential departure from a linear relation is more pronounced when the linear dependence of $\delta_{\rm Zn}$ on [Zn/Fe] is removed and nucleosynthesis is corrected for, that is, α-element enhancement and Mn underabundance. The deviations are not strictly significant (1.8σ, 2σ, 2.5σ, and 5σ for Mg, Ti, Mn, and S, respectively). A statistical analysis to quantify these deviations is presented in Appendix 3.A. The small deviations in relative abundances that we observe in the neutral ISM in the Magellanic Clouds are not randomly distributed among the elements. The overabundance of α-elements (Ti, Mg, and S, and difficult to tell for Si) and underabundance of Mn is systematic. Therefore, these tentative deviations might be due to α-element enhancement and Mn underabundance in the Magellanic Clouds that we did not take into account in our initial assumptions.

The production of α-elements is dominated by core-collapse SNe (Kobayashi et al., 2006; Kobayashi and Nomoto, 2009), while the production of Mn is dominated by SN Ia (Gratton, 1989; Feltzing, Fohlman, and Bensby, 2007; Kobayashi and Nomoto, 2009). This makes it quite likely that the deviations we observe are caused by nucleosynthesis effects. In our initial analysis, we corrected for α-element enhancement and Mn underabundance assuming a distribution of the [α/Fe] with metallicity with a classical plateau - knee distribution (e.g., McWilliam (1997)), also for the Magallanic Clouds.

As described in Section 3.4.3, the exact position of the α-element knee is only poorly constrained in the Magellanic Clouds. However, small changes in the knee position do not affect our results because the points that deviate from the fit are far from the knee position. In addition, the metallicities of the neutral ISM of the systems that show deviations are in the range in which we did not expect α-element enhancement (De Cia et al., 2024).

When we assume a constant over- or underabundance plateau instead, the previously deviating points follow the linear fit. The shapes of the different assumptions on the nucleosynthetic curves for the α-elements and for Mn are shown in Fig. 3.6. The dust depletion sequences for the α-elements and for Mn after correcting for nucleosynthesis effects in the Magellanic Clouds assuming a constant over- or underabundance plateau are shown in Fig. 3.3. All elements after the new corrections follow linearity, except for S, which is known to be further enhanced toward HII regions by ionization. This might mean that the nucleosynthetic curves for the Magellanic Clouds might be much different from what was previously assumed, and there is only a constant plateau instead. This might be due to a recent burst of star formation in the Magellanic Clouds, which implies that their star formation history is likely to be different than in the Milky Way.

The overabundance of α-elements and underabundance of Mn in the Magellanic Clouds was also observed and discussed in previous studies (Vladilo, 2002; Guber and Richter, 2016; Jenkins and Wallerstein, 2017; De Cia, 2018). Hasselquist et al. (2021) observed stellar α-element enhancement in the Magellanic Clouds and an upturn of the [α/Fe] plateau, which they interpreted as due to a very recent burst of star formation. The α-element enhancement may be local and follow the recent star formation activity. On the other hand, other works failed to find a clear [α/Fe] plateau in the LMC (e.g., Van der Swaelmen et al., 2013). It is possible that we observe α-element enhancement and Mn underabundance toward limited individual systems rather than systematically over the entire metallicity range. Our observations probe the neutral ISM toward hot young OB stars, which means that they may be showing α-element enhancement and Mn underabundance. Additionally, it is possible that α-element enhancement can be observed in the neutral ISM toward young stars following a recent star formation burst, while there was no time for a new generation of stars to form and fully show the α-element enhancement.

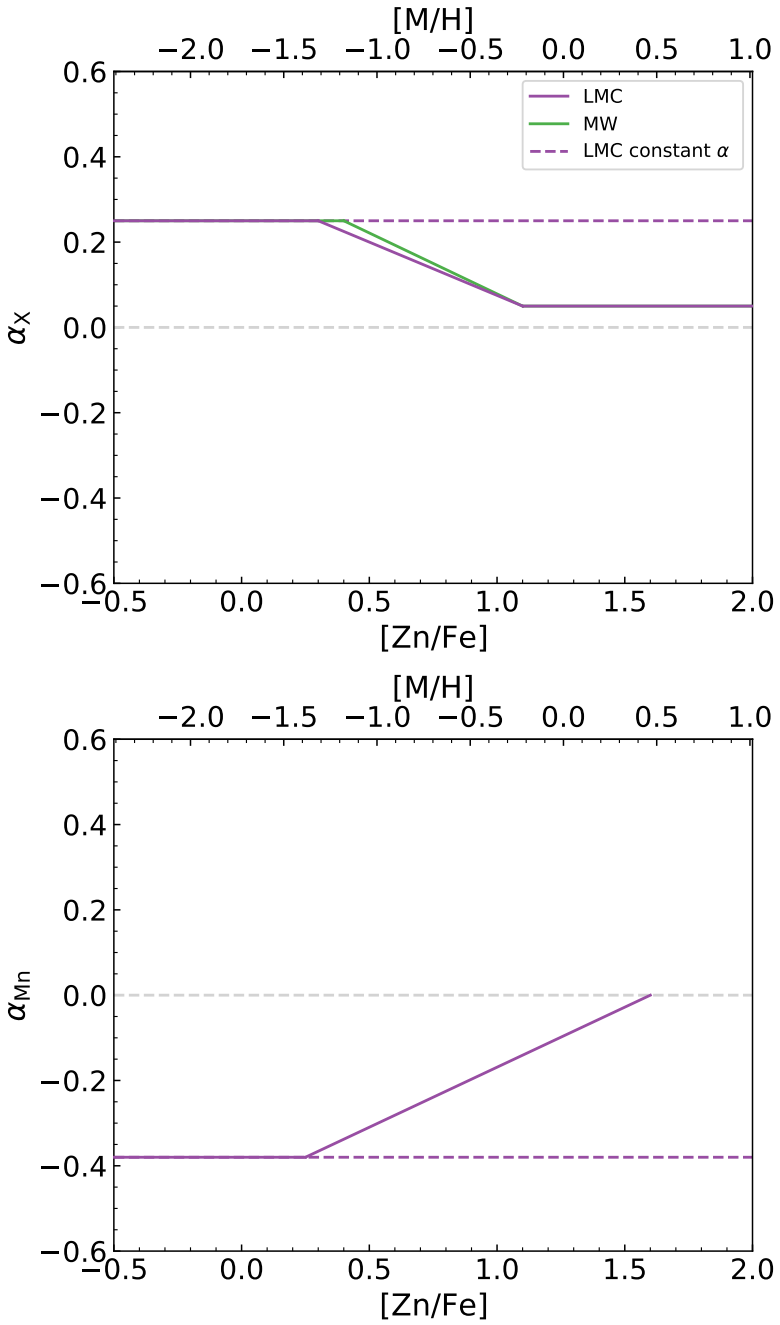


Figure 3.6: Assumed nucleosynthetic over- or underabundances α_X for the α-elements X (S, Si, Mg, and Ti) and Mn with respect to [Zn/Fe] and metallicity [M/H]. The solid green curve shows the Milky Way, the solid purple curve shows the LMC as adopted from de Boer et al. (2014), and the dashed purple curve shows the LMC with a constant over- or underabundance plateau. For the plateau of the α-elements, we used as reference α_S = 0.25.

3.6 SUMMARY AND CONCLUSIONS

We characterized the dust depletion of several metals in different environments from the Milky Way, the Magellanic Clouds, and DLAs toward GRBs and QSOs based on the relative abundances of metals with different refractory properties (or how easily they incorporate into dust grains). We collected all the available literature measurements of metal column densities in these environments, making this a comprehensive study of relative chemical abundances of metals and for different environments. We measured new column densities of Ti and Ni in 70 QSO-DLAs from high-resolution UVES spectra from the sample of De Cia et al. (2016).

We observed and fit the dust depletion sequences and the relative abundances for all the elements. We further focused on the dust depletion of Ti and Ni, for which we also provided new column density measurements.

We observe a slight deviation from the linear fits of the depletion δ_X for Ti, S, Mg, and Mn in the Magellanic Clouds. A potential cause of the anomaly in these elements might be the α-element enhancement and Mn underabundance in the Magellanic Clouds. When a constant over- (under-) abundance plateau of the α-elements (Mn) is assumed, the deviations disappear and all environments for all the elements follow linearity. The observed α-element enhancement and Mn underabundance in the neutral ISM at a wide range of metallcities might be due to recent bursts of star formation in the Magellanic Clouds.

We observe a Cr overabundance of ~ 0.13 dex $\pm$ 0.01. This suggests that it might be affected by an α-element enhancement, while Cr is not typically considered an α-element.

The column densities of SII seem to be higher for local galaxies (Milky Way, SMC, and LMC). This can be explained by an additional contribution of their HII regions to the measured SII column densities.

The tendency of each element to be depleted into dust varies depending on its condensation temperature. This dependence confirms that the the depletion sequences are indeed driven by dust depletion and not by other physical processes.

Overall, the dust depletion of the elements are well described with linear fits to the merged data, despite the small deviations that statistically are not significant for the merged fit. Nevertheless, the small deviations seem to be due to nucleosynthesis and not to dust depletion. The dust depletion sequences are virtually the same for different environments, which implies that dust depletion behaves in the same way, regardless of the environment. This might mean that the process that mostly causes the build-up of dust grains is independent of the star-formation history of the different galaxies, which likely changes dramatically from system to system. This suggests that the growth of dust grains in the ISM is an important process of dust formation.

Acknowledgements: We thank the referee Sandra Savaglio for the detailed and constructive report that improved this manuscript. CK, ADC, JKK and TRH acknowledge support by the Swiss National Science Foundation under grant 185692. KEH acknowledges support from the Carlsberg Foundation Reintegration Fellowship Grant CF21-0103. This paper

makes use of the Python code VoigtFit available on https://github.com/jkrogager/VoigtFit. This research has made use of NASA's Astrophysics Data System.

3. A STATISTICAL ANALYSIS FOR MN AND THE α-ELEMENTS

We estimated the χ^2_ν between the individual datasets (QSO-DLAs, GRB-DLAs, Milky Way, LMC, and SMC) and the merged fit (the fit assuming all datasets merged together) for Mn and for the α-elements Ti, S, Si, and Mg, taking both x and y uncertainties into account. This was used to calculate the difference $\Delta\chi^2_\nu$ by subtracting the χ^2_ν of the merged fit, which can quantify the observed deviations and their significance.

For Ti, the smallest difference from the merged fit is observed for the Milky Way with $\Delta\chi^2_\nu = 0.07$, while the largest difference from the merged fit is observed for the LMC with $\Delta\chi^2_\nu = 0.97$ with a 2σ significance, but with only eight degrees of freedom used for the fit. For the Milky Way, QSO-DLAs, and the LMC, we find a $\chi^2_\nu > 1$. This might be due to underestimated uncertainties, natural scatter of the data, or a poor fit. For the SMC, the uncertainties are probably overestimated, resulting in a $\chi^2_\nu < 1$. The individual fits are well constrained, with r values ranging from -0.99 (SMC) to -0.81 (Milky Way) and high statistical significance, with low p-values ($p \ll 10^{-1}$, see Table 3.5). The lowest statistical significance is recorded for the LMC, but the fit was only performed on ten data points. The linear fit to the Ti depletions in all environments merged together has an r value of -0.97 and a statistical significance ($p \ll 10^{-1}$).

For S, the smallest difference from the merged fit is estimated for QSO-DLAs with $\Delta\chi^2_\nu = 0.02$, and the largest difference is measured for the LMC with $\Delta\chi^2_\nu = 2.02$ with 5σ significance. This deviation is due to ionization effects (see Section 3.5.2), however. Si does not significantly depart from the merged fit, and we do not report any statistically significant deviation for any of the environments. The merged fit remains a good description of the distribution. For Mg, we observe an offset between the merged fit and the Milky Way fit, with a difference of $\Delta\chi^2_\nu = 0.78$ and 1.8σ significance and a large scatter for all the environments. The merged fit remains the best description of the distribution. For Mn, we observe an offset of the Milky Way fit from the merged fit with a difference of $\Delta\chi^2_\nu = 1.05$ within 2.5σ, but only a few points were used for the fit with a large scatter. While the SMC points have a small intrinsic scatter, the difference from the merged fit is $\Delta\chi^2_\nu = 0.93$ within 2.2σ. We conclude that while we see a slight tendency of some elements to depart from the linear fit, none of these deviations are statistically significant, and the overall distribution is best described by the merged linear fit.

3.B ELEMENTS WITH LIMITED COVERAGE

We added many more elements (C, Cl, Kr, Ge, Cu, Co, Al and O) to the current dust depletion scheme whose depletions have not been characterized before using this formalism. We used measurements for the Milky Way and QSO-DLAs, but only few data are available and only some LMC measurements for O. The relative abundances of the elements X as a function of [Zn/Fe] are shown in Fig. 3.7, and their dust depletion sequences are

presented in Fig. 3.8. Because of the small number of degrees of freedom, the fit was made assuming zero intercept ($A2_x$ = 0.00). This can be justified by the fact that there should be zero depletion at the lowest overall strengths of depletion, [Zn/Fe] = 0.

For O and Al, the largest number of QSO-DLA data points are available ofthe elements with limited coverage. However, their depletion coefficients should be used with caution because of potential issues with line saturation. The OI measurements in QSO-DLAs were taken from De Cia et al. (2016), where they were based on high-resolution data and mostly included the few systems for which OI could be estimated based on multiple lines, including weak OI lines in the Ly-α forest, and only in a very few cases using the OI λ1302 line alone when it was not saturated. For the Milky Way, the weak OI lines are typically used (e.g., Jenkins, 2009, and references therein). For AlII, the QSO-DLA measurements were taken from Berg et al. (2015). This is a large collection from the literature of measurements made from the only available AlII λ1670 line, which is often saturated. Therefore, these measurements are not very reliable. This is probably the cause of the large scatter in Fig. 3.8. Nevertheless, because Al is very highly depleted into dust grains, it is still useful to include the rough estimate on its depletion despite the very large uncertainties (e.g., $B2_{Al}$ = -1.66 $\pm$ 0.35). The $A2_X$ ($A2_X$ = 0.00) and $B2_X$ coefficients along with the Pearson correlation coefficients of the dust depletion sequences of elements with limited coverage resulting from the fit are reported along with the rest of the elements in Table 3.4.

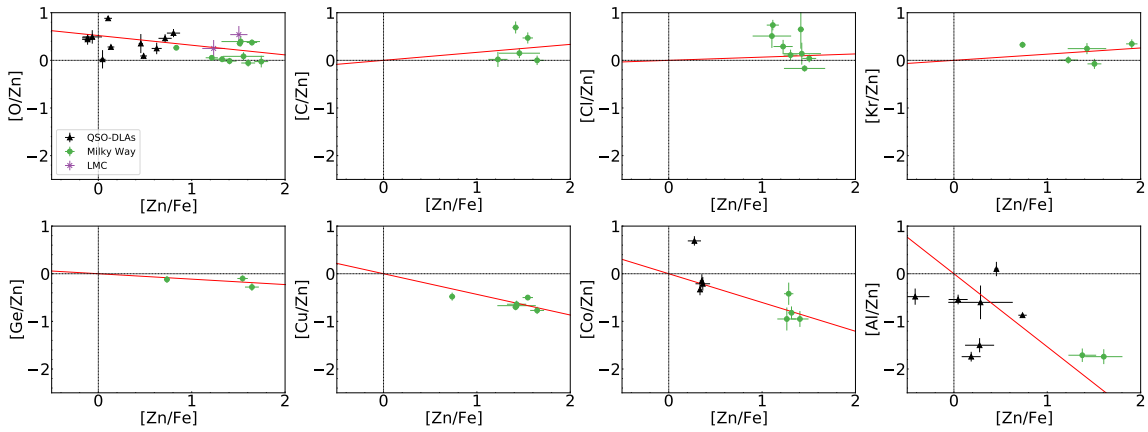


Figure 3.7: Relative abundances of element X with respect to Zn against [Zn/Fe]. The black triangles show QSO-DLAs, the green dots show the Milky Way, and purple stars show the LMC. The red line shows the linear fit to the data.

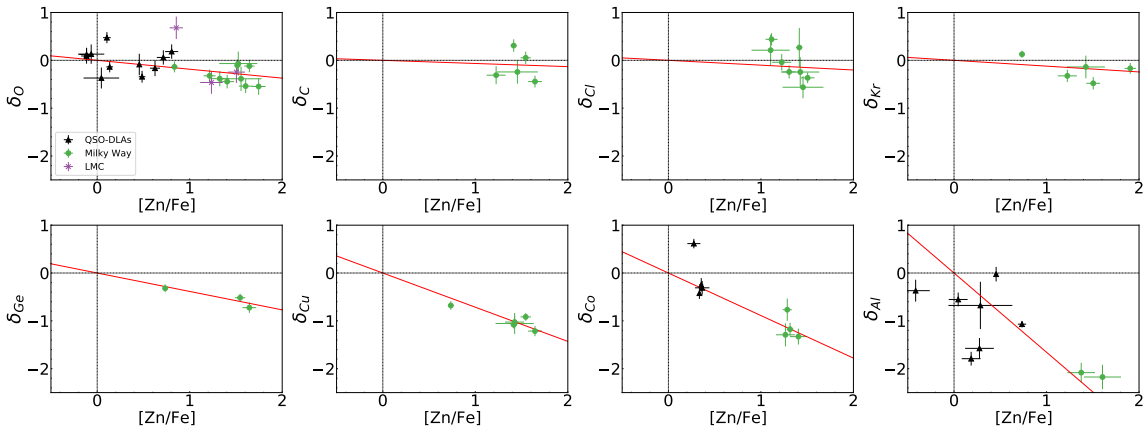


Figure 3.8: Dust depletion of element X (δ_X) against [Zn/Fe]. The black triangles show QSO-DLAs, green dots show the Milky Way, and purple stars show the LMC. The red line shows the linear fit to the data. These elements have limited coverage especially at low depletion levels (QSO-DLAs).

3.C VELOCITY PROFILES OF THE NEW NI AND TI DLA MEASUREMENTS

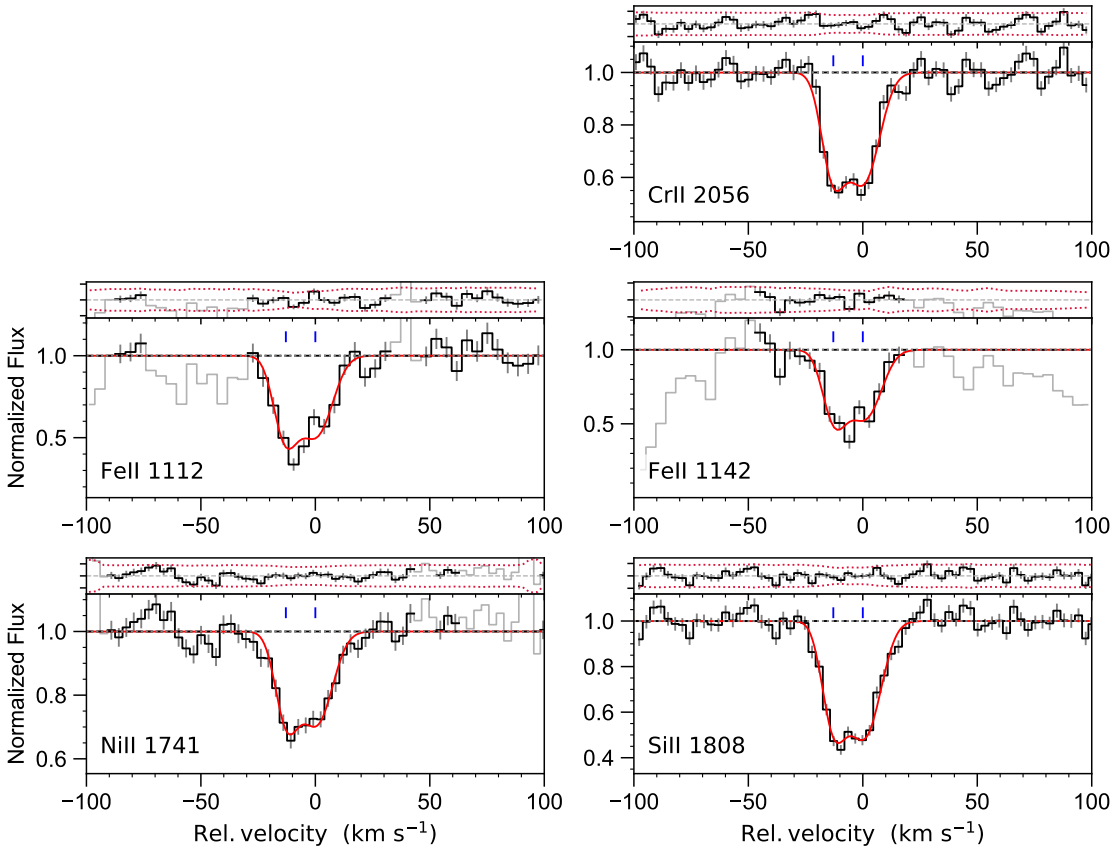


Figure 3.9: Velocity profiles of selected low-ionization transition lines from the DLA system at z_{abs} = 2.02484 toward Q 0010−002. Masked regions are shown in gray. The top subpanels show the residuals, and the blue tick marks show the individual velocity components.

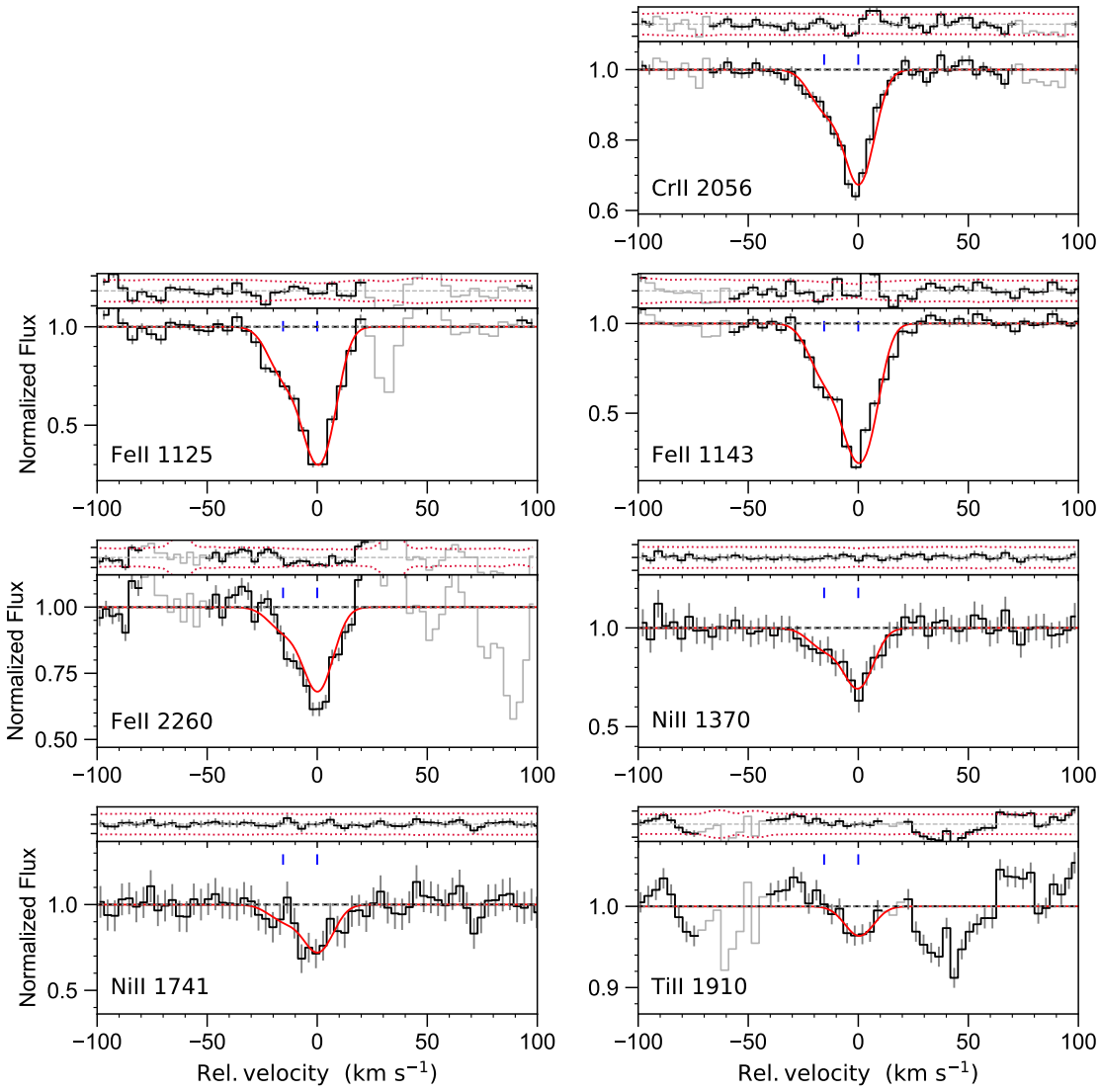


Figure 3.10: Velocity profiles of selected low-ionization transition lines from the DLA system at $z_{abs} = 2.67142$ toward Q 0058−292.

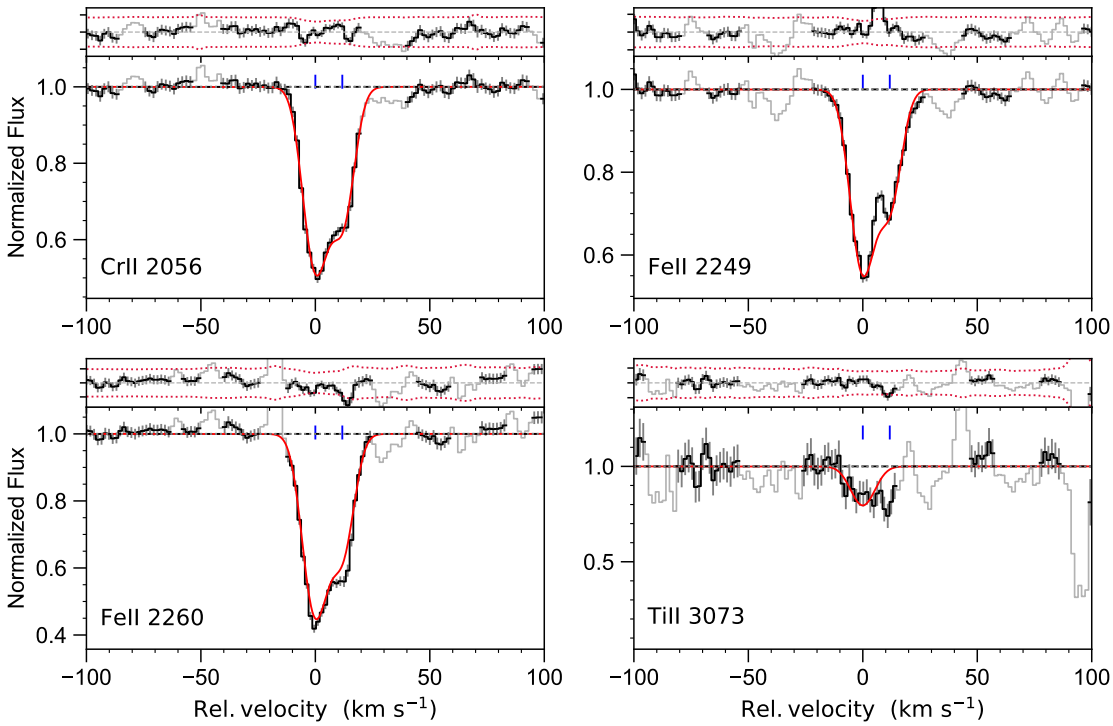


Figure 3.11: Velocity profiles of selected low-ionization transition lines from the DLA system at $z_{abs} = 2.30903$ toward Q 0100+030.

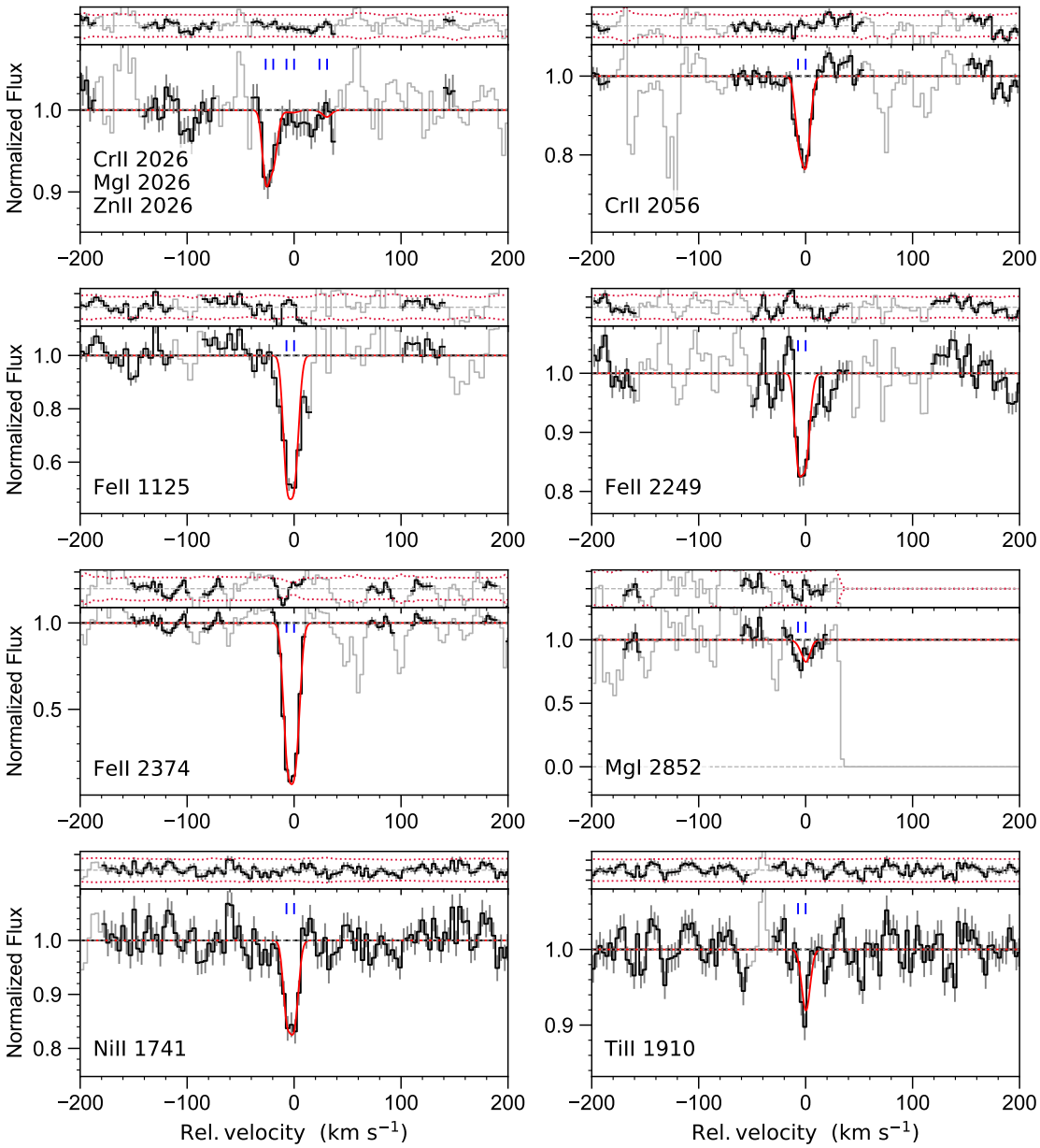


Figure 3.12: Velocity profiles of selected low-ionization transition lines from the DLA system at $z_{abs} = 2.36966$ toward Q 0102−190a.

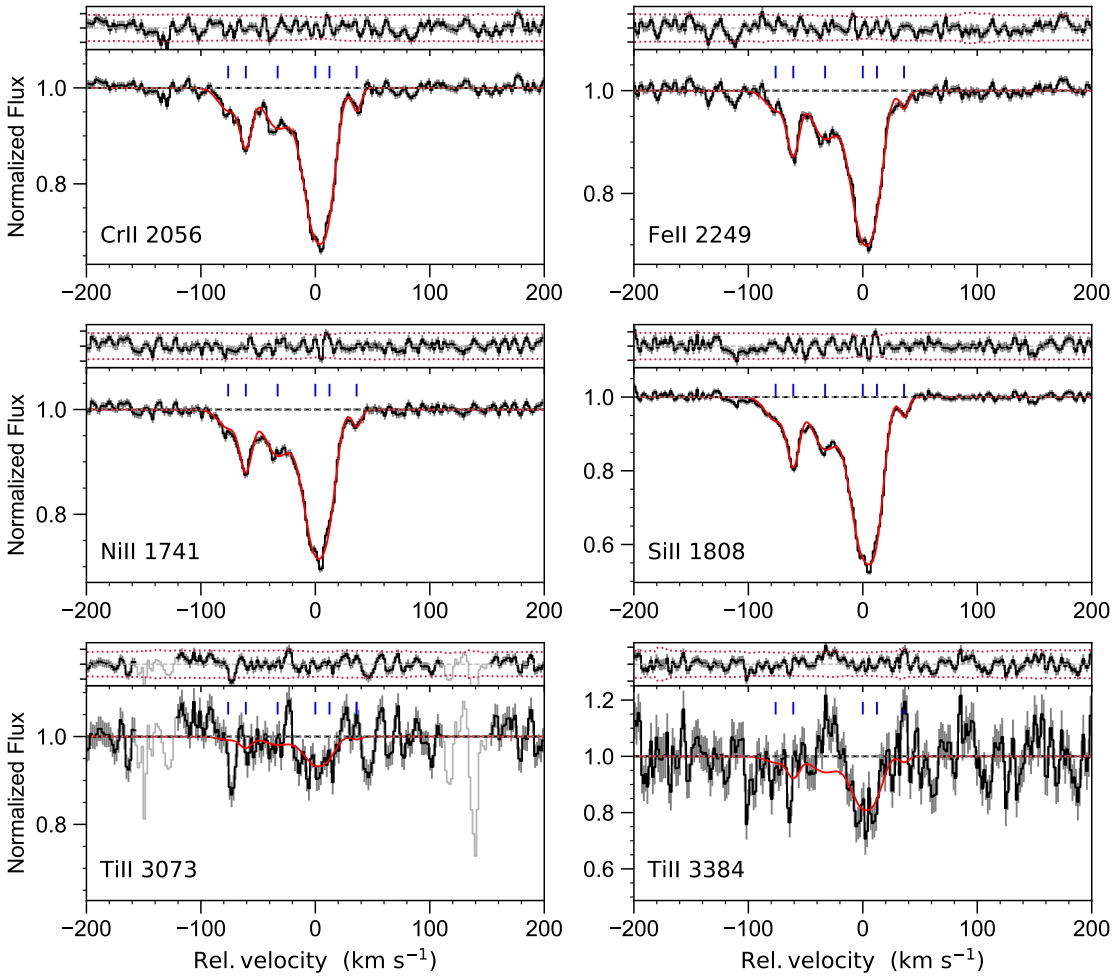


Figure 3.13: Velocity profiles of selected low-ionization transition lines from the DLA system at $z_{abs} = 1.91267$ toward Q 0405−443a.

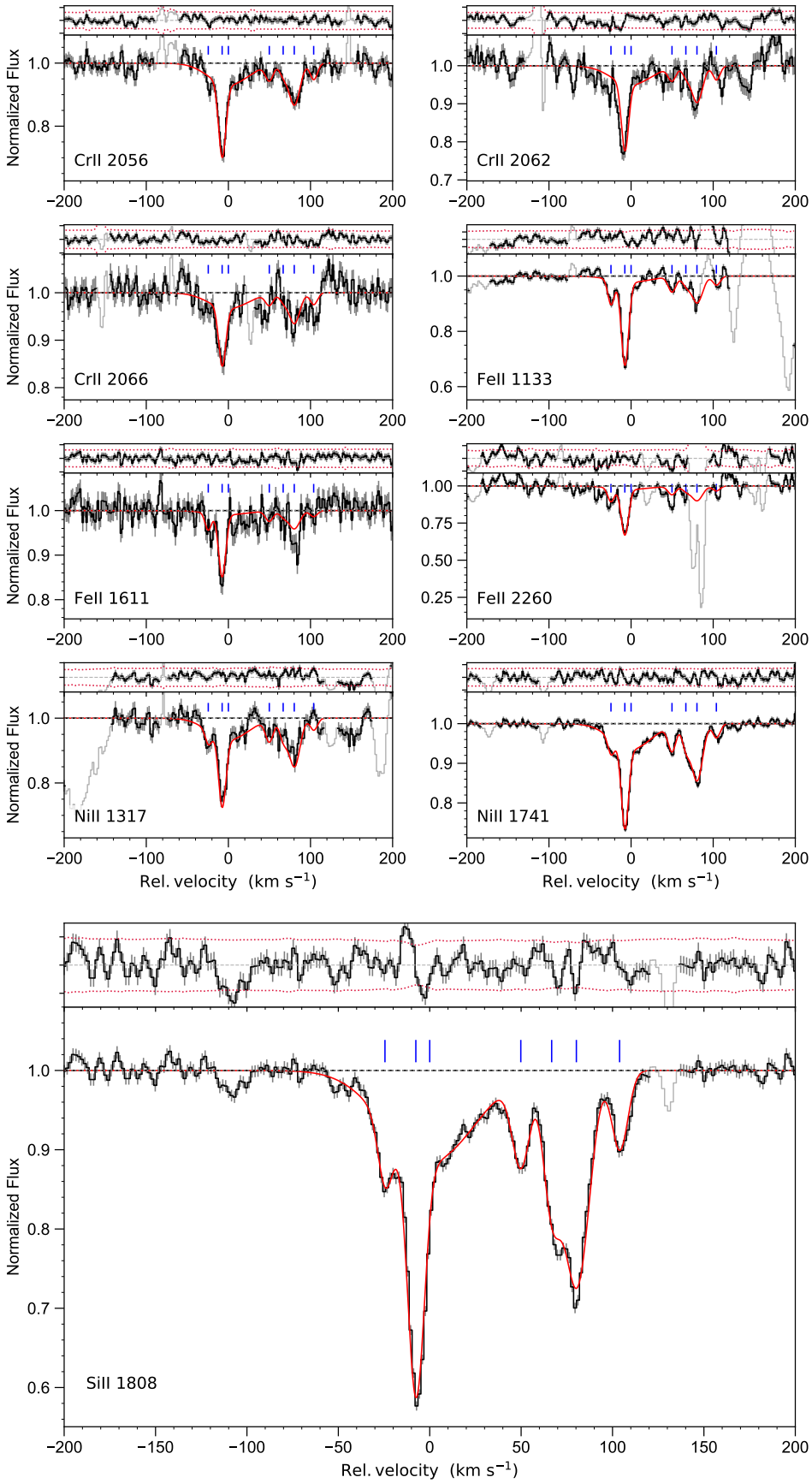


Figure 3.14: Velocity profiles of selected low-ionization transition lines from the DLA system at $z_{abs} = 2.55000$ toward Q 0405−443b.

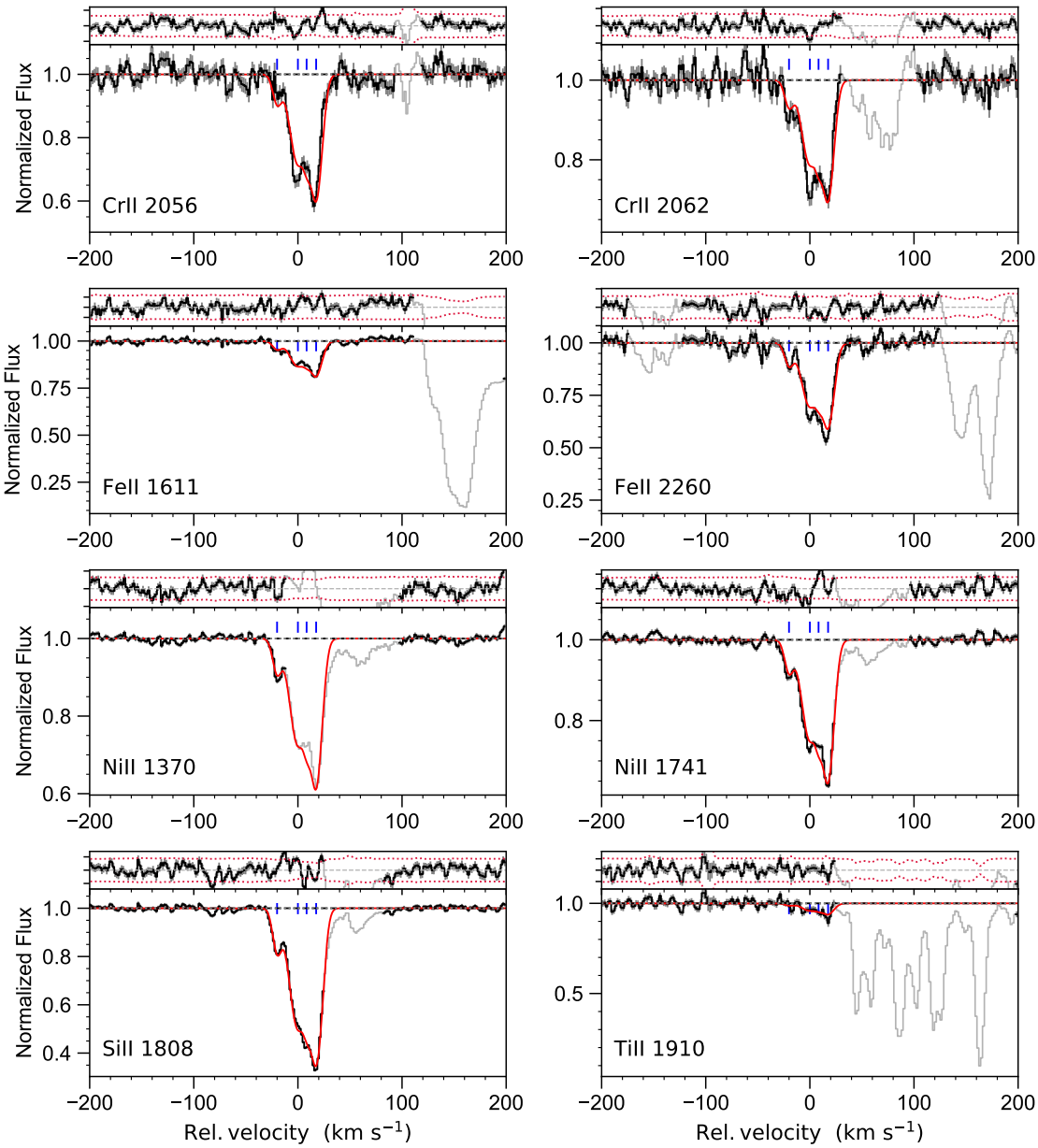


Figure 3.15: Velocity profiles of selected low-ionization transition lines from the DLA system at $z_{abs} = 2.59466$ toward Q 0405−443c.

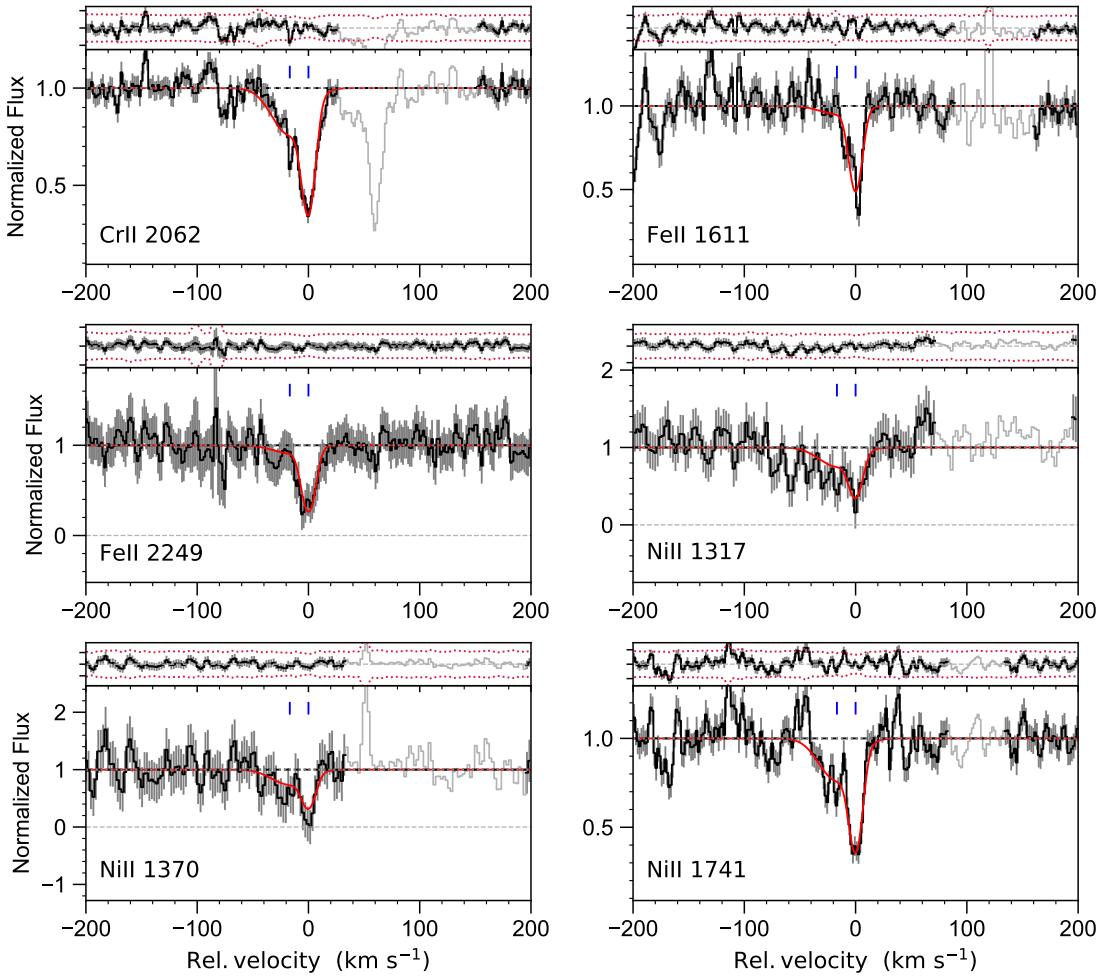
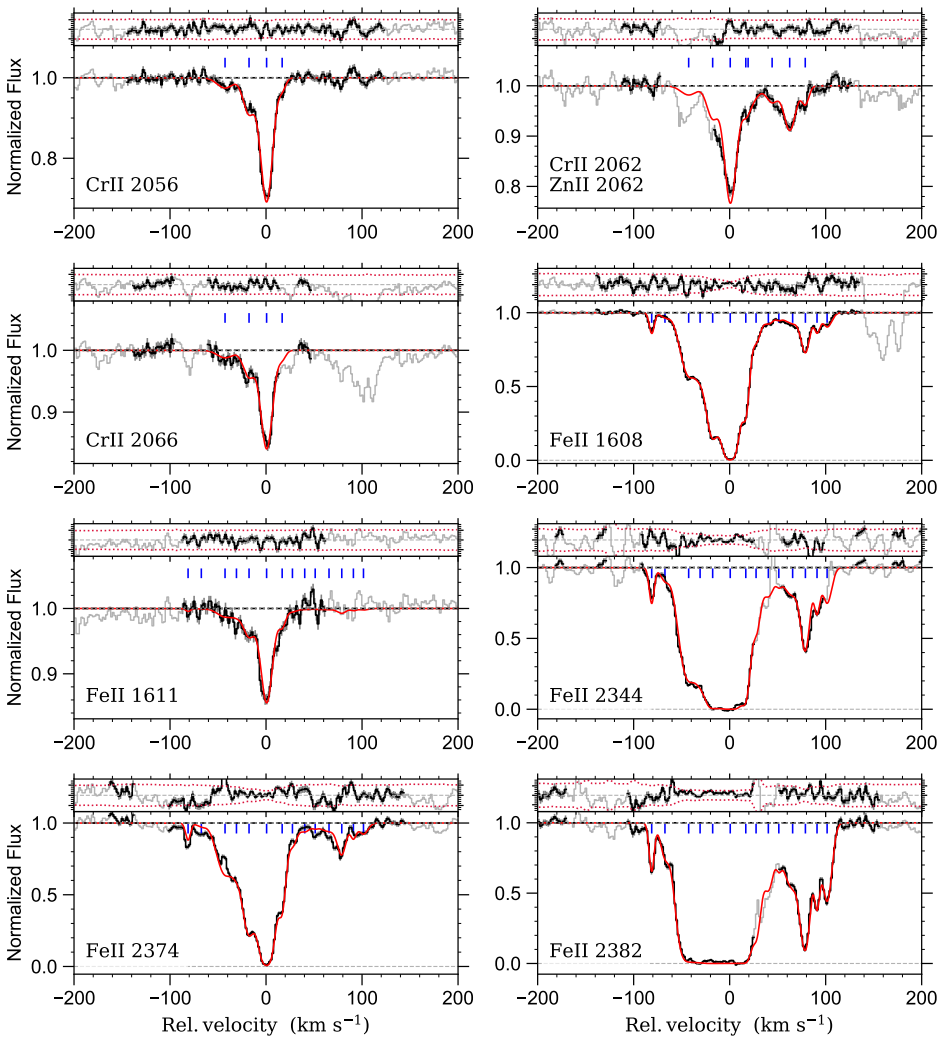


Figure 3.16: Velocity profiles of selected low-ionization transition lines from the DLA system at $z_{abs} = 2.03956$ toward Q 0458−020.


Normalized Flux
CrII 2056
CrII 2062
ZnII 2062
CrII 2066
FeII 1608
FeII 1611
FeII 2344
FeII 2374
FeII 2382
Rel. velocity (km s^{-1})
Rel. velocity (km s^{-1})

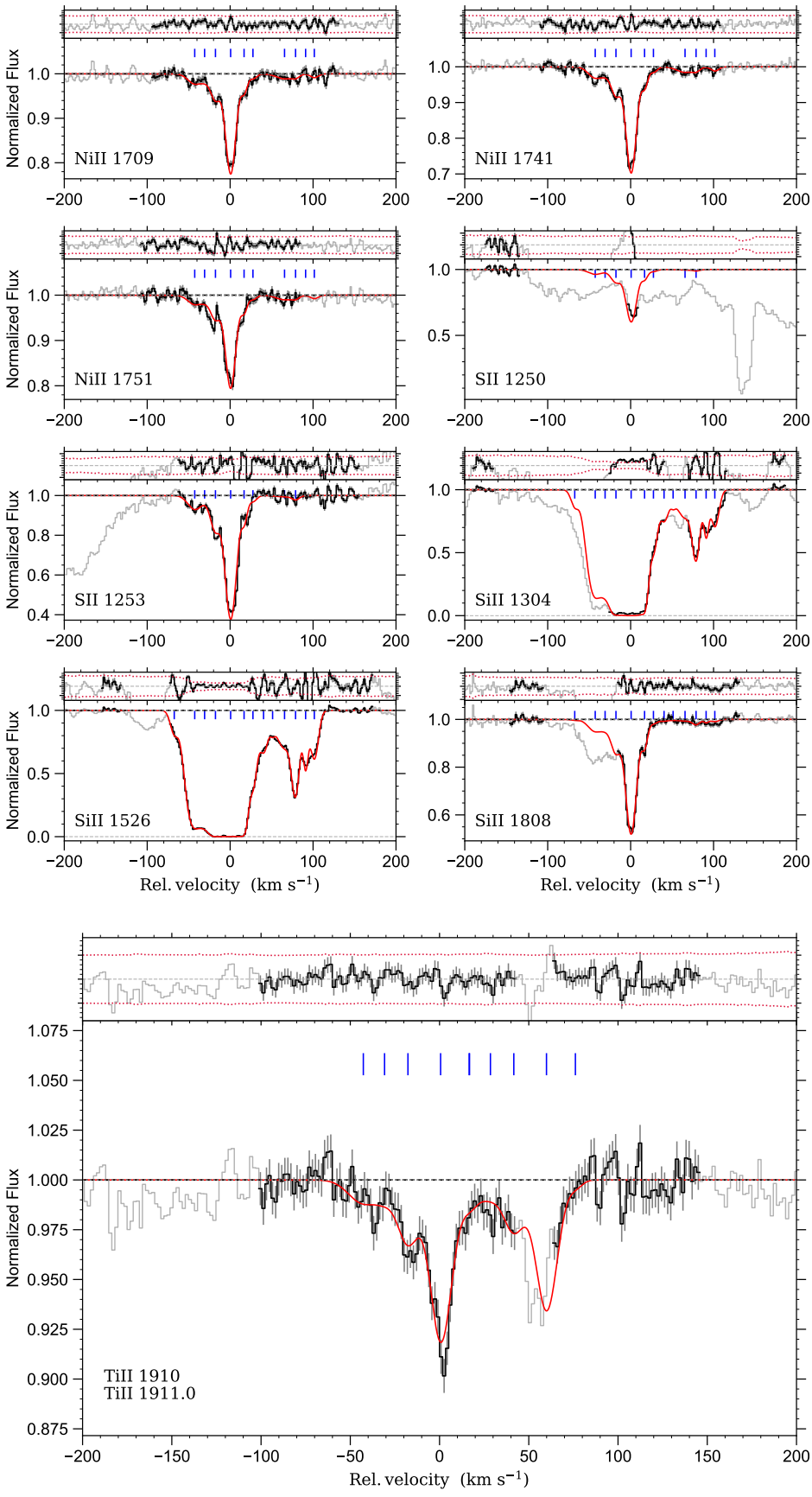
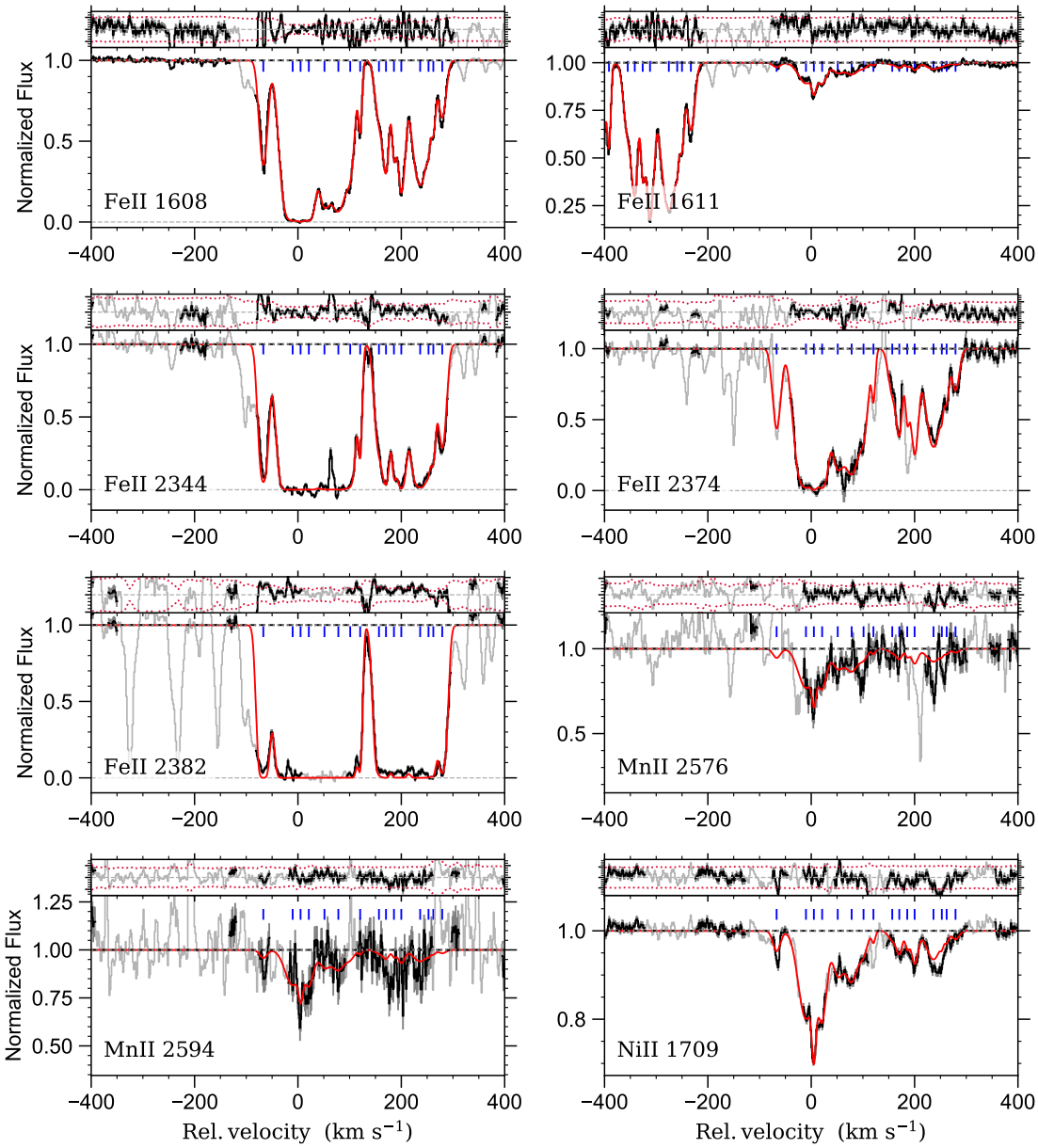


Figure 3.17: Velocity profiles of selected low-ionization transition lines from the DLA system at $z_{abs} = 2.14105$ toward Q 0528−250a.


Normalized Flux
FeII 1608
FeII 1611
FeII 2344
FeII 2374
FeII 2382
MnII 2576
MnII 2594
NiII 1709
Rel. velocity (km s^{-1})
Rel. velocity (km s^{-1})

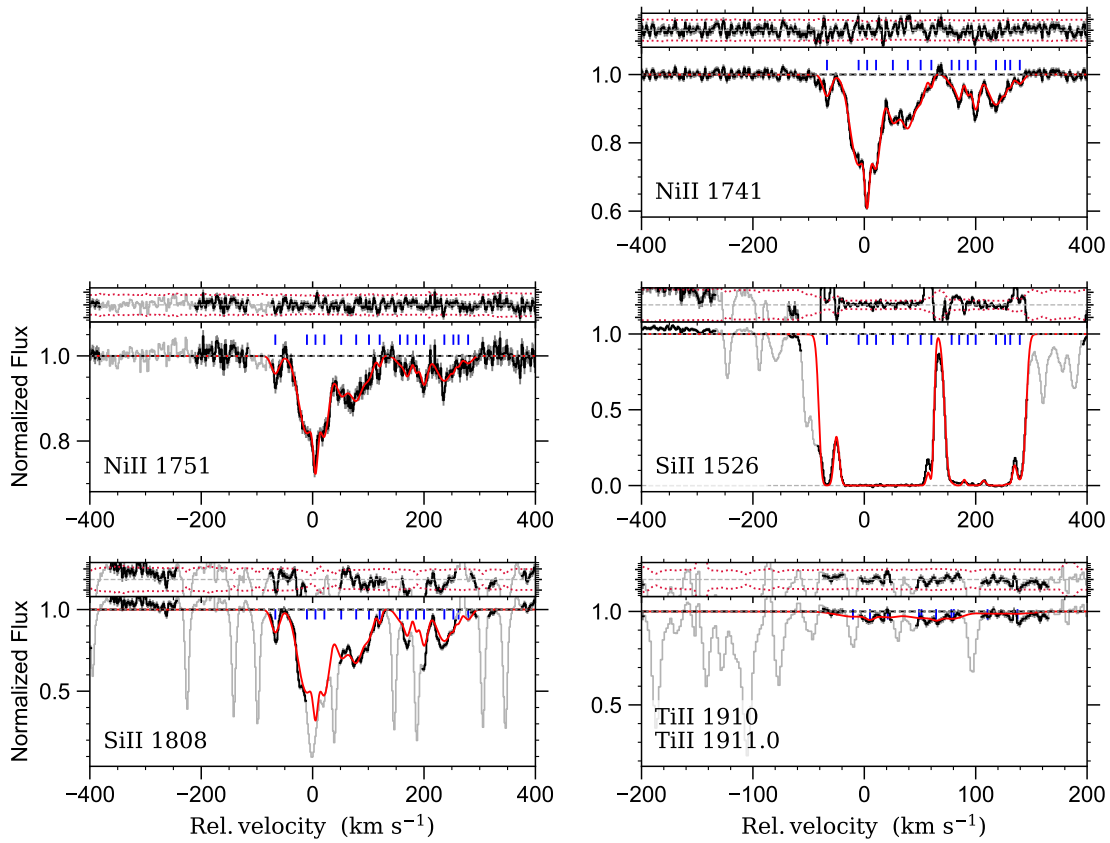


Figure 3.18: Velocity profiles of selected low-ionization transition lines from the DLA system at $z_{abs} = 2.81111$ toward Q 0528−250b.

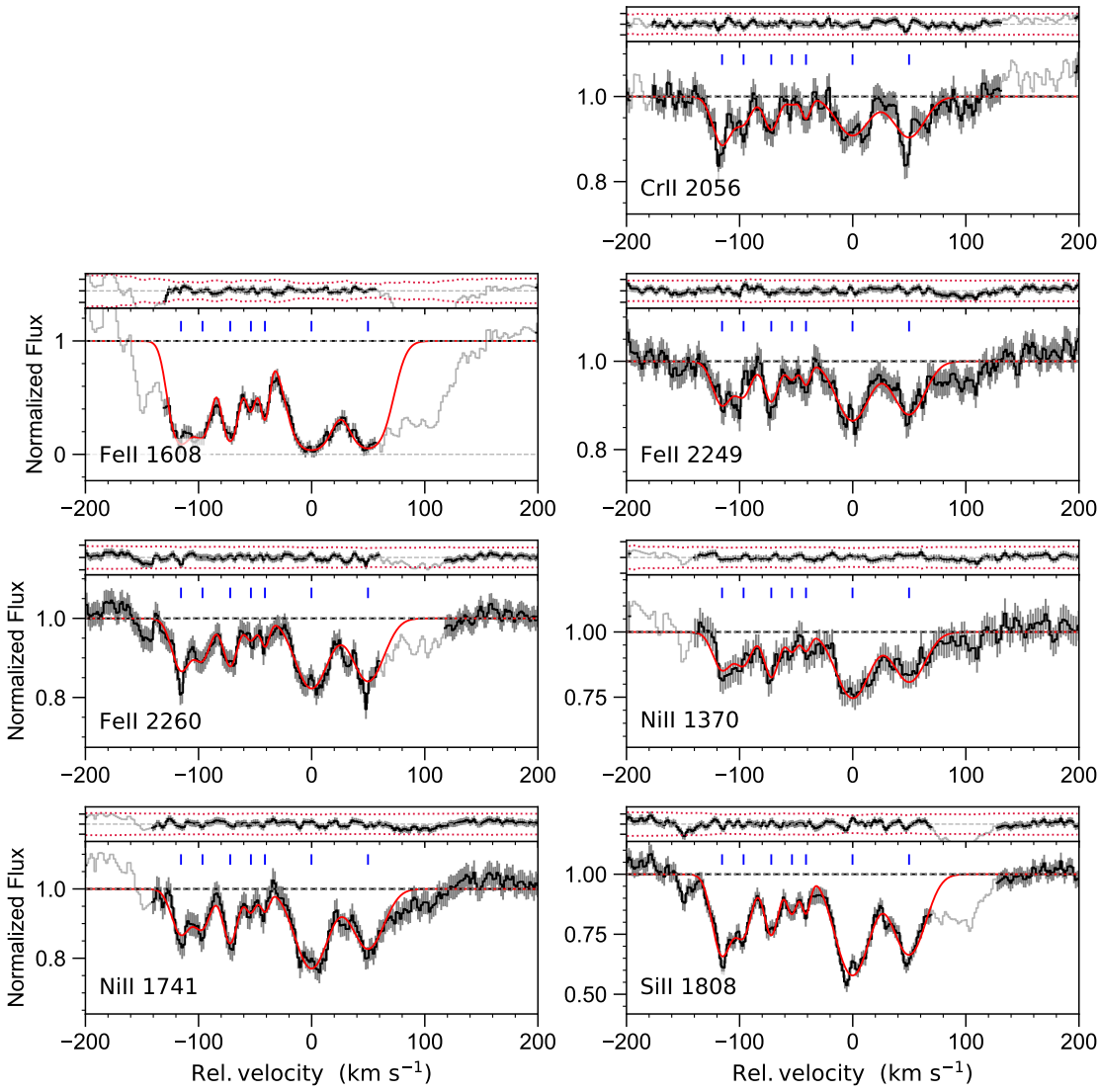
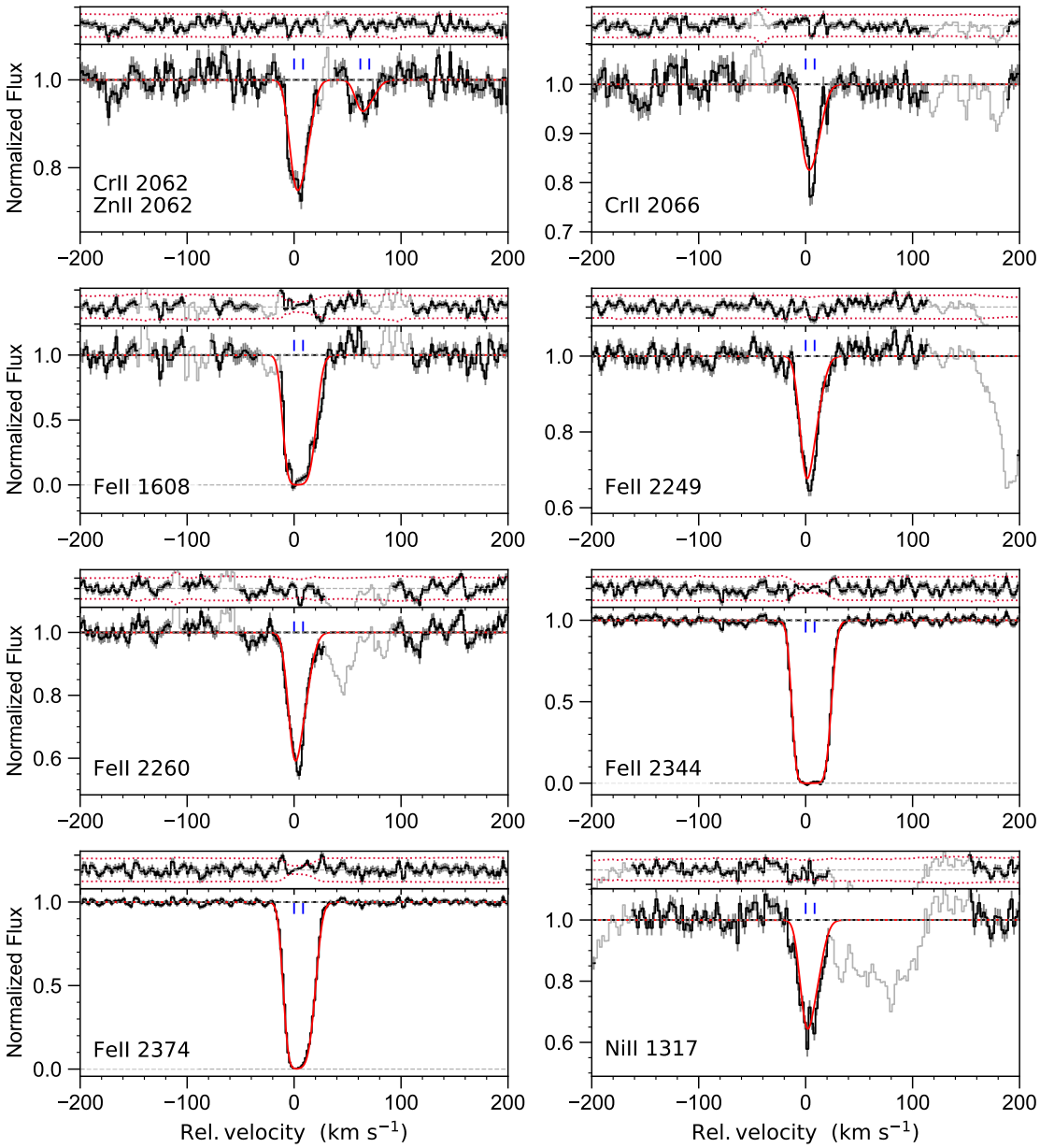


Figure 3.19: Velocity profiles of selected low-ionization transition lines from the DLA system at $z_{abs} = 1.96221$ toward Q 0551−366.


Normalized Flux
CrII 2062
ZnII 2062
CrII 2066
FeII 1608
FeII 2249
FeII 2260
FeII 2344
FeII 2374
NiII 1317
Rel. velocity (km s^{-1})
Rel. velocity (km s^{-1})

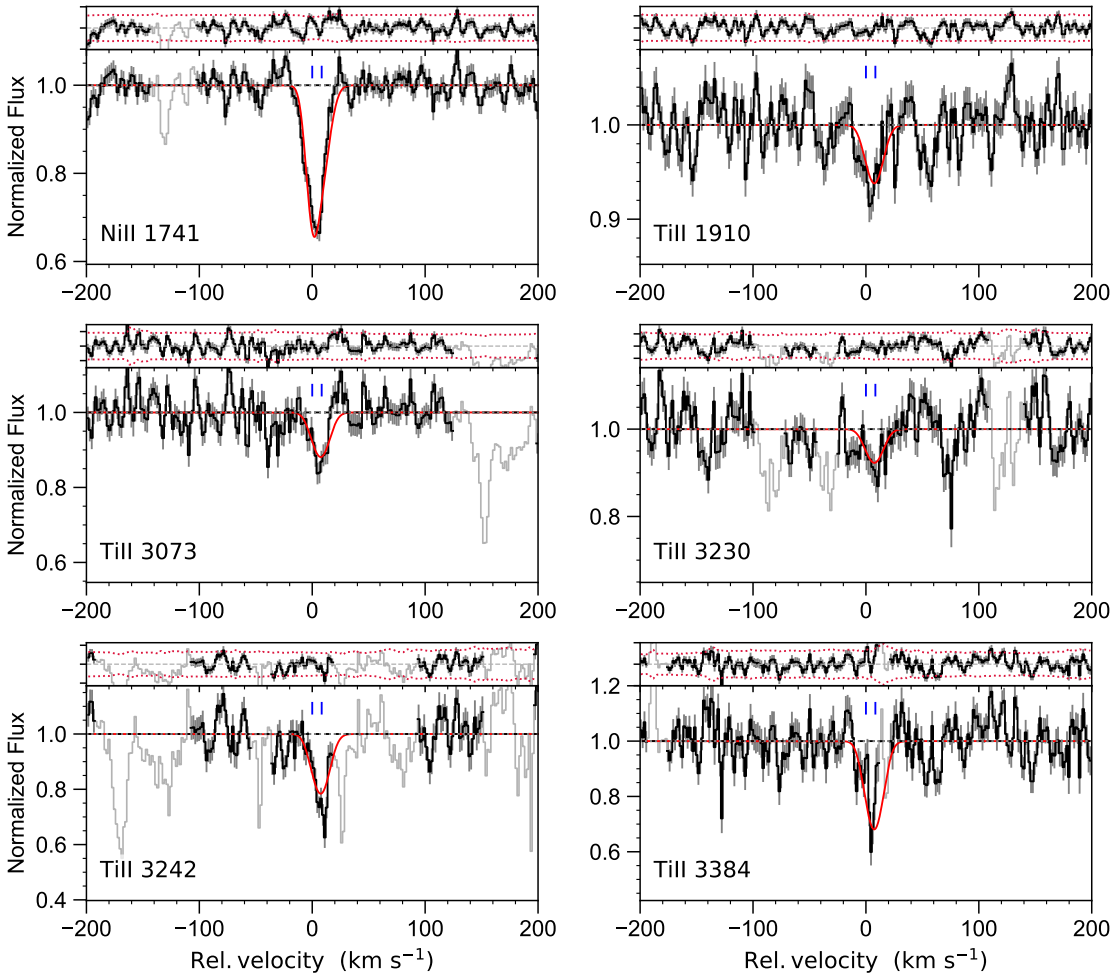


Figure 3.20: Velocity profiles of selected low-ionization transition lines from the DLA system at $z_{abs} = 1.86384$ toward Q 0841+129a.

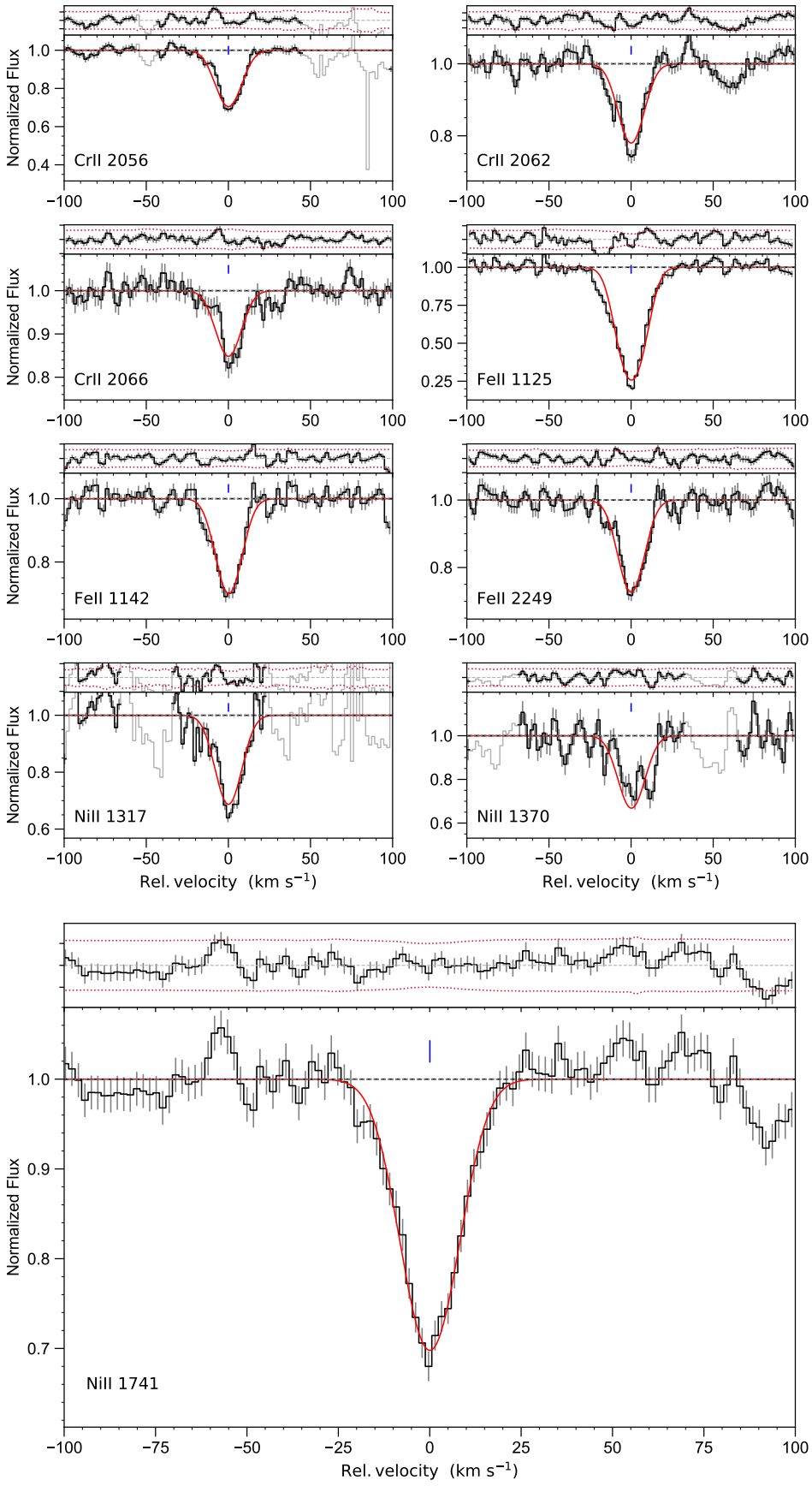


Figure 3.21: Velocity profiles of selected low-ionization transition lines from the DLA system at $z_{abs} = 2.37452$ toward Q 0841+129b.

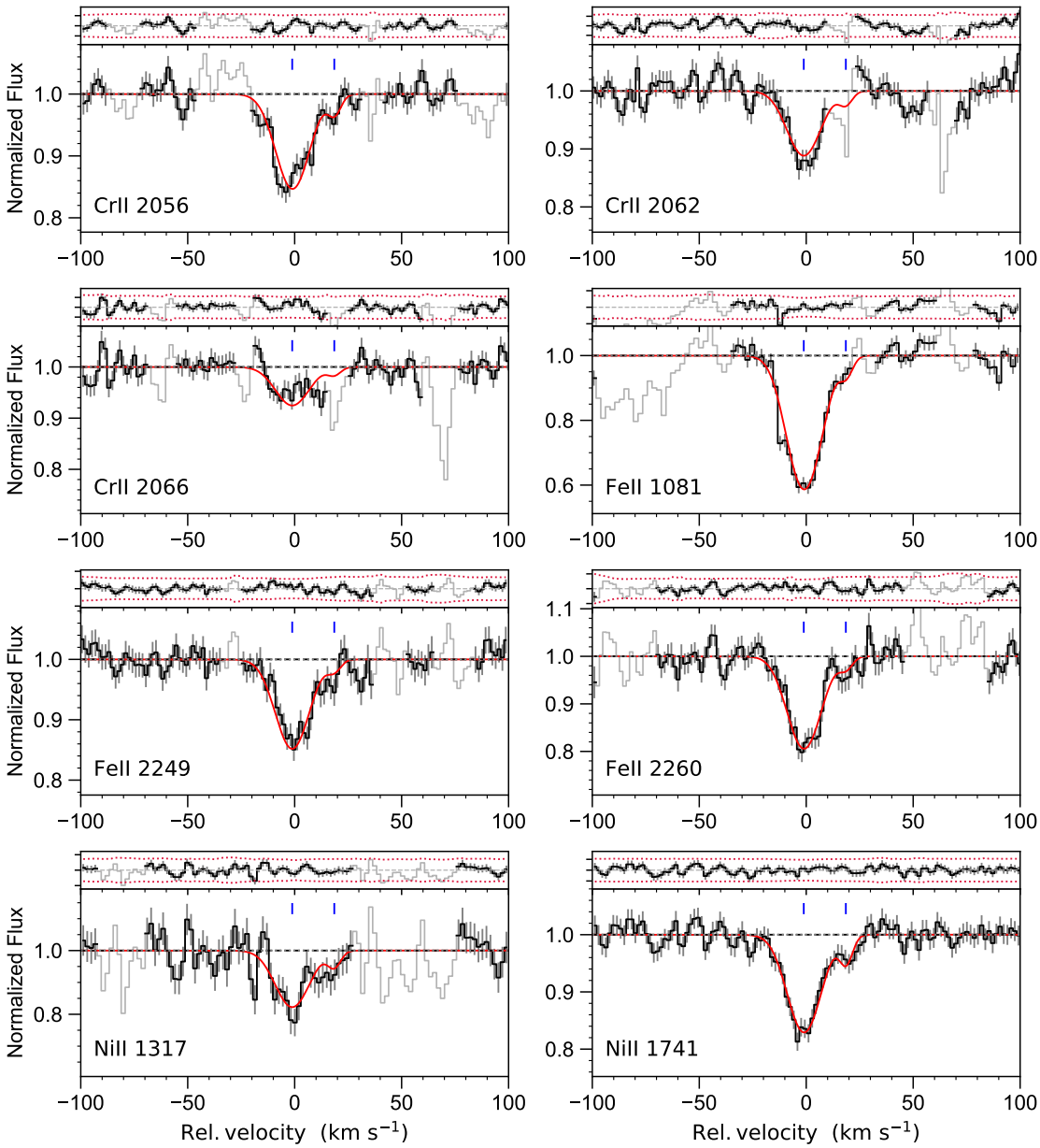


Figure 3.22: Velocity profiles of selected low-ionization transition lines from the DLA system at $z_{abs} = 2.47622$ toward Q 0841+129c.

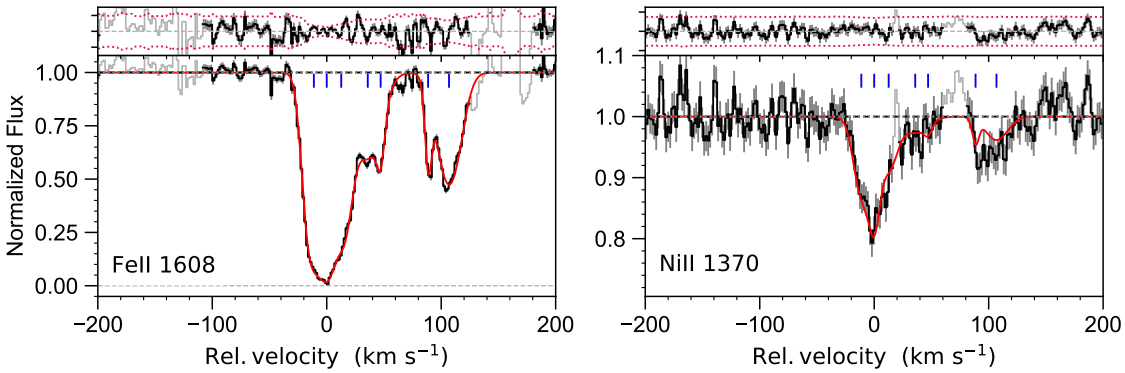


Figure 3.23: Velocity profiles of selected low-ionization transition lines from the DLA system at $z_{abs} = 3.26552$ toward Q 1111−152.

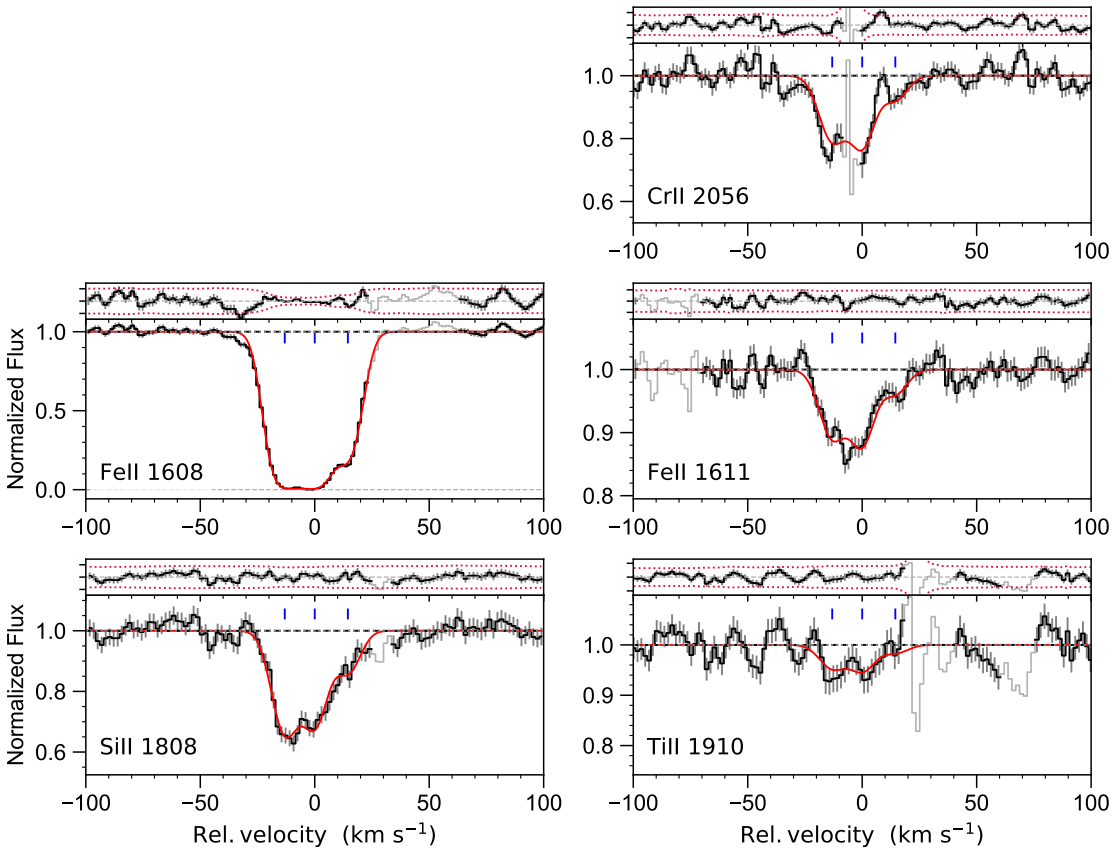


Figure 3.24: Velocity profiles of selected low-ionization transition lines from the DLA system at $z_{abs} = 3.35046$ toward Q 1117−134.

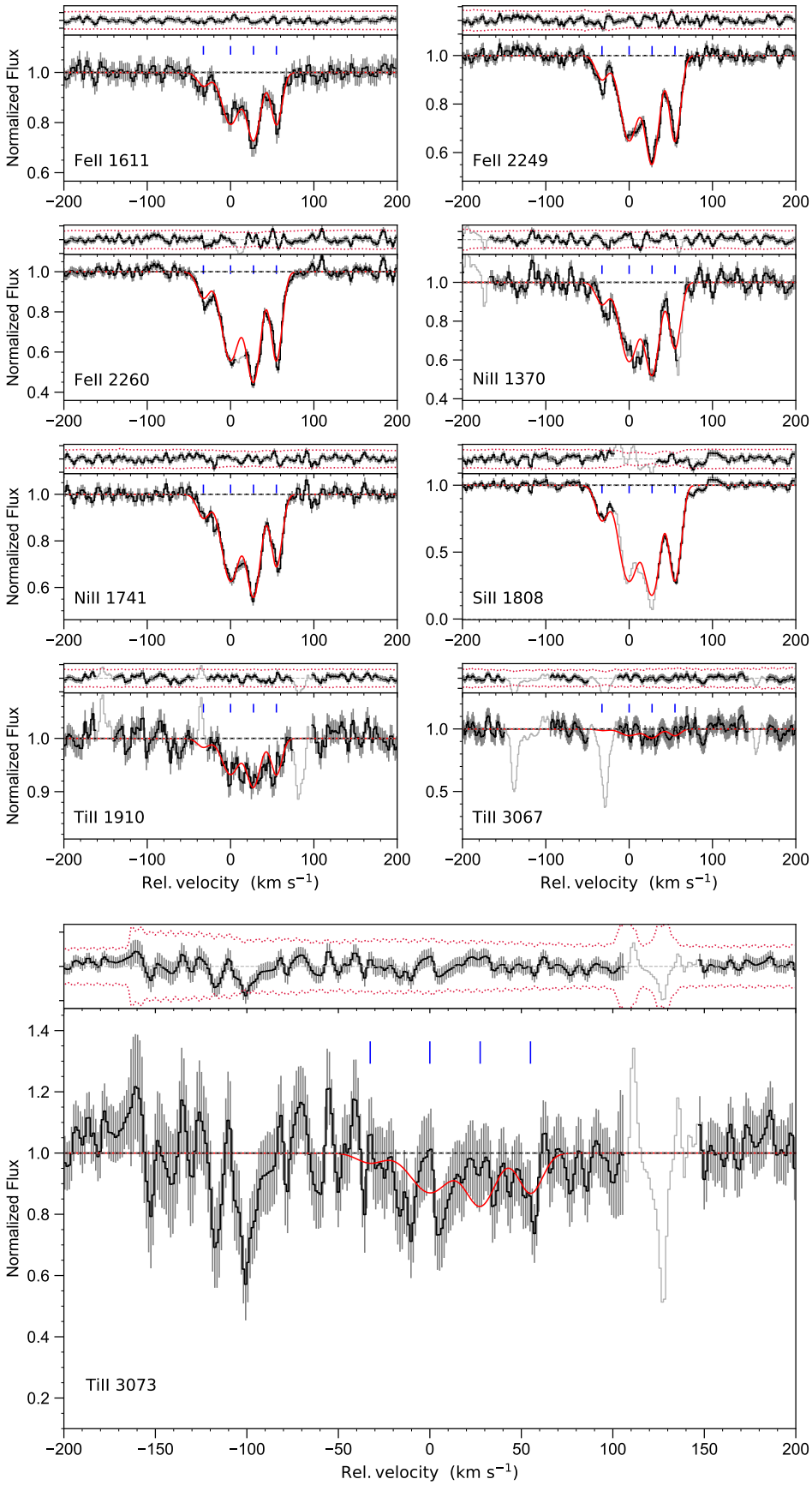


Figure 3.25: Velocity profiles of selected low-ionization transition lines from the DLA system at $z_{abs} = 1.94349$ toward Q 1157+014.

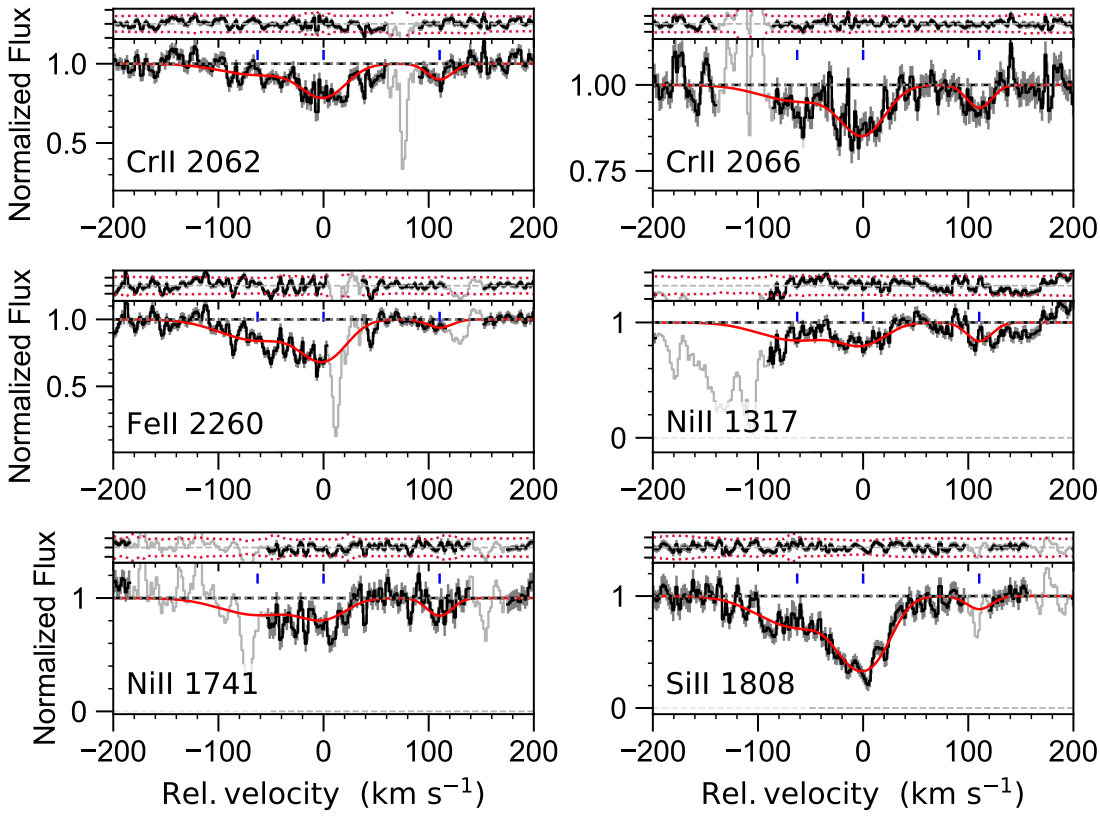


Figure 3.26: Velocity profiles of selected low-ionization transition lines from the DLA system at $z_{abs} = 2.58437$ toward Q 1209+093.

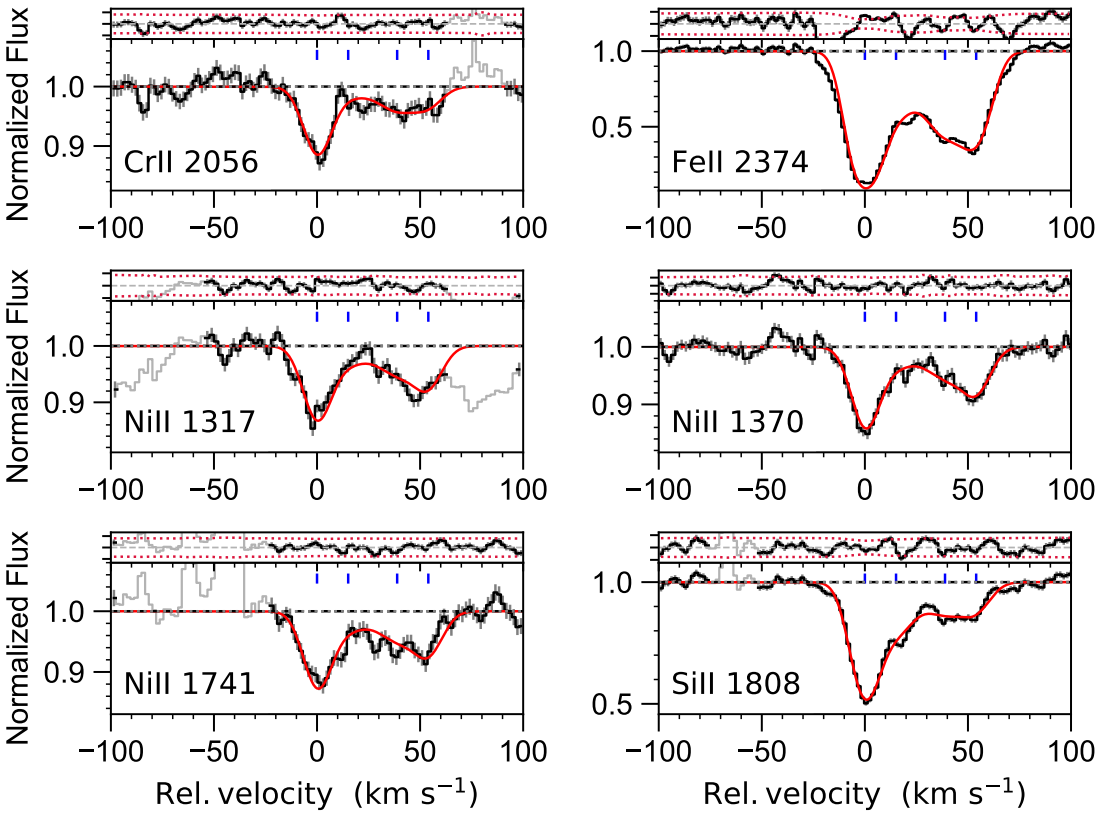


Figure 3.27: Velocity profiles of selected low-ionization transition lines from the DLA system at $z_{abs} = 1.77635$ toward Q 1331+170.

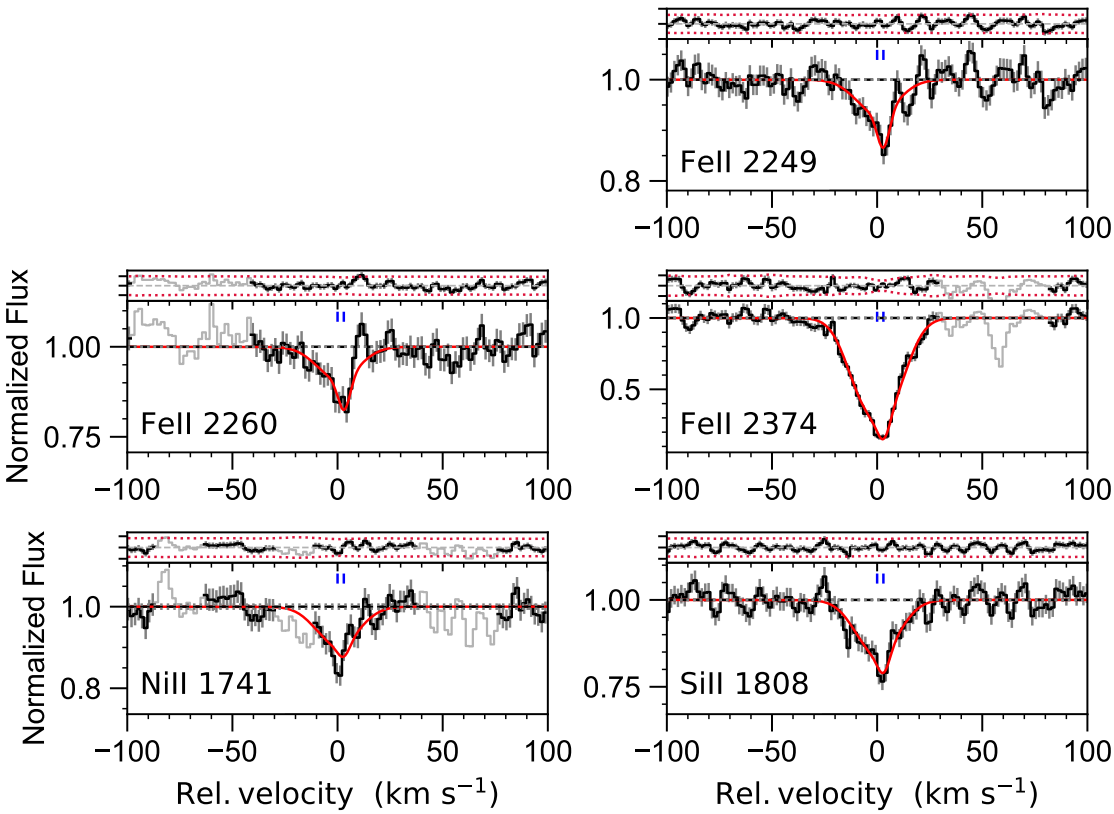


Figure 3.28: Velocity profiles of selected low-ionization transition lines from the DLA system at $z_{abs} = 2.01881$ toward Q 1409+095a.

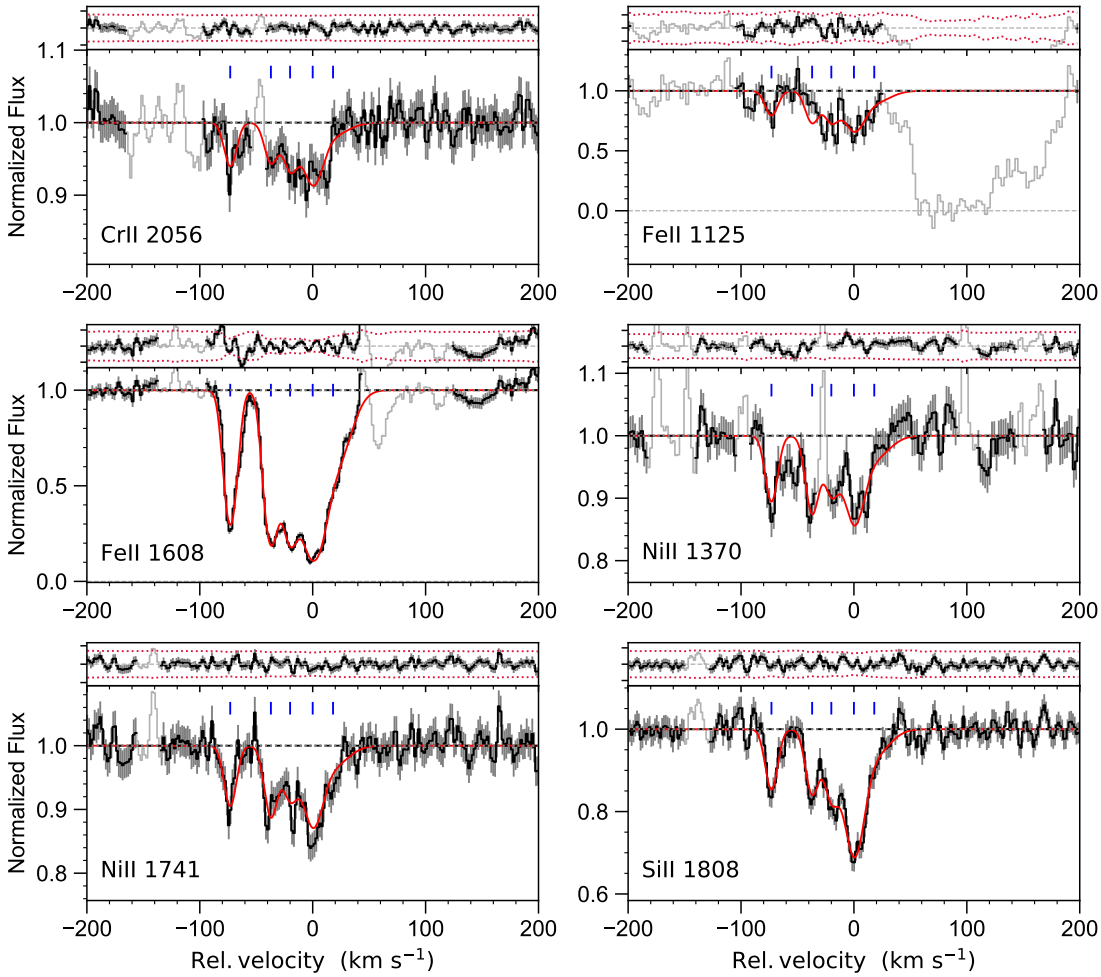


Figure 3.29: Velocity profiles of selected low-ionization transition lines from the DLA system at $z_{abs} = 1.99615$ toward Q 2116−358.

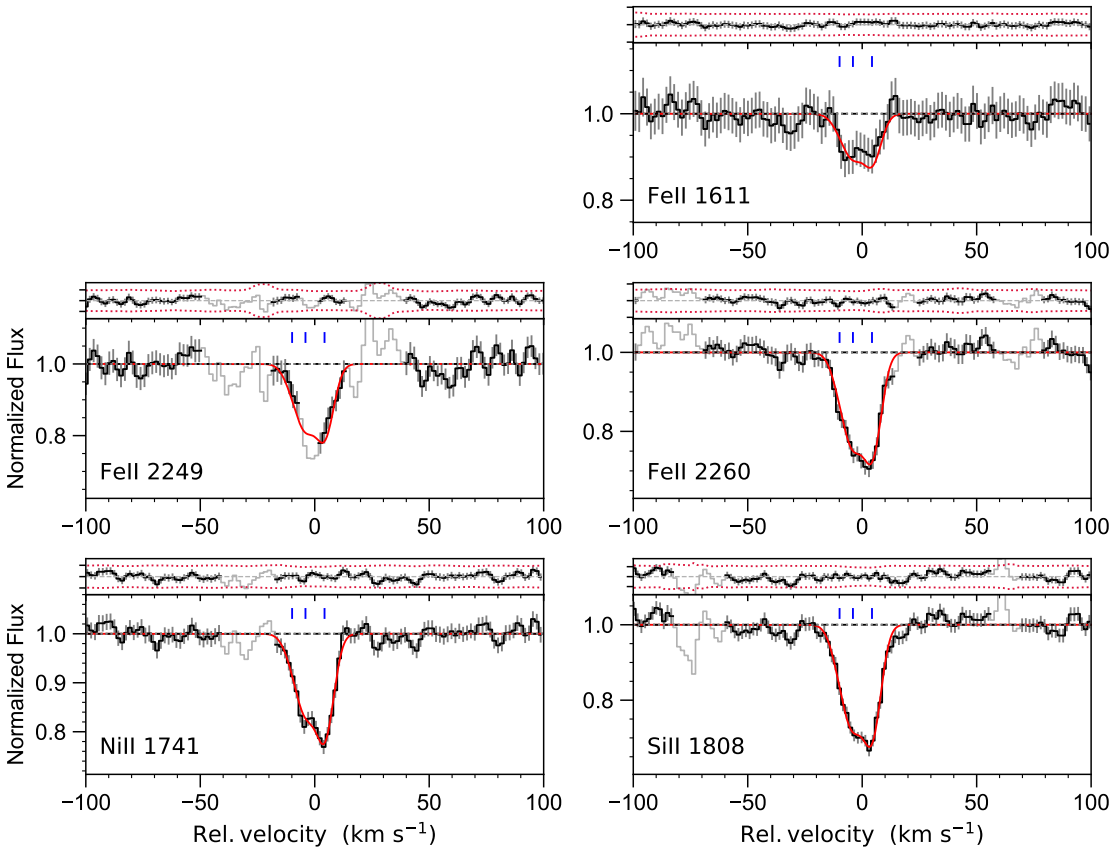
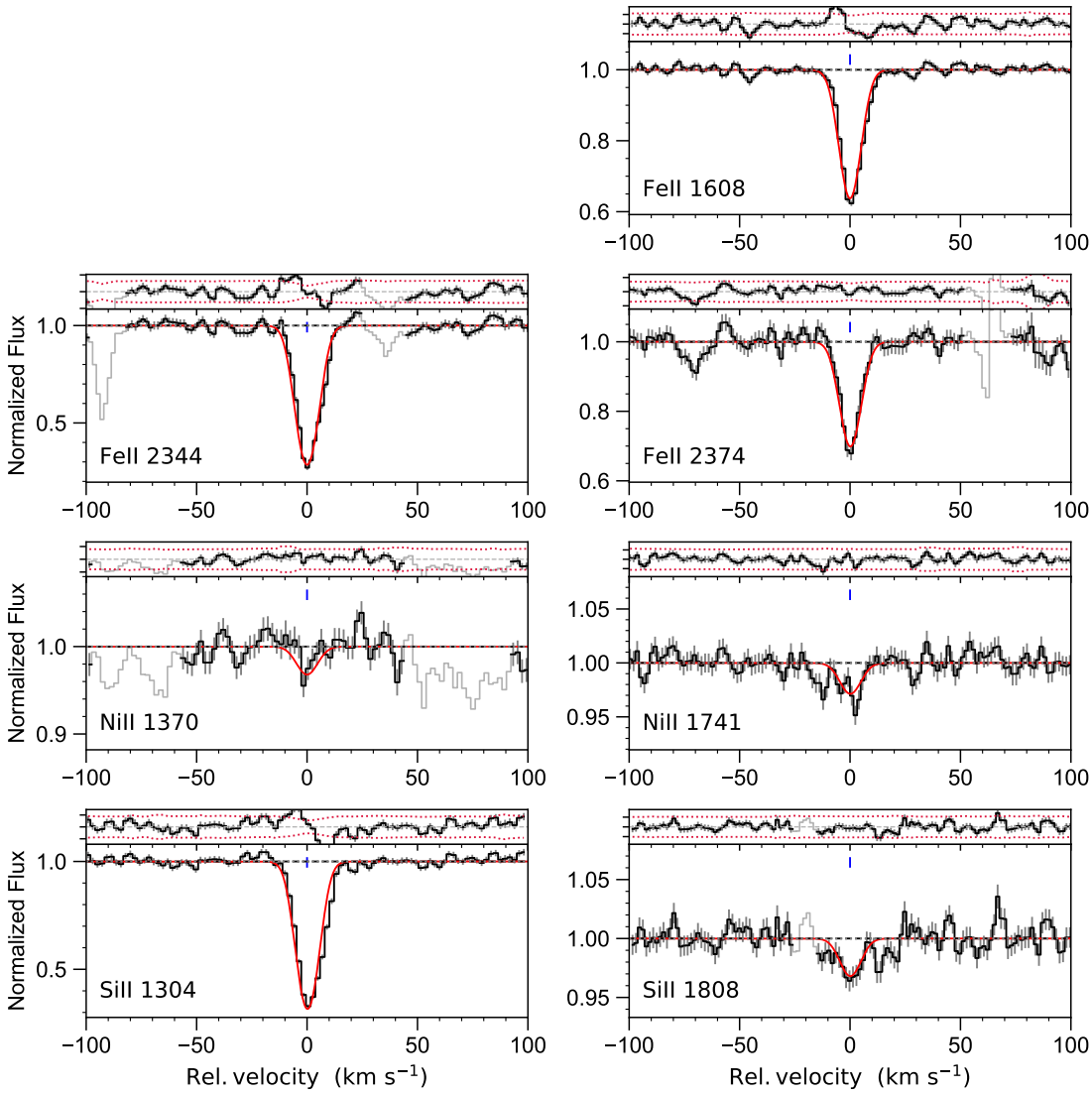


Figure 3.30: Velocity profiles of selected low-ionization transition lines from the DLA system at $z_{abs} = 2.85234$ toward Q 2138−444b.


FeII 1608
FeII 2344
FeII 2374
NiII 1370
NiII 1741
SiII 1304
SiII 1808
Normalized Flux
Rel. velocity (km s^{-1})

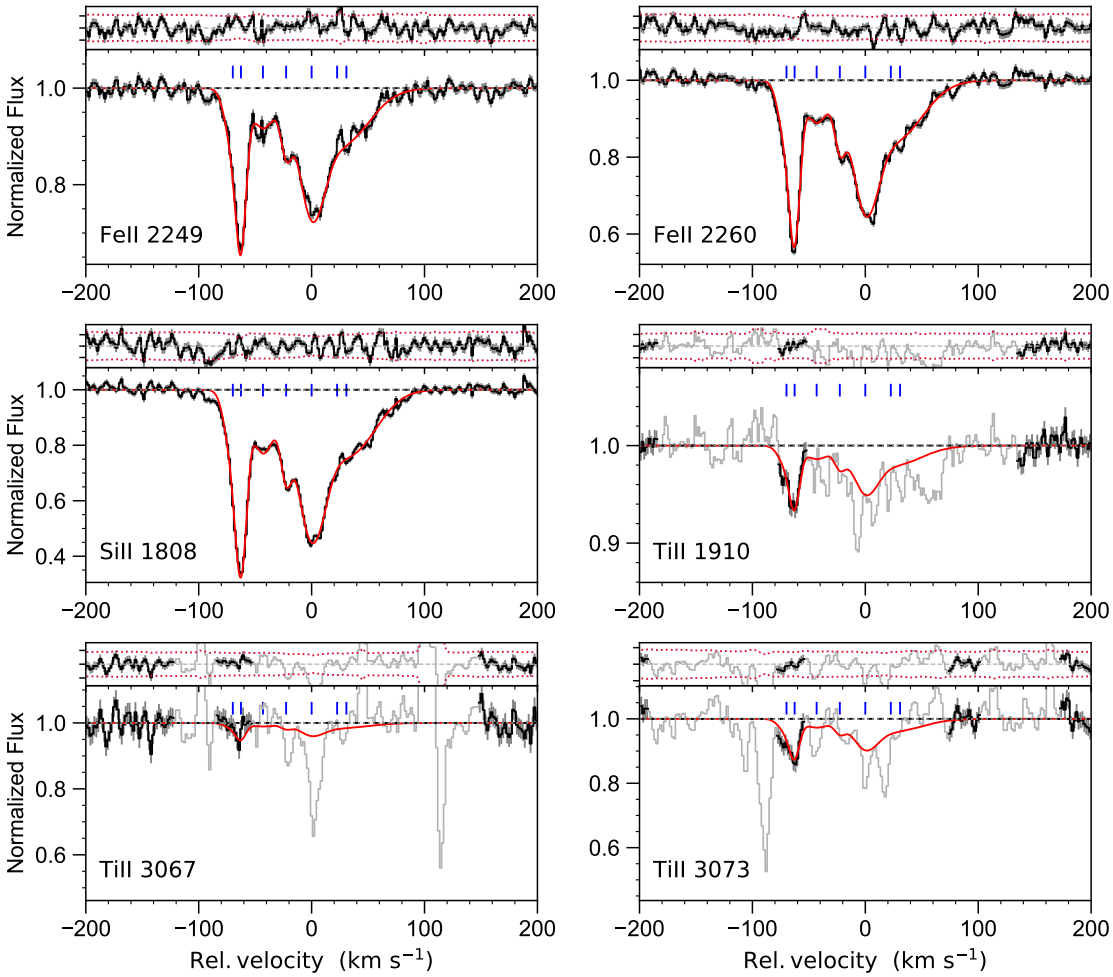


Figure 3.31: Velocity profiles of selected low-ionization transition lines from the DLA system at $z_{abs} = 1.92061$ toward Q 2206−199a.

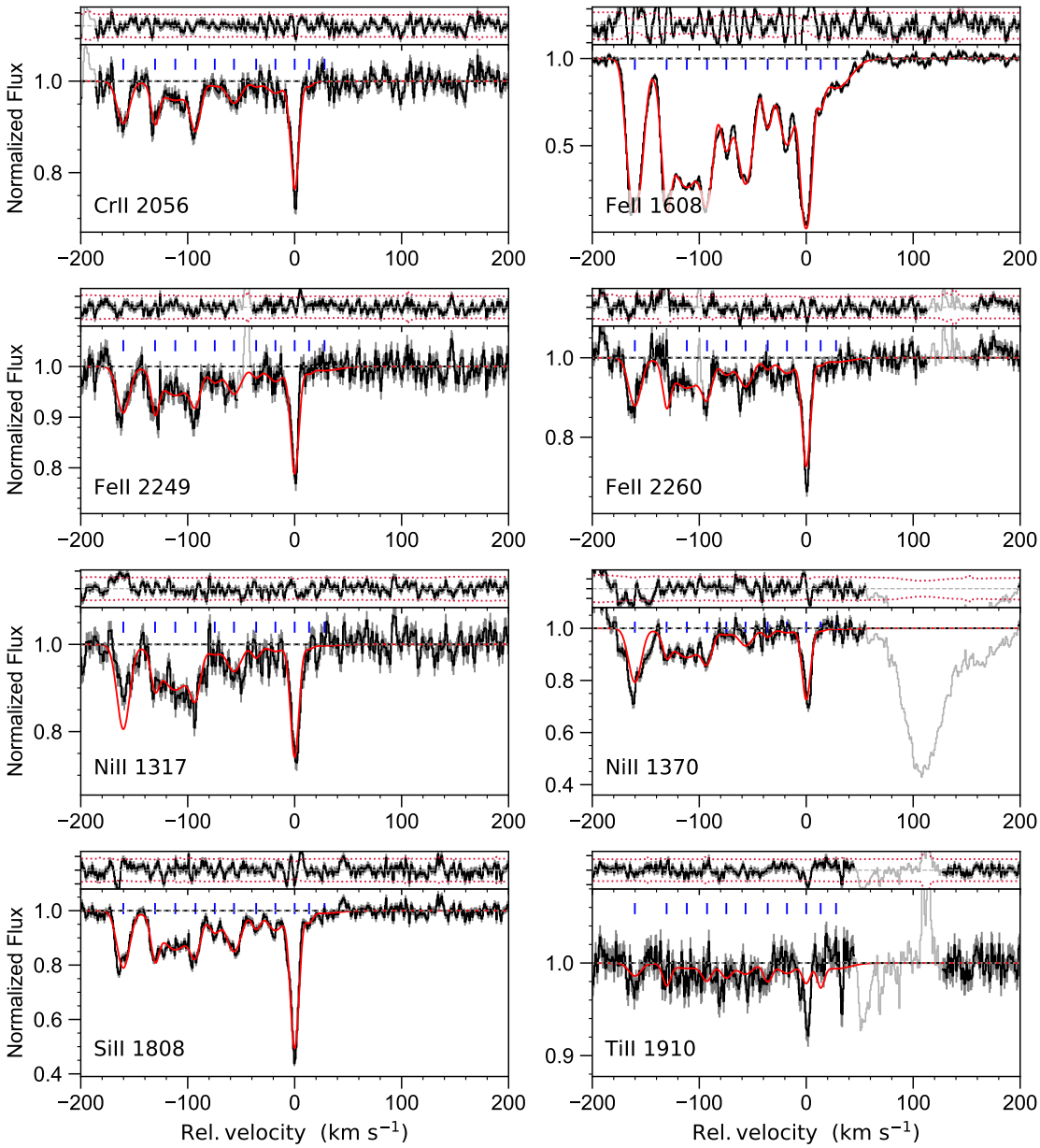


Figure 3.32: Velocity profiles of selected low-ionization transition lines from the DLA system at $z_{abs} = 2.33062$ toward Q 2243−605.

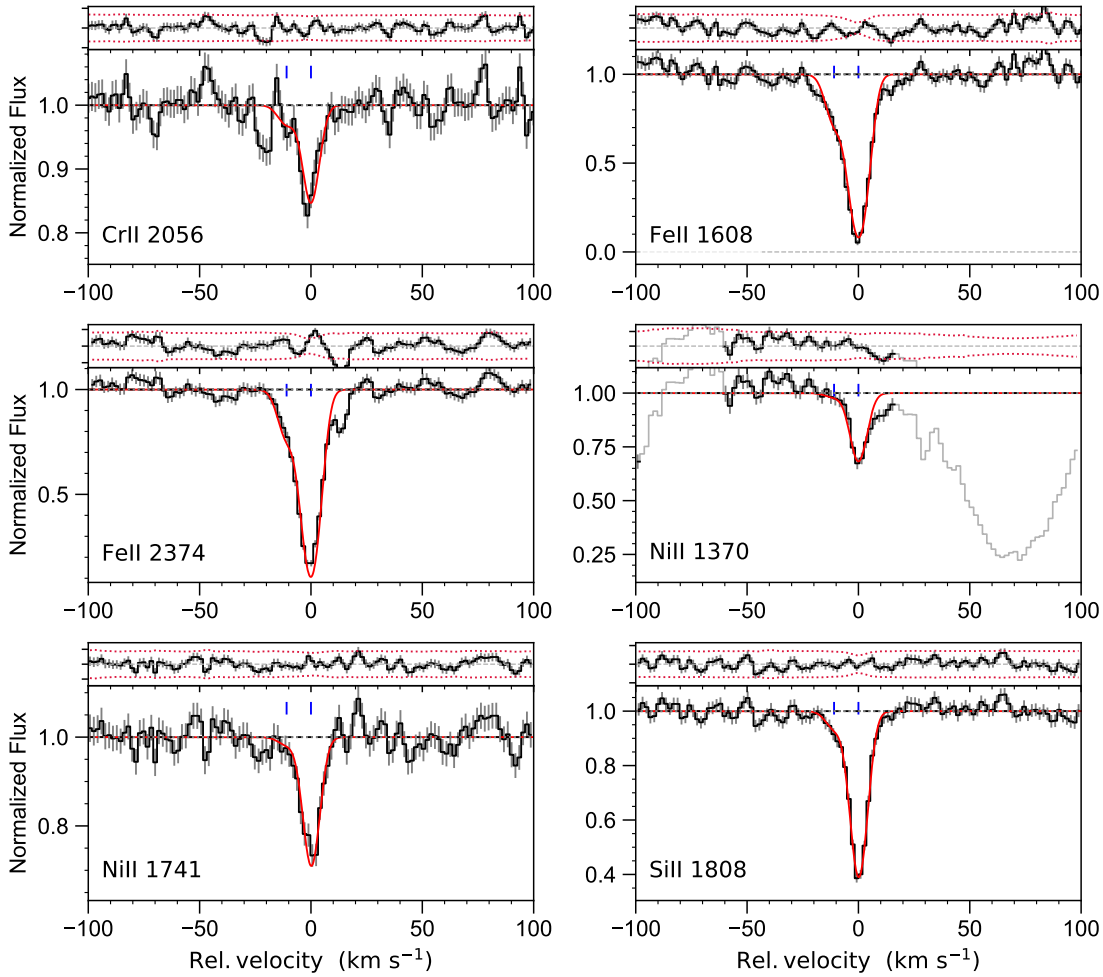


Figure 3.33: Velocity profiles of selected low-ionization transition lines from the DLA system at $z_{abs} = 2.28749$ toward Q 2332−094a.

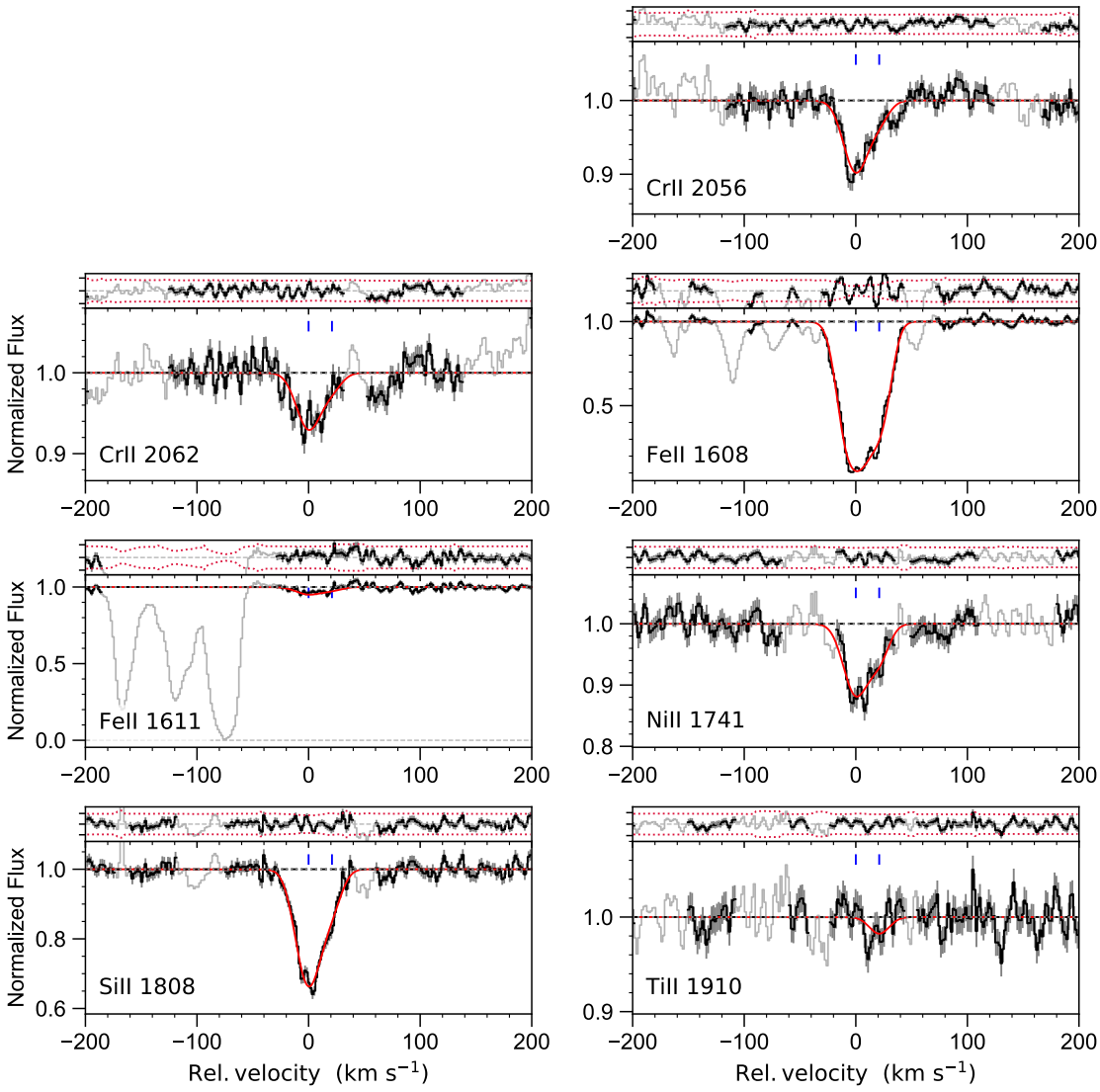


Figure 3.34: Velocity profiles of selected low-ionization transition lines from the DLA system at $z_{abs} = 2.43123$ toward Q 2343+125.

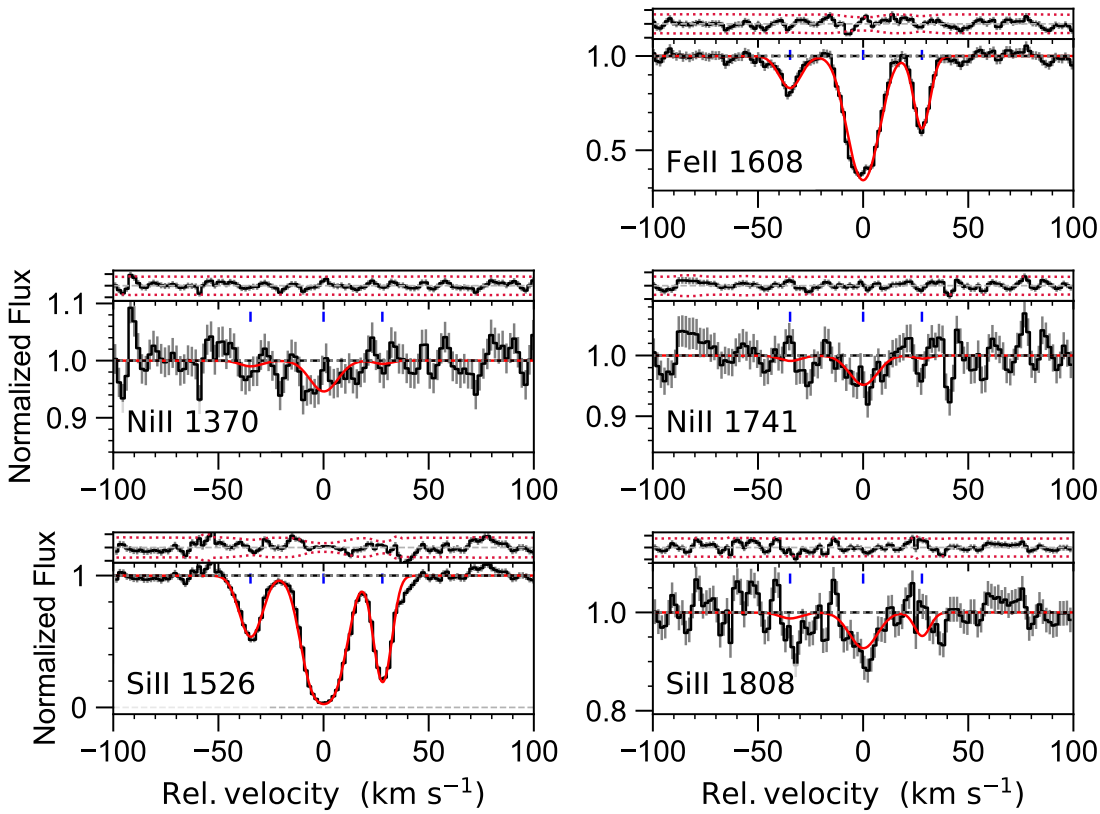


Figure 3.35: Velocity profiles of selected low-ionization transition lines from the DLA system at $z_{abs} = 2.0951$ toward Q 2344+125.

3.D COLUMN DENSITIES OF ALL THE SAMPLES

Table 3.7: QSO-DLA column densities

QSO	z_{abs}	log N(HI)	log N(OI)	log N(MgII)	log N(SiII)	log N(SII)	log N(PII)	log N(TiII)	log N(CrII)	log N(MnII)	log N(FeII)	log N(CoII)	log N(NiII)	log N(ZnII)	Ref
Q0000-263	3.39	21.40±0.08	16.42±0.10	...	14.99±0.02	14.74±0.03	12.72±0.04	...	13.08±0.03	...	14.87±0.03	...	...	11.91±0.05	1
Q0010-002	2.02	20.95±0.10	...	15.54±0.05	15.24±0.03	15.00±0.03	...	<12.38	13.41±0.02	...	15.18±0.04	...	13.69±0.03	12.09±0.04	⋆, 1
Q0013-004	1.97	20.83±0.05	...	...	15.47±0.01	15.48±0.01	14.04±0.01	...	13.17±0.03	13.00±0.04	14.91±0.01	...	...	12.81±0.01	1
Q0058-292	2.67	21.10±0.10	...	15.30±0.00	15.16±0.04	14.96±0.02	...	12.30±0.11	13.11±0.02	...	14.75±0.02	...	13.55±0.08	12.14±0.02	⋆, 1
Q0100+130	2.31	21.35±0.08	...	15.51±0.06	...	15.13±0.01	13.08±0.02	12.72±0.11	13.36±0.01	12.68±0.04	15.05±0.01	...	...	12.34±0.01	⋆, 1
Q0102-190a	2.37	21.00±0.08	...	...	...	14.30±0.02	...	12.20±0.12	12.80±0.02	12.04±0.04	14.44±0.02	...	13.16±0.07	11.61±0.08	⋆, 1
Q0216+080a	1.77	20.30±0.10	...	...	14.83±0.02	14.47±0.13	...	<12.22	12.68±0.07	...	14.47±0.01	...	<13.08	11.87±0.06	⋆, 1
Q0216+080b	2.29	20.50±0.10	...	...	15.34±0.02	...	13.55±0.06	...	13.18±0.04	...	14.88±0.03	...	...	12.31±0.04	1
Q0347-383	3.02	20.73±0.05	16.45±0.11	...	14.71±0.03	14.78±0.02	12.81±0.10	<11.92	12.82±0.05	...	14.35±0.02	...	<13.70	12.13±0.05	⋆, 1
Q0405-443a	1.91	20.80±0.10	...	...	15.36±0.02	...	...	12.48±0.02	13.45±0.02	12.90±0.02	15.16±0.02	...	13.87±0.01	12.34±0.03	⋆, 1
Q0405-443b	2.55	21.15±0.15	...	...	15.29±0.01	14.98±0.01	13.20±0.02	<12.22	13.26±0.02	12.53±0.12	15.05±0.01	...	13.76±0.01	12.36±0.04	⋆, 1
Q0405-443c	2.60	21.05±0.10	...	...	15.42±0.01	15.15±0.01	13.28±0.02	12.55±0.05	13.40±0.02	12.85±0.02	15.08±0.01	...	13.80±0.01	12.50±0.01	⋆, 1
Q0458-020	2.04	21.70±0.10	...	16.07±0.07	...	...	13.81±0.04	<12.72	13.71±0.02	13.19±0.04	15.33±0.04	...	14.06±0.03	13.05±0.02	⋆, 1
Q0528-250a	2.14	20.98±0.05	...	...	15.21±0.01	14.8±0.02	...	12.62±0.07	13.11±0.02	12.57±0.05	14.78±0.02	...	13.65±0.01	12.19±0.04	⋆, 1
Q0528-250b	2.81	21.35±0.07	...	15.87±0.01	16.03±0.01	15.58±0.01	...	12.76±0.06	13.69±0.01	13.35±0.01	15.48±0.01	...	14.29±0.01	13.01±0.01	⋆, 1
Q0551-366	1.96	20.7±0.08	...	...	15.55±0.03	15.42±0.04	13.88±0.16	<12.56	13.25±0.03	13.12±0.02	15.05±0.03	...	14.09±0.01	12.92±0.03	⋆, 1
Q0841+129a	1.86	21.00±0.10	...	...	...	14.73±0.05	...	12.38±0.05	...	12.55±0.04	14.88±0.04	...	13.60±0.02	11.94±0.11	⋆, 1
Q0841+129b	2.38	21.05±0.10	...	15.13±0.04	15.03±0.03	14.77±0.02	12.93±0.03	<13.06	13.06±0.02	12.49±0.02	14.72±0.02	...	13.55±0.01	12.03±0.02	⋆, 1
Q0841+129c	2.48	20.80±0.10	16.12±0.03	14.95±0.05	14.64±0.02	14.48±0.02	12.44±0.05	<11.94	12.82±0.02	12.31±0.02	14.48±0.02	...	13.30±0.02	11.77±0.03	⋆, 1
Q1037-270	2.14	19.7±0.05	...	15.17±0.02	15.18±0.02	14.83±0.01	13.30±0.01	...	12.89±0.01	12.52±0.02	14.74±0.01	...	...	11.96±0.02	1
Q1111-152	3.27	21.30±0.05	...	...	15.03±0.02	14.79±0.02	...	...	13.27±0.04	...	14.82±0.02	...	13.56±0.01	12.22±0.09	⋆, 1
Q1117-134	3.35	20.95±0.10	...	...	15.03±0.02	...	...	12.49±0.05	13.08±0.04	...	14.81±0.03	...	<13.53	12.11±0.05	⋆, 1
Q1157+014	1.94	21.80±0.10	...	15.96±0.02	15.83±0.01	...	13.83±0.04	12.99±0.01	13.78±0.01	13.26±0.01	15.47±0.01	...	14.19±0.01	12.93±0.01	⋆, 1
Q1209+093	2.58	21.4±0.10	...	...	15.90±0.02	15.58±0.02	...	<12.60	13.56±0.02	13.11±0.02	15.36±0.02	...	14.16±0.04	12.96±0.02	⋆, 1
Q1223+178	2.47	21.4±0.10	...	15.82±0.04	15.43±0.01	15.19±0.02	...	12.73±0.06	13.47±0.01	12.86±0.02	15.21±0.01	...	13.86±0.05	12.34±0.02	⋆, 1
Q1331+170	1.78	21.15±0.07	...	15.52±0.03	15.24±0.01	15.11±0.01	13.48±0.02	<11.95	12.86±0.02	12.49±0.02	14.62±0.02	...	13.41±0.02	12.44±0.03	⋆, 1
Q1409+095a	2.02	20.65±0.10	...	...	14.57±0.05	14.14±0.04	...	<12.88	12.62±0.07	...	14.34±0.02	...	13.15±0.08	11.6±0.13	⋆, 1
Q1444+014	2.09	20.25±0.07	...	...	14.32±0.04	14.66±0.04	13.13±0.05	<12.43	12.36±0.11	...	14.00±0.03	...	<12.81	12.02±0.07	⋆, 1
Q1451+123a	2.26	20.35±0.10	...	...	14.89±0.08	...	...	<12.97	12.85±0.10	...	14.42±0.05	...	<13.60	11.85±0.11	⋆, 1
Q2116-358	2.00	20.10±0.07	...	...	15.17±0.05	14.98±0.07	13.34±0.10	<12.43	13.03±0.06	...	14.72±0.05	...	13.61±0.02	12.33±0.08	⋆, 1
Q2138-444a	2.38	20.6±0.05	...	...	14.89±0.01	14.75±0.10	...	<12.64	12.99±0.05	12.45±0.05	14.54±0.01	...	<12.90	12.02±0.08	⋆, 1
Q2138-444b	2.85	20.98±0.05	...	...	14.79±0.02	14.54±0.02	12.45±0.05	<11.83	12.91±0.02	12.21±0.04	14.63±0.02	...	13.33±0.02	11.81±0.02	⋆, 1
Q2206-199a	1.92	20.67±0.05	...	15.71±0.04	15.72±0.01	15.42±0.02	13.98±0.03	12.86±0.02	13.59±0.01	13.10±0.02	15.34±0.01	...	14.16±0.02	12.70±0.01	⋆, 1
Q2243-605	2.33	20.65±0.05	...	...	15.33±0.01	15.05±0.01	13.57±0.01	12.64±0.03	13.19±0.02	12.80±0.03	14.95±0.01	...	13.83±0.02	12.37±0.02	⋆, 1
Q2332-094a	2.29	20.07±0.07	...	...	14.95±0.02	14.67±0.02	...	...	12.51±0.06	12.19±0.05	14.23±0.03	...	13.25±0.04	12.31±0.02	⋆, 1
Q2343+125	2.43	20.40±0.07	...	15.02±0.08	15.04±0.02	14.72±0.02	13.15±0.02	<11.97	12.78±0.02	12.35±0.02	14.51±0.02	...	13.36±0.03	12.05±0.02	⋆, 1
Q2359-022a	2.10	20.65±0.10	...	...	15.37±0.02	15.17±0.04	13.53±0.11	<12.51	13.03±0.09	...	14.47±0.01	...	<13.59	12.38±0.08	⋆, 1
Q1328+307	0.69	21.25±0.10	...	...	...	...	12.50±0.10	...	13.28±0.10	...	14.98±0.10	...	...	12.62±0.10	2
Q1137+3907	0.72	21.10±0.10	...	...	...	...	...	...	13.69±0.20	...	15.45±0.05	...	...	13.33±0.05	2
J1431+3952	0.60	21.20±0.10	...	...	...	...	...	12.70±0.15	13.51±0.18	13.08±0.14	15.15±0.11	...	...	12.93±0.19	2
J2328+0022	0.65	20.32±0.07	...	...	...	...	12.43±0.03	...	13.33±0.19	12.85±0.02	14.84±0.01	...	...	12.33±0.15	2
J0256+0110	0.72	20.70±0.16	...	...	...	...	...	12.27±0.05	13.79±0.05	13.25±0.02	15.13±0.30	...	...	13.09±0.04	2
B0105-008	1.37	21.70±0.15	...	...	...	...	...	13.00±0.20	13.9±0.03	13.30±0.04	15.59±0.03	...	14.25±0.04	12.83±0.04	2
J1107+0048	0.74	21.00±0.05	...	...	...	...	...	...	13.82±0.06	13.28±0.03	15.53±0.02	...	...	12.96±0.15	2
Q1010+0003	1.26	21.52±0.07	...	...	15.80±0.06	...	...	...	13.52±0.07	13.24±0.11	15.26±0.05	...	14.20±0.07	12.86±0.06	2
Q0302-223	1.01	20.36±0.11	...	...	15.11±0.06	...	...	...	13.06±0.06	12.58±0.06	14.67±0.05	...	13.57±0.06	12.35±0.06	2
Q1727+5302	1.03	21.41±0.15	...	...	15.44±0.01	...	...	...	13.31±0.11	13.06±0.02	14.81±0.01	...	...	12.66±0.24	2
Q1727+5302	0.94	21.16±0.10	...	...	15.84±0.08	...	...	...	13.57±0.11	13.52±0.01	15.29±0.01	...	...	13.15±0.11	2
B2355-106	1.17	21.00±0.10	...	...	15.35±0.13	...	...	...	...	12.92±0.1	15.08±0.1	...	14.17±0.12	12.66±0.17	2
J1623+0718	1.34	21.35±0.10	...	...	15.71±0.05	...	...	...	13.53±0.06	13.07±0.06	15.28±0.05	...	14.11±0.07	12.81±0.09	2
HE0515-4414	1.15	20.45±0.15	...	...	14.67±0.18	...	12.6±0.27	...	...	11.94±0.11	14.31±0.2	...	...	12.01±0.04	2
J0927+1543	1.73	...	...	...	15.92±0.05	...	...	...	13.81±0.05	...	15.14±0.24	...	14.17±0.05	13.28±0.05	2

Table 3.7: continued

QSO	z_{abs}	log N(HI)	log N(OI)	log N(MgII)	log N(SiII)	log N(SII)	log N(PII)	log N(TiII)	log N(CrII)	log N(MnII)	log N(FeII)	log N(CoII)	log N(NiII)	log N(ZnII)	Ref
J1142+0701	1.84	21.5±0.15	...	...	16.08±0.13	...	...	...	13.68±0.05	...	15.47±0.05	...	14.01±0.05	13.19±0.05	2
J1313+1441	1.80	...	...	...	16.05±0.05	...	...	...	13.59±0.05	...	15.55±0.05	...	14.27±0.05	13.20±0.05	2
Q0948+433	1.23	21.62±0.06	...	...	...	...	...	13.34±0.07	13.88±0.01	13.31±0.01	15.56±0.01	13.02±0.12	...	13.05±0.01	2
J1056+1208	1.61	21.45±0.15	...	...	16.41±0.09	...	...	...	14.02±0.05	...	15.81±0.05	...	14.69±0.05	13.66±0.05	2
J1310+5424	1.80	21.45±0.15	...	...	16.37±0.05	...	...	...	13.97±0.05	...	15.64±0.05	...	14.45±0.05	13.47±0.05	2
Q0935+417	1.37	20.52±0.10	...	...	...	...	...	...	13.16±0.05	12.46±0.08	14.82±0.10	...	...	12.16±0.02	2
J0008-0958	1.77	20.85±0.15	...	...	15.97±0.05	15.88±0.05	...	...	13.89±0.05	...	15.62±0.05	...	14.46±0.05	13.21±0.05	2
J1454+0941	1.79	20.50±0.15	...	...	15.40±0.05	15.29±0.06	...	...	13.28±0.09	...	15.02±0.12	...	13.89±0.05	12.62±0.05	2
Q1354+258	1.42	21.54±0.06	...	...	15.29±0.08	...	...	...	13.40±0.06	12.76±0.06	15.01±0.04	...	13.11±0.08	12.49±0.08	2
J1417+4132	1.95	21.45±0.25	17.98±0.07	...	...	...	...	...	14.02±0.05	...	15.58±0.05	...	14.55±0.05	13.45±0.05	2
J1552+4910	1.96	...	...	...	15.91±0.05	15.38±0.05	...	...	13.72±0.05	13.40±0.05	15.47±0.05	...	14.24±0.05	12.83±0.05	2
Q1331+17	1.78	21.14±0.08	...	15.53±0.14	15.23±0.01	15.12±0.11	...	...	12.93±0.03	12.51±0.03	14.63±0.03	...	13.44±0.08	12.44±0.02	2
J2340-00	2.05	20.35±0.15	...	...	15.16±0.05	14.99±0.05	...	...	...	...	14.98±0.05	...	13.81±0.05	12.53±0.07	2
Q1755+578	1.97	21.40±0.15	...	...	16.51±0.05	...	...	...	14.07±0.05	13.84±0.05	15.79±0.05	...	14.75±0.05	13.75±0.05	2
J1049-0110	1.66	20.31±0.15	...	...	15.73±0.05	15.51±0.05	...	...	13.47±0.05	...	15.17±0.05	...	14.25±0.05	13.04±0.05	2
SDSS1249-0233	1.78	21.45±0.15	...	...	...	15.57±0.05	...	13.06±0.10	13.89±0.02	13.20±0.02	15.47±0.02	...	14.29±0.05	13.05±0.05	2
Q2230+025	1.86	20.83±0.05	...	...	15.58±0.05	15.33±0.05	...	12.68±0.09	13.38±0.05	13.04±0.03	15.19±0.05	...	14.13±0.05	12.70±0.05	2
Q2228-3954	2.10	21.20±0.10	...	...	...	...	...	...	...	...	15.17±0.02	...	...	12.41±0.06	2
HE1104-1805	1.66	20.85±0.01	16.80±0.20	...	15.31±0.02	...	...	12.28±0.07	13.05±0.01	12.78±0.14	14.77±0.02	...	13.42±0.03	12.38±0.01	2
Q0149+33	2.14	20.5±0.10	...	...	14.50±0.05	...	...	...	12.70±0.04	...	14.2±0.02	...	13.17±0.04	11.4±0.10	2
B2314-409	1.86	20.90±0.10	...	...	15.34±0.10	15.14±0.15	...	...	13.36±0.08	...	15.08±0.10	...	13.84±0.08	12.42±0.10	2
Q0027-1836	2.40	21.75±0.10	...	16.00±0.04	15.60±0.03	15.27±0.02	...	12.61±0.06	13.35±0.01	12.85±0.03	14.97±0.02	...	13.70±0.02	12.69±0.02	2
Q0201+365	2.46	20.38±0.05	...	...	15.46±0.01	15.33±0.01	...	...	13.23±0.03	...	15.01±0.01	...	14.02±0.01	12.37±0.05	2
J0058+0115	2.01	21.10±0.15	...	...	...	15.44±0.05	...	...	13.52±0.05	...	15.18±0.05	...	14.16±0.05	12.85±0.05	2
Q0841+12	2.38	20.99±0.08	...	15.13±0.10	15.14±0.04	14.73±0.05	...	...	13.05±0.02	12.51±0.02	14.76±0.01	...	13.53±0.05	12.00±0.02	2
Q0841+12	2.48	20.78±0.08	16.15±0.10	14.99±0.15	14.92±0.03	14.52±0.10	...	...	12.87±0.06	12.34±0.15	14.50±0.03	...	13.19±0.09	11.59±0.10	2
Q2343+12	2.43	20.34±0.10	...	...	15.22±0.04	...	...	...	12.78±0.03	12.28±0.04	14.66±0.03	...	...	12.14±0.03	2
Q0933+733	1.48	21.62±0.1	...	...	...	...	...	...	13.54±0.01	12.97±0.01	15.19±0.01	...	13.92±0.01	12.61±0.02	2
Q1210+17	1.89	20.63±0.08	...	...	15.26±0.03	15.00±0.02	...	12.34±0.08	13.26±0.03	12.73±0.01	15.01±0.03	...	13.67±0.06	12.30±0.05	2
SDSS2059-0529	2.21	20.8±0.20	...	...	15.29±0.10	...	...	...	13.53±0.12	...	15.00±0.11	...	13.88±0.11	12.84±0.11	2
J1541+3153	2.44	20.95±0.10	...	...	14.90±0.04	...	...	...	12.59±0.14	...	14.50±0.11	...	13.10±0.08	11.93±0.11	2
Q2206-199	1.92	20.65±0.07	...	...	15.73±0.01	...	...	12.77±0.04	13.62±0.01	...	15.30±0.02	12.96±0.14	14.23±0.01	12.81±0.01	2
Q1232+082	2.34	20.90±0.10	...	15.44±0.09	15.17±0.11	14.87±0.10	...	...	...	...	14.68±0.08	...	...	12.61±0.11	2
Q1215+33	2.00	20.95±0.07	...	...	14.96±0.03	...	...	...	13.11±0.03	...	14.75±0.05	...	13.59±0.03	12.23±0.05	2
Q0449-1645	1.01	20.98±0.07	...	...	15.79±0.04	...	...	...	13.45±0.02	12.92±0.03	15.09±0.01	13.51±0.07	...	12.52±0.07	2
Q0100+13	2.31	21.37±0.08	...	15.57±0.09	...	15.13±0.06	...	...	13.35±0.01	...	15.09±0.01	...	13.87±0.01	12.37±0.01	2
FJ0812+32	2.07	21.0±0.10	...	...	15.11±0.01	...	...	12.53±0.03	13.22±0.01	12.66±0.03	14.89±0.02	...	13.62±0.01	12.11±0.02	2
FJ0812+32	2.63	21.35±0.10	17.69±0.07	16.24±0.01	15.91±0.05	15.67±0.07	...	...	13.34±0.05	13.01±0.0	15.09±0.05	...	13.89±0.05	13.05±0.05	2
UM673A	1.63	20.7±0.1	...	...	14.68±0.03	...	...	...	12.76±0.04	...	14.59±0.03	...	12.99±0.04	11.33±0.15	2
Q0528-2505	2.81	21.20±0.04	...	...	15.94±0.03	15.60±0.02	...	...	13.63±0.12	...	15.47±0.02	...	13.89±0.03	13.17±0.03	2
Q0528-2505	2.14	20.95±0.05	...	...	15.15±0.05	14.87±0.04	...	...	13.08±0.04	12.39±0.10	14.85±0.09	...	13.22±0.06	12.15±0.03	2
Q2359-02	2.10	20.70±0.10	...	...	15.38±0.05	15.06±0.06	...	...	12.73±0.09	...	14.56±0.02	12.83±0.0	13.14±0.05	12.45±0.04	2
J1135-0010	2.21	22.05±0.10	...	...	16.42±0.03	...	...	13.28±0.04	14.12±0.01	13.63±0.01	15.76±0.03	...	14.67±0.02	13.52±0.03	2
Q0201+36	2.46	20.38±0.04	...	...	15.46±0.05	15.33±0.05	...	...	13.22±0.05	...	15.01±0.05	...	14.03±0.05	12.66±0.05	2
Q1223+1753	2.47	21.5±0.10	...	...	15.4±0.01	15.18±0.03	...	...	13.47±0.01	...	15.16±0.02	...	13.95±0.01	12.45±0.03	2
Q2318-1107	1.99	20.68±0.05	...	...	15.27±0.01	15.13±0.02	...	...	13.11±0.06	...	14.91±0.01	...	13.82±0.03	12.4±0.03	2
SDSS0225+0054	2.71	21.0±0.15	15.69±0.0	...	15.54±0.07	...	...	...	13.76±0.10	...	15.3±0.08	...	14.17±0.11	12.79±0.11	2
SDSS1116+4118A	2.66	20.48±0.10	...	...	14.98±0.11	...	...	...	...	...	14.36±0.10	...	13.35±0.20	12.3±0.20	2
Q0216+0803	2.29	20.4±0.08	...	...	15.38±0.04	15.03±0.03	...	...	...	...	14.87±0.05	...	13.60±0.07	12.33±0.05	2
HE2243-6031	2.33	20.67±0.02	16.21±0.19	...	15.29±0.02	14.92±0.01	...	...	13.22±0.02	...	14.92±0.01	...	13.86±0.03	12.12±0.03	2
Q0405-443	2.55	21.13±0.10	...	...	15.25±0.04	14.86±0.06	...	...	13.18±0.03	12.87±0.02	14.95±0.06	...	13.94±0.02	12.34±0.05	2
Q2231-00	2.07	20.53±0.08	...	...	15.22±0.04	15.14±0.15	...	12.66±0.08	12.98±0.04	12.60±0.04	14.83±0.03	...	13.54±0.06	12.2±0.05	2
Q0405-443	2.60	21.09±0.10	...	...	15.52±0.03	15.23±0.05	...	...	13.35±0.04	12.88±0.01	15.15±0.02	...	13.86±0.31	12.58±0.02	2
Q0918+1636	2.41	21.26±0.06	...	...	15.93±0.20	...	...	...	13.68±0.21	13.35±0.21	15.51±0.23	...	...	13.13±0.18	2

Table 3.7: continued

QSO	z_{abs}	log N(HI)	log N(OI)	log N(MgII)	log N(SiII)	log N(SII)	log N(PII)	log N(TiII)	log N(CrII)	log N(MnII)	log N(FeII)	log N(CoII)	log N(NiII)	log N(ZnII)	Ref
Q0918+1636	2.58	20.96±0.05	...	...	15.94±0.01	15.86±0.01	...	...	13.70±0.01	13.48±0.01	15.43±0.01	...	14.40±0.01	13.30±0.01	2
Q0642-5038	2.66	20.95±0.08	...	...	15.15±0.06	...	...	...	...	...	14.20±0.03	...	...	11.57±0.04	2
J1240+1455	3.11	21.30±0.20	...	...	15.86±0.03	15.60±0.02	...	...	...	...	14.60±0.03	...	...	12.80±0.07	2
SDSS2100-0641	3.09	21.05±0.15	...	...	15.81±0.05	15.53±0.05	...	...	13.57±0.05	...	15.37±0.05	...	14.23±0.05	13.14±0.05	2
J1604+3951	3.16	21.75±0.20	...	...	...	15.75±0.05	...	...	...	...	15.47±0.05	...	14.24±0.05	13.02±0.05	2
Q1425+6039	2.83	20.3±0.04	...	...	...	...	...	...	...	...	14.48±0.01	...	13.27±0.03	12.08±0.04	2
Q2138-444	2.85	20.98±0.05	...	...	14.79±0.02	14.54±0.02	...	...	...	...	14.63±0.02	...	...	11.81±0.02	2
SDSS1610+4724	2.51	21.15±0.15	...	...	16.09±0.05	...	...	...	13.88±0.05	13.79±0.01	15.62±0.05	...	14.58±0.05	13.46±0.05	2
Q0347-38	3.02	20.63±0.01	16.64±0.01	...	15.17±0.01	14.8±0.04	...	...	12.42±0.04	...	14.43±0.01	...	13.38±0.03	11.69±0.04	2
Q1451+123	2.26	20.30±0.15	...	...	...	...	...	...	12.86±0.14	...	14.33±0.07	...	...	11.75±0.11	2
FJ2334-0908	3.06	20.48±0.05	16.19±0.06	...	14.75±0.03	14.35±0.03	...	...	...	...	14.39±0.03	...	...	12.03±0.02	2
J1200+4015	3.22	20.65±0.15	...	...	...	15.4±0.05	...	12.96±0.03	13.51±0.05	...	15.31±0.05	...	14.18±0.05	12.76±0.05	2
J1155+0530	3.33	21.05±0.10	...	...	15.87±0.05	15.44±0.05	...	...	13.34±0.09	...	15.37±0.05	...	14.07±0.05	12.79±0.07	2
BR1117-1329	3.35	20.84±0.12	...	...	15.06±0.05	...	...	...	13.13±0.03	...	14.83±0.03	...	13.52±0.03	12.16±0.03	2
PSS1253-0228	2.78	21.85±0.20	...	...	...	...	...	...	13.61±0.03	13.43±0.07	15.36±0.04	...	14.17±0.04	12.67±0.07	2
Q0000-262	3.39	21.41±0.08	16.45±0.06	...	14.99±0.02	...	...	...	13.07±0.03	...	14.87±0.03	...	13.39±0.03	11.91±0.05	2
PSSJ2344+0342	3.22	21.25±0.08	...	...	...	...	...	...	13.32±0.10	...	15.06±0.15	...	13.59±0.11	12.13±0.30	2
PSSJ2155+1358	3.32	20.5±0.15	...	...	14.74±0.20	...	...	...	...	...	14.51±0.13	...	...	11.95±0.32	2
BRI1013+0035	3.10	21.1±0.10	...	...	15.71±0.02	...	...	...	...	...	15.18±0.05	...	13.89±0.05	13.23±0.02	2
J1211+0833	2.12	21.00±0.20	...	...	...	...	...	...	12.76±0.14	...	14.77±0.03	...	13.62±0.08	13.48±0.06	2
eHAQ0111+0641	2.03	21.50±0.30	...	...	...	...	...	...	13.88±0.10	...	15.80±0.10	...	...	13.40±0.10	2
J0000+0048	2.52	21.07±0.10	...	...	15.86±0.17	...	...	...	...	...	15.14±0.03	...	13.99±0.04	13.99±0.45	2
J1237+0647	2.69	20.00±0.15	...	...	15.08±0.02	15.43±0.06	...	...	...	...	14.57±0.01	...	13.48±0.03	12.92±0.02	2

Notes: References:(⋆) This work; (1) De Cia et al. (2016); (2) Berg et al. (2015). Revised f-values from Cashman et al. (2017), Kisielius et al. (2014, 2015) and Kurucz (2017).

Table 3.8: Milky Way column densities

Star	log N(PII)	log N(MgII)	log N(SiII)	log N(SII)	log N(TiII)	log N(CrII)	log N(MnII)	log N(FeII)	log N(NiII)	log N(ZnII)	
HD-18100	13.81±0.07	15.18±0.03	15.27±0.03	...	...	12.89±0.04	12.75±0.03	14.67±0.04	13.44±0.05	12.62±0.05	1
KSI-PER	14.62±0.03	15.92±0.04	...	...	11.53±0.05	12.88±0.02	13.53±0.03	14.72±0.03	13.30±0.05	13.39±0.02	1
23O-ORI	14.40±0.04	15.63±0.04	15.37±0.08	...	11.17±0.03	12.72±0.01	13.02±0.04	14.38±0.03	12.96±0.12	13.28±0.07	1
DEL-ORI-A	13.42±0.20	15.09±0.04	...	...	11.11±0.04	12.07±0.05	12.28±0.06	14.06±0.06	...	12.62±0.05	1
EPS-ORI	13.87±0.08	15.27±0.02	...	...	11.36±0.03	12.43±0.05	12.73±0.04	14.21±0.05	...	12.97±0.06	1
MU-COL	13.70±0.02	15.12±0.02	15.09±0.02	15.21±0.02	11.46±0.02	12.61±0.03	12.42±0.02	14.31±0.01	12.94±0.05	12.59±0.08	1
TAU-CMA	...	15.86±0.09	...	...	11.41±0.11	12.90±0.55	12.89±0.07	14.76±0.09	...	13.24±0.05	1
ZET-PUP	13.60±0.05	15.07±0.04	15.16±0.15	15.21±0.04	11.03±0.04	12.22±0.20	12.45±0.04	14.08±0.05	12.68±0.40	12.44±0.20	1
HD-116852	...	15.91±0.04	...	...	...	...	13.45±0.06	15.24±0.02	...	13.23±0.03	1
1-SCO	14.32±0.13	15.84±0.07	...	...	...	13.03±0.05	13.21±0.08	14.81±0.20	13.18±0.08	13.49±0.05	1
PI-SCO	13.99±0.20	15.14±0.20	...	...	10.81±0.10	12.62±0.05	12.89±0.20	14.46±0.10	...	13.14±0.02	1
BET-1-SCO	14.32±0.08	15.72±0.03	...	...	11.14±0.07	12.96±0.05	13.16±0.03	14.81±0.22	...	13.52±0.05	1
ZET-OPH	...	15.42±0.03	15.27±0.03	...	10.98±0.10	12.51±0.03	13.05±0.03	14.39±0.03	12.92±0.02	13.19±0.05	1
V600-HER	...	...	15.73±0.10	...	12.44±0.07	13.42±0.05	13.37±0.06	15.20±0.06	...	13.19±0.05	1
LAM-SCO	12.68±0.05	...	14.02±0.03	14.54±0.03	...	11.74±0.05	...	13.39±0.04	...	11.76±0.06	1
HD-215733	...	15.70±0.16	15.70±0.12	15.80±0.10	...	13.35±0.17	13.25±0.09	15.09±0.10	...	13.16±0.09	1
OMI-PER	...	...	...	...	11.12±0.05	12.91±0.22	...	14.45±0.06	...	13.00±0.07	2
X-PER	...	...	...	...	11.26±0.07	12.82±0.09	...	14.55±0.03	13.34±0.05	13.03±0.04	2
EPS-PER	...	...	14.81±0.06	...	11.12±0.07	12.62±0.14	...	14.20±0.09	...	12.73±0.10	2
62-TAU	...	...	...	...	11.14±0.03	12.58±0.06	...	14.40±0.04	12.95±0.11	13.12±0.08	2
TET01-ORI-C	...	...	...	...	11.53±0.05	13.33±0.02	...	15.07±0.02	13.75±0.04	13.27±0.04	2
IOT-ORI	...	...	14.97±0.09	...	11.31±0.07	12.49±0.14	...	14.20±0.09	...	12.79±0.04	2
ZET-ORI-A	...	...	15.05±0.05	...	11.10±0.07	...	...	14.22±0.06	...	12.79±0.07	2
HD-62542	...	...	15.25±0.02	...	11.48±0.03	...	...	14.48±0.02	13.24±0.04	13.13±0.05	2
HD-73882	...	...	...	...	12.12±0.02	13.33±0.02	...	15.06±0.02	13.80±0.04	13.48±0.10	2
HD-110432	...	...	...	...	11.49±0.03	12.85±0.03	...	14.62±0.03	13.17±0.04	13.29±0.08	2
HR-4908	...	...	...	...	11.94±0.02	13.24±0.02	...	14.93±0.02	13.63±0.04	13.49±0.08	2
TET-MUS	...	...	...	...	12.18±0.02	13.42±0.03	...	15.17±0.02	13.92±0.06	13.64±0.03	2
RHO-OPH-A	...	...	...	...	11.49±0.02	13.10±0.02	...	14.84±0.02	13.56±0.03	13.18±0.07	2
CHI-OPH	...	...	...	...	11.55±0.03	12.97±0.03	...	14.82±0.02	13.36±0.04	13.27±0.03	2
HD-149404	...	...	...	...	12.06±0.02	13.47±0.02	...	15.23±0.02	13.91±0.03	13.79±0.09	2
HD-154368	...	...	...	...	12.00±0.04	13.30±0.05	...	15.03±0.03	...	13.69±0.05	2
HD-164402	...	...	...	...	12.07±0.02	13.36±0.02	...	15.02±0.02	...	13.75±0.05	2
KAP-AQL	...	...	...	...	11.50±0.03	12.90±0.05	...	14.69±0.03	13.20±0.11	13.13±0.04	2
HD-188439	...	...	...	...	...	13.07±0.03	...	14.85±0.02	13.60±0.03	13.21±0.02	2
HD-199579	...	...	...	...	11.63±0.07	13.00±0.04	...	14.80±0.02	13.38±0.06	13.60±0.05	1,2
HD-206267	...	...	...	...	12.01±0.07	13.25±0.02	...	15.02±0.02	...	13.73±0.03	1,2

Notes: References: 1=Jenkins (2009); 2=De Cia et al. (2021). Revised f-values from Cashman et al. (2017), Kisielius et al. (2014, 2015) and Kurucz (2017).

Table 3.9: Milky Way. Elements with limited coverage

Star	log N(OI)	log N(FeII)	log N(ZnII)	log N(CoII)	log N(GeII)	log N(KrI)	log N(ClII)	log N(CuII)	log N(AlII)	log N(CII)	Ref
HD-18100	...	14.67±0.04	12.62±0.05	...	...	...	...	...	...	13.69±0.07	1
KSI-PER	17.81±0.06	14.72±0.03	13.39±0.02	...	...	...	14.54±0.41	12.21±0.07	...	14.50±0.03	1
23O-ORI	17.31±0.10	14.38±0.03	13.28±0.07	...	11.89±0.04	...	13.57±0.68	12.03±0.03	...	14.28±0.04	1
DEL-ORI-A	16.66±0.05	14.06±0.06	12.62±0.05	...	...	...	13.23±0.11	...	...	13.30±0.20	1
EPS-ORI	16.97±0.05	14.21±0.05	12.97±0.06	...	...	11.42±0.09	13.51±0.06	...	...	13.75±0.08	1
MU-COL	...	14.31±0.01	12.59±0.08	...	...	...	...	...	...	13.58±0.02	1
TAU-CMA	17.32±0.04	14.76±0.09	13.24±0.05	...	...	11.77±0.06	14.03±0.13	...	...	...	1
ZET-PUP	...	14.08±0.05	12.44±0.20	...	...	...	13.45±0.15	...	...	13.48±0.05	1
HD-116852	17.55±0.04	15.24±0.02	13.23±0.03	...	12.0±0.07	12.08±0.06	...	12.27±0.08	...	...	1
1-SCO	17.94±0.09	14.81±0.20	13.49±0.05	...	...	12.26±0.11	14.13±0.23	12.34±0.05	...	14.20±0.13	1
PI-SCO	...	14.46±0.10	13.14±0.02	...	...	...	...	12.02±0.07	...	13.87±0.20	1
BET-1-SCO	17.66±0.07	14.81±0.22	13.52±0.05	...	...	...	13.85±0.04	...	...	14.20±0.08	1
ZET-OPH	17.62±0.04	14.39±0.03	13.19±0.05	...	11.98±0.04	...	...	12.21±0.03	...	...	1
LAM-SCO	15.87±0.02	13.39±0.04	11.76±0.06	...	...	...	13.00±0.10	...	...	12.56±0.05	1
HD-73882	...	15.06±0.02	13.48±0.10	12.83±0.22	...	...	...	...	...	...	2
TET-MUS	...	15.17±0.02	13.64±0.03	13.12±0.13	...	...	...	...	...	...	2
HD-149404	...	15.23±0.02	13.79±0.09	13.14±0.14	...	...	...	...	...	...	2
HD-154368	...	15.03±0.03	13.69±0.05	13.47±0.04	...	...	...	...	...	...	2
HD-164402	...	15.02±0.02	13.75±0.05	13.33±0.04	...	...	...	...	...	...	2
KAP-AQL	...	14.69±0.03	13.13±0.04	13.01±0.23	...	...	...	...	...	...	2
HD-206267	...	15.02±0.02	13.73±0.03	13.60±0.12	...	...	...	...	...	...	2,3
DEL-LUP	...	13.75±0.11	12.38±0.10	...	...	...	...	...	12.65±0.10	...	2,3
HD136664	...	12.77±0.10	13.67±0.16	...	...	...	...	...	12.77±0.10	...	2,3
HD135348	...	13.97±0.10	13.10±0.33	...	...	...	...	...	13.10±0.22	...	2,3

Notes: Milky Way column densities of the elements with limited coverage. Revised f-values from Cashman et al. (2017) and Kisielius et al. (2014, 2015) and Kurucz (2017). References: 1=Jenkins (2009); 2=De Cia et al. (2021); 3=Phillips, Gondhalekar, and Pettini (1982).

Table 3.10: GRB-DLAs

GRB	z_{abs}	log N(HI)	log N(OI)	log N(ZnII)	log N(SII)	log N(SiII)[a]	log N(MgII)[a]	log N(MnII)	log N(CrII)[a]	log N(NiII)[a]	log N(FeII)	log N(TiII)[a]
090926A	2.1069	21.58±0.01	>15.00	12.24±0.11	14.52±0.04	15.21±0.05	>14.60	<13.00	<12.90	13.40±0.11	14.21±0.02	<11.60
120327A	2.8143	22.07±0.01	>16.30	13.21±0.04	15.75±0.02	>14.50	16.40±0.23	...	14.10±0.02	14.57±0.04	15.79±0.06	12.69±0.08
120716A	2.4874	21.73±0.03	>15.50	13.65±0.05	16.00±0.14	>16.20	>14.80	13.93±0.18	14.38±0.22	<15.40	15.81±0.22	...
120815A	2.3582	22.09±0.01	>16.00	13.27±0.02	15.51±0.05	>15.40	...	13.29±0.07	13.37±0.08	14.16±0.08	15.11±0.05	<12.50
121024A	2.3005	21.78±0.02	>15.00	13.65±0.06	>15.70	16.62±0.14	>17.80	13.76±0.03	14.07±0.05	14.24±0.34	15.73±0.05	...
140311A	4.9550	22.30±0.02	>15.50	13.28±0.14	15.48±0.12	>14.70	>14.60	13.49±0.03	14.11±0.08	14.40±0.23	15.78±0.15	...
141109A	2.9940	22.18±0.02	>17.20	13.18±0.06	15.81±0.05	>15.60	>15.60	13.57±0.56	13.80±0.03	14.06±0.17	15.54±0.04	<12.80
150403A	2.0571	21.73±0.02	>16.70	13.32±0.04	15.78±0.08	>15.80	>15.70	>13.50	14.06±0.03	14.23±0.10	15.54±0.07	...
151021A	2.3297	22.14±0.03	>16.00	13.79±0.06	15.97±0.15	>16.00	>16.10	13.87±0.03	14.19±0.04	14.61±0.07	15.78±0.06	...

Notes: Redshifts and column densities are taken from Bolmer et al. (2019). Revised f-values from [a]Cashman et al. (2017) and [b] Boissé and Bergeron (2019).

Table 3.11: LMC column densities

Star	log N(HI)	log N(CrII)	log N(FeII)	log N(MgII)	log N(NiII)	log N(OI)	log N(PII)	log N(SII)	log N(SiII)	log N(ZnII)	log N(TiII)
BI173	21.25±0.05	13.57±0.03	15.24±0.03	16.01±0.10	13.94±0.03	...	13.79±0.02	15.86±0.06	15.91±0.20	13.22±0.04	...
BI184	21.15±0.04	13.61±0.06	15.31±0.04	16.05±0.05	14.15±0.10	...	...	...	15.78±0.16	13.19±0.07	...
BI237	21.65±0.03	13.53±0.06	15.23±0.04	16.32±0.05	13.98±0.06	...	...	...	15.84±0.14	13.36±0.06	12.45±0.05
BI253	21.68±0.03	13.72±0.04	15.46±0.03	16.38±0.09	14.17±0.06	...	...	...	...	13.44±0.03	12.71±0.04
PGMW3120	21.48±0.03	13.60±0.06	15.22±0.05	16.05±0.12	14.00±0.06	...	...	...	15.93±0.26	13.34±0.06	...
PGMW3223	21.40±0.06	13.51±0.06	15.24±0.03	16.12±0.11	13.93±0.05	...	...	...	15.84±0.17	13.42±0.05	...
SK-6522	20.66±0.03	13.19±0.06	14.94±0.04	...	13.68±0.07	...	...	15.78±0.11	15.58±0.12	12.92±0.05	...
SK-66172	21.27±0.03	13.15±0.09	14.85±0.05	15.89±0.14	13.65±0.15	...	...	15.68±0.15	...	13.11±0.04	...
SK-6619	21.87±0.07	13.64±0.09	15.32±0.04	16.49±0.16	14.00±0.06	...	...	...	...	13.72±0.12	...
SK-6635	20.85±0.04	...	15.06±0.04	15.88±0.12	13.73±0.05	...	...	15.85±0.11	15.73±0.12	13.05±0.13	...
SK-67101	20.20±0.04	13.22±0.09	14.90±0.06	...	13.63±0.11	...	...	15.26±0.03	15.26±0.09	12.73±0.12	...
SK-67105	21.26±0.04	13.09±0.06	14.86±0.04	15.83±0.19	13.65±0.08	18.22±0.19	...	15.5±0.07	15.29±0.06	12.87±0.06	...
SK-6714	20.24±0.06	...	14.87±0.06	...	13.72±0.07	...	...	15.42±0.05	15.16±0.10	...	...
SK-67191	20.78±0.03	13.31±0.09	15.07±0.04	15.65±0.19	13.81±0.08	...	...	15.71±0.05	15.61±0.12	12.74±0.20	...
SK-672	21.46±0.12	13.89±0.06	14.89±0.06	15.87±0.13	13.52±0.17	...	...	15.55±0.17	...	13.19±0.09	12.09±0.04
SK-67211	20.81±0.04	13.31±0.06	15.06±0.04	15.69±0.12	13.85±0.06	...	13.98±0.48	15.77±0.05	15.80±0.19	12.94±0.05	12.31±0.03
SK-675	21.04±0.04	13.14±0.07	14.90±0.03	15.87±0.09	13.53±0.08	...	...	15.68±0.04	15.72±0.05	13.05±0.04	12.24±0.03
SK-68129	21.62±0.14	13.61±0.05	15.28±0.03	16.50±0.07	...	...	...	...	...	13.76±0.14	...
SK-68135	21.48±0.02	13.70±0.05	15.36±0.03	16.25±0.12	14.07±0.04	...	...	...	...	13.55±0.06	12.66±0.03
SK-68140	21.51±0.11	13.80±0.06	15.38±0.03	16.44±0.19	14.24±0.09	...	...	...	16.20±0.24	13.69±0.10	...
SK-68155	21.47±0.09	13.82±0.04	15.48±0.03	16.50±0.07	14.27±0.09	...	...	...	16.02±0.13	13.69±0.04	...
SK-6826	21.65±0.06	13.65±0.10	15.04±0.05	16.23±0.08	13.90±0.06	...	...	...	...	13.24±0.14	...
SK-6852	21.31±0.06	13.81±0.04	15.26±0.03	15.97±0.13	13.99±0.06	...	...	15.9±0.04	15.69±0.13	12.84±0.12	12.50±0.03
SK-6873	21.68±0.02	13.65±0.03	15.32±0.02	16.49±0.14	14.07±0.04	18.02±0.13	...	...	...	13.71±0.12	12.48±0.03
SK-69104	19.57±0.68	...	14.08±0.08	...	...	...	...	14.61±0.11	15.0±0.12	12.29±0.26	...
SK-69175	20.64±0.03	...	15.05±0.08	...	13.65±0.17	...	...	15.68±0.06	15.36±0.19	12.58±0.09	...
SK-69246	21.48±0.02	13.71±0.03	15.43±0.02	16.31±0.11	14.12±0.03	...	...	15.92±0.15	15.96±0.14	13.38±0.04	12.60±0.03
SK-69279	21.63±0.05	13.80±0.03	15.36±0.03	16.34±0.14	14.04±0.08	...	...	...	15.89±0.13	13.27±0.05	...
SK-70115	21.18±0.08	13.70±0.03	15.43±0.03	16.17±0.11	14.12±0.05	...	...	15.94±0.06	15.99±0.12	13.25±0.04	12.73±0.05
SK-7079	21.34±0.04	...	14.78±0.07	15.82±0.11	13.37±0.13	18.04±0.17	...	15.61±0.15	...	13.44±0.06	...
SK-7145	21.11±0.03	13.62±0.05	15.34±0.03	16.15±0.19	14.04±0.06	...	...	...	15.94±0.15	13.30±0.05	...
SK-7150	21.24±0.05	13.78±0.03	15.54±0.03	15.92±0.22	14.21±0.04	...	...	15.89±0.14	15.87±0.10	13.24±0.04	...

Notes: Column densities are taken from Roman-Duval et al. (2021), except for the PII for BI173, SK-70115, SK-6522, SK-675, SK-7145, SK-66172,SK-68135, which are from Tchernyshyov et al. (2015). Revised f-values from Cashman et al. (2017), Boissé and Bergeron (2019) and Kurucz (2017) for PII.

Table 3.12: SMC column densities

Star	H_{tot}	log N(MgII)	log N(SiII)	log N(SII)	log N(TiII)	log N(CrII)	log N(MnII)	log N(FeII)	log N(NiII)	log N(ZnII)	log N(PII)
AzV18	22.06±0.02	16.68±0.07	...	...	12.94±0.01	13.95±0.06	13.48±0.02	15.61±0.03	14.29±0.04	13.67±0.08	...
AzV26	21.77±0.04	16.11±0.05	16.05±0.05	...	12.86±0.01	13.82±0.02	13.38±0.01	15.51±0.02	14.23±0.02	13.26±0.05	...
AzV47	21.32±0.04	16.07±0.12	15.81±0.06	15.84±0.08	12.78±0.03	13.67±0.04	13.25±0.03	15.37±0.03	14.06±0.04	13.09±0.06	13.86±0.03
AzV80	21.83±0.02	16.37±0.09	...	...	12.77±0.03	13.70±0.03	13.26±0.02	15.39±0.03	14.09±0.04	13.23±0.05	...
AzV95	21.50±0.04	16.02±0.15	15.94±0.06	15.84±0.07	12.78±0.04	13.70±0.04	13.24±0.02	15.37±0.03	14.04±0.04	13.09±0.06	13.86±0.01
AzV104	21.46±0.06	16.14±0.10	15.89±0.11	15.78±0.05	...	13.48±0.09	...	15.31±0.04	14.01±0.04	12.97±0.16	...
AzV207	21.44±0.06	...	15.95±0.22	...	12.45±0.08	13.50±0.06	13.09±0.03	15.16±0.04	...	13.14±0.05	...
AzV216	21.64±0.03	16.33±0.08	...	...	...	13.67±0.05	...	15.41±0.03	14.14±0.04	13.28±0.07	...
AzV229	21.06±0.04	15.82±0.10	15.67±0.05	15.57±0.05	12.34±0.04	13.31±0.08	12.87±0.03	14.88±0.02	13.74±0.04	12.65±0.08	...
AzV242	21.32±0.04	16.03±0.10	15.82±0.06	15.83±0.05	12.46±0.02	13.24±0.21	12.96±0.04	15.08±0.04	13.85±0.05	13.39±0.18	...
AzV321	20.70±0.08	...	15.40±0.09	15.46±0.05	12.06±0.03	...	12.66±0.12	14.66±0.03	13.57±0.13	12.71±0.11	...
AzV332	20.54±0.16	...	15.45±0.06	15.35±0.06	...	13.11±0.03	12.83±0.04	14.82±0.04	13.45±0.12	12.53±0.05	...
AzV388	21.19±0.04	16.08±0.13	15.61±0.06	15.71±0.05	12.10±0.08	...	12.73±0.09	14.74±0.02	...	12.88±0.07	...
AzV456	21.43±0.07	...	15.44±0.10	...	11.97±0.10	...	12.68±0.08	14.60±0.05	...	13.11±0.08	...
AzV476	21.95±0.08	...	...	...	12.78±0.01	13.73±0.03	13.34±0.02	15.43±0.03	14.10±0.07	13.39±0.17	14.11±0.04
SK143	21.43±0.21	...	15.03±0.11	...	11.97±0.07	11.47±0.97	...	14.65±0.03	...	12.57±0.33	...
AzV327	21.62±0.22	...	...	...	...	...	...	14.67±0.02	...	12.75±0.19	13.39±0.13
AzV238	21.41±0.21	...	...	...	...	...	...	14.91±0.02	...	13.05±0.04	13.74±0.04
SK116	21.57±0.21	...	...	...	...	...	...	15.36±0.03	...	13.15±0.02	13.92±0.04

Notes: All column densities are taken from Jenkins and Wallerstein (2017), except for the case of SK143, for which log N(TiII) is taken from Welty and Crowther (2010) and log N(ZnII), log N(FeII) are taken from Tchernyshyov et al. (2015). Revised f-values from Cashman et al. (2017), Boissé and Bergeron (2019) and Kurucz (2017).

3.E UPDATED COLUMN DENSITIES AND COEFFICIENTS FOR PHOSPHORUS

This is a corrigendum published in Astronomy&Astrophysics, Volume 674, C1, 2023
A&A, 674, C1 (2023)

In this erratum we remove duplicate entries from Table D.1 of the original paper for QSO-DLAs. Removing the duplicated entries from Table D.1 has no effect on the results of the original paper.

Additionally, we update the PII column densities for the Milky Way that are taken from Jenkins (2009) adopting the most recent value f= 0.0196 for the λ1301 line of Brown et al. (2018). This value is based on comprehensive beam-foil measurements. In the original paper we homogenized the PII column densities to the oscillator strength f = 0.0053 derived by Kurucz (2017), which is an older value. The updated column densities are given in Table 3.13. The updated and the old $A2_P$ and $B2_P$ coefficients resulting from the fit are presented in Table 3.14, where the difference between the old and new values are small. Figure 3.36 shows the updated fit for [P/Zn] with [Zn/Fe] (top) and the dust depletion δ_P with [Zn/Fe] (bottom).

The updated table for QSO-DLAs without the duplicates is Table 3.15.

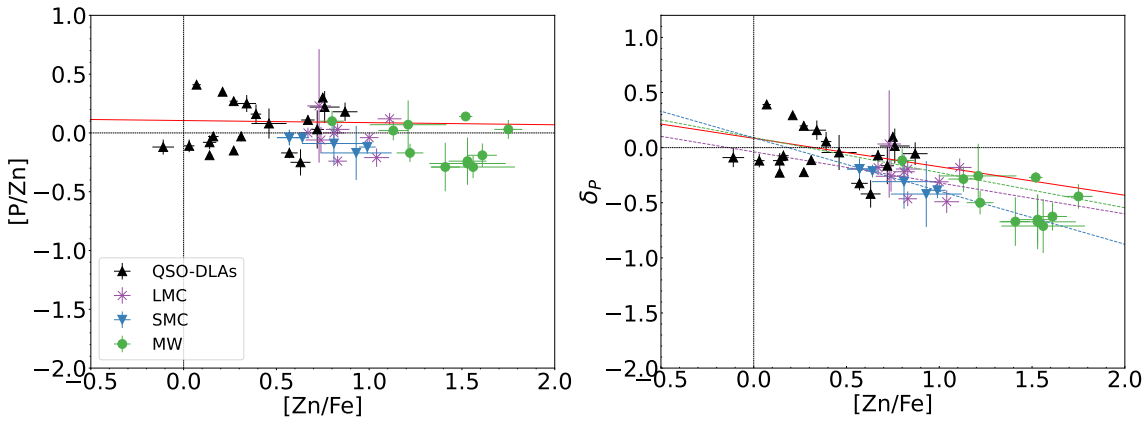


Figure 3.36: Relative abundance of P with respect to Zn against [Zn/Fe] (top). Dust depletion of P against [Zn/Fe] (bottom). The linear fits for the QSO-DLAs (black triangles and black line), for the LMC (purple stars and purple line), for the SMC (blue triangles and blue line) and for the Milky Way (green points and green line) are shown. The solid red line shows the linear fit to the merged data, resulting in the new $A2_P$ and $B2_P$ coefficients given in Table 3.14.

Table 3.13: The updated column densities for PII

Star	log N(PII)
HD-18100	13.53 ± 0.07
KSI-PER	14.34 ± 0.03
23O-ORI	14.12 ± 0.04
DEL-ORI-A	13.14 ± 0.20
EPS-ORI	13.59 ± 0.08
MU-COL	13.42 ± 0.02
ZET-PUP	13.32 ± 0.05
1-SCO	14.04 ± 0.13
PI-SCO	13.71 ± 0.20
BET-1-SCO	14.04 ± 0.08
LAM-SCO	12.40 ± 0.05

Table 3.14: The coefficients for PII

Coefficients	$A2_P$	$B2_P$	r
new	0.08 ± 0.05	-0.26 ± 0.08	-0.74
old	0.03 ± 0.05	-0.21 ± 0.08	-0.46

Table 3.15: QSO-DLA column densities

QSO	z_{abs}	log N(HI)	log N(OI)	log N(MgII)	log N(SiII)	log N(SII)	log N(PII)	log N(TiII)	log N(CrII)	log N(MnII)	log N(FeII)	log N(CoII)	log N(NiII)	log N(ZnII)	Ref
Q0000-263	3.390	21.40±0.08	16.41±0.10	...	14.99±0.02	14.74±0.03	12.60±0.04	...	13.08±0.03	...	14.87±0.03	...	...	11.91±0.05	1
Q0010-002	2.025	20.95±0.10	...	15.54±0.05	15.24±0.03	15.00±0.03	...	<12.38	13.41±0.02	...	15.18±0.04	...	13.69±0.03	12.09±0.04	*,1
Q0013-004	1.973	20.83±0.05	...	...	15.47±0.01	15.48±0.01	13.92±0.01	...	13.17±0.03	13.00±0.04	14.91±0.01	...	...	12.81±0.01	1
Q0058-292	2.671	21.10±0.10	...	...	15.16±0.04	14.96±0.02	...	12.3±0.11	13.11±0.02	...	14.75±0.02	...	13.55±0.08	12.14±0.02	*,1
Q0100+130	2.309	21.35±0.08	...	15.51±0.06	...	15.13±0.01	12.96±0.02	12.72±0.11	13.37±0.01	12.68±0.04	15.05±0.01	...	...	12.34±0.01	*,1
Q0102-190a	2.37	21.00±0.08	...	...	...	14.34±0.02	...	12.2±0.12	12.78±0.02	12.05±0.04	14.44±0.02	...	13.16±0.07	11.61±0.08	*,1
Q0216+080a	1.769	20.30±0.10	...	...	14.83±0.02	14.47±0.13	...	<12.22	12.68±0.07	...	14.47±0.01	...	<13.08	11.87±0.06	*,1
Q0216+080b	2.293	20.50±0.10	...	...	15.34±0.02	...	13.43±0.06	...	13.18±0.04	...	14.88±0.03	...	...	12.37±0.04	1
Q0347-383	3.025	20.73±0.05	16.44±0.11	...	14.71±0.03	14.78±0.02	12.69±0.10	<11.92	12.82±0.05	...	14.35±0.02	...	<13.70	12.13±0.05	*,1
Q0405-443a	1.913	20.80±0.10	...	...	15.35±0.02	...	...	12.48±0.02	13.45±0.02	12.9±0.02	15.16±0.02	...	13.87±0.01	12.34±0.03	*,1
Q0405-443b	2.55	21.15±0.15	...	...	15.29±0.01	14.98±0.01	...	<12.22	13.26±0.02	12.53±0.12	15.05±0.01	...	13.76±0.01	12.36±0.04	*,1
Q0405-443c	2.595	21.05±0.10	...	...	15.42±0.01	15.15±0.01	13.16±0.02	12.55±0.05	13.40±0.02	12.85±0.02	15.08±0.01	...	13.08±0.01	12.5±0.01	*,1
Q0458-020	2.04	21.70±0.10	...	16.07±0.07	...	...	13.69±0.04	<12.72	13.72±0.02	13.19±0.04	15.33±0.04	...	14.06±0.03	13.05±0.02	*,1
Q0528-250a	2.141	20.98±0.05	...	...	15.21±0.01	14.80±0.02	...	12.62±0.07	13.11±0.02	12.56±0.05	14.78±0.02	...	13.65±0.01	12.19±0.04	*,1
Q0528-250b	2.811	21.35±0.07	...	15.87±0.01	16.03±0.01	15.58±0.01	...	12.76±0.06	13.69±0.01	13.35±0.01	15.48±0.01	...	14.29±0.01	13.01±0.01	*,1
Q0551-366	1.962	20.70±0.08	...	...	15.54±0.03	15.42±0.05	13.17±0.11	<12.56	13.26±0.03	13.12±0.02	15.05±0.02	...	14.09±0.01	12.92±0.03	*,1
Q0841+129a	1.864	21.00±0.10	...	...	...	14.73±0.05	...	...	...	12.55±0.04	14.88±0.04	...	12.38±0.05	13.02±0.03	*,1
Q0841+129b	2.375	21.05±0.10	...	15.13±0.04	15.03±0.03	14.77±0.02	12.81±0.03	<13.06	13.06±0.02	12.49±0.02	14.72±0.02	...	13.55±0.01	12.03±0.02	*,1
Q0841+129c	2.476	20.80±0.10	16.11±0.03	14.95±0.05	14.69±0.02	14.48±0.02	12.5±0.05	<11.94	12.82±0.02	12.31±0.02	14.48±0.02	...	13.3±0.02	11.77±0.03	*,1
Q1037-270	2.139	19.70±0.05	...	15.17±0.02	15.17±0.02	14.83±0.01	13.18±0.01	...	12.89±0.01	12.52±0.02	14.74±0.01	...	...	11.96±0.02	1
Q1111-152	3.266	21.30±0.05	...	...	15.03±0.02	14.79±0.02	...	...	13.27±0.04	...	14.82±0.02	...	13.56±0.01	12.22±0.09	*,1
Q1117-134	3.35	20.95±0.10	...	...	15.03±0.02	...	...	12.49±0.05	13.08±0.04	...	14.81±0.03	...	<13.53	12.11±0.05	*,1
Q1157+014	1.944	21.80±0.10	...	15.95±0.02	15.92±0.01	...	13.71±0.04	12.99±0.01	13.78±0.01	13.26±0.01	15.47±0.01	...	14.19±0.01	12.93±0.01	*,1
Q1209+093	2.584	21.40±0.10	...	...	15.9±0.02	15.58±0.02	...	<12.60	13.57±0.02	13.11±0.02	15.36±0.02	...	14.16±0.04	12.96±0.02	*,1
Q1223+178	2.466	21.40±0.10	...	15.82±0.04	15.43±0.01	15.19±0.02	...	12.73±0.06	13.47±0.01	12.86±0.02	15.21±0.01	...	13.86±0.05	12.34±0.02	*,1
Q1331+170	1.776	21.15±0.07	...	15.52±0.03	15.23±0.01	15.11±0.01	13.36±0.02	<11.95	12.86±0.02	12.49±0.02	14.62±0.02	...	13.41±0.02	12.44±0.03	*,1
Q1409+095a	2.019	20.65±0.10	...	...	14.57±0.05	14.14±0.04	...	<12.88	12.63±0.07	...	14.34±0.02	...	13.15±0.08	11.6±0.13	*,1
Q1444+014	2.087	20.25±0.07	...	...	14.31±0.04	14.66±0.04	13.01±0.05	<12.43	12.36±0.11	...	14.0±0.03	...	<12.81	12.02±0.06	*, 1
Q1451+123a	2.255	20.35±0.10	...	...	14.89±0.08	...	...	<12.97	12.86±0.10	...	14.42±0.05	...	<13.60	11.85±0.11	*,1
Q2116-358	1.996	20.10±0.07	...	...	15.17±0.05	14.98±0.07	13.22±0.10	<12.43	13.03±0.06	...	14.72±0.05	...	13.61±0.02	12.33±0.08	*,1
Q2138-444a	2.383	20.60±0.05	...	...	14.89±0.01	14.75±0.10	...	<12.64	12.99±0.05	12.45±0.05	14.54±0.01	...	<12.90	12.02±0.08	*,1
Q2138-444b	2.852	20.98±0.05	...	...	14.79±0.02	14.54±0.02	12.51±0.05	<11.83	12.91±0.02	12.21±0.04	14.63±0.02	...	13.33±0.02	11.81±0.02	*,1
Q2206-199a	1.921	20.67±0.05	...	15.7±0.04	15.72±0.01	15.42±0.02	13.86±0.03	12.86±0.02	13.59±0.01	13.1±0.02	15.34±0.01	...	14.16±0.02	12.7±0.01	*,1
Q2243-605	2.331	20.65±0.05	...	...	15.33±0.01	15.05±0.01	13.45±0.01	12.64±0.03	13.19±0.02	12.8±0.03	14.95±0.01	...	13.83±0.02	12.37±0.02	*,1
Q2332-094a	2.287	20.07±0.07	...	...	14.95±0.02	14.67±0.02	...	...	12.51±0.06	12.19±0.05	14.23±0.03	...	13.25±0.04	12.31±0.02	*,1
Q2343+125	2.431	20.40±0.07	...	15.02±0.08	15.04±0.02	14.72±0.02	13.02±0.08	<11.97	12.78±0.02	12.35±0.02	14.51±0.02	...	13.36±0.03	12.05±0.02	*,1
Q2359-022a	2.095	20.65±0.10	...	...	15.36±0.02	15.17±0.04	13.41±0.11	<12.51	13.04±0.09	...	14.47±0.01	...	<13.59	12.38±0.08	*,1
Q1328+307	0.692	21.25±0.10	...	...	...	...	12.50±0.10	...	13.28±0.10	...	14.98±0.10	...	...	12.62±0.1	2
Q1137+3907	0.720	21.10±0.10	...	...	...	...	...	...	13.69±0.20	...	15.45±0.05	...	...	13.33±0.05	2
J1431+3952	0.602	21.20±0.10	...	...	...	...	...	12.66±0.15	13.51±0.18	13.08±0.14	15.15±0.11	...	...	12.93±0.19	2
J2328+0022	0.652	20.32±0.07	...	...	...	...	12.43±0.03	...	13.33±0.19	12.85±0.02	14.84±0.01	...	...	12.33±0.15	2
J0256+0110	0.720	20.70±0.16	...	...	...	...	...	12.23±0.05	13.79±0.05	13.25±0.02	15.13±0.30	...	...	13.09±0.04	2
B0105-008	1.371	21.70±0.15	...	...	...	...	...	12.96±0.20	13.90±0.03	13.30±0.04	15.59±0.03	...	14.25±0.04	12.83±0.04	2
J1107+0048	0.740	21.00±0.05	...	...	...	...	...	...	13.82±0.06	13.28±0.03	15.53±0.02	...	...	12.96±0.15	2
Q1010+0003	1.265	21.52±0.07	...	...	15.8±0.06	...	...	...	13.52±0.07	13.24±0.11	15.26±0.05	...	14.20±0.07	12.86±0.06	2
Q0302-223	1.009	20.36±0.11	...	...	15.11±0.06	...	...	...	13.06±0.06	12.58±0.06	14.67±0.05	...	13.57±0.06	12.35±0.06	2
Q1727+5302	1.03	21.41±0.15	...	...	15.44±0.01	...	...	...	13.31±0.11	13.06±0.02	14.81±0.01	...	...	12.66±0.24	2
Q1727+5302	0.945	21.16±0.10	...	...	15.84±0.08	...	...	...	13.57±0.11	13.52±0.01	15.29±0.01	...	...	13.15±0.11	2
B2355-106	1.172	21.00±0.10	...	...	15.35±0.13	...	...	...	...	12.92±0.1	15.08±0.10	...	14.17±0.12	12.66±0.17	2
J1623+0718	1.336	21.35±0.10	...	...	15.71±0.05	...	...	...	13.53±0.06	13.07±0.06	15.28±0.05	...	14.11±0.07	12.81±0.09	2
HE0515-4414	1.150	20.45±0.15	...	...	14.67±0.18	...	12.6±0.27	...	...	11.94±0.11	14.31±0.2	...	...	12.01±0.04	2
J0927+1543	1.73	...	...	...	15.92±0.05	...	...	...	13.81±0.05	...	15.14±0.24	...	14.17±0.05	13.28±0.05	2
J1142+0701	1.841	21.50±0.15	...	...	16.08±0.13	...	...	...	13.68±0.05	...	15.47±0.05	...	14.01±0.05	13.19±0.05	2

Table 3.15: continued

QSO	z_{abs}	log N(HI)	log N(OI)	log N(MgII)	log N(SiII)	log N(SII)	log N(PII)	log N(TiII)	log N(CrII)	log N(MnII)	log N(FeII)	log N(CoII)	log N(NiII)	log N(ZnII)	Ref
J1313+1441	1.801	...	...	...	16.05±0.05	...	...	...	13.59±0.05	...	15.55±0.05	...	14.27±0.05	13.2±0.05	2
Q0948+433	1.233	21.62±0.06	...	...	...	...	...	13.3±0.07	13.88±0.01	13.31±0.01	15.56±0.01	13.02±0.12	...	13.05±0.01	2
J1056+1208	1.610	21.45±0.15	...	...	16.41±0.09	...	...	...	14.02±0.05	...	15.81±0.05	...	14.69±0.05	13.66±0.05	2
J1310+5424	1.801	21.45±0.15	...	...	16.37±0.05	...	...	...	13.97±0.05	...	15.64±0.05	...	14.45±0.05	13.47±0.05	2
Q0935+417	1.373	20.52±0.10	...	...	...	...	...	...	13.16±0.05	12.46±0.08	14.82±0.1	...	...	12.16±0.02	2
J0008-0958	1.768	20.85±0.15	...	...	15.97±0.05	15.88±0.05	...	...	13.89±0.05	...	15.62±0.05	...	14.46±0.05	13.21±0.05	2
J1454+0941	1.788	20.50±0.15	...	...	15.4±0.05	15.29±0.06	...	...	13.28±0.09	...	15.02±0.12	...	13.89±0.05	12.62±0.05	2
Q1354+258	1.420	21.54±0.06	...	...	15.29±0.08	...	...	...	13.40±0.06	12.76±0.06	15.01±0.04	...	13.11±0.08	12.49±0.08	1
J1417+4132	1.951	21.45±0.25	17.98±0.07	...	...	...	...	...	14.02±0.05	...	15.58±0.05	...	14.55±0.05	13.45±0.05	2
J1552+4910	1.96	...	...	...	15.91±0.05	15.38±0.05	...	...	13.72±0.05	13.4±0.05	15.47±0.05	...	14.24±0.05	12.83±0.05	2
J2340-00	2.054	20.35±0.15	...	...	15.16±0.05	14.99±0.05	...	...	...	...	14.98±0.05	...	13.81±0.05	12.53±0.07	2
Q1755+578	1.971	21.40±0.15	...	...	16.51±0.05	...	...	...	14.07±0.05	13.84±0.05	15.79±0.05	...	14.75±0.05	13.75±0.05	2
J1049-0110	1.658	20.31±0.15	...	...	15.73±0.05	15.51±0.05	...	...	13.47±0.05	...	15.17±0.05	...	14.25±0.05	13.04±0.05	2
SDSS1249-0233	1.781	21.45±0.15	...	...	...	15.57±0.05	...	13.02±0.10	13.89±0.02	13.20±0.02	15.47±0.02	...	14.29±0.05	13.05±0.05	2
Q2230+025	1.864	20.83±0.05	...	...	15.58±0.05	15.33±0.05	...	12.64±0.09	13.38±0.05	13.04±0.03	15.19±0.05	...	14.13±0.05	12.7±0.05	1
Q2228-3954	2.095	21.2±0.10	...	...	...	...	...	...	...	...	15.17±0.02	...	...	12.41±0.06	2
HE1104-1805	1.662	20.85±0.01	16.80±0.20	...	15.31±0.02	...	...	12.24±0.07	13.05±0.01	12.78±0.14	14.77±0.02	...	13.42±0.03	12.38±0.01	2
Q0149+33	2.141	20.50±0.10	...	...	14.50±0.05	...	...	...	12.70±0.04	...	14.20±0.02	...	13.17±0.04	11.40±0.10	2
B2314-409	1.857	20.90±0.10	...	...	15.34±0.1	15.14±0.15	...	...	13.36±0.08	...	15.08±0.1	...	13.84±0.08	12.42±0.1	2
Q0027-1836	2.402	21.75±0.10	...	16.00±0.04	15.6±0.03	15.27±0.02	...	12.57±0.06	13.35±0.01	12.85±0.03	14.97±0.02	...	13.70±0.02	12.69±0.02	2
Q0201+365	2.463	20.38±0.05	...	...	15.46±0.01	15.33±0.01	...	...	13.23±0.03	...	15.01±0.01	...	14.02±0.01	12.37±0.05	2
J0058+0115	2.010	21.10±0.15	...	...	...	15.44±0.05	...	...	13.52±0.05	...	15.18±0.05	...	14.16±0.05	12.85±0.05	1
Q0933+733	1.479	21.62±0.10	...	...	...	...	...	...	13.54±0.01	12.97±0.01	15.19±0.01	...	13.92±0.01	12.61±0.02	2
Q1210+17	1.892	20.63±0.08	...	...	15.26±0.03	15.0±0.02	...	12.3±0.08	13.26±0.03	12.73±0.01	15.01±0.03	...	13.67±0.06	12.3±0.05	2
SDSS2059-0529	2.210	20.80±0.20	...	...	15.29±0.10	...	...	...	13.53±0.12	...	15.00±0.11	...	13.88±0.11	12.84±0.11	2
J1541+3153	2.444	20.95±0.10	...	...	14.9±0.04	...	...	...	12.59±0.14	...	14.5±0.11	...	13.10±0.08	11.93±0.11	2
Q1232+082	2.338	20.09±0.10	...	15.44±0.09	15.17±0.11	14.87±0.10	...	...	...	...	14.68±0.08	...	...	12.61±0.11	2
Q1215+33	1.999	20.95±0.07	...	...	14.96±0.03	...	...	...	13.11±0.03	...	14.75±0.05	...	13.59±0.03	12.23±0.05	2
Q0449-1645	1.007	20.98±0.07	...	...	15.79±0.04	...	...	...	13.45±0.02	12.92±0.03	15.09±0.01	13.51±0.07	...	12.52±0.07	2
FJ0812+32	2.067	21.00±0.10	...	...	15.11±0.01	...	...	12.49±0.03	13.22±0.01	12.66±0.03	14.89±0.02	...	13.62±0.01	12.11±0.02	2
FJ0812+32	2.626	21.35±0.10	17.69±0.07	16.24±0.01	15.91±0.05	15.67±0.07	...	...	13.34±0.05	...	15.09±0.05	...	13.89±0.05	13.05±0.05	2
UM673A	1.626	20.70±0.10	...	...	14.68±0.03	...	...	...	12.76±0.04	...	14.59±0.03	...	12.99±0.04	11.33±0.15	2
J1135-0010	2.207	22.05±0.10	...	...	16.42±0.03	...	...	13.24±0.04	14.12±0.01	13.63±0.01	15.76±0.03	...	14.67±0.02	13.52±0.03	2
Q2318-1107	1.989	20.68±0.05	...	...	15.27±0.01	15.13±0.02	...	...	13.11±0.06	...	14.91±0.01	...	13.82±0.03	12.4±0.03	2
SDSS0225+0054	2.714	21.00±0.15	...	...	15.54±0.07	...	...	...	13.76±0.10	...	15.30±0.08	...	14.17±0.11	12.79±0.11	2
SDSS1116+4118A	2.662	20.48±0.10	...	...	14.98±0.11	...	...	...	...	...	14.36±0.10	...	13.35±0.20	12.3±0.20	2
Q2231-00	2.066	20.53±0.08	...	...	15.22±0.04	15.14±0.15	...	12.62±0.08	12.98±0.04	12.60±0.04	14.83±0.03	...	13.54±0.06	12.20±0.05	2
Q0918+1636	2.412	21.26±0.06	...	...	15.93±0.20	...	...	...	13.68±0.21	13.35±0.21	15.51±0.23	...	...	13.13±0.18	2
Q0918+1636	2.583	20.96±0.05	...	...	15.94±0.01	15.86±0.01	...	...	13.70±0.01	13.48±0.01	15.43±0.01	...	14.40±0.01	13.30±0.01	2
Q0642-5038	2.662	20.95±0.08	...	...	15.15±0.06	...	...	...	...	...	14.20±0.03	...	...	11.57±0.04	2
J1240+1455	3.108	21.30±0.20	...	...	15.86±0.03	15.60±0.02	...	...	...	...	14.60±0.03	...	...	12.80±0.07	2
SDSS2100-0641	3.092	21.05±0.15	...	...	15.81±0.05	15.53±0.05	...	...	13.57±0.05	...	15.37±0.05	...	14.23±0.05	13.14±0.05	2
J1604+3951	3.163	21.75±0.20	...	...	...	15.75±0.05	...	...	...	...	15.47±0.05	...	14.24±0.05	13.02±0.05	2
Q1425+6039	2.827	20.30±0.04	...	...	...	...	...	...	...	...	14.48±0.01	...	13.27±0.03	12.08±0.04	2
SDSS1610+4724	2.508	21.15±0.15	...	...	16.09±0.05	...	...	...	13.88±0.05	13.79±0.01	15.62±0.05	...	14.58±0.05	13.46±0.05	2
FJ2334-0908	3.057	20.48±0.05	16.19±0.06	...	14.75±0.03	13.97±0.03	...	...	...	...	14.39±0.03	...	...	12.03±0.02	2
J1200+4015	3.220	20.65±0.15	...	...	...	15.40±0.05	...	12.92±0.03	13.51±0.05	...	15.31±0.05	...	14.18±0.05	12.76±0.05	2
J1155+0530	3.326	21.05±0.10	...	...	15.87±0.05	15.44±0.05	...	...	13.34±0.09	...	15.37±0.05	...	14.07±0.05	12.79±0.07	2
PSS1253-0228	2.783	21.85±0.20	...	...	...	...	...	...	13.61±0.03	13.43±0.07	15.36±0.04	...	14.17±0.04	12.67±0.07	2
PSSJ2344+0342	3.220	21.25±0.08	...	...	...	...	...	...	13.32±0.10	...	15.06±0.15	...	13.59±0.11	12.13±0.30	2
BRI1013+0035	3.104	21.10±0.10	...	...	15.71±0.02	...	...	...	...	...	15.18±0.05	...	13.89±0.05	13.23±0.02	2
J1211+0833	2.117	21.00±0.20	...	...	...	...	...	...	12.76±0.14	...	14.77±0.03	...	13.62±0.08	13.48±0.06	2
eHAQ0111+0641	2.027	21.50±0.30	...	...	...	...	...	...	13.88±0.10	...	15.8±0.1	...	...	13.4±0.1	2
J0000+0048	2.525	21.07±0.10	...	...	15.86±0.17	...	...	...	...	...	15.14±0.03	...	13.99±0.04	13.99±0.45	2

Table 3.15: continued

QSO	z_{abs}	log N(HI)	log N(OI)	log N(MgII)	log N(SiII)	log N(SII)	log N(PII)	log N(TiII)	log N(CrII)	log N(MnII)	log N(FeII)	log N(CoII)	log N(NiII)	log N(ZnII)	Ref
J1237+0647	2.690	20.00±0.15	...	...	15.08±0.02	15.43±0.06	...	...	...	...	14.57±0.01	...	13.48±0.03	12.92±0.02	2

Notes: References:(⋆) This work; (1) De Cia et al. (2016); (2) Berg et al. (2015). Revised f-values from Cashman et al. (2017), Kisielius et al. (2014, 2015) and Brown et al. (2018).

4

DUST DEPLETION FROM LOCAL TO DISTANT GALAXIES II: COSMIC DUST-TO-METAL RATIO AND DUST COMPOSITION

In Chapter 3, I presented my work on characterizing dust depletion of several elements in different galactic environments. This included new column density measurements of Ti and Ni, which I measured using Voigt-profile fitting, described in Chapter 2.

Cosmic dust plays a significant role in star formation, metal recycling, and the overall chemical enrichment in galaxies. Yet there are open questions on many of the properties of dust grains, and their production and destruction mechanisms are still only partially understood. The characterization of dust depletion in local and distant galaxies and the extensive compilation of both new and pre-existing literature measurements of metal column densities in Konstantopoulou et al. (2022), enabled a follow-up study using dust depletion to characterize the properties of cosmic dust in these galactic environments.

Here I present my work on the dust properties of different galaxies, which is published in A&A (Konstantopoulou et al., 2024). The aim of this paper is to contribute to our understanding of the properties of dust and the cycle between cosmic dust and metals within the ISM of galaxies. This interplay has a key influence on galaxy evolution. Previous studies have used dust depletion to infer the dust properties of different galaxies. For example, dust depletion can be used to derive the DTM ratio in various environments, providing valuable insights about the dust production mechanisms (e.g., De Cia et al., 2013, 2016; Wiseman et al., 2017; Roman-Duval et al., 2021). Building on my results from Konstantopoulou et al. (2022) on dust depletion, in this paper, I estimate the DTM and DTG ratios in terms of mass and focused on their evolution with metallicity and the amount of dust ([Zn/Fe]) with the goal to understand in which ways dust is formed in different galaxies. Moreover, I estimate, using dust depletion, the dust composition in terms of mass, as well as dust extinction across various galactic environments, including the Milky Way, the Magellanic Clouds, QSO- and GRB-DLAs. The results of this paper underline once again the importance of grain growth in the ISM as a dominant dust production mechanism, agreeing with our previous results.

This chapter contains the following article with title:

"Dust depletion of metals from local to distant galaxies II: Cosmic dust-to-metal ratio and dust composition"

Authors: Christina Konstantopoulou, Annalisa De Cia, Jens-Kristian Krogager, Cédric Ledoux, Pasquier Noterdaeme, Johan P. U. Fynbo, Kasper E. Heintz, Darach Watson, Anja C. Andersen, Iris Jermann and Tanita Ramburuth-Hurt

Published in Astronomy&Astrophysics, Volume 681, Issue A64, January 2024
A&A, 681, A64 (2024) and presented unmodified below.

4.1 ABSTRACT

The evolution of the cosmic dust content and the cycle between metals and dust in the interstellar medium (ISM) plays a fundamental role in galaxy evolution. The chemical enrichment of the Universe can be traced through the evolution of the dust-to-metals ratio (DTM) and the dust-to-gas ratio (DTG) with metallicity. The physical processes through which dust is created and eventually destroyed still remain important open questions. We use a novel method to determine mass estimates of the DTM, DTG and dust composition in terms of fraction of dust mass contributed by element X (f_{M_X}) based on our previous measurements of the depletion of metals in different environments (the Milky Way, the Magellanic Clouds, and damped Lyman-α absorbers, DLAs, toward quasars and towards gamma-ray bursts, GRBs), which were calculated from the relative abundances of metals in the ISM through absorption-line spectroscopy column densities observed mainly from VLT/UVES and X-shooter, and HST/STIS. We also derive the dust extinction from the estimated dust depletion ($A_{V,\mathrm{depl}}$) for GRB-DLAs, the Magellanic Clouds and the Milky Way and compare with the A_V estimated from extinction ($A_{V,\mathrm{ext}}$). We find that the DTM and DTG ratios increase with metallicity and with the dust tracer [Zn/Fe]. This suggests that grain growth in the ISM is a dominant process of dust production, at least in the metallicity range ($-2 \leq [\mathrm{M/H}]_{\mathrm{tot}} \leq 0.5$) and redshift range ($0.6 < z < 6.3$) that we are studying. The increasing trend of the DTM and DTG with metallicity is in good agreement with a dust production and evolution hydrodynamical model. Our data suggest that the stellar dust yield is much lower (about 1%) than the metal yield and thus that the overall amount of dust in the warm neutral medium that is produced by stars is much lower, than previously estimated. The global neutral gas metallicity is decreasing over cosmic time and is traced similarly by quasar- and GRB-DLAs. We find that $A_{V,\mathrm{depl}}$ is overall lower than $A_{V,\mathrm{ext}}$ for the Milky Way and a few Magellanic Clouds lines of sight, a discrepancy that is likely related to the presence of carbonaceous dust associated with dense clumps of cold neutral gas. For the other environments we find an overall good agreement between the

$A_{V,\mathrm{ext}}$ and $A_{V,\mathrm{depl}}$. We show that the main elements ($f_{M_X} > 1\%$) that contribute to the dust composition are, by mass, O, Fe, Si, Mg, C, S, Ni and Al for all the environments, with Si, Mg and C being equivalent contributors. There are, nevertheless, variations in the dust composition depending on the overall amount of dust. The abundances measured at low dust regimes in quasar- and GRB-DLAs suggest the presence of pyroxene and metallic iron in dust. These results give important information on the dust and metal content of galaxies across cosmic times, from the Milky Way up to $z = 6.3$.

4.2 INTRODUCTION

The interplay between the production of metals by stars and the formation and evolution of cosmic dust plays a fundamental role in the chemical enrichment of the interstellar medium (ISM). The cycle of exchanging material between stars, interstellar gas and cosmic dust drives galactic evolution (Maiolino and Mannucci, 2019). Yet the direct observations of the chemical properties of the baryon cycle remains a big challenge.

Metals are formed in stars and are ejected into the ISM by strong stellar winds and supernova explosions. More than 90% of the baryons are found in the gas phase at $z > 2$ (Péroux and Howk, 2020). These metals in the ISM can be incorporated in the next generation of stars. While substantial amount of metals are found in neutral gas, large fractions of these metals are instead locked into dust grains, an effect called dust depletion (Field, 1974; Savage and Sembach, 1996; Phillips, Gondhalekar, and Pettini, 1982; Savaglio, Fall, and Fiore, 2003; Jenkins, 2009; De Cia et al., 2016; Roman-Duval et al., 2021). Potential channels for the production of dust are the cooling ejecta of supernovae (Dunne et al., 2003; Matsuura et al., 2015), grain growth in the ISM (Draine, 2003; Mattsson, Andersen, and Munkhammar, 2012; Dwek, 2016; De Cia et al., 2016) and asymptotic giant branch (AGB) stars (Gail et al., 2009; Höfner and Olofsson, 2018). Around 30% of the light in the Universe is re-radiated by dust grains in the infrared, altering the light that we observe (Calzetti et al., 1995; Witt and Gordon, 2000). Dust is also necessary in the process of star formation, because it is an important direct coolant for star formation and acts as a catalyst for the production of molecular hydrogen (Hollenbach and Salpeter, 1971; Hollenbach and McKee, 1979). Therefore, characterizing the dust properties and also the cycle of metals between the dust and gas is of fundamental importance in our understanding of galaxy formation and evolution.

The fraction of metals in dust can be described by the dust-to-metal ratio and another indicator of the dust content is the dust-to-gas ratio (Draine, 2003). These properties can help us understand the production and destruction mechanisms of the dust and its evolution. They can be used to estimate a number of dust properties, including the dust surface density (see Péroux, De Cia, and Howk, 2023) and the dust composition. One way to infer the dust composition is to observe the abundances of metals in the gas phase ISM through absorption-line spectroscopy and taking into account their depletion into dust grains (e.g, Roman-Duval et al., 2022a). In Konstantopoulou et al. (2022) (hereafter Paper I), we characterized the dust depletion of 18 metals in the Milky Way, the Magellanic Clouds, QSO- and GRB-DLAs using the ISM relative abundances of metals, following the

prescription of (De Cia et al., 2016). Here we use the depletion estimates from Paper I to infer the dust properties, namely the dust-to-gas (DTG) and dust-to-metal (DTM) ratios, dust composition, and dust extinction in a wide range of galactic environments (the Milky Way, the Magellanic Clouds, QSO- and GRB-DLAs) and study how they evolve over cosmic time.

The paper is organized as follows. In Section 2 we briefly present the samples and the method that is used for the dust depletion estimates. In Section 3 we infer the DTM, DTG, the extinction and dust composition from depletion. We discuss our results in Section 4, and finally summarize and conclude in Section 5.

Throughout the paper we use a linear unit for the column densities N in terms of ions cm^{-2}. We refer to relative abundances of elements X and Y as $[X/Y] \equiv \log\frac{N(X)}{N(Y)} - \log\frac{N(X)_\odot}{N(Y)_\odot}$, where reference solar abundances are taken from Asplund, Amarsi, and Grevesse (2021) following the recommendations of Lodders, Palme, and Gail (2009) (see Table 1 in Paper I). We adopt a Λ cold dark matter cosmology (ΛCDM) with $H_0 = 67.7\,km\,s^{-1}\,Mpc^{-1}$, $\Omega_M = 0.3$ and $\Omega_\Lambda = 0.7$ (Planck Collaboration et al., 2020).

4.3 DATA SAMPLES

In this section we briefly present the observational sample that we use for our analysis and the method that is used to estimate the dust depletion of all the metals for the Milky Way, the Magellanic Clouds and for high-redshift QSO- and GRB-DLAs. These can be found in more detail in Paper I.

In Paper I we used a large compilation of metal column densities, measured in a consistent way, in the neutral ISM for the Milky Way, the Magellanic Clouds, QSO- and GRB-DLAs to characterize the dust depletion of 18 metals (C, P, O, Cl, Kr, S, Ge, Mg, Si, Cu, Co, Mn, Cr, Ni, Al, Ti, Zn, and Fe). Our sample probes gas in a wide range of galaxy types and regions. QSO-DLAs trace gas-rich regions in the outskirts of galaxies (Prochaska et al., 2007; Fynbo et al., 2008), while GRB-DLAs probe the inner regions of galaxies hosting GRBs in a way more similar to the Milky Way and the Magellanic Clouds samples but at high redshifts.

The Milky Way sample is from Jenkins (2009), De Cia et al. (2021), Welty and Crowther (2010), and Phillips, Gondhalekar, and Pettini (1982). The Large Magellanic Cloud (LMC) sample from Roman-Duval et al. (2021), the Small Magellanic Cloud (SMC) from Welty and Crowther (2010), Tchernyshyov et al. (2015), Jenkins and Wallerstein (2017) and the QSO-DLAs sample is from De Cia et al. (2016), Berg et al. (2015), De Cia (2018). We also use 36 GRB-DLAs from Savaglio, Fall, and Fiore (2003), Shin et al. (2006), Prochaska et al. (2007), Piranomonte et al. (2008), Ledoux et al. (2009), D'Elia et al. (2011), Wiseman et al. (2017), Zafar and Møller (2019), Bolmer et al. (2019), and Saccardi et al. (2023), as compiled in Heintz et al. (2023), who also presents three new GRB-DLAs.

The column densities are measured mainly from spectra obtained with UVES/VLT, X-SHOOTER/VLT and STIS/HST and were homogenized to the newest oscillator strengths, listed in Paper I. The details of the full sample properties are presented in Paper I.

4.4 METHODS AND RESULTS

4.4.1 *Dust depletion measurements*

In this work we adopt the dust depletions of each metal from Paper I, which were estimated from the relative abundances of metals (De Cia et al., 2016), based on the fact that different metals have different tendencies of being incorporated into dust grains. We note that this is a different approach from the one of Roman-Duval et al. (2021), who also derived dust properties based on depletions, but estimated the depletions from the observed abundances and assuming a given metallicity of the gas. Here we briefly present our method.

The depletion of an element X (δ_X) can be estimated from the relative abundances of two elements that have different refractory properties but follow each other nucleosynthetically. If X is a refractory element and Y is volatile (i.e., is not easily depleted into dust, like Zn) then the dust depletion of X can be expressed using the ratio of the two elements [X/Y]. De Cia et al. (2016) and Paper I relied on [X/Zn] and their relation to the dust tracer to estimate the depletion of X. To trace the overall amount of dust we used the dust tracer [Zn/Fe]. Two corrections are applied: first the dependence on the depletion of Zn is removed by assuming $\delta_{\rm Zn}$ = -0.27×[Zn/Fe], which is derived from the Milky Way and QSO-DLAs (De Cia et al., 2016) and second a correction is applied to account for nucleosynthesis effects, such as α-element enhancement and Mn underabundance, as described in Paper I.

The depletion of X correlates linearly with the dust tracer, such as [Zn/Fe], but others, such as [Si/Ti] or [O/Si] are possible and thus the dust depletion can then be expressed by a simple linear relation as,

$$\delta_X = A2_X + B2_X \times [\mathrm{Zn/Fe}], \tag{4.1}$$

where the $A2_X$ and $B2_X$ coefficients for all the metals are the results of the linear fits to the data and are presented in Table 4 of Paper I. These results are consistent with De Cia et al. (2016). In Paper I the coefficients are estimated using two different assumptions on α-element enhancement and Mn underabundance in the Magellanic Clouds. Here we adopt the coefficients that were estimated using the assumption of constant α-element enhancement and Mn underabundance and are reported in Table 4.1 for completeness.

4.4.2 *Dust-to-metal and dust-to-gas mass ratios*

The total abundance of element X can be expressed as:

$$\left(\frac{N(\mathrm{X})}{N(\mathrm{H})}\right)_{\rm tot} = 10^{([\mathrm{X}/H]_\odot + [M/\mathrm{H}]_{\rm tot})}, \tag{4.2}$$

where $[\mathrm{X/H}]_\odot$ is the solar abundance of element X and $[M/\mathrm{H}]_{\rm tot}$ is the total dust-corrected metallicity of the gas.

Then the DTM mass ratio can be calculated including all the metals as:

$$\mathrm{DTM} = \frac{M_{dust}}{M_{metals}} = \frac{\Sigma_{\mathrm{X}_i}\,(1 - 10^{\delta_{\mathrm{X}_i}})\,10^{[\mathrm{X}_i/H]_\odot}\,\mathrm{W}_{\mathrm{X}_i}}{\Sigma_{\mathrm{X}_i}\,10^{[\mathrm{X}_i/H]_\odot}\,\mathrm{W}_{\mathrm{X}_i}}, \tag{4.3}$$

Table 4.1: Coefficients $A2_X$ and $B2_X$ resulting from the linear fit $\delta_X = A2_X + B2_X \times$ [Zn/Fe] of the depletion sequences of metals presented in Paper I and P from Konstantopoulou et al. (2023).

Element X	$A2_x$	$B2_x$
C	0.00	-0.10 ± 0.10
P	0.08 ± 0.05	-0.26 ± 0.08
O	0.00	-0.20 ± 0.05
Cl	0.00	-0.12 ± 0.09
Kr	0.00	-0.04 ± 0.09
S	0.01 ± 0.02	-0.48 ± 0.04
Zn	0.00 ± 0.01	-0.27 ± 0.03
Ge	0.00	-0.40 ± 0.04
Mg	0.01 ± 0.03	-0.66 ± 0.04
Si	-0.04 ± 0.02	-0.75 ± 0.03
Cu	0.00	-0.73 ± 0.04
Co	0.00	-0.89 ± 0.19
Mn	0.07 ± 0.02	-1.03 ± 0.03
Cr	0.12 ± 0.01	-1.30 ± 0.01
Ni	0.07 ± 0.02	-1.31 ± 0.03
Fe	-0.01 ± 0.03	-1.26 ± 0.04
Al	0.00	-1.66 ± 0.35
Ti	-0.07 ± 0.03	-1.67 ± 0.04

where δ_X is the dust depletion of element X, which are taken from Paper I and W_X the atomic weight of element X. The total dust-corrected metallicity of the gas $[M/H]_{tot}$ cancels out and thus the dust-to-metal ratio is estimated independently of the total metallicity. [1] The sum is over all metals that have an elemental abundance $12 + log\,(X/H) > 3$. In total we use 29 metals, namely, C, P, O, Cl, Kr, S, Ge, Mg, Si, Cu, Co, Mn, Cr, Ni, Al, Ti, N, Ne, Ar, F, Na, K, Ga, V, Sc, Se, Li, Zn, and Fe. The abundance measurements of these metals are done in the neutral gas of the ISM in their dominant ionization state, which is mostly singly ionized. In some cases, some elements should be volatile, although their depletion is not assessed in Paper I. In such cases (namely, N, Ne, Ar, F, Na, K, Ga, V, Sc, Se and Li) we assume that $\delta_X = 0$. These metals make a small difference in the calculation of the DTM and DTG, but we include them because they contribute to the mass of the metals by summing their atomic weights in the denominator of Eq. 4.3. The calculation of the depletions using the method of relative abundances is based on the availability of Zn and Fe. Thus, when Zn and/or Fe were not available, no estimate of the depletion was made in Paper I. In case δ_X was not estimated in Paper I, but [Zn/Fe] has been observed, we use the coefficients $A2_X$ and $B2_X$ listed in Table 4.1 to estimate the depletion δ_X using Eq. 4.1. The dust depletion is typically defined as a negative number, because it removes metals from the gas-phase. In a few cases, however, the observed [Zn/Fe] is slightly negative, and typically consistent with

1 We note that Eq. 4.3 is equivalent to eq. 9 of Roman-Duval et al. (2022a), but the depletions are estimated from the observed abundances. In De Cia et al. (2016) the calculation of DTM is based on $(1 - 10^{\delta_X})$ and only for Fe.

zero within the uncertainties. In such cases, the values of depletion (δ_X) that we strictly derive from the [Zn/Fe] would be slightly positive, which is non-physical (i.e. the presence of dust removes metals from the gas phase, does not add them). We therefore assign zero depletion in such cases. For the cases of GRB-DLAs with no observed [Zn/Fe], we use the estimated $[\mathrm{Zn/Fe}]_{fit}$ from Heintz et al. (2023) to calculate the expected depletions from the coefficients $A2_X$ and $B2_X$, listed in Table 4.1 and using Eq. 4.1. $[\mathrm{Zn/Fe}]_{fit}$ is equivalent to the observed [Zn/Fe], but is derived from the abundances of all the available metals.

The DTG is the total dust mass relative to the total gas mass. It can be expressed as:

$$\mathrm{DTG} = \frac{M_{dust}}{M_{gas}} = DTM \times 10^{[M/H]_{\mathrm{tot}}} \times Z_{\odot}, \tag{4.4}$$

where DTM is defined in Eq. 4.3, $[M/\mathrm{H}]_{\mathrm{tot}}$ is the total dust-corrected metallicity of the gas and $Z_{\odot} = 0.0139$ is the solar metallicity taken from Asplund, Amarsi, and Grevesse (2021). Figures 4.1 and 4.2 show the DTM (top panel) and the DTG (bottom panel) with respect to the dust tracer [Zn/Fe] and the total dust-corrected metallicity $[M/\mathrm{H}]_{\mathrm{tot}}$ respectfully and for all the environments. Our measurements are given in Tables 4.4- 4.8.

4.4.3 *Dust composition*

We estimate the fraction of dust mass contributed by element X, $\mathrm{f_{M_X}}$ as,

$$f_{\mathrm{M_X}} = \frac{(1 - 10^{\delta_X})\ 10^{[\mathrm{X/H}]_{\odot}}\ \mathrm{W}_X}{\Sigma_{X_i}\ (1 - 10^{\delta_{X_i}})\ 10^{[\mathrm{X}_i/\mathrm{H}]_{\odot}}\ \mathrm{W}_{X_i}}, \tag{4.5}$$

where $[\mathrm{X/H}]_{\odot}$ is the solar abundance of element X, δ_X is the dust depletion of element X and W_X the atomic weight of element X.[2]

Figure 4.3 shows the evolution of dust composition with [Zn/Fe] for the elements that contribute at least 1% to the dust composition ($\mathrm{f_{M_X}} > 1\%$). In case a measurement of δ_X is unavailable for a given system, we calculate it from the measurements of dust depletion of a given metal. This is done using Eq. 4.1 and the coefficients presented in Table 4.1. This means that in such cases the measurements of the dust depletion are extrapolated from the general behaviour of the other environments, and our estimates on the dust composition are indicative. For the cases of targets that have less than three measurements of metals, the calculation of $\mathrm{f_{M_X}}$ is not reliable and thus we exclude them. Figures 4.9 to 4.13 show the dust composition with respect to [Zn/Fe] for all the environments. The systems for which we have a measurement of dust depletion for each metal are shown with filled symbols and those calculated from the coefficients with empty symbols.

4.4.4 *Dust extinction A_V from depletion*

The extinction of light by dust grains depends on several factors, such as their density, their size distribution, and composition (e.g. Draine, 2003). While typically the dust extinction

2 We note that Eq. 4.5 is equivalent to Eq. 12 of Roman-Duval et al. (2022a), but the depletions are estimated in a different way (see Sect. 4.4.1).

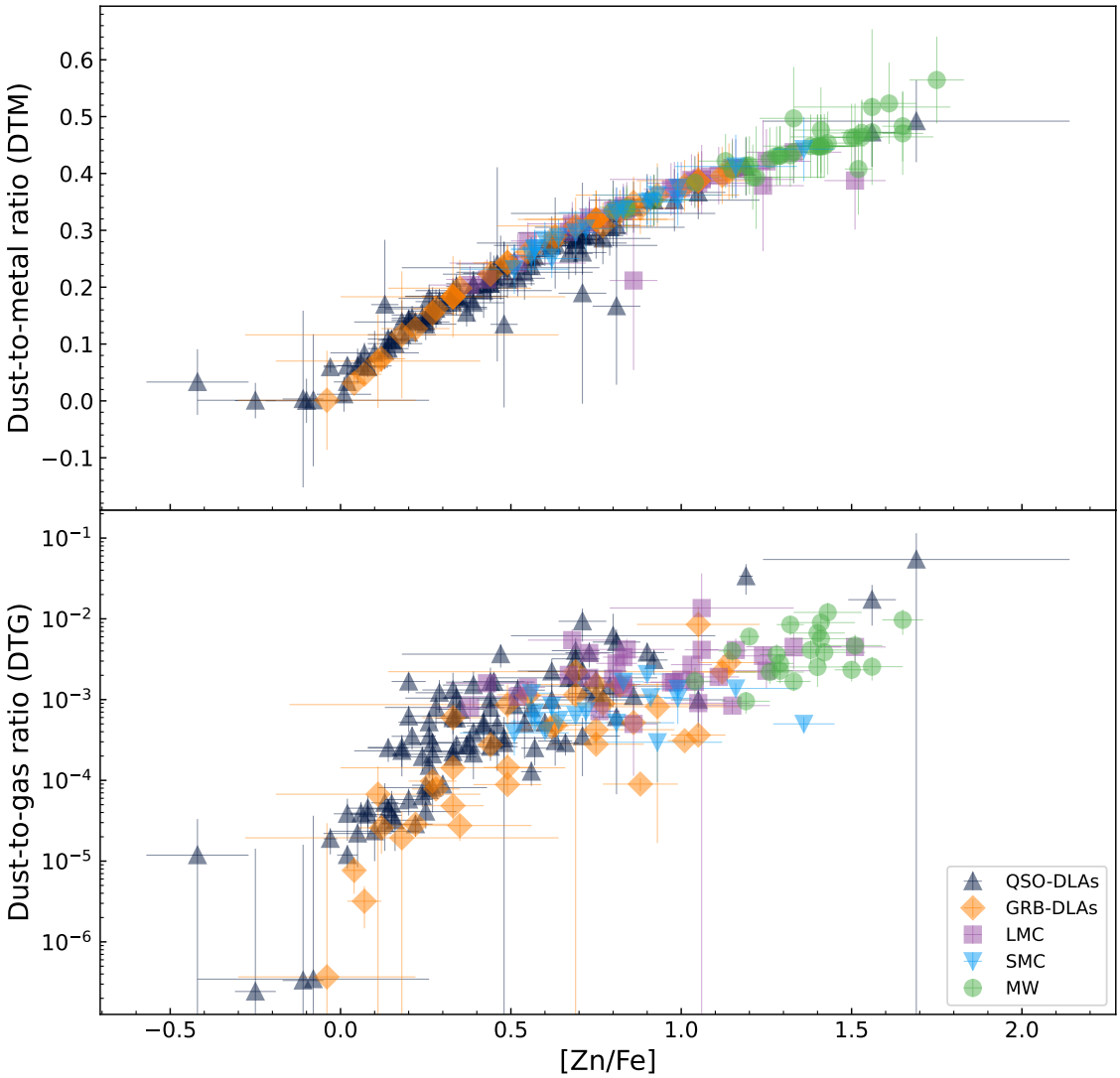


Figure 4.1: (Top): Dust-to-metal ratio as a function of the dust tracer [Zn/Fe]. (Bottom): Dust-to-gas ratio as a function of [Zn/Fe]. The black triangles are for QSO-DLAs, the purple squares are for the LMC, the blue triangles are for the SMC, the orange diamonds for the GRB-DLAs and the green circles are for the Milky Way.

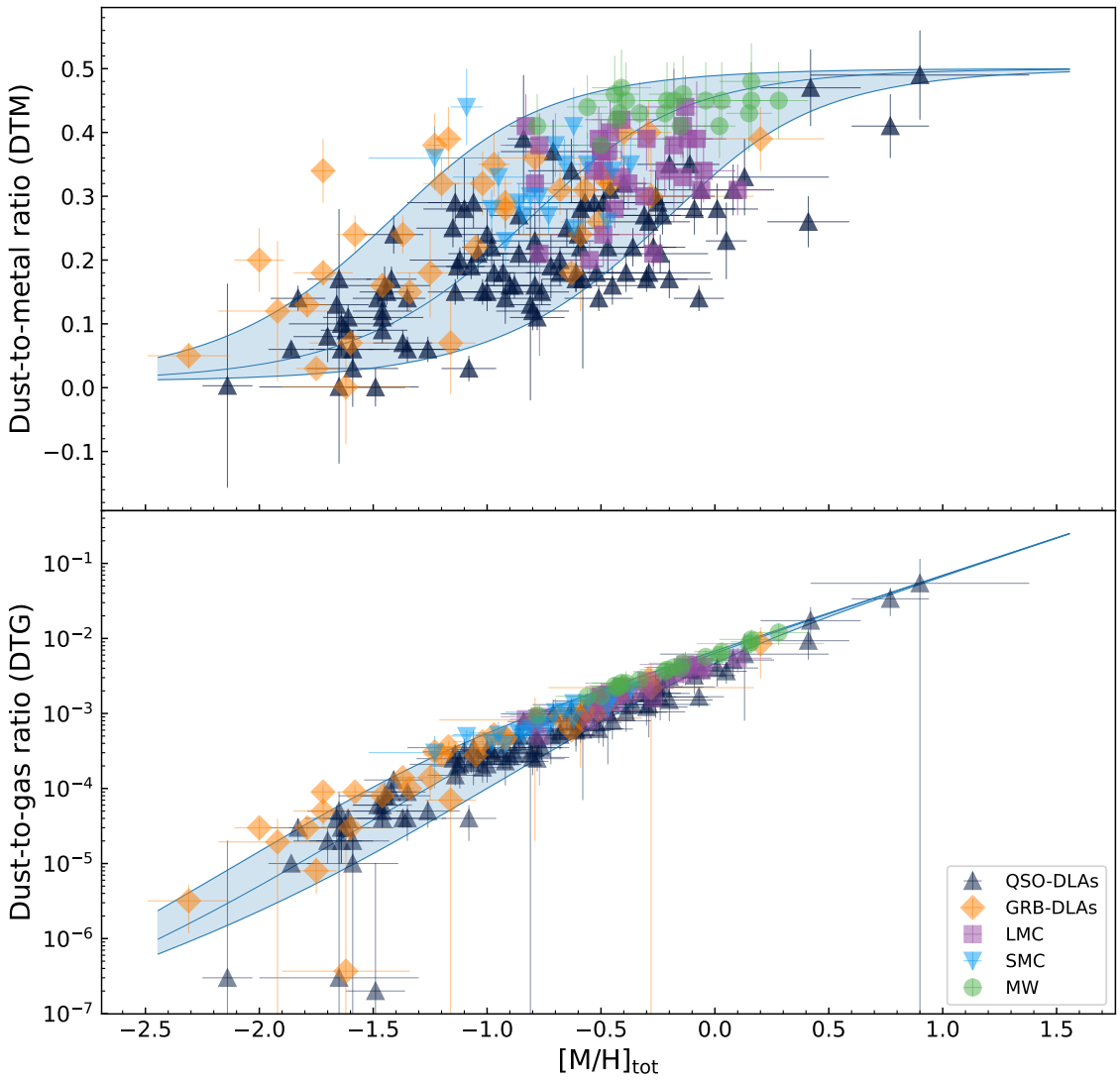


Figure 4.2: (Top): Dust-to-metal ratio as a function of the total dust-corrected gas metallicity $[M/\mathrm{H}]_{\mathrm{tot}}$. (Bottom): Dust-to-gas ratio as a function of the total dust-corrected gas metallicity $[M/\mathrm{H}]_{\mathrm{tot}}$. The symbols are the same as in Fig. 4.1. For the Milky Way metallicities $[M/\mathrm{H}]_{\mathrm{tot}}$ are from De Cia et al. (2021). There is a clear increasing trend of the DTM and DTG ratios with $[M/\mathrm{H}]_{\mathrm{tot}}$ and a tight correlation of the DTG with $[M/\mathrm{H}]_{\mathrm{tot}}$. The blue shaded regions show the analytic the dust production and evolution model from Mattsson (2020) with varying $\delta = \epsilon$ from 1 to 16.

A_V is measured from the variations on the spectral continuum, it is also possible to estimate an A_V from the dust depletion (and the dust-to-metals ratio), which we refer to as $A_{V,depl}$. However, because dust extinction depends on the cross section of the dust grains, it is more sensitive to the number of grains, rather than the mass of the individual grains. Therefore, we derive the $A_{V,depl}$ based on a DTM that is defined in terms of number of atoms (or column densities), which we refer to as $\mathrm{DTM_N}$. We derive the $\mathrm{DTM_N}$ in terms of column density by number as,

$$\mathrm{DTM}_N = \frac{\Sigma_{X_i}\,(1-10^{\delta_{X_i}})\,10^{[X_i/H]_\odot}}{\Sigma_{X_i}\,10^{[X_i/H]_\odot}}, \tag{4.6}$$

The DTM in terms of column density ($\mathrm{DTM_N}$) is on average 0.05 times lower than the DTM in terms of mass (DTM), as expected because Eq. 4.6 is equivalent to Eq. 4.3 without adding the atomic weights W_X of the elements. However, the overall trend is the same. Figure 4.8 shows the relation between the DTM by mass and the DTM by column density ($\mathrm{DTM_N}$). Our measurements of both DTM and $\mathrm{DTM_N}$ are given in Tables 4.4 - 4.8.

The dust extinction A_V can be derived from the depletion estimated $\mathrm{DTM_N}$ as,

$$A_{V,depl} = \frac{\mathrm{DTM}_N}{DTM_{N,Gal}} \times \left(\frac{A_V}{N(\mathrm{H})}\right)_{Gal} \times N(\mathrm{H}) \times 10^{[M/\mathrm{H}]_{tot}}, \tag{4.7}$$

where $\left(\frac{A_V}{N(H)}\right)_{\mathrm{Gal}} = 0.45 \times 10^{-21}$ mag cm^2 is the Galactic DTM ratio from Watson (2011). $\mathrm{DTM_{N,Gal}} = 0.354$ is the dust-to-metal ratio for the Galaxy in terms of column density, derived using Eq. 4.6 and assuming an average [Zn/Fe] = 1.22 for the Milky Way. N(H) is the total column density of H, defined as N(H) = N(HI) + 2 N(H2), although for most QSO- and GRB-DLAs only HI is measured and H2 is negligible (e.g., the mean molecular fraction measured in QSO-DLAs in Noterdaeme et al., 2008, is $\log f_{\mathrm{H2}} \sim -6.2$). $[M/\mathrm{H}]_{\mathrm{tot}}$ is the total dust-corrected metallicity.

Figure 4.4 shows the distribution of $A_{V,depl}$ with [Zn/Fe] (left panel) and with the total dust corrected metallicity $[M/\mathrm{H}]_{\mathrm{tot}}$ (right panel). The DTM, DTG, $\mathrm{DTM_N}$ and $A_{V,depl}$ results for all the environments are reported in Tables 4.4- 4.8.

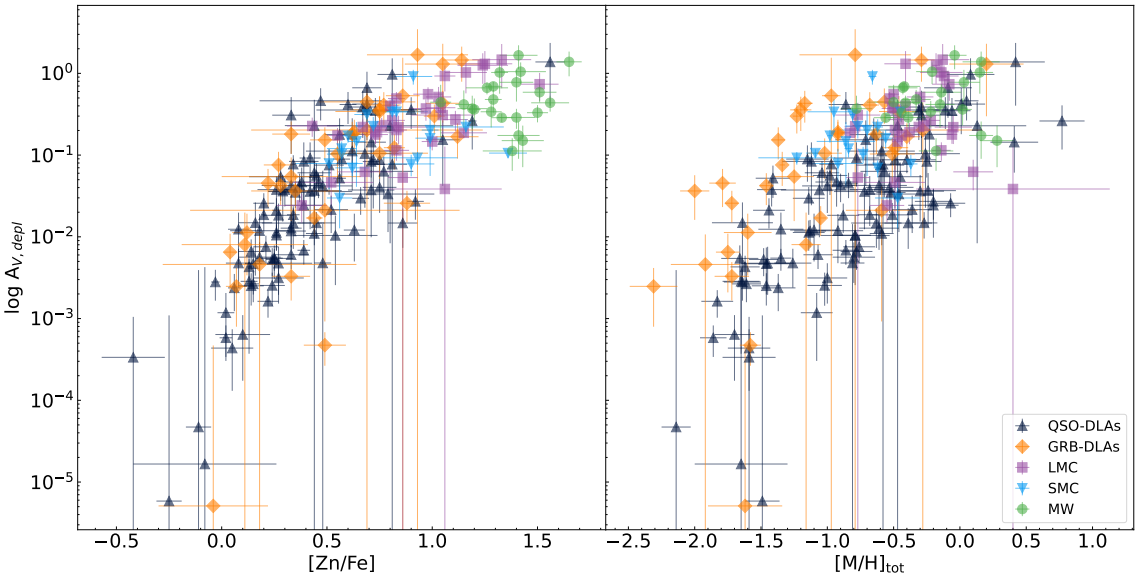


Figure 4.4: Dust extinction $A_{V,depl}$ as a function of [Zn/Fe] (left panel) and as a function of the total dust-corrected metallicity $[M/H]_{tot}$ (right panel). For the Milky Way metallicities $[M/H]_{tot}$ are from De Cia et al. (2021).

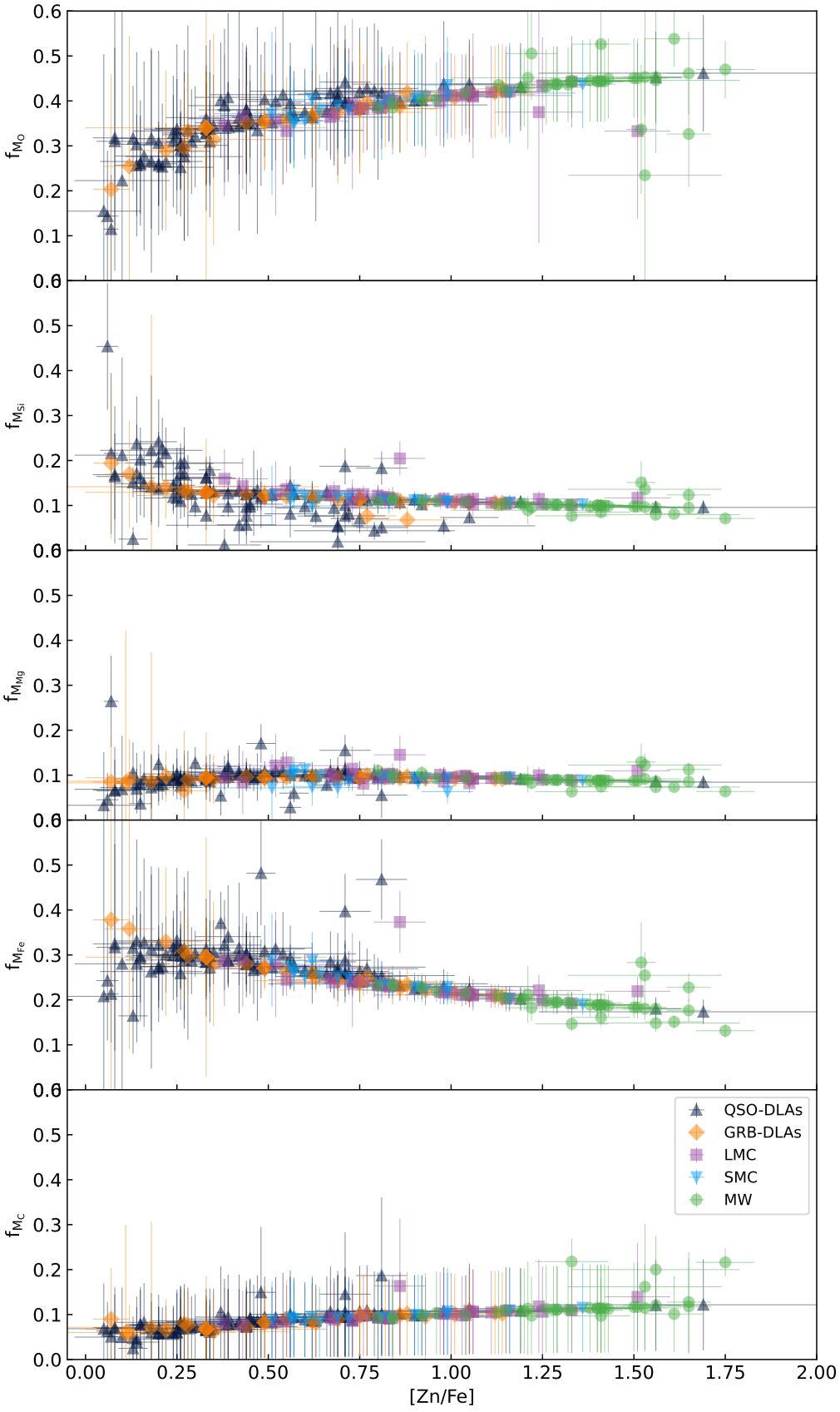


Figure 4.3: Fraction of dust mass contributed by element X, f_{M_X} as a function of the dust tracer [Zn/Fe] for the five most abundant contributors in dust (O, Fe, Si, Mg, C) for QSO- and GRB-DLAs, LMC, SMC and the Milky Way.

4.5 DISCUSSION

4.5.1 *DTM, DTG, and the origin of dust*

The evolution of the DTM and DTG ratios with metallicity gives us clues about the origin of interstellar dust. The three candidate mechanisms for the formation of the bulk of cosmic dust are dust condensation in the envelopes of AGB stars (Gail et al., 2009), condensation in SNe ejecta (Dunne et al., 2003; Matsuura et al., 2015), and grain growth in the ISM (Draine, 2003; Mattsson, Andersen, and Munkhammar, 2012; Dwek, 2016; De Cia et al., 2016).

Different dust production mechanisms can produce different types of dust. AGB stars produce C-rich dust as well as silicates, while SNe produce mostly silicates. Type Ia SNe are the major Fe producers but dust produced by Type Ia SNe has generally not been observed, with the exception of Dwek (2016) and Nagao, Maeda, and Yamanaka (2018). ISM grain growth by condensation upon existing seeds produced by stars is the mechanism that can produce silicates but also the amounts of C- and Fe-dust observed.

Different mechanisms of dust production have different dependencies on the environment metallicity. Dust that is mostly built up with ISM grain growth has DTM ratios that increase with metallicity, because the grain growth rate is metallicity dependent. On the other hand, SNe-produced dust should show a constant DTM (Mattsson et al., 2014), because dust production by SNe is weakly dependent on metallicity. AGB stars are often considered secondary for dust production, because of their longer lifetimes, although they cannot be neglected on short timescales ($\sim$500 Myr, Valiante et al., 2009).

Although grain growth in the ISM can occur at any time during the lifetime of a galaxy, Zhukovska, Gail, and Trieloff (2008) show that there is likely a critical metallicity above which grain growth in the ISM becomes dominant over other sources of dust production. Their evolution model shows that at very low metallicities $[M/\mathrm{H}]_{\mathrm{tot}} \leq -2$ in the solar neighbourhood the grain growth timescale exceeds by about 10 Myr the average lifetime of the molecular cloud. This means that until this point, not a lot is added to the dust content of the interstellar matter. When the metallicity of the ISM has reached $[M/\mathrm{H}]_{\mathrm{tot}} = -2$ some dust starts to condensate in the ISM and at $[M/\mathrm{H}]_{\mathrm{tot}} \sim -1$ the rate of growth increases rapidly and grain growth is the dominant mechanism of dust production in the diffuse ISM (Zhukovska, Gail, and Trieloff, 2008). At high metallicities, such as in the Milky Way, the DTM ratio has a smaller dependence with metallicity. This is possibly because dust production depends not only on metallicity, but also temperature, density and pressure. In the Milky Way the presence of cold dense gas and high pressure provide favorable conditions for the formation of dust. In this case, due to the higher dependence of ISM grain growth on density and pressure, the metallicity dependence is lower (Blitz and Rosolowsky, 2006).

The top panel of Fig. 4.1 shows the DTM ratio with respect to the dust tracer [Zn/Fe] for the Milky Way, LMC, SMC, QSO- and GRB-DLAs. It is evident that there is a tight correlation between the DTM and [Zn/Fe], which is expected by the fact that the depletions that are used for the DTM calculation are linearly correlated with [Zn/Fe] (see Eq. 4.1). The DTM is lower for QSO-DLAs and increases with increasing [Zn/Fe], i.e., for dustier systems, like the Milky Way.

The bottom panel of Fig. 4.1 shows the DTG with respect to [Zn/Fe] for the Milky Way, LMC, SMC, DLA- and GRB-DLAs. The DTG ratio is increasing with [Zn/Fe] and there is a larger scatter in the linear relation than what we see for the DTM (top panel of Fig. 4.1). Fig. 4.2 shows the DTM (top panel) and DTG (bottom panel) with respect to the total dust-corrected metallicity $[M/\mathrm{H}]_{\mathrm{tot}}$. We find that overall the DTM is increasing with metallicity. For QSO-DLAs, we see a relatively sharp decline of the DTM at low metallicities (at $[M/\mathrm{H}]_{\mathrm{tot}} < -1$), indicating that the net dust production rate is lower at low metallicities. This decline of the DTM could indicate that dust is destroyed more efficiently than being formed in this low-metallicity regime. However, uncertainties are large for these few systems probably as a result of the low amounts of dust, which is difficult to measure with this method.

The analytic dust production and evolution model tracks from Mattsson (2020) are also shown in Fig. 4.2. The model is overplotted, using eq. 42 of Mattsson (2020) and assuming that the dust destruction parameter δ is essentially equal to the growth parameter ϵ. The model considers all sources of dust, i.e., stellar sources (AGB stars, SNe) and grain growth in the ISM, involves several simplifying assumptions and is based on an idealised model of grain growth in turbulent cold molecular clouds. Some parameters are modified to fit the observational data well, that is, the stellar dust yield (y_d) is lowered by an order of magnitude with respect to Mattsson (2020) and the solar abundance $Z_\odot$ is updated to the most recent value from Asplund, Amarsi, and Grevesse (2021). The parameters for the model are then $y_Z = 0.01$, $y_d = 1\times 10^{-4}$, $\delta = \epsilon$ and $Z_\odot = 0.0139$. The shaded regions in the plots show the parts of the DTM-$[M/\mathrm{H}]_{\mathrm{tot}}$ and DTG-$[M/\mathrm{H}]_{\mathrm{tot}}$ planes that are covered by varying $\delta = \epsilon$ from 1 to 16. Surprisingly, the predicted (stellar) dust yield is only 1% of the metals yield, while the previous estimates by Mattsson (2020) indicated 10-20%. This suggests that the overall stellar population (and not individual cases) produce much less dust than previously estimated. We note that with our data we probe the integrated metals and dust recycled by the stellar sources (AGB stars, SNe) in the warm diffuse ISM. We might be missing the dust produced by stars in the dense and dustier regions around AGB stars or SNe.

The fact that the DTM is increasing with metallicity indicates that grain growth in the ISM, is likely the dominant mechanism for dust production. This is supported by the fact that the data fit well the dust production and evolution model trend from Mattsson (2020). We note that due to the nature of the measurements used in this paper (column densities of the metals in the warm neutral gas from UV absorption-line spectroscopy), there is a selection effect that gives privilege to sampling of environments where there is dust growth in the (more diffuse) ISM. Moreover, with the depletion measurements we probably cannot distinguish between grain growth and dust destruction/sputtering in the diffuse ISM. With our method we do not directly probe the very dense envelopes of AGB stars, or regions of condensations in SNe ejecta, but any dust that has been produced or recycled into the warm neutral ISM. In addition the number of SNe or AGB stars along a line of sight depends on the star-formation history of the local environment sampled. As shown in Paper I, the depletions sequences are independent of the star-formation histories of the different galaxies that were sampled. This means that the total budget of dust grains in the warm neutral medium does not depend on the star-formation histories of the galaxies. However,

our technique does not probe dust in the densest regions of the ISM (cold and molecular neutral medium) and in particular C-rich dust grains, which contribute significantly to the dust budget.

We find that the increase of the DTM with metallicity is not developing with the same rate for all the environments (49 % increase for QSO-DLAs, 40 % for GRB-DLAs, 23 % for the LMC, 21 % for the SMC and 23 % for the Milky Way). In environments that have high metallicity and large amounts of cold dense gas (high pressure), like in the Milky Way disk, the dependence on the metallicity seems to become less important. In this case, grain growth in the ISM depends more strongly on pressure and thus molecular production and ISM grain growth (Blitz and Rosolowsky, 2006). This can cause a shallower increase in the DTM with metallicity for environments with higher pressure.

Overall, the DTM is larger for dustier and higher metallicity systems, like the Milky Way and lower for QSO-DLAs. An increase of the DTM with metallicity has been observed in local and distant galactic environments (e.g. De Cia et al., 2013, 2016; Wiseman et al., 2017), with this tendency somehow flattening above 0.1 $Z_{\odot}$ and reaching the Milky Way values. However, there are differences between the DTM calculations in these works. In our method, we use all the metals that contribute into dust, including C, by using the depletion of C that is estimated either from measurements for the Milky Way or from its empirical relation with [Zn/Fe] (calibrated with Milky Way data only) for the rest of the environments. We also calculate the DTM in terms of mass, by weighting each element for its atomic weight. De Cia et al. (2013) and De Cia et al. (2016) derive DTM_N in terms of column density and only based on the depletion of Fe. Wiseman et al. (2017) calculate the DTM_N in terms of column density and not including C.All these works refer to a normalized DTM_N with respect to the Milky Way. If we consider this, our DTM_N is consistent with the DTM_N estimated by Wiseman et al. (2017) within the uncertainties.

In Fig. 4.2, the DTM suggests that GRB-DLAs are dustier than QSO-DLAs for equal amounts of metals, while in Figs. 4.1 and 4.2 the DTG indicates that GRB-DLAs exhibit more gas with respect to QSO-DLAs along the lines of sight. In addition, most systems lying above the model expectations in Fig 4.2 are GRB-DLAs at low metallicity, while those below are QSO-DLAs at $[M/\mathrm{H}]_{\mathrm{tot}} > -0.3$. A possible explanation for these effects is the increased amount of colder dense gas and pressure in GRB hosts with respect to the more diffuse and warmer gas probed by QSO DLAs. This is vastly a geometrical effect of GRB lines of sight crossing through more central parts of their host galaxy, while QSO-DLAs probe more peripheral regions of the absorbing galaxy (e.g., Fynbo et al., 2008, Krogager et al. in prep). Overall, our results suggest that the production of dust is not only dependent on the metallicity - or the availability of metals - but also on gas temperature, pressure and density in each environment. The scatter that we observe in the DTM values at a given metallicity may be due to the different dynamical timescales that the stellar and ISM sources contribute to dust at various redshifts. At higher redshifts but for the same $[M/\mathrm{H}]_{\mathrm{tot}}$ it is possible that some sources did not have enough time to form dust in such short timescales (the Universe is just ~ 1 Gyr old at $z = 6$). The scatter in our DTM values suggest a complex interplay of factors within galactic environments. With our method we primarily probe the characteristics of dust within the diffuse ISM. We acknowledge that our approach may not fully capture contributions from specific stellar

sources, such as carbonaceous dust from AGB stars, in denser regions. It is indeed possible that the scatter observed in our DTM values arises from the combined effects of sampling different combinations of more diffuse and denser ISM, as well as regions with varying star-formation histories. The results presented in Paper I indicate that in the diffuse ISM, dust origin appears to be less dependent on the star formation history of galaxies. As our study predominantly focuses on the diffuse ISM, we recognize the need for further research to explore methods that better represent denser regions, which may be influenced by variations in star formation history. The DTM overall tends to decrease with redshift, which is likely due to the dependence of the DTM on the decreasing metallicity (Heintz et al., 2023).

The DTG shows a clear increasing trend with metallicity for all the environments (see bottom panel of Fig. 4.2). The increase of DTG with metallicity has been consistently observed in previous works (Issa, MacLaren, and Wolfendale, 1990; Lisenfeld and Ferrara, 1998; Draine and Li, 2007; Galliano, Dwek, and Chanial, 2008; Rémy-Ruyer et al., 2014; De Vis et al., 2017; Galliano, Galametz, and Jones, 2018; Li, Narayanan, and Davé, 2019; Roman-Duval et al., 2022b). The observed DTG trend with metallicity is in agreement with the dust production and evolution model from Mattsson (2020). Roman-Duval et al. (2022b) compare their observed DTG-metallicity trend with the model tracks from Feldmann (2015), which fits well the FIR observations of galaxies from Rémy-Ruyer et al. (2014). In this comparison, these author find a discrepancy of the QSO-DLA observations with the FIR observations from Rémy-Ruyer et al. (2014), which is still present in our current observational dataset. This discrepancy highlights that FIR observations probe a very different kind of environment, likely the most dense clouds around star-forming regions and AGB stars that may have dust with a different nature from what is observed in the diffuse ISM. The DTG-metallicity trend that we observe is consistent with the one observed in Roman-Duval et al. (2022b).

4.5.2 *Cosmic metallicity evolution of the neutral gas - Comparison between QSO- and GRB-DLAs*

In Fig. 4.5 we compare the metallicity evolution with redshift between QSO- and GRB-DLAs. We calculate the HI-weighted mean from the linear metallicities in five redshift bins for QSO- and GRB-DLAs and plot the points at the mean redshift. We fit the HI-weighted mean metallicities, taking into account the y-axis uncertainties. The individual metallicity measurements in different environments are shown in Fig. 4.5. The two linear fits result to $[M/\mathrm{H}]_{\mathrm{tot}} = (-0.38 \pm 0.07) + (-0.18 \pm 0.03) \times z$ for QSO-DLAs and $[M/\mathrm{H}]_{\mathrm{tot}} = (-0.53 \pm 0.05) + (-0.18 \pm 0.01) \times z$ for GRB-DLAs, where z is the redshift. There is a small difference between the fits, which we quantify by calculating the difference between the reduced χ^2_ν of the two fits ($\Delta\chi^2_\nu = 0.04$). We note that the two samples have different redshift ranges, with most of the targets concentrating in the redshift range $1.8 < z < 3.2$. In this range, the observed scatter is large, and is reflecting the diversity in metallicity of galaxies at any given time. This is not complete, however, since optically- or UV-selected QSOs tend to have lower $[M/\mathrm{H}]_{\mathrm{tot}}$, because their selection is biased by the presence of dust (Krogager et al., 2019). At higher and lower redshifts there are less data points due

to observational limitations. The effect of dust bias will be further investigated with the 4MOST–Gaia Purely Astrometric Quasar Survey (4G-PAQS) (Krogager et al., 2023).

The HI-weighted mean metallicity is a measure of the metallicity in the neutral gas in the Universe, rather than the metallicity of the individual systems. The agreement between the two fits suggests that QSO- and GRB-DLA may be arising from a similar population of galaxies, or at least probe the neutral gas in the Universe in a similar way (see also Krogager et al. in prep.). We find a decrease of neutral gas metallicity with redshift ($0.6 < z < 6.3$), in agreement with previous studies (e.g. De Cia, 2018; Mattsson et al., 2019; Péroux and Howk, 2020). The inclusion of GRB-DLAs extends the study of the cosmic chemical evolution to $z > 6$ (Heintz et al., 2023; Saccardi et al., 2023).

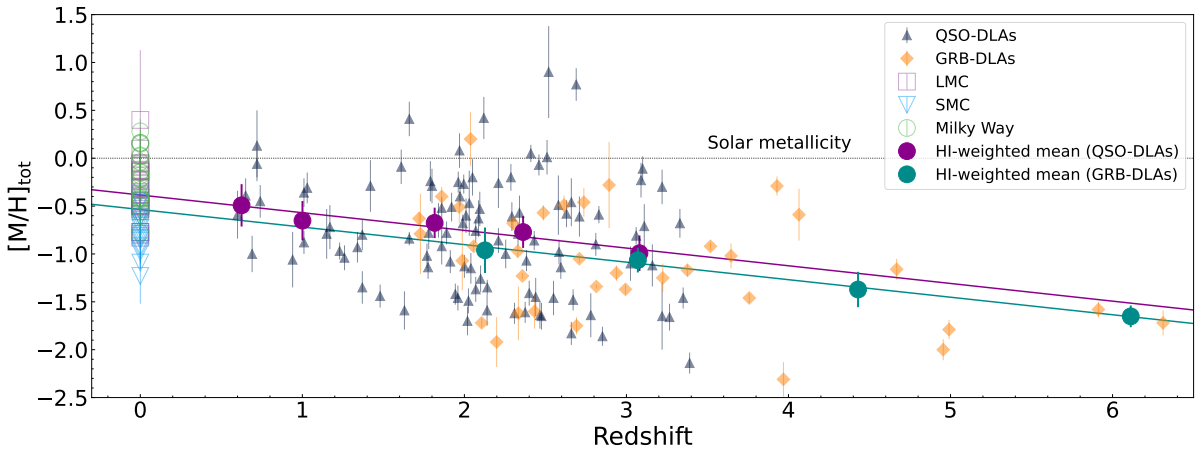


Figure 4.5: Total dust-corrected metallicity $[M/H]_{tot}$ evolution with redshift z for GRB-DLAs (orange diamonds) and QSO-DLAs (black triangles). The larger points (green for GRB-DLAs and purple for QSO-DLAs) show the HI-weighted mean metallicities binned in redshift and the lines are their corresponding linear fits. The open symbols at redshift $z = 0$ refer to the Milky Way (green), the LMC (purple) and the SMC (blue). The dotted line shows the solar metallicity ($[M/H]_{tot} = 0$).

4.5.3 *Dust composition*

Figure 4.3 shows the evolution of dust composition derived from the dust depletion, with [Zn/Fe] for the elements that contribute at least 1 % to the dust composition ($f_{M_X} > 1\%$). Dust depletion can be used to get information on the dust composition in various ways (Savage and Sembach, 1996; Jenkins, 2014; De Cia et al., 2016; Mattsson et al., 2019; Roman-Duval et al., 2022a).

In each panel of Fig. 4.3 we can see that the main components of dust are by mass, O, Fe, Si, Mg, C, S, Ni and Al. The distribution of the elements that compose dust varies, however, with the amount of dust in the system measured with [Zn/Fe]. Figure 4.6 visualizes this distribution of metals that compose dust for the least dusty systems (upper panel, e.g. [Zn/Fe] < 0.3), the distribution of metals in the middle range of [Zn/Fe] (middle panel, e.g. $0.3 \leq$ [Zn/Fe] ≤ 0.9) and for most dusty systems (lower panel, e.g. 0.9 < [Zn/Fe] < 1.2).

Systems with low dust content ([Zn/Fe] < 0.3) are observed among QSO- and GRB-DLAs, which tend to have a low metallicity. In these systems, the most abundant elements in dust are Fe, O, and after these Si. On the contrary, in the average [Zn/Fe] and high dust content regime (0.9 < [Zn/Fe] < 1.2) O is more abundant than Fe in all the galactic environments. Overall, in GRB-DLAs and QSO-DLAs the contribution of Fe and Si to dust increases steeply as we go towards lower [Zn/Fe] (i.e. less dust), while O decreases. We speculate that this least dusty regime may be one where the seeds of dust grains did not undergo as much grain growth by the gradual accumulation of matter in the ISM, because there was not enough time, or underwent a more efficient dust destruction process by SNe shocks. In low metallicity and low dust environments the dust grains are small and are more easily destroyed by SNe shocks.

The main dust destruction processes in the ISM are either from sputtering by high-velocity SN shocks and photo-destruction by high-energy photons (Dwek, Foster, and Vancura, 1996; Jones, Tielens, and Hollenbach, 1996; Bocchio, Jones, and Slavin, 2014; Slavin, Dwek, and Jones, 2015), or from consumption of interstellar dust by star formation (astration).

In Table 4.2 we present the gas- and solid phase abundances in parts-per-million (ppm) of the main elements that contribute to the dust composition for systems in different environments and for the three different intervals of [Zn/Fe] defined above. At low-depletion levels ([Zn/Fe] < 0.3), where dust starts to form, we find for QSO- and GRB-DLAs that the O abundance in dust is ~ 3 times higher than the Si abundance. This suggests that the presence of pyroxene ($Mg_xFe_{(1-x)}SiO_3$) is likely. The amounts of Fe and Mg observed in the least-dusty regime suggest a significant contribution of enstatites ($MgSiO_3$) and metallic Fe. There is no need to invoke oxydation of Fe (e.g. FeO) in the least dusty regime, because all the oxygen can in principle be included in pyroxenes. A more detailed analysis of the dust composition, such as the one presented in Mattsson et al. (2019), is required to accurately constrain the dust composition of the different environments.

The different environments considered in this study span different ranges of dust content ([Zn/Fe], see Fig. 4.3). Here we discuss their average properties. For the full range of [Zn/Fe], for all the environments, we find that the largest fraction of dust mass is contributed by O and is increasing with [Zn/Fe] with a smaller increase in the Milky Way and the largest increase for QSO-DLAs. The largest amount of O in dust is found in the Milky Way (44 %) and the smallest in GRB-DLAs (35 %). The second most abundant element in dust is Fe, which is decreasing with [Zn/Fe] for all the environments. A possible cause for the opposite evolutions of the mass abundance of O and C with respect to Fe and other refractory elements is the following. For the least dusty systems, at low levels of [Zn/Fe], most of the Fe and other refractory elements are available in the gas-phase and they are the ones that can more easily be incorporated in dust grains. On the other hand, for very dusty systems, at high levels of dust depletion, there are much fewer atoms of Fe and refractory metals available in the gas-phase to form additional dust, while O and C are always very abundant in the gas-phase. Layers of complexity will need to be added to this simplified picture when considering systems that have intrinsically very low abundance of Fe and heavily refractory metals, for example in the very distant Universe. The chemical evolution of galactic environments and their local star-formation histories influence the availability

Table 4.2: Gas- and solid-phase abundances of the main elements that contribute to the dust composition for systems in different environments and for different intervals of [Zn/Fe].

Element X	$[X/H]_{gas}$ (ppm)	$[X/H]_{dust}$ (ppm)					Interval [Zn/Fe]
		QSO-DLAs	GRB-DLAs	Milky Way	LMC	SMC	
O	490	35	27	...	...	...	[Zn/Fe] < 0.3
		102	118	154	126	125	0.3 ≤ [Zn/Fe] ≤ 0.9
		186	178	181	172	168	0.9 < [Zn/Fe] < 1.2
Fe	29	10	27	...	...	...	[Zn/Fe] < 0.3
		23	23	26	25	25	0.3 ≤ [Zn/Fe] ≤ 0.9
		27	27	27	27	27	0.9 < [Zn/Fe] < 1.2
Si	32	13	8	...	...	...	[Zn/Fe] < 0.3
		14	20	25	25	22	0.3 ≤ [Zn/Fe] ≤ 0.9
		21	25	27	26	27	0.9 < [Zn/Fe] < 1.2
Mg	35	7	5	...	...	...	[Zn/Fe] < 0.3
		18	20	27	24	20	0.3 ≤ [Zn/Fe] ≤ 0.9
		24	27	28	22	26	0.9 < [Zn/Fe] < 1.2
C	288	10	8	...	...	...	[Zn/Fe] < 0.3
		34	37	48	43	40	0.3 ≤ [Zn/Fe] ≤ 0.9
		56	33	81	48	54	0.9 < [Zn/Fe] < 1.2
S	14	3	2	...	...	...	[Zn/Fe] < 0.3
		5	6	8	6	5	0.3 ≤ [Zn/Fe] ≤ 0.9
		7	10	8	8	9	0.9 < [Zn/Fe] < 1.2
Ni	2	1	0.3	...	...	...	[Zn/Fe] < 0.3
		1	1	1	1	1	0.3 ≤ [Zn/Fe] ≤ 0.9
		1	1	2	1	1	0.9 < [Zn/Fe] < 1.2
Al	3	1	1	...	...	...	[Zn/Fe] < 0.3
		2	2	3	3	2	0.3 ≤ [Zn/Fe] ≤ 0.9
		3	3	3	2	3	0.9 < [Zn/Fe] < 1.2

of metals for dust formation. In regions with lower metallicity and lower dust content, which are chemically less evolved, there might be a reduced abundance of heavy elements crucial for dust production. Si, C, Mg, S, Ni and Al have smaller contributions in dust (< 12%) in all the environments.

Our current data suggest that C has a similar mass abundance in dust for all the environments, 8 %, 9 %, 10 %, 10 %, 12 % for QSO-DLAs, GRB-DLAs, LMC, SMC and Milky Way respectively. However, the Milky Way and Magellanic clouds have substantially different extinction curves, in particular the presence and strength of the 2175 feature (e.g. Pei, 1992). The origin of the 2175 feature remains unclear and it is likely that a combination of several species that produce it. Some candidates that may produce the feature have been proposed, such as non-graphitic C (Mathis, 1994) or polycyclic aromatic hydrocarbons (PAHs, Draine, 2003). This indicates that the Milky Way has a much higher content of C-rich dust, possibly polycyclic aromatic hydrocarbons (PAH) (Shivaei et al., 2022), than the LMC and even more the SMC. The SMC extinction curve does mostly not show the 2175 feature, with few exceptions e.g. Gordon and Clayton, 1998a; Gordon et al., 2003; Welty and Crowther, 2010. Most GRB afterglows also do not show a 2175 feature in their extinction curve (e.g. Zafar et al., 2011; Schady et al., 2012), with some exceptions (Elíasdóttir et al., 2009; Zafar et al., 2012; Heintz et al., 2019b). Thus, one could expect a smaller contribution of PAH grains,

and possibly C-rich dust and smaller grain sizes to their dust composition. The distribution of PAHs may actually vary with location, being more strongly associated with molecular clouds (Sandstrom et al., 2010). The dust depletion analysis probes more efficiently the warm neutral medium in galaxies, and may be not very sensitive to dust located in dense molecular clouds. Thus our results on the dust composition are only representative of the dust in the warm neutral medium, while the dust located in dense molecular clouds might have a different composition.

The depletion of C in dust is very uncertain for GRB- and QSO-DLAs, because the typical CII line used to measure the C content is normally highly saturated. In Paper I we derived the depletion of C based only on five Milky Way measurements. This can only give a rough estimate of the C dust depletion. We extrapolate these estimates on the C depletion for the other environments and this is probably the cause of the similar percentages of C dust composition that we obtain, regardless of the presence or not of strong C-dust features in their extinction curves (i.e. SMC, LMC). This highlights the importance of a detailed study of the C depletion and the need for more and reliable measurements for systems in all environments.

Similar C fractions in dust can also result from the fact that most of C is produced by C-rich AGB stars (Gustafsson et al., 1999; Mattsson, 2010), the presence of which does not depend on the environment. Although, C-rich massive stars may significantly contribute to the C budget (Gustafsson, 2022).

Table 4.3: Average percentage of the main elements that contribute to the dust composition for systems in different environments.

X	QSO-DLAs	GRB-DLAs	LMC	SMC	Milky Way
O	36 %	35 %	38 %	39 %	44 %
Fe	27 %	27 %	23 %	24 %	19 %
Si	11 %	12 %	12 %	11 %	10 %
Mg	9 %	9 %	10 %	9 %	9 %
C	8 %	9 %	10 %	10 %	12 %
S	4 %	4 %	4 %	3 %	4 %
Ni	2 %	1 %	1 %	1 %	1 %
Al	1 %	1 %	1 %	1 %	1 %

4.5.4 *Dust extinction from depletion compared to extinction from SED*

Figure 4.4 shows the distribution of $A_{V,depl}$ with [Zn/Fe] (left panel) and with the total dust corrected metallicity $[M/H]_{tot}$ (right panel). The $A_{V,depl}$ for QSO-DLAs is generally small and is increasing with the dust tracer [Zn/Fe] and with the total dust corrected metallicity $[M/H]_{tot}$. At higher metallicities and [Zn/Fe], the dust extinction is also expected to be higher. The right panel of Fig. 4.4 shows that, for a given metallicity, QSO-DLAs tend to have a lower $A_{V,depl}$ than the other systems. This is probably due to the fact that QSO-DLAs probe outer galactic regions than GRB-DLAs (Prochaska et al., 2007; Fynbo et al., 2008) and absorbing systems towards OB stars in local galaxies.

We compare the $A_{V,depl}$ with $A_{V,ext}$, which we measured from the reddening $A_V = E(B-V) \times R_V$, assuming R_V = 3.08, for the Milky Way , R_V = 3.16 for the LMC and $R_V = 2.93$ for the SMC (Pei, 1992). In the case of GRB-DLAs we compare the $A_{V,depl}$ with the $A_{V,ext}$ measured from the SED in Heintz et al. (2023). The comparison between $A_{V,depl}$ and $A_{V,ext}$ is shown in Fig. 4.7. The green circles in 4.7 highlight systems in the Magellanic Clouds that show a 2175 feature in their dust extinction curve. $A_{V,ext}$ for QSO-DLAs are difficult to obtain and no measurements are available for the systems that we are studying here. The dust extinction $A_{V,ext}$ of a sample of QSO-DLAs has been measured in previous studies (Krogager et al., 2016; Heintz et al., 2016), but is only possible for strong absorbers and/or for cases with the 2175 bump present in their spectra. We find that $A_{V,depl}$ is much lower than $A_{V,ext}$ for the Milky Way. This could be due to the fact that with $A_{V,depl}$ we are probing only the warm diffuse ISM, while $A_{V,ext}$ is the cumulative extinction along the full line of sight, including the warm ISM and also regions of cold dense gas. On the other hand, for the LMC, SMC and GRB-DLAs the $A_{V,depl}$ is generally in good agreement with $A_{V,ext}$, with some exceptions that lie above or below the 1:1 line of equality. In the LMC and the SMC most of the systems lie below the line of equality ($A_{V,ext} > A_{V,depl}$). We quantify the correlation between the two measurements of A_V by calculating the χ^2_ν between $A_{V,ext}$ and $A_{V,depl}$ for all the environments. The Milky Way has the highest χ^2_ν with χ^2_ν = 2.18 and then the SMC with χ^2_ν = 2.14. GRB-DLAs have χ^2_ν = 1.03 and finally the LMC χ^2_ν = 0.63. We additionally estimate the Pearson's correlation coefficients r and report: r = 0.55 (GRBs), r = 0.71 (LMC), r = 0.30 (SMC), r = 0.48 (Milky Way). These indicate that the LMC points have the tightest correlation and the SMC the smallest. However, the low r for the SMC is driven only by the outlier marked in the green circle, which if excluded would give r = 0.61. Because this point has different properties due to the presence of the 2175 bump in the dust extinction curve for this system and is a physical outlier.

Savaglio and Fall (2004), Wiseman et al. (2017), and Bolmer et al. (2019) also compare their estimates of the dust extinction derived from depletion $A_{V,depl}$ with the dust extinction derived from SED ($A_{V,ext}$) for GRB-DLAs. They find that some systems lie above or below the line of equality, with an overall larger scatter that is observed in this paper, and they report that most lines of sight have a larger $A_{V,depl}$ than $A_{V,ext}$. The difference in our method is that we include C, as well as several more metals in the derivation of the $A_{V,depl}$ (all those that have an elemental abundance $12 + log\,(X/H) > 3$). Dust extinction depends on the composition of the dust, but also on the grain size distribution (Mathis, Rumpl, and Nordsieck, 1977; Pei, 1992; Hoffman and Draine, 2016; Mattsson, 2020), and gray dust has previously been suggested (e.g., Wiseman et al., 2017) as a solution for the high $A_{V,depl}$, but low reddening in some sources. If grains are big enough, then the extinction depends less on the wavelength and more on the geometrical cross section, which has been observed in some cases (e.g., Friis et al., 2015). In this case, the extinction curve is achromatic and $A_{V,ext}$ would be lower because each measurement is sensitive only to wavelength dependent extinction. On the other hand, $A_{V,depl}$ is an average of the dust extinction in the warm neutral medium of the absorbing galaxies and would be more sensitive to gray dust. The presence of gray dust would result to $A_{V,depl} > A_{V,ext}$. Most of the $A_{V,ext}$ measurements for GRB-DLAs are done adopting an X-ray spectral slope (e.g., Heintz et al., 2019b) and this makes them more robust in presence of gray dust. In any case, we observe only a few

systems with significant $A_{V,depl} > A_{V,ext}$, which possibly limits the effects of gray dust in this work.

The shape of the extinction curves depend on several properties, and can be steeper at lower metallicities (e.g. Shivaei et al., 2020), like for GRB-DLAs. $A_{V,ext}$ and $A_{V,depl}$ may be probing different types of dust and different regions with lower or higher densities. The methods used to measure $A_{V,ext}$ and $A_{V,depl}$ are very different, so that $A_{V,ext}$ represents a sum of the extinction integrated along the line of sight, including clumps of dense cold regions and intervening systems at lower z, while $A_{V,depl}$ represents an average value in the warm neutral medium through galaxies. On the other hand, the composition of dust plays a role in dust extinction, because the $A_{V,ext}$ is very sensitive to C-rich dust, but the depletion of C is challenging to constrain. For the calculation of $A_{V,depl}$ we do take into account C. However, only five Milky Way measurements are available (see Fig. B.2 of Paper I). These are based on only one weak transition (λ 2325), since the allowed transitions at λ 1036 and λ 1335 are strongly saturated (Jenkins, 2009). In Paper I we adopted the laboratory oscillator strength measurements with no additional correction for the oscillator strength of C.

In Paper I using the depletion coefficients we extrapolated the C depletion measured from a few Milky Way systems to the other environments where no measurements are available. This could mean that the depletion of C might be underestimated and might lead to a lower $A_{V,depl}$. On the other hand, $A_{V,ext}$ is estimated probing also C grains, especially in the Milky Way that has the strongest 2175 feature. This could partly explain the higher values of $A_{V,ext}$ and the large discrepancy with $A_{V,depl}$ for the cases where C is present, like for most of the targets in the Milky Way.

In fact, the presence of C-rich dust confined in molecular clouds may explain the discrepancy between $A_{V,depl}$ and $A_{V,ext}$ in a few outliers in the Magellanic Clouds as well as in the Milky Way (see Fig. 4.7). The highly deviating points, Sk 143 (SMC) at $A_{V,ext}$ = 0.97 and Sk 672 (LMC) at $A_{V,ext}$ = 0.76, that are marked with green circles in Fig. 4.7, are moderately reddened stars and the lines of sight with the highest molecular fraction and CN absorption within the SMC and LMC sample (Cartledge et al., 2006; Welty et al., 2006). Sk 143 is, in fact, the only SMC line of sight known to exhibit a Milky Way-like extinction curve, with a 2175 extinction bump (Gordon et al., 2003; Welty and Crowther, 2010). In the LMC, Sk 6619 fits a Milky Way-like extinction curve (Gordon et al., 2003) and is marked with a green circle point above the 1:1 line seen in Fig. 4.7.

The good agreement of the two extinction estimates for GRB-DLAs can be explained by the fact the two measurements may be probing dust with more similar composition - because there may be less C-rich dust given the low metallicity - and in more similar regions - because the GRB is expected to photo-dissociate the surrounding dense region, (e.g., Ledoux et al., 2009), possibly leading to $A_{V,ext}$ being more representative of the diffuse warm neutral medium in the host galaxy. In general, the measurements of $A_{V,ext}$ in GRB afterglows are reliable (Watson et al., 2006; Zafar and Watson, 2013; Perley et al., 2013; Heintz et al., 2019b), because the intrinsic afterglow spectrum is known to be either a power law or a broken power law (e.g. Sari, Piran, and Narayan, 1998).

Overall, $A_{V,depl}$ and $A_{V,ext}$ do not measure dust in the same way or in the same regions. $A_{V,depl}$ measures the average extinction along the line of sight, while only dusty clouds

contribute to $A_{V,ext}$ (i.e., the latter is not sensitive to the dust-free segments of the line of sight). The analysis of the depletion is mostly probing the warm neutral medium, and less sensitive to the dense clumps of cold molecular gas, which may contain large fractions of C-rich dust. This is a likely cause of the discrepancy between $A_{V,depl}$ and $A_{V,ext}$ observed in the Milky Way and a few lines of sight in the Magellanic Clouds.

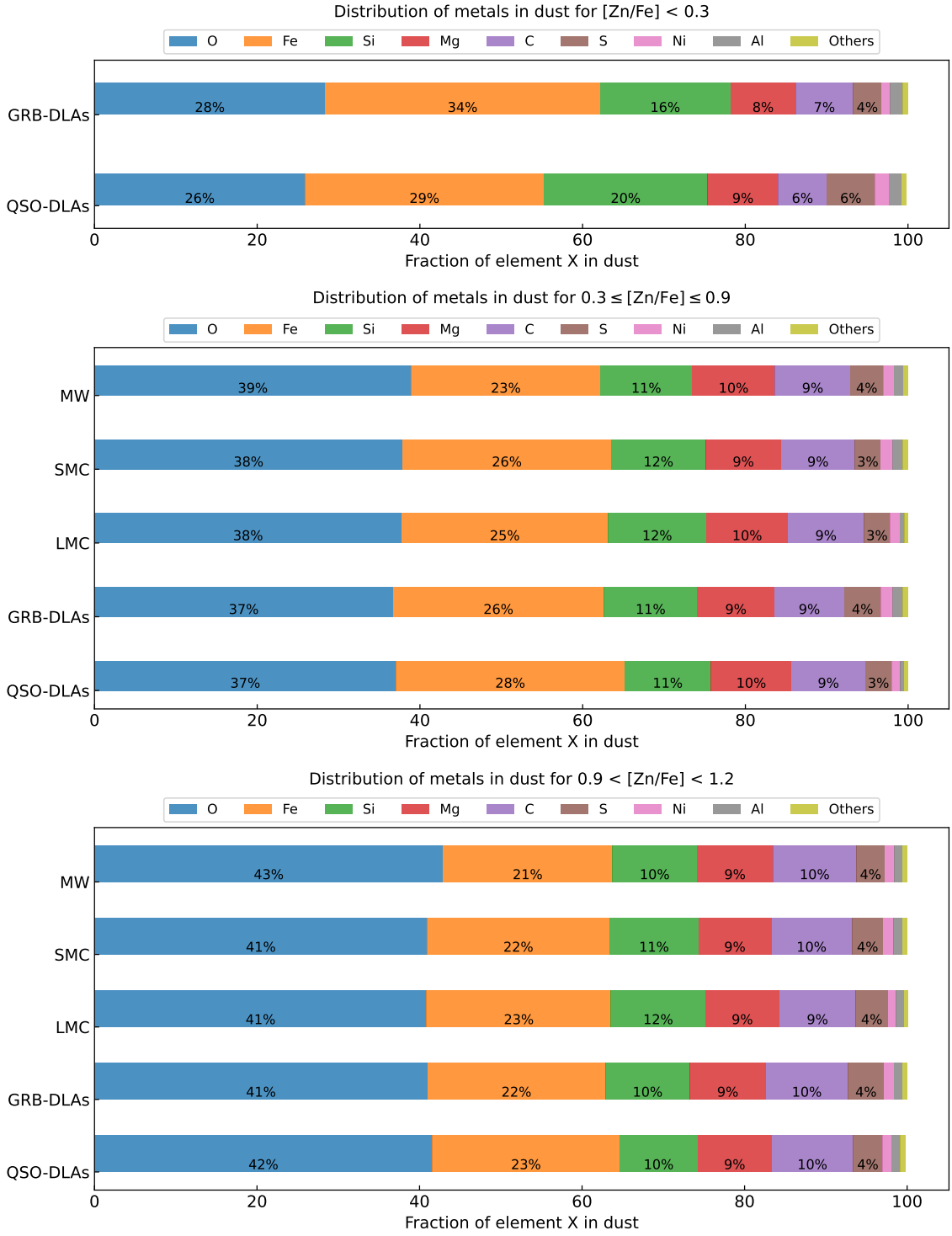


Figure 4.6: Distribution of metals that compose dust for the main elements ($f_{M_X} > 1\%$) that contribute into dust. The top panel shows the distribution of elements for [Zn/Fe] < 0.3 in QSO- and GRB-DLAs, the middle panel for the average [Zn/Fe] in all the environments and the bottom panel for 0.9 < [Zn/Fe] < 1.2. The average f_{M_X} on the full range of [Zn/Fe] are averaged over different ranges of [Zn/Fe] in different environments.

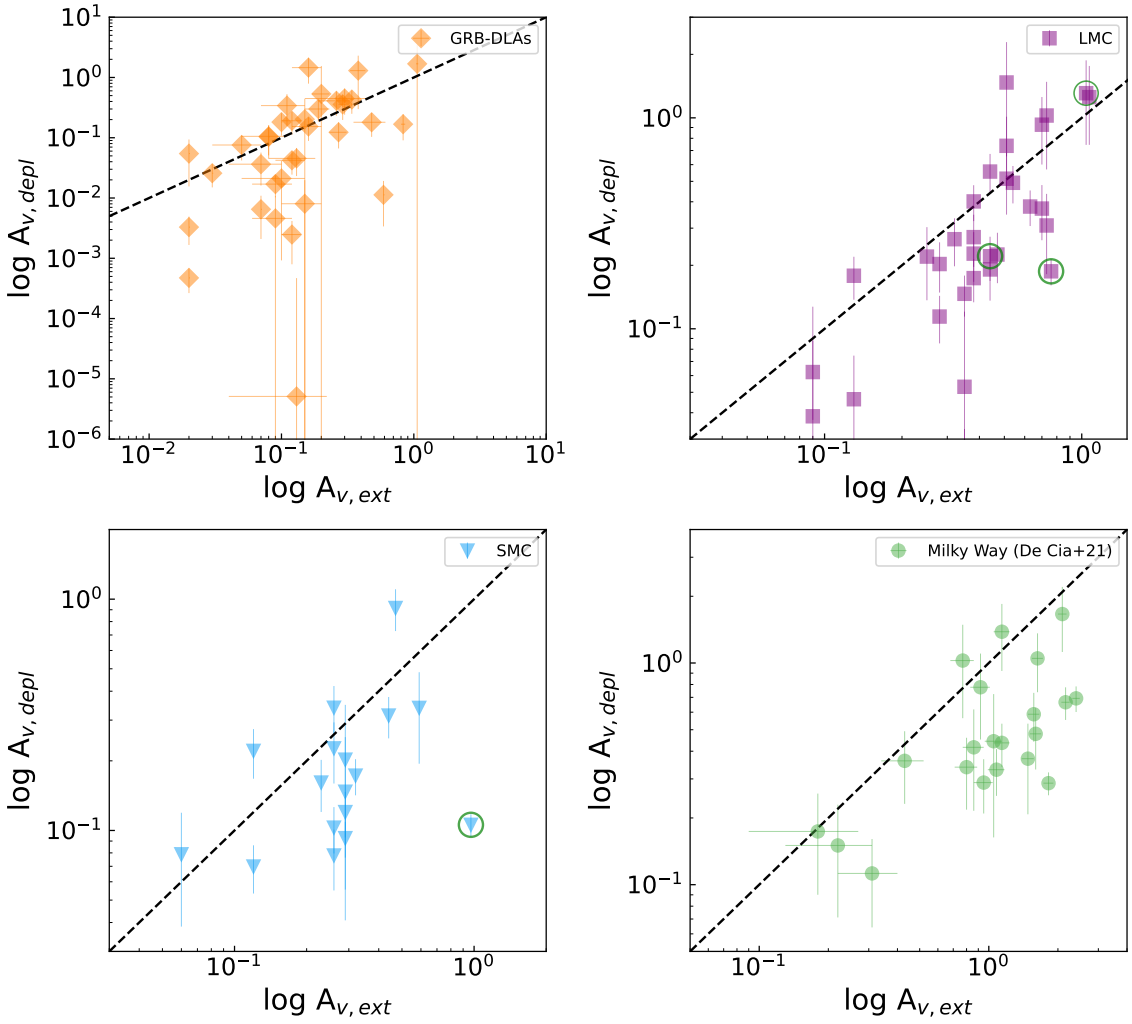


Figure 4.7: Dust extinction A_V as measured from extinction against the A_V calculated using the dust depletion for GRB-DLAs, LMC, SMC and the Milky Way. The black dashed line indicates the 1:1 conversion between the two. The green circles show targets with a 2175 feature or signs of carbonaceous dust.

4.6 CONCLUSIONS

In this paper we measure the dust-to-metal (DTM), dust-to-gas (DTG) ratios, dust extinction from depletion $A_{V,depl}$ and the fraction of dust mass contributed by element X (f_{M_X}) from the dust depletion of all the elements that contribute to dust. We do this for systems in different environments, QSO-DLAs, GRB-DLAs, LMC, SMC and the Milky Way. We study the DTM, DTG and $A_{V,depl}$ evolution with the total dust-corrected metallicity and the dust tracer [Zn/Fe]. The evolution of the DTM and DTG with metallicity gives us clues on the dominant mechanisms of dust production. We find that the DTM and DTG ratios increase with metallicity and with [Zn/Fe], which suggests that the dominant mechanism for dust production in the metallicity range (-2 $\leq$ $[M/H]_{tot}$ $\leq$ 0.5) and redshift range ($0.6 < z < 6.3$) that we study is grain growth in the ISM. Our data are in very good agreement with the dust production and evolution model from Mattsson (2020). The comparison of our data with the model indicates that the stellar dust yield is only 1% of the metals yield, which suggests that the net amount of dust that the overall stellar population produces is about ten times less than what was previously estimated. However, we note that this could be an effect of observational bias, since our data probe sightlines of warm diffuse gas and, as a result, might be missing some dust production contributions from stellar sources.

We investigate the cosmic metallicity evolution of the neutral gas and find a declining evolution with increasing redshift, which is probed both with QSO- and GRB-DLAs in a similar way.

The main elements that contribute to dust are, in order of abundance in mass, O, Fe, Si, Mg, C, S, Ni and Al for different environments and with overall similar percentages. Si, Mg and C have similar contributions by mass in dust in all the environments and vary with the amount of dust in each system, as traced by [Zn/Fe]. O and Fe have the highest fractions among all studied elements and show opposite trends with [Zn/Fe] between each other. O (and C) is increasing, while Fe is decreasing with [Zn/Fe]. This opposite evolution may be due to larger availability of Fe in systems with lower levels of depletions. In the low-dust regime ([Zn/Fe] < 0.3), we find that the amount of O in dust is about three times that of Si. This suggests the presence of pyroxenes as the main dust species.

We calculate the dust-to-metal ratio in terms of column density (DTM_N), in order to estimate the dust extinction using dust depletion ($A_{V,depl}$). The dust extinction $A_{V,depl}$ is increasing with metallicity and with [Zn/Fe]. At any given metallicity, we find lower values of $A_{V,depl}$ for QSO-DLAs than for GRB-DLAs, Mikly Way, and Magellanic Clouds. This suggests that not only metallicity but also the presence of dense cold gas at high pressure (such as in galaxy disks) are determinant factors to facilitate the growth of dust in the ISM.

We compare the dust extinction estimated from depletion ($A_{V,depl}$) with the one estimated from SED or from the reddening ($A_{V,ext}$). We find an overall good agreement between $A_{V,depl}$ and $A_{V,ext}$. However, we find that $A_{V,depl}$ is much lower than $A_{V,ext}$ for the Milky Way, as well as in a few systems in the SMC and LMC. In all these cases, the systems show a 2175 bump in their extinction curves. The likely cause of the discrepancy is the presence of C-rich dust in clumps of dense cold gas, such as molecular clouds, which are not probed by the depletion measurements. Overall, $A_{V,depl}$ and $A_{V,ext}$ do not measure the amount of dust

in the same way and in the same regions, with $A_{V,depl}$ measuring an average extinction along the line of sight and $A_{V,ext}$ being sensitive to dust-rich clouds. Nevertheless, in this work we refine the measurements of $A_{V,depl}$ and find a better consistency with $A_{V,ext}$. The reasons for the discrepancies that remain are probably related to C-rich dust in clumps of cold dense gas.

Acknowledgements: *We thank the anonymous referee for the useful and constructive comments that improved this manuscript. CK, ADC and TRH acknowledge support by the Swiss National Science Foundation under grant 185692. KEH acknowledges support from the Carlsberg Foundation Reintegration Fellowship Grant CF21-0103. ACA would like to acknowledge support by the Carlsberg Foundation. The Cosmic Dawn Center (DAWN) is funded by the Danish National Research Foundation under grant No. 140. This research has made use of NASA's Astrophysics Data System.*

4.A ADDITIONAL FIGURES

Here we present additional figures for the relation between the DTM by mass and the DTM by column density (DTM_N) and for the dust composition f_{M_X} with respect to [Zn/Fe] for all the elements that contribute to dust with $f_{M_X} > 1\%$, namely O, S, Si, Mg, Fe, Ni, Al and C. In the dust composition figgures, we show the targets that have dust depletion measurements with filled symbols and the ones whose dust depletion is calculated from the coefficients listed in Table 4.1 with empty symbols. This is shown for each environment: QSO- and GRB-DLAs, the Milky Way, the LMC and the SMC.

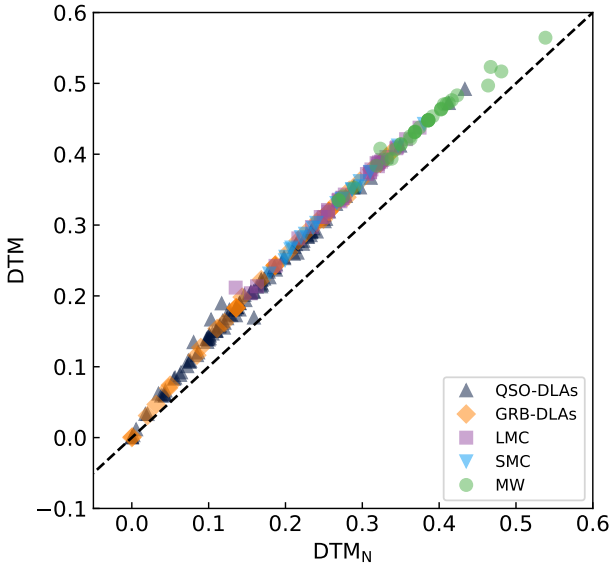


Figure 4.8: Relation between the DTM calculated in terms of mass and the DTM calculated in terms of column density (DTM_N) for QSO- and GRB-DLAs, LMC, SMC and the Milky Way. The dashed line is the 1:1 line of equality. DTM is on average ~ 0.05 times higher than DTM_N.

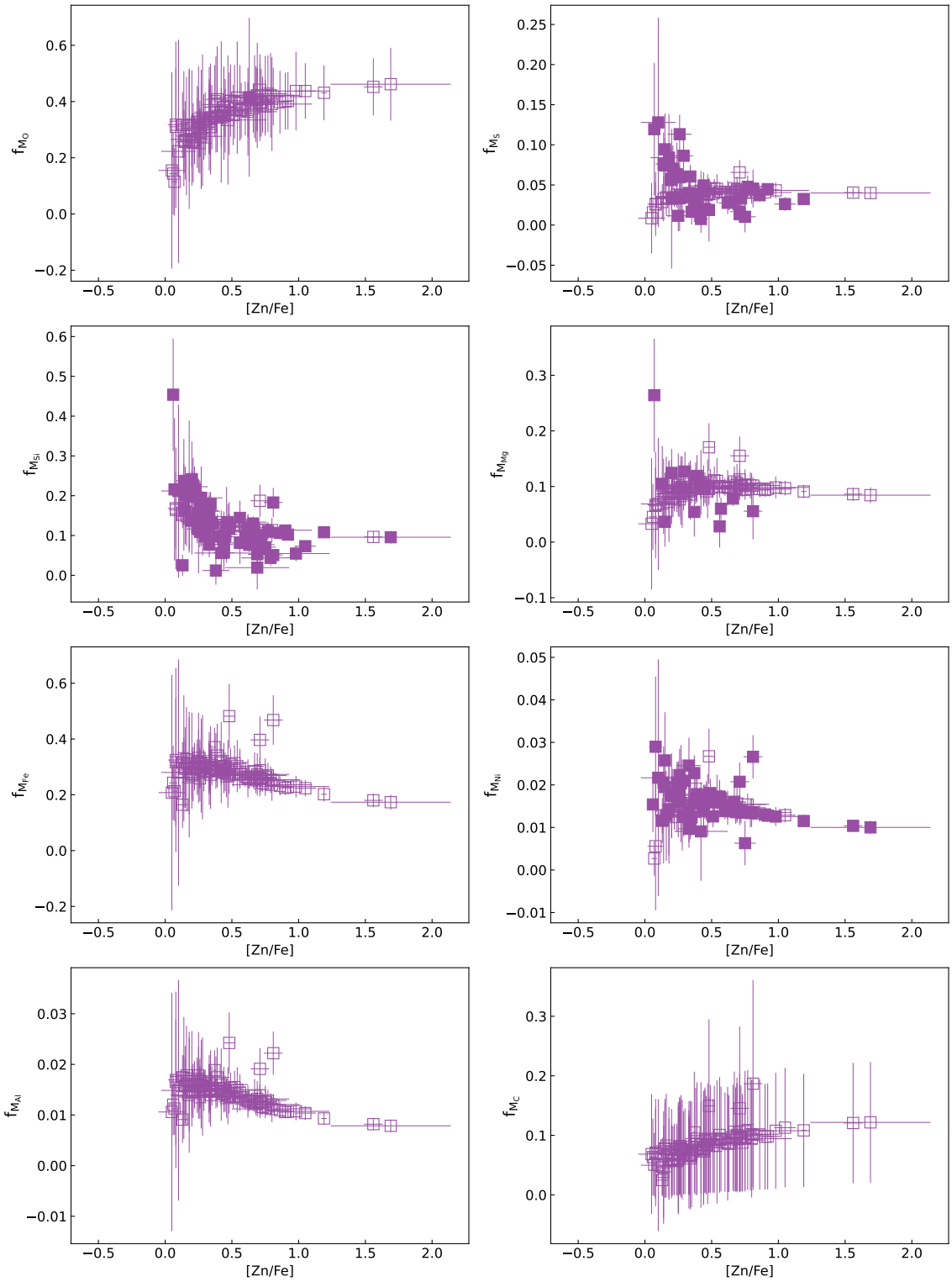


Figure 4.9: Fraction of dust mass contributed by element X, f_{M_X} as a function of the dust tracer [Zn/Fe] for QSO-DLAs. The filled squares indicate the targets that have a dust depletion measurement and the empty symbols indicate the targets whose dust depletion is calculated from the coefficients listed in Table 4.1.

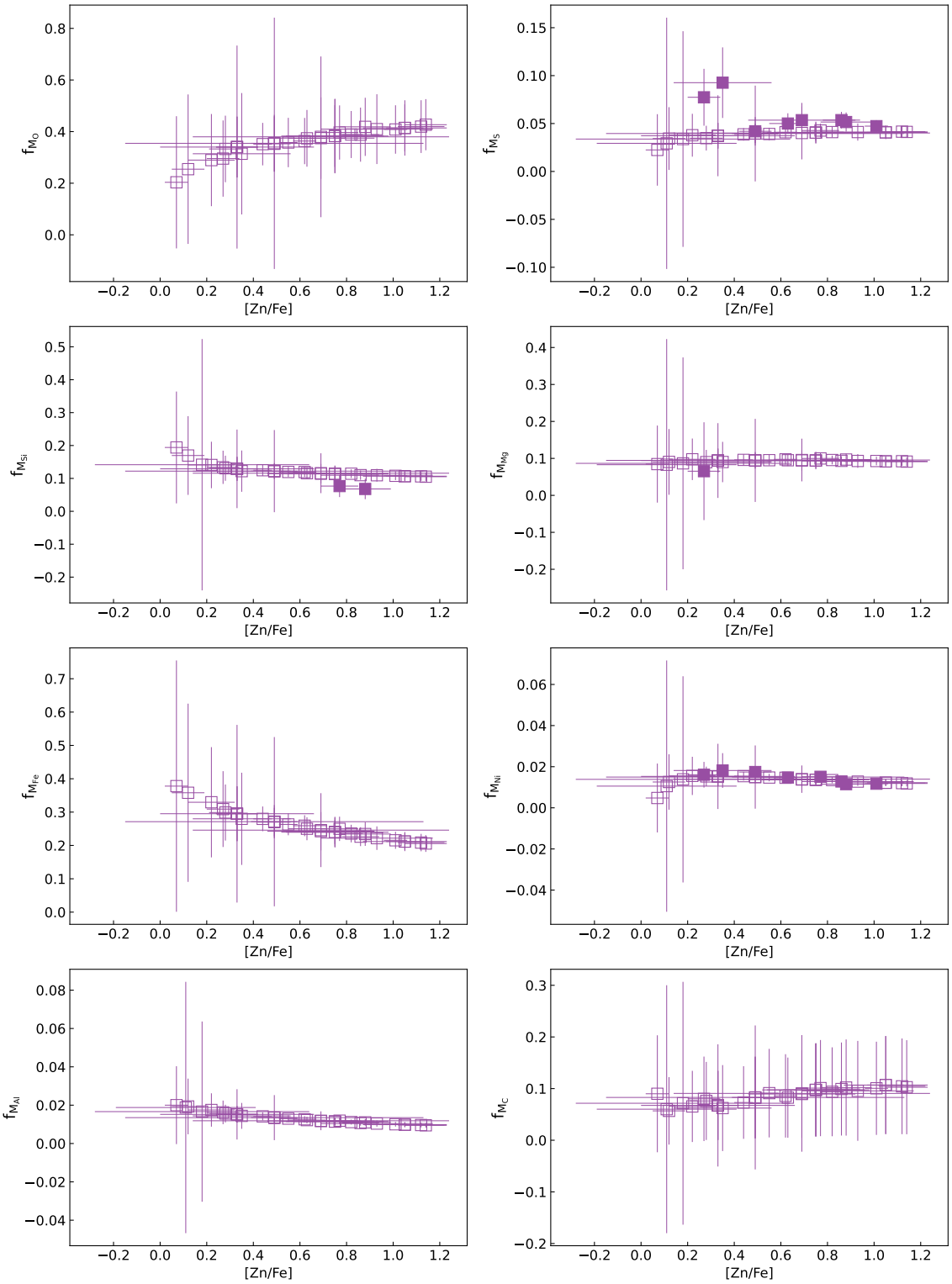


Figure 4.10: Fraction of dust mass contributed by element X, f_{M_X} as a function of the dust tracer [Zn/Fe] for GRB-DLAs.

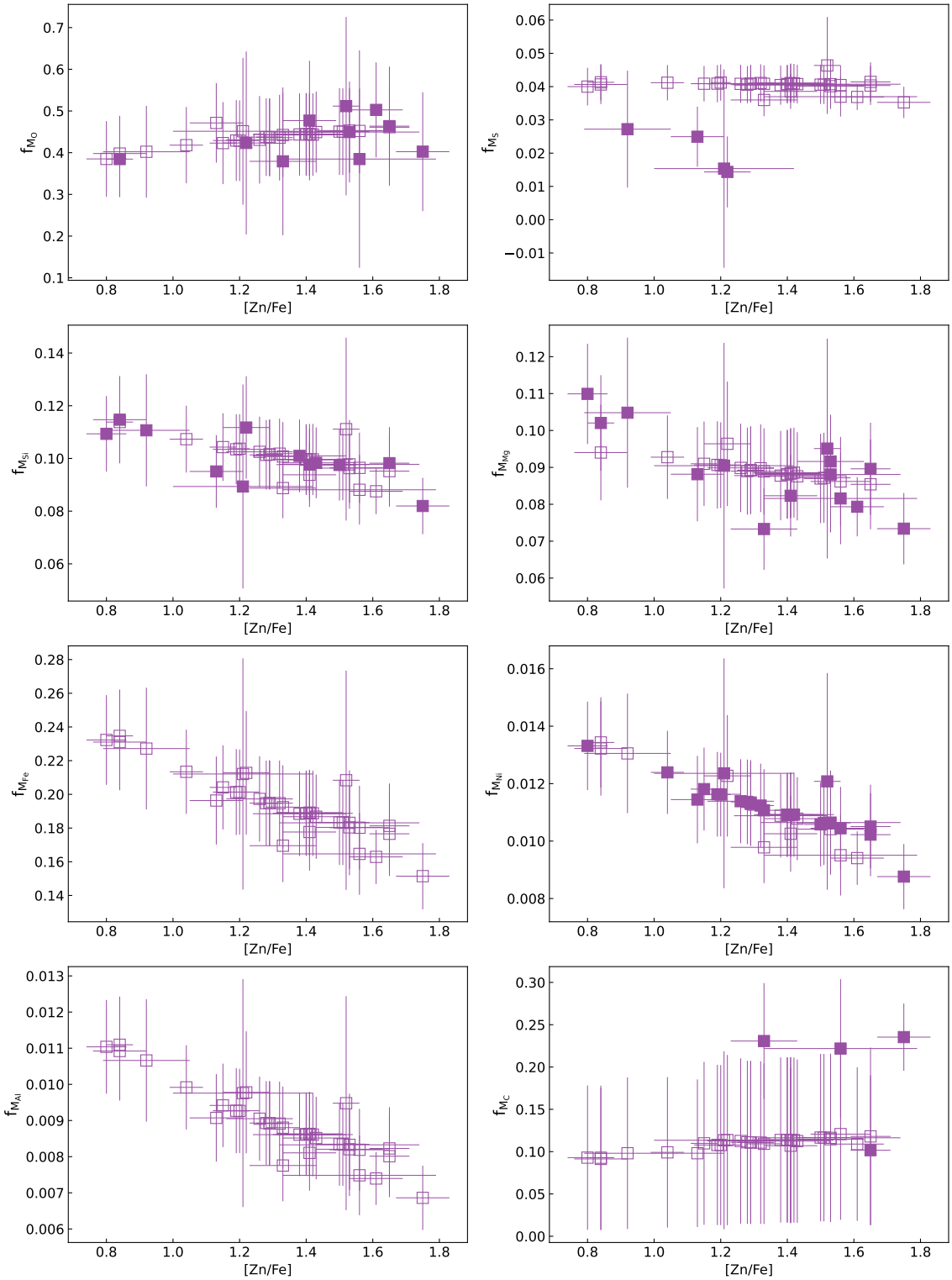


Figure 4.11: Fraction of dust mass contributed by element X, f_{M_X} as a function of the dust tracer [Zn/Fe] for the Milky Way.

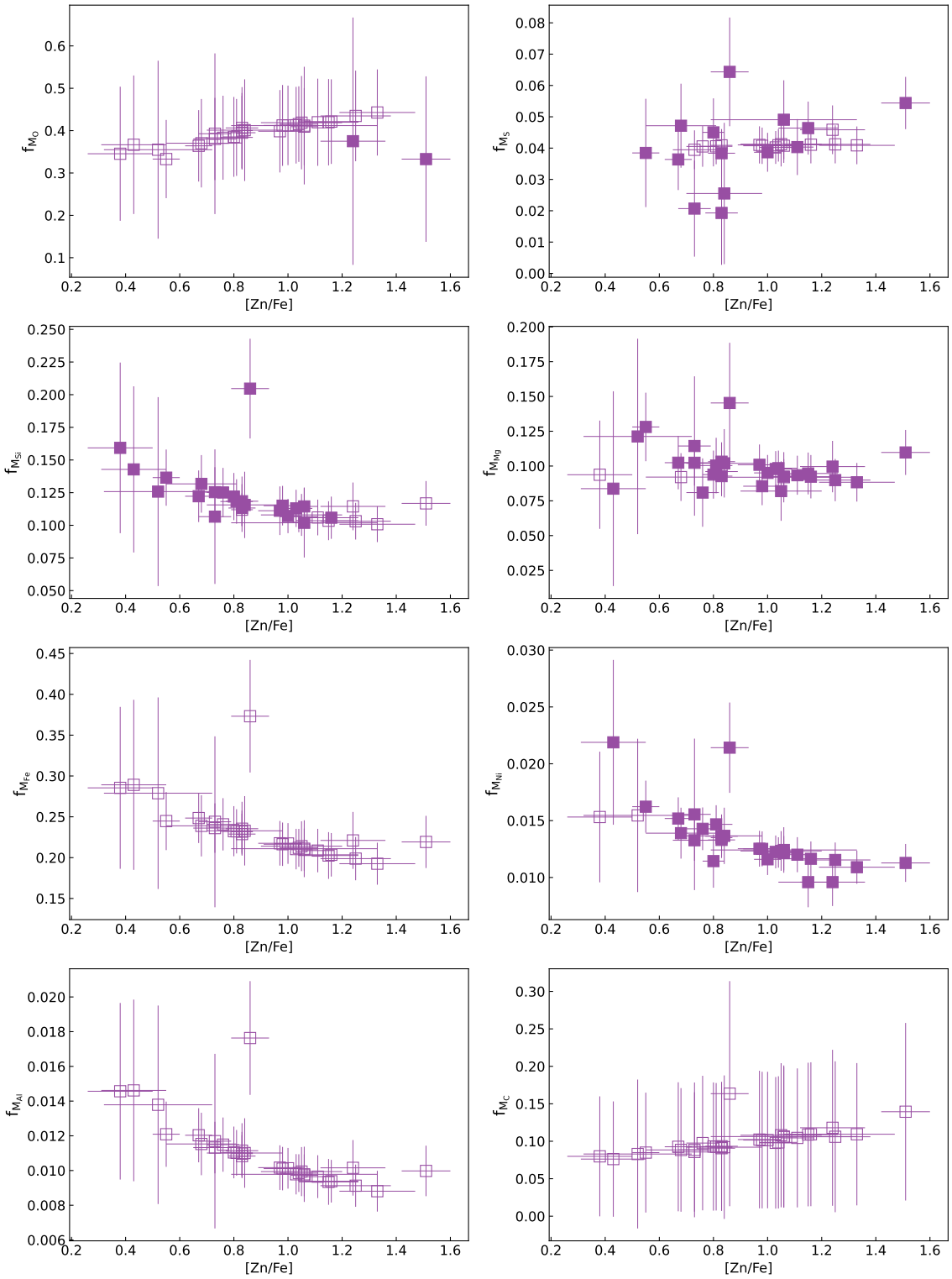


Figure 4.12: Fraction of dust mass contributed by element X, f_{M_X} as a function of the dust tracer [Zn/Fe] for the LMC.

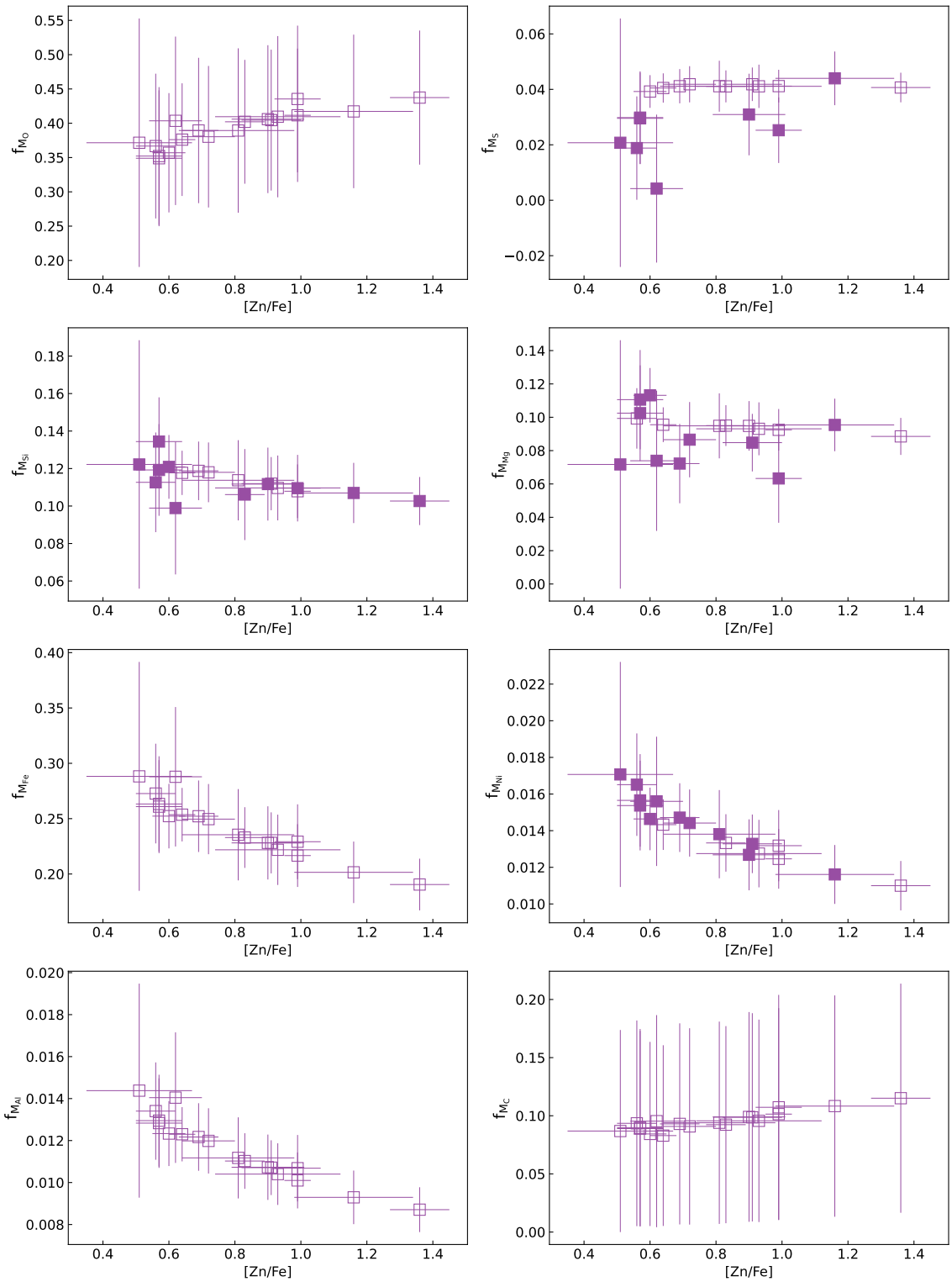


Figure 4.13: Fraction of dust mass contributed by element X, f_{M_X} as a function of the dust tracer [Zn/Fe] for the SMC.

4.B DUST PROPERTIES OF THE DATA SAMPLE

Here we present the tables of the dust properties for QSO- and GRB-DLAs, the Milky Way, LMC and SMC. We include the redshift z_{abs}, the column densities of HI, HII, the dust tracer [Zn/Fe], the DTM and DTG in terms of mass, the DTM in terms of column density (DTM_N), the dust extinction estimated from the dust depletion $A_{V,depl}$ and the total dust-corrected metallicity $[M/H]_{tot}$. We note that the DTM in terms of column density (DTM_N) is not normalized by the Galactic DTM. We also report the references of the data samples.

Table 4.4: QSO-DLAs dust properties

QSO	z_{abs}	log N(HI)	log N(H2)	[Zn/Fe]	DTM	DTG	DTM_N	$A_{V,depl}$	$[M/H]_{tot}$	Ref
B0105-008	1.371	21.70±0.15	...	0.08±0.05	0.06±0.02	4.00e-05±2.00e-05	0.04±0.01	0.01±0.01	-1.35±0.17	*,2,3
B2314-409	1.857	20.90±0.10	...	0.18±0.14	0.14±0.04	2.30e-04±1.20e-04	0.10±0.03	0.01±0.01	-0.92±0.19	*,2,3
B2355-106	1.173	21.00±0.10	...	0.42±0.20	0.19±0.05	5.10e-04±3.00e-04	0.15±0.05	0.04±0.02	-0.72±0.23	*,2,3
BRI1013+0035	3.104	21.10±0.10	...	0.90±0.05	0.35±0.04	3.82e-03±1.24e-03	0.29±0.06	0.36±0.15	-0.11±0.13	*,2,3
FJ0812+32	2.626	21.35±0.10	...	0.81±0.07	0.17±0.14	6.10e-04±5.40e-04	0.10±0.15	0.08±0.12	-0.58±0.14	*,2,3
FJ0812+32	2.067	21.00±0.10	...	0.06±0.03	0.07±0.02	4.00e-05±1.00e-05	0.04±0.01	...	-1.37±0.13	*,2,3
FJ2334-0908	3.057	20.48±0.05	...	0.48±0.04	0.13±0.15	2.90e-04±3.20e-04	0.08±0.16	0.003±0.001	-0.81±0.09	*,2,3
HE0515-4414	1.150	20.45±0.15	...	0.54±0.20	0.23±0.05	5.10e-04±3.20e-04	0.18±0.05	0.01±0.01	-0.79±0.26	*,2,3
HE1104-1805	1.662	20.85±0.01	...	0.46±0.02	0.39±0.10	7.80e-04±2.30e-04	0.35±0.10	0.05±0.02	-0.84±0.07	*,2,3
J0000+0048	2.525	21.07±0.10	...	1.69±0.45	0.49±0.07	5.43e-02±6.06e-02	0.43±0.09	5.14±5.91	0.90±0.48	*,2,3
J0008-0958	1.768	20.85±0.15	...	0.44±0.07	0.21±0.03	...	0.16±0.03	...	0.0±0.18	*,2,3
J0058+0115	2.010	21.10±0.15	...	0.51±0.07	0.24±0.03	8.50e-04±3.70e-04	0.19±0.04	0.08±0.04	-0.60±0.18	*,2,3
J0256+0110	0.725	20.70±0.16	...	0.80±0.30	0.33±0.06	6.18e-03±5.38e-03	0.27±0.07	0.23±0.22	0.13±0.37	*,2,3
J0927+1543	1.731	...	...	0.98±0.25	0.35±0.06	...	0.30±0.07	...	...	*,2,3
J1049-0110	1.658	20.31±0.15	...	0.71±0.07	0.26±0.04	9.32e-03±4.11e-03	0.22±0.05	0.14±0.08	0.41±0.18	*,2,3
J1056+1208	1.610	21.45±0.15	...	0.69±0.07	0.28±0.04	3.20e-03±1.39e-03	0.23±0.05	0.67±0.39	-0.09±0.18	*,2,3
J1107+0048	0.740	21.00±0.05	...	0.28±0.105	0.16±0.03	8.00e-04±3.50e-04	0.12±0.03	0.05±0.03	-0.45±0.17	*,2,3
J1135-0010	2.207	22.05±0.10	...	0.60±0.04	0.27±0.03	5.20e-04±1.70e-04	0.21±0.04	0.42±0.18	-0.86±0.13	*,2,3
J1142+0701	1.841	21.50±0.15	...	0.56±0.07	0.25±0.03	7.90e-04±3.40e-04	0.20±0.04	0.18±0.10	-0.65±0.18	*,2,3
J1155+0530	3.326	21.05±0.10	...	0.26±0.09	0.18±0.02	5.20e-04±1.90e-04	0.13±0.03	0.04±0.02	-0.68±0.15	*,2,3
J1200+4015	3.220	20.65±0.15	...	0.29±0.07	0.17±0.02	1.22e-03±5.30e-04	0.13±0.03	0.04±0.02	-0.30±0.18	*,2,3
J1211+0833	2.117	21.00±0.20	...	1.56±0.07	0.47±0.06	1.73e-02±9.02e-03	0.41±0.08	1.38±0.98	0.42±0.22	*,2,3
J1237+0647	2.690	20.00±0.15	...	1.19±0.02	0.41±0.05	3.37e-02±1.38e-02	0.35±0.07	0.26±0.15	0.77±0.17	*,2,3
J1240+1455	3.108	21.30±0.20	...	1.05±0.08	0.37±0.05	9.90e-04±5.40e-04	0.31±0.06	0.15±0.11	-0.71±0.23	*,2,3
J1310+5424	1.801	21.45±0.15	...	0.67±0.07	0.26±0.05	1.85e-03±8.30e-04	0.21±0.05	0.39±0.23	-0.29±0.18	*,2,3
J1313+1441	1.795	...	...	0.49±0.07	0.21±0.03	...	0.17±0.04	...	...	*,2,3
J1417+4132	1.951	21.45±0.25	...	0.71±0.07	0.19±0.19	...	0.12±0.21	...	...	*,2,3
J1431+3952	0.602	21.20±0.10	...	0.62±0.22	0.28±0.05	9.90e-04±5.90e-04	0.22±0.05	0.11±0.08	-0.59±0.25	*,2,3
J1454+0941	1.788	20.50±0.15	...	0.44±0.13	0.21±0.03	1.65e-03±8.40e-04	0.16±0.04	0.04±0.02	-0.24±0.21	2
J1541+3153	2.444	20.95±0.10	...	0.27±0.16	0.16±0.03	8.00e-05±4.00e-05	0.12±0.03	...	-1.45±0.20	*,2,3
J1552+4910	1.960	...	...	0.20±0.07	0.12±0.03	6.00e-05±2.00e-05	0.09±0.02	...	-1.46±0.13	*,2,3
J1604+3951	3.163	21.75±0.20	...	0.39±0.07	0.20±0.02	2.10e-04±1.10e-04	0.15±0.03	0.08±0.06	-1.12±0.22	*,2,3
J1623+0718	1.336	21.35±0.10	...	0.38±0.10	0.18±0.03	3.00e-04±1.20e-04	0.14±0.03	0.05±0.02	-0.93±0.16	*,2,3
J2328+0022	0.652	20.32±0.07	...	0.34±0.15	0.18±0.03	1.04e-03±4.70e-04	0.14±0.04	0.01±0.01	-0.39±0.18	*,2,3
J2340-00	2.054	20.35±0.15	...	0.39±0.09	0.17±0.03	1.51e-03±7.20e-04	0.14±0.04	0.02±0.01	-0.20±0.19	*,2,3
PSS1253-0228	2.783	21.85±0.20	...	0.16±0.08	0.10±0.02	3.00e-05±2.00e-05	0.07±0.02	0.01±0.01	-1.64±0.23	*,2,3
PSSJ2344+0342	3.220	21.25±0.08	...	-0.08±0.34	0.0011±0.120	3.00e-07±4.00e-05	0.001 ±0.08	...	-1.65±0.35	*,2,3
Q0000-263	3.390	21.40±0.08	...	-0.11±0.06	0.003±0.16	3.00e-07±2.00e-05	0.003±0.16	...	-2.14±0.11	*,1,3
Q0010-002	2.025	20.95±0.10	...	-0.25±0.06	0.0005±0.030	2.00e-07±1.00e-05	0.001±0.03	...	-1.49±0.13	*,1,3
Q0013-004	1.973	20.83±0.05	18.86±1.14	0.75±0.01	0.32±0.04	1.77e-03±4.60e-04	0.26±0.05	0.09±0.03	-0.40±0.10	*,1,3
Q0027-1836	2.402	21.75±0.10	17.30±0.07	0.56±0.03	0.24±0.03	1.30e-04±4.00e-05	0.19±0.04	0.05±0.02	-1.41±0.13	*,2,3
Q0058-292	2.671	21.10±0.10	...	0.24±0.03	0.14±0.01	6.00e-05±2.00e-05	0.10±0.02	0.01±0.001	-1.48±0.11	*,1,3
Q0100+130	2.309	21.35±0.08	...	0.13±0.01	0.09±0.01	3.00e-05±1.00e-05	0.06±0.01	...	-1.62±0.11	*,1,3
Q0102-190a	2.370	21.00±0.08	...	0.01±0.08	0.01±0.03	...	0.01±0.02	...	...	*,1,3
Q0149+33	2.141	20.50±0.10	...	0.05±0.10	0.06±0.03	2.00e-05±1.00e-05	0.04±0.02	...	-1.59±0.16	*,2,3
Q0201+365	2.463	20.38±0.05	...	0.20±0.05	0.14±0.02	1.67e-03±4.70e-04	0.10±0.02	0.03±0.01	-0.07±0.11	*,2,3
Q0216+080a	1.769	20.30±0.10	...	0.24±0.06	0.15±0.02	1.90e-04±7.00e-05	0.1±0.02	...	-1.02±0.13	*,1,3
Q0216+080b	2.293	20.50±0.10	...	0.33±0.05	0.17±0.02	5.90e-04±2.20e-04	0.13±0.03	0.01±0.01	-0.61±0.15	*,1,3
Q0302-223	1.009	20.36±0.11	...	0.52±0.08	0.22±0.03	1.31e-03±4.90e-04	0.17±0.04	0.02±0.01	-0.36±0.15	*,2,3
Q0347-383	3.025	20.73±0.05	14.53±0.06	0.63±0.05	0.28±0.08	3.10e-04±1.50e-04	0.22±0.09	0.01±0.01	-1.10 ±0.18	*,1,3
Q0405-443a	1.913	20.80±0.10	...	0.02±0.04	0.03±0.02	4.00e-05±2.00e-05	0.02±0.01	...	-1.08±0.12	*,1,3
Q0405-443b	2.550	21.15±0.15	...	0.15±0.04	0.11±0.02	5.00e-05±2.00e-05	0.08±0.02	...	-1.46±0.18	*,1,3
Q0405-443c	2.595	21.05±0.10	18.14±0.07	0.26±0.01	0.15±0.02	1.50e-04±4.00e-05	0.11±0.02	0.01±0.001	-1.14±0.12	*,1,3
Q0449-1645	1.007	20.98±0.07	...	0.27±0.07	0.16±0.02	2.90e-04±9.00e-05	0.11±0.03	0.02±0.01	-0.88±0.12	*,2,3
Q0458-020	2.040	21.70±0.10	...	0.57±0.04	0.25±0.03	2.50e-04±1.00e-04	0.2±0.04	0.09±0.04	-1.15±0.16	*,1,3
Q0528-250a	2.141	20.98±0.05	...	0.25±0.04	0.14±0.02	9.00e-05±2.00e-05	0.1±0.02	0.010±0.001	-1.35±0.08	*,1,3
Q0528-250b	2.811	21.35±0.07	18.22±0.11	0.37±0.01	0.16±0.02	2.70e-04±9.00e-05	0.12±0.03	0.04±0.02	-0.90±0.12	*,1,3
Q0551-366	1.962	20.70±0.08	17.42±0.14	0.71±0.04	0.29±0.04	2.26e-03±6.50e-04	0.23±0.05	0.08±0.03	-0.25±0.11	*,1,3
Q0642-5038	2.659	20.95±0.08	...	0.22±0.05	0.14±0.02	3.00e-05±1.00e-05	0.10±0.02	...	-1.83±0.12	*,2,3

Table 4.4: continued

QSO	z_{abs}	log N(HI)	log N(H2)	[Zn/Fe]	DTM	DTG	DTM_N	$A_{V,depl}$	$[M/H]_{tot}$	Ref
Q0841+129a	1.864	21.00±0.10	...	-0.10±0.12	0.00017±0.04	...	0.0002±0.03	...	...	1
Q0841+129b	2.375	21.05±0.10	...	0.15±0.03	0.11±0.02	4.00e-05±1.00e-05	0.08±0.02	...	-1.61±0.11	*,1,3
Q0841+129c	2.476	20.80±0.10	...	0.13±0.04	0.17±0.11	5.00e-05±4.00e-05	0.16±0.12	...	-1.65±0.14	*,1,3
Q0918+1636	2.583	20.96±0.05	...	0.72±0.01	0.29±0.04	1.31e-03±9.50e-04	0.23±0.05	0.09±0.07	-0.49±0.31	*,2,3
Q0918+1636	2.412	21.26±0.06	...	0.47±0.29	0.23±0.06	3.65e-03±1.16e-03	0.18±0.06	0.46±0.20	0.05±0.09	*,2,3
Q0933+733	1.479	21.62±0.10	...	0.26±0.02	0.15±0.02	8.00e-05±2.00e-05	0.11±0.02	0.02±0.01	-1.44±0.12	*,2,3
Q0935+417	1.373	20.52±0.10	...	0.18±0.10	0.12±0.03	2.60e-04±1.10e-04	0.08±0.02	0.01±0.0	-0.80±0.16	*,2,3
Q0948+433	1.233	21.62±0.06	...	0.34±0.01	0.18±0.02	2.70e-04±6.00e-05	0.14±0.02	0.08±0.02	-0.97±0.09	*,2,3
Q1010+0003	1.265	21.52±0.07	...	0.44±0.08	0.21±0.03	2.60e-04±9.00e-05	0.16±0.03	0.06±0.02	-1.04±0.13	*,2,3
Q1037-270	2.139	19.70±0.05	...	0.07±0.02	0.08±0.02	...	0.05±0.02	...	...	*,1,3
Q1111-152	3.266	21.30±0.05	...	0.25±0.09	0.13±0.03	4.00e-05±2.00e-05	0.10±0.03	0.010±0.001	-1.66±0.14	*,1,3
Q1117-134	3.350	20.95±0.10	...	0.14±0.06	0.09±0.02	4.00e-05±1.00e-05	0.06±0.02	...	-1.46±0.11	*,1,3
Q1137+3907	0.720	21.10±0.10	...	0.73±0.07	0.31±0.04	3.80e-03±1.31e-03	0.25±0.05	0.35±0.15	-0.06±0.14	*,2,3
Q1157+014	1.944	21.80±0.10	...	0.30±0.01	0.17±0.02	9.00e-05±3.00e-05	0.12±0.03	0.04±0.02	-1.42±0.11	*,1,3
Q1209+093	2.584	21.40±0.10	...	0.45±0.03	0.22±0.03	3.20e-04±1.00e-04	0.17±0.03	0.06±0.02	-0.98±0.13	*,1,3
Q1210+17	1.892	20.63±0.08	...	0.14±0.06	0.11±0.02	2.50e-04±8.00e-05	0.07±0.02	0.010±0.001	-0.78±0.12	*,2,3
Q1215+33	1.999	20.95±0.07	...	0.33±0.07	0.19±0.02	2.00e-04±6.00e-05	0.14±0.03	0.01±0.0	-1.13±0.12	*,2,3
Q1223+178	2.466	21.40±0.10	...	-0.03±0.02	0.06±0.01	2.00e-05±1.00e-05	0.040±0.001	...	-1.64±0.14	*,1,3
Q1232+082	2.338	20.90±0.10	...	0.77±0.14	0.29±0.05	1.07e-03±4.70e-04	0.23±0.06	0.06±0.03	-0.57±0.18	*,2,3
Q1328+307	0.692	21.25±0.10	...	0.48±0.14	0.24±0.04	3.30e-04±1.60e-04	0.19±0.04	0.04±0.02	-1.00±0.19	*,2,3
Q1331+170	1.776	21.15±0.07	...	0.66±0.04	0.29±0.03	2.90e-04±9.00e-05	0.23±0.04	0.03±0.01	-1.14±0.12	*,1,3
Q1354+258	1.420	21.54±0.06	...	0.33±0.09	0.18±0.02	1.32e-03±8.40e-04	0.14±0.03	0.31±0.20	-0.29±0.27	*,2,3
Q1409+095a	2.019	20.65±0.10	...	0.10±0.13	0.08±0.04	2.00e-05±1.00e-05	0.06±0.03	...	-1.70±0.15	*,1,3
Q1425+6039	2.827	20.30±0.04	...	0.44±0.04	0.22±0.02	8.00e-04±1.80e-04	0.17±0.03	0.01±0.0	-0.59±0.09	*,2,3
Q1444+014	2.087	20.25±0.07	18.16±0.14	0.86±0.07	0.34±0.05	1.11e-03±5.10e-04	0.28±0.06	0.01±0.01	-0.63±0.19	*,1,3
Q1451+123a	2.255	20.35±0.10	...	0.27±0.12	0.15±0.03	2.10e-04±9.00e-05	0.11±0.03	...	-1.00±0.15	*,1,3
Q1727+5302	1.031	21.41±0.15	...	0.69±0.24	0.27±0.05	1.86e-03±7.70e-04	0.22±0.06	0.36±0.20	-0.31±0.16	*,2,3
Q1727+5302	0.945	21.16±0.10	...	0.71±0.11	0.29±0.04	3.50e-04±2.40e-04	0.23±0.05	0.04±0.03	-1.06±0.29	*,2,3
Q1755+578	1.971	21.40±0.15	...	0.81±0.07	0.31±0.04	5.16e-03±2.24e-03	0.25±0.05	0.97±0.56	0.08±0.18	*,2,3
Q2116-358	1.996	20.10±0.07	...	0.45±0.09	0.22±0.03	1.67e-03±4.50e-04	0.17±0.04	0.01±0.01	-0.27±0.10	*,1,3
Q2138-444a	2.383	20.60±0.05	...	0.33±0.08	0.19±0.02	2.20e-04±6.00e-05	0.14±0.03	0.01±0.0	-1.07±0.11	*,1,3
Q2138-444b	2.852	20.98±0.05	...	0.02±0.03	0.06±0.01	1.00e-05±0.00e+00	0.03±0.01	...	-1.86±0.10	*,1,3
Q2206-199a	1.921	20.67±0.05	...	0.20±0.01	0.14±0.02	6.20e-04±2.20e-04	0.10±0.02	0.02±0.01	-0.51±0.15	*,1,3
Q2228-3954	2.095	21.20±0.10	...	0.08±0.06	0.06±0.02	5.00e-05±2.00e-05	0.04±0.01	...	-1.26±0.14	*,2,3
Q2230+025	1.864	20.83±0.05	...	0.35±0.07	0.18±0.02	7.60e-04±2.20e-04	0.13±0.03	0.03±0.01	-0.52±0.11	*,2,3
Q2231-00	2.066	20.53±0.08	...	0.21±0.06	0.15±0.02	3.50e-04±1.10e-04	0.10±0.02	0.01±0.0	-0.76±0.12	*,2,3
Q2243-605	2.331	20.65±0.05	...	0.26±0.02	0.16±0.02	3.50e-04±1.10e-04	0.11±0.02	0.01±0.0	-0.79±0.12	*,1,3
Q2318-1107	1.989	20.68±0.05	15.49±0.03	0.34±0.03	0.20±0.02	5.80e-04±1.40e-04	0.15±0.02	0.02±0.01	-0.68±0.09	*,2,3
Q2332-094a	2.287	20.07±0.07	...	0.92±0.04	0.35±0.04	3.09e-03±1.07e-03	0.29±0.06	0.03±0.01	-0.20±0.14	*,1,3
Q2343+125	2.431	20.40±0.07	13.69±0.09	0.39±0.03	0.21±0.02	3.90e-04±1.00e-04	0.16±0.03	0.01±0.0	-0.86±0.10	*,1,3
Q2359-022a	2.095	20.65±0.10	...	0.75±0.08	0.29±0.04	1.19e-03±5.20e-04	0.24±0.05	0.04±0.02	-0.53±0.18	*,1,3
SDSS0225+0054	2.714	21.00±0.15	...	0.33±0.14	0.18±0.03	6.30e-04±3.20e-04	0.14±0.04	0.04±0.03	-0.61±0.21	*,2,3
SDSS1116+4118A	2.662	20.48±0.10	...	0.79±0.22	0.31±0.05	1.47e-03±8.80e-04	0.25±0.06	0.03±0.02	-0.46±0.25	*,2,3
SDSS1249-0233	1.781	21.45±0.15	...	0.42±0.05	0.21±0.02	4.70e-04±1.90e-04	0.15±0.03	0.09±0.05	-0.78±0.17	*,2,3
SDSS1610+4724	2.508	21.15±0.15	...	0.69±0.07	0.28±0.04	4.04e-03±1.76e-03	0.23±0.05	0.42±0.24	0.01±0.18	*,2,3
SDSS2059-0529	2.210	20.80±0.20	...	0.68±0.16	0.30±0.04	2.26e-03±1.39e-03	0.24±0.05	0.1±0.08	-0.26±0.26	*,2,3
SDSS2100-0641	3.092	21.05±0.15	...	0.62±0.07	0.27±0.03	2.23e-03±9.60e-04	0.21±0.04	0.18±0.10	-0.23±0.18	*,2,3
UM673A	1.626	20.70±0.10	...	-0.42±0.15	0.03±0.06	1.00e-05±2.00e-05	0.02±0.05	...	-1.59±0.20	*,2,3
eHAQ0111+0641	2.027	21.50±0.30	...	0.44±0.14	0.22±0.04	1.05e-03±8.40e-04	0.17±0.04	0.23±0.25	-0.47±0.34	*,2,3

References: Measurements of the DTM, DTG, DTM_N and $A_{V,depl}$ are from ($\star$) this work, column densities from (1) De Cia et al. (2016); (2) Berg et al. (2015) and total dust-corrected metallicities from De Cia (2018).

Table 4.5: Milky Way dust properties

Star	log N(HI)	log N(H2)	[Zn/Fe]	DTM	DTG	DTM_N	$A_{V,depl}$	$[M/H]_{tot}$	Ref
1-SCO	...	...	1.53±0.21	0.46±0.06	...	0.40±0.08	...	...	*,2
23O-ORI	...	...	1.75±0.08	0.56±0.08	...	0.54±0.08	...	...	*,2
62-TAU	20.95±0.10	20.79±0.10	1.56±0.09	0.47±0.06	2.55e-03±8.30e-04	0.41±0.08	0.44±0.23	-0.41±0.13	*,1
BET-1-SCO	...	...	1.56±0.23	0.52±0.14	...	0.48±0.15	...	...	*,2
CHI-OPH	21.13±0.10	20.63±0.10	1.29±0.04	0.43±0.05	2.80e-03±7.90e-04	0.37±0.07	0.48±0.24	-0.33±0.11	*,1
DEL-ORI-A	...	...	1.41±0.08	0.48±0.08	...	0.42±0.09	...	...	*,2
EPS-ORI	...	...	1.61±0.08	0.52±0.07	...	0.47±0.09	...	...	*,2
EPS-PER	20.45±0.10	19.52±0.10	1.38±0.14	0.45±0.06	4.12e-03±1.33e-03	0.39±0.07	0.11±0.06	-0.18±0.13	*,1
HD-110432	20.85±0.10	20.64±0.10	1.51±0.08	0.46±0.06	4.67e-03±1.72e-03	0.40±0.08	0.59±0.33	-0.14±0.15	*,1
HD-116852	...	...	0.84±0.04	0.34±0.04	...	0.27±0.05	...	...	*,2
HD-149404	21.40±0.10	20.79±0.10	1.41±0.09	0.45±0.06	5.68e-03±1.37e-03	0.39±0.07	1.66±0.80	-0.04±0.09	*,1
HD-154368	21.00±0.10	21.16±0.10	1.29±0.04	0.43±0.05	2.28e-03±6.90e-04	0.37±0.07	0.69±0.36	-0.42±0.12	*,1
HD-164402	21.11±0.10	19.49±0.10	1.15±0.04	0.41±0.05	4.00e-03±1.13e-03	0.34±0.07	0.42±0.21	-0.15±0.11	*,1
HD-18100	...	...	0.80±0.06	0.33±0.04	...	0.27±0.05	...	...	*,2
HD-188439	20.78±0.10	19.95±0.10	1.20±0.03	0.41±0.05	6.03e-03±1.22e-03	0.35±0.07	0.36±0.17	0.02±0.07	*,1
HD-199579	21.04±0.10	20.53±0.10	1.65±0.06	0.48±0.06	9.71e-03±3.37e-03	0.42±0.08	1.38±0.75	0.16±0.14	*,1
HD-206267	21.30±0.10	20.86±0.10	1.42±0.12	0.45±0.06	3.84e-03±1.16e-03	0.39±0.07	1.05±0.54	-0.21±0.12	*,1
HD-215733	...	...	0.92±0.13	0.35±0.05	...	0.29±0.06	...	...	*,2
HD-62542	20.70±0.10	20.81±0.10	1.50±0.05	0.46±0.06	2.34e-03±6.60e-04	0.40±0.08	0.33±0.28	-0.44±0.11	*,1
HD-73882	21.11±0.10	21.11±0.10	1.26±0.10	0.42±0.06	2.19e-03±6.30e-04	0.36±0.07	0.67±0.34	-0.43±0.11	*,1
HR-4908	21.08±0.10	20.14±0.10	1.40±0.08	0.45±0.06	6.67e-03±2.02e-03	0.39±0.07	0.78±0.40	0.03±0.12	*,1
IOT-ORI	20.20±0.10	14.69±0.10	1.43±0.10	0.45±0.06	1.200e-02±3.88e-03	0.39±0.07	0.15±0.08	0.28±0.13	*,1
KAP-AQL	20.90±0.10	20.31±0.10	1.28±0.05	0.43±0.05	3.61e-03±1.24e-03	0.37±0.07	0.34±0.18	-0.22±0.14	*,1
KSI-PER	...	...	1.52±0.04	0.41±0.08	...	0.32±0.10	...	...	*,2
LAM-SCO	...	...	1.22±0.07	0.39±0.09	...	0.33±0.10	...	...	*,2
MU-COL	...	...	1.13±0.08	0.42±0.05	...	0.36±0.06	...	...	*,2
OMI-PER	20.82±0.10	20.60±0.10	1.40±0.09	0.45±0.06	2.54e-03±1.10e-03	0.39±0.07	0.29±0.17	-0.39±0.18	*,1
PI-SCO	...	...	1.53±0.10	0.47±0.06	...	0.41±0.08	...	...	*,2
RHO-OPH-A	21.63±0.10	20.57±0.10	1.19±0.07	0.41±0.05	9.50e-04±2.90e-04	0.35±0.07	0.37±0.19	-0.78±0.12	1
TAU-CMA	...	...	1.33±0.10	0.50±0.09	...	0.46±0.10	...	...	*,2
TET-MUS	21.15±0.10	19.83±0.10	1.32±0.04	0.43±0.06	8.48e-03±2.24e-03	0.37±0.07	1.03±0.51	0.15±0.10	*,1
TET01-ORI-C	21.54±0.10	17.25±0.10	1.04±0.05	0.38±0.05	1.69e-03±8.00e-04	0.32±0.06	0.44±0.28	-0.50±0.20	*,1
V600-HER	...	...	0.84±0.08	0.34±0.04	...	0.28±0.05	...	...	*,2
X-PER	20.73±0.1	20.92±0.10	1.33±0.05	0.44±0.05	1.68e-03±4.10e-04	0.37±0.07	0.29±0.14	-0.56±0.09	*,1
ZET-OPH	...	...	1.65±0.06	0.47±0.07	...	0.41±0.09	...	...	*,2
ZET-ORI-A	20.39±0.10	15.86±0.10	1.41±0.10	0.45±0.06	8.99e-03±2.17e-03	0.39±0.07	0.17±0.08	0.16±0.09	*,1
ZET-PUP	...	...	1.21±0.21	0.39±0.06	...	0.34±0.07	...	...	*,2

References: Measurements of the DTM, DTG, DTM_N and $A_{V,depl}$ are from ($\star$) this work, column densities from (1) De Cia et al. (2021); (2) Jenkins (2009) and total dust-corrected metallicities from De Cia et al. (2021).

Table 4.6: LMC dust properties

Star	log N(HI)	log N(H2)	[Zn/Fe]	DTM	DTG	DTM_N	$A_{V,depl}$	$[M/H]_{tot}$	Ref
BI173	21.25±0.05	15.64±0.10	0.83±0.05	0.34±0.04	1.54e-03±3.00e-04	0.28±0.05	0.20±0.05	-0.49±0.07	*,1,2
BI184	21.15±0.04	19.65±0.10	0.73±0.08	0.32±0.04	1.86e-03±4.80e-04	0.26±0.05	0.19±0.06	-0.38±0.10	*,1,2
BI237	21.65±0.03	20.05±0.10	0.98±0.07	0.37±0.05	1.65e-03±2.50e-04	0.31±0.06	0.56±0.12	-0.50±0.04	*,1,2
BI253	21.68±0.03	19.76±0.10	0.83±0.04	0.34±0.04	1.39e-03±1.90e-04	0.27±0.05	0.49±0.10	-0.53±0.03	*,1,2
PGMW3120	21.48±0.03	18.30±0.10	0.97±0.08	0.37±0.05	1.64e-03±4.00e-04	0.31±0.06	0.37±0.11	-0.50±0.09	*,1,2
PGMW3223	21.40±0.06	18.69±0.10	1.03±0.06	0.39±0.05	2.71e-03±7.00e-04	0.32±0.06	0.51±0.17	-0.30±0.10	*,1,2
SK 6522	20.66±0.03	14.93±0.10	0.83±0.06	0.33±0.04	3.36e-03±6.70e-04	0.27±0.05	0.11±0.03	-0.14±0.07	*,1,2
SK 66172	21.27±0.03	18.21±0.10	1.11±0.06	0.40±0.05	1.91e-03±4.30e-04	0.33±0.06	0.27±0.08	-0.46±0.08	*,1,2
SK-6619	21.87±0.07	20.20±0.10	1.25±0.13	0.42±0.06	2.28e-03±8.90e-04	0.36±0.07	1.31±0.59	-0.41±0.16	*,1,2
SK 6635	20.85±0.04	19.30±0.10	0.84±0.14	0.34±0.05	4.19e-03±1.47e-03	0.27±0.06	0.22±0.09	-0.05±0.14	*,1,2
SK 67101	20.20±0.04	14.14±0.10	0.68±0.13	0.31±0.04	5.45e-03±2.00e-03	0.25±0.05	0.06±0.03	0.10±0.15	*,1,2
SK 67105	21.26±0.04	19.13±0.10	0.86±0.07	0.21±0.16	5.00e-04±3.90e-04	0.14±0.17	0.05±0.07	-0.77±0.09	*,1,2
SK-67191	20.78±0.03	14.28±0.10	0.52±0.20	0.24±0.05	1.09e-03±6.20e-04	0.19±0.06	0.05±0.03	-0.49±0.23	*,1,2

SK 672	21.46±0.12	20.95±0.10	1.15±0.11	0.41±0.05	8.40e-04±1.70e-04	0.35±0.07	0.19±0.07	-0.83±0.07	*,1,2
SK 67211	20.81±0.04	13.98±0.10	0.73±0.06	0.31±0.04	3.77e-03±5.80e-04	0.25±0.05	0.18±0.04	-0.06±0.04	*,1,2
SK 675	21.04±0.04	19.46±0.10	1.00±0.05	0.37±0.05	1.76e-03±2.70e-04	0.31±0.06	0.15±0.03	-0.47±0.04	*,1,2
SK 68129	21.62±0.14	20.20±0.10	1.33±0.14	0.44±0.05	4.51e-03±2.15e-03	0.37±0.07	1.47±0.87	-0.13±0.20	*,1,2
SK 68135	21.48±0.02	19.87±0.10	1.04±0.07	0.39±0.05	1.66e-03±2.30e-04	0.32±0.06	0.38±0.08	-0.51±0.03	*,1,2
SK 68140	21.51±0.11	20.11±0.10	1.16±0.10	0.41±0.05	4.11e-03±1.60e-03	0.34±0.07	1.03±0.50	-0.14±0.16	*,1,2
SK 68155	21.47±0.09	19.99±0.10	1.06±0.05	0.39±0.05	4.13e-03±1.16e-03	0.33±0.06	0.93±0.35	-0.12±0.11	*,1,2
SK 6826	21.65±0.06	20.38±0.10	1.05±0.15	0.38±0.05	9.00e-04±3.70e-04	0.32±0.07	0.31±0.14	-0.77±0.17	*,1,2
SK 6852	21.31±0.06	19.47±0.10	0.43±0.12	0.21±0.04	1.59e-03±2.80e-04	0.16±0.04	0.23±0.06	-0.27±0.03	*,1,2
SK 6873	21.68±0.02	20.09±0.10	1.24±0.12	0.38±0.12	3.48e-03±1.08e-03	0.31±0.13	1.25±0.53	-0.18±0.03	*,1,2
SK 69104	19.57±0.68	14.03±0.10	1.06±0.27	0.39±0.06	1.36e-02±2.30e-02	0.32±0.07	0.04±0.09	0.40±0.73	*,1,2
SK 69175	20.64±0.03	14.28±0.10	0.38±0.12	0.20±0.03	8.00e-04±2.70e-04	0.15±0.04	0.02±0.01	-0.55±0.13	*,1,2
SK 69246	21.48±0.02	19.71±0.10	0.80±0.04	0.33±0.04	1.81e-03±2.30e-04	0.27±0.05	0.40±0.08	-0.41±0.02	*,1,2
SK 69279	21.63±0.05	20.31±0.10	0.76±0.06	0.32±0.04	7.20e-04±1.60e-04	0.26±0.05	0.22±0.07	-0.79±0.08	*,1,2
SK 70115	21.18±0.08	19.94±0.10	0.67±0.05	0.30±0.03	2.02e-03±2.50e-04	0.23±0.04	0.22±0.06	-0.31±0.02	*,1,2
SK 7079	21.34±0.04	20.26±0.10	1.51±0.09	0.39±0.09	4.48e-03±1.67e-03	0.32±0.10	0.74±0.33	-0.08±0.13	*,1,2
SK 7145	21.11±0.03	18.63±0.10	0.81±0.06	0.34±0.04	2.81e-03±5.60e-04	0.27±0.05	0.27±0.07	-0.22±0.07	*,1,2
SK 7150	21.24±0.05	20.13±0.10	0.55±0.05	0.28±0.03	1.42e-03±2.80e-04	0.22±0.04	0.17±0.05	-0.44±0.07	*,1,2

References: Measurements of the DTM, DTG, DTM_N and $A_{V,depl}$ are from ($\star$) this work, column densities fromd (1) Roman-Duval et al. (2021); and total dust-corrected metallicities from (2) De Cia et al. (2024)

Table 4.7: SMC dust properties

Star	log N(HI)	log N(H2)	[Zn/Fe]	DTM	DTG	DTM_N	$A_{V,depl}$	$[M/H]_{tot}$	Ref
AzV18	22.04±0.02	20.36±0.08	0.91±0.09	0.35±0.04	1.07e-03±1.60e-04	0.29±0.06	0.92±0.20	-0.66±0.03	*,1,2
AzV26	21.70±0.06	20.63±0.06	0.60±0.05	0.28±0.03	4.10e-04±5.00e-05	0.22±0.04	0.17±0.04	-0.98±0.02	*,1,2
AzV47	21.32±0.04	18.54±0.70	0.57±0.07	0.27±0.03	6.90e-04±1.00e-04	0.21±0.04	0.10±0.02	-0.73±0.03	*,1,2
AzV80	21.81±0.02	20.08±0.30	0.69±0.06	0.30±0.04	6.40e-04±9.00e-05	0.24±0.05	0.31±0.07	-0.81±0.02	*,1,2
AzV95	21.49±0.04	19.40±0.09	0.57±0.07	0.27±0.03	5.30e-04±8.00e-05	0.21±0.04	0.12±0.03	-0.84±0.03	*,1,2
AzV104	21.45±0.06	19.23±0.30	0.51±0.16	0.23±0.04	3.90e-04±1.80e-04	0.18±0.05	0.08±0.04	-0.92±0.19	*,1,2
AzV207	21.43±0.06	19.40±0.10	0.83±0.06	0.34±0.04	1.66e-03±2.50e-04	0.27±0.05	0.34±0.08	-0.45±0.04	*,1,2
AzV216	21.64±0.03	18.78±1.30	0.72±0.08	0.30±0.04	7.20e-04±1.70e-04	0.24±0.05	0.23±0.07	-0.77±0.09	*,1,2
AzV229	21.06±0.04	15.66±0.30	0.62±0.08	0.25±0.03	8.30e-04±1.30e-04	0.20±0.04	0.07±0.02	-0.62±0.03	*,1,2
AzV242	21.32±0.04	17.21±1.30	1.16±0.18	0.41±0.06	1.37e-03±2.30e-04	0.35±0.07	0.22±0.05	-0.62±0.04	*,1,2
AzV321	20.70±0.08	14.44±1.30	0.90±0.11	0.35±0.05	2.07e-03±3.60e-04	0.29±0.06	0.08±0.02	-0.37±0.05	*,1,2
AzV332	20.54±0.16	14.50±0.12	0.56±0.06	0.26±0.03	1.20e-03±5.00e-04	0.20±0.04	0.03±0.02	-0.47±0.17	*,1,2
AzV388	21.18±0.04	19.40±0.10	0.99±0.07	0.35±0.05	1.36e-03±2.60e-04	0.30±0.06	0.16±0.04	-0.56±0.06	*,1,2
AzV456	21.00±0.06	20.93±0.10	1.36±0.09	0.44±0.06	5.00e-04±1.00e-04	0.38±0.07	0.11±0.03	-1.09±0.07	*,1,2
AzV476	21.85±0.07	20.95±0.30	0.81±0.17	0.33±0.04	5.20e-04±2.50e-04	0.27±0.05	0.34±0.18	-0.95±0.20	*,1,2
AzV327	20.93±0.10	14.79±0.10	0.93±0.19	0.36±0.05	3.00e-04±2.00e-04	0.30±0.06	0.09±0.08	-1.23±0.29	*,1,2
AzV238	21.41±0.10	15.95±0.10	0.99±0.04	0.38±0.05	1.04e-03±5.40e-04	0.31±0.06	0.20±0.15	-0.70±0.22	*,1,2
SK116	21.57±0.10	18.53±0.10	0.64±0.04	0.29±0.03	5.50e-04±2.90e-04	0.23±0.04	0.15±0.11	-0.86±0.22	*,1,2

References: Measurements of the DTM, DTG, DTM_N and $A_{V,depl}$ are from ($\star$) this work, column densities from (1) Jenkins and Wallerstein (2017); and total dust-corrected metallicities from (2) De Cia et al. (2024)

Table 4.8: GRB-DLAs dust properties

GRB	z_{abs}	log N(HI)	log N(H2)	[Zn/Fe]	DTM	DTG	DTM_N	$A_{V,depl}$	$[M/H]_{tot}$	Ref
000926	2.0380	21.30±0.20	...	1.05±0.18	0.39±0.05	8.53e-03±5.62e-03	0.32±0.07	1.30±1.00	0.20±0.28	*,1
030226	1.9870	20.50±0.30	...	-0.19±0.12	...	...	...	...	-1.07±0.31	*,1
050730	3.9690	22.10±0.10	...	0.07±0.05	0.05±0.02	3.18e-06±2.00e-06	0.03±0.01	...	-2.31±0.18	*,1
050820A	2.6150	21.05±0.10	...	0.82±0.05	0.33±0.04	1.49e-03±3.90e-04	0.27±0.05	0.12±0.06	-0.49±0.10	*,1
050922C	2.1990	21.55±0.10	...	0.18±0.46	0.12±0.11	1.94e-05±2.00e-05	0.08±0.10	0.005±0.006	-1.92±0.26	*,1
071031	2.6920	22.15±0.05	...	0.04±0.03	0.03±0.01	8.00e-06±4.00e-06	0.02±0.01	0.007±0.004	-1.75±0.09	*,1
080413A	2.4330	21.85±0.15	...	0.12±0.07	0.07±0.02	3.00e-05±1.00e-05	0.05±0.02	0.01±0.01	-1.60±0.18	*,1
081008	1.9685	21.11±0.10	...	0.55±0.04	0.26±0.03	1.12e-03±4.60e-04	0.20±0.04	0.10±0.06	-0.51±0.17	*,1
090809A	2.7373	21.48±0.07	...	0.75±0.21	0.32±0.05	1.54e-03±5.80e-04	0.26±0.06	0.34±0.19	-0.46±0.15	*,1
090926A	2.1069	21.58±0.01	...	0.88±0.11	0.34±0.05	9.00e-05±2.00e-05	0.28±0.06	0.03±0.01	-1.72±0.05	*,1
100219A	4.6676	21.28±0.02	...	0.11±0.30	0.07±0.08	7.00e-05±8.00e-05	0.05±0.07	0.01±0.01	-1.16±0.11	*,1
111008A	4.9910	22.39±0.01	...	0.22±0.10	0.13±0.02	3.00e-05±1.00e-05	0.09±0.02	0.05±0.02	-1.79±0.10	*,1
111107A	2.8930	21.10±0.04	...	0.69±0.55	0.30±0.09	2.21e-03±2.39e-03	0.24±0.10	0.20±0.24	-0.28±0.45	*,1
120119A	1.7285	22.44±0.12	...	0.93±0.24	0.36±0.06	8.20e-04±8.00e-04	0.30±0.07	1.69±1.78	-0.79±0.42	*,1
120327A	2.8143	22.07±0.01	17.39±0.13	0.27±0.07	0.15±0.03	1.00e-04±2.00e-05	0.11±0.03	0.08±0.03	-1.34±0.02	*,1
120716A	2.4874	21.73±0.03	...	0.69±0.23	0.31±0.05	1.15e-03±2.80e-04	0.24±0.06	0.45±0.21	-0.57±0.08	*,1
120815A	2.3582	22.09±0.01	20.42±0.08	1.01±0.05	0.38±0.05	3.10e-04±4.00e-05	0.31±0.06	0.30±0.12	-1.23±0.03	*,1
120909A	3.9290	21.82±0.02	...	1.14±0.09	0.40±0.05	2.87e-03±7.50e-04	0.34±0.06	1.46±0.67	-0.29±0.10	*,1
121024A	2.3005	21.78±0.02	19.9±0.17	0.77±0.08	0.31±0.04	9.00e-04±1.90e-04	0.25±0.05	0.41±0.18	-0.68±0.07	*,1
130408A	3.7579	21.90±0.01	...	0.28±0.07	0.16±0.02	8.00e-05±1.00e-05	0.12±0.03	0.04±0.02	-1.46±0.05	*,1
130606A	5.9127	19.88±0.01	...	0.49±0.10	0.24±0.03	9.00e-05±2.00e-05	0.19±0.04	...	-1.58±0.08	*,1
140311A	4.9550	22.30±0.02	...	0.35±0.21	0.20±0.05	3.00e-05±1.00e-05	0.14±0.05	0.04±0.02	-2.00±0.11	*,1
141028A	2.3333	20.39±0.03	...	-0.04±0.26	0.001±0.090	3.68e-07±3.00e-05	0.001±0.062	...	-1.62±0.28	*,1
141109A	2.9940	22.18±0.02	18.02±0.12	0.49±0.07	0.24±0.03	1.40e-04±2.00e-05	0.19±0.04	0.15±0.06	-1.37±0.05	*,1
150403A	2.0571	21.73±0.02	19.90±0.14	0.63±0.08	0.29±0.04	4.80e-04±8.00e-05	0.23±0.04	0.19±0.08	-0.92±0.05	*,1
151021A	2.3297	22.14±0.03	18.99±1.28	0.86±0.08	0.35±0.05	5.20e-04±1.10e-04	0.28±0.06	0.53±1.02	-0.97±0.07	*,1
151027B	4.0650	20.54±0.07	...	0.49±0.64	0.24±0.12	8.70e-04±6.80e-04	0.19±0.12	0.02±0.02	-0.59±0.27	*,1
160203A	3.5187	21.74±0.02	...	0.62±0.05	0.28±0.03	4.60e-04±7.00e-05	0.22±0.04	0.18±0.07	-0.92±0.04	*,1
161023A	2.7100	20.95±0.01	...	0.44±0.04	0.22±0.02	2.80e-04±4.00e-05	0.17±0.03	0.02±0.01	-1.05±0.04	*,1
170202A	3.6456	21.53±0.04	...	0.75±0.23	0.32±0.05	4.20e-04±1.40e-04	0.26±0.06	0.11±0.05	-1.02±0.13	*,1
181020A	2.9379	22.24±0.03	...	0.75±0.14	0.32±0.04	2.80e-04±6.00e-05	0.26±0.06	0.36±0.16	-1.20±0.08	*,1
190114A	3.3764	22.19±0.05	...	1.05±0.08	0.39±0.05	3.60e-04±7.00e-05	0.32±0.06	0.43±0.18	-1.17±0.06	*,1
190106A	1.8599	21.00±0.04	...	1.12±0.10	0.40±0.05	2.19e-03±5.80e-04	0.33±0.06	0.17±0.08	-0.40±0.10	*,1
190919B	3.2241	21.75±0.06	...	0.33±0.33	0.18±0.07	1.40e-04±7.00e-05	0.14±0.07	0.05±0.04	-1.25±0.15	*,1
191011A	1.7204	21.65±0.08	...	0.33±0.09	0.18±0.02	6.00e-04±1.20e-04	0.14±0.03	0.18±0.08	-0.63±0.07	*,1
210905A	6.3118	21.00±0.02	...	0.33±0.09	0.18±0.02	5.00e-05±2.00e-05	0.14±0.03	...	-1.72±0.13	*,1

References: ($\star$) This work; (1) Heintz et al. (2023)

5

DUNE: DUST DEPLETION UNIFIED METHOD ACROSS COSMIC TIME AND ENVIRONMENTS

"He who controls the spice controls the Universe."
∼ Dune by Frank Herbert ∼

The large collection of column density measurements in several environments has enabled different types of analysis in this sample, including the characterization of dust depletion in local and distant galaxies (Chapter 3), the investigation of important scaling relations, such as the DTM and DTG up to $z = 6.3$, the dust composition as well as dust extinction in different galaxies, using dust depletion (Chapter 4) estimated using the relative abundances of metals. The main assumption of this method is the preferential usage of Zn in the relative abundances, including the dust tracer [Zn/Fe]. Zn, broadly following Fe in nucleosynthesis but with a partial α-element behavior, faces an ongoing debate about whether it can be reliably used, in the relative abundance [Zn/Fe], as a dust tracer. On the other hand, the F_* method, i.e. the other main method to estimate dust depletion, can include the information on all available metals, without the preferential use of any. However, it faces another caveat, that one has to assume a certain metallicity for the gas and this cannot be characterized for distant galaxies. This introduces limitations regarding the galactic environments that the F_* method can be applied to. The question arises then about whether we can improve our methods.

Considering the above, we developed a new method to characterize dust depletion, with the aim to limit the assumptions of the previous methods and combining their strengths. In this Chapter, I present DUNE: Dust depletion UNified method across cosmic time and environments, which is re-submitted to A&A. In this method, I use the data collection from Konstantopoulou et al. (2022), with additional Milky Way measurements from Ritchey et al. (2023b) and find correlations among all possible relative abundances of metals. I describe the development of the method, the observed correlations and the characterization of dust depletion in different galactic environments. Using the new method, I provide the refined coefficients to characterize dust depletion of individual elements. Finally, I offer guidelines of the different applications of the method showing simple examples. Overall, I provide a new formalism for the characterization of dust depletion, that is applicable to any environment, it does not make any assumption on the metallicity of the gas, it makes optimal use of all possible metals, and it is not affected by nucleosynthesis effects.

This chapter contains the following article with title:

"DUNE: Dust depletion UNified method across cosmic time and Environments"

Authors: Christina Konstantopoulou, Annalisa De Cia, Jens-Kristian Krogager, Cédric Ledoux, Julia Roman-Duval, Edward B. Jenkins, Tanita Ramburuth-Hurt and Anna Velichko

Published in Astronomy&Astrophysics, Volume 691, Issue A129, November 2024 A&A, 691, A29 (2024) and presented unmodified below.

5.1 ABSTRACT

We present a novel method to characterize dust depletion, namely, the depletion of metals into dust grains. We used observed correlations among relative abundances combining a total of 17 metals in diverse galactic environments, including the Milky Way (MW), Large Magellanic Cloud (LMC), Small Magellanic Cloud (SMC), and damped Lyman-α absorbers (DLAs) towards quasars and gamma-ray bursts (GRBs). We only considered the relative abundances of metals that qualify as tracers of dust and we used all available dust tracers. We find linear correlations among all studied dust tracers in a multidimensional space, where each dimension corresponds to an individual dust tracer. The fit to the linear correlations among the dust tracers describes the tendencies of different elements when depleting into dust grains. We determined the overall strength of dust depletion, Δ, along individual lines of sight, based on the correlations among different dust tracers. We avoided any preference for specific dust tracers or any other assumptions by including all available dust tracers in this multidimensional space. We also determined the dust depletion of Kr, C, O, Cl, P, Zn, Ge, Mg, Cu, Si, Fe, Ni, and Ti. Finally, we offer simple guidelines for the application of the method to the study of the observed patterns of abundances and relative abundances. This has allowed for a straightforward determination of the overall strength of depletion and the dust depletion of individual elements. We also obtained an estimate for the gas-phase metallicity and identified any additional deviations due to the nucleosynthesis of specific stellar populations. Thus, we have established a unified methodology for characterizing dust depletion across cosmic time and diverse galactic environments, offering a valuable new approach to the study of dust depletion in studies of the chemical evolution of galaxies.

5.2 INTRODUCTION

Metals are produced within stars and released into the interstellar medium (ISM) of galaxies. While some of these metals remain in the gas-phase of the ISM, a significant amount is instead incorporated into dust grains, an effect called dust depletion (Field, 1974; Savage and Sembach, 1996; Phillips, Gondhalekar, and Pettini, 1982; Savaglio, Fall, and Fiore, 2003; Jenkins, 2009; De Cia et al., 2016; Roman-Duval et al., 2021; Konstantopoulou et al., 2022). Gas-phase metal abundances, resulting from column density measurements of metals, HI and HII, obtained through absorption-line spectroscopy, can vary depending on dust depletion, but also on metallicity variations in the gas and the nucleosynthetic history of metals. Understanding dust depletion is still a challenge, especially because of the difficulties in disentangling these different phenomena that affect the observed abundances.

Dust depletion is a critical phenomenon within the ISM of galaxies (Roman-Duval et al., 2022a; Konstantopoulou et al., 2024; De Cia et al., 2024). Understanding dust depletion is important for several reasons. Applying depletion corrections for damped Lyman-α absorbers (DLAs) is essential for tracking the chemical enrichment of the universe over cosmic time and it provides an estimate of the dust-to-gas ratio that is independent of FIR data, which can suffer from limited sensitivity and resolution (Roman-Duval et al., 2014, 2021). Therefore, depletion corrections improve the accuracy of dust and gas mass estimates across all redshifts and help us understand the variations of dust properties in galaxies. Therefore, a comprehensive study of dust depletion is crucial to understanding how dust is formed and how metals are distributed within the ISM of galaxies. During dust formation, metals are collected from the gas and incorporated into dust grains, while dust destruction (e.g., by SN shocks) releases them back into the gas-phase of the ISM. The interplay of metals between gas-phase, dust-phase, and stars is fundamental for the chemical evolution of galaxies.

Jenkins (2009) developed a unified scheme of elemental depletions in the ISM of the Milky Way. This method arises from the discovery that the observed abundances [X/H] of different metals are correlated with each other. For example, [Mg/H] is correlated with [Fe/H], which, in turn, is correlated with [P/H] and so on (see Fig. 1 of Jenkins, 2009). The observed abundances are used as a proxy for the elemental depletions. This approach shows that different lines of sight have a continuous range of depletions (as opposed to discrete depletion patterns (e.g., Savage and Sembach, 1996). The overall strength of dust depletion along an individual line of sight is represented by the factor F_* in Jenkins (2009). The value of F_* is defined to be $F_* = 1$, for lines of sight exhibiting the strongest depletions, while for those with the lowest depletions F_* is assigned to be $F_* = 0$. This scale is somewhat arbitrary because the $F_* = 0$ and $F_* = 1$ end points are tied to the particular sample studied in Jenkins (2009). In the Jenkins (2009) formalism, the depletion of individual elements increases with F_*. This increase in depletion is often associated with denser and/or colder gas environments. Lines of sight with lower depletion may indicate that grains have undergone partial destruction through sputtering in interstellar shocks and/or they have not grown as much as the grains in the denser ISM from the accretion of metals from the gas-phase. This progression from low-density diffuse atomic gas to higher-density diffuse

molecular clouds can be interpreted as grain growth in the ISM. Hereafter, we refer this method, developed by Jenkins (2009), as the "F_* method".

The main strength of the F_* method is that it uses all the observed abundances of metals, without favoring any metal in particular, to estimate the overall strength of depletion along individual lines of sight. It identifies correlations among different elements and finds continuous trends in elemental depletions, characterizing each line of sight with a single measure of the overall strength of depletion. However, it assumes that the total (gas+dust) abundance in the ISM is equal to the photospheric abundances of young stars. Moreover, the usage of all the observed abundances of metals is only valid for the Jenkins (2009) sample. For other samples in other galaxies or even the MW, we have to use the Fe depletion to define F_* based on the Jenkins (2009) coefficients. In addition, the transport of metals from stars to the ISM is unaccounted for. More specifically, the determination of abundances of metals is complicated by variations in metallicity and nucleosynthesis effects, such as α-element enhancement, in the gas of the ISM. These effects are not trivial to disentangle and can affect the observed trends, which are interpreted as dust depletion within the F_* method. Moreover, the F_* method assumes a fixed metallicity for the gas, and specifically for the MW it assumes solar metallicity. This may serve as a reasonable approximation for the MW but cannot be assumed for other galaxies. To use the F_* method in other galaxies, we have to assume a different metallicity than solar. Additionally, the F_* scale is tied to specific lines of sight in the Jenkins (2009) sample and, thus, this scale is arbitrary. Therefore, we must use Fe depletions to define F_*, based on the Jenkins (2009) coefficients. In fact, even the metallicity of the MW remains puzzling. While Ritchey et al. (2023b) have found that the metallicity of the MW is fairly homogeneous, large variations in metallicity have been observed in the neutral ISM in the vicinity of the Sun (De Cia et al., 2021). One important difference between the two studies is that Ritchey et al. (2023b) included volatile elements in their analysis, thus probing higher metallicity gas; whereas De Cia et al. (2021) excluded volatile elements, probing mostly lower metallicity gas. Hence, while the F_* method offers valuable insights and has become one of the key pillars for the study of dust depletion, its assumptions should be approached with caution when we are considering environments beyond the MW.

De Cia et al. (2016) developed an independent study of dust depletion, based on observations of the MW and distant galaxies. De Cia (2018) extended this, to study dust depletion using observations in the Magellanic Clouds. This method uses relative abundances (meaning abundance ratios) of metals as dust tracers rather than observed abundances to estimate the depletion of different elements because different metals have different tendencies to deplete into dust grains. A relative abundance [X/Y] can be a dust tracer if X and Y follow each other in nucleosynthesis, but have very different refractory properties. De Cia et al. (2016) mainly used [Zn/Fe] as a dust tracer, but note that others are possible (e.g., [Si/Ti]). The depletion of element X is then obtained from the observed correlation between [X/Zn] (a quantity dominated by the depletion of X because Zn is rather volatile) and the dust tracer [Zn/Fe]. Hereafter, we refer to this method, developed by De Cia et al. (2016), as the "relative method".

The main strength of the relative method is the use of relative abundances of metals, making it possible to disentangle effects, such as dust depletion, metallicity, and nucleosyn-

thesis. If there are variations in metallicity, the relative abundances are not affected. On the other hand, variations in specific metals that do not follow dust depletion, such α-element enhancements, can be identified and are indeed observed in the ISM (De Cia et al., 2024; Velichko et al., 2024). Consequently, this methodology can be applied across a wide range of galactic environments, including distant galaxies and low-metallicity systems, extending the study of dust depletion beyond the MW. However, the main weakness of this method is that Zn has a preferential role in the method's formalism. The use of [X/Zn] introduces a dependency on the depletion of Zn, which is built-in by assuming a certain slope for the expected depletion of Zn with the dust tracer [Zn/Fe]. The impact of this assumption on the recovered depletions in DLAs is investigated in Roman-Duval et al. (2022c). Nevertheless, the accuracy of the estimated Zn depletion is solely based on Zn abundances and may not be precise. Furthermore, there is an uncertainty regarding the reliability of [Zn/Fe] as a dust tracer. While [Zn/Fe] is often considered a good tracer of dust (e.g., De Cia et al., 2016; De Cia, 2018; Konstantopoulou et al., 2022), due to the fact that Zn and Fe trace each other in the Solar neighborhood ([Zn/Fe] ~ 0 for $-2 <$ [Fe/H] < 0 dex), the nucleosynthetic behavior of Zn is complex as it does not strictly belong to the Fe-peak or α-element group. This means that Zn can show an enhancement that resembles α-element enhancement, albeit with a smaller amplitude (e.g., Nissen and Schuster, 2011; Barbuy et al., 2015; Duffau et al., 2017). This effect has recently been observed in the ISM as well (De Cia et al., 2024; Velichko et al., 2024). Finally, the methodology of De Cia et al. (2016) also made an assumption on the shape of the α-element enhancement curves to be able to convert the observed relative abundances [X/Zn] to depletions. Hence, the relative method offers a new approach to studying dust depletion across diverse galactic environments and its reliance on Zn, as well as any assumptions placed on nucleosynthesis; however, it does introduce caveats that need to be taken into consideration.

Motivated by the above two existing methods for estimating dust depletion, the aim of this paper is to combine their strengths and overcome their limitations, by developing a Dust depletion UNified method across cosmic time and Environments (DUNE). In this method, we use correlations among all relative abundances that are valid dust tracers, to estimate the dust depletion of different metals in diverse galactic environments, including the MW, LMC, SMC, and QSO- and GRB-DLAs.

The paper is organized as follows. In Sect. 5.3, we briefly present the data samples compiled from the literature. The development of the method is presented in Sect. 5.4. We discuss our results in Sect. 5.6. Finally, we summarize and conclude in Sect. 5.7. Throughout the paper, we use a linear unit for the column densities, N, in terms of ions cm^{-2}. We refer to relative abundances of elements X and Y as $[X/Y] \equiv \log\frac{N(X)}{N(Y)} - \log\frac{N(X)_\odot}{N(Y)_\odot}$, where reference solar abundances are taken from Asplund, Amarsi, and Grevesse (2021) following the recommendations of Lodders, Palme, and Gail (2009).

5.3 SAMPLES

We compiled a broad literature sample of metal column densities in the neutral ISM for 528 lines of sight and in diverse galactic environments: the MW, the LMC, the SMC, and QSO-

and GRB-DLAs. We use the data collected in Konstantopoulou et al. (2022), which includes column densities from Jenkins (2009), De Cia et al. (2021), Welty and Crowther (2010), and Phillips, Gondhalekar, and Pettini (1982) for the MW, from Roman-Duval et al. (2021) for the LMC , from Welty and Crowther (2010), Tchernyshyov et al. (2015), and Jenkins and Wallerstein (2017) for the SMC, from Berg et al. (2015) and De Cia (2018) for QSO-DLAs and from Bolmer et al. (2019) for GRB-DLAs. We additionally include column densities for the MW from Ritchey et al. (2023b). We cross-matched samples within the same galactic environment and combined column densities of different metals corresponding to the same line of sight. For the MW, column densities from Ritchey et al. (2023b) are preferred, because they include also higher resolution data (R∼114,000, Ritchey et al., 2023a). Our final sample consists of column densities for 17 metals in their dominant ionization state, namely: OI, MgII, SiII, SII, PII, TiII, CrII, FeII, CoII, NiII, ZnII, AlII, GeII, KrI, ClII, CuII, and CII. The column densities were measured through absorption-line spectroscopy in spectra observed mainly with VLT/UVES, VLT/X-SHOOTER, HST/STIS, and HST/COS. They are homogenized to the most recent published oscillator strengths from Konstantopoulou et al. (2022) and Ritchey et al. (2023b).

5.4 METHODS AND RESULTS

In the following sections, we describe our methodology. Specifically, we describe the selection of dust tracers in Sect. 5.4.1, the correlations among different dust tracers in Sect. 5.4.2, the derivation of the overall strength of depletion in Sect. 5.4.3, the usage of indirect reference dust tracers in Sect. 5.4.4, and the determination of the dust depletion of individual elements in Sect. 5.4.5. We additionally provide examples of some possible applications of our method in Sect. 5.5.

5.4.1 *Stage 1: Designing DUNE*

In our method, we use the correlations between all observed relative abundances of metals [X/Y] that qualify as dust tracers, to estimate the overall strength of depletion along individual lines of sight. A relative abundance [X/Y] qualifies as a dust tracer if it fulfills the following criteria:

1. X is less refractory than Y. We assess this by calculating the difference between the refractory indices $B2_X$ of X and Y, which are taken from Table 4 of Konstantopoulou et al. (2022) (using the constant α_X assumption) and from Konstantopoulou et al. (2023) for P. We select relative abundances with $\Delta B2_X > 0$, to ensure that X is less refractory than Y. This criterion only gives an initial selection of [X/Y] as likely dust tracers and rejects the specular [Y/X]. No relative abundances [X/Y] were rejected based on the $B2_X$, as the $B2_X$ coefficients result from the relative method. Because we are seeking an independent criterion instead, the dust tracers are later filtered based on the strength of their correlation (see Sect. 5.4.2).

2. X and Y follow each other in terms of the process of nucleosynthesis, to a first approximation. We categorize elements into two distinct groups depending on whether they are affected (group 1) or not (group 2) by α-element enhancement: group 1 includes the α-elements (O, S, Si, Mg, and Ti, Kobayashi et al., 2006); whereas group 2 includes non-α elements (meaning all other elements that do not exhibit α-element enhancement). Those are Fe, Cr, Ni, P, Kr, Ge, Co, Cu, Al, C, Cl, and Zn. We treated the two groups separately, namely, we did not mix group 1 with group 2 to obtain relative abundances, to ensure that our relative abundances [X/Y] are not affected by α-element enhancements. We further tested the exclusion of Zn from the analysis to ensure the robustness of the method (see Appendix 5.A).

The elements are only categorized based on whether α-element enhancement has been observed, rather than strictly by their production channels. As a result, our non-α element group (group 1) includes such elements as Ge and Kr, which are produced through different channels; however, their common characteristic is that they do not show α-element enhancement. Similarly, Ti, although it is both an Fe-peak and an α-element, is included in group 1 with the α-elements, because it exhibits α-element enhancement. Here, Ti is mostly produced in core-collapse SNe (e.g., Kobayashi, Karakas, and Lugaro, 2020). Group 2 is a mixed group containing Fe-peak elements as well as any other non-α elements. Then, Ge is vastly produced in Type II SNe, and not at all in SNe Type Ia. However, it is not affected by α-element enhancement and is included in group 2. Similarly, Kr is created chiefly by s-process neutron capture (e.g., Sneden, Cowan, and Gallino, 2008) and is not an Fe-peak element. However, it is not affected by α-element enhancement and is included in group 2.

A reliable dust tracer is characterized by a large difference between the refractory indices of X and Y. The larger the difference in the tendencies of X and Y to deplete into dust, the larger the expected values of dust tracers [X/Y]. For example, [Si/Ti], [Zn/Fe], and [Ge/Ni] exhibit large $\Delta B2_{XY}$ differences, with $\Delta B2_{SiTi} = 0.92$, $\Delta B2_{ZnFe} = 0.99$, and $\Delta B2_{GeNi} = 0.91$, respectively, and are sensitive tracers of dust. Due to the strength of these dust tracers, we used them as "reference dust tracers". On the other hand, other dust tracers are less sensitive, such as [O/Mg] with $\Delta B2_{OMg} = 0.40$, while the most sensitive dust tracer in our sample is [O/Ti] with $\Delta B2_{OTi} = 1.44$, but with scarce data available for O. Due to our selection criteria (defined above), reliable dust tracers are not affected by metallicity variation or nucleosynthesis effects, and any effect on them is due to dust depletion. When elements are grouped by nucleosynthetic history, meaning that they are not affected by α-element enhancement, each set of dust tracers [X1/Y1] and [X2/Y2] is proportional to the overall strength of depletion and, thus, correlates with the other. We identified 70 dust tracers, after applying the above selection criteria. The identified dust tracers, along with their $\Delta B2_{XY}$ differences, are reported in Table C.1 (available on Zenodo).

5.4.2 *Correlations among dust tracers*

We observed linear correlations between multiple dust tracers, 70 in total, considering a diversity of galactic environments (the MW, LMC, SMC, and QSO- and GRB-DLAs). In fact, all dust tracers are linearly correlated with each other in a multidimensional space. Figure

5.1 shows the linear correlation between three different dust tracers ([Si/Ti], [Zn/Fe], and [P/Cr]) in a three-dimensional (3D) space.

Driven by the observation that all dust tracers exhibit correlations within a multidimensional space, we found all possible correlations among relative abundances (dust tracers) and assess their correlation strength using Pearson's correlation coefficients (r). Valid correlations must meet the following criteria: 1) the correlation coefficient between the dust tracer and the reference dust tracer (r_{XY}) must be $r_{XY} > 0.6$. We chose this threshold to ensure a strong correlation between the two dust tracers. 2) We selected only pairs of relative abundances with at least four common data points and with uncertainties of the relative abundances involved in each correlation less than 0.5 dex.

We fit the valid correlations using orthogonal distance regression, which takes errors in both the x-axis and y-axis into account. We implement this by using the Python package scipy.odr, which determines the parameters that minimize the sum of the squared error for each data point during the regression. We fit assuming a fixed intercept at zero. This is justified by the expectation that all dust tracers should be at zero if no dust is present. Indeed, the observations agree very well with this when sufficient data is available. We chose three strong dust tracers as references to project the correlations on these most reliable axes. We assigned a priority to [Si/Ti] as our primary reference dust tracer. We expect Si and Ti to trace each other closely in nucleosynthesis, because not only they are both α-elements, but they are also produced in the explosive environments of core-collapse SNe (e.g., Nomoto et al., 2006), as opposed to quiescent burning in their progenitors. We then assigned [Zn/Fe] as the second priority and the [Ge/Ni] as third priority reference dust tracers. We used [Ge/Ni] as a reference dust tracer instead of [P/Cr] (shown in Fig. 5.1 due to better visualization in all the environments). While both elements are abundantly available, Ge has more consistent and reliable measurements (Ritchey et al., 2023b) than P does. We refer to [Zn/Fe] and [Ge/Ni] as "indirect reference dust tracers" and discuss their usage in Sect. 5.4.4. Correlations of different valid dust tracers with the primary dust tracer [Si/Ti] and their fits are shown in Fig. 5.2. The parameters resulting from the fit among valid correlations between different dust tracers ([X/Y]) with respect to [Si/Ti], [Zn/Fe], and [Ge/Ni] are reported in Table 2 (available on Zenodo). Large slopes C_{XY} resulting from the fit between two dust tracers denote strong dust tracers.

5.4.3 *Overall strength of depletion:* Δ

The overall strength of depletion per line of sight represents the collective contribution of dust tracers to dust depletion along a line of sight. In the hyperspace of the correlated dust tracers, the overall strength of depletion, Δ, is a measure of the distance along the correlation from the origin (which is the point of no depletion). We calculate Δ with respect to [Si/Ti], and therefore it inherits its dynamical range. The overall strength of dust depletion, Δ, has values that are overall similar to [Si/Ti], but are actually calculated from all the available dust tracers.

To derive Δ, we calculate the sum of all the available dust tracers in each line of sight and normalize by the corresponding slopes of all the involved dust tracers with a "reference dust tracer". Each valid dust tracer [X/Y] is weighted by its correlation with a reference

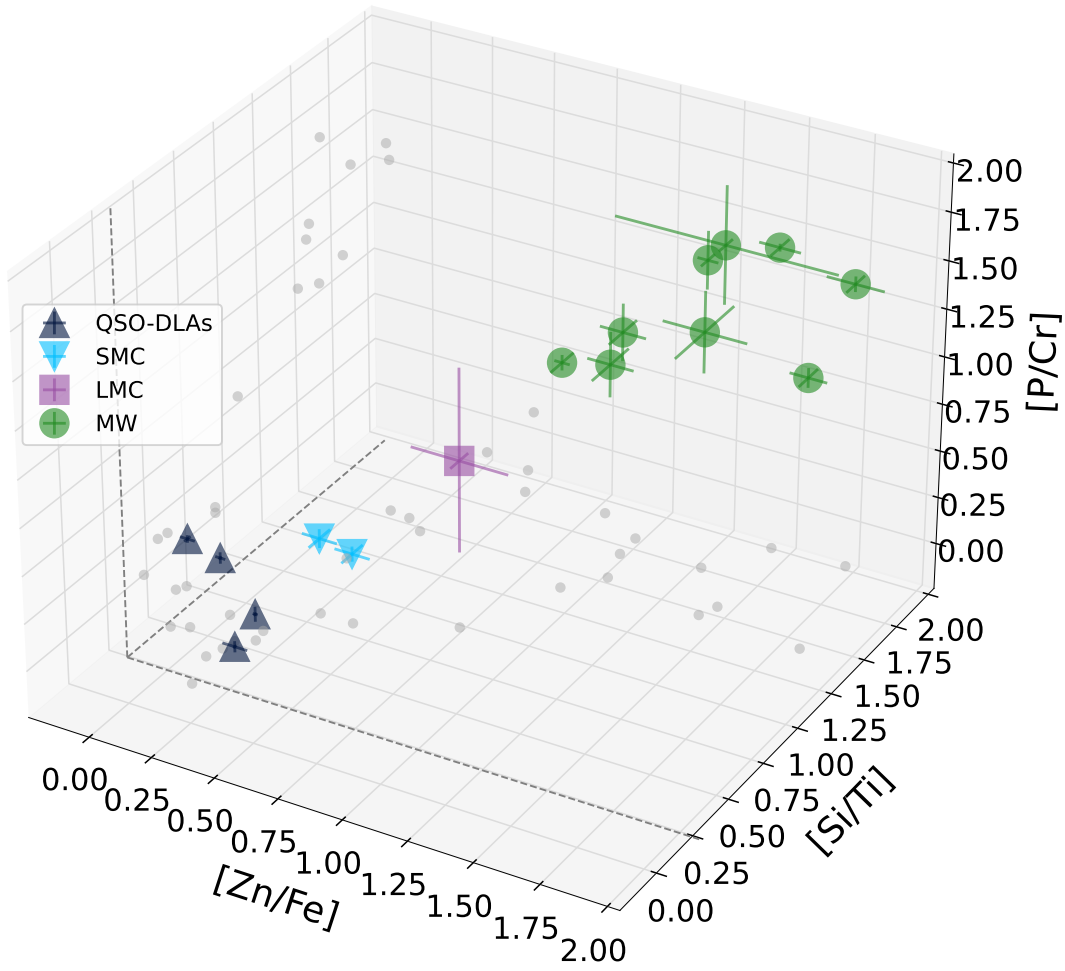


Figure 5.1: 3-dimensional correlation between the dust tracers [Si/Ti], [Zn/Fe] and [P/Cr]. The black triangles are for QSO-DLAs, the purple squares are for the LMC, the blue triangles are for the SMC and the green circles are for the Milky Way. The gray dots are the projections of the points in each plane.

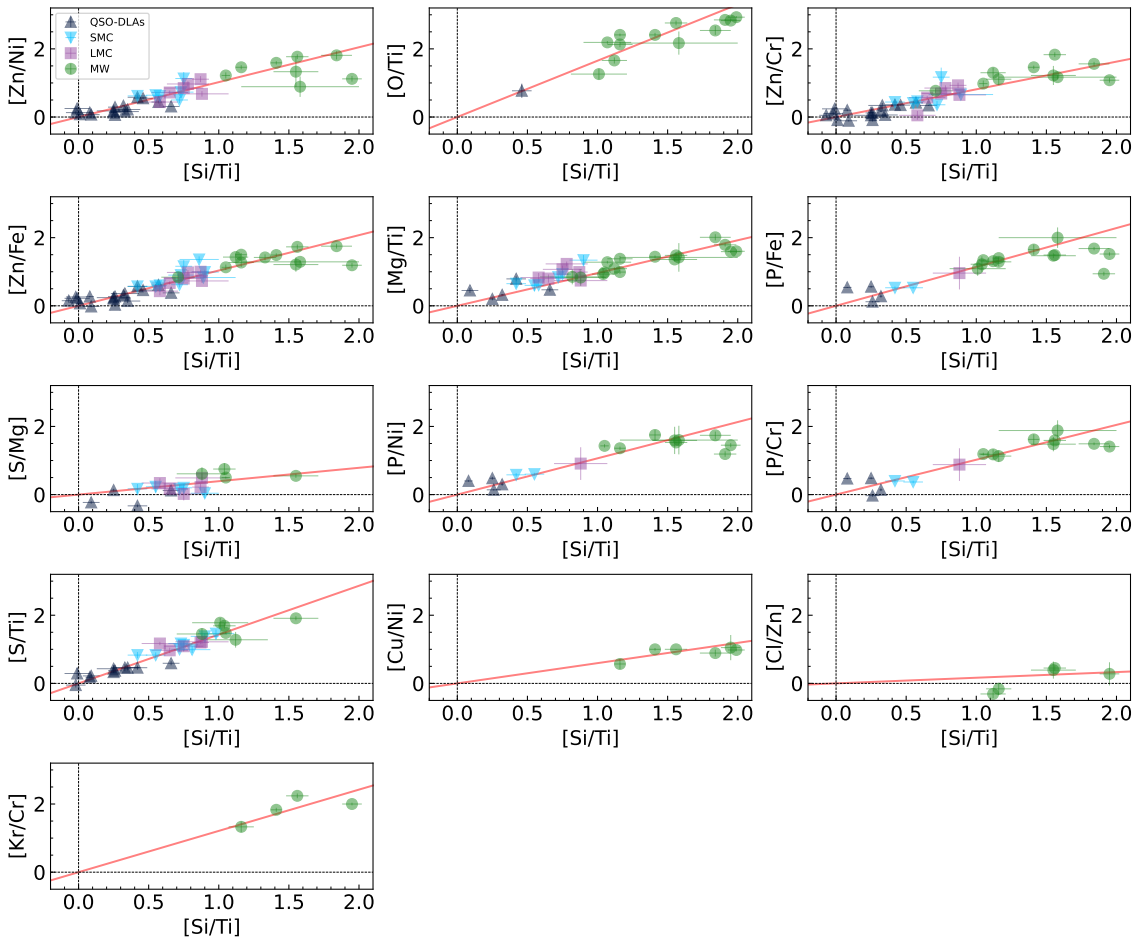


Figure 5.2: Correlations of different dust tracer with the primary reference dust tracer [Si/Ti]. The black triangles are for QSO-DLAs, the blue triangles for the SMC, the purple squares for the LMC and green circles for the MW. The red solid line is the linear fit to all the environments.

dust tracer. We use [Si/Ti] as our primary reference dust tracer, given its $\Delta B2_X$ strength ($\Delta B2_{X_{SiTi}} = 0.92$). The overall strength of depletion for each line of sight can be estimated as

$$\Delta = \frac{\sum_i [X/Y]_i \times W_i \times \frac{1}{C_{XY_i}}}{\sum_i W_i} \tag{5.1}$$

where each dust tracer $[X/Y]_i$ is weighted by W_i as

$$W_i = \frac{r_{XY_i}}{\sigma^2} \tag{5.2}$$

where r_{XY_i} is the correlation coefficient between each dust tracer with the primary reference dust tracer [Si/Ti] and C_{XY_i} is the slope of each dust tracer with respect to the reference dust tracer. Then, σ is given by the combined uncertainties of [X/Y] and C_{XY_i} and is estimated as

$$\sigma = \sqrt{\left(\frac{\sigma([X/Y])}{C_{XY}}\right)^2 + \left(\frac{[X/Y] \times \sigma(C_{XY})}{C_{XY}^2}\right)^2}. \tag{5.3}$$

By taking into account the weights W_i for the calculation of the overall strength of depletion (Eq. 5.1), we make sure that dust tracers with large uncertainties and poor correlations have a smaller influence on the calculation. The uncertainty on the overall strength of depletion can be estimated as

$$\sigma(\Delta) = (\Sigma_i W_i)^{-1/2}. \tag{5.4}$$

The correlations of different dust tracers with the primary dust tracer [Si/Ti] are shown in Fig. 5.2.

5.4.4 *Indirect reference dust tracers*

In cases where [Si/Ti] was not observed for a specific line of sight and there is no correlation between the [X/Y] and [Si/Ti] (and no $C_{XY_{SiTi}}$), alternative dust tracers were used as references. Given the $\Delta B2_X$ strength of [Zn/Fe], [Ge/Ni] and their reliability as dust tracers (as described in Sect. 5.4.1), we use them as indirect reference dust tracers. All valid dust tracers are correlated with each other and with [Si/Ti], when sufficient data are available. We calculate Δ for the cases where indirect reference dust tracers ([Zn/Fe] and [Ge/Ni]) are used, by substituting the slope C_{XY_i} in Eq. 5.1 with the indirect slope $C_{XY_{ind}}$. When [Zn/Fe] is used as an indirect reference dust tracer the indirect slope is estimated as

$$C_{XY_{ind}} = C_{XY_{ZnFe}} \times C_{ZnFe_{SiTi}}, \tag{5.5}$$

where $C_{XY_{ZnFe}}$ is the slope of each dust tracer [X/Y] with the indirect reference dust tracer [Zn/Fe] and $C_{ZnFe_{SiTi}}$ is the slope of [Zn/Fe] with the primary reference tracer [Si/Ti]. Each dust tracer [X/Y] is weighted by W_i using Eq. 5.2, where r_{XY_i} is given by the indirect correlation $r_{XY_{ind}}$. When [Zn/Fe] is the indirect reference dust tracer the indirect correlation is estimated as

$$r_{XY_{ind}} = r_{XY_{ZnFe}} \times r_{ZnFe_{SiTi}}, \tag{5.6}$$

where $r_{XY_{ZnFe}}$ is the correlation coefficient between each dust tracer [X/Y] with the indirect reference dust tracer [Zn/Fe] and $r_{ZnFe_{SiTi}}$ is the correlation coefficient between [Zn/Fe] with the primary reference tracer [Si/Ti].

In the case where [Ge/Ni] is used as an indirect reference dust tracer (third priority dust tracer), we use the indirect slope $C_{XY_{ind}}$ instead, which is estimated as

$$C_{XY_{ind}} = C_{XY_{GeNi}} \times C_{GeNi_{ZnFe}} \times C_{ZnFe_{SiTi}}, \tag{5.7}$$

where $C_{XY_{GeNi}}$ is the slope of each dust tracer [X/Y] with the third priority indirect tracer [Ge/Ni], $C_{GeNi_{ZnFe}}$ is the slope of [Ge/Ni] with the indirect reference tracer [Zn/Fe], and $C_{ZnFe_{SiTi}}$ is the slope of [Zn/Fe] with the primary reference tracer [Si/Ti]. The indirect correlation is estimated, in this case, as

$$r_{XY_{ind}} = r_{XY_{GeNi}} \times r_{GeNi_{ZnFe}} \times r_{ZnFe_{SiTi}}, \tag{5.8}$$

where $r_{XY_{GeNi}}$ is the correlation coefficient between each dust tracer [X/Y] with the indirect reference dust tracer [Ge/Ni], $r_{GeNi_{ZnFe}}$ is the correlation coefficient of [Ge/Ni] with the indirect reference tracer [Zn/Fe] and $r_{ZnFe_{SiTi}}$ is the correlation coefficient of [Zn/Fe] with the primary reference tracer [Si/Ti]. We adopt this approach for [Ge/Ni] as an indirect tracer due to its poor correlation with [Si/Ti], which is reflected by their very low correlation coefficient (r = 0.0021). However, [Ge/Ni] exhibits a strong correlation with [Zn/Fe] and, subsequently, with [Si/Ti], enabling an indirect correlation of [Ge/Ni] with [Si/Ti] through [Zn/Fe]. We note that the weak correlation between [Ge/Ni] and [Si/Ti] is due to the lack of data at low levels of depletion. The correlations among different dust tracers with the primary and indirect reference dust tracers color coded by the overall strength of depletion are shown in Figs. B.2, B.3, and B.4, (available on Zenodo).

5.4.5 *Dust depletion of individual elements*

At this stage, we have calculated the overall strength of depletion per line of sight, which represents the collective contribution of the depletion of all available elements. We can then focus on determining the dust depletion of individual elements, utilizing the derived overall strength of depletion and the observed relative abundances of metals. Given that the overall strength of depletion (Δ) considers the contribution of all the elements, there must be a correlation between Δ and the depletion of individual elements.

The dust depletion of element X, δ_X, can be derived from a relative abundance of an element that is highly volatile, and correcting for the depletion of the volatile element. In our sample, Kr is the least depleted metal (e.g., Konstantopoulou et al., 2022). Because we measure Kr column densities from KrI, and we do not actually expect Kr to be depleted, we assume that Kr has no depletion. We discuss this in more detail in Sect. 5.6.4. Then we can derive the dust depletion of each element as

$$\delta_X - \delta_{Kr} = [\mathrm{X/Kr}] = B_X \times \Delta \sim \delta_X, \tag{5.9}$$

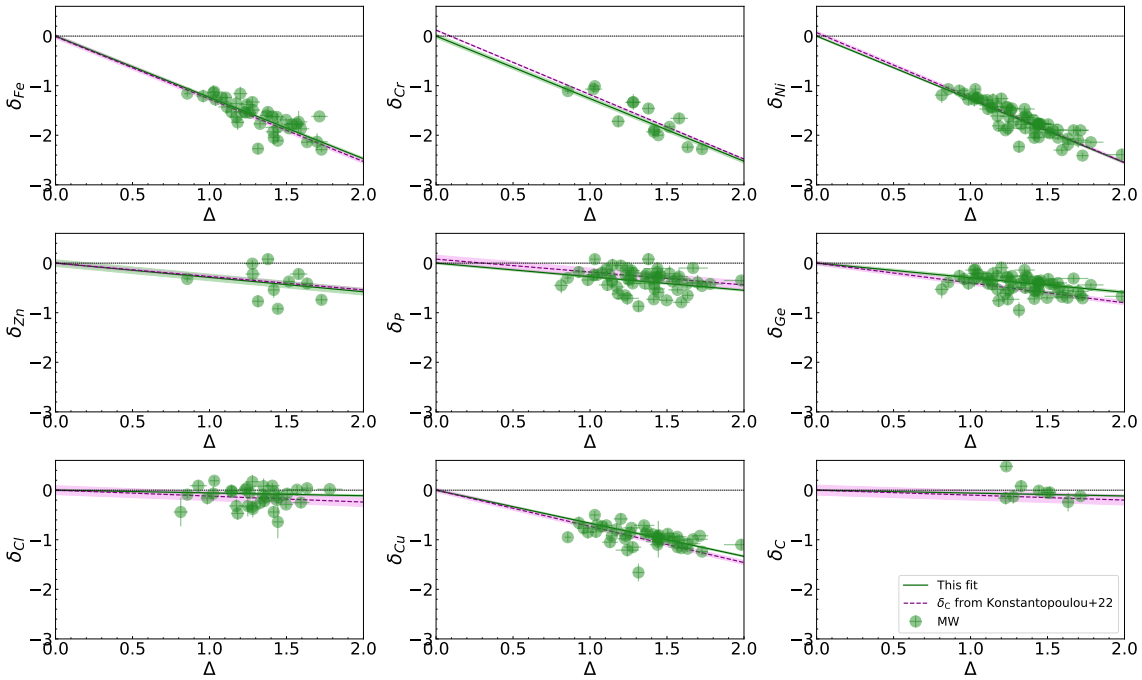


Figure 5.3: Dust depletion of element X against the overall strength of depletion Δ for lines of sight in the MW. The green solid line shows the linear fit to the data and the dashed purple line shows the depletion of element X (δ_X) from Konstantopoulou et al. (2022). The colored surfaces show the uncertainty areas of the fits.

where B_X is the slope of the linear fit unique to each element X and Δ is the overall strength of depletion derived from Eq. 5.1. The coefficients B_X are reported in Table 5.2.

Figure 5.3 shows the dust depletion of element X (δ_X) (for X: Cl, P, Ni, Cu, Cr, Zn, Ge, Fe, and C) with respect to the overall strength of depletion Δ for the MW. We observe a linear relation between δ_X and Δ among all the elements that were studied and fit the data with orthogonal distance regression.

Table 5.1: Parameters[a] resulting from the linear fit ($[X/Y]_{ref} = C_{XY} \times [X/Y]$) between valid correlations among different dust tracers [X/Y] with the reference dust tracers ($[X/Y]_{ref}$ = [Si/Ti], [Zn/Fe], [Ge/Ni]).

[X/Y]	[Si/Ti]			[Zn/Fe]			[Ge/Ni]		
	C_{XY}	r_{XY}	ν_{XY}	C_{XY}	r_{XY}	ν_{XY}	C_{XY}	r_{XY}	ν_{XY}
O/Si	0.71 ± 0.07	0.38	11	0.71 ± 0.05	0.57	14	0.71 ± 0.03	0.01	8
O/S	...	...	...	0.01 ± 0.16	0.33	6	...	...	...
O/Mg	0.72 ± 0.06	0.25	9	0.65 ± 0.05	0.41	23	0.61 ± 0.01	0.53	80
O/Ti	1.65 ± 0.07	0.89	11	1.66 ± 0.06	0.66	21	1.66 ± 0.03	0.82	44
S/Mg	0.39 ± 0.08	0.70	16	0.29 ± 0.05	0.39	32	...	...	...
S/Si	0.47 ± 0.06	0.58	28	0.41 ± 0.03	0.51	72	...	...	...
S/Ti	1.43 ± 0.03	0.95	28	1.32 ± 0.07	0.90	27	...	...	...
Si/Ti	1.00 ± 0.00	1.00	53	0.96 ± 0.04	0.91	42	1.12 ± 0.10	0.00	6
Mg/Si	-0.10 ± 0.03	-0.58	30	-0.03 ± 0.03	-0.17	47	-0.02 ± 0.03	0.07	8
Mg/Ti	0.96 ± 0.03	0.91	31	1.04 ± 0.03	0.85	48	1.07 ± 0.02	0.78	44
P/Co	...	...	...	...	...	...	...	...	...
P/Zn	0.01 ± 0.09	0.15	15	0.16 ± 0.05	0.12	51	0.02 ± 0.03	0.17	8
P/Fe	1.14 ± 0.10	0.84	18	1.21 ± 0.05	0.90	52	1.01 ± 0.02	0.70	35
P/Ni	1.06 ± 0.09	0.90	14	1.03 ± 0.05	0.93	30	1.06 ± 0.01	0.89	70
P/Cr	1.02 ± 0.10	0.92	14	1.06 ± 0.07	0.89	47	0.99 ± 0.02	0.93	10
P/Ge	-0.01 ± 0.03	-0.38	4	0.06 ± 0.03	0.33	10	0.07 ± 0.01	-0.05	69
P/Cu	0.39 ± 0.04	-0.47	3	0.44 ± 0.04	0.62	11	0.47 ± 0.02	0.27	53
P/Al	...	...	...	...	...	...	...	...	...
Zn/Ni	1.02 ± 0.05	0.88	34	0.95 ± 0.02	0.93	148	1.02 ± 0.03	0.86	9
Zn/Cr	0.81 ± 0.05	0.90	37	0.86 ± 0.01	0.96	172	0.97 ± 0.04	0.84	8
Zn/Fe	1.04 ± 0.04	0.91	42	1.00 ± 0.00	1.00	200	0.99 ± 0.03	0.80	9
Zn/Co	...	...	...	0.61 ± 0.30	0.78	4	...	...	...
Zn/Cu	0.47 ± 0.05	-0.53	3	0.47 ± 0.03	0.72	16	0.47 ± 0.04	-0.04	8
Zn/Al	...	...	...	...	...	...	...	...	...
Zn/Ge	0.03 ± 0.06	-0.53	3	0.02 ± 0.11	0.22	12	0.03 ± 0.03	-0.06	9
Co/Fe	...	...	...	0.85 ± 0.37	0.06	4	...	...	...
Co/Al	...	...	...	...	...	...	...	...	...
Co/Ni	...	...	...	0.42 ± 0.10	0.31	2	...	...	...
Co/Cr	...	...	...	0.62 ± 0.30	0.20	4	...	...	...
C/Co	...	...	...	...	...	...	...	...	...
C/Cl	0.12 ± 0.09	0.23	2	0.06 ± 0.11	-0.52	2	0.22 ± 0.10	-0.51	3
C/Cu	0.44 ± 0.04	-0.33	3	0.54 ± 0.06	-0.45	3	0.69 ± 0.08	-0.40	6
C/Zn	0.13 ± 0.12	0.29	3	0.10 ± 0.10	-0.61	5	0.15 ± 0.12	-0.62	3
C/Cr	1.04 ± 0.10	-0.03	3	1.10 ± 0.10	0.04	6	1.17 ± 0.08	-0.08	3
C/Ge	0.23 ± 0.05	0.12	5	0.03 ± 0.23	0.30	4	0.33 ± 0.06	-0.83	8
C/Ni	1.03 ± 0.07	0.05	6	1.23 ± 0.10	0.13	4	1.36 ± 0.05	0.10	8
C/Fe	0.94 ± 0.08	-0.27	6	1.16 ± 0.10	-0.03	6	1.29 ± 0.07	0.23	8
C/Al	...	...	...	...	...	...	...	...	...
C/P	0.17 ± 0.09	0.47	4	0.08 ± 0.07	-0.07	5	0.27 ± 0.10	-0.74	6
Cr/Ni	0.03 ± 0.03	-0.13	31	0.05 ± 0.02	-0.00	131	0.01 ± 0.02	0.34	12
Cr/Al	...	...	...	...	...	...	...	...	...
Cl/Co	...	...	...	...	...	...	...	...	...
Cl/Fe	1.13 ± 0.11	0.21	6	1.18 ± 0.06	0.36	12	1.27 ± 0.03	0.71	20
Cl/Al	...	...	...	...	...	...	...	...	...
Cl/Zn	0.17 ± 0.11	0.78	3	0.08 ± 0.07	-0.37	12	0.29 ± 0.07	0.16	3
Cl/Cu	...	...	...	0.79 ± 0.12	0.60	1	0.71 ± 0.03	0.22	26
Cl/Ge	0.32 ± 0.06	-0.09	2	0.27 ± 0.17	-0.04	4	0.25 ± 0.02	0.01	42
Cl/Ni	1.19 ± 0.14	-0.11	3	1.28 ± 0.07	0.67	5	1.27 ± 0.02	0.84	42
Cl/Cr	1.28 ± 0.14	0.49	3	1.19 ± 0.06	0.35	12	1.32 ± 0.06	0.77	5
Ge/Ni	0.89 ± 0.08	0.00	6	1.01 ± 0.03	0.80	9	1.00 ± 0.00	1.00	83
Ge/Cu	0.32 ± 0.05	-0.66	4	0.38 ± 0.02	0.21	10	0.42 ± 0.01	0.35	63
Ge/Al	...	...	...	...	...	...	...	...	...
Ge/Co	...	...	...	...	...	...	...	...	...
Ge/Cr	0.92 ± 0.09	-0.31	2	1.07 ± 0.11	0.12	11	0.95 ± 0.02	0.97	12
Ge/Fe	0.82 ± 0.09	-0.26	6	1.04 ± 0.09	0.13	12	0.96 ± 0.01	0.86	43
Kr/Ge	0.33 ± 0.03	0.03	5	0.34 ± 0.21	0.18	7	0.32 ± 0.01	0.31	59
Kr/Al	...	...	...	...	...	...	...	...	...
Kr/Ni	1.18 ± 0.11	-0.07	5	1.41 ± 0.06	0.85	5	1.32 ± 0.01	0.87	59
Kr/Co	...	...	...	...	...	...	...	...	...
Kr/Cu	0.53 ± 0.08	-0.77	3	0.75 ± 0.06	0.42	5	0.72 ± 0.02	0.50	41
Kr/Cr	1.21 ± 0.10	0.70	2	1.30 ± 0.07	0.64	8	1.31 ± 0.05	0.90	8
Kr/Fe	1.10 ± 0.12	-0.05	6	1.35 ± 0.07	0.59	9	1.29 ± 0.02	0.82	33
Kr/Zn	0.38 ± 0.07	0.54	3	0.29 ± 0.07	-0.03	9	0.41 ± 0.06	0.37	5
Fe/Al	...	...	...	...	...	...	...	...	...
Ni/Al	...	...	...	...	...	...	...	...	...
Cu/Al	...	...	...	...	...	...	...	...	...
Cu/Ni	0.59 ± 0.04	0.68	4	0.63 ± 0.03	0.58	14	0.59 ± 0.01	0.89	63
Cu/Fe	0.51 ± 0.06	0.40	4	0.56 ± 0.02	0.55	16	0.55 ± 0.01	0.75	32
Cu/Co	...	...	...	...	...	...	...	...	...
Cu/Cr	0.60 ± 0.08	-0.16	2	0.53 ± 0.03	0.68	14	0.60 ± 0.03	0.88	8

Notes: [a] C_{XY} is the slope between the reference dust tracer and [X/Y], ν_{XY} the degrees of freedom and r_{XY} the Pearson's correlation coefficients.

5.5 STAGE 2: APPLICATION OF THE METHOD

In this section, we provide practical guidance on how to apply the methodology described above to derive the overall strength of depletion, Δ, and analyze the abundance patterns, metal patterns, and relative metal patterns.

5.5.1 *Abundance patterns when* H *is known*

An analysis of the abundance patterns can be carried out when H is known. It can be used to derive the overall amount of dust depletion, metallicity of the gas, and eventual deviations from the metal pattern of specific elements, for example, due to nucleosynthesis effects such as α-element enhancements from core-collapse SNe.

This analysis is analogous to figure 3 of De Cia et al. (2024), but using the DUNE coefficients. Figure 5.4 shows an example of the study of an abundance pattern. The abundance pattern shows the observed abundances [X/H] (on the y-axis) with respect to the tendencies of each metal to deplete into dust, which is quantified by the parameter B_X (x-axis), which we call the DUNE refractory index. The total metallicity $[M/H]_{tot}$ and the overall strength of depletion Δ can be derived as

$$[X/H] = [M/H]_{tot} + \Delta \times B_X, \tag{5.10}$$

which can be written as a linear relation, $y = a + b\,x$, where the values of B_X and [X/H] are the known x and y data (tabulated and observed, respectively). The normalization of the linear fit gives the metallicity of the gas ($a = [M/H]_{tot}$), the slope gives the overall strength of depletion (b = Δ), and any deviations on individual elements can be identified, are due to nucleosynthesis effects. The coefficients B_X, are reported in Table 5.2. In principle, one can calculate Δ already from one relative abundance [X/Y] of a dust tracer, as described in Sect. 5.5.3.

5.5.2 *Metal patterns when* H *is unknown*

The analysis of the metal patterns can be done in case H is unknown, including for individual components of the line profiles (Ramburuth-Hurt et al., 2023). The metal patterns can be useful to derive the overall amount of dust depletion, Δ, and to identify eventual deviations from the metal pattern of specific elements, for example, due to nucleosynthesis effects, such as α-element enhancement from core-collapse SNe. The metal patterns can be described by rewriting Eq. 5.10, as follows

$$y = a + B_X \times \Delta \tag{5.11}$$

where

$$y = \log N(X) - X_\odot + 12, \tag{5.12}$$
$$a = [M/H] + \log N(H) \tag{5.13}$$

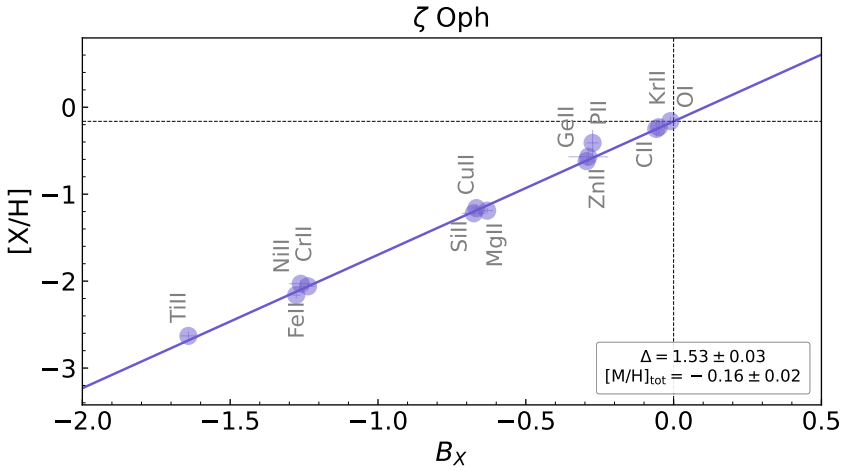


Figure 5.4: Abundances [X/H] with respect to the coefficients B_X (abundance pattern) resulting from Eq. 5.9 for ζ Oph in the MW. The solid line is the fit to the points, the slope of which gives the overall strength of depletion Δ along the line of sight. The y intercept gives the total metallicity $[M/H]_{tot}$.

In this case, y shows the equivalent metal column densities of metals (abundances normalized by their equivalent solar abundance), rather than the metal abundances, as shown in Sect. 5.5.1. Figure 5.5 shows the metal pattern for ζ Oph in the MW. The y-intercept of the linear fit to the data gives the equivalent metal column density, a = $[M/H] + \log N(H)$ – or the total amount of metals after correcting for dust depletion – and the slope gives the overall strength of depletion, Δ. Deviations of individual elements from the linear fit, are due to nucleosynthesis effects, such as α-element enhancement. These deviations (i.e., the distance in the y-axis of the observed data from the main linear fit) can be used to quantify the alpha-element enhancements in the ISM or potential other nucleosytnhesis signatures.

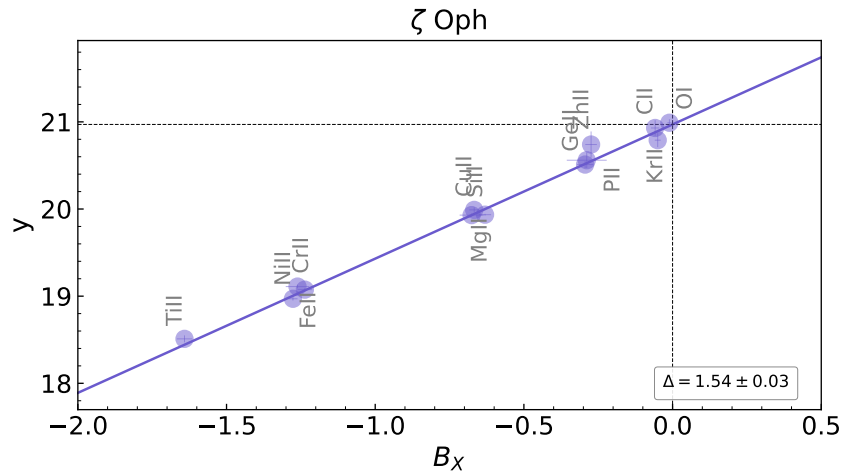


Figure 5.5: Metal pattern for ζ Oph in the MW. The solid line is the fit to the points, the slope of which gives the overall strength of depletion Δ along the line of sight.

5.5.3 *Relative metal patterns*

The analysis of the relative metal patterns can only be used to determine dust depletion. This means that the relative metal patterns should not be used in cases where potential deviations due to nucleosynthesis effects might occur. Instead, it is recommended to use [X/Y] ratios that are pure dust tracers, avoiding mixtures of elements with different nucleosynthetic origins (e.g., α and non-α elements). The overall strength of depletion Δ can then be calculated as

$$\Delta = \frac{[X/Y]}{C_{XY}}, \tag{5.14}$$

using the observed relative abundances [X/Y] and the coefficients C_{XY}, which are reported in Table 2. Equation 5.14 is technically Eq. 5.1 if applied to one dust tracer and for $W_i = 1$. In Fig. 5.6, we provide an example of how the user can practically obtain Δ. It shows the relative abundances [X/Y] against their slopes with the reference dust tracer [Si/Ti] ($C_{XY_{SiTi}}$) for ζ Oph in the MW. The slope of the linear fit to the data gives the overall strength of depletion. Δ.

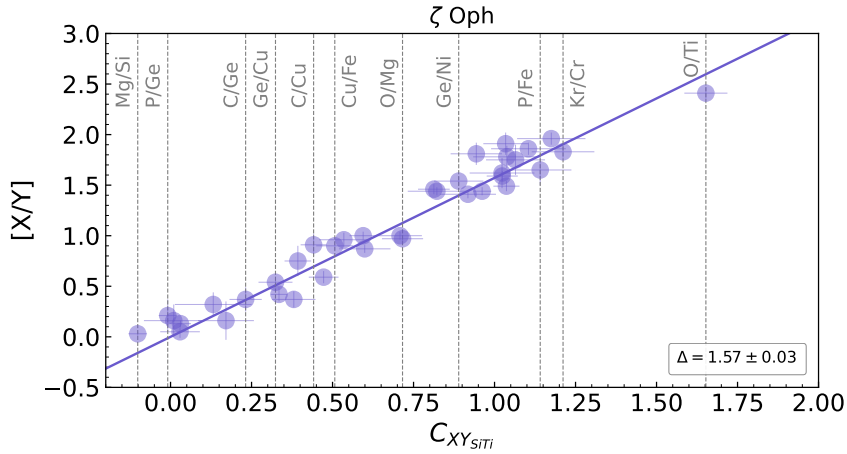


Figure 5.6: Relative abundances [X/Y] with respect to their corresponding slopes with the dust tracer [Si/Ti] ($C_{XY_{SiTi}}$) for ζ Oph in the MW. The solid line is the fit to the points, the slope of which gives the overall strength of depletion Δ along the line of sight. The vertical dashed lines show the dust tracers that can be found in the $C_{XY_{SiTi}}$ range.

5.6 DISCUSSION

5.6.1 *Strengths and limitations*

While our method is one of the most robust methodologies available so far, since it combines strengths from previous methods and overcomes their weaknesses, it also faces some limitations. One of the key strengths of our approach is its ability to derive dust depletion without relying on assumptions regarding α-element enhancement, metallicity,

or dust behavior, thus offering a more reliable determination of both the overall strength of depletion and the dust depletion of individual metals. Additionally, our method can be applied to individual gas clouds, allowing for a more detailed analysis of dust depletion within specific components of the ISM.

However, one limitation that our method is facing, lies in the use of Kr for the determination of the depletion of individual elements through Eq. 5.9. To obtain the depletion of X through the relative abundance [X/Kr], without applying any additional corrections, the depletion of Kr has to be consistent with zero. We estimated the depletion of Kr, from the slope of the linear relation [Kr/H] = $B_{Kr} \times \Delta$, to be B_{Kr} = -0.05 $\pm$ 0.01. However, there is a large scatter in the data, as seen in Fig. 5.7, which might be an effect of metallicity variations in the gas. In addition, the data span a short dynamical range in the x-axis (Δ), not allowing for an accurate determination of the slope.

Another limitation is the availability of metals. Because we are using relative abundances of metals, at least four different metal measurements need to be available in each line of sight, in order to make it possible to obtain correlations among them and consequently the coefficients for their fits. Therefore, we have not been able to provide coefficients for some metals, due to a lack of sufficient measurements, for example, S, Cl, P, Al, Cu, and Co.

We tested whether our methodology is affected by lines of sight that have broken linear relations in their abundance patterns due to multiple gas components with different depletions, as found in De Cia et al. (2021) and Ritchey et al. (2023b). To test this we exclude from the analysis lines of sight that exhibit "upturns" of the volatile elements in the Ritchey et al. (2023b) sample. The derived depletions are not significantly affected by the presence of these lines of sight, thus, we include them here.

Therefore, while our method provides the most solid way to derive dust depletions so far, some limitations are still present mainly due to the availability and quality of metal column density measurements.

5.6.2 *Comparison with previous methods*

Here, we give some examples of how our results compare with the results obtained with the relative method (De Cia et al., 2021) and with the F_* method (Jenkins, 2009; Ritchey et al., 2023b). The Δ determined in DUNE is related with F_* by the linear relation F_* = 0.86 $\times$ Δ - 0.54, based on F_* data from Ritchey et al. (2023b). The relation between Δ and [Zn/Fe] is [Zn/Fe] = 1.05 $\times$ Δ - 0.03, based on the data of this work. We convert our Δ to [Zn/Fe] and to F_* to be able to compare the results of the three methods on a similar scale.

Taking a line of sight that is in common in the three methods, for example, ϵ Per in the MW, we can compare the values on the overall strength of depletion and the gas-phase metallicity. With DUNE we find the overall strength of depletion, found with the abundance pattern, of Δ = 1.26 $\pm$ 0.09. This corresponds to [Zn/Fe] = 1.29 $\pm$ 0.02. With the relative method De Cia et al. (2021) find $[Zn/Fe]_{fit}$ = 1.24 $\pm$ 0.13, which is consistent with the [Zn/Fe] we calculate using its relation to Δ. Converting to F_* we derive F_* = 0.54 $\pm$ 0.17, which is consistent with the F_* = 0.68 $\pm$ 0.04 derived in Jenkins (2009). For the metallicity, we find $[M/H]_{tot}$ = -0.14 $\pm$ 0.09, while De Cia et al. (2021) find $[M/H]_{tot}$ = -0.18

$\pm$ 0.13. Therefore, our results on the depletion and metallicity for ϵ Per are consistent with the results from Jenkins (2009) and De Cia et al. (2021), within the uncertainties.

For ζ Oph, which is featured in Figs. 5.4, 5.5, 5.6, in DUNE we find using the abundance pattern an overall strength of depletion Δ = 1.53 $\pm$ 0.03. This corresponds to F_* = 0.78 $\pm$ 0.15. Jenkins (2009) finds F_* = 1.05 $\pm$ 0.02 while Ritchey et al. (2023b) find F_* = 0.85 $\pm$ 0.05. Our estimate of the overall strength of depletion is in better agreement with Ritchey et al. (2023b). In DUNE we find a metallicity $[M/H]_{tot}$ = -0.16 $\pm$ 0.03, assuming a fit to all the metals. In Ritchey et al. (2023b) they find using the F_* method $[M/H]_{tot}$ = -0.07 $\pm$ 0.06, fitting all the metals, consistent within the uncertainties with our findings. This line of sight was not studied in De Cia et al. (2021).

5.6.3 *Coefficients for mixed groups*

As previously highlighted, our methodology strictly avoids mixing groups of elements when defining dust tracers. This means that we never include relative abundances such as [group1/group2], ensuring that α-elements are not mixed with non-α elements. This is to avoid the influence of α-element enhancement, in the relative abundances (dust tracers). Alternatively, corrections for nucleosynthesis effects would be necessary, as described in De Cia et al. (2016) and Konstantopoulou et al. (2022). This would require the assumption of nucleosynthetic curves for each environment. However, the exact shape of the nucleosynthetic curves, and especially the position of the α-element knee, is uncertain or poorly constrained for QSO-DLAs and for the Magellanic Clouds. A first determination of the distribution of the α-element enhancement in QSO-DLAs is presented in Velichko et al. (2024).

For the ease of use of the reader, particularly in cases where only a limited number of elements are available, we provide coefficients resulting from the fit δ_X = [X/Kr] = $B_X \times \Delta$, shown in Fig. B.5 (available on Zenodo), where X is an α-element. This is done only for the MW data, where nucleosynthesis effects are not present. Specifically, coefficients are provided for correlations of O, Mg, Si and Ti with non-α elements. This extended set of coefficients ensures that our method can be applied even when only few elements are observed. The coefficients for correlations between mixed elements are reported in Table C.2 (available on Zenodo).

5.6.4 *Krypton*

Krypton being a noble gas, remains chemically inert and does not easily create bonds with other elements. As a result, Kr is primarily found in the gas phase of the ISM and it is hard to see how it could be incorporated into dust grains. However, it is important to note that the ISM is a complex environment with a variety of physical processes occurring, including the formation and destruction of dust grains. While Kr may not directly form dust itself, it could potentially be indirectly associated with dust through other processes, which may not yet be understood.

In our method, we aim to avoid assumptions that can compromise the validity of our results. Therefore, even though it seems unlikely that Kr depletes into dust, due to its nature, we examined the possibility of slight depletion. In our methodology, we use relative abundances rather than metal abundances to estimate dust depletion of different elements. This approach helps to avoid complications that can arise from metallicity variations or nucleosynthesis effects, such as α-element enhancement. However, Kr being highly volatile, noble gas and created by s-process neutron capture (Sneden, Cowan, and Gallino, 2008), it remains insensitive to variations of low-metallicity gas and is not affected by nucleosynthesis effects. This is demonstrated in the abundance patterns observed by De Cia et al. (2021) and Ritchey et al. (2023b), where deviations from linearity, or upturns, of volatile elements in the MW indicate the complex nature of the ISM, comprising a mix of gases with different metallicities and dust depletions. In De Cia et al. (2024), they show that these upturns of the volatile elements arise in the presence of high-metallicity gas, indicating that volatiles are less sensitive to variations in low-metallicity gas. Additionally, our analysis of Kr depletion focuses on the MW, where nucleosynthesis effects are not present. While variations of low-metallicity gas do not affect the abundance of Kr, high-metallicity gas can influence its abundance.

We investigate whether there is independent evidence for the depletion of Kr by studying the relation between the abundance of Kr ([Kr/H]) with respect to the overall strength of depletion, Δ, and the dust tracers [Si/Ti], [Zn/Fe], and [Ge/Ni] in the MW (as shown in Fig. 5.7). The top panel of Fig. 5.7 shows the abundance of Kr ([Kr/H]) with respect to Δ and the dust tracers [Si/Ti], [Zn/Fe], and [Ge/Ni]. We fit the data using orthogonal distance regression, with the resulting slopes labeled in Fig. 5.7. The average slope among the different panels of Fig. 5.7 is -0.09 $\pm$ 0.04. This is consistent, within the uncertainties, with the slope obtained from the fit with Δ (see Sect. 5.4.5). The slope obtained from [X/Kr] = $B_{Kr} \times \Delta$ is also consistent, within the uncertainties, with the result from Konstantopoulou et al. (2022), who reported $B2_{Kr}$ = -0.04 $\pm$ 0.09. Jenkins (2009) finds, using the F_* method, that the depletion of Kr get progressively stronger as F_* increases (A_{Kr} = -0.17 $\pm$ 0.10) and Ritchey, Federman, and Lambert (2018) find the same slope but with an improved significance level in their measurement (A_{Kr} = -0.17 $\pm$ 0.06). A_{Kr} corresponds to $B2_{Kr}$ = -0.18 $\pm$ 0.06 using the relation $B2_X = 1.05 \times A_X$. Jenkins (2019) attempts to explain this puzzling depletion of Kr, although only marginally significant, with various scenarios. One explanation given by Jenkins (2019) is that Kr atoms could attach more strongly to surfaces if those surfaces were hit by energetic protons, which create free radicals and broken bonds that can chemically attract noble gas atoms, such as Kr (Hohenberg, Thonnard, and Meshik, 2002). Ionizing radiation might also create such strong binding sites. This would mean that the Kr depletion is influenced by the presence of dust grains but also by higher levels of UV radiation, which can make surfaces more chemically active. As discussed in Jenkins (2009) laboratory experiments and studies of meteoritic materials suggest that noble gases can bind to certain compounds or charged molecular complexes under specific conditions, but these mechanisms do not fully explain the observed depletions in the ISM. Additionally, noble gas atoms can bind to positive ions and charged molecular complexes, such as H^+, H_2^+, and H_3^+. This phenomenon has been observed for interstellar ArH^+ in spectra, however, the concentrations have typically been low. It is unlikely that such molecular

complexes cause significant depletions of Kr. Another possibility is that KrI, as a neutral species, can easily be ionized. In that case, Kr would be ionized more efficiently than hydrogen, lowering the apparent gas-phase [Kr/H] in the warm phase of the ISM that we are probing, where most singly ionized species lie. However, this would result in a roughly flat trend of the Kr abundance [Kr/H] with log N(HI). Instead, we observed a slightly decreasing trend of [Kr/H] with increasing log N(HI), which suggests little or no ionization. This is because, as the total hydrogen column density decreases in the neutral gas, Kr abundance appears to increase if Kr is not depleted into dust. In addition, we do not observe a trend between [O/Kr] with respect to log N(HI). Figure B.6 (available on Zenodo) shows the relations between [Kr/H] and [O/Kr] with log N(HI). A suitable alternative reference instead of KrI could be ArI, which is also a noble gas and not depleted into dust grains. However, Jenkins (2013) demonstrated that ArI can still be ionized in the partly ionized ISM. In addition, ArI is not sufficiently measured in the Milky Way, while KrI has been measured in several lines of sight in our sample.

A mild depletion of Kr would have a small systematic effect on our estimate of the depletion of all metals, which is relatively more important for volatile elements. We can simply subtract it from the B_X coefficients as (B_X - B_{Kr}, where B_{Kr} = -0.09 $\pm$ 0.04). However, we do not consider this apparent Kr depletion significant, since it is not supported by other observed trends. On the contrary, our results on the depletion of individual elements, without the need to assume Kr depletion, agree very well with previous studies De Cia et al. (2016), Jenkins (2009), and Konstantopoulou et al. (2022). The behavior of Kr remains puzzling and further observational evidence would be needed to resolve the discrepancies.

Table 5.2: Coefficients B_X resulting from the linear fit $\delta_X = B_X \times \Delta$ shown in Figs. 5.7, 5.3, and B.5 and the degrees of freedom ν.

X	B_X	ν
Kr	-0.05 $\pm$ 0.01	33
Cl	-0.06 $\pm$ 0.02	30
C	-0.07 $\pm$ 0.02	5
P	-0.27 $\pm$ 0.02	51
Zn	-0.29 $\pm$ 0.07	9
Ge	-0.29 $\pm$ 0.03	61
Cu	-0.67 $\pm$ 0.02	40
Fe	-1.24 $\pm$ 0.02	37
Cr	-1.26 $\pm$ 0.04	12
Ni	-1.28 $\pm$ 0.02	59
	α-elements[a]	
O	-0.06 $\pm$ 0.01	61
Mg	-0.63 $\pm$ 0.02	63
Si	-0.68 $\pm$ 0.04	8
Ti	-1.64 $\pm$ 0.03	39

Note: [a] We provide coefficients for a/non-α group elements only for the MW and only for the convenience of the user (see Sect. 5.6.3). We do not use mixed groups for the development of the method.

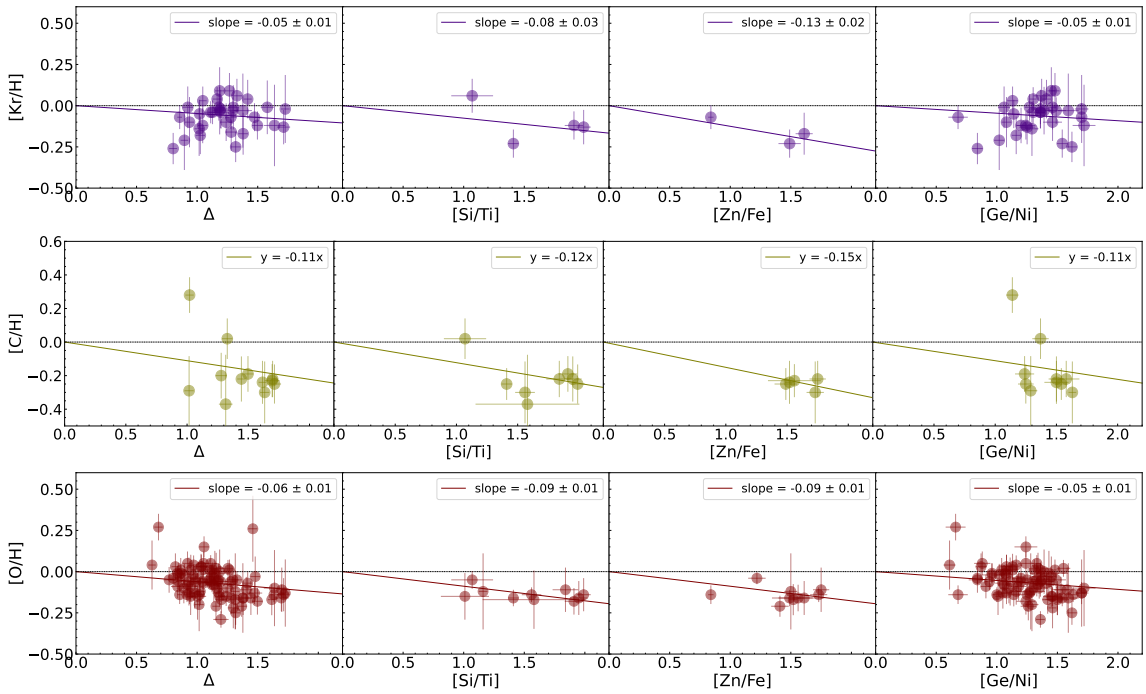


Figure 5.7: Abundances with respect to the overall strength of depletion Δ and the dust tracers [Si/Ti], [Zn/Fe] and [Ge/Ni] for MW data. Top panel: [Kr/H], Middle panel: [C/H], Bottom panel: [O/H], Bottom panel: [O/H]. The solid lines shows the linear fit to the MW data. The slope of the fits gives the depletions of Kr, C and O respectively. ($\delta_{\rm Kr}$, $\delta_{\rm C}$, $\delta_{\rm O}$).

5.6.5 *Carbon and oxygen*

Carbon plays a significant role in dust composition, with considerable amounts found in dust grains. The bulk of C is found in the form of submicron-sized carbon dust grains, such as amorphous carbon or graphite (Mishra and Li, 2017), but also in the form of polycyclic aromatic hydrocarbons (PAHs). PAHs are the main candidates for the origin of the 2175 extinction feature, observed in the MW (e.g, Fitzpatrick and Massa, 1986; Gordon et al., 2003; Valencic, Clayton, and Gordon, 2004; Gordon et al., 2023; Lin, Yang, and Li, 2023), in local galaxies (e.g, Gordon and Clayton, 1998b; Gordon et al., 1999, 2003; Maíz Apellániz and Rubio, 2012), but also in distant galaxies (e.g., Motta et al., 2002; York et al., 2006; Elíasdóttir et al., 2009; Zafar et al., 2011; Witstok et al., 2023). While different studies on dust grains may differ regarding the composition and form of dust grains, they all require the presence of carbon dust, for example in the form of graphite or PAH (e.g., Mattsson et al., 2019; Roman-Duval et al., 2022a; Konstantopoulou et al., 2024). Additionally, most models require carbon to explain the 2175 extinction feature (e.g., Li and Draine, 2001; Draine, 2003). From the fit in Fig. 5.3 we find a slope $B_C = -0.06 \pm 0.02$, which is consistent within the uncertainties with Konstantopoulou et al. (2022), who find $B2_C = -0.10 \pm 0.10$ and Jenkins (2009) who find A_C = -0.10 $\pm$ 0.23, which corresponds to $B2_C$ = -0.11 $\pm$ 0.23. We exclude from the fit the point at δ_C = 0.51 $\pm$ 0.09. This highly positive δ_C arises from a high C column density. For this line of sight, the measurement of the C column density is done in Sofia et al. (2004) and may be overestimated because of the noise structure in the data. Thus, we consider this measurement unreliable and exclude it from the fit.

We estimate the amount of C in dust in particles per million (ppm) in the case of maximum overall strength of depletion Δ. Considering that B_C = -0.07 $\pm$ 0.02 we estimate the maximum amount of C depletion as $\delta_{C_{max}} = B_C \times \Delta_{C_{max}}$. Then the amount of C in dust in terms of particles per million is estimated as $[C/H]_{dust}=[C/H]_{ISM}(1\text{-}10^{\delta_{C_{max}}})$ = 82 $\pm$ 31 ppm, where we adopt $[C/H]_{ISM}$ = 339 $\pm$ 39 ppm for C from Zuo, Li, and Zhao (2021a) and Hensley and Draine (2021). This is consistent with $[C/H]_{dust}$ estimated at maximum amount of dust for the Milky Way in Konstantopoulou et al. (2024) and with the dust-phase C abundance estimated by Cardelli et al. (1996).

The middle panel of Fig. 5.7 shows the gas-phase observed C abundance ([C/H]) with respect to Δ and the dust tracers [Si/Ti], [Zn/Fe], [Ge/Ni]. We fit the data resulting in the slopes labeled in Fig. 5.7, which represent the depletion of C. The average slope of the distribution of [C/H] with respect of different dust tracers (see Fig. 5.3) is -0.13 $\pm$ 0.05 and it is consistent with the slope obtained from the fit with Δ within the uncertainties (see Sect. 5.4.5). Because C is very lightly depleted, a small change in the depletion of Kr can make a bigger difference in the [C/Kr] relative abundance, than for strongly depleted elements.

Oxygen plays a crucial role in ISM dust composition, especially as a component of silicates, contributing significantly to the overall dust mass. However, using Eq. 5.9 we find that $B_O = -0.01 \pm 0.01$. This is contradicting what is already known about the role of O in dust composition. Indeed, dust depletion studies, such as those presented by Jenkins (2009), De Cia et al. (2016), and Konstantopoulou et al. (2022), have revealed substantial depletions of O, with values ranging from -0.09 to -0.23. Jenkins (2009) found $A_O = -0.23 \pm 0.05$

(corresponding to B_O = -0.24 ± 0.05), whereas De Cia et al. (2016) found $B2_O = -0.15 \pm 0.09$ and Konstantopoulou et al. (2022) found $B2_O = -0.20 \pm 0.05$.

The bottom panel of Fig. 5.7 shows the O abundance ([O/H]) with respect to Δ and the dust tracers [Si/Ti], [Zn/Fe], [Ge/Ni]. We fit the data resulting in the slope B_O, which represents the depletion of O (δ_O). The average slope of the distribution of [O/H] with respect to different dust tracers (see Fig. 5.7) is -0.08 ± 0.03. This is consistent, within the uncertainties, with the B_O obtained from the fit with Δ (see Sect. 5.4.5). This is also consistent within the uncertainties with De Cia et al. (2016) and is lower than the results from Jenkins (2009) and Konstantopoulou et al. (2022). Therefore, Fig. 5.7 provides a better representation of the depletion of O than Fig. B.5. Because O is mildly depleted, even a small change in the depletion of Kr can make a bigger difference in the [O/Kr] relative abundance, than for strongly depleted elements.

However, the depletion of Kr into dust grains is highly unlikely, due to its noble gas nature, and the bonding of gas-phase atoms into solids is not observed in the ISM. The constant [O/Kr] with Δ suggests that, while O is known to deplete into dust grains, this depletion is balanced out by other processes in the ISM that maintain the [O/Kr] ratio stable throughout different amounts of dust. This trend remains puzzling, and more data and analysis are needed to understand the underlying causes of the [O/Kr] trend and the behavior of O and Kr in the complex ISM. Although there is uncertainty in the nature of the [O/Kr] - Δ trend which hints to δ_O = -0.01 ± 0.01, the observed oxygen abundance ([O/H]) with respect to the amount of dust (see Fig. 5.7), imply a larger depletion of O with an average δ_O = -0.08 ± 0.03. Additional measurements of O and/or Kr would be necessary to refine the determination of the B_O coefficient.

We estimate the O abundance in dust in terms of particles per million, assuming maximum overall strength of depletion Δ_{max} and estimating the maximum depletion of O as $\delta_{O_{max}} = B_O \times \Delta_{max}$, where B_O = -0.06 ± 0.01 is slope of [O/H] with Δ shown in the bottom panel of Fig. 5.7. We find $[O/H]_{dust}$ = 141 ± 60 ppm estimated as $[O/H]_{dust} = [O/H]_{ISM} \times (1 - 10^{\delta_O})$, where $[O/H]_{ISM}$ = 589 ± 68 ppm from Zuo, Li, and Zhao (2021a) and Hensley and Draine (2021). This means that if we assume the maximum amount of depletion, 141 particles per million of O are expected to be in dust, corresponding to 24% of O being locked in dust grains. This is consistent with other studies, which find that O is present in substantial amounts in dust. Jenkins (2009) estimates an excess of O in dust with respect to what is expected for the formation of known oxygen-rich compounds, in what he calls the 'oxygen crisis'. We estimate the Si abundance into dust for maximum depletion as $[Si/H]_{dust}$ = 40 ± 4 ppm, assuming $[Si/H]_{ISM}$ = 43 ± 4 ppm from Zuo, Li, and Zhao (2021a) and Hensley and Draine (2021). Therefore, up to 93% of Si is in the form of dust at maximum levels of depletion. The abundances in dust of O and Si are consistent with O being largely incorporated in silicates. For pure olivine $Mg_{2x}Fe_{2(1-x)}SiO_4$, $4[Si/H]_{dust}$ = 120 ppm, consistent, within the uncertainties, with the O abundance in dust. Some oxygen may also be incorporated in iron oxides. Studies on dust composition, such as Roman-Duval et al. (2022a,c) and Konstantopoulou et al. (2024) find that O is the most abundant element by mass in dust in all the galactic environments studied (MW, LMC, SMC, QSO- and GRB-DLAs). Their results on dust composition suggest the presence of significant amounts of pyroxenes ($MgSiO_3$) in dust, as observed also by Mattsson et al.

(2014). Specifically, Konstantopoulou et al. (2024) estimate the maximum amount of O in dust to be 181 ppm and a minimum 154 ppm in the MW, which is consistent with our findings. Nevertheless, with $[O/H]_{dust} = 141 \pm 60$ ppm (as derived here) and typical gas-phase interstellar abundance of $[O/H]_{gas} = 310$ ppm (Meyer, Jura, and Cardelli, 1998), we derive a total O abundance of 450 ppm. This is considerably lower than the interstellar abundance of $[O/H]_{ISM} = 589 \pm 68$ ppm, implying 138 ppm (= 589 ppm - 451 ppm) of O remains unaccounted for in the ISM, consistent with earlier studies of Whittet (2010) and Wang, Li, and Jiang (2015). Therefore, the missing O problem is not solved, but the tension is not strong (1.5σ level).

[O/Ti] is our most sensitive dust tracer due to the large difference in the refractory properties of O and Ti ($\Delta B2_{OTi} = 1.44$) and it correlates well with both [Zn/Fe] (see Fig. B.1, available on Zenodo) and with [Si/Ti] (see Fig. 5.2). The strong correlation between the relative abundances [O/Ti] and [Si/Ti] is partially by construction, due to the fact that Ti is present in both x- and y-axis. The steeper slope than the 1:1 relation between [O/Ti] and [Si/Ti] of Fig. 5.2 indicates that O is depleted into dust much less severely than Si, which agrees with the results from De Cia et al. (2016), Roman-Duval et al. (2021), and Konstantopoulou et al. (2022). O is a volatile element, that remains for longer time in the gas-phase than Si, and has a weaker tendency to incorporate into dust compared to Si which is more refractory.

5.6.6 *Sulfur depletion in the diffuse ISM*

In the past, S was believed to not deplete into dust grains in the diffuse ISM, until the study of Jenkins (2009). Later studies on dust depletion of metals in the diffuse ISM confirmed that S, being a volatile element, is mildly depleted into dust grains (De Cia et al., 2016; Roman-Duval et al., 2021; Konstantopoulou et al., 2022). The panels showing [S/Ti] and [S/Mg] vs. [Si/Ti] in Fig. 5.2 give us insights into the dust depletion behavior of S in the diffuse ISM. The strong correlations between the relative abundances of metals show they follow the same sequences. The strong correlation between [S/Ti] and [S/Mg] with [Si/Ti] shown in Fig. 5.2 suggest that S is indeed depleted into dust grains at a lesser degree than Ti and Mg. If S would not deplete into dust grains one would expect a flat trend between [S/Ti] and [S/Mg] vs. [Si/Ti], which is clearly not observed. We note that the panel showing [S/Ti] vs. [Si/Ti] involves Ti in both x- and y-axis. This means that a strong correlation is created by construction. The steep slope between [S/Ti] and [Si/Ti] indicates that S is indeed depleted into dust but at a lesser degree than Si, and both S, Si deplete less heavily than Ti. These are consistent with the findings of De Cia et al. (2016), Roman-Duval et al. (2021), and Konstantopoulou et al. (2022). Other recent works, such as Yang, Hua, and Li (2024), discuss the depletion of S in the ISM, and specifically examine the possibility of the incorporation of S into dust grains or molecular forms that are less easily detected. This study reinforces the result that S is depleted, even in the diffuse ISM, in agreement with previous studies.

5.6.7 *Variations of the dust depletion with interstellar conditions*

The formation of molecules often occurs on the surface of dust grains. Therefore, we investigate the variation of the overall strength of depletion with the molecular fraction, defined as $f_{H_2} = 2\mathrm{N}(H_2)/[\mathrm{N(HI)} + \mathrm{N}(H_2)]$, which expresses the fraction of hydrogen nuclei bound to H_2. Figure 5.8 shows the relation between the overall strength of depletion with respect to the molecular fraction f_{H_2} for the MW, LMC, SMC and QSO-DLAs. We find no significant trend with the dust depletion Δ. This is consistent with the findings of De Cia et al. (2024), who find no clear correlation between the molecular fraction and the amount of dust depletion, which they trace with [Zn/Fe] (see their Fig. 12), and with Tumlinson et al. (2002) who find no clear correlation between f_{H_2} and the color excess $E(B-V)$ (see their Fig. 7). Dust depletion probes the warm neutral medium of the ISM. On the other hand, H_2 molecules are known to form in the molecular medium, it is likely that they do not survive or form as abundantly in the warmer and diffuse phase of the ISM.

There is no clear variation in the abundances [O/H], [C/H] with interstellar conditions, for example with the molecular fraction f_{H_2}. This is consistent with previous results from Cardelli et al. (1996), who found the gas-phase [C/H] abundance to be about 140 ppm, independent of the interstellar conditions, such as f_{H_2} (see their Fig. 2). It is also consistent with Meyer, Jura, and Cardelli (1998), who found the gas-phase [O/H] abundance to be about 310 ppm, also independent of the interstellar conditions. The agreement between the different studies is reassuring, since such gas-phase abundances of [C/H] and [O/H] have been frequently used to constrain dust models, such as Mathis (1996), Li and Greenberg (1997), Jones et al. (2013), and Zuo, Li, and Zhao (2021a,b).

Additionally, we do not expect to have variations of the dust depletion with the hydrogen number density n_H of the dense molecular clouds. The [O/H] and [C/H] abundances and the estimated overall strength of depletion Δ do not vary with the n_H measurements from Meyer, Jura, and Cardelli (1998) and Klimenko et al. (2024), in agreement with the conclusions of Meyer, Jura, and Cardelli (1998). We note that Jenkins (2009) found a relation between the strength of depletion (F_*) and the average n_H in the warm neutral medium and cold neutral medium.

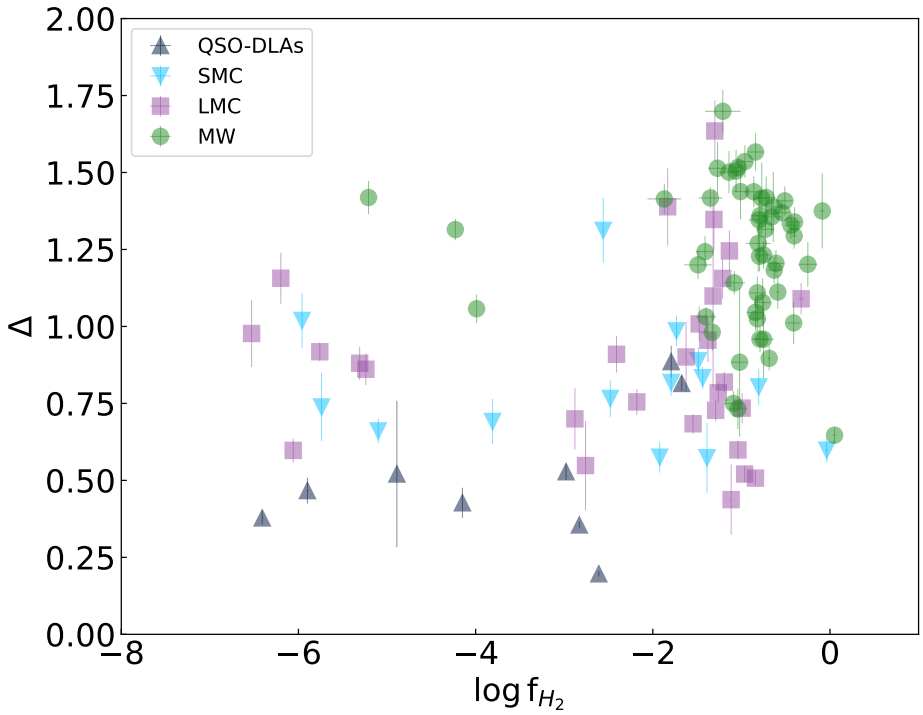


Figure 5.8: Overall strength of depletion Δ with respect to the molecular fraction f_{H_2}. The black triangles are for QSO-DLAs, the blue triangles for the SMC, the purple squares for the LMC and green circles for the MW.

5.7 SUMMARY AND CONCLUSIONS

Each metal exhibits a different tendency to deplete into dust grains, thus, their relative abundances can allow us to trace the amount of dust. In this work, we present a novel method to characterize the depletion of metals into dust using known correlations among relative abundances of metals that qualify as tracers of dust. This new method aims at taking full advantage of the strengths of the two main existing methods of estimating dust depletion (the F_* and relative methods), while overcoming their weaknesses.

Using a comprehensive literature sample, we compiled the column densities of 17 metals for diverse galactic environments, including the MW, LMC, SMC, and QSO- and GRB-DLAs. To avoid complications arising from nucleosynthesis effects, we divided our elements into two groups: group 1, comprised of the α-elements (O, S, Si, Mg, and Ti), and group 2, comprised of the non-α elements (Fe, Cr, Ni, P, Kr, Ge, Co, Cu, Al, C, Cl, and Zn). We observed the linear correlations among all valid observed relative abundances of metals [X/Y] (dust tracers) across all the studied environments.

Our method uses all the available dust tracers and the resulting parameters describing their correlations to estimate the overall strength of depletion, Δ, along individual lines of sight. All dust tracers are correlated with each other, so there is no preferential use of

any of them in the determination of the overall strength of depletion. We de-projected these correlations with respect to one reference dust tracer, [Si/Ti], so that the value of Δ is comparable to the observed values of [Si/Ti]. In cases where [Si/Ti] was not observed, we used the correlations between [Si/Ti] with [Ge/Ni] or [Zn/Fe] observed for the whole sample.

Moreover, we provide updated dust depletion estimates, on Cl, P, Ni, Cu, Cr, Zn, Ge, Fe, C, and Kr, which directly result from our methodology. To benefit users, we used MW data to also provide dust depletion estimates on O, Si, Mg, and Ti, which result from the relative abundances of a mix of α-elements with Kr (a refractory element). For the development of our methodology and the derivation of the overall strength of depletion, we strictly avoid mixing α-elements with refractory elements when defining the relative abundances [X/Y].

In addition, we provide users with straightforward tools to determine the overall strength of depletion along individual lines of sight (Δ), the gas-phase metallicity ([M/H]), and any deviations due to a nucleosynthesis effect, from the study of the abundance patterns, when H is known. When H is unknown, we guide users on using metal patterns to determine the dust depletion and any deviations due to nucleosynthesis effect. Lastly, we offer simple guidelines on using any observed relative abundances of metals [X/Y] (or relative metal patterns) to estimate the overall strength of depletion. For these applications, we provide the required coefficients B_X and C_{XY}. This novel method offers valuable insights into the chemical evolution of galaxies and the role of dust in shaping their galactic environments.

Data availability: Table 2 and appendices B-C are available on Zenodo at https://doi.org/10.5281/zenodo.13889072.

Acknowledgements: *We thank the anonymous referee for the useful and constructive comments that improved this manuscript. Edward B. Jenkins passed away just before the submission of this paper. Ed was one of the great fathers of UV astronomy and his scientific work on the ISM was immensely impactful and inspiring. We are grateful to have had the opportunity to work with and learn from him. His legacy will live on. CK, ADC, TRH and AV acknowledge support by the Swiss National Science Foundation under grant 185692. This research has made use of NASA's Astrophysics Data System.*

5. A TESTING OUR METHODOLOGY WITHOUT ZN

When defining the two groups we included Zn in the non α-element group. The nucleosynthetic origin of Zn is complex and it is not considered an α-element nor an Fe-peak element. However, prior studies (e.g., Saito et al., 2009) have shown that Zn generally traces Fe in the metallicity range that we are studying here ($-2 \leq$ [M/H] ≤ 0). Additionally, [Zn/Fe] is the strongest dust tracer in this study, demonstrated by the large difference between the refractory indices of Zn and Fe ($\Delta B2_{ZnFe} = 0.99$) and the large amount of data points. Therefore, Zn is included in group 2.

However, we acknowledge that Zn can show a small enhancement, but of smaller amplitude than the α-elements (e.g., Barbuy et al., 2015; Velichko et al., 2024). This small

amplitude is, however, not affecting our analysis. First, the correlations involving Zn are not affected, as shown in Fig. 5.2, where the QSO-DLA points (black triangles) pass through zero, despite the scatter caused by inhomogeneities in the Berg et al. (2015) sample. Second, we tested the analysis by excluding Zn and our results remain unaffected.

Although there is still some debate on the reliability of [Zn/Fe] as a dust tracer, it remains the strongest dust tracer in our study, demonstrated by the large difference between the refractory indices of Zn and Fe ($\Delta B2_{ZnFe} = 0.99$). Therefore, [Zn/Fe] is used in our methodology as an indirect reference dust tracer and Zn is involved in several other dust tracers, as well, e.g., [Zn/Ni], [Zn/Cr], [Zn/Co]. To assess the impact of Zn on our results, we conduct a comparative analysis by recalculating the overall strength of depletion, Δ, without including Zn. For this test, we limit the analysis to a subset of lines of sight with available Si and Ti measurements, using only [Si/Ti] as a reference dust tracer.

The comparison between the overall strength of depletion calculated with (Δ) and without Zn (Δ_{noZn}) is shown in Fig. 5.9. The data follow a 1:1 relationship, represented by the slope ($B_X = 1.00 \pm 0.02$) of the linear fit. This reassures the validity of our methodology. Additionally, [Zn/Fe] shows strong correlations with multiple other dust tracers, as illustrated in Figure B.1. This analysis confirms that the inclusion of Zn does not compromise the reliability of our method, and the use of [Zn/Fe] as an indirect reference dust tracer is justified. This comparative analysis supports the non-privileged treatment of any dust tracer in our methodology, since all dust tracers are correlated with each other in a multidimensional space.

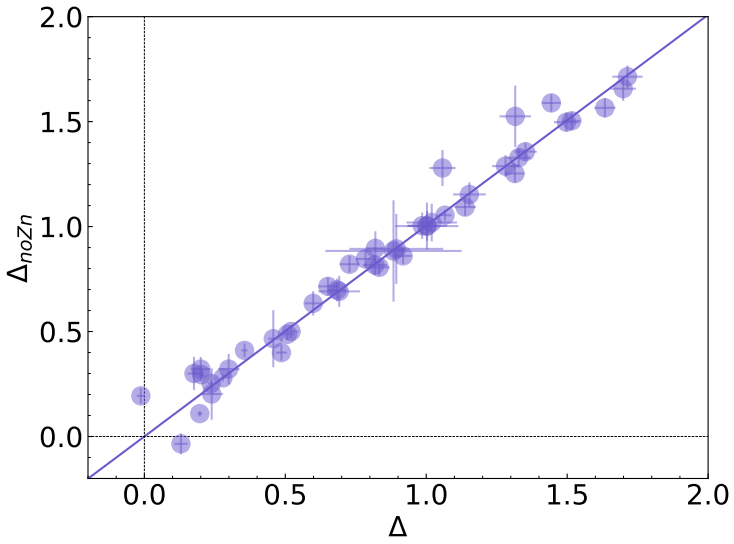


Figure 5.9: Comparison of the overall strength of depletion obtained from eq. 5.1 including Zn (Δ) and the overall strength of depletion after excluding Zn from the analysis (Δ_{noZn}).

5.B ADDITIONAL FIGURES

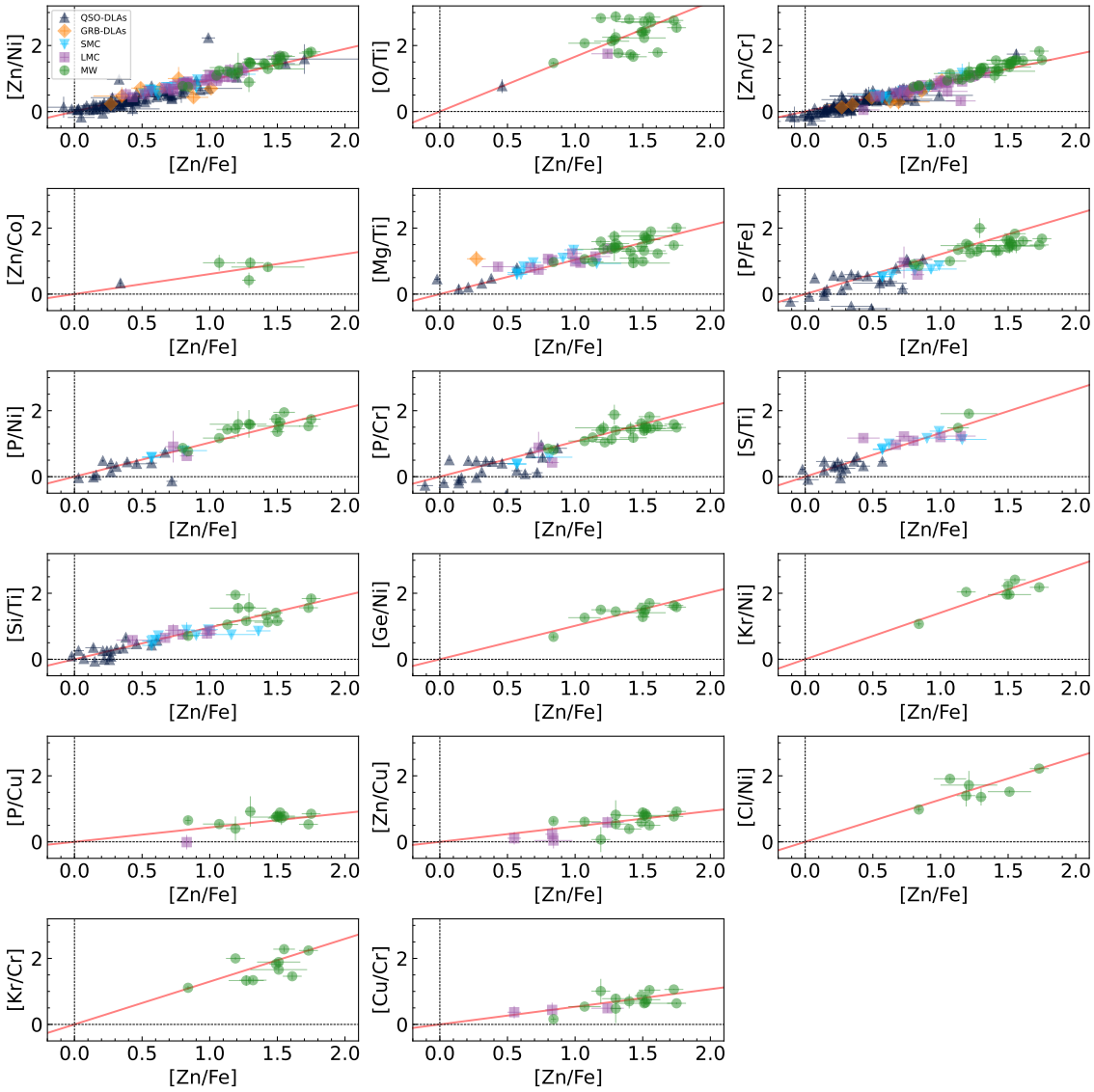


Figure 5.10: Correlations of different dust tracers with the indirect reference dust tracer [Zn/Fe]. The black triangles are for QSO-DLAs, the orange diamonds are for QSO-DLAs, the blue triangles for the SMC, the purple squares for the LMC and green circles for the MW. The red solid line is the linear fit to all the environments.

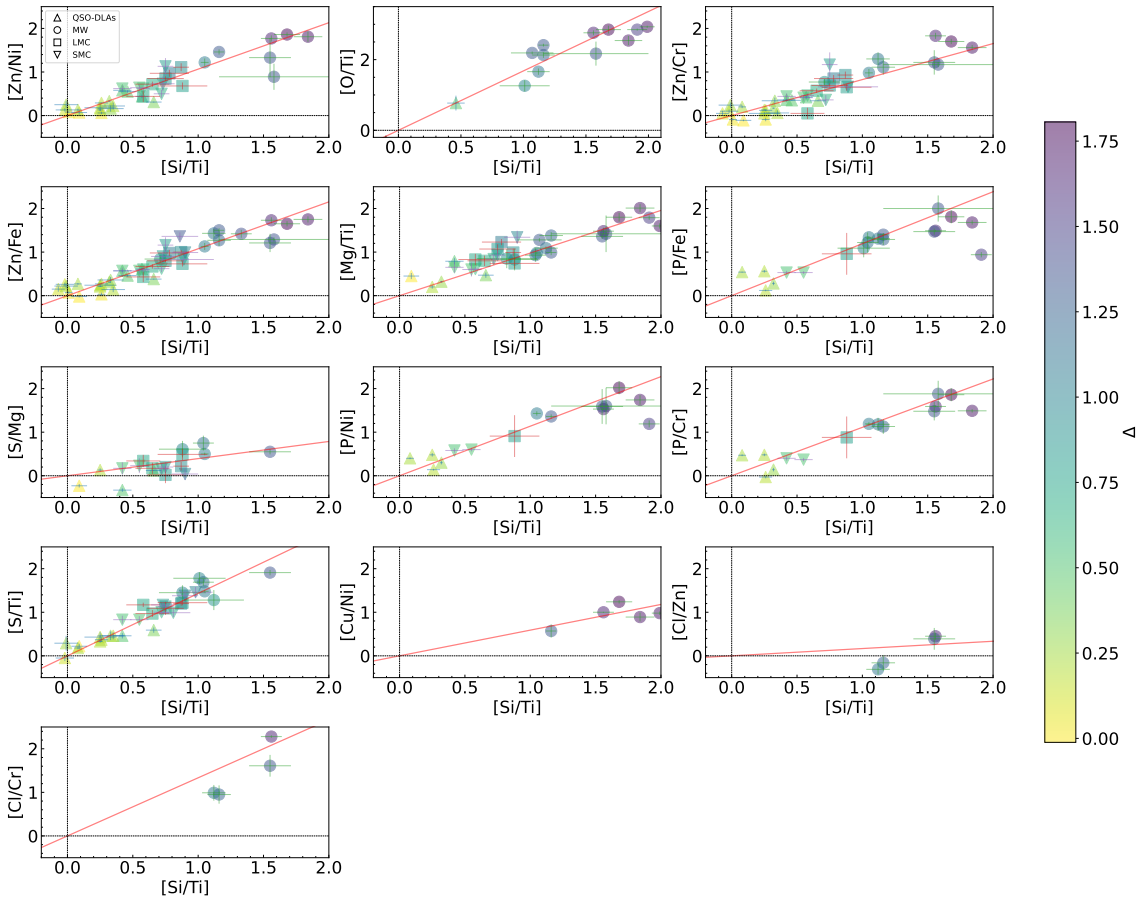


Figure 5.11: Correlations of different dust tracers with the primary reference dust tracer [Si/Ti], color coded by the overall strength of depletion (Δ). The red solid line shows the linear fit to the data.

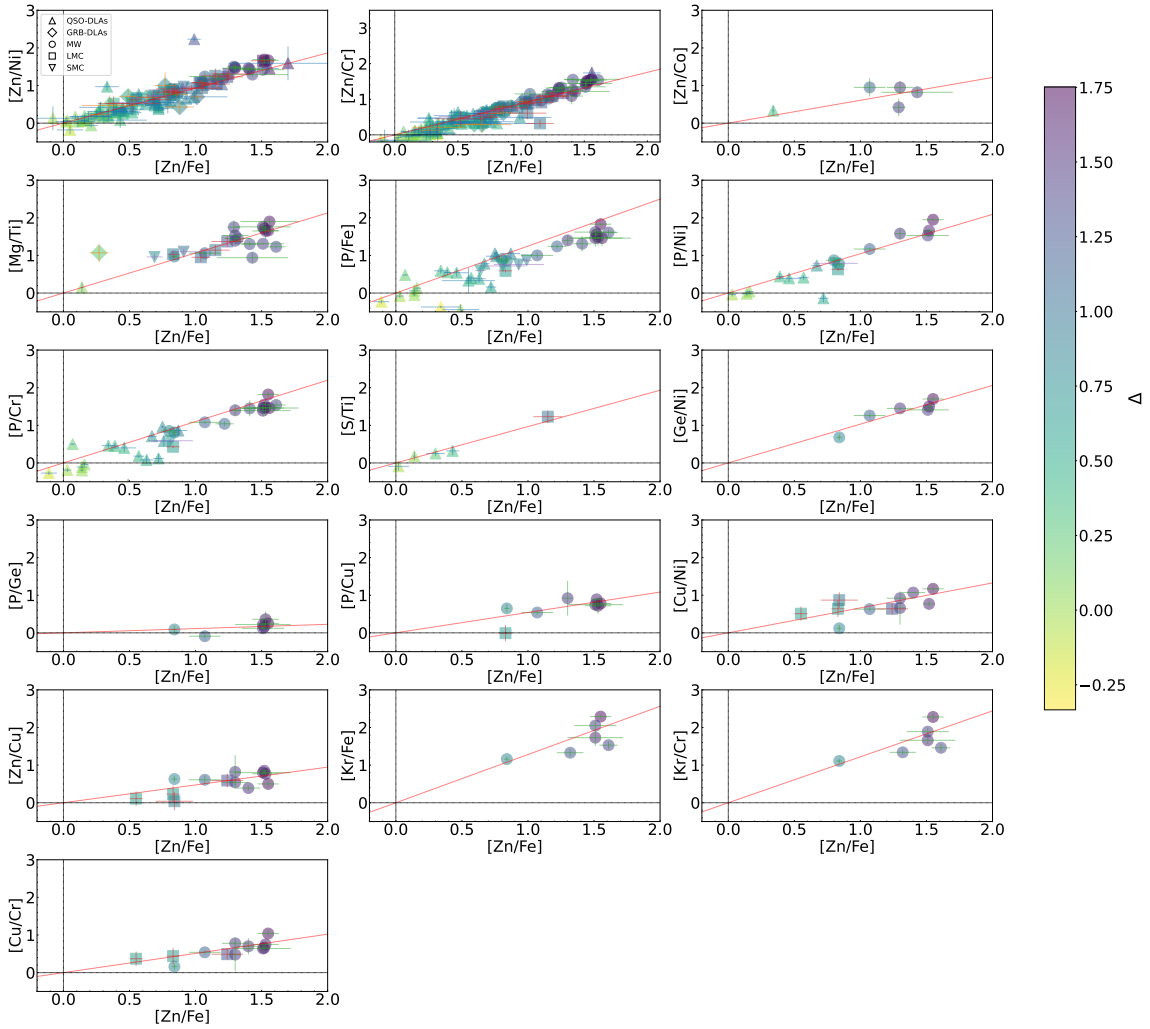


Figure 5.12: Correlations of different dust tracers with the indirect dust tracer [Zn/Fe], color coded by the overall strength of depletion (Δ). The red solid line shows the linear fit to the data.

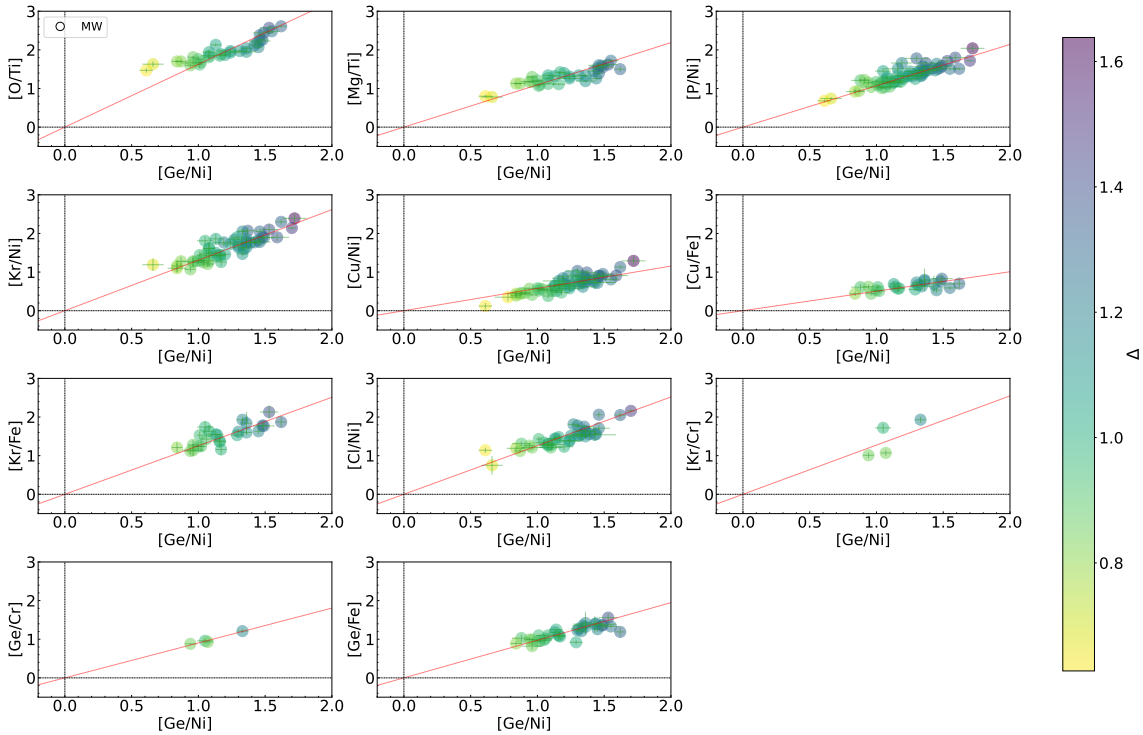


Figure 5.13: Correlations of different dust tracers with the indirect dust tracer [Ge/Ni], color coded by the overall strength of depletion (Δ). The red solid line shows the linear fit to the data.

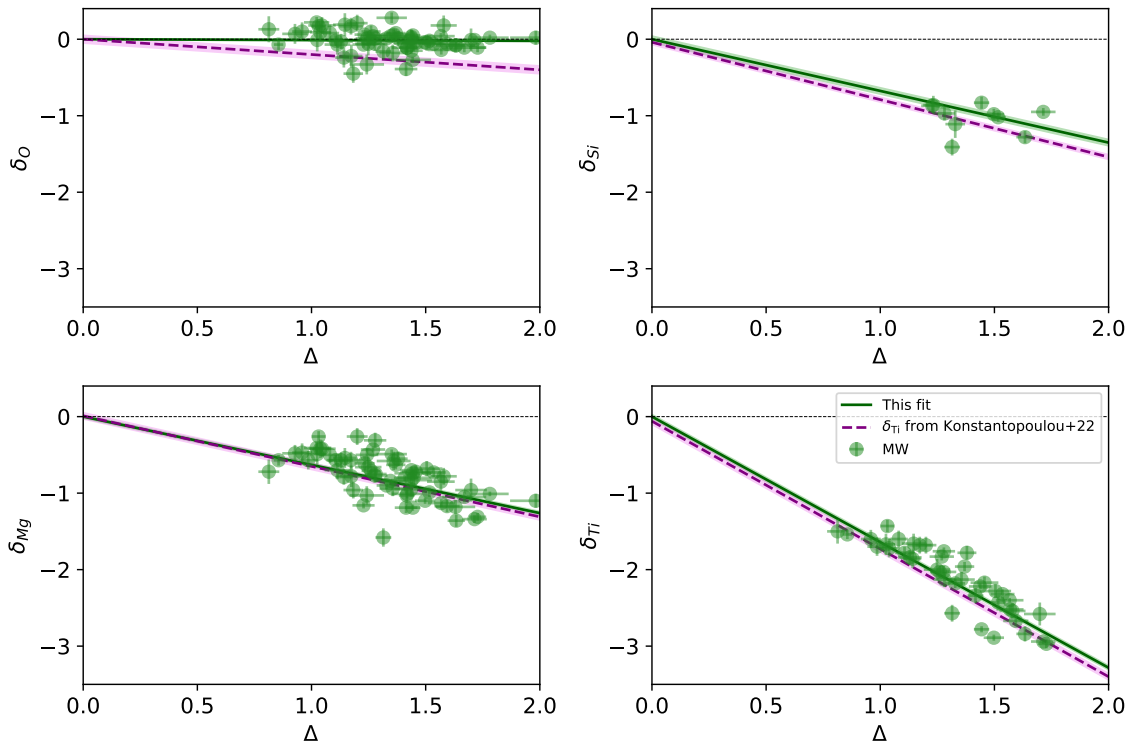


Figure 5.14: Relative abundance of element X with respect to Kr against the overall strength of depletion Δ for lines of sight in the MW. The black solid line shows the linear fit to the data and the dashed red line shows the depletion of element X (δ_X) from Konstantopoulou et al. (2022).

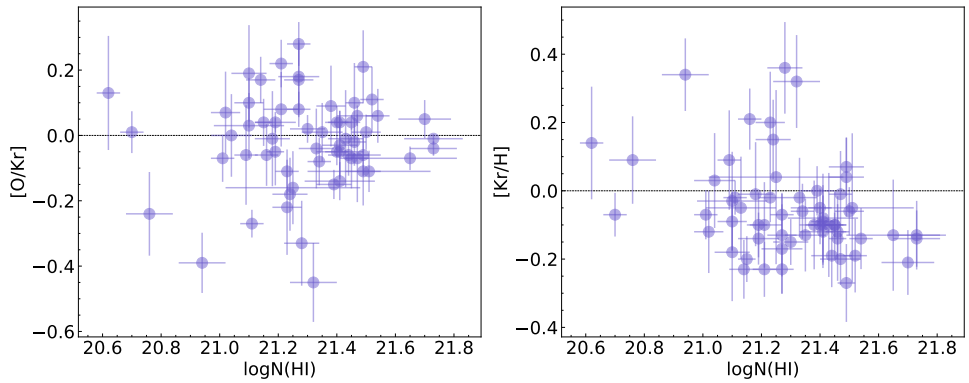


Figure 5.15: [O/Kr] with respect to log N(HI (left panel) and [Kr/H] with respect to log N(HI (right panel).

5.C ADDITIONAL TABLES

Table 5.3: The 70 dust tracers identified in our method after applying the selection criteria described in Section 5.4.1. $\Delta B2_X$ is the difference between the refractory indices $B2_X$ of X and Y. The $B2_X$ coefficients are taken from Konstantopoulou et al. (2022).

[X/Y]	$\Delta B2_{XY}$	[X/Y]	$\Delta B2_{XY}$
Kr/Al	1.62±0.36	P/Co	0.63±0.21
C/Al	1.56±0.36	Zn/Co	0.62±0.19
Cl/Al	1.54±0.36	Cl/Cu	0.61±0.10
O/Ti	1.47±0.06	Cu/Ni	0.58±0.05
P/Al	1.40±0.36	Cu/Cr	0.57±0.04
Zn/Al	1.39±0.35	O/Si	0.55±0.06
Kr/Ni	1.27±0.09	Cu/Fe	0.53±0.06
Kr/Cr	1.26±0.09	Ge/Co	0.49±0.19
Ge/Al	1.26±0.35	P/Cu	0.47±0.09
Kr/Fe	1.22±0.10	O/Mg	0.46±0.06
C/Ni	1.21±0.10	Zn/Cu	0.46±0.05
C/Cr	1.20±0.10	Co/Ni	0.42±0.19
Cl/Ni	1.19±0.09	Co/Cr	0.41±0.19
S/Ti	1.19±0.06	Fe/Al	0.40±0.35
Cl/Cr	1.18±0.09	Co/Fe	0.37±0.19
C/Fe	1.16±0.11	Kr/Ge	0.36±0.10
Cl/Fe	1.14±0.10	Cr/Al	0.36±0.35
P/Ni	1.05±0.09	Ni/Al	0.35±0.35
P/Cr	1.04±0.08	Ge/Cu	0.33±0.06
Zn/Ni	1.04±0.04	C/Ge	0.30±0.11
Zn/Cr	1.03±0.03	O/S	0.28±0.06
Mg/Ti	1.01±0.06	Cl/Ge	0.28±0.10
P/Fe	1.00±0.09	S/Si	0.27±0.05
Zn/Fe	0.99±0.05	Kr/Zn	0.23±0.09
Cu/Al	0.93±0.35	S/Mg	0.18±0.06
Si/Ti	0.92±0.05	C/Zn	0.17±0.10
Ge/Ni	0.91±0.05	C/P	0.16±0.13
Ge/Cr	0.90±0.04	Cu/Co	0.16±0.19
Ge/Fe	0.86±0.06	Cl/Zn	0.15±0.09
Kr/Co	0.85±0.21	P/Ge	0.14±0.09
C/Co	0.79±0.21	Zn/Ge	0.13±0.05
Cl/Co	0.77±0.21	Mg/Si	0.09±0.05
Co/Al	0.77±0.40	C/Cl	0.02±0.13
Kr/Cu	0.69±0.10	P/Zn	0.01±0.09
C/Cu	0.63±0.11	Cr/Ni	0.01±0.03

Table 5.4: Same as Table 5.1 but for mixed groups of elements.

[X/Y]	[Si/Ti]			[Zn/Fe]			[Ge/Ni]		
	C_{XY}	r_{XY}	ν_{XY}	C_{XY}	r_{XY}	ν_{XY}	C_{XY}	r_{XY}	ν_{XY}
Ti/Fe	-0.49 ± 0.04	-0.94	18	-0.43 ± 0.04	-0.07	28	-0.50 ± 0.04	-0.40	31
Ti/Cr	-0.42 ± 0.02	-0.70	8	-0.48 ± 0.20	-0.06	26	-0.42 ± 0.03	-0.66	9
Ti/Ni	-0.41 ± 0.03	-0.67	11	-0.38 ± 0.04	0.01	20	-0.34 ± 0.02	-0.27	44
Ti/Zn	-1.38 ± 0.07	-0.70	10	-1.44 ± 0.04	-0.72	28	-1.39 ± 0.04	-0.87	9
Ti/P	-1.38 ± 0.05	-0.84	11	-1.43 ± 0.06	-0.48	18	-1.40 ± 0.02	-0.90	37
Ti/Co	...	...	...	-0.83 ± 0.18	-0.30	2	...	...	...
Ti/Ge	-1.23 ± 0.05	-0.86	6	-1.43 ± 0.09	-0.53	10	-1.35 ± 0.02	-0.90	44
Ti/Kr	-1.60 ± 0.09	-0.87	6	-1.82 ± 0.17	-0.32	7	-1.70 ± 0.03	-0.83	35
Ti/Cl	-1.56 ± 0.10	-0.75	5	-1.49 ± 0.10	-0.48	9	-1.59 ± 0.05	-0.78	22
Ti/Cu	-1.01 ± 0.04	-0.91	3	-1.00 ± 0.05	-0.78	10	-0.93 ± 0.03	-0.81	33
Ti/Al	...	...	...	...	...	...	...	...	...
Ti/C	-1.47 ± 0.05	-0.62	6	-1.72 ± 0.20	-0.16	5	-1.85 ± 0.10	0.18	6
Si/Fe	0.60 ± 0.04	0.40	18	0.56 ± 0.03	-0.08	13	0.54 ± 0.02	0.70	8
Si/Cr	0.57 ± 0.02	0.79	8	0.55 ± 0.05	-0.30	11	0.58 ± 0.04	-0.72	2
Si/Ni	0.61 ± 0.03	0.77	11	0.63 ± 0.06	0.16	7	0.64 ± 0.03	0.54	8
Si/Zn	-0.42 ± 0.06	0.12	10	-0.47 ± 0.04	-0.94	13	-0.44 ± 0.09	-0.31	3
Si/P	-0.40 ± 0.04	0.09	11	-0.41 ± 0.02	-0.62	10	-0.37 ± 0.04	-0.52	6
Si/Co	...	...	...	...	...	...	...	...	...
Si/Ge	-0.30 ± 0.05	0.65	6	-0.38 ± 0.02	-0.84	3	-0.36 ± 0.03	-0.45	8
Si/Kr	-0.59 ± 0.07	0.55	6	-0.80 ± 0.06	-0.82	3	-0.74 ± 0.04	-0.37	7
Si/Cl	-0.66 ± 0.09	-0.10	5	-0.74 ± 0.10	-0.44	3	-0.78 ± 0.05	-0.85	2
Si/Cu	-0.05 ± 0.03	-0.40	3	-0.06 ± 0.04	-0.39	2	-0.05 ± 0.03	-0.48	5
Si/Al	...	...	...	...	...	...	...	...	...
Si/C	-0.47 ± 0.05	0.39	6	-0.53 ± 0.11	-0.40	3	-0.65 ± 0.07	0.19	7
Mg/Fe	0.50 ± 0.06	-0.18	14	0.60 ± 0.02	0.49	23	0.63 ± 0.02	0.37	43
Mg/Cr	0.52 ± 0.02	0.81	7	0.71 ± 0.15	-0.03	22	0.63 ± 0.02	0.81	12
Mg/Ni	0.53 ± 0.05	0.48	10	0.67 ± 0.04	0.59	16	0.71 ± 0.01	0.77	82
Mg/Zn	-0.42 ± 0.06	0.24	8	-0.39 ± 0.02	-0.87	23	-0.38 ± 0.04	-0.45	9
Mg/P	-0.41 ± 0.04	0.09	10	-0.43 ± 0.02	-0.34	19	-0.36 ± 0.01	-0.60	70
Mg/Co	...	...	...	0.29 ± 0.13	-0.46	2	...	...	...
Mg/Ge	-0.35 ± 0.04	0.08	6	-0.36 ± 0.04	-0.19	10	-0.29 ± 0.01	-0.67	82
Mg/Kr	-0.67 ± 0.05	-0.25	6	-0.81 ± 0.10	-0.28	7	-0.65 ± 0.02	-0.61	59
Mg/Cl	-0.69 ± 0.10	-0.57	4	-0.63 ± 0.08	-0.15	9	-0.59 ± 0.03	-0.54	41
Mg/Cu	-0.07 ± 0.07	-0.28	3	0.03 ± 0.04	-0.40	9	0.13 ± 0.02	-0.33	58
Mg/Al	...	...	...	...	...	...	...	...	...
Mg/C	-0.55 ± 0.06	-0.14	6	-0.47 ± 0.12	0.23	5	-0.71 ± 0.08	0.36	8
S/Fe	1.18 ± 0.05	0.17	4	0.96 ± 0.22	-0.93	2	...	...	...
S/Cr	...	...	...	0.92 ± 0.15	-0.90	2	...	...	...
S/Ni	1.23 ± 0.09	0.65	1	...	...	...	...	...	...

Table 5.4: continued

[X/Y]	[Si/Ti]			[Zn/Fe]			[Ge/Ni]		
	C_{XY}	r_{XY}	ν_{XY}	C_{XY}	r_{XY}	ν_{XY}	C_{XY}	r_{XY}	ν_{XY}
S/Zn	...	...	...	-0.14 ± 0.25	-0.99	2	...	...	...
S/P	-0.06 ± 0.05	-0.42	2	-0.01 ± 0.08	0.79	1	...	...	...
S/Co	...	...	...	...	...	...	...	...	...
S/Ge	...	...	...	...	...	...	...	...	...
S/Kr	...	...	...	...	...	...	...	...	...
S/Cl	...	...	...	...	...	...	...	...	...
S/Cu	...	...	...	...	...	...	...	...	...
S/Al	...	...	...	...	...	...	...	...	...
S/C	...	...	...	...	...	...	...	...	...
O/Fe	1.20 ± 0.12	0.30	10	1.27 ± 0.05	0.47	18	1.25 ± 0.02	0.81	43
O/Cr	1.16 ± 0.07	0.69	5	1.24 ± 0.07	0.23	17	1.26 ± 0.02	0.91	12
O/Ni	1.25 ± 0.11	0.06	7	1.38 ± 0.07	0.49	12	1.31 ± 0.01	0.89	81
O/Zn	0.30 ± 0.08	0.36	6	0.23 ± 0.05	-0.41	18	0.30 ± 0.05	0.10	9
O/P	0.37 ± 0.05	0.36	8	0.28 ± 0.04	-0.14	16	0.26 ± 0.01	0.16	68
O/Co	...	...	...	...	...	...	...	...	...
O/Ge	0.32 ± 0.03	-0.07	6	0.32 ± 0.03	-0.03	9	0.30 ± 0.01	0.09	81
O/Kr	-0.01 ± 0.00	0.47	5	-0.04 ± 0.02	-0.34	6	-0.01 ± 0.01	-0.18	58
O/Cl	0.00 ± 0.06	0.24	4	0.00 ± 0.05	0.12	9	0.06 ± 0.02	0.00	39
O/Cu	0.56 ± 0.07	-0.96	3	0.70 ± 0.04	0.03	9	0.71 ± 0.01	0.40	60
O/Al	...	...	...	...	...	...	...	...	...
O/C	0.03 ± 0.01	0.34	6	0.05 ± 0.01	-0.10	5	0.00 ± 0.04	0.58	8
Fe/Ti	0.49 ± 0.04	0.94	18	0.43 ± 0.04	0.07	28	0.50 ± 0.04	0.40	31
Fe/Si	-0.60 ± 0.04	-0.40	18	-0.56 ± 0.03	0.08	13	-0.54 ± 0.02	-0.70	8
Fe/Mg	-0.50 ± 0.06	0.18	14	-0.60 ± 0.02	-0.49	23	-0.63 ± 0.02	-0.37	43
Fe/S	-1.18 ± 0.05	-0.17	4	-0.96 ± 0.22	0.93	2	...	...	...
Fe/O	-1.20 ± 0.12	-0.30	10	-1.27 ± 0.05	-0.47	18	-1.25 ± 0.02	-0.81	43
Cr/Ti	0.42 ± 0.02	0.70	8	0.48 ± 0.20	0.06	26	0.42 ± 0.03	0.66	9
Cr/Si	-0.57 ± 0.02	-0.79	8	-0.55 ± 0.05	0.30	11	-0.58 ± 0.04	0.72	2
Cr/Mg	-0.52 ± 0.02	-0.81	7	-0.71 ± 0.15	0.03	22	-0.63 ± 0.02	-0.81	12
Cr/S	...	...	...	-0.92 ± 0.15	0.90	2	...	...	...
Cr/O	-1.16 ± 0.07	-0.69	5	-1.24 ± 0.07	-0.23	17	-1.26 ± 0.02	-0.91	12
Ni/Ti	0.41 ± 0.03	0.67	11	0.38 ± 0.04	-0.01	20	0.34 ± 0.02	0.27	44
Ni/Si	-0.61 ± 0.03	-0.77	11	-0.63 ± 0.06	-0.16	7	-0.64 ± 0.03	-0.54	8
Ni/Mg	-0.53 ± 0.05	-0.48	10	-0.67 ± 0.04	-0.59	16	-0.71 ± 0.01	-0.77	82
Ni/S	-1.23 ± 0.09	-0.65	1	...	...	...	...	...	...
Ni/O	-1.25 ± 0.11	-0.06	7	-1.38 ± 0.07	-0.49	12	-1.31 ± 0.01	-0.89	81
Zn/Ti	1.38 ± 0.07	0.70	10	1.44 ± 0.04	0.72	28	1.39 ± 0.04	0.87	9
Zn/Si	0.42 ± 0.06	-0.12	10	0.47 ± 0.04	0.94	13	0.44 ± 0.09	0.31	3
Zn/Mg	0.42 ± 0.06	-0.24	8	0.39 ± 0.02	0.87	23	0.38 ± 0.04	0.45	9

Table 5.4: continued

[X/Y]	[Si/Ti]			[Zn/Fe]			[Ge/Ni]		
	C_{XY}	r_{XY}	ν_{XY}	C_{XY}	r_{XY}	ν_{XY}	C_{XY}	r_{XY}	ν_{XY}
Zn/S	...	...	...	0.14 ± 0.25	0.99	2	...	...	...
Zn/O	-0.30 ± 0.08	-0.36	6	-0.23 ± 0.05	0.41	18	-0.30 ± 0.05	-0.10	9
P/Ti	1.38 ± 0.05	0.84	11	1.43 ± 0.06	0.48	18	1.40 ± 0.02	0.90	37
P/Si	0.40 ± 0.04	-0.09	11	0.41 ± 0.02	0.62	10	0.37 ± 0.04	0.52	6
P/Mg	0.41 ± 0.04	-0.09	10	0.43 ± 0.02	0.34	19	0.36 ± 0.01	0.60	70
P/S	0.06 ± 0.05	0.42	2	0.01 ± 0.08	-0.79	1	...	...	...
P/O	-0.37 ± 0.05	-0.36	8	-0.28 ± 0.04	0.14	16	-0.26 ± 0.01	-0.16	68
Co/Ti	...	...	...	0.83 ± 0.18	0.30	2	...	...	...
Co/Si	...	...	...	...	...	...	...	...	...
Co/Mg	...	...	...	-0.29 ± 0.13	0.46	2	...	...	...
Co/S	...	...	...	...	...	...	...	...	...
Co/O	...	...	...	...	...	...	...	...	...
Ge/Ti	1.23 ± 0.05	0.86	6	1.43 ± 0.09	0.53	10	1.35 ± 0.02	0.90	44
Ge/Si	0.30 ± 0.05	-0.65	6	0.38 ± 0.02	0.84	3	0.36 ± 0.03	0.45	8
Ge/Mg	0.35 ± 0.04	-0.08	6	0.36 ± 0.04	0.19	10	0.29 ± 0.01	0.67	82
Ge/S	...	...	...	...	...	...	...	...	...
Ge/O	-0.32 ± 0.03	0.07	6	-0.32 ± 0.03	0.03	9	-0.30 ± 0.01	-0.09	81
Kr/Ti	1.60 ± 0.09	0.87	6	1.82 ± 0.17	0.32	7	1.70 ± 0.03	0.83	35
Kr/Si	0.59 ± 0.07	-0.55	6	0.80 ± 0.06	0.82	3	0.74 ± 0.04	0.37	7
Kr/Mg	0.67 ± 0.05	0.25	6	0.81 ± 0.10	0.28	7	0.65 ± 0.02	0.61	59
Kr/S	...	...	...	...	...	...	...	...	...
Kr/O	0.01 ± 0.00	-0.47	5	0.04 ± 0.02	0.34	6	0.01 ± 0.01	0.18	58
Cl/Ti	1.56 ± 0.10	0.75	5	1.49 ± 0.10	0.48	9	1.59 ± 0.05	0.78	22
Cl/Si	0.66 ± 0.09	0.10	5	0.74 ± 0.10	0.44	3	0.78 ± 0.05	0.85	2
Cl/Mg	0.69 ± 0.10	0.57	4	0.63 ± 0.08	0.15	9	0.59 ± 0.03	0.54	41
Cl/S	...	...	...	...	...	...	...	...	...
Cl/O	-0.00 ± 0.06	-0.24	4	-0.00 ± 0.05	-0.12	9	-0.06 ± 0.02	-0.00	39
Cu/Ti	1.01 ± 0.04	0.91	3	1.00 ± 0.05	0.78	10	0.93 ± 0.03	0.81	33
Cu/Si	0.05 ± 0.03	0.40	3	0.06 ± 0.04	0.39	2	0.05 ± 0.03	0.48	5
Cu/Mg	0.07 ± 0.07	0.28	3	-0.03 ± 0.04	0.40	9	-0.13 ± 0.02	0.33	58
Cu/S	...	...	...	...	...	...	...	...	...
Cu/O	-0.56 ± 0.07	0.96	3	-0.70 ± 0.04	-0.03	9	-0.71 ± 0.01	-0.40	60
Al/Ti	...	...	...	...	...	...	...	...	...
Al/Si	...	...	...	...	...	...	...	...	...
Al/Mg	...	...	...	...	...	...	...	...	...
Al/S	...	...	...	...	...	...	...	...	...
Al/O	...	...	...	...	...	...	...	...	...
C/Ti	1.47 ± 0.05	0.62	6	1.72 ± 0.20	0.16	5	1.85 ± 0.10	-0.18	6
C/Si	0.47 ± 0.05	-0.39	6	0.53 ± 0.11	0.40	3	0.65 ± 0.07	-0.19	7

Table 5.4: continued

[X/Y]	[Si/Ti]			[Zn/Fe]			[Ge/Ni]		
	C_{XY}	r_{XY}	ν_{XY}	C_{XY}	r_{XY}	ν_{XY}	C_{XY}	r_{XY}	ν_{XY}
C/Mg	0.55 ± 0.06	0.14	6	0.47 ± 0.12	-0.23	5	0.71 ± 0.08	-0.36	8
C/S	...	...	...	...	...	...	...	...	...
C/O	-0.03 ± 0.01	-0.34	6	-0.05 ± 0.01	0.10	5	-0.00 ± 0.04	-0.58	8

Notes: [a] C_{XY} is the slope between the reference dust tracer and [X/Y], ν_{XY} the degrees of freedom and r_{XY} the Pearson's correlation coefficients.

6

A HUNT FOR CLOSE PROJECTED QUASAR PAIRS

"Twinkle, twinkle, quasi-star,
Biggest puzzle from afar,
How unlike the other ones,
Brighter than a billion suns."
∼ The Creation of the Universe by George Gamow ∼

During the first year of my PhD, I conducted a side project to astrometrically select and observe candidate close projected QSO pairs. The aim was to evaluate the efficiency of astrometric selection of QSOs in identifying and classifying QSOs that have been missed by spectroscopic surveys, like the Sloan Digital Sky Survey (SDSS). Creating large samples of classified QSOs is important for understanding the clustering of quasars on small scales and the ISM along close lines of sight. Particularly interesting cases can be selected from these samples, for follow-up high-resolution observations. The follow-up high-resolution observations are valuable for studies of the chemical enrichment of the ISM, for example, observing absorption lines through closely spaced lines of sight can provide detailed information about variations in the ISM and its chemical composition. In this Chapter, I briefly describe the project, target selection and results.

Due to their great cosmological importance, numerous surveys are dedicated to the selection and study of QSOs. A common objective of these surveys is to obtain complete and unbiased samples of the QSO population. In order to achieve that, several color selection techniques have been proposed, but they all suffer from different kinds of biases. For example, some surveys manage to achieve high completeness by identifying QSOs in a wide range of redshifts, but with high contamination from stars due to their similar colors (e.g., Richards et al., 2006). Others limit the contamination from stars by using stricter color cuts, but miss a significant population of QSOs (e.g., Maddox et al., 2008).

With the launch of ESA's Gaia satellite, offering unprecedented accuracy, another characteristic of QSOs can be used: their zero proper motion in the sky relative to stars. Using a combination of astrometric criteria, such as proper motion and parallax from Gaia, as well as, photometry from the optical (SDSS), the near-infrared (UKIDSS), and the mid-infrared (WISE) surveys, it has been shown that it is possible to minimize stellar contamination (e.g., Heintz, Fynbo, and Høg, 2015; Heintz et al., 2018; Geier et al., 2019). Using these combination criteria, hundreds of QSOs have been identified including some rare findings

- serendipitous discoveries of physical QSO pairs with angular separation in the sky <10 arcsec (e.g., see Heintz et al., 2016; Altamura et al., 2019). In those discoveries, the second member of the QSO pair was coincidentally placed on the slit during the target acquisition of its companion. The number of known QSO pairs with separation <10 arcsec in SDSS at the time was only 30 (Pâris et al., 2018), and the serendipitous discovery of not just one, but two QSO pairs with such small separation, suggests that the number of these unusually close binaries is significantly underestimated. Moreover, the two members of the QSOs have significantly different optical colors. While traditionally, QSO pairs have been selected based on their similar optical colors, these discoveries demonstrate that they can also be found with different colors and, therefore, in such cases, photometric selection which is based on QSO colors is not efficient. In addition, fiber spectroscopy (such as SDSS, DESI, WEAVE and 4MOST) is limited in how close they can place fibers. Therefore, closely separated QSOs are missed by such surveys due to fiber collision. For example, the fiber collision radius for SDSS is about 55 arcsec. This means that if two objects are closer than 55 arcsec on the sky, only one of them can be observed spectroscopically in a single observation. Future surveys have smaller collision radii, for example the 4-metre Multi-Object Spectrograph Telescope (4MOST) has a fiber collision radius of ∼15 arcsec, which still is not close enough for these cases of close projected pair QSOs.

6.1 TARGET SELECTION

The purpose of this study is to spectroscopically confirm QSO pairs with separation <10 arcsec in a color-unbiased sample of candidates from Gaia, to explore their potentially underestimated numbers, and to evaluate Gaia-assisted QSO selection. To achieve this, I applied astrometric criteria during the target selection, specifically using parallax and proper motion criteria from Gaia DR2 (Pâris et al., 2018) and early DR3 (Gaia Collaboration et al., 2021). The objects are first extracted from a catalog of 1,172,157 QSO candidates selected from the photometric imaging data of SDSS DR6 (Richards et al., 2009). The objects are selected to have a close companion (< 10 arcseconds) using the nearest neighbors algorithm and focused on sources with r < 20 mag.

The extracted objects were then shortlisted to those flagged as non-moving targets and those not previously spectroscopically confirmed. The second phase involved cross-matching with SDSS DR12 to exclude pairs both spectroscopically confirmed after the release of SDSS DR6 (Richards et al., 2009), and cross-matching with Gaia DR2 and EDR3 (Gaia Collaboration et al., 2018, 2021) to apply the parallax and proper motion criteria. Specifically, candidates were selected to have zero parallax within 2σ uncertainty and proper motions consistent with zero within 3σ uncertainty. The final list includes 22 candidate QSO pairs, that have none or only one of the members spectroscopically confirmed.

6.2 OBSERVATIONS WITH THE NORDIC OPTICAL TELESCOPE

In period 62 (2020 Oct 1 - 2021 Apr 1) I was awarded 19 hours of observing time (62-020; PI: Konstantopoulou) at the 2.5m Nordic Optical Telescope (NOT), operated by the Spanish

Observatorio del Roque de los Muchachos in La Palma. As part of this proposal, I obtained spectra of candidate close projected QSO pairs using the low resolution spectrograph Alhambra Faint Object Spectrograph and Camera (ALFOSC). Grism #4 was used, that covers the wavelength range from 3200 Å to 9600 Å and 1.0" or 1.3" slit depending on the seeing. To avoid second order contamination blocking filter #94 was used. The aim was to achieve a signal-to-noise ratio (SNR) of at least 10 for r-band magnitude at 6500 Å. I secured the spectra on two nights (29/01/2021 and 30/01/2021), under variable observing conditions. As the primary purpose of the observations is to classify the targets, and not to derive detailed properties (e.g. abundances or precise stellar parameters), high signal-to-noise is not required. It was thus possible to use spectra obtained under poor conditions as long as the nature of the targets can be concluded. I calculated the exposure times calculated accordingly. I chose the slit orientation with a parallactic angle (PA) that allows both quasars to be in the same slit and be observed simultaneously. This approach makes observations highly efficient and saves valuable telescope time. In total, 22 candidate pair QSOs were observed. I also obtained bias, flat field and arc frames, required for calibration, each night. In Table 6.1, the observations log is provided for all targets.

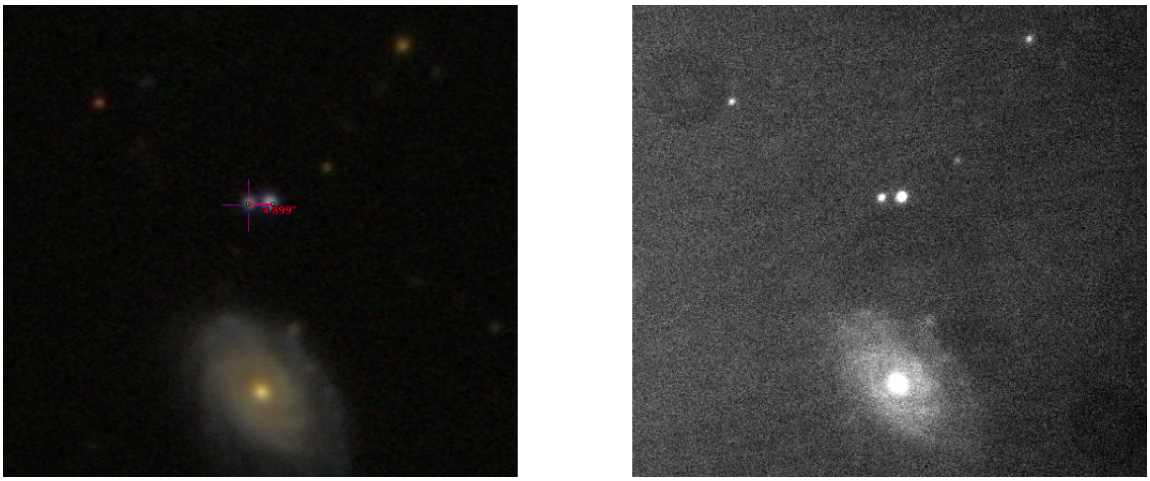


Figure 6.1: Observation of the pair QSOs J0836+4841A and J0836+4841B. (Left:) Aladin image cutout on the QSO pair J0836+4841. The cross is centered on J0836+4841A and the arrow shows the projected distance of the two QSOs on the sky, which is d = 4.899". (Right:) Cutout of the NOT image acquisition of the QSO pair J0836+4841. The orientation is chosen so that both of the QSOs are aligned in the same slit.

Target	Slit	Seeing	r (mag)	d (arcsec)	PA (deg)	Exptime
SP0305+261	1, 1.3	1, 1.4	8	-	-	2x15
SP0644+375	1, 1.3	1	12.1	-	-	2x150
J0728+2607AB	1.3	1.3, 1.4	19.82, 18.84	2.25	197.09	2x1200
J0753+1734AB	1	1.2, 1.3	19.35, 20.06	4.14	131.80	1x1200, 1x1500
J0811+0825AB	1.3	1.6	19.67, 19.99	4.26	260.20	2x1200
J0811+1527AB	1	1.1	18.88, 19.53	5.89	202.30	2x1000
J0836+4841AB	1.3	1	18.39, 19.18	4.04	190.80	2x1000
J0902+2816AB	1.3	1.3, 1,1	19.27, 18.37	8.35	98.10	2x1200
J0920+1311AB	1.3	1.6, 1.4	19.22, 19.49	6.21	146.60	2x1200
J0922−0117AB	1	0.97, 0.87	18.94, 19.72	6.10	179.40	2x1000
J0930+4200AB	1.3	1.7	19.32, 19.85	5.35	156.90	2x1200
J1114+1549AB	1	0.9, 0.7	19.87, 19.79	8.79	124.00	2x1000
J1125+3256AB	1.3	1.6	18.90, 19.10	7.07	112.80	2x1000
J1148+0936AB	1	0.8	17.96, 19.74	8.73	217.60	2x1000
J1151+3156AB	1.3	1.6	19.39, 19.21	8.56	159.10	2x900
J1215+0225AB	1	1	19.69, 19.16	5.98	195.60	2x1000
J1301+0536AB	1	0.9	18.94, 18.89	7.13	254.10	2x900
J1430+1539AB	1.3	1.9	19.66, 19.73	5.30	143.60	2x1000
J1433+1450AB	1	1	19.15, 19.40	3.57	140.00	2x900
J1510+3741AB	1	1	19.38, 19.66	5.83	211.20	2x900
J1558+5742AB	1.3	1.5	18.99, 19.69	5.83	172.20	2x1000
J1649+1733AB	1	1.04, 1.2	19.58, 19.16	3.79	232.70	2x900
J1657+2117AB	1.3	1.8	18.83, 18.67	6.85	186.80	2x1000
j1713+5530AB	1.3	1.4	18.60, 18.65	5.94	113.40	2x1000

Table 6.1: Observations log for the 22 pair QSOs and flux standard stars.

6.3 DATA REDUCTION

I performed the data reduction using standard procedures mostly in IRAF,[1] but also using similar procedures written in Python[2]. I flux calibrated the spectra using observations of spectrophotometric standard stars, observed on the same nights as the science targets.

Bias frames are used to correct for electronic readout noise from the CCD detector. To create a master bias, I obtained 44 bias frames and then inspected for overscan regions, which are areas not exposed to light. I computed the median of the overscan region and subtracted from the rest of the image pixels. I then combined these bias frames using IRAF to produce a master bias, reducing readout noise and providing an accurate estimate of the bias level. I subsequently subtracted the master bias from the raw images.

Flat fields correct for pixel-to-pixel variations in the CCD caused by different quantum efficiencies. For this, I obtained 15 halogen lamp flat frames (dome flats). After subtracting the master bias from these flat frames, I combined them to create a master flat. I then normalized this master flat by dividing by the mean pixel value, resulting in a frame with average pixel values close to one.

Cosmic ray removal is another important step, as cosmic ray hits can affect image quality. This is addressed by iteratively correcting each of the two exposures of each spectrum using IRAF, since cosmic rays typically do not affect all exposures simultaneously. The two bias-subtracted, flat, and cosmic ray-corrected frames of each object are then combined to improve the quality of spectrum extraction. Figure 6.2 shows a part of the spectrum of QSO J0836++4841 before and after cosmic ray removal.

The extraction process involves defining apertures around the object and tracing the 2D spectrum. I performed variance-weighted optimal extraction, assigning different weights to different parts of the spectrum, and average background subtraction is done after defining background regions around the object. This results in the extraction of the 1D spectrum. The final reduced 2D spectrum is shown in Figure 6.3.

Wavelength calibration is performed by assigning each pixel of the dispersion axis to the corresponding wavelength. This is achieved using HeNe arc lamps, which I obtained immediately before each target observation. I identified emission lines in the arc frames using ALFOSC arc maps[3] for He and Ne of grism #4, and the calibrated arc spectrum serves as a reference for calibrating the quasar spectra. Finally, flux calibration determines the system sensitivity as a function of wavelength. This is done using the spectral flux of standard stars observed with the same telescope setup as the science frames, and applying atmospheric extinction corrections.

1 The Image Reduction and Analysis Facility (IRAF) is distributed by the National Optical Astronomy Observatory, which is operated by the Association of Universities for Research in Astronomy (AURA) under a cooperative agreement with the National Science Foundation.

2 https://github.com/christinakonst/Data-Reduction

3 http://www.not.iac.es/instruments/alfosc/lamps/

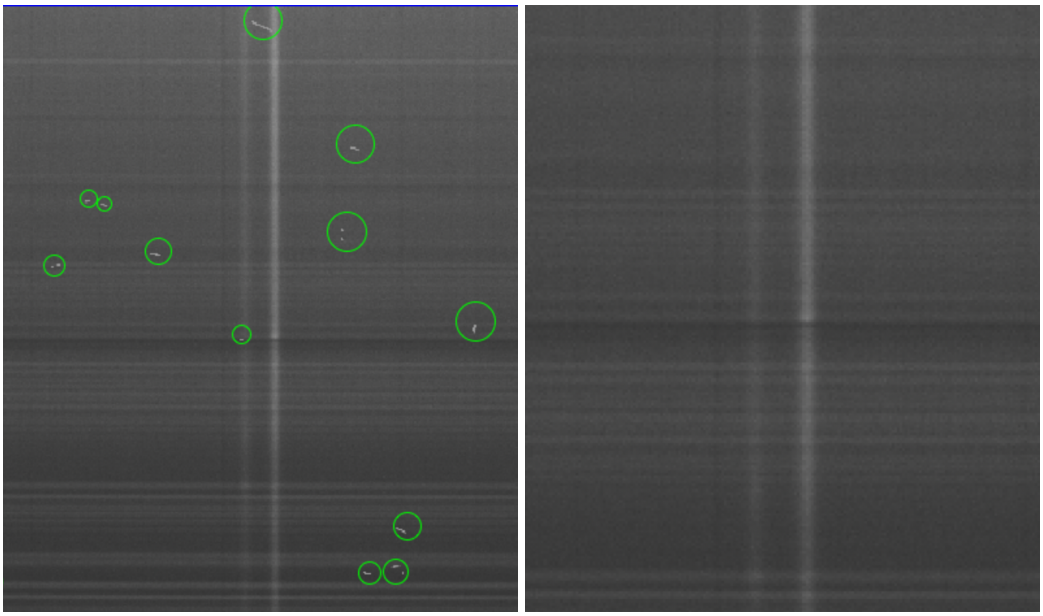


Figure 6.2: Cutout of the spectrum of J0836++4841 before (left panel) and after (right panel) cosmic ray removal. Cosmic ray hits are marked in green circles in the left panel.

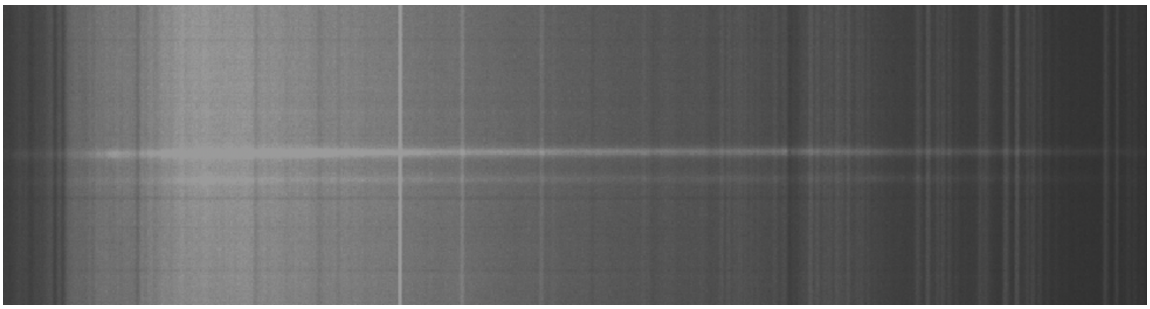


Figure 6.3: The reduced 2D spectrum of J0836++4841 before sky subtraction. The spectrum is 90° rotated.

6.4 RESULTS

6.4.1 *Spectroscopic confirmation of quasar pairs*

Quasars can be identified by the presence of strong broad emission lines in their spectra. I determined the redshifts of these QSOs by visually identifying prominent emission lines in the spectrum of each target and measuring their shifted wavelengths. I then confirmed the estimated redshifts by fitting the composite QSO template by Selsing et al. (2016) to each spectrum. The redshift range of the spectroscopically confirmed QSOs is $0.22 < z < 3.55$ with seperations $2.1 < d < 8.79$ arcsec. Out of the 44 individual spectroscopically confirmed QSOs in this work, only 17 were previously confirmed by SDSS, while out of the 22 QSO pairs, only three pairs had both QSOs confirmed by SDSS, indicating that 86% of the observed QSO pairs were newly discovered pairs in this work.

I explore the possibility that some of the observed QSO pairs gravitationally lensed by visually inspecting and comparing their features (redshift, emission lines, flux). Five QSO pairs have identical redshifts and features, suggesting they might be lensed QSOs. However, a more thorough analysis of their spectra would be needed to confirm this. Figure 6.4 shows the offsets in redshifts between the observed QSO pairs in relation to the projected separation of the QSO pairs. It is evident that the possible lensed QSOs are clustered at $\Delta z \sim 0$. Although there are more QSO pairs that exhibit $\Delta z \sim 0$, I do not consider them possible lenses, since their spectra show differences. J0811+1527B is the highest redshift QSO in the sample at z = 3.55. The largest offset in redshifts is observed between J1558+5742A and J1558+5742B with $\Delta z = 2.51$. Although the initial selection is done based on a large photometric catalog of 1,172,157 candidate quasars, this does not exclude the possibility of stellar contamination. As a result, the initial catalog by Richards et al. (2009) also contains stellar sources. To address stellar contamination we applied astrometric selection criteria, which successfully secured a clean sample of QSO candidates with no stellar contaminants.

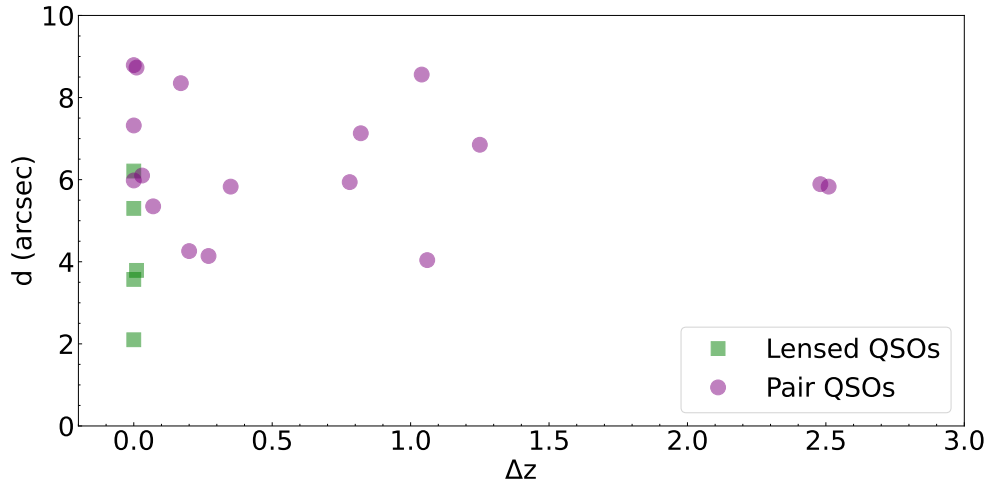


Figure 6.4: Spectroscopic redshift offset Δz between the observed pairs with respect to the seperation d. Purple triangles show the confirmed pair QSOs, while the green squares are possible lensed QSOs.

6.4.2 *Dust extinction*

For each quasar, I determine the line-of-sight visual extinction (A_V, the extinction in the V-band) as follows. I fit the quasar composite spectrum from Selsing et al. (2016) to the observed spectra and to the available photometry from SDSS and UKIDSS (u, g, r, i, z, Y, J, H, Ks bands). I then scale the spectra to the SDSS photometric r-band and normalize to the wavelength range 5700-6600 Å. This approach improves the representation of the spectra by excluding points blueward of Lyman-α and any other areas with strong absorption.

Target	RA (deg)	DEC (deg)	Redshift z	A_V
J0728+2607A	07:28:27.747	+26:07:01.304	1.02	0
J0728+2607B	07:28:27.876	+26:07:02.550	1.02	0
J0753+1734A	07:53:39.863	+17:34:10.660	1.23	0
J0753+1734B	07:53:40.080	+17:34:07.980	0.96	0
J0811+0825A	08:11:56.137	+08:25:58.100	1.16	0.7
J0811+0825B	08:11:56.414	+08:25:58.792	0.96	0
J0811+1527A	08:11:24.192	+15:27:49.249	1.07	0
J0811+1527B	08:11:24.332	+15:27:54.674	3.55	0
J0836+4841A	08:36:49.459	+48:41:50.104	0.65	0
J0836+4841B	08:36:49.557	+48:41:54.062	1.71	0
J0902+2816A	09:02:08.611	+28:16:05.554	0.79	0
J0902+2816B	09:02:09.223	+28:16:04.430	0.62	0
J0920+1311A	09:20:56.010	+13:11:02.690	2.44	0.2
J0920+1311B	09:20:56.238	+13:10:57.469	2.44	0.2
J0922−0117A	09:22:17.533	-01:17:55.768	1.67	0
J0922−0117B	09:22:17.537	-01:17:49.738	1.70	0
J0930+4200A	09:30:15.022	+42:00:33.680	1.20	0
J0930+4200B	09:30:14.824	+42:00:38.689	1.27	0
J1114+1549A	11:14:33.763	+15:49:49.802	1.77	0.6
J1114+1549B	11:14:34.262	+15:49:44.856	1.77	0
J1125+3256A	11:25:01.374	+32:56:22.804	1.30	0.2
J1125+3256B	11:25:01.906	+32:56:19.908	1.30	0
J1148+0936A	11:48:36.045	+09:36:53.300	1.41	0
J1148+0936B	11:48:36.401	+09:37:00.060	1.40	0
J1151+3156A	11:51:29.839	+31:56:41.628	0.89	0
J1151+3156B	11:51:30.053	+31:56:33.850	1.93	0
J1215+0225A	12:15:46.721	+02:25:58.066	1.44	0
J1215+0225B	12:15:46.622	+02:25:52.516	1.44	0
J1301+0536A	13:01:32.941	+05:36:37.550	1.29	0
J1301+0536B	13:01:32.511	+05:36:35.116	0.47	0
J1430+1539A	14:30:03.889	+15:39:49.398	0.91	0
J1430+1539B	14:30:03.563	+15:39:45.236	0.91	0
J1433+1450A	14:33:50.942	+14:50:08.168	1.51	0
J1433+1450B	14:33:51.086	+14:50:05.575	1.51	0
J1510+3741A	15:10:55.971	+37:41:24.215	0.96	0
J1510+3741B	15:10:55.732	+37:41:19.343	1.31	0
J1558+5742A	15:58:13.037	+57:42:06.465	3.02	0
J1558+5742B	15:58:13.133	+57:42:00.584	0.51	0
J1649+1733A	16:49:29.000	+17:33:08.557	2.08	0
J1649+1733B	16:49:28.791	+17:33:06.494	2.09	0
J1657+2117A	16:57:16.932	+21:17:52.168	1.47	0
J1657+2117B	16:57:17.005	+21:17:58.335	0.22	0
j1713+5530A	17:13:34.418	+55:30:50.243	2.06	0
j1713+5530B	17:13:35.042	+55:30:47.789	1.28	0

Table 6.2: Spectroscopically confirmed QSOs, the estimated redshifts and dust extinction A_V.

The observed flux of the spectra is affected by intervening Milky Way dust, so Galactic extinction corrections are applied to all the spectra and photometry to retrieve the original flux of the targets. I perform these corrections using the SFD dust maps (Schlegel, Finkbeiner, and Davis, 1998) and taking into account the color excess $E(B-V)$ values, which indicate the amount of dust. I calculate the $E(B-V)$ value of each target using the SFD maps based on the Galactic coordinates of each target. I determine the intrinsic dust extinction in the rest-frame of the QSO using the SMC extinction curve parameterized by Pei (1992). I compare the redshifted and reddened model to the data to obtain the best-fitting A_V. The fitting function covering all wavelengths is

$$\xi(\lambda) = A_0 + \sum_{i=1}^{6} \frac{a_i}{\left(\frac{\lambda}{\lambda_i}\right)^{n_i} + \left(\frac{\lambda_i}{\lambda}\right)^{n_i} + b_i} \tag{6.1}$$

where A_0 is the flux of the composite spectrum in microns (rest-frame) scaled to zero. Taking into account the estimated extinction A_V of the V photometric band, the extinction A_λ at a wavelength λ is expressed as

$$A_\lambda = \xi(\lambda) \cdot A_V \tag{6.2}$$

and finally the model of the flux of the reddened composite spectrum is given by

$$F_{model} = (10^{-0.4 \cdot A_\lambda}) \cdot F_c \tag{6.3}$$

where F_c is the flux of the composite spectrum (unreddened) at a given wavelength, with the wavelength expressed in microns.

The conversion from r-band magnitudes to flux is given by

$$F_r = 10^{0.4(-48.6-r)} \cdot \frac{3 \cdot 10^{18}}{\lambda_r} \tag{6.4}$$

where the wavelength λ_r is in Å and the converted flux F_r is expressed in erg cm^{-2} s^{-1} Å^{-1}. The spectra of the QSO pair J1125+3256AB at z = 1.3 is shown in Figure 6.5. All the resulting reduced and analyzed spectra of the pair QSOs are presented in the Appendix B.

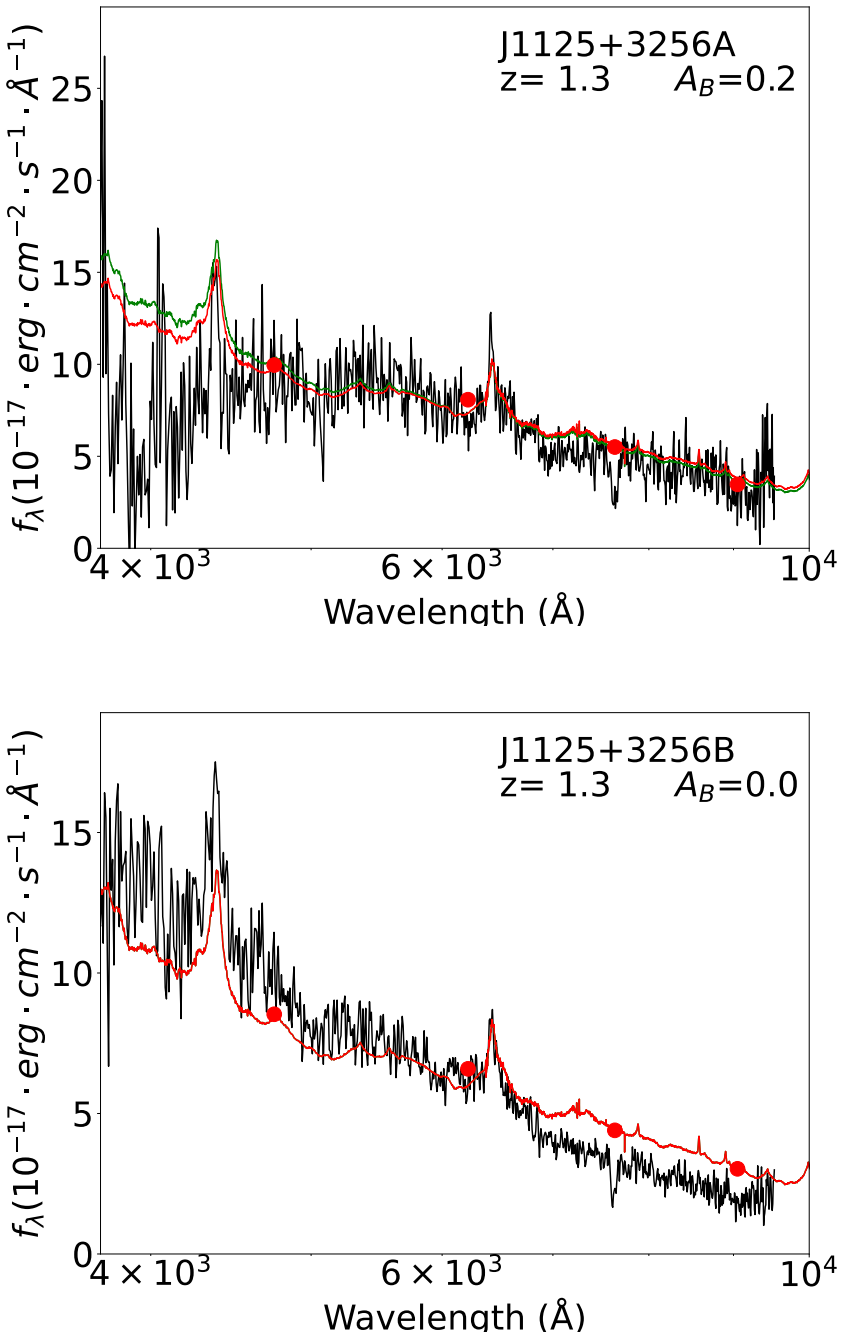


Figure 6.5: The spectra of the two members of the QSO pair J1125+3256AB at z = 1.3. (Top panel:) The spectrum of QSO J1125+3256A is in black, the composite QSO template in green and the reddened composite template in red. The dust extinction is determined to be A_V = 0.2. The red filled circles are the photometric points of the u, g, r, i, z, Y, J, H, Ks bands, from SDSS and UKIDSS. (Bottom panel:) The spectrum of QSO J1125+3256B at the same redshift (z = 1.3) but with no dust extinction (A_V = 0).

6.4.3 *Efficiency of astrometric selection in identifying QSO pairs*

All the targets that were observed as part of this work have measured photometric redshifts from Richards et al. (2009). In Fig. 6.6 the photometric redshifts from Richards et al. (2009) are compared to the spectroscopic redshift determinations from this work. The agreement is overall very good, with few outliers. Pair QSOs previously confirmed spectroscopically by SDSS DR16 are marked with green hexagons. Out of the 22 pair QSOs, only three (J1125+3256AB, J1510+3741AB, and J1558+5742AB) have been confirmed by SDSS. These pairs have projected separations d = 7.32, 5.83 and 5.83 arcsec respectively. This highlights the efficiency of astrometric selection in identifying sources missed by other photometric surveys, like SDSS, due to fiber collisions that prevent distinguishing closely separated objects (closer than 55 arcsec). The fiber collision radius for 4MOST is only 15 arcsec. However, even with the small collision radius of 4MOST, it would still not be possible to observe such closely separated quasar candidates unless one observes multiple times the same region of the sky (Krogager et al., 2023).

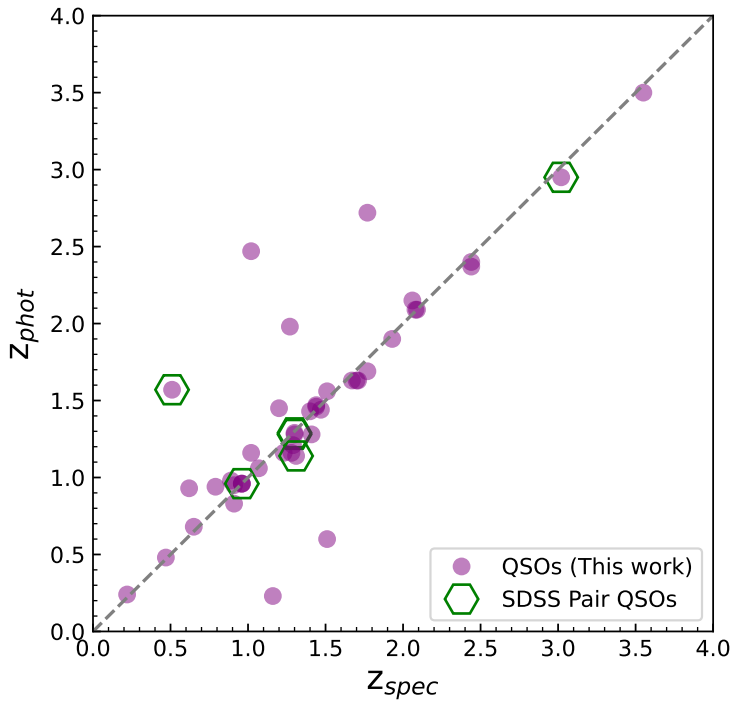


Figure 6.6: Comparison between the photometric redshifts estimated by Richards et al. (2009) and the spectroscopic redshifts determined in this work. The purple filled circles show the pair QSOs observed as part of this work and the green empty hexagons indicate the pair QSOs that have already been detected by SDSS DR16.

6.4.4 *The special configuration of a close projected pair of QSOs*

This project highlights the importance of creating clean catalogs of QSOs and discovering new ways to select them. From such catalogs, interesting objects can be identified and studied in greater detail with follow-up higher-resolution observations. From this sample of pair QSOs, we have identified a unique case of QSO pairs with a special configuration. Specifically, QSOs J0820+0357A and J0820+0357B, at redshifts of $z = 1.56$ and $z = 1.87$, respectively, are separated by an angular distance of only 6.5″ on the sky (corresponding to 57 kpc at $z = 1.56$). The spectra of both quasars show absorption from a foreground galaxy at $z_{\rm abs} = 1.175$ as well as absorption lines related to the quasar at $z = 1.56$ (see Fig. 6.7). The projected separation at the redshift of the foreground galaxy at $z_{\rm abs} = 1.175$ corresponds to $\sim$55 kpc. By further studying this galaxy we can obtain important information about the chemical enrichment of the CGM. This is a rare configuration for the pair QSOs, as it is the only such case out of the 22 close quasar pairs observed.

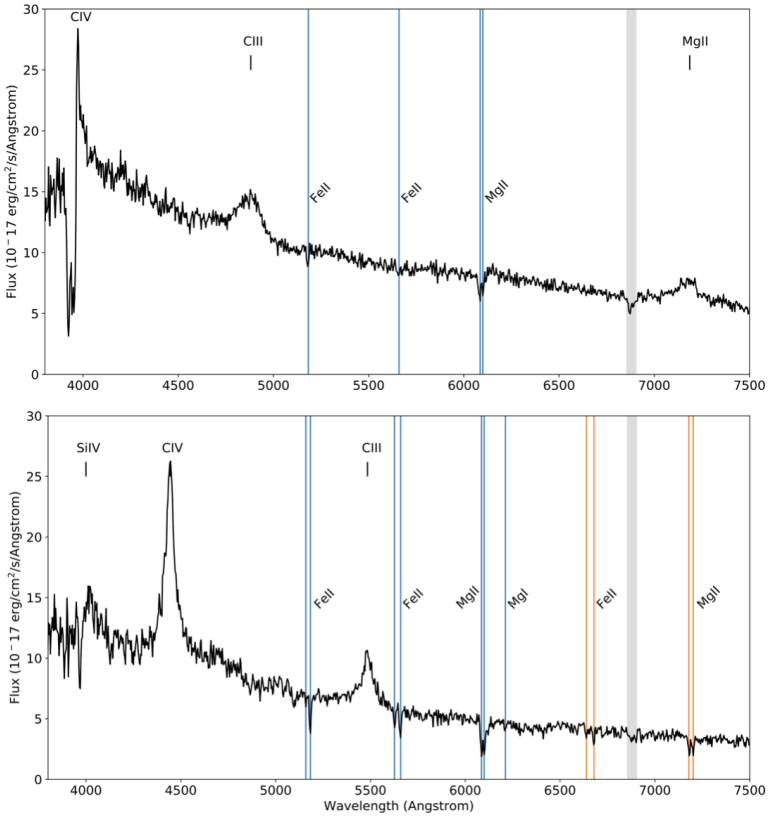


Figure 6.7: The observed NOT spectra of the QSO pair: The top left panel shows the QSO J0820+0357B at $z = 1.87$ and the bottom left panel shows the QSO J0820+0357A at $z = 1.56$. The observed NOT spectra of the QSO pair: The top panel shows the QSO J0820+0357B at $z = 1.87$ and the bottom panel shows the QSO J0820+0357A at $z = 1.56$. Marked with blue lines are the absorption features seen in both lines of sight at $z_{\rm abs} = 1.175$. The orange dashed lines show the absorption features at the redshift of the foreground QSO ($z_{\rm abs} = 1.56$). Telluric absorption is marked by the grey shaded area at $\sim$ 6880 Å.

In addition, the quasar at $z = 1.56$, J0820+0357A, shows broad, blue-shifted C IV absorption, indicating an outflow from the central engine. We observe absorption from C IV, Mg II and Fe II in the second line of sight at a transverse separation of ∼57 kpc at this redshift $z = 1.56$, indicating metal-enriched gas spread out over large distances. Therefore, this unique QSO pair can be used to study the chemical enrichment of the CGM in two separate environments, the foreground galaxy and the quasar outflow, both along two close different lines of sight simultaneously. It is important to highlight that this particular case does not represent typical DLAs, like the ones studied in this thesis. Unlike typical DLAs, which are selected or identified by strong HI absorption seen in the spectra of background QSOs, this configuration involves a QSO pair which can be used to study the CGM through different lines of sight.

6.5 CONCLUSIONS

Using astrometric selection and observations of 22 close projected QSO pairs with the NOT, I spectroscopically confirmed all observed candidates as QSO pairs. Except for three, these pairs were missed by spectroscopic surveys like SDSS due to fiber collision constraints. This study highlights the efficiency of astrometric selection in identifying quasars as stationary objects, effectively minimizing stellar contamination. Given the significance of QSOs as cosmic probes of the ISM in the distant universe, building clean and extensive catalogs of QSOs is essential. Although conducted on a small scale, this study showcases the potential for expanding to larger astrometric catalogs of QSOs, such as Heintz et al. (2020) and Krogager et al. (2023). Unique objects identified from these catalogs can be then followed up using higher-resolution spectroscopy, and used for detailed studies of the chemical enrichment of the CGM and ISM, using, for example, methods described in Chapters 3 and 5.

This research also identified a rare QSO pair configuration, presenting an opportunity to study the chemical properties of a foreground galaxy at z_{abs} = 1.175 and outflowing gas from the QSOs at z = 1.56. The projected separation at the redshift of the foreground galaxy at z_{abs} = 1.175 corresponds to ∼55 kpc. Observing absorption lines along closely projected lines of sight (e.g., d $\leq$ 10 arcsec) with high resolution spectroscopy offers detailed information about variations in the ISM and its chemical composition, crucial for understanding galaxy evolution and star formation. The findings suggest that the number of closely separated QSO pairs is significantly underestimated, emphasizing the importance of astrometric selection for discovering such pairs, with limited contaminations by stars. Expanding this approach to larger astrometric catalogs will not only enhance the completeness of QSO samples but also provide invaluable insights of the processes dominating gas outflows and gas accretion around galaxies, which is fundamental for the understanding of galaxy evolution and star formation..

7

CONCLUSIONS AND FUTURE PERSPECTIVES

"I've done the math enough to know
The dangers of our second guessing
Doomed to crumble unless we grow
And strengthen our communication."
∼ Schism by Tool ∼

During my PhD I conducted research that mainly aimed at characterizing dust depletion in different galactic environments. This work involved assembling and homogenizing a comprehensive dataset of column densities of metals for local and distant galaxies, allowing for the development of new methodologies with the goal of shedding light into the properties of cosmic dust and unraveling the secrets of dust depletion. In this section, I will summarize my work on dust depletion, described in the main chapters of this thesis, and finally I will outline potential future perspectives in the study of chemical enrichment of the ISM.

7.1 SUMMARY AND CONCLUSIONS

The work in this thesis focuses on the characterization of the dust depletion from the (relative) abundances in the gas of local and distant galaxies used to investigate the properties of cosmic dust. To achieve this, I have used an extensive collection of data from the literature as well as additional new column density measurements that I obtained through absorption-line spectroscopy. By analyzing the absorption lines in spectra from bright background sources, such as QSOs, GRBs, or stars, one can eventually obtain in great detail the abundances and relative abundances of various elements in the gas inside and around different galaxies. This method is valuable for studying both local and distant galaxies, offering unique insights into the chemical enrichment of their gas. The high resolution of instruments like UVES at the VLT and STIS at the HST are important for identifying and measuring the absorption lines accurately. During my PhD, I analyzed the UVES spectra from 70 QSO-DLAs, using Voigt-profile fitting, and specifically the software VoigtFit. In Chapter 2, I described the technique of absorption-line spectroscopy, highlighted its importance and presented in detail the functionality of VoigtFit. Voigt-profile fitting is particularly effective in analyzing absorption lines, allowing for precise determination of the column densities of various metals, which in turn can be used for metal abundance

estimates. In my case, instead of metal abundances, I estimated relative abundances of metals, which are used extensively in this thesis. These are vital for understanding the effects of dust depletion and how it can be used to characterize the properties of cosmic dust.

Dust depletion significantly affects the observable metal abundances in the ISM of galaxies, because metals are incorporated into dust grains. Therefore, it is important to characterize it and build dust depletion schemes that include extensive amounts of metals and galactic environments. Using absorption-line spectroscopy, the column densities of 18 metals where determined in the Milky Way, LMC, SMC, QSO- and GRB-DLAs. During my PhD, I measured the column densities of NiII and TiII in 70 QSO-DLAs and the rest were measured in previous studies (Ledoux, Bergeron, and Petitjean, 2002; Jenkins, 2009; Berg et al., 2015; De Cia et al., 2016; Roman-Duval et al., 2021; De Cia et al., 2021; Bolmer et al., 2019) for OI, CII, ClII, KrI, SII, SiII, MgII, MnII, ZnII, PII, CrII, GeII, CoII, AlII, CuII, FeII, NiII and NiII. Additionally, I updated all the compiled column densities to the newest, at that time, oscillator strengths to homogenize the sample. As presented in Chapter 3, featuring Konstantopoulou et al. (2022, Paper I), I used these column densities to measure relative abundances of metals and examine their trends with the dust tracer [Zn/Fe]. I estimated the dust depletion of the 18 metals in different galactic environments (the Milky Way, LMC, SMC, QSO- and GRB-DLAs) using the relative abundances, instead of abundances of metals that have commonly been used in the past (e.g., Savage and Sembach, 1996; Jenkins, 2009; Roman-Duval et al., 2021). The usage of relative abundances allows for the characterization of dust depletion without the need to assume a certain metallicity for the gas, and also allows to include distant galaxies (e.g., QSO- and GRB-DLAs) on the same scale of dust depletion strength as local ones (Milky Way, Magellanic Clouds). This is particularly important, because the metallicity of the gas is often not known, for example for QSO-DLAs, which is a mixed bag of galaxies with different metallicities and masses. Overall, this paper uses the methodology of De Cia et al. (2016), but expands it to more metals and environments.

The discovery of linear relations between the depletion of metals with the dust tracer [Zn/Fe], the so-called depletion sequences, across different galactic environments, offers intriguing insights about the origin of cosmic dust (De Cia et al., 2016). The continuous trends of dust depletion suggest that the dominant dust production mechanism is common. Given that the dust production mechanism is common, this mechanism cannot be related to the specific star-formation history of galaxies, This is because different galaxies exhibit different star-formation histories, yet they share the same dust depletion sequences. This highlights the importance of grain growth in the ISM as a significant process of dust production, because grain growth depends on the physical conditions in the ISM regardless of the star-formation history of galaxies. Furthermore, we observed peculiar nucleosynthesis effects in the Magellanic Clouds. Specifically, we observed a potential deviation from linearity in the dust depletion sequences for Ti, Mg, S, and Mn in the Magellanic Clouds. This observed overabundance of α-elements and Mn underabundance is systematic for these elements and therefore, might be due to nucleosynthesis effects that we did not take into account in our initial assumptions. Instead, when we assumed a constant α-element enhancements and Mn underabundance in the Magellanic Clouds, these deviations disappear and the

dust depletion sequences are linear and the same for all galaxies. These nucleosynthesis effects that we observed are potentially caused by recent bursts of star-formation in the Magellanic Clouds. This was further confirmed by De Cia et al. (2024), who characterized the α-element enhancements from the study of the abundance patterns in individual lines of sight toward the Magellanic Clouds. Finally, in Konstantopoulou et al. (2023) (Section 3.E), I updated the P column densities from Paper I, using the newest possible oscillator strengths and removed duplicate entries in the QSO-DLA sample.

The compilation of a large amount of column densities, for several metals, and for a wide range of galactic environments allowed me to further discover the properties of dust. In Chapter 4, I presented my work from Konstantopoulou et al. (2024, Paper II), which is built up on my previous work (Paper I) on dust depletion of several elements. I utilized the dust depletion estimates from Paper I to derive, based on dust depletion, the cosmic dust-to-metal ratio (DTM), the dust-to-gas ratio (DTG), dust extinction and dust composition across different galactic environments. Enriching the previous sample with new GRB-DLA column density measurements from Heintz et al. (2023) and Saccardi et al. (2023), I expanded the sample to $z = 6.3$, enabling the study of the dust properties at even higher redshifts. We developed a new method for the derivation of the DTG, DTM, and dust composition in terms of mass and by using all the metals that contribute into dust and gas. We found that the DTM and DTG ratios increase with the overall amount of dust (as traced by [Zn/Fe]) and with metallicity. We find DTM ratios that increase with metallicity, indicating that grain growth in the ISM is a dominant process of dust production, in the warm neutral ISM that we are probing. This is due to the fact that grain growth in the ISM is metallicity dependent, while stellar dust production shows a constant DTM with metallicity according to dust production and evolution models, such as in Mattsson et al. (2014). The observed trends of DTM and DTG ratios with metallicity are in good agreement with the analytic dust production and evolution model by Mattsson (2020). Moreover, we found that the stellar dust yield is significantly lower than previously estimated, contributing about 1% compared to the metals yield. Overall, we observe a high DTM ratio for dustier and higher metallicity systems, such as in the Milky Way. However, in environments with high metallicity and large amounts of cold dense gas (and as a result high pressure), like in the Milky Way disk, the increase of the DTM ratio is less steep, implying a less pronounced dependence of the DTM ratio with metallicity.

Additionally, I used dust depletion to derive the dust composition, defined as the fraction of dust mass contributed by element X. The results highlight the presence of variations in dust composition depending on the environment's dust content, with the main elements contributing to the dust being, by mass, O, Fe, Si, Mg, C and to a smaller extent S, Ni, and Al, for all the galactic environments. In the least dusty regime, we found that O is three times more abundant in dust than Si, which suggests the presence of pyroxenes ($Mg_xFe_{(1-x)}SiO_3$) as main dust species. In addition, I estimated the dust extinction (A_V) using dust depletion. Comparing to the dust extinction that is estimated from SED, we found an overall agreement between the two estimates of A_V. However, we found a discrepancy in the two measurements, for a few systems in the LMC and SMC and for most systems in the Milky Way. This discrepancy is associated with lines of sight that exhibit the 2175Å feature in the spectra. The 2175Å is related to the presence of C-rich dust, or

carbonaceous dust, and specifically PAHs. As such, a likely cause in the discrepancy is the presence of C-dust in clumps of cold dense gas, which we do not probe with dust depletion. I also investigated the cosmic metallicity evolution of the neutral gas with redshift, using QSO- and GRB-DLAs. The cosmic metallicity evolution of the neutral gas is decreasing with redshift and there is a good agreement between the fits of the two groups. This might suggest that QSO-DLAs and GRB-DLAs arise from a similar population of galaxies, or that they might probe the neutral gas in the Universe in a similar way.

In Chapter 5, I described DUNE - a Dust Depletion UNified method across cosmic time and Environments. In this project I introduced a comprehensive method to characterize dust depletion by analyzing the correlations among the relative abundances of 17 metals across various galactic environments (the Milky Way, LMC, SMC, QSO- and GRB-DLAs). The development of DUNE was motivated by the need to reconcile the two main existing dust depletion methods, the F_* method developed by Jenkins (2009) and the relative method developed by De Cia et al. (2016). While both methods have significantly advanced our understanding of dust depletion and the properties of dust, they also have limitations that DUNE aims to overcome. The F_* method is based on the observation of the abundances of all available metals, which correlate among each other, also because of dust depletion. This method uses observed abundances of metals to estimate the overall strength of depletion, as a proxy for the depletions of metals, having to assume a fixed metallicity for the gas of the galaxy. This introduces limitations for the expansion of the method to diverse galactic environments and also prevents the study of potential variations in metallicity of the gas, or nucleosynthesis signatures. The relative method uses observed relative abundances of metals, enabling the application of the method to distant galaxies, as well as the possibility to study variations in metallicity of the gas and nucleosynthesis signatures. However, the relative method relies on a specific and possibly not ideal dust tracer like [Zn/Fe], making its application challenging in environments with varying nucleosynthetic histories.

With DUNE, we provide a unified approach to accurately estimate the dust depletion of individual elements δ_x and the overall strength of depletion Δ, by combining the strengths of the previous methods (Jenkins, 2009; De Cia et al., 2016) and overcoming their limitations. Different elements have different tendencies in depleting into dust grains, so that their relative abundances can trace the overall dust content. We call these dust tracers. Unlike previous methods, which need to rely on a single dust tracer or assume a fixed metallicity, DUNE uses all possible relative abundances that qualify as dust tracer, which correlate among each other. Then I do a multi-dimensional analysis of 70 dust tracers among different galactic environments (the Milky Way, LMC, SMC, QSO- and GRB-DLAs). For the development of DUNE, I have combined a large literature sample of 528 lines of sight in different galactic environments, compiling column density measurements of the 17 metals in their dominant ionization state: OI, CII, ClII, KrI, SII, SiII, MgII, ZnII, PII, CrII, GeII, CoII, AlII, CuII, FeII, TiII and NiII. An important principle of DUNE is that we do not mix α-elements and non-α elements, so that the dust tracers are not affected by α element enhancement. After assessing the correlation strength among the different dust tracers, and filtering out weak correlations, I performed linear regression fits to the valid correlations. I estimated the overall strength of depletion, Δ, by summing the weighted contribution by

all dust tracers. The overall strength of depletion, representing the collective contribution of the depletion of all elements, increases with the amount of dust. Additionally, I estimated the dust depletion of Cl, P, Ni, Cu, Cr, Zn, Ge, Fe, C, O, Si, Mg, Ti and Kr, refining their dust depletion coefficients. Finally, I provided simple guidelines for the different applications of DUNE. Specifically, I offer examples of the study of abundance, metal and relative metal patterns and how the user can simply utilize them to derive the overall strength of depletion, metallicity and potential deviations of individual elements from linearity, hinting nucleosynthesis effects. Overall, DUNE's strength lies in the ability to be applied universally in different galactic environments. By avoiding assumptions regarding α-element enhancement and metallicity variations, DUNE is not affected by nucleosynthesis effects and metallicity assumptions, offering a unified method that acknowledges the complexity and diversity of galactic environments. DUNE is thus applicable to diverse galactic environments without relying on simplifying assumptions, making it a powerful tool for the study of dust depletion in a wide range of galaxies.

In the first year of my PhD, I conducted a side project, using observations of my accepted telescope proposal at the Nordic Optical Telescope (NOT). In this project, which I describe in Chapter 6, I investigated close projected QSO pairs using astrometric selection criteria to identify and spectroscopically confirm such QSO pairs that have been missed by surveys like the SDSS. The study aims at evaluating the strength of astrometric selection of QSOs and spectroscopically confirm close projected QSO pairs ($<$ 10arcsec). I detail the observations with the NOT as well as the data reduction of the observed 22 candidate QSO pairs. I spectroscopically confirmed the candidates, as either QSO pairs or possible gravitational lenses, highlighting the efficiency of astrometric selection. I describe the identification process of their redshifts and dust reddening. Most of these pairs were missed by SDSS due to fiber collision constraints. With this project I emphasize the importance of using astrometric data to build extensive and unbiased QSO catalogs. Additionally, from this sample, I showcase a rare QSO pair configuration, which allows for detailed study of the chemical properties of a foreground galaxy and outflowing gas from QSOs, potentially contributing to our understanding of the ISM and galaxy evolution. My analysis suggests that the number of closely separated QSO pairs is significantly underestimated and highlights the need for expanding the astrometric approach to create large QSO catalogs. This will enable the discovery of missed QSOs, and follow-up studies with large telescopes, such as the VLT, revealing the chemical properties of galaxies through several lines of sight.

The main focus of my PhD has been to characterize the dust depletion as well as to study the properties of cosmic dust in a wide range of galactic environments. This work has facilitated further studies of the ISM of galaxies, including the study of the ISM in GRB afterglows at the reionization epoch (Saccardi et al., 2023), the componenent-by-component analysis of the gas in distant galaxies (Ramburuth-Hurt et al., 2023), the cosmic buildup of dust and metals using GRBs (Heintz et al., 2023), the study α-element enhancement and metallicity determinations in the LMC and SMC (De Cia et al., 2024) and the α-element enhancement in the gas of distant galaxies (Velichko et al., 2024).

7.2 OPEN QUESTIONS AND FUTURE PERSPECTIVES

The metal enrichment of the gas inside and around galaxies is fundamental to understanding the evolution of galaxies. As research in this direction progresses, it seems clear that an approach using various methodologies, including the depletion of metals into dust grains to understand the abundances of metals as well as the properties of dust, will enable us to unveil the complexities of the ISM of galaxies across cosmic time. In this section, I describe future perspectives in this regard, focusing on the contribution of dust depletion and other complementary techniques, as well as upcoming surveys and research programs that have the ambition to advance our knowledge.

The study of dust depletion has been indeed crucial in uncovering the incorporation of metals into dust grains, therefore depleting them from the observed gas-phase of the ISM. As our observational techniques, telescopes and instruments advance, a few things can be anticipated. New instruments, including 4MOST, a second-generation instrument built for ESO's 4.1m Visible and Infrared Survey Telescope for Astronomy (VISTA) telescope, will perform large spectroscopic surveys. It will offer spectra of 2400 objects observed simultaneously in one pointing of the telescope. 4MOST will start operations in 2025 and will conduct both Galactic and Extragalactic surveys. On the extragalactic side, The 4MOST–Gaia Purely Astrometric Quasar Survey (4G-PAQS, PI: Jens-Kristian Krogager), which I am part of, will carry out the first large-scale quasar survey exclusively based on astrometric data from Gaia (Krogager et al., 2023). This survey will provide us with spectra of $\sim$ 1000 DLAs observed at spectral resolution R = 5000-8000, which will be valuable for studying the gas in and around distant galaxies. The main objective of the survey is to quantify the selection effects of color-selected samples. It will quantify the dust bias, improving our view to the chemical enrichment of neutral gas. With the availability of these data, our understanding on dust depletion and the distribution of metals in these galaxies will advance. In particular, having direct access to these data, I will be able to expand the application of DUNE, described in Chapter 5, to this extended dataset, to refine the characterization of dust depletion of several elements at a larger and diverse sample of galaxies, the derivation of gas-phase metallicities in different galaxies and the identification and quantification of α-element enhancement. At the same time, the Gaia mission has revolutionized astrometric data, offering precise measurements of proper motion and parallax. The Gaia Data release 4 (DR4) which is expected not before mid 2026, will refine the identification of stationary objects, such as QSOs, improving the selection of targets for dust depletion studies.

The HST remains the only telescope that is able to provide us with high resolution UV spectroscopy of individual stars in nearby galaxies. As discussed in Section 1.3, by observing bright OB stars in nearby galaxies, one can obtain detailed abundances of metals in the ISM of these galaxies (De Cia et al., 2021; Roman-Duval et al., 2021). Such observations are unique for ISM studies. The HST will possibly remain operational until the mid 2030s, although its future is uncertain. The HST's ambitious program ULLYSES, the Ultraviolet Legacy Library of Young Stars as Essential Standards, (Roman-Duval et al., 2020), has gathered data since 2020 creating a UV spectroscopic library of young high and low mass stars in the local Universe. This legacy program, is designed to deliver

fundamental properties of massive OB stars, such as spectral type, luminosity class, and metallicity, in the Magellanic Clouds and two other lower metallicity nearby galaxies. This will enable not only extended metal abundance studies in the ISM of these galaxies, but also a synergy between stellar and ISM studies, enabling the comparison between stellar and ISM metallicities. A fully complementary to ULYSSES program, is STIS-ISM (PI: Annalisa De Cia, Program ID: GO 17703), which I am part of, is designed to observe at high-spectral resolution massive OB stars in the Milky Way with the aim to investigate the ISM complexity. This will be achieved by conducting in-depth component-by-component analysis of the ISM, based on a comprehensive set of metals from the highest resolution spectra. It will study the diffuse ISM, the cold molecular gas as well as stellar metallicities, providing a legacy dataset. The main goal of this program is to answer the question of whether there are local metallicity variations in the Milky Way ISM. Answering this question will reflect on several astrophysical fields, including the study of the baryon cycle, stellar evolution, GRBs and the formation of stars and planets from gas of different metallicities. The programs that were discussed above will take dust depletion into account. The UV capabilities of HST are, and are expected to remain, unique until the beginning of operations of the NASA's future flagship space telescope, the Habitable Worlds Observatory (HWO).

The HWO (aka "Super Hubble") is the successor of HST and is expected in the 2040's. It will cover wavelength ranges from the UV to the IR and is designed to explore several science themes, contributing to the study of the ISM. Its high spectral resolution and multi-wavelength observations will be valuable for both absorption- and emission-line studies of the ISM in different galaxies. Additionally it will provide UV spectroscopy of hot OB stars in the Milky Way and the Magellanic Clouds, nearby galaxies, as well as distant QSOs. These can be complementary to gas-phase metallicities, giving the opportunity to link individual stars to the material from which they are formed, and therefore infer chemical enrichment processes.

Emission-line spectroscopy may complement absorption studies by providing information concerning different phases of the ISM. A full understanding of the chemical content, distribution and extent of the cool gas surrounding galaxies requires its study both in absorption and emission. Instruments like the Multi Unit Spectroscopic Explorer (MUSE) on the VLT deliver detailed 3D spectroscopy, that allows the study of ionized regions and their chemical composition. MUSE can be used to identify in emission galaxies associated with intervening absorbers (Hennawi and Prochaska, 2013), and can measure emission lines to constrain star formation rates and kinematics of these galaxies. MUSE has also been employed in several absorption studies, such as Schroetter et al. (2016) and Wendt et al. (2021), to observationally probe galaxy orientations, as well as, the distribution of metallicity and the baryon cycle, finding metal-enriched gas, associated with outflows in galaxies. However, its spectral resolution is relatively low compared to other instruments, which can limit the ability to resolve narrow spectral lines. MUSE enables spatially resolved spectroscopy, offering a three-dimensional view of the CGM. This becomes especially valuable for mapping the distribution of metals and understanding the physical processes by which gas is flowing though and around galaxies.

JWST has already opened a new era for high-z galaxy research and has provided new insights into the dust and gas content in the early Universe (Witstok et al., 2023; Heintz et al., 2024). By observing galaxies both in absorption and in emission one can obtain important information about the dust and metal content of the gas in galaxies. With the application of DUNE to metal absorption lines and comparison with JWST emission line data, we can obtain exciting new results. We will be able to characterize the dust depletion and dust properties at high-z, offering new insights into the dust content of these galaxies and into the dust production and destruction mechanisms, which are still unclear in the early Universe.

The ELT, is expected to see first light in the late 2020s and will be equipped with the high-resolution spectrograph ANDES (ArmazoNes high Dispersion Echelle Spectrograph) in the early 2030s. Thanks to the high spectral resolution ($R \sim 100{,}000$) and wavelength coverage from the UV to NIR, ANDES will significantly enhance our understanding of the dust and metal content of the early Universe. Because it will be more sensitive than UVES, ANDES will also allow us to detect less abundant elements (like Kr or Ge), which have not been detected yet in distant galaxies. A comprehensive understanding of dust depletion will be necessary to disentangle the effects of dust and nucleosynthesis of specific stellar populations and signatures from PopIII stars (D'Odorico et al., 2023).

As an extension to this, submillimeter observations will further uncover the nature of cold dust and its interaction with surrounding gas. The Atacama Large Millimeter Array (ALMA) is playing a very important role in the understanding of the cold and dusty components of the Universe, as it provides an unprecedented view on the dust content and of the cold molecular gas of the ISM (Palla et al., 2024; Algera et al., 2024). In the radio regime, the Square Kilometer Array (SKA) will become the largest radio telescope worldwide, aiming at observing the neutral ISM throughout the Universe. Its sensitivity to atomic hydrogen (HI) will allow for detailed studies on the distribution and dynamics of the ISM, including regions heavily affected by dust depletion.

Additionally, developing more sophisticated dust models that incorporate a variety of dust grain types, sizes, and compositions will help in accurately interpreting observational data. These models will account for grain growth in the ISM, destruction processes, and the varying depletion patterns of different elements. Accurate dust models are important for the interpretation of observational data.

The future of the study of the chemical enrichment of gas in and around galaxies is incredibly bright, with numerous developments in observational techniques and data analysis on the horizon. Complementing emission-line with absorption-line spectroscopy, and thus combining the properties of the neutral ISM/CGM/dust in galaxies (from dust depletion) and the properties of stars and ionized-gas in galaxies, will be important for unveiling the processes that drive the chemical evolution galaxies. The extension of current surveys (e.g., ULYSSES), combined with revolutionary future surveys and upcoming missions, telescopes and instruments (e.g., 4MOST, ELT, JWST, HWO), will provide unprecedented data, giving the opportunity to study the details of gas properties across diverse galactic environments and epochs. This will open a new era in the study of the chemical evolution of galaxies over cosmic time.

A

LIST OF PUBLICATIONS

This is the full list of publications I have contributed to during my PhD (as of October 2024).

FIRST AUTHOR

○ "*DUNE: Dust depletion UNified method across cosmic times and Environments*" **Konstantopoulou, C**, De Cia, A., et al. A&A, 691, A129 (2024), featured in Chapter 5.

○ "*Dust depletion from local to distant galaxies II: Dust-to-metal ratio and cosmic dust composition*" **Konstantopoulou, C.**, De Cia, A., Ledoux, C., et al. A&A, 681, A64 (2023), featured in Chapter 4.

○ "*Dust depletion of metals from local to distant galaxies I: Peculiar nucleosynthesis effects and grain growth in the ISM (Corrigendum)*" **Konstantopoulou, C.**, De Cia, A., Krogager, J. -K., et al. A&A, 674, C1 (2023), featured in Section 3.E.

○ "*Dust depletion of metals from local to distant galaxies I: Peculiar nucleosynthesis effects and grain growth in the ISM*" **Konstantopoulou, C.**, De Cia, A., Krogager, J. -K., et al. A&A, 666, A12 (2022), featured in Section 3.

CO-AUTHOR

○ "*The α-element enrichment of gas in distant galaxies*" Velichko, A., De Cia, A., **Konstantopoulou C.**, et al. A&A, 685, A103 (2024)

○ "*α-element enhancements in the ISM of the LMC and SMC: Evidence of recent star formation*" De Cia, A., Roman-Duval, J., **Konstantopoulou C.**, et al. A&A, 683, A216 (2024)

○ "*The cosmic buildup of dust and metals. Accurate abundances from GRB-selected star-forming galaxies at* $1.7 < z < 6.3$, Heintz, K. E., De Cia, A., Thöne, C. C., ..., **Konstantopoulou C.**, et al. A&A, 679, A91 (2023)

○ "*Dissecting the interstellar medium of a* $z = 6.3$ *galaxy. X-shooter spectroscopy and HST imaging of the afterglow and environment of the Swift GRB 210905A*, Saccardi, A., Vergani, S. D., De Cia, A., ..., **Konstantopoulou C.**, et al. A&A, 671, A84 (2023)

- "*Chemical diversity of gas in distant galaxies. Metal and dust enrichment and variations within absorbing galaxies*, Ramburuth-Hurt, T., De Cia, A., Krogager, J. -K., ..., **Konstantopoulou C.**, et al. A&A, 672, A68 (2023)

- "*Addendum: Large metallicity variations in the Galactic interstellar medium*, De Cia, A., Jenkins, E., Fox, A.,..., **Konstantopoulou C.**, et al. Nature, 605, E8 (2022)

- "*Large metallicity variations in the Galactic interstellar medium*, De Cia, A., Jenkins, E., Fox, A.,..., **Konstantopoulou C.**, et al. Nature, 597, 206–208 (2021)

- "*Investigating chemical variations between interstellar gas clouds in the Solar neighbourhood*, Ramburuth-Hurt, T., De Cia, A., Krogager, J. -K., ..., **Konstantopoulou C.**, et al. (submitted to A&A)

B

ADDITIONAL VOIGT-PROFILE FITS

Here I show additional line profiles of QSO-DLAs, which I fit using VoigtFit, but are not published in Konstantopoulou et al. (2022) due to the lack of either Ti, Ni, Zn or Fe detection, which was required for the selection of the sample. The process followed is the same as in Konstantopoulou et al. (2022).

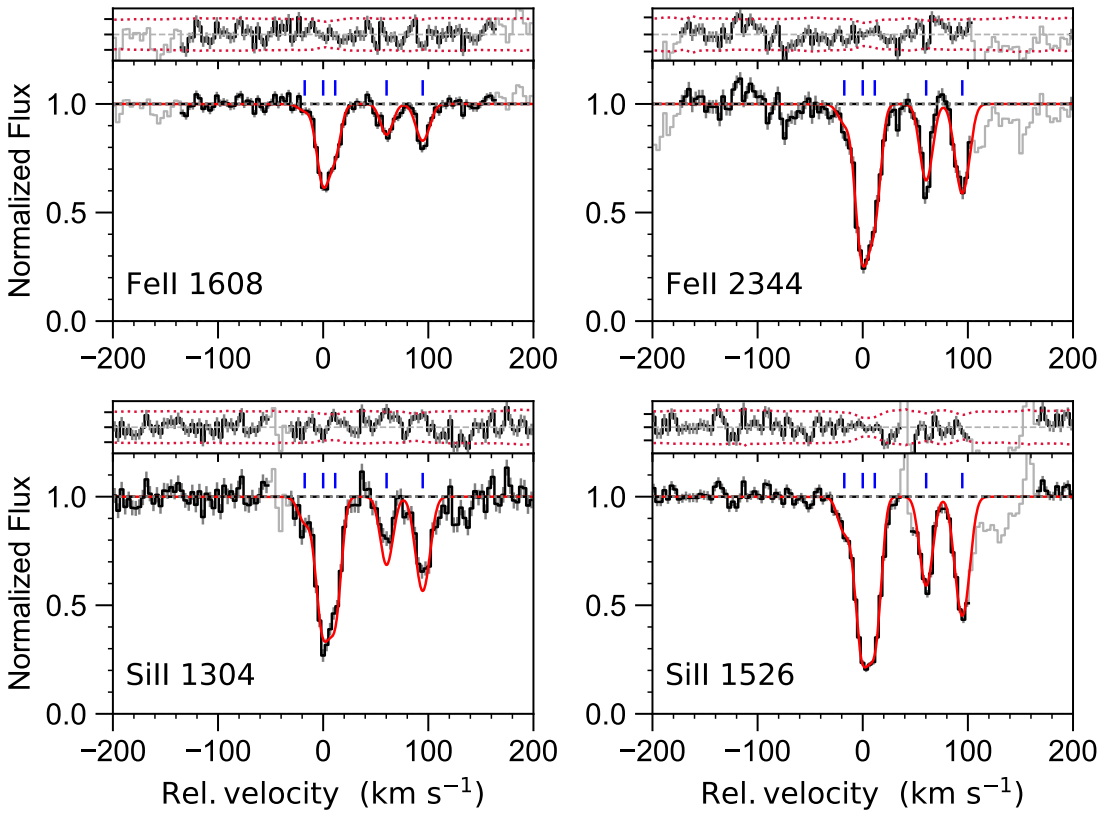


Figure A2.1: Velocity profiles of selected low-ionization transition lines from the DLA system at z_{abs} = 2.92648 toward Q 0102−190. Masked regions are shown in gray. The top subpanels show the residuals, and the blue tick marks show the individual velocity components.

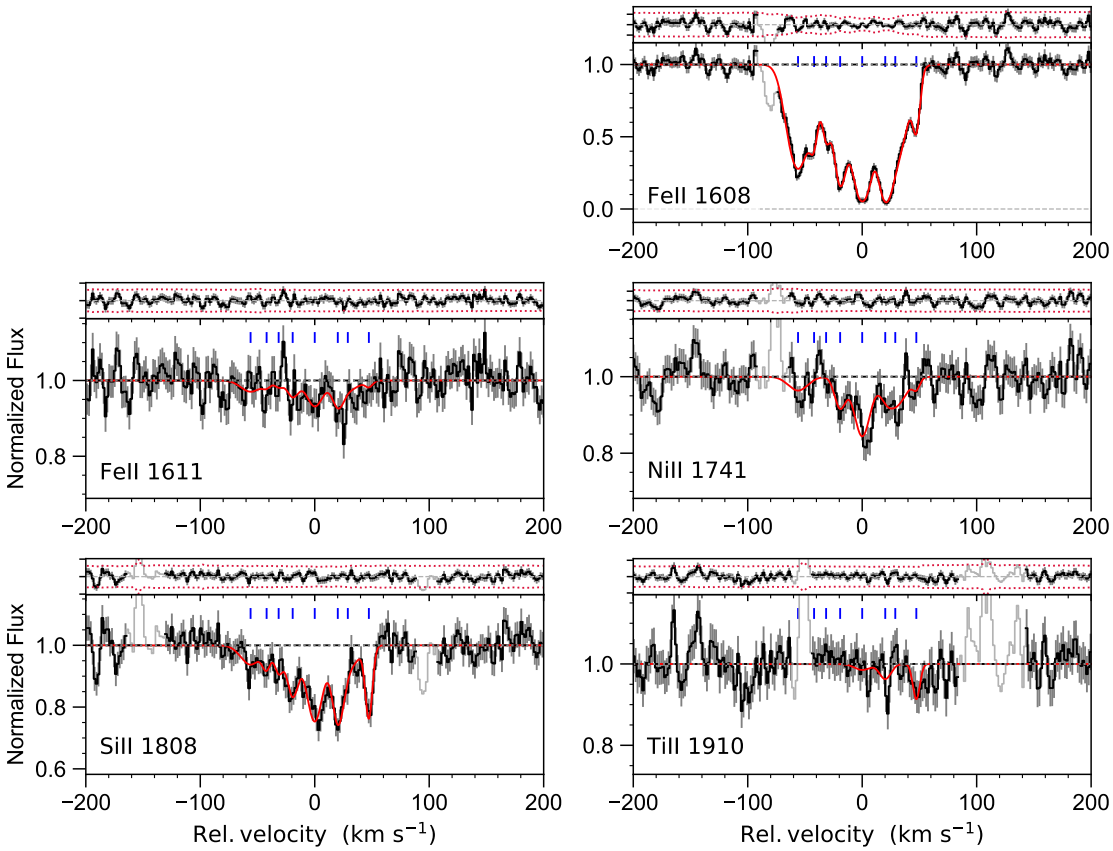


Figure A2.2: Velocity profiles of selected low-ionization transition lines from the DLA system at $z_{\rm abs}$ = 2.42322 toward Q 0112+030.

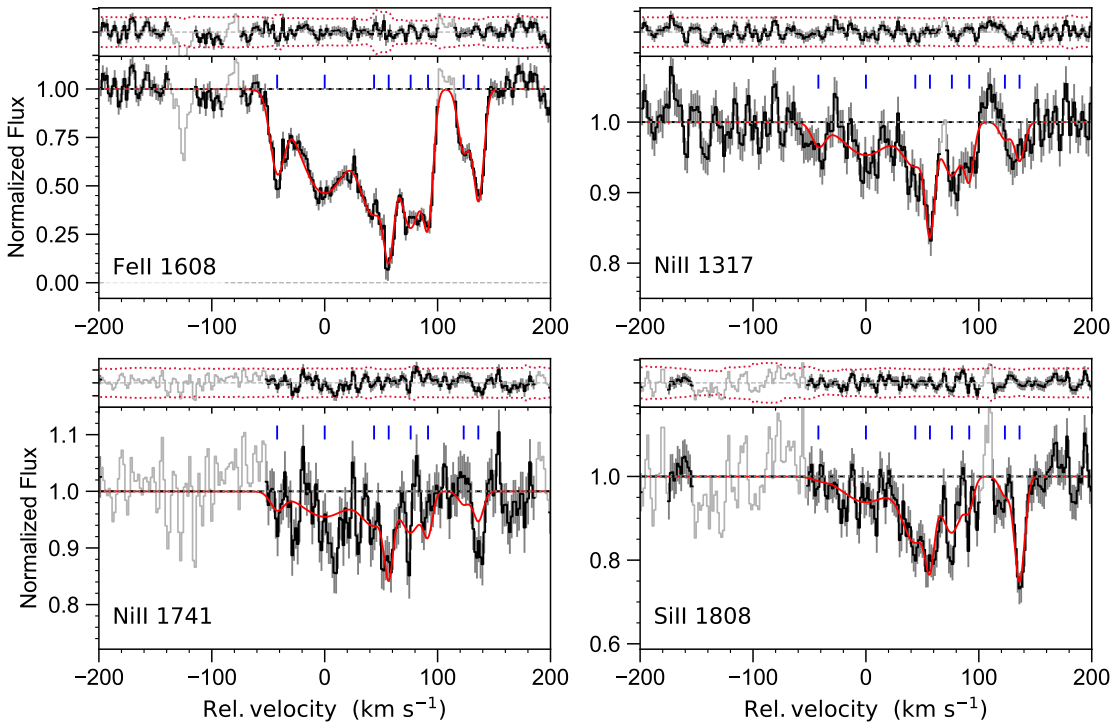


Figure A2.3: Velocity profiles of selected low-ionization transition lines from the DLA system at $z_{\rm abs} = 2.70163$ toward Q 0112−306.

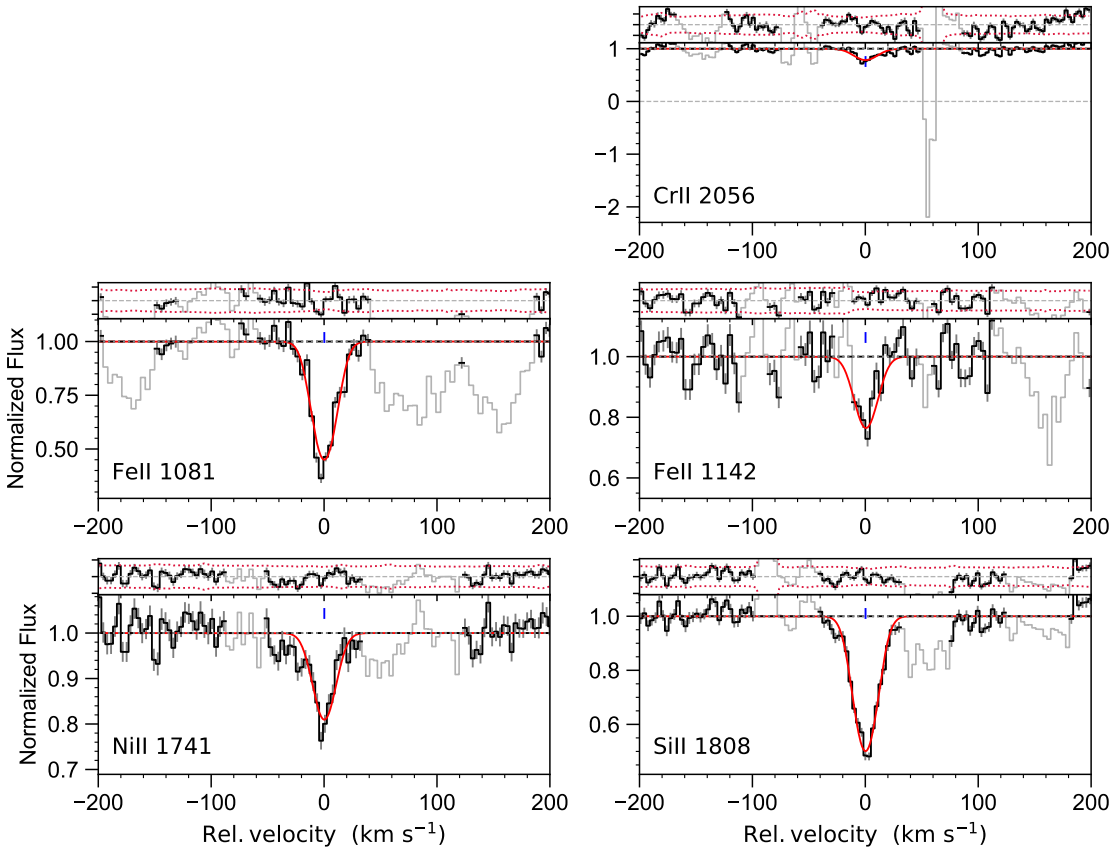


Figure A2.4: Velocity profiles of selected low-ionization transition lines from the DLA system at $z_{\rm abs} = 3.06209$ toward Q 0336−017.

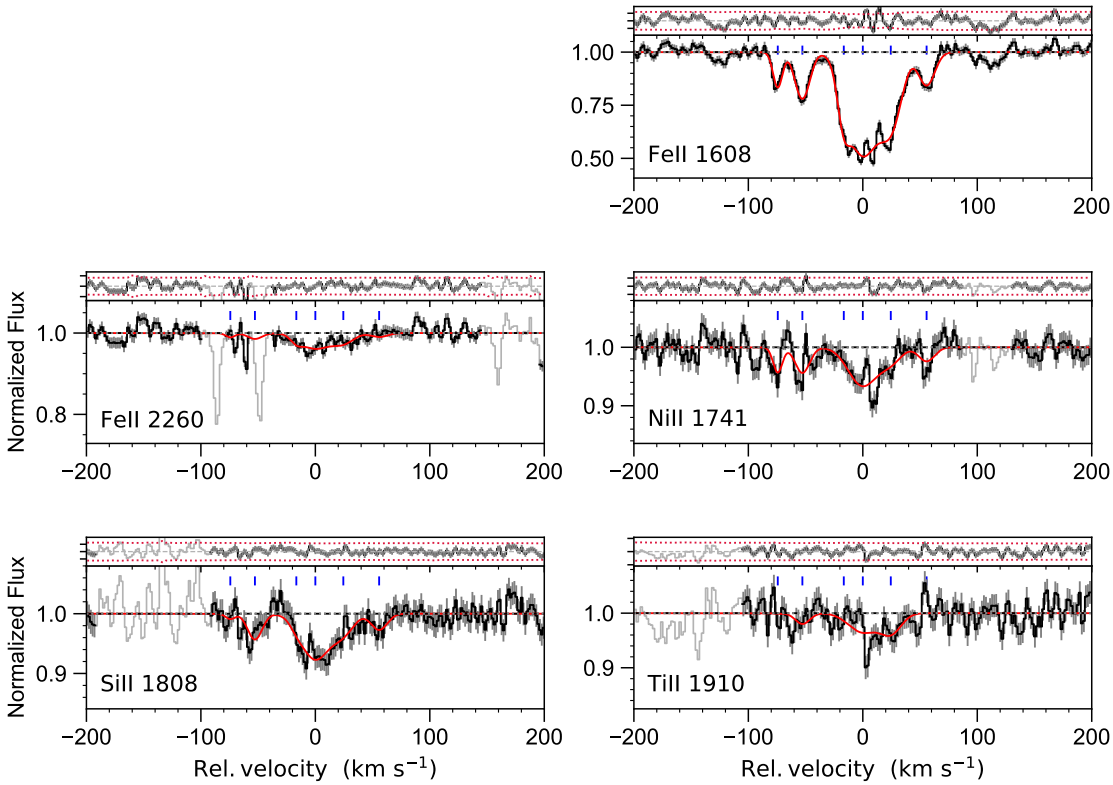


Figure A2.5: Velocity profiles of selected low-ionization transition lines from the DLA system at $z_{\rm abs} = 2.06658$ toward Q 0450−131.

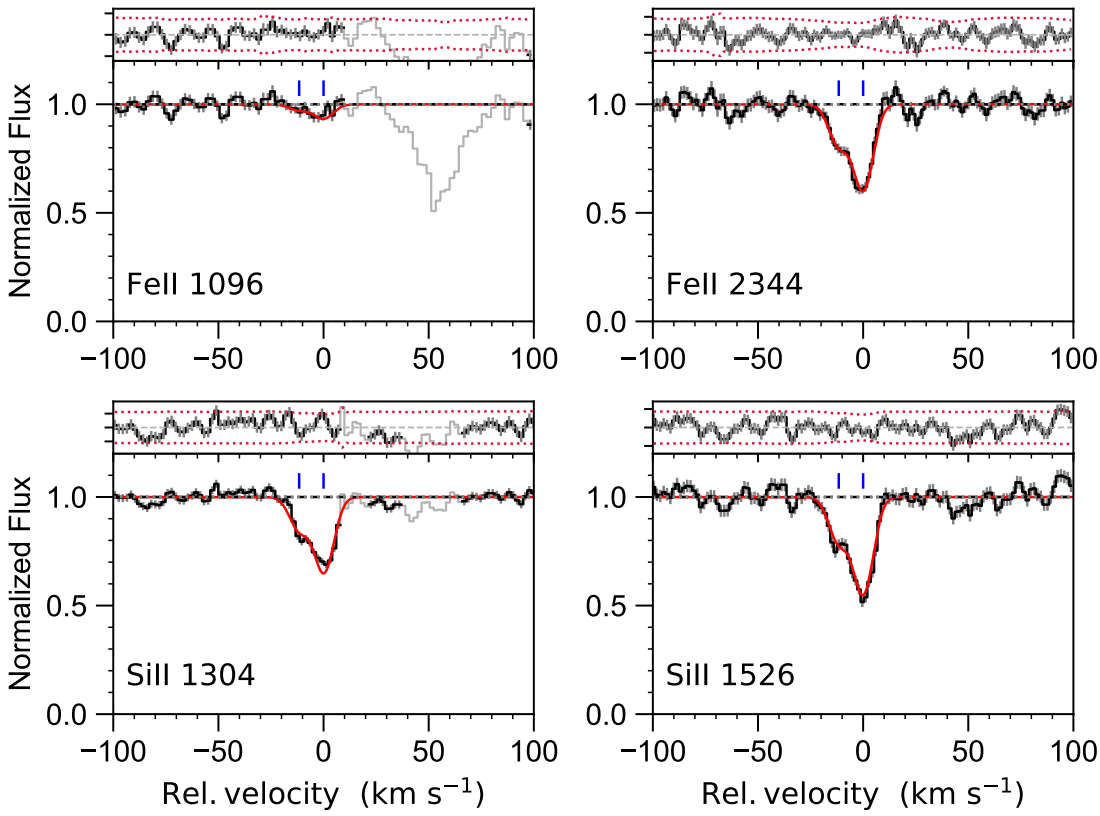


Figure A2.6: Velocity profiles of selected low-ionization transition lines from the DLA system at $z_{\rm abs}$ = 2.61843 toward Q 0913+072.

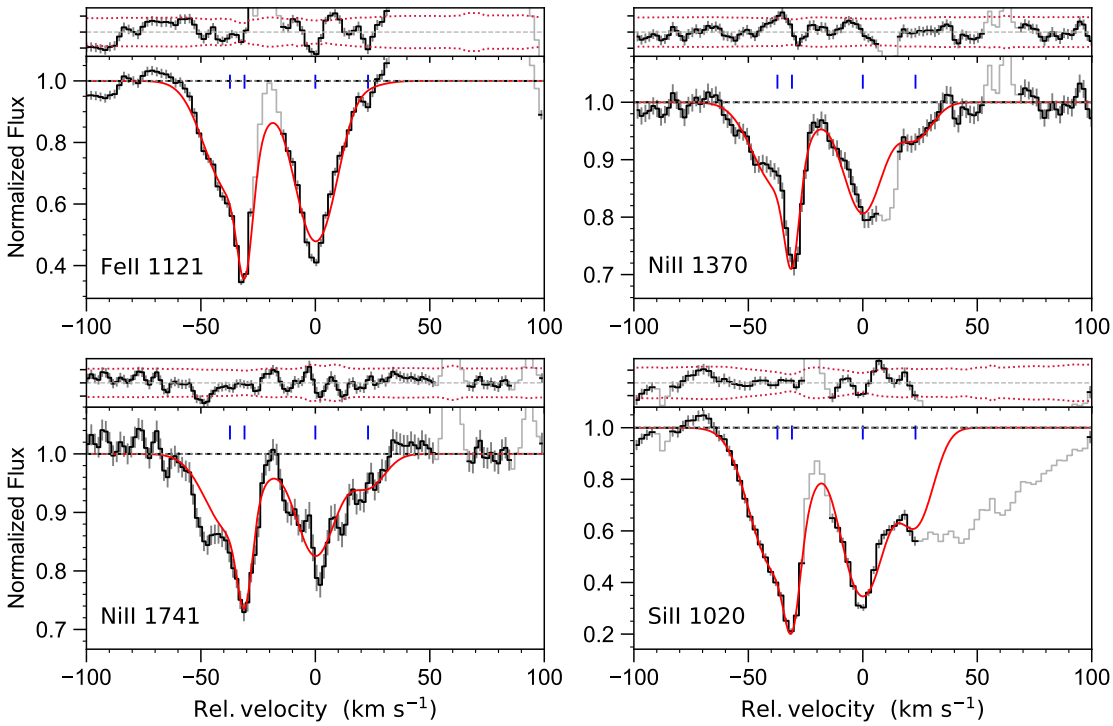


Figure A2.7: Velocity profiles of selected low-ionization transition lines from the DLA system at $z_{\rm abs} = 2.77779$ toward Q 1036−229.

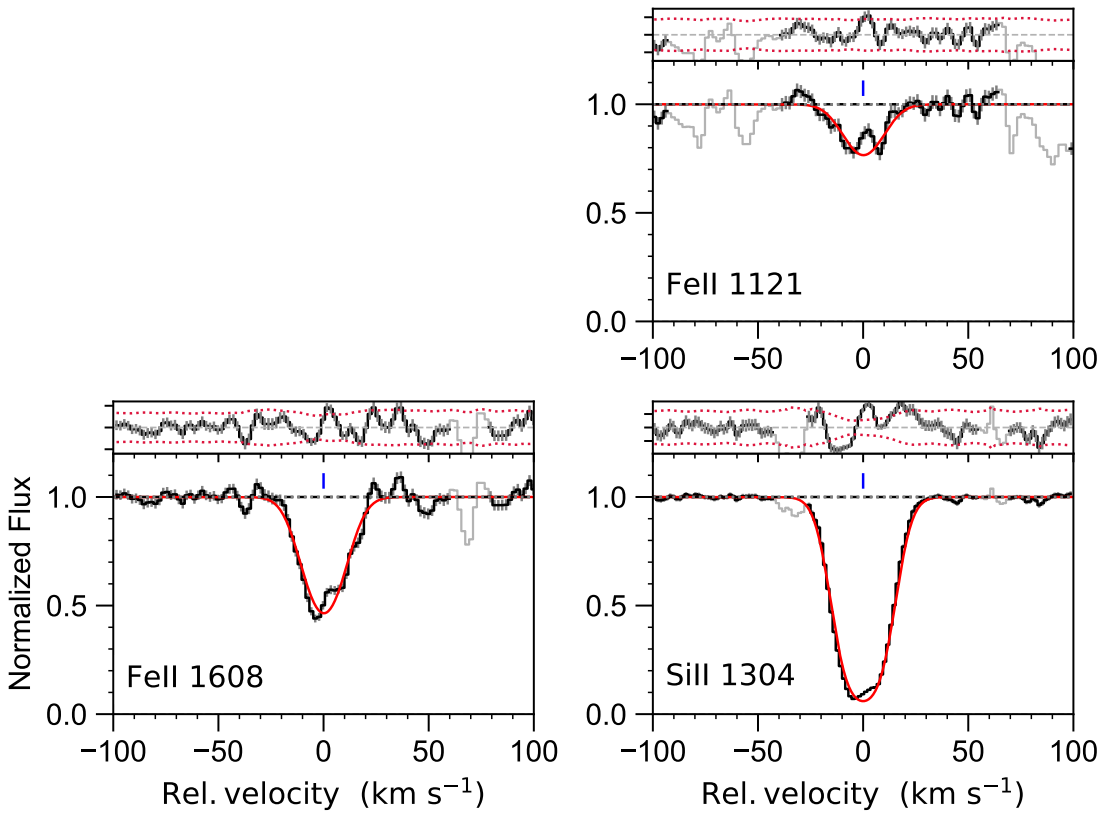


Figure A2.8: Velocity profiles of selected low-ionization transition lines from the DLA system at $z_{\rm abs} = 3.48185$ toward Q 1108−077.

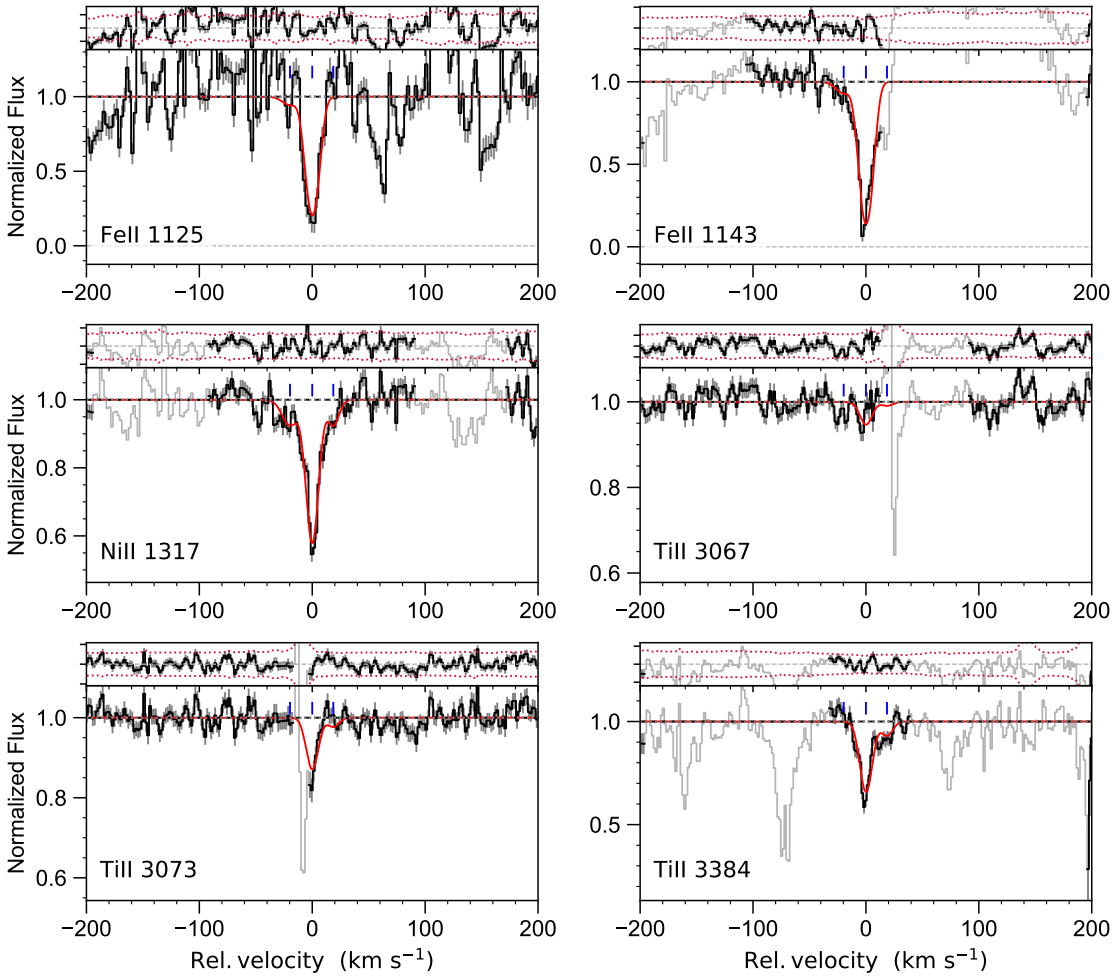


Figure A2.9: Velocity profiles of selected low-ionization transition lines from the DLA system at $z_{abs} = 1.89177$ toward Q 1210+175.

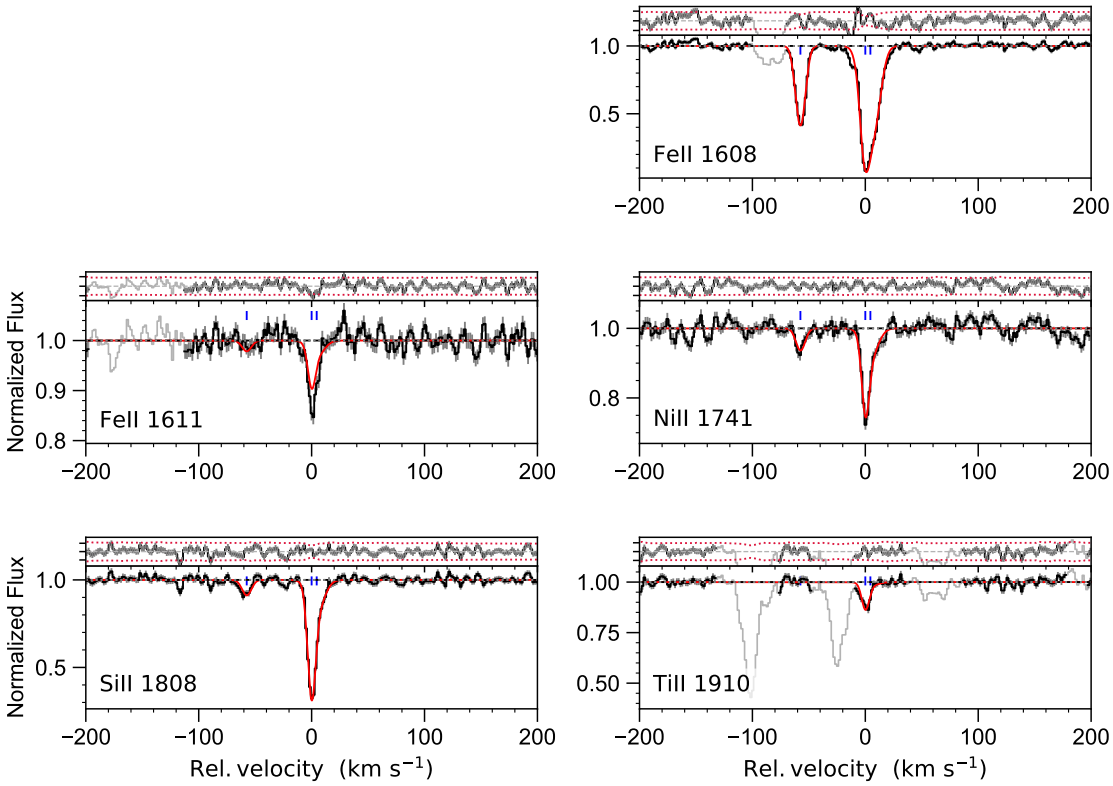


Figure A2.10: Velocity profiles of selected low-ionization transition lines from the DLA system at $z_{\rm abs}$ = 2.33771 toward Q 1232+082.

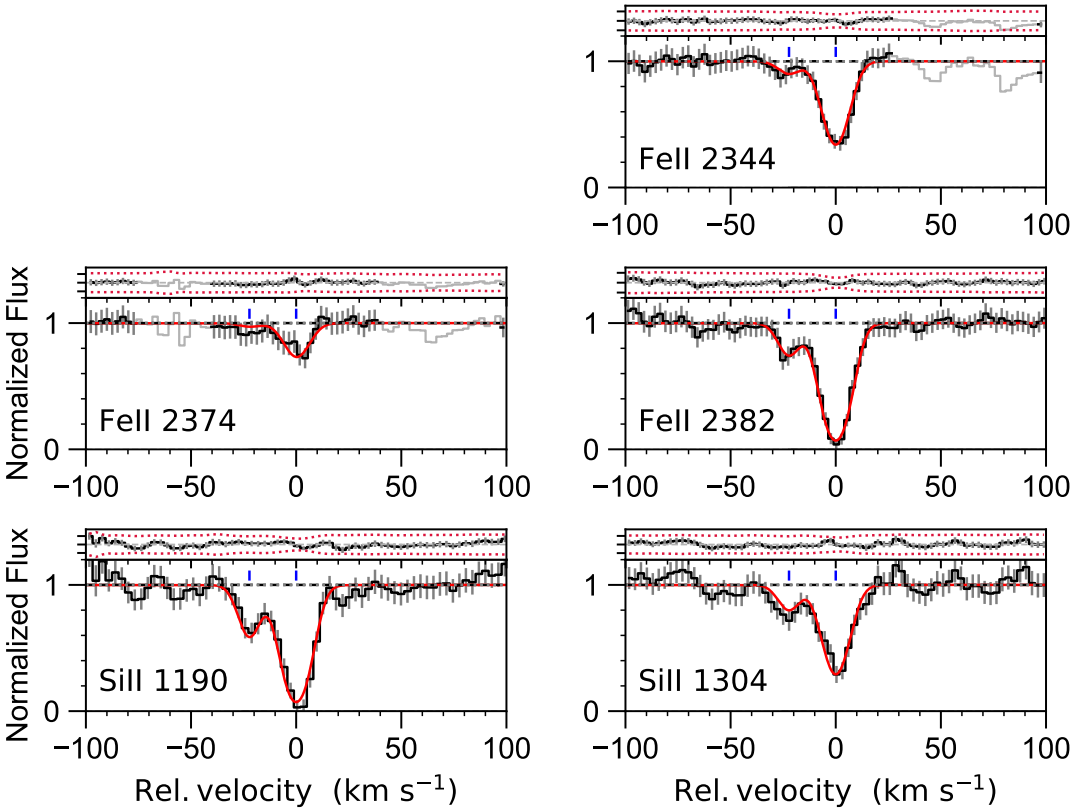


Figure A2.11: Velocity profiles of selected low-ionization transition lines from the DLA system at $z_{\rm abs} = 2.50792$ toward Q 1337+113.

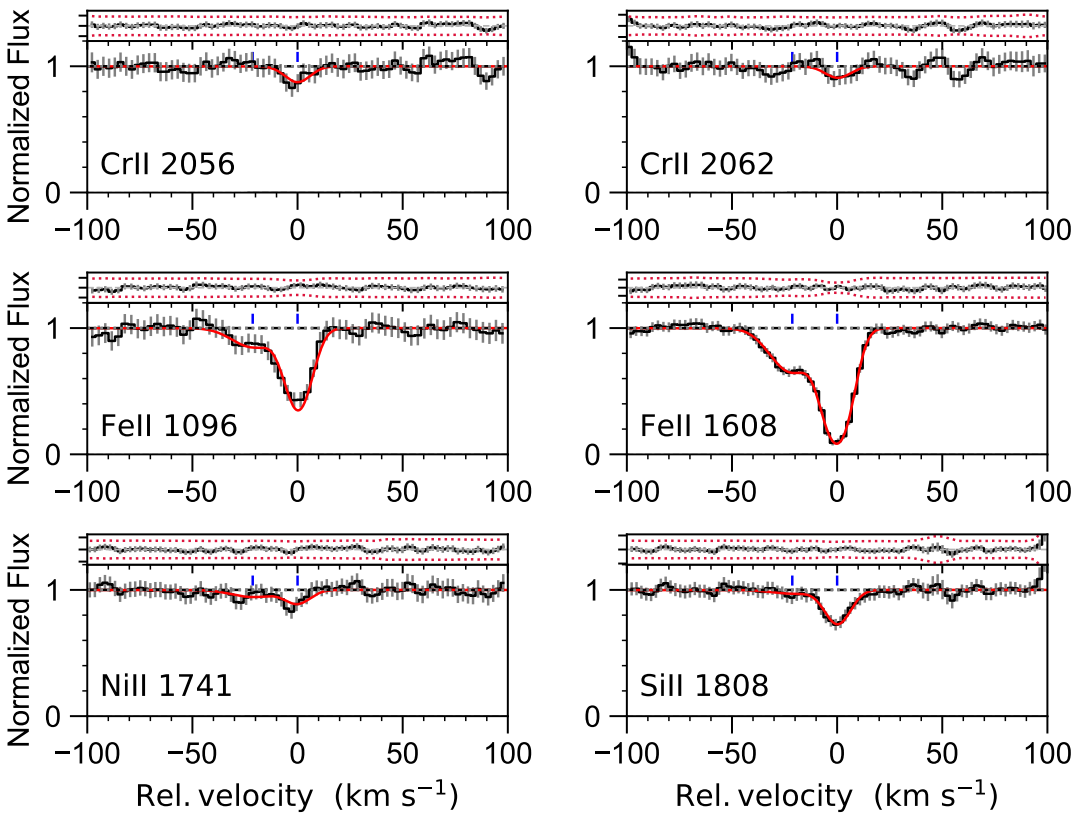


Figure A2.12: Velocity profiles of selected low-ionization transition lines from the DLA system at $z_{\rm abs}$ = 2.79584 toward Q 1337+113.

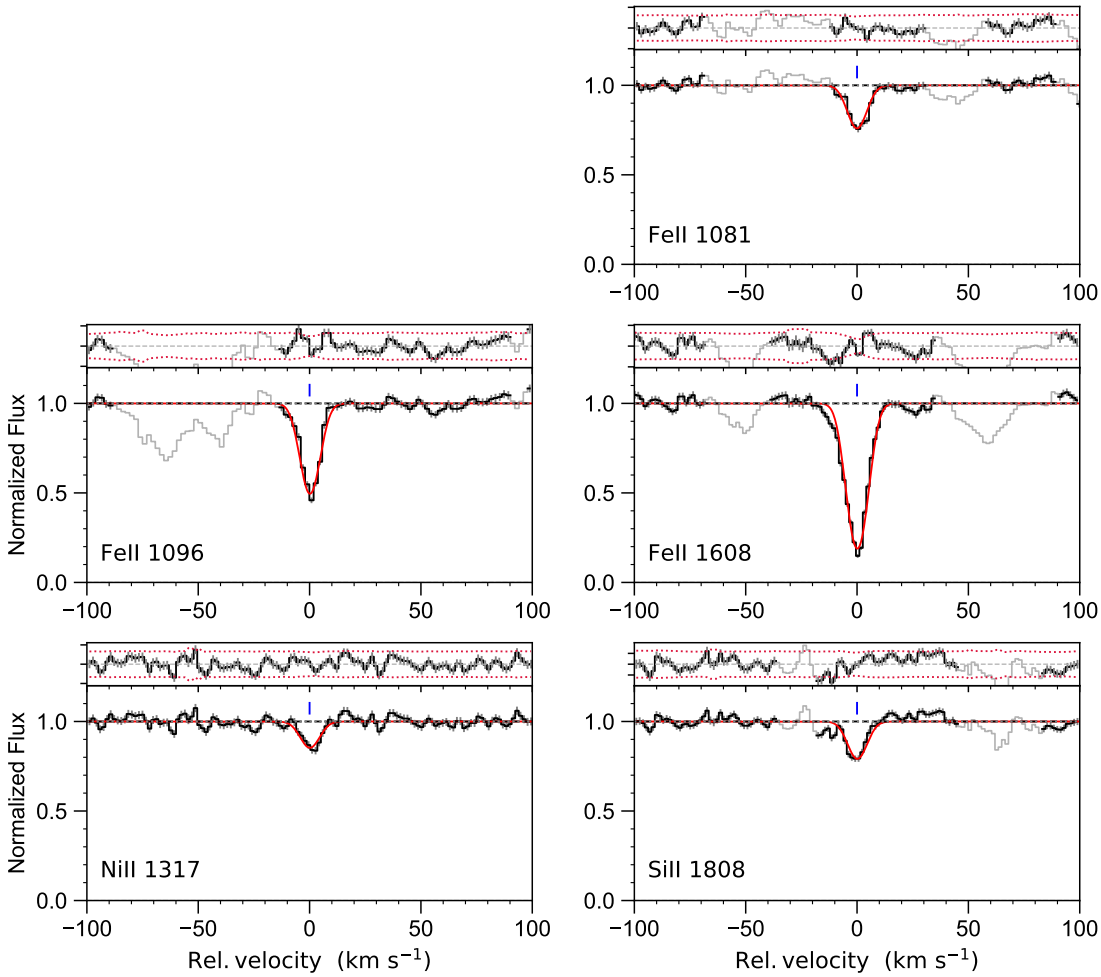


Figure A2.13: Velocity profiles of selected low-ionization transition lines from the DLA system at $z_{\rm abs} = 3.11835$ toward Q 1340−136.

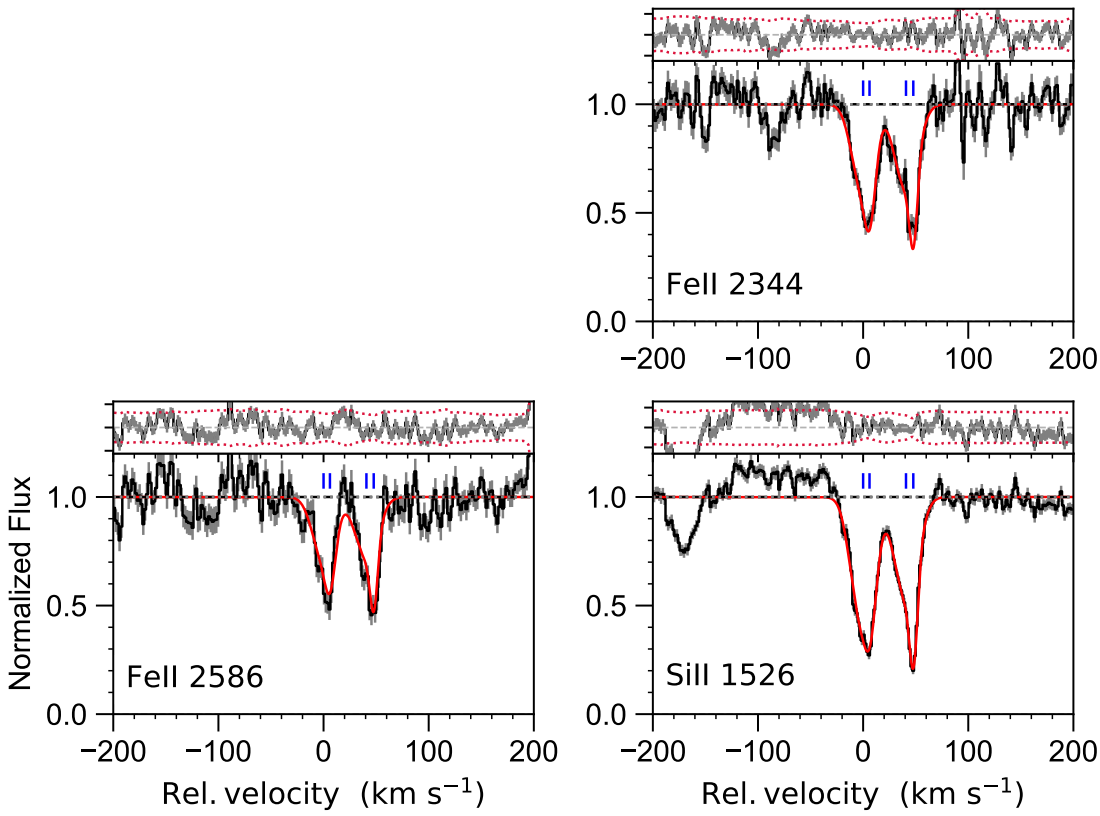


Figure A2.14: Velocity profiles of selected low-ionization transition lines from the DLA system at $z_{\rm abs}$ = 2.45593 toward Q 1409+095.

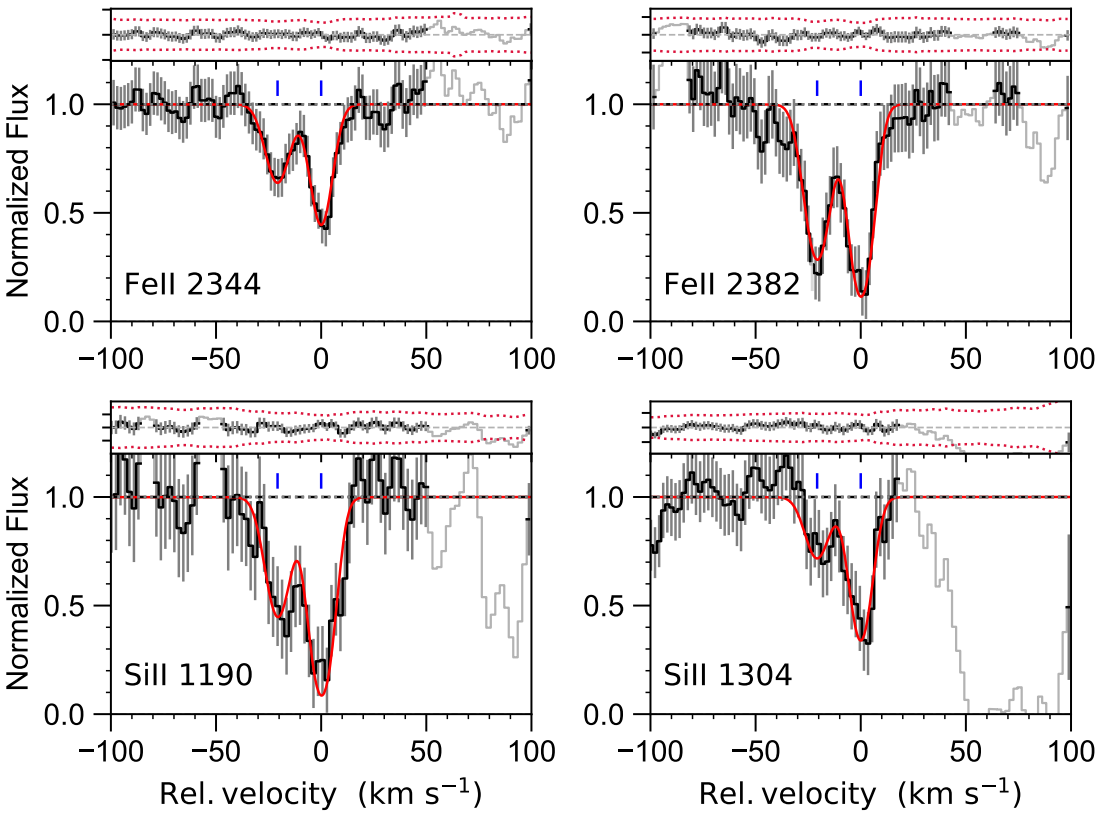


Figure A2.15: Velocity profiles of selected low-ionization transition lines from the DLA system at $z_{\rm abs}$ = 2.25466 toward Q 1451+123.

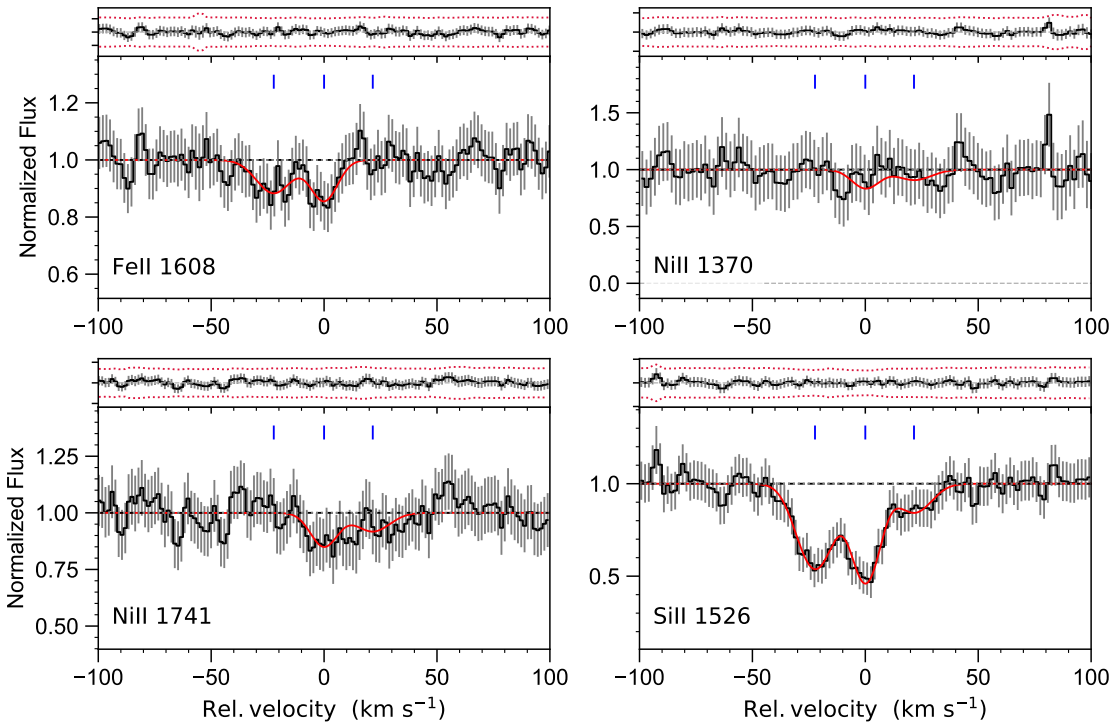


Figure A2.16: Velocity profiles of selected low-ionization transition lines from the DLA system at $z_{\rm abs} = 2.46921$ toward Q 1451+123.

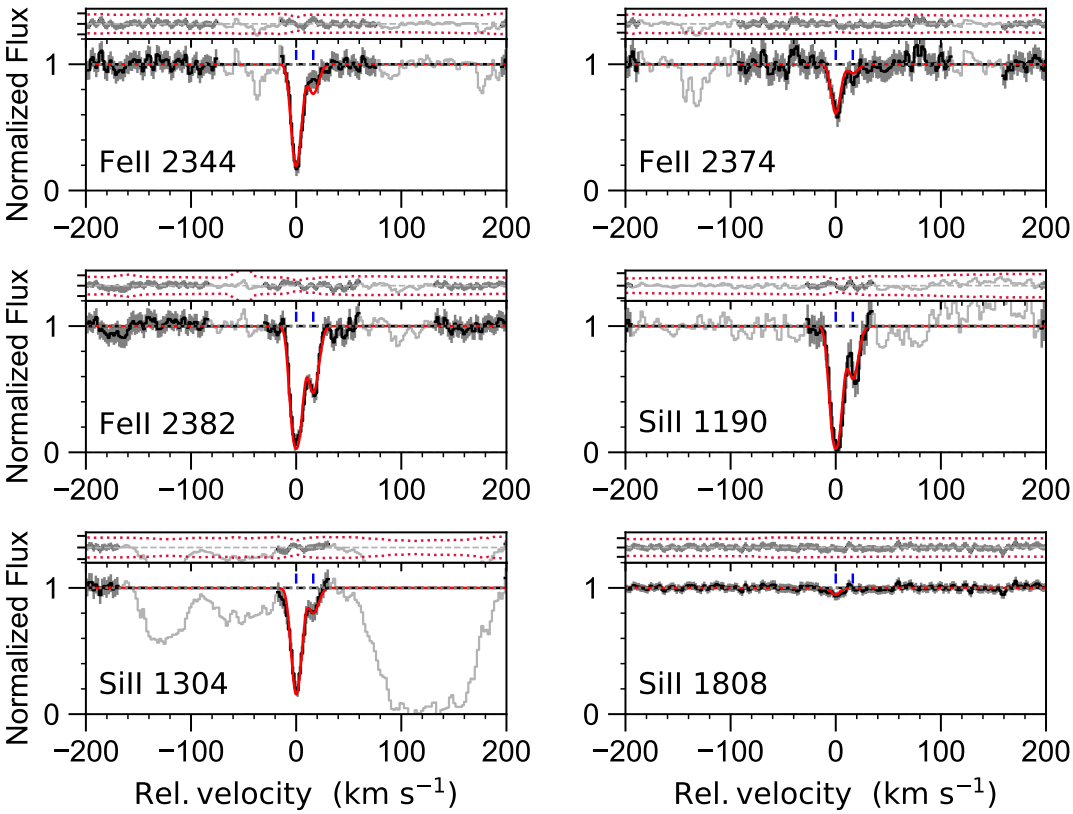


Figure A2.17: Velocity profiles of selected low-ionization transition lines from the DLA system at $z_{\rm abs} = 2.50734$ toward Q 2059−360.

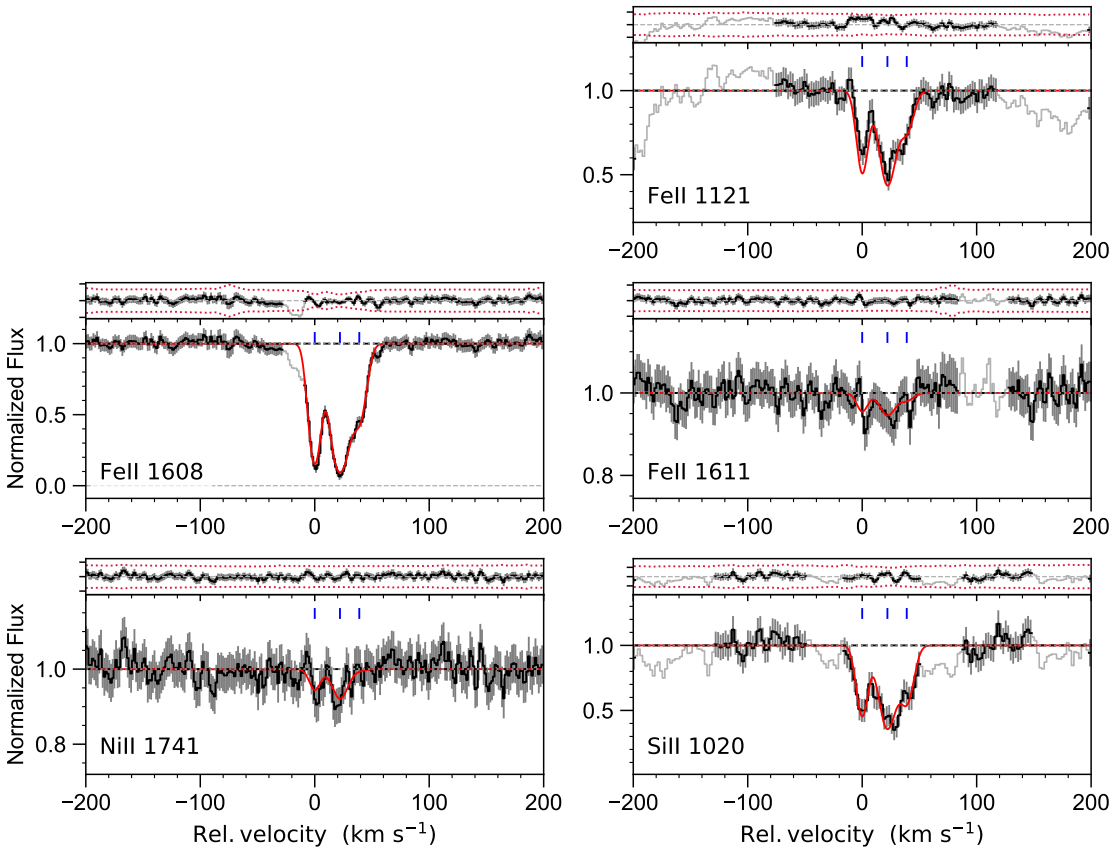


Figure A2.18: Velocity profiles of selected low-ionization transition lines from the DLA system at $z_{\rm abs} = 3.08291$ toward Q 2059−360.

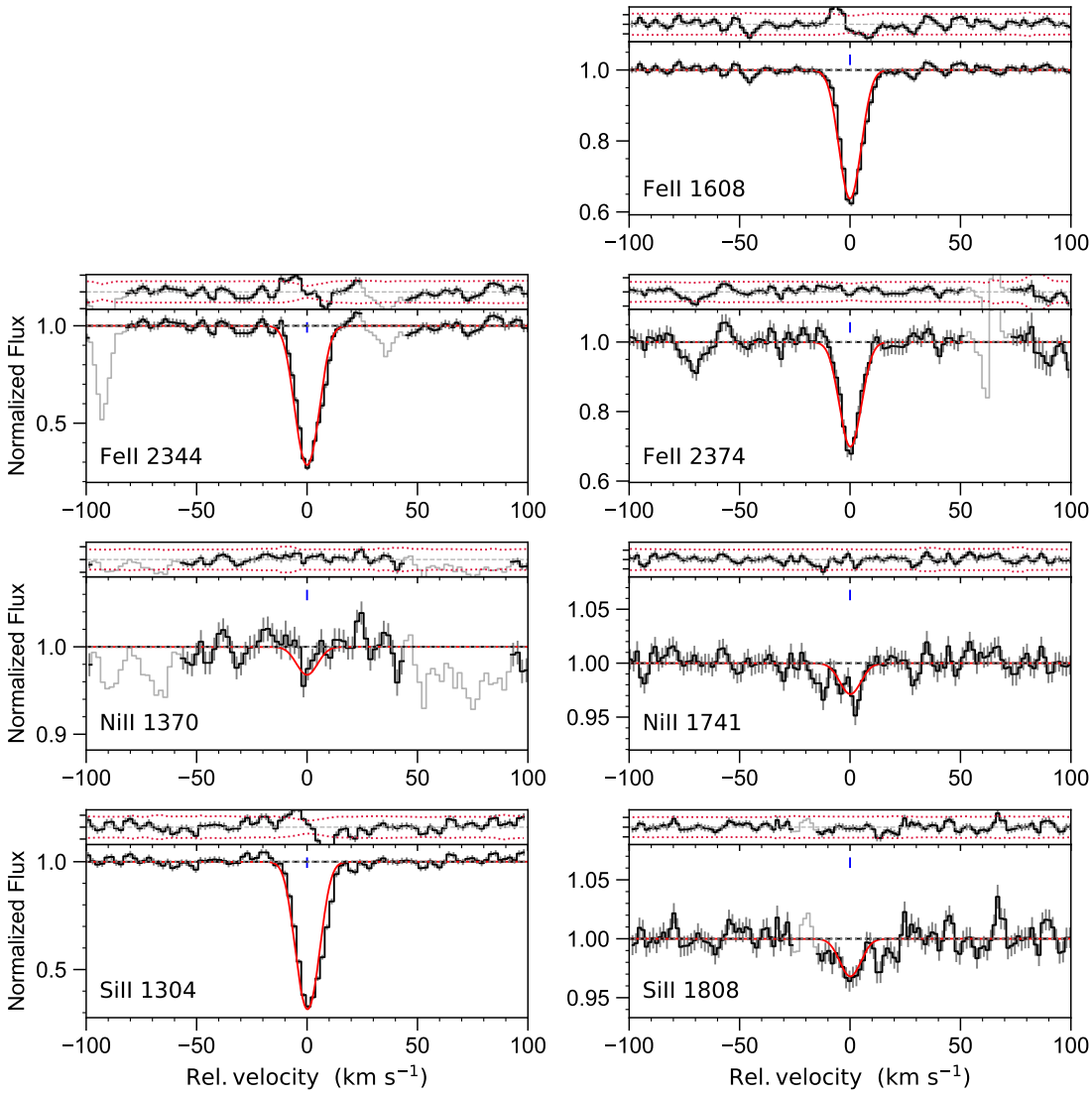


Figure A2.19: Velocity profiles of selected low-ionization transition lines from the DLA system at $z_{\rm abs} = 2.07622$ toward Q 2206−199.

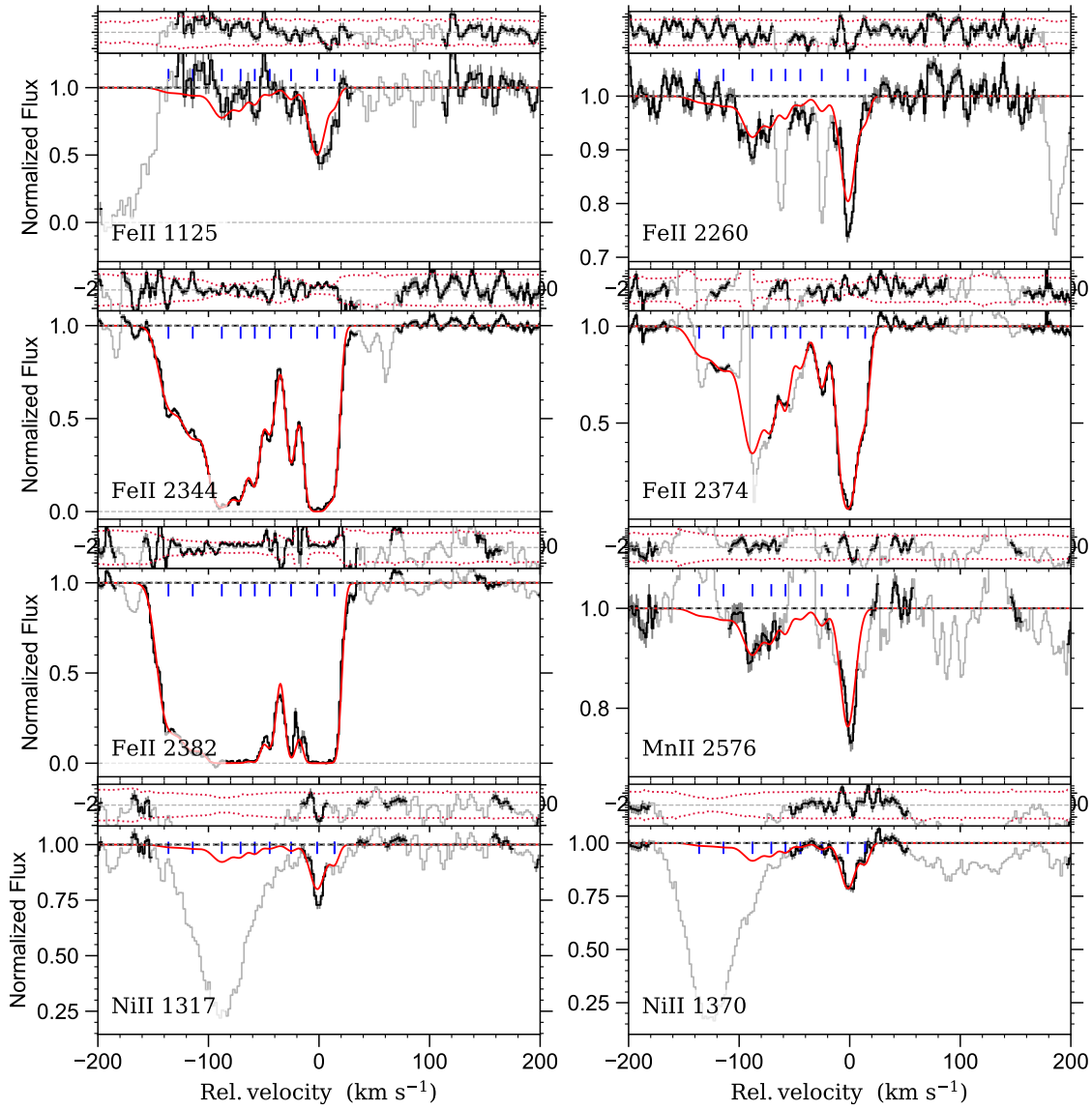


Figure A2.20: Velocity profiles of selected low-ionization transition lines from the DLA system at $z_{\rm abs} = 2.06552$ toward Q 2231−002.

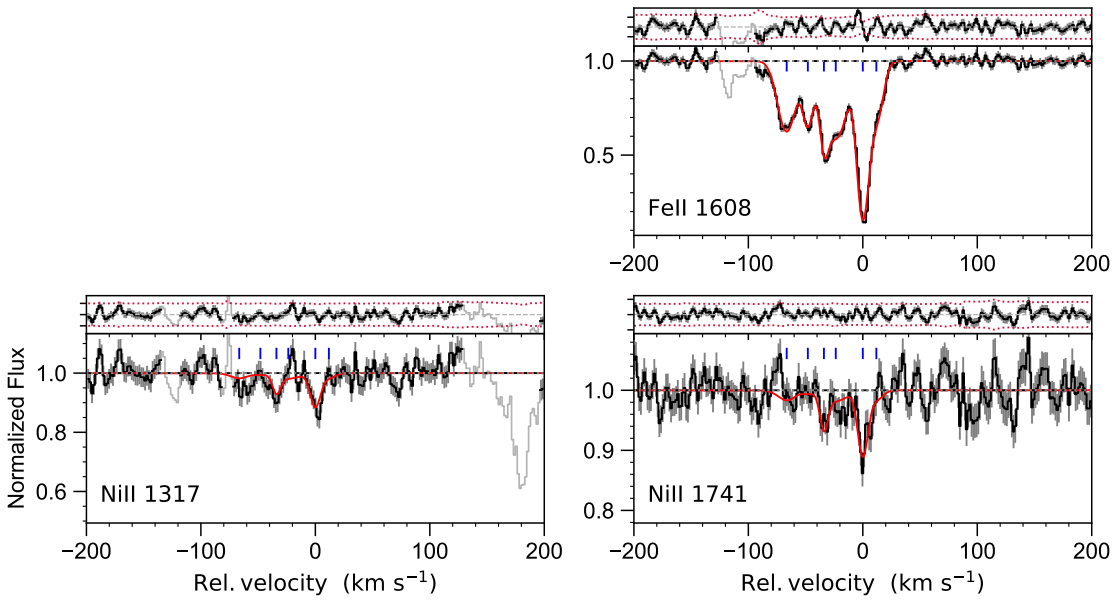


Figure A2.21: Velocity profiles of selected low-ionization transition lines from the DLA system at $z_{\rm abs} = 3.05722$ toward Q 2332−094.

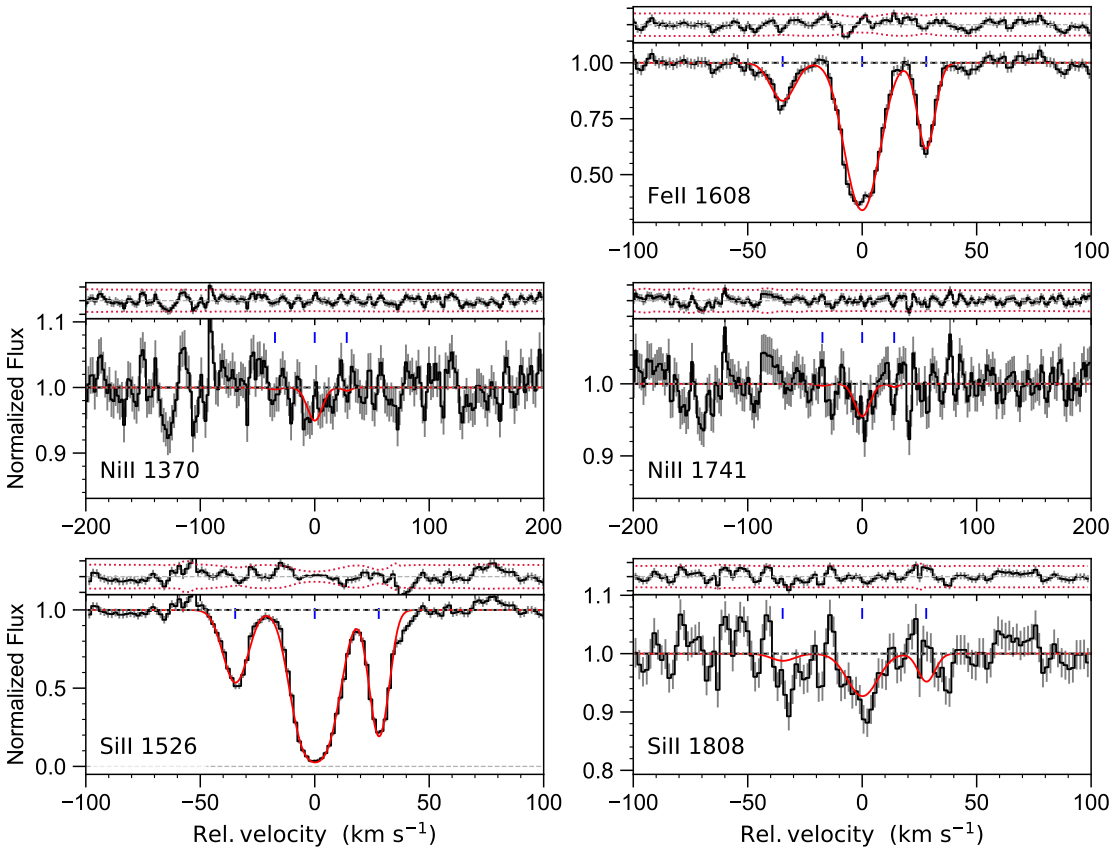


Figure A2.22: Velocity profiles of selected low-ionization transition lines from the DLA system at $z_{\rm abs} = 2.53787$ toward Q 2344+125.

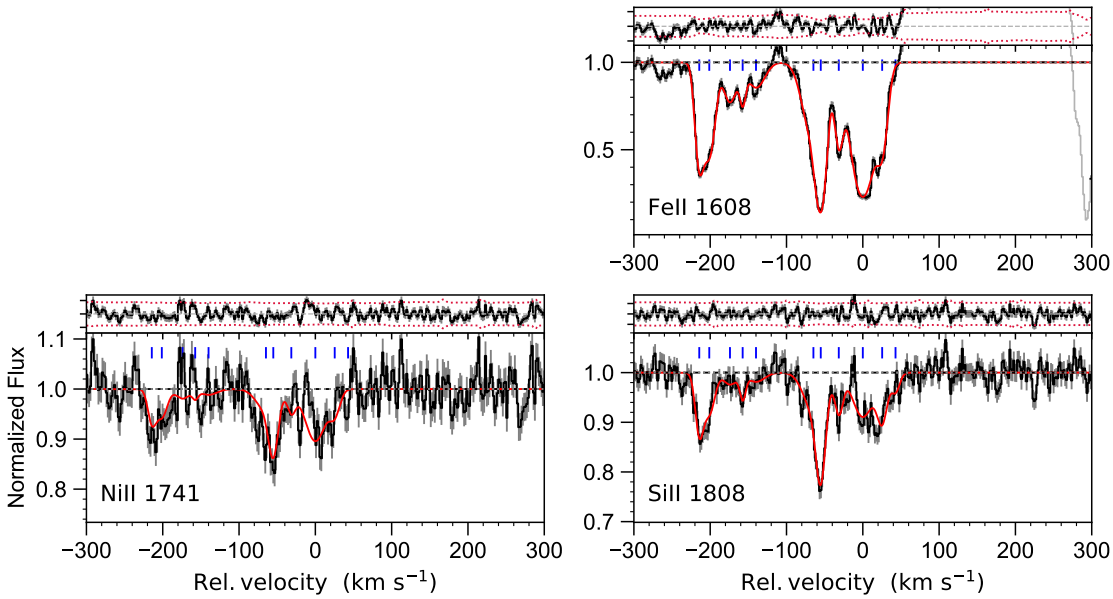


Figure A2.23: Velocity profiles of selected low-ionization transition lines from the DLA system at $z_{\rm abs} = 2.42695$ toward Q 2348−011.

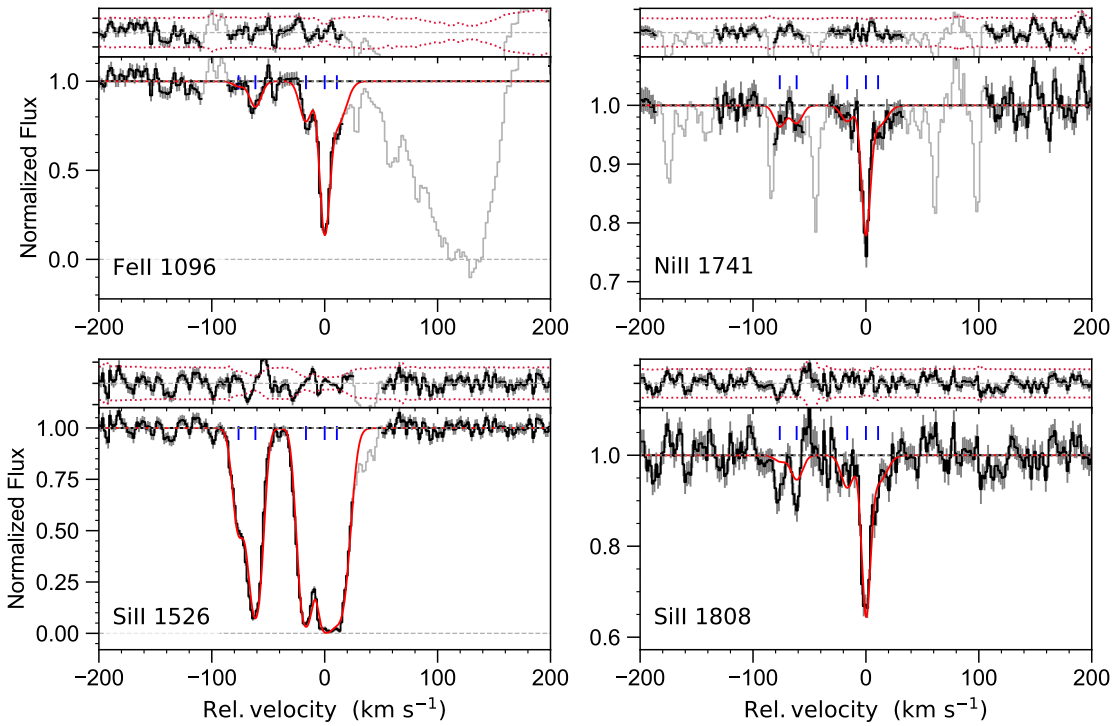
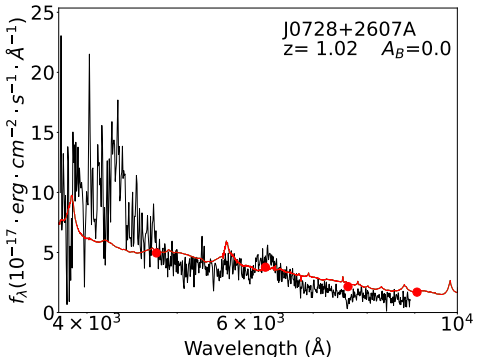


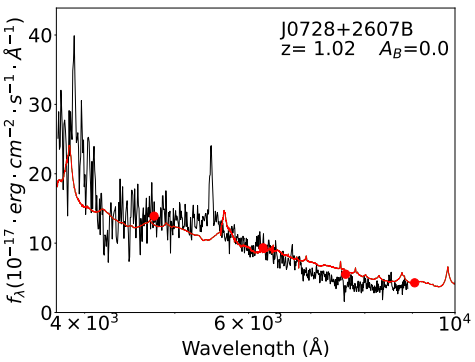
Figure A2.24: Velocity profiles of selected low-ionization transition lines from the DLA system at $z_{\rm abs} = 2.61473$ toward Q 2348−011.

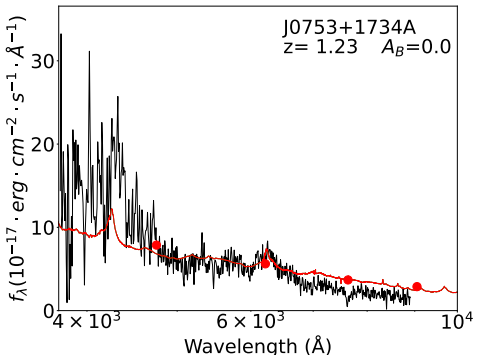
C

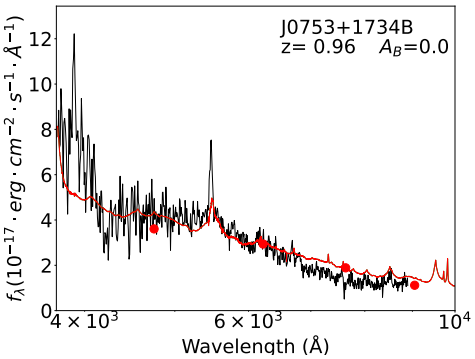
QSO PAIRS SPECTRA

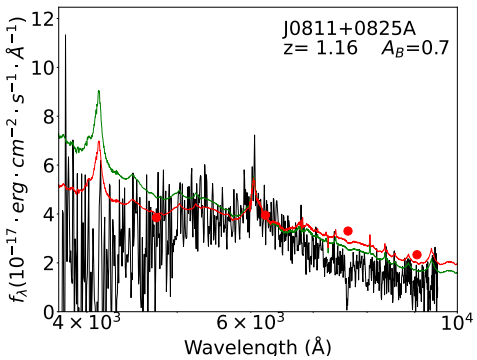
Full set of quasar pairs observed with the NOT and spectroscopically confirmed. The QSO spectrum is plotted in black, a QSO unreddened template is overplotted in green and the best-fit dust-reddened QSO template is in red. The red dots are the photometric data points of the u, g, r, i, z, Y, J, H, Ks bands, from SDSS and UKIDSS.

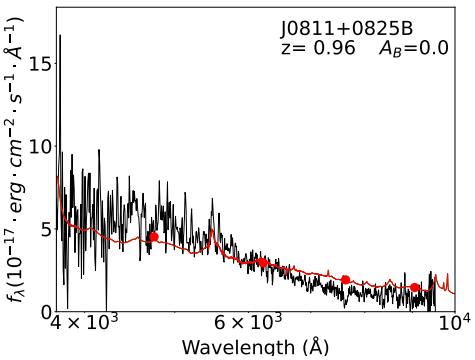

J0728+2607A
z= 1.02 A_B=0.0
$f_\lambda(10^{-17} \cdot erg \cdot cm^{-2} \cdot s^{-1} \cdot \AA^{-1})$
Wavelength (Å)

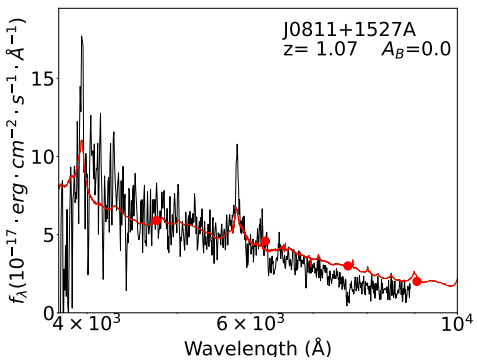

J0728+2607B
z= 1.02 A_B=0.0
$f_\lambda(10^{-17} \cdot erg \cdot cm^{-2} \cdot s^{-1} \cdot \AA^{-1})$
Wavelength (Å)

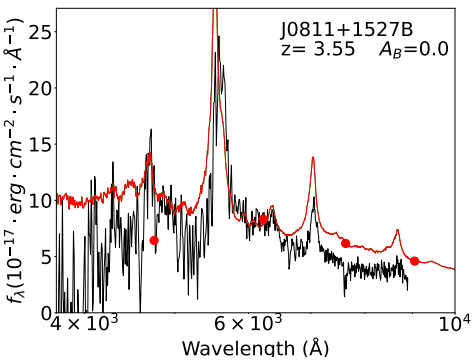

J0753+1734A
z= 1.23 A_B=0.0
$f_\lambda(10^{-17} \cdot erg \cdot cm^{-2} \cdot s^{-1} \cdot \AA^{-1})$
Wavelength (Å)

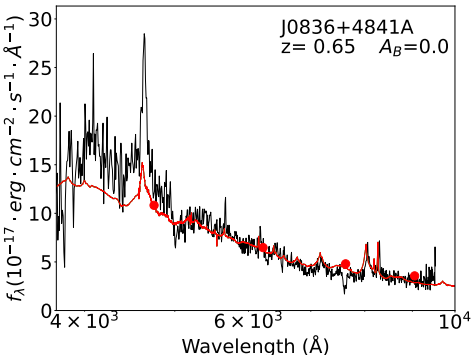

J0753+1734B
z= 0.96 A_B=0.0
$f_\lambda(10^{-17} \cdot erg \cdot cm^{-2} \cdot s^{-1} \cdot \AA^{-1})$
Wavelength (Å)

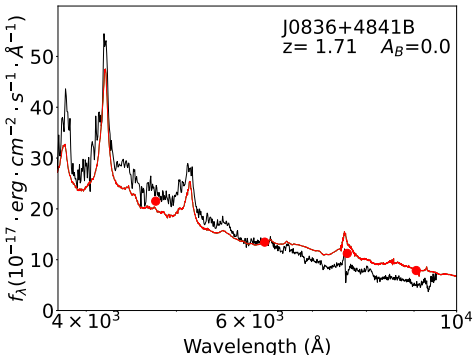

J0811+0825A
z= 1.16 A_B=0.7
$f_\lambda(10^{-17} \cdot erg \cdot cm^{-2} \cdot s^{-1} \cdot \AA^{-1})$
Wavelength (Å)

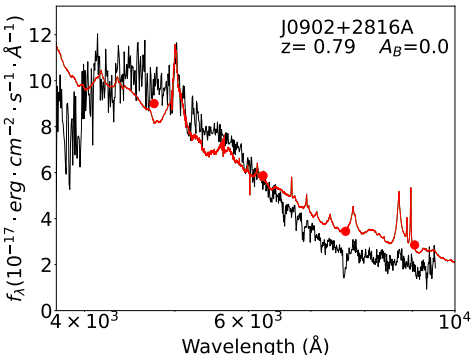

J0811+0825B
z= 0.96 A_B=0.0
$f_\lambda(10^{-17} \cdot erg \cdot cm^{-2} \cdot s^{-1} \cdot \AA^{-1})$
Wavelength (Å)

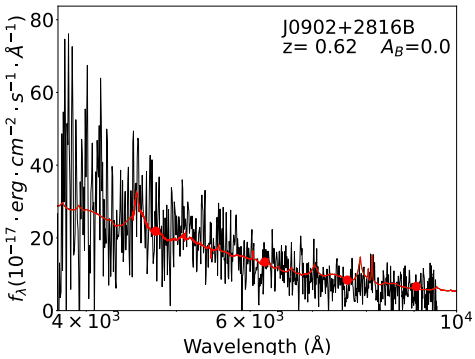

J0811+1527A
z= 1.07 A_B=0.0
$f_\lambda(10^{-17} \cdot erg \cdot cm^{-2} \cdot s^{-1} \cdot \AA^{-1})$
Wavelength (Å)

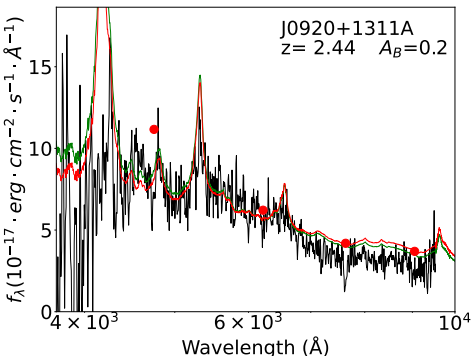

J0811+1527B
z= 3.55 A_B=0.0
$f_\lambda(10^{-17} \cdot erg \cdot cm^{-2} \cdot s^{-1} \cdot \AA^{-1})$
Wavelength (Å)

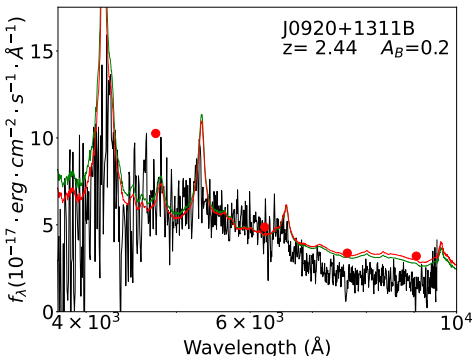

J0836+4841A
z= 0.65 A_B=0.0
$f_\lambda(10^{-17} \cdot erg \cdot cm^{-2} \cdot s^{-1} \cdot \AA^{-1})$
Wavelength (Å)

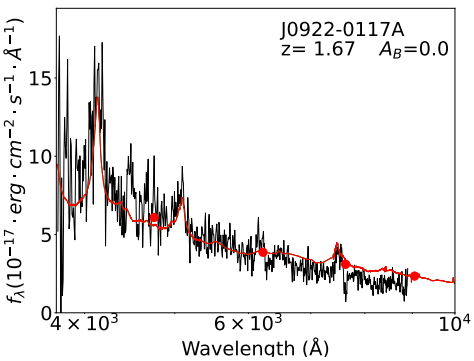

J0836+4841B
z= 1.71 A_B=0.0
$f_\lambda(10^{-17} \cdot erg \cdot cm^{-2} \cdot s^{-1} \cdot \AA^{-1})$
Wavelength (Å)

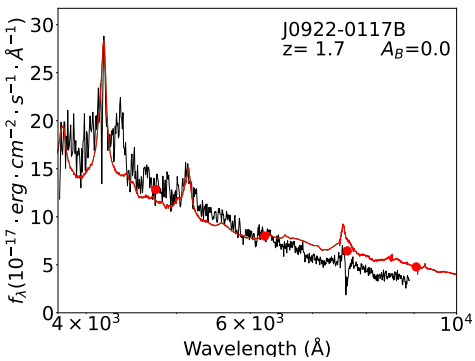

J0902+2816A
z= 0.79 A_B=0.0
$f_\lambda(10^{-17} \cdot erg \cdot cm^{-2} \cdot s^{-1} \cdot \AA^{-1})$
Wavelength (Å)

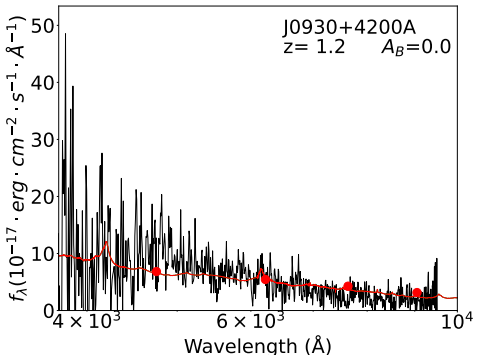

J0902+2816B
z= 0.62 A_B=0.0
$f_\lambda(10^{-17} \cdot erg \cdot cm^{-2} \cdot s^{-1} \cdot \AA^{-1})$
Wavelength (Å)

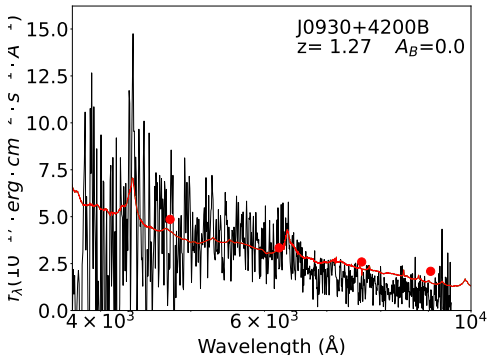

J0920+1311A
z= 2.44 A_B=0.2
$f_\lambda(10^{-17} \cdot erg \cdot cm^{-2} \cdot s^{-1} \cdot \AA^{-1})$
Wavelength (Å)

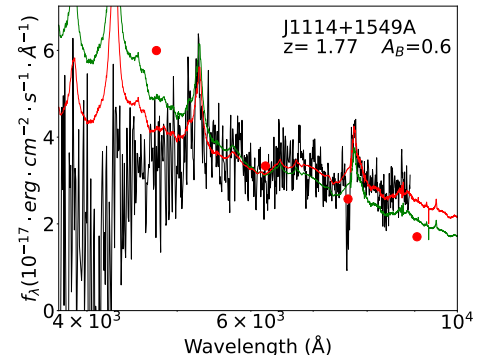

J0920+1311B
z= 2.44 A_B=0.2
$f_\lambda(10^{-17} \cdot erg \cdot cm^{-2} \cdot s^{-1} \cdot \AA^{-1})$
Wavelength (Å)

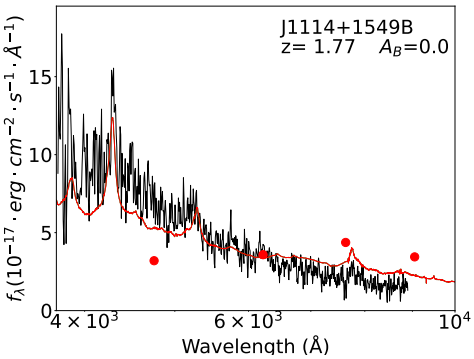

J0922-0117A
z= 1.67 A_B=0.0
$f_\lambda(10^{-17} \cdot erg \cdot cm^{-2} \cdot s^{-1} \cdot \AA^{-1})$
Wavelength (Å)

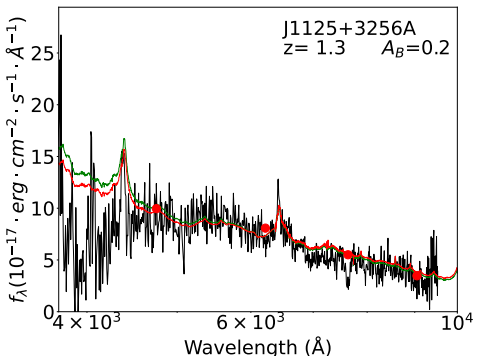

J0922-0117B
z= 1.7 A_B=0.0
$f_\lambda(10^{-17} \cdot erg \cdot cm^{-2} \cdot s^{-1} \cdot \AA^{-1})$
Wavelength (Å)

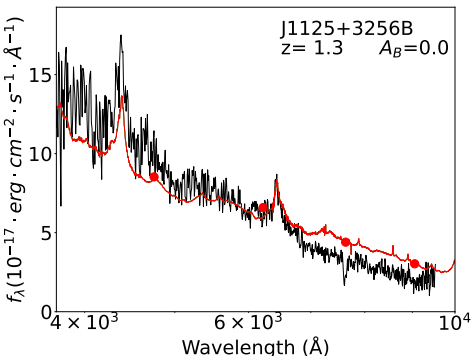

J0930+4200A
z= 1.2 A_B=0.0
$f_\lambda(10^{-17} \cdot erg \cdot cm^{-2} \cdot s^{-1} \cdot \AA^{-1})$
Wavelength (Å)

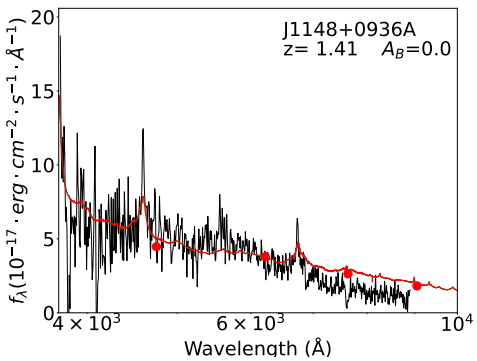

J0930+4200B
z= 1.27 A_B=0.0
Wavelength (Å)

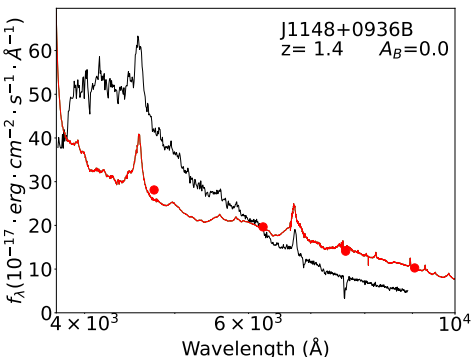

J1114+1549A
z= 1.77 A_B=0.6
$f_\lambda(10^{-17} \cdot erg \cdot cm^{-2} \cdot s^{-1} \cdot \AA^{-1})$
Wavelength (Å)

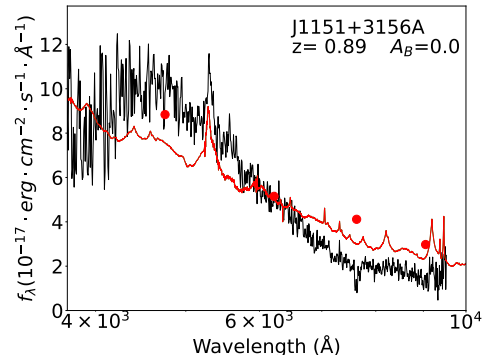

J1114+1549B
z= 1.77 A_B=0.0
$f_\lambda(10^{-17} \cdot erg \cdot cm^{-2} \cdot s^{-1} \cdot \AA^{-1})$
Wavelength (Å)

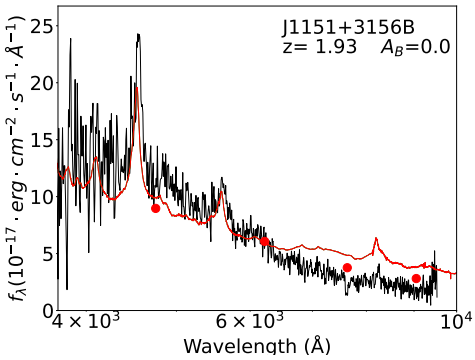

J1125+3256A
z= 1.3 A_B=0.2
$f_\lambda(10^{-17} \cdot erg \cdot cm^{-2} \cdot s^{-1} \cdot \AA^{-1})$
Wavelength (Å)

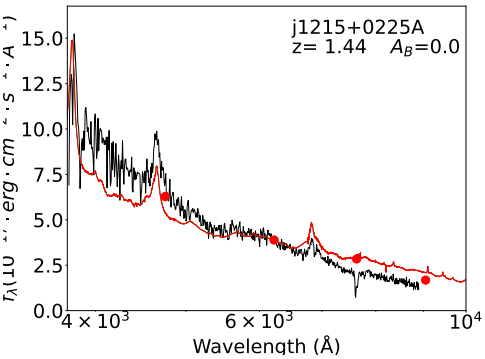

J1125+3256B
z= 1.3 A_B=0.0
$f_\lambda(10^{-17} \cdot erg \cdot cm^{-2} \cdot s^{-1} \cdot \AA^{-1})$
Wavelength (Å)

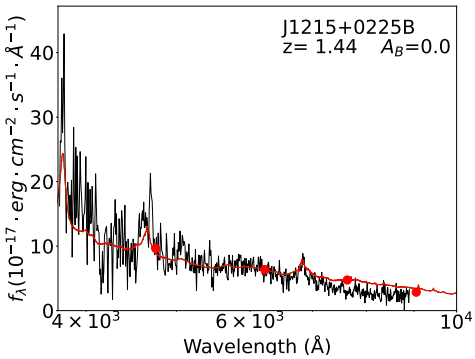

J1148+0936A
z= 1.41 A_B=0.0
$f_\lambda(10^{-17} \cdot erg \cdot cm^{-2} \cdot s^{-1} \cdot \AA^{-1})$
Wavelength (Å)

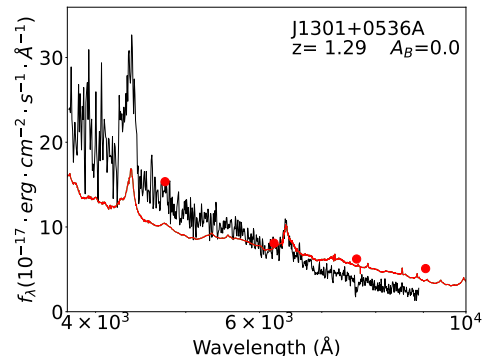

J1148+0936B
z= 1.4 A_B=0.0
$f_\lambda(10^{-17} \cdot erg \cdot cm^{-2} \cdot s^{-1} \cdot \AA^{-1})$
Wavelength (Å)

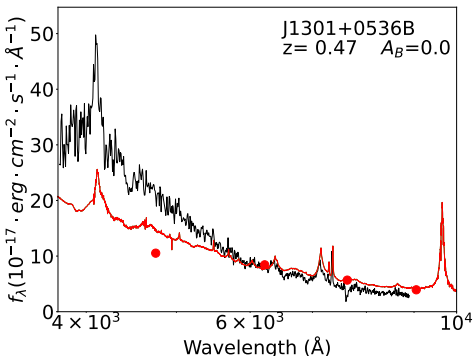

J1151+3156A
z= 0.89 A_B=0.0
$f_\lambda(10^{-17} \cdot erg \cdot cm^{-2} \cdot s^{-1} \cdot \AA^{-1})$
Wavelength (Å)

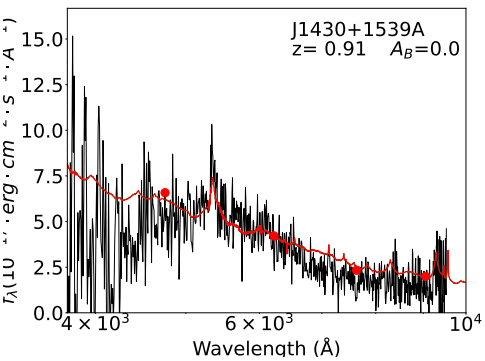

J1151+3156B
z= 1.93 A_B=0.0
$f_\lambda(10^{-17} \cdot erg \cdot cm^{-2} \cdot s^{-1} \cdot \AA^{-1})$
Wavelength (Å)

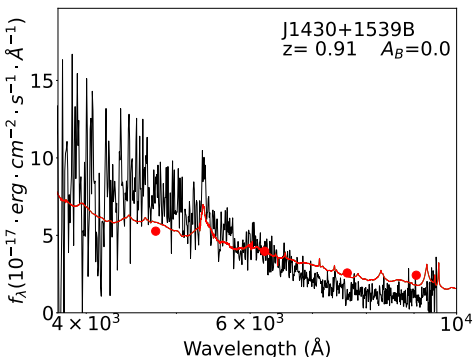

j1215+0225A
z= 1.44 A_B=0.0
Wavelength (Å)

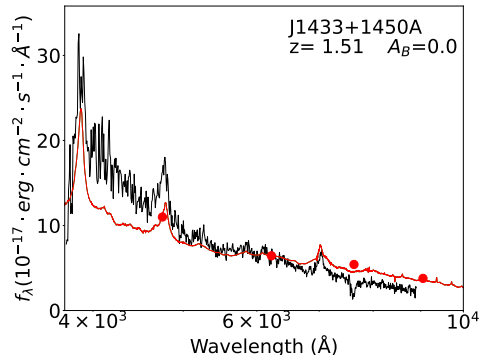

J1215+0225B
z= 1.44 A_B=0.0
$f_\lambda(10^{-17} \cdot erg \cdot cm^{-2} \cdot s^{-1} \cdot \AA^{-1})$
Wavelength (Å)

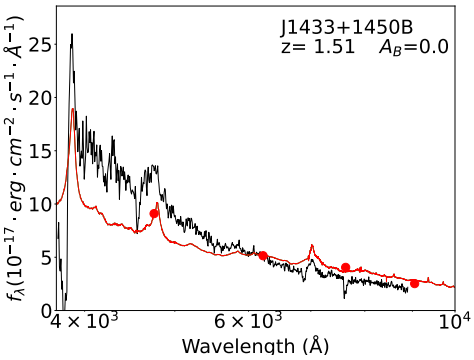

J1301+0536A
z= 1.29 A_B=0.0
$f_\lambda(10^{-17} \cdot erg \cdot cm^{-2} \cdot s^{-1} \cdot \AA^{-1})$
Wavelength (Å)

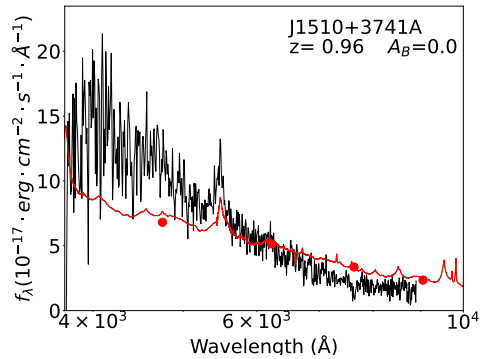

J1301+0536B
z= 0.47 A_B=0.0
$f_\lambda(10^{-17} \cdot erg \cdot cm^{-2} \cdot s^{-1} \cdot \AA^{-1})$
Wavelength (Å)

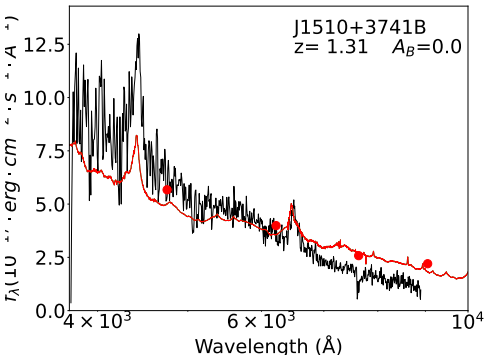

J1430+1539A
z= 0.91 A_B=0.0
Wavelength (Å)

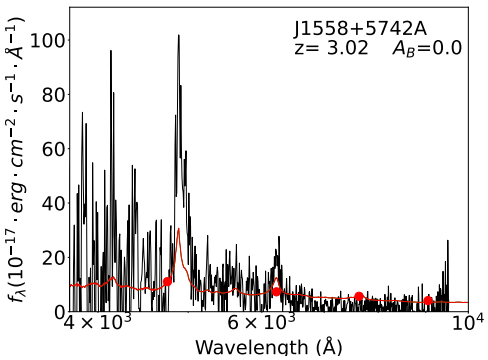

J1430+1539B
z= 0.91 A_B=0.0
$f_\lambda(10^{-17} \cdot erg \cdot cm^{-2} \cdot s^{-1} \cdot \AA^{-1})$
Wavelength (Å)

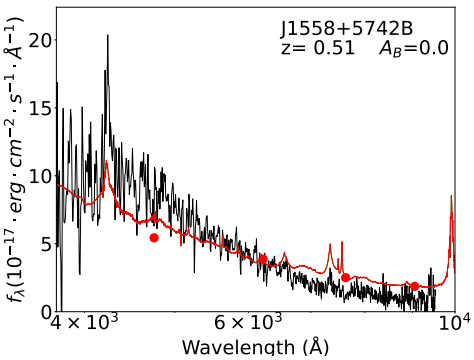

J1433+1450A
z= 1.51 A_B=0.0
$f_\lambda(10^{-17} \cdot erg \cdot cm^{-2} \cdot s^{-1} \cdot \AA^{-1})$
Wavelength (Å)

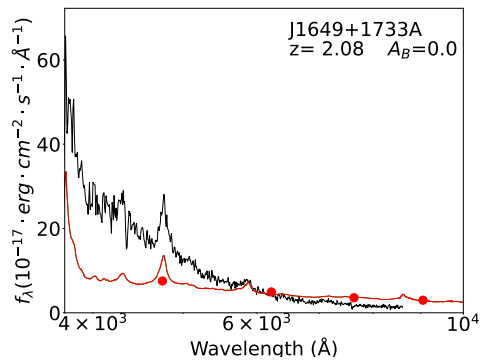

J1433+1450B
z= 1.51 A_B=0.0
$f_\lambda(10^{-17} \cdot erg \cdot cm^{-2} \cdot s^{-1} \cdot \AA^{-1})$
Wavelength (Å)

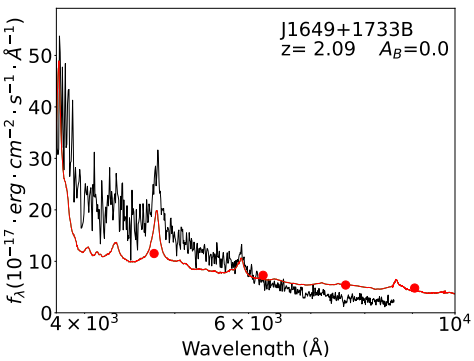

J1510+3741A
z= 0.96 A_B=0.0
$f_\lambda(10^{-17} \cdot erg \cdot cm^{-2} \cdot s^{-1} \cdot \AA^{-1})$
Wavelength (Å)

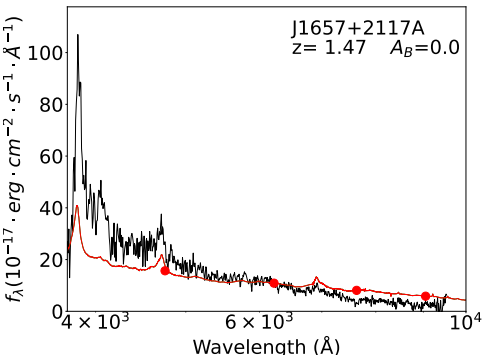

J1510+3741B
z= 1.31 A_B=0.0
Wavelength (Å)

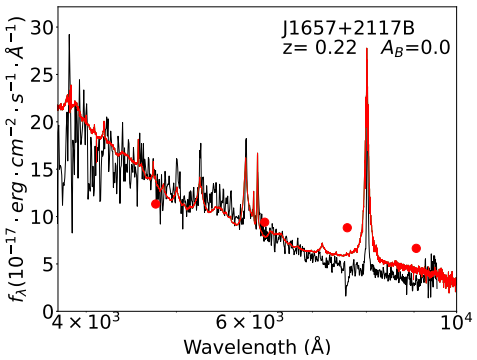

J1558+5742A
z= 3.02 A_B=0.0
$f_\lambda(10^{-17} \cdot erg \cdot cm^{-2} \cdot s^{-1} \cdot \AA^{-1})$
Wavelength (Å)

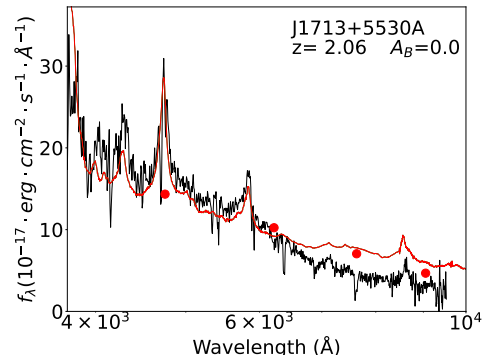

J1558+5742B
z= 0.51 A_B=0.0
$f_\lambda(10^{-17} \cdot erg \cdot cm^{-2} \cdot s^{-1} \cdot \AA^{-1})$
Wavelength (Å)

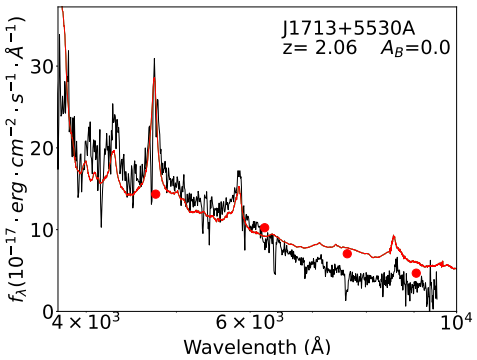

J1649+1733A
z= 2.08 A_B=0.0
$f_\lambda(10^{-17} \cdot erg \cdot cm^{-2} \cdot s^{-1} \cdot \AA^{-1})$
Wavelength (Å)


J1649+1733B
z= 2.09 A_B=0.0
$f_\lambda(10^{-17} \cdot erg \cdot cm^{-2} \cdot s^{-1} \cdot \AA^{-1})$
Wavelength (Å)


J1657+2117A
z= 1.47 A_B=0.0
$f_\lambda(10^{-17} \cdot erg \cdot cm^{-2} \cdot s^{-1} \cdot \AA^{-1})$
Wavelength (Å)


J1657+2117B
z= 0.22 A_B=0.0
$f_\lambda(10^{-17} \cdot erg \cdot cm^{-2} \cdot s^{-1} \cdot \AA^{-1})$
Wavelength (Å)


J1713+5530A
z= 2.06 A_B=0.0
$f_\lambda(10^{-17} \cdot erg \cdot cm^{-2} \cdot s^{-1} \cdot \AA^{-1})$
Wavelength (Å)


J1713+5530A
z= 2.06 A_B=0.0
$f_\lambda(10^{-17} \cdot erg \cdot cm^{-2} \cdot s^{-1} \cdot \AA^{-1})$
Wavelength (Å)

D

CONTRIBUTIONS

During my PhD I have also contributed to a series of projects that have led to peer-reviewed publications in scientific journals. Below I provide a list of the articles to which I have contributed. I also include a short abstract for each, and a description of the work I have done for each article.

Title: The α-element enrichment of gas in distant galaxies

Journal: Astronomy & Astrophysics, Issue 685, A103 (2024);
doi:10.1051/0004-6361/202348601

Authors: Anna Velichko, Annalisa De Cia, **Christina Konstantopoulou**, Cédric Ledoux, Jens-Kristian Krogager and Tanita Ramburuth-Hurt

Description: This study analyzed the metallicities, dust depletion, and α-element enhancements in the neutral ISM of distant gas-rich, mostly metal-poor galaxies (DLAs). The authors found systematic deviations in the abundance patterns of various elements, interpreted as α-element enhancements and Mn underabundance, with less massive galaxies showing α-element enhancement at lower metallicities. This work provides new insights into the chemical evolution of distant galaxies, suggesting that more massive galaxies evolve to higher metallicities before Type Ia supernovae contributions balance those of core-collapse supernovae.

My contribution: In this work, I contributed by providing the coefficients (refractory index) for the 11 metals used, including an updated coefficient for PII, after correcting for the most recent oscillator strengths. These coefficients are from the published Konstantopoulou et al. (2022). I have also provided the column density measurements and limits for TiII and NiII, using VoigtFit, of the additional QSOs-DLAs included in this work. Finally, I provided general comments throughout the manuscript.

Title: α-element enhancements in the ISM of the LMC and SMC: Evidence of recent star formation

Journal: Astronomy & Astrophysics, Issue 683, A216 (2024);
doi:10.1051/0004-6361/202346611

Authors: Annalisa De Cia, Julia Roman-Duval, **Christina Konstantopoulou**, Pasquier Noterdaeme, Tanita Ramburuth-Hurt, Anna Velichko, Andrew J. Fox, Cédric Ledoux, Patrick Petitjean, Iris Jermann, and Jens-Kristian Krogager

Description: This article describes the measurements of metallicity and dust depletion in the neutral ISM of the Large Magellanic Cloud (LMC) and Small Magellanic Cloud (SMC). α-element enhancements and Mn underabundance are found, likely due to recent bursts of star formation. Most regions show well-mixed metallicities similar to hot star metallicities, except for some lower metallicity areas near the Magellanic Bridge.

My contribution: In this work, I have contributed by providing the coefficients (refractory index) for the 18 metals used, including an updated coefficient for P, after correcting for the most recent oscillator strengths and providing general comments throughout the manuscript. The provided coefficients are from the published Konstantopoulou et al. (2022).

Title: The cosmic buildup of dust and metals. Accurate abundances from GRB-selected star-forming galaxies at $1.7 < z < 6.3$

Journal: Astronomy & Astrophysics, Issue 679, A91 (2023);
doi:10.1051/0004-6361/202347418

Authors: K. E. Heintz, A. De Cia, C. C. Thöne, J.-K. Krogager, R. M. Yates, S. Vejlgaard, **C. Konstantopoulou**, J. P. U. Fynbo, D. Watson, D. Narayanan, S. N. Wilson, M. Arabsalmani, S. Campana, V. D'Elia, M. De Pasquale, D. H. Hartmann, L. Izzo, P. Jakobsson, C. Kouveliotou, A. Levan, Q. Li, D. B. Malesani, A. Melandri, B. Milvang-Jensen, P. Møller, E. Palazzi, J. Palmerio, P. Petitjean, G. Pugliese, A. Rossi, A. Saccardi, R. Salvaterra, S. Savaglio, P. Schady, G. Stratta, N. R. Tanvir, A. de Ugarte Postigo, S. D. Vergani, K. Wiersema, R. A. M. J. Wijers, and T. Zafar

Description: This study investigates the evolution of gas-phase metallicities, dust-to-gas (DTG), and dust-to-metal (DTM) ratios in 36 star-forming galaxies at redshifts $1.7<z<6.3$, using data from gamma-ray bursts (GRBs). The authors determined a linear relation for the dust-corrected gas-phase metallicity with redshift. The study also reveals that both DTG and DTM ratios are strongly correlated with gas-phase metallicity and show a mild evolution with redshift, providing important insights into the dust and metal content of

high-redshift galaxies and highlighting significant deviations from average Galactic values in low-metallicity, high-redshift environments.

My contribution: In this work, I have contributed by providing the DTM and DTG measurements of the SMC and LMC, published in Konstantopoulou et al. (2024), that were used for comparisons. I also provided the coefficients (refractory index) of metals, which are published in Konstantopoulou et al. (2022). I also contributed to the scientific discussion and methodology of DTM and DTG ratios and provided general comments.

Title: Chemical diversity of gas in distant galaxies. Metal and dust enrichment and variations within absorbing galaxies

Journal: Astronomy & Astrophysics, Issue 672, A68 (2023);
doi:10.1051/0004-6361/202244609

Authors: T. Ramburuth-Hurt, A. De Cia, J.-K. Krogager, C. Ledoux, P. Petitjean, C. Péroux, M. Dessauges-Zavadsky, J. Fynbo, M. Wendt, N. F. Bouché, **C. Konstantopoulou**, and I. Jermann

Description: This article analyzes the chemical enrichment within 64 damped Lyman-α absorption systems (DLAs) at redshifts $1.7<z<4.2$ using high-resolution spectra from VLT/UVES. The component-by-component analysis revealed significant chemical diversity within DLAs, with dust depletion ($[Zn/Fe]_{fit}$) varying up to 0.62 dex within a single system. The authors found that the most chemically enriched systems are at lower redshifts, while dust-poor components are present at all redshifts, likely due to pristine gas accretion. Over-abundances of α-elements and under-abundances of Mn are identified, indicating core-collapse supernovae nucleosynthesis in the ISM.

My contribution: In this work, I have contributed by providing the coefficients (refractory index) for the 9 metals used, including an updated coefficient for P, after correcting for the most recent oscillator strengths, published in Konstantopoulou et al. (2022). I also contributed in the scientific discussion and general comments throughout the manuscript.

Title: Dissecting the interstellar medium of a z = 6.3 galaxy. X-shooter spectroscopy and HST imaging of the afterglow and environment of the Swift GRB 210905A

Journal: Astronomy & Astrophysics, Issue 671, A84 (2023);
doi:10.1051/0004-6361/202244205

Authors: A. Saccardi, S. D. Vergani, A. De Cia, V. D'Elia, K. E. Heintz, L. Izzo, J. T. Palmerio, P. Petitjean, A. Rossi, A. de Ugarte Postigo, L. Christensen, **C. Konstantopoulou**, A. J. Levan, D. B. Malesani, P. Møller, T. Ramburuth-Hurt, R. Salvaterra, N. R. Tanvir, C. C. Thöne, S. Vejlgaard, J. P. U. Fynbo, D. A. Kann, P. Schady, D. J. Watson, K. Wiersema, S. Campana, S. Covino, M. De Pasquale, H. Fausey, D. H. Hartmann, A. J. van der Horst, P. Jakobsson, E. Palazzi, G. Pugliese, S. Savaglio, R. L. C. Starling, G. Stratta, and T. Zafar

Description: This article studies the ISM properties of the GRB host galaxy (GRB 210905A) at z=6.3, using VLT/X-shooter afterglow spectra. The analysis is done to calculate the total metallicity and dust-to-metal ratio, as well as identify nucleosynthesis signatures from massive stars. The low-ionization gas clouds are found several kiloparsecs from the GRB, suggesting a significant impact of ionizing photons. The study highlights the potential of GRBs to provide detailed insights into the metal enrichment, gas kinematics, and dust content of very high-redshift galaxies.

My contribution: In this work, I have contributed by providing the coefficients (refractory index) for carbon and aluminium, published in Konstantopoulou et al. (2022), and general comments throughout the manuscript.

Title: Large metallicity variations in the Galactic interstellar medium

Journal: Nature, Volume 597, p.206–208 (2021); doi:10.1038/s41586-021-03780-0

Authors: Annalisa De Cia, Edward B. Jenkins, Andrew J. Fox, Cédric Ledoux, Tanita Ramburuth-Hurt, **Christina Konstantopoulou**, Patrick Petitjean & Jens-Kristian Krogager

Description: This article measures the dust-corrected metallicity of the neutral ISM towards 25 stars in the Milky Way, revealing significant variations in metallicity by a factor of ten. The average metallicity is found to be 55% of the solar value, and includes regions of low metallicity, down to about 17% of solar metallicity. The results of this work suggests that these chemical inhomogeneities are caused by pristine gas accreting onto the Galactic disk from high-velocity clouds, which does not efficiently mix into the ISM.

My contribution: In this work, I have helped measuring column densities towards eight targets with VoigtFit for a cross-check of the results. I also reviewed the depletion methods and assumptions and collected data from Galactic extinction maps.

LIST OF FIGURES

Figure 1.1 A cartoon view of the CGM from Tumlinson, Peeples, and Werk (2017). 5
Figure 1.2 A cartoon illustration of the likely differences between QSO-DLA and GRB-DLA lines of sight (following Prochaska et al. (2007)). . . 10
Figure 1.3 Gaia map of interstellar dust in the Milky Way. 13
Figure 1.4 Gas-phase metal abundances with respect to their condensation temperatures T_c for the cool diffuse interstellar cloud toward ζ Oph from Savage and Sembach (1996). 15
Figure 1.5 Dust masses produced by SNe IIP as a function of post-explosion time from Schneider and Maiolino (2024). 18
Figure 1.6 Evolution of dust mass fraction in the ISM with time, as modeled by (Zhukovska, Gail, and Trieloff, 2008), for the three main sources of dust. 20
Figure 1.7 Composition of interstellar dust grains formed by different production mechanisms. 22
Figure 2.1 An example of absorption line spectroscopy towards a background quasar from (Péroux and Howk, 2020). 26
Figure 2.2 Example of the fitting process on the spectrum of the QSO-DLA towards Q 2348-011b. 32
Figure 2.3 Velocity profiles of selected transition lines (FeII 1096, NiII 1741, SiII 1526, SiII 1808) from the QSO-DLA system at z_{abs} = 2.61473 towards Q 2348-011b. 33
Figure 2.4 The shapes of the nucleosynthetic curves of different elements. . . . 38
Figure 3.1 Relative abundances of element X with respect to Zn against the amount of dust. 52
Figure 3.2 Dust depletion of element X (δ_X) against the amount of dust. 52
Figure 3.3 Same as Fig. 3.2 for the α-elements and Mn after assuming a constant overabundance for the α-elements and an underabundance plateau for Mn in the Magellanic Clouds. 53
Figure 3.4 Relative abundances of Ti and Ni with respect to Zn against the amount of dust. 54
Figure 3.5 Merged fits of the dust depletion (δ_X) as a function of the amount of dust for all the elements (left) and the slopes of the fits of the depletion sequences $B2_X$ (or refractory index) as a function of the respective element condensation temperature T_c. 56
Figure 3.6 Assumed nucleosynthetic over- or underabundances α_X for the α-elements X (S, Si, Mg, and Ti) and Mn with respect to the amount of dust and metallicity. 60

Figure 3.7 Relative abundances of element X with respect to Zn against the amount of dust . . . 63
Figure 3.8 Dust depletion of element X (δ_X) against the amount of dust 64
Figure 3.9 Velocity profiles of selected low-ionization transition lines from the DLA system at z_{abs} = 2.02484 toward Q 0010−002. Masked regions are shown in gray. The top subpanels show the residuals, and the blue tick marks show the individual velocity components. 65
Figure 3.10 Velocity profiles of selected low-ionization transition lines from the DLA system at z_{abs} = 2.67142 toward Q 0058−292. 66
Figure 3.11 Velocity profiles of selected low-ionization transition lines from the DLA system at z_{abs} = 2.30903 toward Q 0100+030. 67
Figure 3.12 Velocity profiles of selected low-ionization transition lines from the DLA system at z_{abs} = 2.36966 toward Q 0102−190a. 68
Figure 3.13 Velocity profiles of selected low-ionization transition lines from the DLA system at z_{abs} = 1.91267 toward Q 0405−443a. 69
Figure 3.14 Velocity profiles of selected low-ionization transition lines from the DLA system at z_{abs} = 2.55000 toward Q 0405−443b. 70
Figure 3.15 Velocity profiles of selected low-ionization transition lines from the DLA system at z_{abs} = 2.59466 toward Q 0405−443c. 71
Figure 3.16 Velocity profiles of selected low-ionization transition lines from the DLA system at z_{abs} = 2.03956 toward Q 0458−020. 72
Figure 3.17 Velocity profiles of selected low-ionization transition lines from the DLA system at z_{abs} = 2.14105 toward Q 0528−250a. 74
Figure 3.18 Velocity profiles of selected low-ionization transition lines from the DLA system at z_{abs} = 2.81111 toward Q 0528−250b. 76
Figure 3.19 Velocity profiles of selected low-ionization transition lines from the DLA system at z_{abs} = 1.96221 toward Q 0551−366. 77
Figure 3.20 Velocity profiles of selected low-ionization transition lines from the DLA system at z_{abs} = 1.86384 toward Q 0841+129a. 79
Figure 3.21 Velocity profiles of selected low-ionization transition lines from the DLA system at z_{abs} = 2.37452 toward Q 0841+129b. 80
Figure 3.22 Velocity profiles of selected low-ionization transition lines from the DLA system at z_{abs} = 2.47622 toward Q 0841+129c. 81
Figure 3.23 Velocity profiles of selected low-ionization transition lines from the DLA system at z_{abs} = 3.26552 toward Q 1111−152. 82
Figure 3.24 Velocity profiles of selected low-ionization transition lines from the DLA system at z_{abs} = 3.35046 toward Q 1117−134. 82
Figure 3.25 Velocity profiles of selected low-ionization transition lines from the DLA system at z_{abs} = 1.94349 toward Q 1157+014. 83
Figure 3.26 Velocity profiles of selected low-ionization transition lines from the DLA system at z_{abs} = 2.58437 toward Q 1209+093. 84
Figure 3.27 Velocity profiles of selected low-ionization transition lines from the DLA system at z_{abs} = 1.77635 toward Q 1331+170. 85

Figure 3.28 Velocity profiles of selected low-ionization transition lines from the DLA system at $z_{abs} = 2.01881$ toward Q 1409+095a. 86
Figure 3.29 Velocity profiles of selected low-ionization transition lines from the DLA system at $z_{abs} = 1.99615$ toward Q 2116−358. 87
Figure 3.30 Velocity profiles of selected low-ionization transition lines from the DLA system at $z_{abs} = 2.85234$ toward Q 2138−444b. 88
Figure 3.31 Velocity profiles of selected low-ionization transition lines from the DLA system at $z_{abs} = 1.92061$ toward Q 2206−199a. 90
Figure 3.32 Velocity profiles of selected low-ionization transition lines from the DLA system at $z_{abs} = 2.33062$ toward Q 2243−605. 91
Figure 3.33 Velocity profiles of selected low-ionization transition lines from the DLA system at $z_{abs} = 2.28749$ toward Q 2332−094a. 92
Figure 3.34 Velocity profiles of selected low-ionization transition lines from the DLA system at $z_{abs} = 2.43123$ toward Q 2343+125. 93
Figure 3.35 Velocity profiles of selected low-ionization transition lines from the DLA system at $z_{abs} = 2.0951$ toward Q 2344+125. 94
Figure 3.36 Relative abundance of P with respect to Zn against the amount of dust (top). Dust depletion of P against the amount of dust (bottom). 102
Figure 4.1 (Top): Dust-to-metal ratio as a function of the dust tracer. (Bottom): Dust-to-gas ratio as a function of the dust tracer. 114
Figure 4.2 (Top): Dust-to-metal ratio as a function of the total dust-corrected gas metallicity. (Bottom): Dust-to-gas ratio as a function of the total dust-corrected gas metallicity. 115
Figure 4.4 Dust extinction $A_{V,depl}$ as a function of the amount of dust (left panel) and as a function of the total dust-corrected metallicity (right panel). 117
Figure 4.3 Fraction of dust mass contributed by element X, f_{M_X} as a function of the dust tracer [Zn/Fe] for the five most abundant contributors in dust (O, Fe, Si, Mg, C) for QSO- and GRB-DLAs, LMC, SMC and the Milky Way. 118
Figure 4.5 Total dust-corrected metallicity evolution with redshift z for GRB-DLAs (orange diamonds) and QSO-DLAs (black triangles). 123
Figure 4.6 Distribution of metals that compose dust for the main elements that contribute into dust. 130
Figure 4.7 Dust extinction A_V as measured from extinction against the A_V calculated using the dust depletion for GRB-DLAs, LMC, SMC and the Milky Way. 131
Figure 4.8 Relation between the DTM calculated in terms of mass and the DTM calculated in terms of column density (DTM_N) for QSO- and GRB-DLAs, LMC, SMC and the Milky Way. 134

Figure 4.9 Fraction of dust mass contributed by element X, f_{M_X} as a function of the dust tracer [Zn/Fe] for QSO-DLAs. The filled squares indicate the targets that have a dust depletion measurement and the empty symbols indicate the targets whose dust depletion is calculated from the coefficients listed in Table 4.1. . . . 135
Figure 4.10 Fraction of dust mass contributed by element X, f_{M_X} as a function of the dust tracer [Zn/Fe] for GRB-DLAs. . . . 136
Figure 4.11 Fraction of dust mass contributed by element X, f_{M_X} as a function of the dust tracer [Zn/Fe] for the Milky Way. . . . 137
Figure 4.12 Fraction of dust mass contributed by element X, f_{M_X} as a function of the dust tracer [Zn/Fe] for the LMC. . . . 138
Figure 4.13 Fraction of dust mass contributed by element X, f_{M_X} as a function of the dust tracer [Zn/Fe] for the SMC. . . . 139
Figure 5.1 3-dimensional correlation between the dust tracers. . . . 155
Figure 5.2 Correlations of different dust tracer with the primary reference dust tracer. . . . 156
Figure 5.3 Dust depletion of element X against the overall strength of depletion Δ for lines of sight in the MW. . . . 159
Figure 5.4 Abundances with respect to the coefficients B_X (abundance pattern) resulting from eq. 5.9 for ζ Oph in the MW. . . . 162
Figure 5.5 Metal pattern for ζ Oph in the MW. . . . 162
Figure 5.6 Relative abundances with respect to their corresponding slopes with the dust tracer ($C_{XY_{SiTi}}$) for ζ Oph in the MW. . . . 163
Figure 5.7 Abundances with respect to the overall strength of depletion Δ and the dust tracers for MW data. . . . 168
Figure 5.8 Overall strength of depletion Δ with respect to the molecular fraction f_{H_2}. The black triangles are for QSO-DLAs, the blue triangles for the SMC, the purple squares for the LMC and green circles for the MW. . . . 173
Figure 5.9 Comparison of the overall strength of depletion obtained from eq. 5.1 including Zn (Δ) and the overall strength of depletion after excluding Zn from the analysis (Δ_{noZn}). . . . 175
Figure 5.10 Correlations of different dust tracers with the indirect reference dust tracer. . . . 177
Figure 5.11 Correlations of different dust tracers with the primary reference dust tracer, color coded by the overall strength of depletion (Δ) . . . 178
Figure 5.12 Correlations of different dust tracers with the indirect dust tracer [Zn/Fe], color coded by the overall strength of depletion (Δ). The red solid line shows the linear fit to the data. . . . 179
Figure 5.13 Correlations of different dust tracers with the indirect dust tracer [Ge/Ni], color coded by the overall strength of depletion (Δ). The red solid line shows the linear fit to the data. . . . 180
Figure 5.14 Relative abundance of element X with respect to Kr against the overall strength of depletion Δ for lines of sight in the MW. . . . 181

Figure 5.15 [O/Kr] with respect to log N(HI (left panel) and [Kr/H] with respect to log N(HI (right panel). 181
Figure 6.1 Observation of the pair QSOs J0836+4841A and J0836+4841B. 191
Figure 6.2 Cut-out of the spectrum of J0836++4841 before (left panel) and after (right panel) cosmic ray removal. 194
Figure 6.3 The final reduced 2D spectrum of of J0836++4841. 194
Figure 6.4 Spectroscopic redshift offset Δz between the observed pairs with respect to the seperation d 195
Figure 6.5 The spectra of the QSO pair J1125+3256AB at z = 1.3. 198
Figure 6.6 Comparison between the photometric redshifts estimated by Richards et al. (2009) and the spectroscopic redshifts determined in this work. 199
Figure 6.7 The observed NOT spectra of the QSO pair: The top left panel shows the QSO J0820+0357B at $z = 1.87$ and the bottom left panel shows the QSO J0820+0357A at $z = 1.56$. 200
Figure A2.1 Velocity profiles of selected low-ionization transition lines from the DLA system at z_{abs} = 2.92648 toward Q 0102−190. 217
Figure A2.2 Velocity profiles of selected low-ionization transition lines from the DLA system at z_{abs} = 2.42322 toward Q 0112+030. 218
Figure A2.3 Velocity profiles of selected low-ionization transition lines from the DLA system at z_{abs} = 2.70163 toward Q 0112−306. 219
Figure A2.4 Velocity profiles of selected low-ionization transition lines from the DLA system at z_{abs} = 3.06209 toward Q 0336−017. 220
Figure A2.5 Velocity profiles of selected low-ionization transition lines from the DLA system at z_{abs} = 2.06658 toward Q 0450−131. 221
Figure A2.6 Velocity profiles of selected low-ionization transition lines from the DLA system at z_{abs} = 2.61843 toward Q 0913+072. 222
Figure A2.7 Velocity profiles of selected low-ionization transition lines from the DLA system at z_{abs} = 2.77779 toward Q 1036−229. 223
Figure A2.8 Velocity profiles of selected low-ionization transition lines from the DLA system at z_{abs} = 3.48185 toward Q 1108−077. 224
Figure A2.9 Velocity profiles of selected low-ionization transition lines from the DLA system at z_{abs} = 1.89177 toward Q 1210+175. 225
Figure A2.10 Velocity profiles of selected low-ionization transition lines from the DLA system at z_{abs} = 2.33771 toward Q 1232+082. 226
Figure A2.11 Velocity profiles of selected low-ionization transition lines from the DLA system at z_{abs} = 2.50792 toward Q 1337+113. 227
Figure A2.12 Velocity profiles of selected low-ionization transition lines from the DLA system at z_{abs} = 2.79584 toward Q 1337+113. 228
Figure A2.13 Velocity profiles of selected low-ionization transition lines from the DLA system at z_{abs} = 3.11835 toward Q 1340−136. 229
Figure A2.14 Velocity profiles of selected low-ionization transition lines from the DLA system at z_{abs} = 2.45593 toward Q 1409+095. 230
Figure A2.15 Velocity profiles of selected low-ionization transition lines from the DLA system at z_{abs} = 2.25466 toward Q 1451+123. 231

Figure A2.16 Velocity profiles of selected low-ionization transition lines from the DLA system at z_{abs} = 2.46921 toward Q 1451+123. 232
Figure A2.17 Velocity profiles of selected low-ionization transition lines from the DLA system at z_{abs} = 2.50734 toward Q 2059−360. 233
Figure A2.18 Velocity profiles of selected low-ionization transition lines from the DLA system at z_{abs} = 3.08291 toward Q 2059−360. 234
Figure A2.19 Velocity profiles of selected low-ionization transition lines from the DLA system at z_{abs} = 2.07622 toward Q 2206−199. 235
Figure A2.20 Velocity profiles of selected low-ionization transition lines from the DLA system at z_{abs} = 2.06552 toward Q 2231−002. 236
Figure A2.21 Velocity profiles of selected low-ionization transition lines from the DLA system at z_{abs} = 3.05722 toward Q 2332−094. 237
Figure A2.22 Velocity profiles of selected low-ionization transition lines from the DLA system at z_{abs} = 2.53787 toward Q 2344+125. 238
Figure A2.23 Velocity profiles of selected low-ionization transition lines from the DLA system at z_{abs} = 2.42695 toward Q 2348−011. 239
Figure A2.24 Velocity profiles of selected low-ionization transition lines from the DLA system at z_{abs} = 2.61473 toward Q 2348−011. 239

LIST OF TABLES

Table 1.1 Most prominent dust species produced by different production mechanisms 22
Table 2.1 New UVES QSO-DLA Ti and Ni measurements or limits 34
Table 3.1 Solar abundances. 43
Table 3.2 Number of Ti and Ni measurements for the Milky Way, QSO-DLAs, the LMC, SMC, and GRB-DLAs. 45
Table 3.3 New UVES QSO-DLA Ti and Ni measurements 47
Table 3.4 Coefficients $A2_X$ and $B2_X$ resulting from the linear merged fit of the depletion sequences. 51
Table 3.5 Orthogonal distance regression results of the fits for the depletion of Ti in the different environments. 51
Table 3.6 Same as Table 3.5, but for Ni. 53
Table 3.7 QSO-DLA column densities 96
Table 3.7 continued 97
Table 3.7 continued 98
Table 3.8 Milky Way column densities 99
Table 3.9 Milky Way. Elements with limited coverage 99
Table 3.10 GRB-DLAs 100

Table 3.11 LMC column densities . . . 100
Table 3.12 SMC column densities . . . 101
Table 3.13 The updated column densities for PII . . . 102
Table 3.14 The coefficients for PII . . . 102
Table 3.15 QSO-DLA column densities . . . 103
Table 3.15 continued . . . 104
Table 3.15 continued . . . 105
Table 4.1 Coefficients $A2_X$ and $B2_X$ resulting from the linear fit of the depletion sequences of metals. . . . 112
Table 4.2 Gas- and solid-phase abundances of the main elements that contribute to the dust composition for systems in different environments and for different intervals of [Zn/Fe]. . . . 125
Table 4.3 Average percentage of the main elements that contribute to the dust composition for systems in different environments. . . . 126
Table 4.4 QSO-DLAs dust properties . . . 141
Table 4.4 continued . . . 142
Table 4.5 Milky Way dust properties . . . 143
Table 4.6 LMC dust properties . . . 143
Table 4.7 SMC dust properties . . . 144
Table 4.8 GRB-DLAs dust properties . . . 145
Table 5.1 Parameters[a] resulting from the linear fit ($[X/Y]_{ref} = C_{XY} \times [X/Y]$) between valid correlations among different dust tracers [X/Y] with the reference dust tracers ($[X/Y]_{ref}$ = [Si/Ti], [Zn/Fe], [Ge/Ni]). . . . 160
Table 5.2 Coefficients B_{XY}. . . . 167
Table 5.3 The 70 dust tracers identified in our method after applying the selection criteria described in Section 5.4.1. $\Delta B2_X$ is the difference between the refractory indices $B2_X$ of X and Y. The $B2_X$ coefficients are taken from Konstantopoulou et al. (2022). . . . 183
Table 5.4 Same as Table 5.1 but for mixed groups of elements. . . . 184
Table 5.4 continued . . . 185
Table 5.4 continued . . . 186
Table 5.4 continued . . . 187
Table 6.1 Observations log for the 22 pair QSOs and flux standard stars. . . . 192
Table 6.2 Spectroscopically confirmed QSOs, the estimated redshifts and dust extinction A_V. . . . 196

BIBLIOGRAPHY

ALMA Partnership, C. L. Brogan, et al. (July 2015). «The 2014 ALMA Long Baseline Campaign: First Results from High Angular Resolution Observations toward the HL Tau Region». In: *ApJ* 808.1, L3, p. L3. DOI: 10.1088/2041-8205/808/1/L3. arXiv: 1503.02649 [astro-ph.SR] (Cited on page 12).

Abbott, B. P., R. Abbott, et al. (Oct. 2017). «Gravitational Waves and Gamma-Rays from a Binary Neutron Star Merger: GW170817 and GRB 170817A». In: *ApJ* 848.2, L13, p. L13. DOI: 10.3847/2041-8213/aa920c. arXiv: 1710.05834 [astro-ph.HE] (Cited on page 8).

Algera, Hiddo, Hanae Inami, et al. (Aug. 2024). «Accurate Simultaneous Constraints on the Dust Mass, Temperature and Emissivity Index of a Galaxy at Redshift 7.31». In: *arXiv e-prints*, arXiv:2408.02267, arXiv:2408.02267. DOI: 10.48550/arXiv.2408.02267. arXiv: 2408.02267 [astro-ph.GA] (Cited on page 210).

Altamura, E., S. Brennan, et al. (Dec. 2019). «Discovery of a binary quasar at z = 1.76». In: *Contributions of the Astronomical Observatory Skalnate Pleso* 49.3, pp. 528–531 (Cited on page 190).

Arnett, David (1996). *Supernovae and Nucleosynthesis: An Investigation of the History of Matter from the Big Bang to the Present* (Cited on page 4).

Arrigoni, Matías, Scott C. Trager, et al. (Feb. 2010). «Galactic chemical evolution in hierarchical formation models - I. Early-type galaxies in the local Universe». In: *MNRAS* 402.1, pp. 173–190. DOI: 10.1111/j.1365-2966.2009.15924.x. arXiv: 0905.4189 [astro-ph.CO] (Cited on page 41).

Asplund, M., A. M. Amarsi, and N. Grevesse (Sept. 2021). «The chemical make-up of the Sun: A 2020 vision». In: *A&A* 653, A141, A141. DOI: 10.1051/0004-6361/202140445. arXiv: 2105.01661 [astro-ph.SR] (Cited on pages 7, 35, 43, 110, 113, 120, 151).

Asplund, Martin, Nicolas Grevesse, et al. (Sept. 2009). «The Chemical Composition of the Sun». In: *ARA&A* 47.1, pp. 481–522. DOI: 10.1146/annurev.astro.46.060407.145222. arXiv: 0909.0948 [astro-ph.SR] (Cited on page 35).

Barbuy, B., A. C. S. Friaça, et al. (Aug. 2015). «Zinc abundances in Galactic bulge field red giants: Implications for damped Lyman-α systems». In: *A&A* 580, A40, A40. DOI: 10.1051/0004-6361/201525694. arXiv: 1506.01612 [astro-ph.GA] (Cited on pages 48, 151, 174).

Battistini, Chiara and Thomas Bensby (May 2015). «The origin and evolution of the odd-Z iron-peak elements Sc, V, Mn, and Co in the Milky Way stellar disk». In: *A&A* 577, A9, A9. DOI: 10.1051/0004-6361/201425327. arXiv: 1502.01152 [astro-ph.GA] (Cited on page 49).

Bensby, T., S. Feltzing, and I. Lundström (Nov. 2003). «Elemental abundance trends in the Galactic thin and thick disks as traced by nearby F and G dwarf stars». In: *A&A* 410, pp. 527–551. DOI: 10.1051/0004-6361:20031213 (Cited on page 38).

Berg, Trystyn A. M., Sara L. Ellison, et al. (Oct. 2015). «The chemistry of the most metal-rich damped Lyman α systems at z $\sim$ 2 - II. Context with the Local Group». In: *MNRAS* 452.4, pp. 4326–4346. DOI: 10.1093/mnras/stv1577. arXiv: 1507.08311 [astro-ph.GA] (Cited on pages 43–45, 63, 98, 105, 110, 142, 152, 175, 204).

Bernstein, Rebecca A., Wendy L. Freedman, and Barry F. Madore (May 2002). «The First Detections of the Extragalactic Background Light at 3000, 5500, and 8000 Å. I. Results». In: *ApJ* 571.1, pp. 56–84. DOI: 10.1086/339422. arXiv: astro-ph/0112153 [astro-ph] (Cited on page 11).

Bestenlehner, Joachim M., Paul A. Crowther, et al. (Dec. 2020). «The R136 star cluster dissected with Hubble Space Telescope/STIS - II. Physical properties of the most massive stars in R136». In: *MNRAS* 499.2, pp. 1918–1936. DOI: 10.1093/mnras/staa2801. arXiv: 2009.05136 [astro-ph.SR] (Cited on page 44).

Bianchi, Simone and Raffaella Schneider (July 2007). «Dust formation and survival in supernova ejecta». In: *MNRAS* 378.3, pp. 973–982. DOI: 10.1111/j.1365-2966.2007.11829.x. arXiv: 0704.0586 [astro-ph] (Cited on pages 17, 21).

Blair, William P., Parviz Ghavamian, et al. (June 2007). «Spitzer Space Telescope Observations of Kepler's Supernova Remnant: A Detailed Look at the Circumstellar Dust Component». In: *ApJ* 662.2, pp. 998–1013. DOI: 10.1086/518414. arXiv: astro-ph/0703660 [astro-ph] (Cited on page 21).

Blandford, R. D. and R. L. Znajek (May 1977). «Electromagnetic extraction of energy from Kerr black holes.» In: *MNRAS* 179, pp. 433–456. DOI: 10.1093/mnras/179.3.433 (Cited on page 8).

Blitz, Leo and Erik Rosolowsky (Oct. 2006). «The Role of Pressure in GMC Formation II: The H_2-Pressure Relation». In: *ApJ* 650.2, pp. 933–944. DOI: 10.1086/50541710.48550/arXiv.astro-ph/0605035. arXiv: astro-ph/0605035 [astro-ph] (Cited on pages 119, 121).

Bloom, J. S., D. A. Perley, et al. (Jan. 2009). «Observations of the Naked-Eye GRB 080319B: Implications of Nature's Brightest Explosion». In: *ApJ* 691.1, pp. 723–737. DOI: 10.1088/0004-637X/691/1/723. arXiv: 0803.3215 [astro-ph] (Cited on page 9).

Bocchio, Marco, Anthony P. Jones, and Jonathan D. Slavin (Oct. 2014). «A re-evaluation of dust processing in supernova shock waves». In: *A&A* 570, A32, A32. DOI: 10.1051/0004-6361/201424368 (Cited on page 124).

Boggs, P., R. Byrd, et al. (1992). «User's reference guide for ODRPACK version 2.01:: software for weighted orthogonal distance regression». In: *User's reference guide for ODRPACK version 2.01:: software for weighted orthogonal distance regression* (Cited on page 50).

Boissé, P. and J. Bergeron (Feb. 2019). «Improved Ni II oscillator strengths from quasar absorption systems». In: *A&A* 622, A140, A140. DOI: 10.1051/0004-6361/201834308 (Cited on pages 44, 46, 100, 101).

Bolmer, J., C. Ledoux, et al. (Mar. 2019). «Evidence for diffuse molecular gas and dust in the hearts of gamma-ray burst host galaxies. Unveiling the nature of high-redshift damped

Lyman-α systems». In: *A&A* 623, A43, A43. DOI: 10.1051/0004-6361/201834422. arXiv: 1810.06403 [astro-ph.GA] (Cited on pages 9, 27, 35, 42–45, 55, 100, 110, 127, 152, 204).

Brooker, Ezra S., Sarah M. Stangl, et al. (June 2022). «Dependence of Dust Formation on the Supernova Explosion». In: *ApJ* 931.2, 85, p. 85. DOI: 10.3847/1538-4357/ac57c3. arXiv: 2103.12781 [astro-ph.HE] (Cited on page 17).

Brown, M. S., R. B. Alkhayat, et al. (Nov. 2018). «Oscillator Strengths for Ultraviolet Transitions in P II: The Multiplet at 1308 Å». In: *ApJ* 868.1, 42, p. 42. DOI: 10.3847/1538-4357/aae688. arXiv: 1810.04533 [physics.atom-ph] (Cited on pages 101, 105).

Calura, F., A. Pipino, and F. Matteucci (Mar. 2008). «The cycle of interstellar dust in galaxies of different morphological types». In: *A&A* 479.3, pp. 669–685. DOI: 10.1051/0004-6361:20078090. arXiv: 0706.2197 [astro-ph] (Cited on page 41).

Calzetti, Daniela, Ralph C. Bohlin, et al. (June 1995). «Scattering Properties of the Dust in the Reflection Nebula IC 435». In: *ApJ* 446, p. L97. DOI: 10.1086/187939 (Cited on page 109).

Cameron, Alex J., Deanne B. Fisher, et al. (Sept. 2021). «The DUVET Survey: Direct T_e-based Metallicity Mapping of Metal-enriched Outflows and Metal-poor Inflows in Markarian 1486». In: *ApJ* 918.1, L16, p. L16. DOI: 10.3847/2041-8213/ac18ca. arXiv: 2108.13211 [astro-ph.GA] (Cited on page 4).

Cardelli, Jason A., Geoffrey C. Clayton, and John S. Mathis (Oct. 1989). «The Relationship between Infrared, Optical, and Ultraviolet Extinction». In: *ApJ* 345, p. 245. DOI: 10.1086/167900 (Cited on pages 13, 21).

Cardelli, Jason A., David M. Meyer, et al. (Aug. 1996). «The Abundance of Interstellar Carbon». In: *ApJ* 467, p. 334. DOI: 10.1086/177608 (Cited on pages 169, 172).

Cartledge, Stefan I. B., J. T. Lauroesch, et al. (Apr. 2006). «The Homogeneity of Interstellar Elemental Abundances in the Galactic Disk». In: *ApJ* 641.1, pp. 327–346. DOI: 10.1086/500297. arXiv: astro-ph/0512312 [astro-ph] (Cited on page 128).

Cashman, Frances H., Varsha P. Kulkarni, et al. (May 2017). «Atomic Data Revisions for Transitions Relevant to Observations of Interstellar, Circumgalactic, and Intergalactic Matter». In: *ApJS* 230.1, 8, p. 8. DOI: 10.3847/1538-4365/aa6d84. arXiv: 1701.04847 [astro-ph.GA] (Cited on pages 44, 46, 98–101, 105).

Cayrel, R., E. Depagne, et al. (Mar. 2004). «First stars V - Abundance patterns from C to Zn and supernova yields in the early Galaxy». In: *A&A* 416, pp. 1117–1138. DOI: 10.1051/0004-6361:20034074. arXiv: astro-ph/0311082 [astro-ph] (Cited on page 38).

Christensen, L., P. Møller, et al. (Nov. 2014). «Verifying the mass-metallicity relation in damped Lyman α selected galaxies at $0.1 < z < 3.2$». In: *MNRAS* 445.1, pp. 225–238. DOI: 10.1093/mnras/stu1726. arXiv: 1404.6529 [astro-ph.GA] (Cited on pages 41, 49).

Crowther, Paul A., S. M. Caballero-Nieves, et al. (May 2016). «The R136 star cluster dissected with Hubble Space Telescope/STIS. I. Far-ultraviolet spectroscopic census and the origin of He II λ1640 in young star clusters». In: *MNRAS* 458.1, pp. 624–659. DOI: 10.1093/mnras/stw273. arXiv: 1603.04994 [astro-ph.SR] (Cited on page 44).

D'Elia, V., S. Campana, et al. (Nov. 2011). «Very Large Telescope/Ultraviolet and Visual Echelle Spectrograph and FORS2 spectroscopy of the GRB 081008 afterglow». In: *MNRAS* 418.1, pp. 680–690. DOI: 10.1111/j.1365-2966.2011.19517.x (Cited on page 110).

D'Odorico, V., S. Cristiani, et al. (Dec. 2016). «Metals in the z $\sim$ 3 intergalactic medium: results from an ultra-high signal-to-noise ratio UVES quasar spectrum». In: *MNRAS* 463.3, pp. 2690–2707. DOI: 10.1093/mnras/stw2161. arXiv: 1608.06116 [astro-ph.GA] (Cited on page 26).

D'Odorico, Valentina, James S. Bolton, et al. (Nov. 2023). «Galaxy Formation and Symbiotic Evolution with the Inter-Galactic Medium in the Age of ELT-ANDES». In: *arXiv e-prints*, arXiv:2311.16803, arXiv:2311.16803. DOI: 10.48550/arXiv.2311.16803. arXiv: 2311.16803 [astro-ph.GA] (Cited on page 210).

D'Odorico, Valentina, Stefano Cristiani, et al. (July 2004). «Chemical abundances in QSO host galaxies and environments from narrow absorption line systems». In: *MNRAS* 351.3, pp. 976–988. DOI: 10.1111/j.1365-2966.2004.07840.x. arXiv: astro-ph/0402043 [astro-ph] (Cited on page 27).

Danziger, I. J., C. Gouiffes, et al. (Mar. 1989). «Supernova 1987A in the Large Magellanic Cloud». In: *IAU Circ.* 4746, p. 1 (Cited on page 17).

De Cia, A., C. Ledoux, et al. (Dec. 2013). «Dust-to-metal ratios in damped Lyman-α absorbers. Fresh clues to the origins of dust and optical extinction towards γ-ray bursts». In: *A&A* 560, A88, A88. DOI: 10.1051/0004-6361/201321834. arXiv: 1305.1153 [astro-ph.CO] (Cited on pages 107, 121).

De Cia, A., C. Ledoux, et al. (Dec. 2016). «Dust-depletion sequences in damped Lyman-α absorbers. A unified picture from low-metallicity systems to the Galaxy». In: *A&A* 596, A97, A97. DOI: 10.1051/0004-6361/201527895. arXiv: 1608.08621 [astro-ph.GA] (Cited on pages 12, 14, 16, 17, 19, 22, 23, 27, 34, 36, 39, 41–49, 51, 56, 61, 63, 98, 105, 107, 109–112, 119, 121, 123, 142, 149–151, 165, 167, 169–171, 204, 206).

De Cia, Annalisa (May 2018). «Metals and dust in the neutral ISM: the Galaxy, Magellanic Clouds, and damped Lyman-α absorbers». In: *A&A* 613, L2, p. L2. DOI: 10.1051/0004-6361/201833034. arXiv: 1805.05365 [astro-ph.GA] (Cited on pages 16, 42–44, 48, 59, 110, 123, 142, 150–152).

De Cia, Annalisa, Edward B. Jenkins, et al. (Sept. 2021). «Large metallicity variations in the Galactic interstellar medium». In: *Nature* 597.7875, pp. 206–208. DOI: 10.1038/s41586-021-03780-0. arXiv: 2109.03249 [astro-ph.GA] (Cited on pages 10, 25, 28, 30, 36, 42, 43, 45, 99, 110, 115, 117, 143, 150, 152, 164–166, 204, 208).

De Cia, Annalisa, Cédric Ledoux, et al. (Apr. 2018). «The cosmic evolution of dust-corrected metallicity in the neutral gas». In: *A&A* 611, A76, A76. DOI: 10.1051/0004-6361/201731970. arXiv: 1709.06578 [astro-ph.GA] (Cited on page 27).

De Cia, Annalisa, Julia Roman-Duval, et al. (Mar. 2024). «α-element enhancements in the ISM of the LMC and SMC: Evidence of recent star formation». In: *A&A* 683, A216, A216. DOI: 10.1051/0004-6361/202346611 (Cited on pages 36, 58, 144, 149, 151, 161, 166, 172, 205, 207).

De Vis, P., H. L. Gomez, et al. (Oct. 2017). «Using dust, gas and stellar mass-selected samples to probe dust sources and sinks in low-metallicity galaxies». In: *MNRAS* 471.2, pp. 1743–

1765. DOI: 10.1093/mnras/stx981. arXiv: 1705.02340 [astro-ph.GA] (Cited on page 122).

Dekker, Hans, Sandro D'Odorico, et al. (Aug. 2000). «Design, construction, and performance of UVES, the echelle spectrograph for the UT2 Kueyen Telescope at the ESO Paranal Observatory». In: *Optical and IR Telescope Instrumentation and Detectors*. Ed. by Masanori Iye and Alan F. Moorwood. Vol. 4008. Society of Photo-Optical Instrumentation Engineers (SPIE) Conference Series, pp. 534–545. DOI: 10.1117/12.395512 (Cited on page 27).

Dessauges-Zavadsky, M., J. X. Prochaska, et al. (Jan. 2006). «A new comprehensive set of elemental abundances in DLAs. II. Data analysis and chemical variation studies». In: *A&A* 445.1, pp. 93–113. DOI: 10.1051/0004-6361:20053200. arXiv: astro-ph/0511031 [astro-ph] (Cited on page 57).

Domainko, W., M. Mair, et al. (June 2006). «Enrichment of the ICM of galaxy clusters due to ram-pressure stripping». In: *A&A* 452.3, pp. 795–802. DOI: 10.1051/0004-6361:20053921. arXiv: astro-ph/0507605 [astro-ph] (Cited on page 4).

Draine, B. T. (Sept. 1989). «Interstellar extinction in the infrared». In: *Infrared Spectroscopy in Astronomy*. Ed. by Erika Böhm-Vitense, p. 93 (Cited on page 13).

— (Jan. 2003). «Interstellar Dust Grains». In: *ARA&A* 41, pp. 241–289. DOI: 10.1146/annurev.astro.41.011802.094840. arXiv: astro-ph/0304489 [astro-ph] (Cited on pages 11, 13, 17, 19, 21, 22, 109, 113, 119, 125, 169).

Draine, B. T. and Aigen Li (Mar. 2007). «Infrared Emission from Interstellar Dust. IV. The Silicate-Graphite-PAH Model in the Post-Spitzer Era». In: *ApJ* 657.2, pp. 810–837. DOI: 10.1086/511055. arXiv: astro-ph/0608003 [astro-ph] (Cited on pages 21, 122).

Draine, B. T. and E. E. Salpeter (July 1979). «Destruction mechanisms for interstellar dust.» In: *ApJ* 231, pp. 438–455. DOI: 10.1086/157206 (Cited on pages 17, 19).

Draine, Bruce T. (2011). *Physics of the Interstellar and Intergalactic Medium* (Cited on pages 6, 41).

Duffau, S., E. Caffau, et al. (Aug. 2017). «The Gaia-ESO Survey: Galactic evolution of sulphur and zinc». In: *A&A* 604, A128, A128. DOI: 10.1051/0004-6361/201730477. arXiv: 1704.02981 [astro-ph.SR] (Cited on page 151).

Dunne, Loretta, Stephen Eales, et al. (July 2003). «Type II supernovae as a significant source of interstellar dust». In: *Nature* 424.6946, pp. 285–287. DOI: 10.1038/nature01792. arXiv: astro-ph/0307320 [astro-ph] (Cited on pages 17, 109, 119).

Dwek, Eli (July 1998). «The Evolution of the Elemental Abundances in the Gas and Dust Phases of the Galaxy». In: *ApJ* 501, p. 643. DOI: 10.1086/305829. arXiv: astro-ph/9707024 [astro-ph] (Cited on page 41).

— (July 2016). «Iron: A Key Element for Understanding the Origin and Evolution of Interstellar Dust». In: *ApJ* 825.2, 136, p. 136. DOI: 10.3847/0004-637X/825/2/13610.48550/arXiv.1605.01957. arXiv: 1605.01957 [astro-ph.GA] (Cited on pages 17, 109, 119).

Dwek, Eli, Scott M. Foster, and Olaf Vancura (Jan. 1996). «Cooling, Sputtering, and Infrared Emission from Dust Grains in Fast Nonradiative Shocks». In: *ApJ* 457, p. 244. DOI: 10.1086/176725 (Cited on page 124).

Edvardsson, B., J. Andersen, et al. (Aug. 1993). «The Chemical Evolution of the Galactic Disk - Part One - Analysis and Results». In: *A&A* 275, p. 101 (Cited on page 38).

Elíasdóttir, Á., J. P. U. Fynbo, et al. (June 2009). «Dust Extinction in High-z Galaxies with Gamma-Ray Burst Afterglow Spectroscopy: The 2175 Å Feature at z = 2.45». In: *ApJ* 697.2, pp. 1725–1740. DOI: 10.1088/0004-637X/697/2/1725. arXiv: 0810.2897 [astro-ph] (Cited on pages 14, 125, 169).

Fall, S. M. and G. Efstathiou (Oct. 1980). «Formation and rotation of disc galaxies with haloes.» In: *MNRAS* 193, pp. 189–206. DOI: 10.1093/mnras/193.2.189 (Cited on page 4).

Feldmann, Robert (May 2015). «The equilibrium view on dust and metals in galaxies: Galactic outflows drive low dust-to-metal ratios in dwarf galaxies». In: *MNRAS* 449.3, pp. 3274–3292. DOI: 10.1093/mnras/stv552. arXiv: 1412.2755 [astro-ph.GA] (Cited on pages 12, 22, 122).

Feltzing, S., M. Fohlman, and T. Bensby (May 2007). «Manganese trends in a sample of thin and thick disk stars. The origin of Mn». In: *A&A* 467.2, pp. 665–677. DOI: 10.1051/0004-6361:20065797. arXiv: astro-ph/0703488 [astro-ph] (Cited on page 58).

Ferrarotti, A. S. and H. P. Gail (Feb. 2006). «Composition and quantities of dust produced by AGB-stars and returned to the interstellar medium». In: *A&A* 447.2, pp. 553–576. DOI: 10.1051/0004-6361:20041198 (Cited on pages 17, 18, 22).

Field, G. B. (Feb. 1974). «Interstellar abundances: gas and dust.» In: *ApJ* 187, pp. 453–459. DOI: 10.1086/152654 (Cited on pages 12, 14, 15, 25, 36, 41, 56, 109, 149).

Fitzpatrick, E. L. and D. Massa (Aug. 1986). «An Analysis of the Shapes of Ultraviolet Extinction Curves. I. The 2175 Angstrom Bump». In: *ApJ* 307, p. 286. DOI: 10.1086/164415 (Cited on pages 13, 41, 169).

Fitzpatrick, Edward L. and Derck Massa (Jan. 1990). «An Analysis of the Shapes of Ultraviolet Extinction Curves. III. an Atlas of Ultraviolet Extinction Curves». In: *ApJS* 72, p. 163. DOI: 10.1086/191413 (Cited on page 21).

Flesch, E. W. (July 2023). *VizieR Online Data Catalog: The Million Quasars (Milliquas) catalogue, version 8 (Flesch, 2023)*. VizieR On-line Data Catalog: VII/294. Originally published in: 2023OJAp....6E..49F (Cited on page 8).

Fontana, A., L. Pozzetti, et al. (Sept. 2004). «The K20 survey. VI. The distribution of the stellar masses in galaxies up to z = 2». In: *A&A* 424, pp. 23–42. DOI: 10.1051/0004-6361:20035626. arXiv: astro-ph/0405055 [astro-ph] (Cited on page 9).

Fox, A. J., P. Petitjean, et al. (Apr. 2007). «Hot halos around high redshift protogalaxies. Observations of O VI and N V absorption in damped Lyman-α systems». In: *A&A* 465.1, pp. 171–184. DOI: 10.1051/0004-6361:20066157. arXiv: astro-ph/0701392 [astro-ph] (Cited on page 27).

Fox, Andrew and Romeel Davé, eds. (Jan. 2017). *Gas Accretion onto Galaxies*. Vol. 430. Astrophysics and Space Science Library. DOI: 10.1007/978-3-319-52512-9 (Cited on page 4).

Friis, M., A. De Cia, et al. (July 2015). «The warm, the excited, and the molecular gas: GRB 121024A shining through its star-forming galaxy». In: *MNRAS* 451.1, pp. 167–183. DOI: 10.1093/mnras/stv960. arXiv: 1409.6315 [astro-ph.GA] (Cited on page 127).

Fynbo, J. P. U., L. Christensen, et al. (Nov. 2023). «The galaxy counterpart and environment of the dusty damped Lyman-α absorber at z = 2.226 towards Q 1218+0832». In: *A&A* 679, A30, A30. DOI: 10.1051/0004-6361/202347403. arXiv: 2308.15781 [astro-ph.GA] (Cited on page 14).

Fynbo, J. P. U., J. K. Krogager, et al. (Sept. 2017). «The High A_V Quasar Survey: A z = 2.027 metal-rich damped Lyman-α absorber towards a red quasar at z = 3.21». In: *A&A* 606, A13, A13. DOI: 10.1051/0004-6361/201730726. arXiv: 1706.07016 [astro-ph.GA] (Cited on page 44).

Fynbo, J. P. U., C. Ledoux, et al. (June 2011). «Galaxy counterparts of metal-rich damped Lyα absorbers - II. A solar-metallicity and dusty DLA at z_{abs}= 2.58». In: *MNRAS* 413.4, pp. 2481–2488. DOI: 10.1111/j.1365-2966.2011.18318.x. arXiv: 1011.5312 [astro-ph.CO] (Cited on page 14).

Fynbo, Johan P. U., J. Xavier Prochaska, et al. (Aug. 2008). «Reconciling the Metallicity Distributions of Gamma-Ray Burst, Damped Lyα, and Lyman Break Galaxies at z $\approx$ 3». In: *ApJ* 683.1, pp. 321–328. DOI: 10.1086/589555. arXiv: 0801.3273 [astro-ph] (Cited on pages 9, 43, 110, 121, 126).

Gaia Collaboration, A. G. A. Brown, et al. (Aug. 2018). «Gaia Data Release 2. Summary of the contents and survey properties». In: *A&A* 616, A1, A1. DOI: 10.1051/0004-6361/201833051. arXiv: 1804.09365 [astro-ph.GA] (Cited on page 190).

Gaia Collaboration, A. G. A. Brown, et al. (May 2021). «Gaia Early Data Release 3. Summary of the contents and survey properties». In: *A&A* 649, A1, A1. DOI: 10.1051/0004-6361/202039657. arXiv: 2012.01533 [astro-ph.GA] (Cited on pages 12, 190).

Gail, H. P. and E. Sedlmayr (Jan. 1998). «Inorganic dust formation in astrophysical environments». In: *Faraday Discussions* 109, p. 303. DOI: 10.1039/a709290c (Cited on page 18).

Gail, H. P., S. V. Zhukovska, et al. (June 2009). «Stardust from Asymptotic Giant Branch Stars». In: *ApJ* 698.2, pp. 1136–1154. DOI: 10.1088/0004-637X/698/2/1136 (Cited on pages 17, 109, 119).

Galliano, Frédéric, Eli Dwek, and Pierre Chanial (Jan. 2008). «Stellar Evolutionary Effects on the Abundances of Polycyclic Aromatic Hydrocarbons and Supernova-Condensed Dust in Galaxies». In: *ApJ* 672.1, pp. 214–243. DOI: 10.1086/523621. arXiv: 0708.0790 [astro-ph] (Cited on page 122).

Galliano, Frédéric, Maud Galametz, and Anthony P. Jones (Sept. 2018). «The Interstellar Dust Properties of Nearby Galaxies». In: *ARA&A* 56, pp. 673–713. DOI: 10.1146/annurev-astro-081817-051900. arXiv: 1711.07434 [astro-ph.GA] (Cited on pages 11, 122).

Gehren, T., Y. C. Liang, et al. (Jan. 2004). «Abundances of Na, Mg and Al in nearby metal-poor stars». In: *A&A* 413, pp. 1045–1063. DOI: 10.1051/0004-6361:20031582 (Cited on page 38).

Geier, S. J., K. E. Heintz, et al. (May 2019). «Gaia-assisted selection of a quasar reddened by dust in an extremely strong damped Lyman-α absorber at z = 2.226». In: *A&A* 625, L9, p. L9. DOI: 10.1051/0004-6361/201935108. arXiv: 1904.01686 [astro-ph.GA] (Cited on pages 14, 189).

Gomez, H. L., C. J. R. Clark, et al. (Mar. 2012). «Dust in historical Galactic Type Ia supernova remnants with Herschel». In: *MNRAS* 420.4, pp. 3557–3573. DOI: 10.1111/j.1365-2966.2011.20272.x. arXiv: 1111.6627 [astro-ph.GA] (Cited on page 21).

Gordon, Karl D. and Geoffrey C. Clayton (June 1998a). «Starburst-like Dust Extinction in the Small Magellanic Cloud». In: *ApJ* 500.2, pp. 816–824. DOI: 10.1086/305774. arXiv: astro-ph/9802003 [astro-ph] (Cited on pages 14, 125).

— (June 1998b). «Starburst-like Dust Extinction in the Small Magellanic Cloud». In: *ApJ* 500.2, pp. 816–824. DOI: 10.1086/305774. arXiv: astro-ph/9802003 [astro-ph] (Cited on page 169).

Gordon, Karl D., Geoffrey C. Clayton, et al. (Sept. 2003). «A Quantitative Comparison of the Small Magellanic Cloud, Large Magellanic Cloud, and Milky Way Ultraviolet to Near-Infrared Extinction Curves». In: *ApJ* 594.1, pp. 279–293. DOI: 10.1086/376774. arXiv: astro-ph/0305257 [astro-ph] (Cited on pages 13, 14, 41, 125, 128, 169).

Gordon, Karl D., Geoffrey C. Clayton, et al. (June 2023). «One Relation for All Wavelengths: The Far-ultraviolet to Mid-infrared Milky Way Spectroscopic R(V)-dependent Dust Extinction Relationship». In: *ApJ* 950.2, 86, p. 86. DOI: 10.3847/1538-4357/accb59. arXiv: 2304.01991 [astro-ph.GA] (Cited on pages 14, 169).

Gordon, Karl D., M. M. Hanson, et al. (July 1999). «The Dusty Starburst Nucleus of M33». In: *ApJ* 519.1, pp. 165–176. DOI: 10.1086/307350. arXiv: astro-ph/9902043 [astro-ph] (Cited on page 169).

Gratton, R. G. (Jan. 1989). «Abundance of manganese in metal-poor stars.» In: *A&A* 208, pp. 171–178 (Cited on page 58).

Gratton, R. G., E. Carretta, et al. (June 2003). «Abundances for metal-poor stars with accurate parallaxes. I. Basic data». In: *A&A* 404, pp. 187–210. DOI: 10.1051/0004-6361:20030439. arXiv: astro-ph/0303653 [astro-ph] (Cited on page 38).

Greenstein, J. L. and M. Schmidt (July 1964). «The Quasi-Stellar Radio Sources 3C 48 and 3C 273.» In: *ApJ* 140, p. 1. DOI: 10.1086/147889 (Cited on page 8).

Guber, C. R. and P. Richter (June 2016). «Dust depletion of Ca and Ti in QSO absorption-line systems». In: *A&A* 591, A137, A137. DOI: 10.1051/0004-6361/201628466. arXiv: 1605.03054 [astro-ph.GA] (Cited on page 59).

Gustafsson, B., T. Karlsson, et al. (Feb. 1999). «The origin of carbon, investigated by spectral analysis of solar-type stars in the Galactic Disk». In: *A&A* 342, pp. 426–439. DOI: 10.48550/arXiv.astro-ph/9811303. arXiv: astro-ph/9811303 [astro-ph] (Cited on page 126).

Gustafsson, Bengt (2022). «Chemical Tracing and the Origin of Carbon in the Galactic Disk». In: *Universe* 8.8. ISSN: 2218-1997. DOI: 10.3390/universe8080409. URL: https://www.mdpi.com/2218-1997/8/8/409 (Cited on page 126).

Harris, Jason and Dennis Zaritsky (Nov. 2009). «The Star Formation History of the Large Magellanic Cloud». In: *AJ* 138.5, pp. 1243–1260. DOI: 10.1088/0004-6256/138/5/1243. arXiv: 0908.1422 [astro-ph.CO] (Cited on page 44).

Hasselquist, Sten, Christian R. Hayes, et al. (Dec. 2021). «APOGEE Chemical Abundance Patterns of the Massive Milky Way Satellites». In: *ApJ* 923.2, 172, p. 172. DOI: 10.3847/1538-4357/ac25f9. arXiv: 2109.05130 [astro-ph.GA] (Cited on pages 44, 59).

Heintz, K. E., J. Bolmer, et al. (Sept. 2019a). «New constraints on the physical conditions in H_2-bearing GRB-host damped Lyman-α absorbers». In: *A&A* 629, A131, A131. DOI: 10.1051/0004-6361/201936250. arXiv: 1908.02309 [astro-ph.GA] (Cited on pages 27, 42).

Heintz, K. E., A. De Cia, et al. (Nov. 2023). «The cosmic buildup of dust and metals. Accurate abundances from GRB-selected star-forming galaxies at $1.7 < z < 6.3$». In: *A&A* 679, A91, A91. DOI: 10.1051/0004-6361/202347418. arXiv: 2308.14812 [astro-ph.GA] (Cited on pages 9, 27, 110, 113, 122, 123, 127, 145, 205, 207).

Heintz, K. E., J. P. U. Fynbo, and E. Høg (June 2015). «A study of purely astrometric selection of extragalactic point sources with Gaia». In: *A&A* 578, A91, A91. DOI: 10.1051/0004-6361/201526038. arXiv: 1503.02874 [astro-ph.HE] (Cited on page 189).

Heintz, K. E., J. P. U. Fynbo, et al. (Oct. 2016). «Determining the fraction of reddened quasars in COSMOS with multiple selection techniques from X-ray to radio wavelengths». In: *A&A* 595, A13, A13. DOI: 10.1051/0004-6361/201628836. arXiv: 1605.00701 [astro-ph.HE] (Cited on pages 127, 190).

Heintz, K. E., J. P. U. Fynbo, et al. (July 2018). «Unidentified quasars among stationary objects from Gaia DR2». In: *A&A* 615, L8, p. L8. DOI: 10.1051/0004-6361/201833396. arXiv: 1805.03394 [astro-ph.GA] (Cited on page 189).

Heintz, K. E., J. P. U. Fynbo, et al. (Dec. 2020). «Spectroscopic classification of a complete sample of astrometrically-selected quasar candidates using Gaia DR2». In: *A&A* 644, A17, A17. DOI: 10.1051/0004-6361/202039262. arXiv: 2010.05934 [astro-ph.GA] (Cited on page 201).

Heintz, K. E., C. Ledoux, et al. (Jan. 2019b). «Cold gas in the early Universe. Survey for neutral atomic-carbon in GRB host galaxies at $1 < z < 6$ from optical afterglow spectroscopy». In: *A&A* 621, A20, A20. DOI: 10.1051/0004-6361/201834246. arXiv: 1810.11064 [astro-ph.GA] (Cited on pages 14, 27, 42, 125, 127, 128).

Heintz, Kasper E., Darach Watson, et al. (May 2024). «Strong damped Lyman-α absorption in young star-forming galaxies at redshifts 9 to 11». In: *Science* 384.6698, pp. 890–894. DOI: 10.1126/science.adj0343. arXiv: 2306.00647 [astro-ph.GA] (Cited on page 210).

Hennawi, Joseph F. and J. Xavier Prochaska (Mar. 2013). «Quasars Probing Quasars. IV. Joint Constraints on the Circumgalactic Medium from Absorption and Emission». In: *ApJ* 766.1, 58, p. 58. DOI: 10.1088/0004-637X/766/1/58. arXiv: 1303.2708 [astro-ph.CO] (Cited on page 209).

Hensley, Brandon S. and B. T. Draine (Jan. 2021). «Observational Constraints on the Physical Properties of Interstellar Dust in the Post-Planck Era». In: *ApJ* 906.2, 73, p. 73. DOI: 10.3847/1538-4357/abc8f1. arXiv: 2009.00018 [astro-ph.GA] (Cited on pages 169, 170).

Herbert-Fort, Stéphane, Jason X. Prochaska, et al. (Aug. 2006). «The Metal-strong Damped Lyα Systems». In: *PASP* 118.846, pp. 1077–1097. DOI: 10.1086/507653. arXiv: astro-ph/0607430 [astro-ph] (Cited on page 44).

Hjorth, Jens, Jesper Sollerman, et al. (June 2003). «A very energetic supernova associated with the γ-ray burst of 29 March 2003». In: *Nature* 423.6942, pp. 847–850. DOI: 10.1038/nature01750. arXiv: astro-ph/0306347 [astro-ph] (Cited on page 8).

Hoffman, John and B. T. Draine (Feb. 2016). «Accurate Modeling of X-ray Extinction by Interstellar Grains». In: *ApJ* 817.2, 139, p. 139. DOI: 10.3847/0004-637X/817/2/139. arXiv: 1509.08987 [astro-ph.HE] (Cited on page 127).

Höfner, Susanne and Hans Olofsson (Jan. 2018). «Mass loss of stars on the asymptotic giant branch. Mechanisms, models and measurements». In: *A&A Rev.* 26.1, 1, p. 1. DOI: 10.1007/s00159-017-0106-5 (Cited on pages 18, 109).

Hohenberg, C. M., N. Thonnard, and A. Meshik (Feb. 2002). «Active capture and anomalous adsorption: New mechanisms for the incorporation of heavy noble gases». In: *maps* 37.2, pp. 257–267. DOI: 10.1111/j.1945-5100.2002.tb01108.x (Cited on page 166).

Hollenbach, D. and C. F. McKee (Nov. 1979). «Molecule formation and infrared emission in fast interstellar shocks. I. Physical processes.» In: *ApJS* 41, pp. 555–592. DOI: 10.1086/190631 (Cited on pages 11, 109).

Hollenbach, David and E. E. Salpeter (Jan. 1971). «Surface Recombination of Hydrogen Molecules». In: *ApJ* 163, p. 155. DOI: 10.1086/150754 (Cited on pages 11, 109).

Honda, Satoshi, Wako Aoki, et al. (2004). «Spectroscopic Studies of Extremely Metal-Poor Stars with the Subaru High Dispersion Spectrograph. II. The r-Process Elements, Including Thorium*». In: *The Astrophysical Journal* 607.1, p. 474. DOI: 10.1086/383406. URL: https://dx.doi.org/10.1086/383406 (Cited on page 38).

Indebetouw, R., M. Matsuura, et al. (Feb. 2014). «Dust Production and Particle Acceleration in Supernova 1987A Revealed with ALMA». In: *ApJ* 782.1, L2, p. L2. DOI: 10.1088/2041-8205/782/1/L2. arXiv: 1312.4086 [astro-ph.SR] (Cited on page 17).

Indu, G. and A. Subramaniam (Nov. 2011). «The recent star-formation history of the Large and Small Magellanic Clouds». In: *A&A* 535, A115, A115. DOI: 10.1051/0004-6361/201117298. arXiv: 1109.1061 [astro-ph.CO] (Cited on page 44).

Issa, M. R., I. MacLaren, and A. W. Wolfendale (Sept. 1990). «Dust-to-gas ratio and metallicity variations in nearby galaxies.» In: *A&A* 236, p. 237 (Cited on page 122).

Jakobsson, P., J. Hjorth, et al. (Dec. 2004). «The line-of-sight towards GRB 030429 at z =2.66: Probing the matter at stellar, galactic and intergalactic scales». In: *A&A* 427, pp. 785–794. DOI: 10.1051/0004-6361:20041233. arXiv: astro-ph/0407439 [astro-ph] (Cited on page 9).

Jenkins, Edward B. (Aug. 2009). «A Unified Representation of Gas-Phase Element Depletions in the Interstellar Medium». In: *ApJ* 700.2, pp. 1299–1348. DOI: 10.1088/0004-637X/700/2/1299. arXiv: 0905.3173 [astro-ph.GA] (Cited on pages 10, 12, 14–17, 23, 25, 36, 39, 41–43, 45, 49, 54, 56, 58, 63, 99, 101, 109, 110, 128, 143, 149, 150, 152, 164–167, 169–172, 204, 206).

— (Feb. 2013). «The Fractional Ionization of the Warm Neutral Interstellar Medium». In: *ApJ* 764.1, 25, p. 25. DOI: 10.1088/0004-637X/764/1/25. arXiv: 1301.3144 [astro-ph.GA] (Cited on pages 35, 167).

— (Feb. 2014). «Depletions of Elements from the Gas Phase: A Guide on Dust Compositions». In: *arXiv e-prints*, arXiv:1402.4765, arXiv:1402.4765. DOI: 10.48550/arXiv.1402.4765. arXiv: 1402.4765 [astro-ph.GA] (Cited on pages 22, 123).

— (Feb. 2019). «A Closer Look at Some Gas-phase Depletions in the ISM: Trends for O, Ge, and Kr versus {F}_{* }, f(H_2), and Starlight Intensity». In: *ApJ* 872.1, 55, p. 55. DOI:

10.3847/1538-4357/aafe81. arXiv: 1902.01521 [astro-ph.GA] (Cited on page 166).

Jenkins, Edward B. and Todd M. Tripp (Jan. 2006). «Measurements of the f-Values of the Resonance Transitions of Ni II at 1317.217 and 1370.132 Å». In: *ApJ* 637.1, pp. 548–552. DOI: 10.1086/498226. arXiv: astro-ph/0509648 [astro-ph] (Cited on page 19).

Jenkins, Edward B. and George Wallerstein (Apr. 2017). «Interstellar Gas-phase Element Depletions in the Small Magellanic Cloud: A Guide to Correcting for Dust in QSO Absorption Line Systems». In: *ApJ* 838.2, 85, p. 85. DOI: 10.3847/1538-4357/aa64d4. arXiv: 1705.02675 [astro-ph.GA] (Cited on pages 25, 41, 43–45, 58, 59, 101, 110, 144, 152).

Jones, A. P., L. Fanciullo, et al. (Oct. 2013). «The evolution of amorphous hydrocarbons in the ISM: dust modelling from a new vantage point». In: *A&A* 558, A62, A62. DOI: 10.1051/0004-6361/201321686. arXiv: 1411.6293 [astro-ph.GA] (Cited on page 172).

Jones, A. P., A. G. G. M. Tielens, and D. J. Hollenbach (Oct. 1996). «Grain Shattering in Shocks: The Interstellar Grain Size Distribution». In: *ApJ* 469, p. 740. DOI: 10.1086/177823 (Cited on pages 19, 124).

Jones, A. P., A. G. G. M. Tielens, et al. (Oct. 1994). «Grain Destruction in Shocks in the Interstellar Medium». In: *ApJ* 433, p. 797. DOI: 10.1086/174689 (Cited on page 19).

Jones, Tucker, Daniel P. Stark, and Richard S. Ellis (Aug. 2018). «Dust in the Wind: Composition and Kinematics of Galaxy Outflows at the Peak Epoch of Star Formation». In: *ApJ* 863.2, 191, p. 191. DOI: 10.3847/1538-4357/aad37f. arXiv: 1805.01484 [astro-ph.GA] (Cited on page 55).

Joshi, Y. C. and A. Panchal (Aug. 2019). «Reddening map and recent star formation in the Magellanic Clouds based on OGLE IV Cepheids». In: *A&A* 628, A51, A51. DOI: 10.1051/0004-6361/201834574. arXiv: 1906.04481 [astro-ph.GA] (Cited on page 44).

Karakas, Amanda I. (2017). «Low- and Intermediate-Mass Stars». In: *Handbook of Supernovae*. Ed. by Athem W. Alsabti and Paul Murdin, p. 461. DOI: 10.1007/978-3-319-21846-5_117 (Cited on page 4).

Kemper, F., A. J. Markwick, and Paul M. Woods (May 2011). «The crystalline fraction of interstellar silicates in starburst galaxies». In: *MNRAS* 413.2, pp. 1192–1199. DOI: 10.1111/j.1365-2966.2011.18204.x. arXiv: 1012.3251 [astro-ph.CO] (Cited on page 11).

Kemper, F., W. J. Vriend, and A. G. G. M. Tielens (July 2004). «The Absence of Crystalline Silicates in the Diffuse Interstellar Medium». In: *ApJ* 609.2, pp. 826–837. DOI: 10.1086/421339. arXiv: astro-ph/0403609 [astro-ph] (Cited on page 22).

Kirchschlager, Florian, Franziska D. Schmidt, et al. (Apr. 2023). «Dust survival rates in clumps passing through the Cas A reverse shock - II. The impact of magnetic fields». In: *MNRAS* 520.4, pp. 5042–5064. DOI: 10.1093/mnras/stad290. arXiv: 2210.06763 [astro-ph.SR] (Cited on page 17).

Kirk, Jason M., Derek Ward-Thompson, et al. (Nov. 2009). «The Spitzer Survey of Interstellar Clouds in the Gould Belt. II. The Cepheus Flare Observed with IRAC and MIPS». In:

ApJS 185.1, pp. 198–249. DOI: 10.1088/0067-0049/185/1/198. arXiv: 0903.4063 [astro-ph.GA] (Cited on page 12).

Kisielius, Romas, Varsha P. Kulkarni, et al. (Jan. 2014). «Atomic Data for S II—Toward Better Diagnostics of Chemical Evolution in High-redshift Galaxies». In: *ApJ* 780.1, 76, p. 76. DOI: 10.1088/0004-637X/780/1/76. arXiv: 1311.2553 [astro-ph.IM] (Cited on pages 44, 98, 99, 105).

Kisielius, Romas, Varsha P. Kulkarni, et al. (May 2015). «Atomic Data for Zn II: Improving Spectral Diagnostics of Chemical Evolution in High-redshift Galaxies». In: *ApJ* 804.1, 76, p. 76. DOI: 10.1088/0004-637X/804/1/76. arXiv: 1504.01667 [astro-ph.GA] (Cited on pages 44, 46, 98, 99, 105).

Klimenko, V. V., S. A. Balashev, et al. (Sept. 2024). «Excitation of CO molecules in diffuse gas over cosmic history». In: *MNRAS* 533.2, pp. 1367–1393. DOI: 10.1093/mnras/stae1863 (Cited on page 172).

Knight, C., E. Peeters, et al. (Sept. 2021). «Tracing PAH Size in Prominent Nearby Mid-Infrared Environments». In: *ApJ* 918.1, 8, p. 8. DOI: 10.3847/1538-4357/ac02c6. arXiv: 2106.01519 [astro-ph.GA] (Cited on page 12).

Kobayashi, Chiaki, Amanda I. Karakas, and Maria Lugaro (Sept. 2020). «The Origin of Elements from Carbon to Uranium». In: *ApJ* 900.2, 179, p. 179. DOI: 10.3847/1538-4357/abae65. arXiv: 2008.04660 [astro-ph.GA] (Cited on pages 4, 36, 57, 153).

Kobayashi, Chiaki and Ken'ichi Nomoto (Dec. 2009). «The Role of Type Ia Supernovae in Chemical Evolution. I. Lifetime of Type Ia Supernovae and Metallicity Effect». In: *ApJ* 707.2, pp. 1466–1484. DOI: 10.1088/0004-637X/707/2/1466. arXiv: 0801.0215 [astro-ph] (Cited on pages 57, 58).

Kobayashi, Chiaki, Hideyuki Umeda, et al. (Dec. 2006). «Galactic Chemical Evolution: Carbon through Zinc». In: *ApJ* 653.2, pp. 1145–1171. DOI: 10.1086/508914. arXiv: astro-ph/0608688 [astro-ph] (Cited on pages 36, 57, 58, 153).

Konstantopoulou, De Cia, Annalisa, et al. (2023). «Dust depletion of metals from local to distant galaxies - I. Peculiar nucleosynthesis effects and grain growth in the ISM (Corrigendum)». In: *A&A* 674, p. C1. DOI: 10.1051/0004-6361/202243994e. URL: https://doi.org/10.1051/0004-6361/202243994e (Cited on pages 112, 152, 205).

Konstantopoulou, Christina, Annalisa De Cia, et al. (Oct. 2022). «Dust depletion of metals from local to distant galaxies. I. Peculiar nucleosynthesis effects and grain growth in the ISM». In: *A&A* 666, A12, A12. DOI: 10.1051/0004-6361/202243994. arXiv: 2207.08804 [astro-ph.GA] (Cited on pages 12, 23, 24, 28, 30, 31, 39, 107, 109, 147, 149, 151, 152, 158, 159, 165–167, 169–171, 181, 183, 204, 217, 249–252, 259).

Konstantopoulou, Christina, Annalisa De Cia, et al. (Jan. 2024). «Dust depletion of metals from local to distant galaxies. II. Cosmic dust-to-metal ratio and dust composition». In: *A&A* 681, A64, A64. DOI: 10.1051/0004-6361/202347171. arXiv: 2310.07709 [astro-ph.GA] (Cited on pages 12, 23, 107, 149, 169–171, 205, 251).

Krogager, J. K., J. P. U. Fynbo, et al. (Nov. 2016). «The Extended High A(V) Quasar Survey: Searching for Dusty Absorbers toward Mid-infrared-selected Quasars». In: *ApJ* 832.1, 49, p. 49. DOI: 10.3847/0004-637X/832/1/49. arXiv: 1608.08404 [astro-ph.GA] (Cited on pages 14, 127).

Krogager, J. K., K. M. Leighly, et al. (Mar. 2023). «The 4MOST–Gaia Purely Astrometric Quasar Survey (4G-PAQS)». In: *The Messenger* 190, pp. 38–41. DOI: 10.18727/0722-6691/5310 (Cited on pages 123, 199, 201, 208).

Krogager, J. K., P. Møller, et al. (Aug. 2017). «Consensus report on 25 yr of searches for damped Ly α galaxies in emission: confirming their metallicity-luminosity relation at $z \gtrsim 2$». In: *MNRAS* 469.3, pp. 2959–2981. DOI: 10.1093/mnras/stx1011. arXiv: 1704.08075 [astro-ph.GA] (Cited on page 49).

Krogager, Jens-Kristian (2018). *VoigtFit: A Python package for Voigt profile fitting*. arXiv: 1803.01187 [astro-ph.IM] (Cited on pages 30, 45).

Krogager, Jens-Kristian, Johan P. U. Fynbo, et al. (July 2019). «The effect of dust bias on the census of neutral gas and metals in the high-redshift Universe due to SDSS-II quasar colour selection». In: *MNRAS* 486.3, pp. 4377–4397. DOI: 10.1093/mnras/stz1120. arXiv: 1904.06966 [astro-ph.GA] (Cited on page 122).

Kulkarni, Varsha P., Debopam Som, et al. (Dec. 2015). «Keck and VLT Observations of Super-Damped Lyman-Alpha Absorbers at z 2- 2.5: Constraints on Chemical Compositions and Physical Conditions». In: *ApJ* 815.1, 24, p. 24. DOI: 10.1088/0004-637X/815/1/24. arXiv: 1510.05342 [astro-ph.GA] (Cited on pages 27, 42).

Kurucz, Robert L. (Sept. 2017). «Including all the lines: data releases for spectra and opacities». In: *Canadian Journal of Physics* 95.9, pp. 825–827. DOI: 10.1139/cjp-2016-0794 (Cited on pages 44, 98–101).

Lambert, David L. (June 1987). «Chemical evolution of the galaxy: abundances of the light elements (sodium to calcium).» In: *Journal of Astrophysics and Astronomy* 8, pp. 103–122. DOI: 10.1007/BF02714309 (Cited on page 49).

Laporte, N., R. S. Ellis, et al. (Mar. 2017). «Dust in the Reionization Era: ALMA Observations of a z = 8.38 Gravitationally Lensed Galaxy». In: *ApJ* 837.2, L21, p. L21. DOI: 10.3847/2041-8213/aa62aa. arXiv: 1703.02039 [astro-ph.GA] (Cited on page 19).

Ledoux, C., J. Bergeron, and P. Petitjean (Apr. 2002). «Dust depletion and abundance pattern in damped Lyalpha systems: A sample of Mn and Ti abundances at z < 2.2». In: *A&A* 385, pp. 802–815. DOI: 10.1051/0004-6361:20020198. arXiv: astro-ph/0202134 [astro-ph] (Cited on pages 16, 27, 35, 41, 42, 204).

Ledoux, C., P. Petitjean, et al. (Oct. 2006). «Velocity-metallicity correlation for high-z DLA galaxies: evidence of a mass-metallicity relation?» In: *A&A* 457.1, pp. 71–78. DOI: 10.1051/0004-6361:20054242. arXiv: astro-ph/0606185 [astro-ph] (Cited on pages 27, 41).

Ledoux, C., P. M. Vreeswijk, et al. (Nov. 2009). «Physical conditions in high-redshift GRB-DLA absorbers observed with VLT/UVES: implications for molecular hydrogen searches». In: *A&A* 506.2, pp. 661–675. DOI: 10.1051/0004-6361/200811572. arXiv: 0907.1057 [astro-ph.CO] (Cited on pages 110, 128).

Leśniewska, Aleksandra and Michał Jerzy Michałowski (Apr. 2019). «Dust production scenarios in galaxies at z ∼6-8.3». In: *A&A* 624, L13, p. L13. DOI: 10.1051/0004-6361/201935149. arXiv: 1904.11185 [astro-ph.GA] (Cited on page 19).

Li, A. and J. M. Greenberg (July 1997). «A unified model of interstellar dust.» In: *A&A* 323, pp. 566–584 (Cited on page 172).

Li, Aigen and B. T. Draine (June 2001). «Infrared Emission from Interstellar Dust. II. The Diffuse Interstellar Medium». In: *ApJ* 554.2, pp. 778–802. DOI: 10.1086/323147. arXiv: astro-ph/0011319 [astro-ph] (Cited on page 169).

Li, Qi, Desika Narayanan, and Romeel Davé (Nov. 2019). «The dust-to-gas and dust-to-metal ratio in galaxies from z = 0 to 6». In: *MNRAS* 490.1, pp. 1425–1436. DOI: 10.1093/mnras/stz2684. arXiv: 1906.09277 [astro-ph.GA] (Cited on pages 11, 122).

Lin, Qi, X. J. Yang, and Aigen Li (Oct. 2023). «Polycyclic aromatic hydrocarbon molecules and the 2175Å interstellar extinction bump». In: *MNRAS* 525.2, pp. 2380–2387. DOI: 10.1093/mnras/stad2405. arXiv: 2308.04084 [astro-ph.GA] (Cited on pages 14, 169).

Lisenfeld, U. and A. Ferrara (Mar. 1998). «Dust-to-Gas Ratio and Metal Abundance in Dwarf Galaxies». In: *ApJ* 496.1, pp. 145–154. DOI: 10.1086/305354. arXiv: astro-ph/9705037 [astro-ph] (Cited on page 122).

Lodders, K. (July 2003). «Abundances and Condensation Temperatures of the Elements». In: *Meteoritics and Planetary Science Supplement* 38, p. 5272 (Cited on pages 7, 56).

Lodders, K., H. Palme, and H. P. Gail (Jan. 2009). «Abundances of the Elements in the Solar System». In: *Landolt & Börnstein* 4B, p. 712. DOI: 10.1007/978-3-540-88055-4_34. arXiv: 0901.1149 [astro-ph.EP] (Cited on pages 43, 110, 151).

López, S., V. D'Odorico, et al. (Oct. 2016). «XQ-100: A legacy survey of one hundred $3.5 \lesssim z \lesssim 4.5$ quasars observed with VLT/X-shooter». In: *A&A* 594, A91, A91. DOI: 10.1051/0004-6361/201628161. arXiv: 1607.08776 [astro-ph.GA] (Cited on page 8).

Lyke, Brad W., Alexandra N. Higley, et al. (Sept. 2020). «The Sloan Digital Sky Survey Quasar Catalog: Sixteenth Data Release». In: *ApJS* 250.1, 8, p. 8. DOI: 10.3847/1538-4365/aba623. arXiv: 2007.09001 [astro-ph.GA] (Cited on page 8).

Ma, Jingzhe, Gabriel Brammer, et al. (Apr. 2018). «Revealing the Host Galaxy of a Quasar 2175 Å Dust Absorber at z = 2.12». In: *ApJ* 857.2, L12, p. L12. DOI: 10.3847/2041-8213/aabc51. arXiv: 1804.02410 [astro-ph.GA] (Cited on page 57).

Ma, Jingzhe, Paul Caucal, et al. (Dec. 2015). «Cold gas and a Milky Way-type 2175-Å bump in a metal-rich and highly depleted absorption system». In: *MNRAS* 454.2, pp. 1751–1766. DOI: 10.1093/mnras/stv2073. arXiv: 1509.01593 [astro-ph.GA] (Cited on page 44).

Maddox, Natasha, Paul C. Hewett, et al. (May 2008). «Luminous K-band selected quasars from UKIDSS». In: *MNRAS* 386.3, pp. 1605–1624. DOI: 10.1111/j.1365-2966.2008.13138.x. arXiv: 0802.3650 [astro-ph] (Cited on page 189).

Maiolino, R. and F. Mannucci (Feb. 2019). «De re metallica: the cosmic chemical evolution of galaxies». In: *A&A Rev.* 27.1, 3, p. 3. DOI: 10.1007/s00159-018-0112-2. arXiv: 1811.09642 [astro-ph.GA] (Cited on page 109).

Maíz Apellániz, J. and M. Rubio (May 2012). «Ultraviolet extinction toward a quiescent molecular cloud in the Small Magellanic Cloud». In: *A&A* 541, A54, A54. DOI: 10.1051/0004-6361/201118712. arXiv: 1201.6230 [astro-ph.CO] (Cited on page 169).

Mann, Ingrid (Sept. 2010). «Interstellar Dust in the Solar System». In: *ARA&A* 48, pp. 173–203. DOI: 10.1146/annurev-astro-081309-130846 (Cited on page 22).

Marasco, Antonino, Filippo Fraternali, et al. (Sept. 2022). «Intermediate- and high-velocity clouds in the Milky Way - II. Evidence for a Galactic fountain with collimated outflows and diffuse inflows». In: *MNRAS* 515.3, pp. 4176–4190. DOI: 10.1093/mnras/stac1172. arXiv: 2202.05852 [astro-ph.GA] (Cited on page 4).

Mathis, J. S., W. Rumpl, and K. H. Nordsieck (Oct. 1977). «The size distribution of interstellar grains.» In: *ApJ* 217, pp. 425–433. DOI: 10.1086/155591 (Cited on pages 11, 127).

Mathis, John S. (Feb. 1994). «The Origin of Variations in the 2175 Angstrom Extinction Bump». In: *ApJ* 422, p. 176. DOI: 10.1086/173715 (Cited on page 125).

— (Dec. 1996). «Dust Models with Tight Abundance Constraints». In: *ApJ* 472, p. 643. DOI: 10.1086/178094 (Cited on page 172).

Matsuura, M., E. Dwek, et al. (Feb. 2015). «A Stubbornly Large Mass of Cold Dust in the Ejecta of Supernova 1987A». In: *ApJ* 800.1, 50, p. 50. DOI: 10.1088/0004-637X/800/1/5010.48550/arXiv.1411.7381. arXiv: 1411.7381 [astro-ph.SR] (Cited on pages 17, 109, 119).

Matsuura, M., R. Indebetouw, et al. (Aug. 2017). «ALMA spectral survey of Supernova 1987A - molecular inventory, chemistry, dynamics and explosive nucleosynthesis». In: *MNRAS* 469.3, pp. 3347–3362. DOI: 10.1093/mnras/stx830. arXiv: 1704.02324 [astro-ph.SR] (Cited on page 17).

Matsuura, Mikako, Paul M. Woods, and Patrick J. Owen (Mar. 2013). «The global gas and dust budget of the Small Magellanic Cloud». In: *MNRAS* 429.3, pp. 2527–2536. DOI: 10.1093/mnras/sts521. arXiv: 1212.1468 [astro-ph.GA] (Cited on page 19).

Matteucci, Francesca (2012). *Chemical Evolution of Galaxies*. DOI: 10.1007/978-3-642-22491-1 (Cited on page 4).

Mattsson, L. (June 2010). «The origin of carbon: Low-mass stars and an evolving, initially top-heavy IMF?» In: *A&A* 515, A68, A68. DOI: 10.1051/0004-6361/200913315. arXiv: 1003.3474 [astro-ph.GA] (Cited on page 126).

Mattsson, Lars (Dec. 2020). «On the grain-sized distribution of turbulent dust growth». In: *MNRAS* 499.4, pp. 6035–6043. DOI: 10.1093/mnras/staa3114. arXiv: 2010.01953 [astro-ph.GA] (Cited on pages 19, 22, 115, 120, 122, 127, 132, 205).

Mattsson, Lars, Anja C. Andersen, and Joakim D. Munkhammar (June 2012). «On the dust abundance gradients in late-type galaxies - I. Effects of destruction and growth of dust in the interstellar medium». In: *MNRAS* 423.1, pp. 26–37. DOI: 10.1111/j.1365-2966.2012.20575.x. arXiv: 1201.3375 [astro-ph.CO] (Cited on pages 17, 56, 109, 119).

Mattsson, Lars, Annalisa De Cia, et al. (May 2014). «On the (in)variance of the dust-to-metals ratio in galaxies». In: *MNRAS* 440.2, pp. 1562–1570. DOI: 10.1093/mnras/stu370. arXiv: 1403.0502 [astro-ph.GA] (Cited on pages 12, 22, 119, 170, 205).

Mattsson, Lars, Annalisa De Cia, et al. (Apr. 2019). «Dust-depletion sequences in damped Lyman-α absorbers. II. The composition of cosmic dust, from low-metallicity systems to the Galaxy». In: *A&A* 624, A103, A103. DOI: 10.1051/0004-6361/201731482. arXiv: 1901.04710 [astro-ph.GA] (Cited on pages 19, 21, 22, 41, 123, 124, 169).

Mattsson, Lars, Haley L. Gomez, et al. (June 2015). «From flux to dust mass: Does the grain-temperature distribution matter for estimates of cold dust masses in supernova remnants?» In: *MNRAS* 449.4, pp. 4079–4090. DOI: 10.1093/mnras/stv487. arXiv: 1504.02664 [astro-ph.SR] (Cited on page 19).

McKinnon, Ryan, Mark Vogelsberger, et al. (Aug. 2018). «Simulating galactic dust grain evolution on a moving mesh». In: *MNRAS* 478.3, pp. 2851–2886. DOI: 10.1093/mnras/sty1248. arXiv: 1805.04521 [astro-ph.GA] (Cited on page 11).

McWilliam, Andrew (Jan. 1997). «Abundance Ratios and Galactic Chemical Evolution». In: *ARA&A* 35, pp. 503–556. DOI: 10.1146/annurev.astro.35.1.503 (Cited on pages 49, 58).

Meyer, David M., M. Jura, and Jason A. Cardelli (Jan. 1998). «The Definitive Abundance of Interstellar Oxygen». In: *ApJ* 493.1, pp. 222–229. DOI: 10.1086/305128. arXiv: astro-ph/9710163 [astro-ph] (Cited on pages 171, 172).

Mishenina, T., T. Gorbaneva, et al. (Dec. 2015). «Mn abundances in the stars of the Galactic disc with metallicities -1.0 < [Fe/H] < 0.3». In: *MNRAS* 454.2, pp. 1585–1594. DOI: 10.1093/mnras/stv2038. arXiv: 1509.05341 [astro-ph.GA] (Cited on page 49).

Mishra, Ajay and Aigen Li (Dec. 2017). «Interstellar Silicon Depletion and the Ultraviolet Extinction». In: *ApJ* 850.2, 138, p. 138. DOI: 10.3847/1538-4357/aa937a. arXiv: 1710.04905 [astro-ph.GA] (Cited on page 169).

Mo, Houjun, Frank C. van den Bosch, and Simon White (2010). *Galaxy Formation and Evolution* (Cited on page 3).

Molster, Frank and Ciska Kemper (Aug. 2005). «Crystalline Silicates». In: *Space Sci. Rev.* 119.1-4, pp. 3–28. DOI: 10.1007/s11214-005-8066-x (Cited on page 11).

Montargès, M., E. Cannon, et al. (Mar. 2023). «The VLT/SPHERE view of the ATOMIUM cool evolved star sample. I. Overview: Sample characterization through polarization analysis». In: *A&A* 671, A96, A96. DOI: 10.1051/0004-6361/202245398. arXiv: 2301.02081 [astro-ph.SR] (Cited on page 19).

Morgan, H. L. and M. G. Edmunds (Aug. 2003). «Dust formation in early galaxies». In: *MNRAS* 343.2, pp. 427–442. DOI: 10.1046/j.1365-8711.2003.06681.x. arXiv: astro-ph/0302566 [astro-ph] (Cited on page 19).

Morton, Donald C. (Nov. 2003). «Atomic Data for Resonance Absorption Lines. III. Wavelengths Longward of the Lyman Limit for the Elements Hydrogen to Gallium». In: *ApJS* 149.1, pp. 205–238. DOI: 10.1086/377639 (Cited on pages 44, 46).

Moseley, S. H., E. Dwek, et al. (Aug. 1989). «Far-infrared observations of thermal dust emission from supernova 1987A». In: *Nature* 340.6236, pp. 697–699. DOI: 10.1038/340697a0 (Cited on page 17).

Motta, V., E. Mediavilla, et al. (Aug. 2002). «Detection of the 2175 Å Extinction Feature at z = 0.83». In: *ApJ* 574.2, pp. 719–725. DOI: 10.1086/341118. arXiv: astro-ph/0204130 [astro-ph] (Cited on page 169).

Nagao, Takashi, Keiichi Maeda, and Masayuki Yamanaka (June 2018). «Polarization as a probe of dusty environments around Type Ia supernovae: radiative transfer models for SN 2012dn». In: *MNRAS* 476.4, pp. 4806–4813. DOI: 10.1093/mnras/sty538. arXiv: 1802.08954 [astro-ph.HE] (Cited on page 119).

Nissen, P. E., C. Akerman, et al. (July 2007). «Sulphur and zinc abundances in Galactic halo stars revisited». In: *A&A* 469.1, pp. 319–330. DOI: 10.1051/0004-6361:20077344. arXiv: astro-ph/0702689 [astro-ph] (Cited on page 48).

Nissen, P. E., Y. Q. Chen, et al. (Mar. 2004). «Sulphur and zinc abundances in Galactic stars and damped Lyα systems». In: *A&A* 415, pp. 993–1007. DOI: 10.1051/0004-6361:20034063. arXiv: astro-ph/0311529 [astro-ph] (Cited on page 48).

Nissen, P. E. and W. J. Schuster (June 2011). «Two distinct halo populations in the solar neighborhood. II. Evidence from stellar abundances of Mn, Cu, Zn, Y, and Ba». In: *A&A* 530, A15, A15. DOI: 10.1051/0004-6361/201116619. arXiv: 1103.4755 [astro-ph.GA] (Cited on page 151).

Nomoto, K., K. Iwamoto, et al. (Feb. 1997). «Nucleosynthesis in type Ia supernovae». In: *Nucl. Phys. A* 621, pp. 467–476. DOI: 10.1016/S0375-9474(97)00291-1. arXiv: astro-ph/9706025 [astro-ph] (Cited on pages 37, 48, 57).

Nomoto, K., F. K. Thielemann, and K. Yokoi (Nov. 1984). «Accreting white dwarf models for type I supern. III. Carbon deflagration supernovae.» In: *ApJ* 286, pp. 644–658. DOI: 10.1086/162639 (Cited on page 7).

Nomoto, Ken'ichi, Nozomu Tominaga, et al. (Oct. 2006). «Nucleosynthesis yields of core-collapse supernovae and hypernovae, and galactic chemical evolution». In: *Nucl. Phys. A* 777, pp. 424–458. DOI: 10.1016/j.nuclphysa.2006.05.008. arXiv: astro-ph/0605725 [astro-ph] (Cited on pages 37, 38, 48, 57, 154).

Noterdaeme, P., J. K. Krogager, et al. (Jan. 2017). «Discovery of a Perseus-like cloud in the early Universe. H I-to-H_2 transition, carbon monoxide and small dust grains at $z_{abs} \approx$ 2.53 towards the quasar J0000+0048». In: *A&A* 597, A82, A82. DOI: 10.1051/0004-6361/201629173. arXiv: 1609.01422 [astro-ph.GA] (Cited on page 44).

Noterdaeme, P., C. Ledoux, et al. (Apr. 2008). «Molecular hydrogen in high-redshift damped Lyman-α systems: the VLT/UVES database». In: *A&A* 481.2, pp. 327–336. DOI: 10.1051/0004-6361:20078780. arXiv: 0801.3682 [astro-ph] (Cited on pages 16, 35, 48, 116).

Noterdaeme, P., P. Petitjean, et al. (Oct. 2009). «Evolution of the cosmological mass density of neutral gas from Sloan Digital Sky Survey II - Data Release 7». In: *A&A* 505.3, pp. 1087–1098. DOI: 10.1051/0004-6361/200912768. arXiv: 0908.1574 [astro-ph.CO] (Cited on page 9).

Noterdaeme, P., P. Petitjean, et al. (Nov. 2010). «A translucent interstellar cloud at z = 2.69. CO, H_2, and HD in the line-of-sight to SDSS J123714.60+064759.5». In: *A&A* 523, A80, A80. DOI: 10.1051/0004-6361/201015147. arXiv: 1008.0637 [astro-ph.CO] (Cited on page 44).

Nozawa, Takaya, Takashi Kozasa, and Asao Habe (Sept. 2006). «Dust Destruction in the High-Velocity Shocks Driven by Supernovae in the Early Universe». In: *ApJ* 648.1, pp. 435–451. DOI: 10.1086/505639. arXiv: astro-ph/0605193 [astro-ph] (Cited on page 17).

Nozawa, Takaya, Takashi Kozasa, et al. (Sept. 2007). «Evolution of Dust in Primordial Supernova Remnants: Can Dust Grains Formed in the Ejecta Survive and Be Injected into the Early Interstellar Medium?» In: *ApJ* 666.2, pp. 955–966. DOI: 10.1086/520621. arXiv: 0706.0383 [astro-ph] (Cited on page 17).

Nozawa, Takaya, Keiichi Maeda, et al. (July 2011). «Formation of Dust in the Ejecta of Type Ia Supernovae». In: *ApJ* 736.1, 45, p. 45. DOI: 10.1088/0004-637X/736/1/45. arXiv: 1105.0973 [astro-ph.SR] (Cited on pages 17, 22).

O'Donnell, James E. and John S. Mathis (Apr. 1997). «Dust Grain Size Distributions and the Abundance of Refractory Elements in the Diffuse Interstellar Medium». In: *ApJ* 479.2, pp. 806–817. DOI: 10.1086/303903 (Cited on page 19).

O'Meara, J. M., N. Lehner, et al. (Oct. 2015). «The First Data Release of the KODIAQ Survey». In: *AJ* 150.4, 111, p. 111. DOI: 10.1088/0004-6256/150/4/111. arXiv: 1505.03529 [astro-ph.CO] (Cited on page 8).

Oppenheimer, Benjamin D. and Romeel Davé (June 2008). «Mass, metal, and energy feedback in cosmological simulations». In: *MNRAS* 387.2, pp. 577–600. DOI: 10.1111/j.1365-2966.2008.13280.x. arXiv: 0712.1827 [astro-ph] (Cited on page 4).

Ostriker, Jeremiah P. and Paul Steinhardt (June 2003). «New Light on Dark Matter». In: *Science* 300.5627, 1909–1913. ISSN: 1095-9203. DOI: 10.1126/science.1085976. URL: http://dx.doi.org/10.1126/science.1085976 (Cited on page 3).

Palla, Marco, Ilse De Looze, et al. (Feb. 2024). «Metal and dust evolution in ALMA REBELS galaxies: insights for future JWST observations». In: *MNRAS* 528.2, pp. 2407–2427. DOI: 10.1093/mnras/stae160. arXiv: 2311.16071 [astro-ph.GA] (Cited on page 210).

Pâris, Isabelle, Patrick Petitjean, et al. (May 2018). «The Sloan Digital Sky Survey Quasar Catalog: Fourteenth data release». In: *A&A* 613, A51, A51. DOI: 10.1051/0004-6361/201732445. arXiv: 1712.05029 [astro-ph.GA] (Cited on page 190).

Peebles, P. J. E. (Jan. 1980). «Nature of the matter distribution now and at Z = 1000.» In: *Phys. Scr* 21.5, pp. 720–724. DOI: 10.1088/0031-8949/21/5/025 (Cited on page 3).

Pei, Yichuan C. (Aug. 1992). «Interstellar Dust from the Milky Way to the Magellanic Clouds». In: *ApJ* 395, p. 130. DOI: 10.1086/171637 (Cited on pages 13, 21, 41, 125, 127, 197).

Perley, D. A., A. J. Levan, et al. (Dec. 2013). «A Population of Massive, Luminous Galaxies Hosting Heavily Dust-obscured Gamma-Ray Bursts: Implications for the Use of GRBs as Tracers of Cosmic Star Formation». In: *ApJ* 778.2, 128, p. 128. DOI: 10.1088/0004-637X/778/2/128. arXiv: 1301.5903 [astro-ph.CO] (Cited on page 128).

Péroux, Céline, Annalisa De Cia, and J. Christopher Howk (July 2023). «Observed dust surface density across cosmic times». In: *MNRAS* 522.4, pp. 4852–4861. DOI: 10.1093/mnras/stad1235 (Cited on page 109).

Péroux, Céline and J. Christopher Howk (Aug. 2020). «The Cosmic Baryon and Metal Cycles». In: *ARA&A* 58, pp. 363–406. DOI: 10.1146/annurev-astro-021820-120014. arXiv: 2011.01935 [astro-ph.GA] (Cited on pages 4, 9, 25, 26, 42, 109, 123, 253).

Petitjean, P., C. Ledoux, and R. Srianand (Mar. 2008). «The nitrogen and oxygen abundances in the neutral gas at high redshift». In: *A&A* 480.2, pp. 349–357. DOI: 10.1051/0004-6361:20078607. arXiv: 0712.2760 [astro-ph] (Cited on pages 27, 42).

Pettini, Max, Linda J. Smith, et al. (May 1994). «Metal Enrichment, Dust, and Star Formation in Galaxies at High Redshifts. III. Zn and CR Abundances for 17 Damped Lyman-Alpha Systems». In: *ApJ* 426, p. 79. DOI: 10.1086/174041 (Cited on page 42).

Phillips, A. P., P. M. Gondhalekar, and M. Pettini (Aug. 1982). «A study of element depletions in interstellar gas.» In: *MNRAS* 200, pp. 687–703. DOI: 10.1093/mnras/200.3.687 (Cited on pages 12, 14, 43, 45, 99, 109, 110, 149, 152).

Pilbratt, G. L., J. R. Riedinger, et al. (July 2010). «Herschel Space Observatory. An ESA facility for far-infrared and submillimetre astronomy». In: *A&A* 518, L1, p. L1. DOI: 10.1051/0004-6361/201014759. arXiv: 1005.5331 [astro-ph.IM] (Cited on page 12).

Piranomonte, S., P. A. Ward, et al. (Dec. 2008). «Probing the complex environments of GRB host galaxies and intervening systems: high resolution spectroscopy of GRB050922C». In: *A&A* 492.3, pp. 775–785. DOI: 10.1051/0004-6361:20079015. arXiv: 0811.0989 [astro-ph] (Cited on page 110).

Planck Collaboration, P. A. R. Ade, et al. (Sept. 2016). «Planck 2015 results. XIII. Cosmological parameters». In: *A&A* 594, A13, A13. DOI: 10.1051/0004-6361/201525830. arXiv: 1502.01589 [astro-ph.CO] (Cited on pages 3, 12).

Planck Collaboration, N. Aghanim, et al. (Sept. 2020). «Planck 2018 results. VI. Cosmological parameters». In: *A&A* 641, A6, A6. DOI: 10.1051/0004-6361/201833910. arXiv: 1807.06209 [astro-ph.CO] (Cited on page 110).

Popping, Gergö, Rachel S. Somerville, and Maud Galametz (Nov. 2017). «The dust content of galaxies from z = 0 to z = 9». In: *MNRAS* 471.3, pp. 3152–3185. DOI: 10.1093/mnras/stx1545. arXiv: 1609.08622 [astro-ph.GA] (Cited on page 12).

Primas, Francesca, Eric Brugamyer, et al. (Jan. 2000). «Copper and Zinc Abundances in Metal-Poor Stars». In: *The First Stars*. Ed. by Achim Weiss, Tom G. Abel, and Vanessa Hill, p. 51. DOI: 10.1007/10719504_7 (Cited on page 48).

Prochaska, Jason X., Hsiao-Wen Chen, et al. (Sept. 2007). «Probing the Interstellar Medium near Star-forming Regions with Gamma-Ray Burst Afterglow Spectroscopy: Gas, Metals, and Dust». In: *ApJ* 666.1, pp. 267–280. DOI: 10.1086/520042. arXiv: astro-ph/0703665 [astro-ph] (Cited on pages 9, 10, 27, 42, 43, 110, 126, 253).

Prochaska, Jason X. and Arthur M. Wolfe (Apr. 1999). «Chemical Abundances of the Damped Lyα Systems at z>1.5». In: *ApJS* 121.2, pp. 369–415. DOI: 10.1086/313200. arXiv: astro-ph/9810381 [astro-ph] (Cited on pages 7, 25, 27, 41).

— (Feb. 2002). «The UCSD HIRES/Keck I Damped Lyα Abundance Database. II. The Implications». In: *ApJ* 566.1, pp. 68–92. DOI: 10.1086/338080. arXiv: astro-ph/0110351 [astro-ph] (Cited on page 57).

Prochaska, Jason X., Arthur M. Wolfe, et al. (Nov. 2001). «The UCSD HIRES/Keck I Damped Lyα Abundance Database. I. The Data». In: *ApJS* 137.1, pp. 21–73. DOI: 10.1086/322542. arXiv: astro-ph/0110350 [astro-ph] (Cited on page 16).

Psaradaki, I., L. Corrales, et al. (May 2024). «Elemental Abundances in the Diffuse Interstellar Medium from Joint Far-ultraviolet and X-Ray Spectroscopy: Iron, Oxygen, Carbon, and Sulfur». In: *AJ* 167.5, 217, p. 217. DOI: 10.3847/1538-3881/ad306b. arXiv: 2403.02664 [astro-ph.GA] (Cited on page 12).

Quiret, S., C. Péroux, et al. (June 2016). «The ESO UVES advanced data products quasar sample - VI. Sub-damped Lyman α metallicity measurements and the circumgalactic medium». In: *MNRAS* 458.4, pp. 4074–4121. DOI: 10.1093/mnras/stw524. arXiv: 1602.02564 [astro-ph.GA] (Cited on page 55).

Racusin, J. L., S. V. Karpov, et al. (Sept. 2008). «Broadband observations of the naked-eye γ-ray burst GRB080319B». In: *Nature* 455.7210, pp. 183–188. DOI: 10.1038/nature07270. arXiv: 0805.1557 [astro-ph] (Cited on page 9).

Ramburuth-Hurt, T., A. De Cia, et al. (Apr. 2023). «Chemical diversity of gas in distant galaxies. Metal and dust enrichment and variations within absorbing galaxies». In: *A&A* 672, A68, A68. DOI: 10.1051/0004-6361/202244609. arXiv: 2302.00131 [astro-ph.GA] (Cited on pages 29, 161, 207).

Rémy-Ruyer, A., S. C. Madden, et al. (Mar. 2014). «Gas-to-dust mass ratios in local galaxies over a 2 dex metallicity range». In: *A&A* 563, A31, A31. DOI: 10.1051/0004-6361/201322803. arXiv: 1312.3442 [astro-ph.GA] (Cited on page 122).

Richards, Gordon T., Adam D. Myers, et al. (Jan. 2009). «Efficient Photometric Selection of Quasars from the Sloan Digital Sky Survey. II. ~1,000,000 Quasars from Data Release 6». In: *ApJS* 180.1, pp. 67–83. DOI: 10.1088/0067-0049/180/1/67. arXiv: 0809.3952 [astro-ph] (Cited on pages 8, 190, 195, 199, 257).

Richards, Gordon T., Michael A. Strauss, et al. (June 2006). «The Sloan Digital Sky Survey Quasar Survey: Quasar Luminosity Function from Data Release 3». In: *AJ* 131.6, pp. 2766–2787. DOI: 10.1086/503559. arXiv: astro-ph/0601434 [astro-ph] (Cited on page 189).

Riechers, Dominik A., C. M. Bradford, et al. (Apr. 2013). «A dust-obscured massive maximum-starburst galaxy at a redshift of 6.34». In: *Nature* 496.7445, pp. 329–333. DOI: 10.1038/nature12050. arXiv: 1304.4256 [astro-ph.CO] (Cited on page 19).

Ritchey, A. M., S. R. Federman, and D. L. Lambert (June 2018). «Abundances and Depletions of Neutron-capture Elements in the Interstellar Medium». In: *ApJS* 236.2, 36, p. 36. DOI: 10.3847/1538-4365/aab71e. arXiv: 1803.01089 [astro-ph.GA] (Cited on page 166).

Ritchey, Adam M., J. M. Brown, et al. (May 2023a). «A Reexamination of Phosphorus and Chlorine Depletions in the Diffuse Interstellar Medium». In: *ApJ* 948.2, 139, p. 139. DOI: 10.3847/1538-4357/acc179. arXiv: 2301.09727 [astro-ph.GA] (Cited on page 152).

Ritchey, Adam M., Edward B. Jenkins, et al. (July 2023b). «The Distribution of Metallicities in the Local Galactic Interstellar Medium». In: *ApJ* 952.1, 57, p. 57. DOI: 10.3847/1538-4357/acda25. arXiv: 2301.09743 [astro-ph.GA] (Cited on pages 10, 28, 36, 147, 150, 152, 154, 164–166).

Rogantini, D., E. Costantini, et al. (Sept. 2020). «Magnesium and silicon in interstellar dust: X-ray overview». In: *A&A* 641, A149, A149. DOI: 10.1051/0004-6361/201936805. arXiv: 2007.03329 [astro-ph.HE] (Cited on page 12).

Roman-Duval, J. C., G. De Rosa, et al. (Jan. 2020). «Overview of the ULLYSES Director's Discretionary HST program». In: *American Astronomical Society Meeting Abstracts #235*. Vol. 235. American Astronomical Society Meeting Abstracts, 232.03, p. 232.03 (Cited on page 208).

Roman-Duval, Julia, Karl D. Gordon, et al. (Dec. 2014). «Dust and Gas in the Magellanic Clouds from the HERITAGE Herschel Key Project. II. Gas-to-dust Ratio Variations across Interstellar Medium Phases». In: *ApJ* 797.2, 86, p. 86. DOI: 10.1088/0004-637X/797/2/86. arXiv: 1411.4552 [astro-ph.GA] (Cited on page 149).

Roman-Duval, Julia, Edward B. Jenkins, et al. (Apr. 2021). «METAL: The Metal Evolution, Transport, and Abundance in the Large Magellanic Cloud Hubble Program. II. Variations of Interstellar Depletions and Dust-to-gas Ratio within the LMC». In: *ApJ* 910.2, 95, p. 95. DOI: 10.3847/1538-4357/abdeb6. arXiv: 2101.09399 [astro-ph.GA] (Cited on pages 10, 12, 14, 16, 19, 25, 28, 36, 39, 41, 43, 45, 100, 107, 109–111, 144, 149, 152, 171, 204, 208).

Roman-Duval, Julia, Edward B. Jenkins, et al. (Mar. 2022a). «METAL: The Metal Evolution, Transport, and Abundance in the Large Magellanic Cloud Hubble Program. III. Interstellar Depletions, Dust-to-Metal, and Dust-to-Gas Ratios versus Metallicity». In: *ApJ* 928.1, 90, p. 90. DOI: 10.3847/1538-4357/ac524810.48550/arXiv.2202.04765. arXiv: 2202.04765 [astro-ph.GA] (Cited on pages 22, 109, 112, 113, 123, 149, 169, 170).

— (Aug. 2022b). «METAL: The Metal Evolution, Transport, and Abundance in the Large Magellanic Cloud Hubble Program. IV. Calibration of Dust Depletions versus Abundance Ratios in the Milky Way and Magellanic Clouds and Application to Damped Lyα Systems». In: *ApJ* 935.2, 105, p. 105. DOI: 10.3847/1538-4357/ac7713 (Cited on pages 16, 21, 122).

Roman-Duval, Julia, Edward B. Jenkins, et al. (Aug. 2022c). «METAL: The Metal Evolution, Transport, and Abundance in the Large Magellanic Cloud Hubble Program. IV. Calibration of Dust Depletions versus Abundance Ratios in the Milky Way and Magellanic Clouds and Application to Damped Lyα Systems». In: *ApJ* 935.2, 105, p. 105. DOI: 10.3847/1538-4357/ac7713. arXiv: 2206.03639 [astro-ph.GA] (Cited on pages 151, 170).

Ryan, Sean G., John E. Norris, and Timothy C. Beers (Nov. 1996). «Extremely Metal-poor Stars. II. Elemental Abundances and the Early Chemical Enrichment of the Galaxy». In: *ApJ* 471, p. 254. DOI: 10.1086/177967 (Cited on page 38).

Rybicki, George B. and Alan P. Lightman (1979). *Radiative processes in astrophysics* (Cited on page 28).

Saccardi, A., S. D. Vergani, et al. (Mar. 2023). «Dissecting the interstellar medium of a z = 6.3 galaxy. X-shooter spectroscopy and HST imaging of the afterglow and environment of the Swift GRB 210905A». In: *A&A* 671, A84, A84. DOI: 10.1051/0004-6361/202244205. arXiv: 2211.16524 [astro-ph.GA] (Cited on pages 9, 27, 110, 123, 205, 207).

Saito, Yu-Ji, Masahide Takada-Hidai, et al. (June 2009). «Chemical Evolution of Zinc in the Galaxy». In: *PASJ* 61, p. 549. DOI: 10.1093/pasj/61.3.549 (Cited on pages 48, 174).

Sandstrom, Karin M., Alberto D. Bolatto, et al. (June 2010). «The Spitzer Survey of the Small Magellanic Cloud (S^3MC): Insights into the Life Cycle of Polycyclic Aromatic Hydrocarbons». In: *ApJ* 715.2, pp. 701–723. DOI: 10.1088/0004-637X/715/2/701. arXiv: 1003.4516 [astro-ph.CO] (Cited on page 126).

Santini, P., R. Maiolino, et al. (July 2010). «The dust content of high-z submillimeter galaxies revealed by Herschel». In: *A&A* 518, L154, p. L154. DOI: 10.1051/0004-6361/201014748. arXiv: 1005.5678 [astro-ph.CO] (Cited on page 19).

Sarangi, Arkaprabha and Isabelle Cherchneff (Mar. 2015). «Condensation of dust in the ejecta of Type II-P supernovae». In: *A&A* 575, A95, A95. DOI: 10.1051/0004-6361/201424969. arXiv: 1412.5522 [astro-ph.SR] (Cited on pages 17, 21).

Sari, Re'em, Tsvi Piran, and Ramesh Narayan (Apr. 1998). «Spectra and Light Curves of Gamma-Ray Burst Afterglows». In: *ApJ* 497.1, pp. L17–L20. DOI: 10.1086/311269. arXiv: astro-ph/9712005 [astro-ph] (Cited on page 128).

Savage, B. D. and J. S. Mathis (Jan. 1979). «Observed properties of interstellar dust.» In: *ARA&A* 17, pp. 73–111. DOI: 10.1146/annurev.aa.17.090179.000445 (Cited on page 14).

Savage, Blair D. and Kenneth R. Sembach (Jan. 1996). «Interstellar Abundances from Absorption-Line Observations with the Hubble Space Telescope». In: *ARA&A* 34, pp. 279–330. DOI: 10.1146/annurev.astro.34.1.279 (Cited on pages 7, 12, 14, 15, 19, 25, 36, 41, 56, 109, 123, 149, 204, 253).

Savaglio, Sandra and S. Michael Fall (Oct. 2004). «Dust Depletion and Extinction in a Gamma-Ray Burst Afterglow». In: *ApJ* 614.1, pp. 293–300. DOI: 10.1086/423447. arXiv: astro-ph/0406430 [astro-ph] (Cited on page 127).

Savaglio, Sandra, S. Michael Fall, and Fabrizio Fiore (Mar. 2003). «Heavy-Element Abundances and Dust Depletions in the Host Galaxies of Three Gamma-Ray Bursts». In: *ApJ* 585.2, pp. 638–646. DOI: 10.1086/346225. arXiv: astro-ph/0203154 [astro-ph] (Cited on pages 12, 14, 36, 41, 109, 110, 149).

Schady, P., T. Dwelly, et al. (Jan. 2012). «The dust extinction curves of gamma-ray burst host galaxies». In: *A&A* 537, A15, A15. DOI: 10.1051/0004-6361/201117414. arXiv: 1110.3218 [astro-ph.CO] (Cited on page 125).

Schady, P., K. O. Mason, et al. (May 2007). «Dust and gas in the local environments of gamma-ray bursts». In: *MNRAS* 377.1, pp. 273–284. DOI: 10.1111/j.1365-2966.2007.11592.x. arXiv: astro-ph/0702122 [astro-ph] (Cited on page 14).

Schlegel, David J., Douglas P. Finkbeiner, and Marc Davis (June 1998). «Maps of Dust Infrared Emission for Use in Estimation of Reddening and Cosmic Microwave Background Radiation Foregrounds». In: *ApJ* 500.2, pp. 525–553. DOI: 10.1086/305772. arXiv: astro-ph/9710327 [astro-ph] (Cited on page 197).

Schmidt, M. (Mar. 1963). «3C 273 : A Star-Like Object with Large Red-Shift». In: *Nature* 197, p. 1040. DOI: 10.1038/1971040a0 (Cited on page 8).

Schneider, Donald P., Gordon T. Richards, et al. (Feb. 2002). «The Sloan Digital Sky Survey Quasar Catalog. I. Early Data Release». In: *AJ* 123.2, pp. 567–577. DOI: 10.1086/338434. arXiv: astro-ph/0110629 [astro-ph] (Cited on page 8).

Schneider, Raffaella and Roberto Maiolino (Apr. 2024). «The formation and cosmic evolution of dust in the early Universe: I. Dust sources». In: *A&A Rev.* 32.1, 2, p. 2. DOI: 10.1007/s00159-024-00151-2. arXiv: 2310.00053 [astro-ph.GA] (Cited on pages 17, 18, 253).

Schneider, Raffaella, Kazuyuki Omukai, et al. (Dec. 2011). «The first low-mass stars: critical metallicity or dust-to-gas ratio?» In: *Monthly Notices of the Royal Astronomical Society* 419.2, pp. 1566–1575. ISSN: 0035-8711. DOI: 10.1111/j.1365-2966.2011.19818.x. eprint: https://academic.oup.com/mnras/article-pdf/419/2/1566/

3126417/mnras0419-1566.pdf. URL: https://doi.org/10.1111/j.1365-2966.2011.19818.x (Cited on page 7).

Schroetter, I., N. Bouché, et al. (Dec. 2016). «Muse Gas Flow and Wind (MEGAFLOW). I. First MUSE Results on Background Quasars». In: *ApJ* 833.1, 39, p. 39. DOI: 10.3847/1538-4357/833/1/39. arXiv: 1605.03412 [astro-ph.GA] (Cited on page 209).

Selsing, J., J. P. U. Fynbo, et al. (Jan. 2016). «An X-Shooter composite of bright 1 < z < 2 quasars from UV to infrared». In: *A&A* 585, A87, A87. DOI: 10.1051/0004-6361/201527096. arXiv: 1510.08058 [astro-ph.GA] (Cited on pages 194, 195).

Shahbandeh, Melissa, Arkaprabha Sarangi, et al. (Aug. 2023). «JWST observations of dust reservoirs in type IIP supernovae 2004et and 2017eaw». In: *MNRAS* 523.4, pp. 6048–6060. DOI: 10.1093/mnras/stad1681. arXiv: 2301.10778 [astro-ph.HE] (Cited on page 18).

Shao, Yali, Ran Wang, et al. (May 2019). «Star Formation and ISM Properties in the Host Galaxies of Three Far-infrared Luminous Quasars at z $\sim$ 6». In: *ApJ* 876.2, 99, p. 99. DOI: 10.3847/1538-4357/ab133d. arXiv: 1903.01105 [astro-ph.GA] (Cited on page 19).

Shin, Min-Su, Edo Berger, et al. (Aug. 2006). «High-Resolution Spectroscopy of GRB030226: Features of a Massive Star Progenitor or Intervening Absorption Systems?» In: *arXiv e-prints*, astro-ph/0608327, astro–ph/0608327. DOI: 10.48550/arXiv.astro-ph/0608327. arXiv: astro-ph/0608327 [astro-ph] (Cited on page 110).

Shivaei, Irene, Leindert Boogaard, et al. (Aug. 2022). «The UV 2175Å attenuation bump and its correlation with PAH emission at z 2». In: *MNRAS* 514.2, pp. 1886–1894. DOI: 10.1093/mnras/stac1313. arXiv: 2203.09153 [astro-ph.GA] (Cited on page 125).

Shivaei, Irene, Behnam Darvish, et al. (Nov. 2020). «Dependence of the IRX-β Dust Attenuation Relation on Metallicity and Environment». In: *ApJ* 903.2, L28, p. L28. DOI: 10.3847/2041-8213/abc1ef. arXiv: 2010.10538 [astro-ph.GA] (Cited on page 128).

Slavin, Jonathan D., Eli Dwek, and Anthony P. Jones (Apr. 2015). «Destruction of Interstellar Dust in Evolving Supernova Remnant Shock Waves». In: *ApJ* 803.1, 7, p. 7. DOI: 10.1088/0004-637X/803/1/7. arXiv: 1502.00929 [astro-ph.GA] (Cited on pages 22, 124).

Slavin, Jonathan D., Eli Dwek, et al. (Oct. 2020). «The Dynamics, Destruction, and Survival of Supernova-formed Dust Grains». In: *ApJ* 902.2, 135, p. 135. DOI: 10.3847/1538-4357/abb5a4. arXiv: 2009.01895 [astro-ph.HE] (Cited on page 17).

Sneden, C., J. J. Cowan, and R. Gallino (Sept. 2008). «Neutron-capture elements in the early galaxy.» In: *ARA&A* 46, pp. 241–288. DOI: 10.1146/annurev.astro.46.060407.145207 (Cited on pages 153, 166).

Sofia, Ulysses J., James T. Lauroesch, et al. (Apr. 2004). «Interstellar Carbon in Translucent Sight Lines». In: *ApJ* 605.1, pp. 272–277. DOI: 10.1086/382592. arXiv: astro-ph/0401510 [astro-ph] (Cited on page 169).

Sparre, M., O. E. Hartoog, et al. (Apr. 2014). «The Metallicity and Dust Content of a Redshift 5 Gamma-Ray Burst Host Galaxy». In: *ApJ* 785.2, 150, p. 150. DOI: 10.1088/0004-637X/785/2/150. arXiv: 1309.2940 [astro-ph.CO] (Cited on page 9).

Springel, Volker, Carlos S. Frenk, and Simon D. M. White (Apr. 2006). «The large-scale structure of the Universe». In: *Nature* 440.7088, pp. 1137–1144. DOI: 10.1038/nature04805. arXiv: astro-ph/0604561 [astro-ph] (Cited on page 3).

Stebbins, Joel, C. M. Huffer, and A. E. Whitford (Jan. 1939). «No. 617. Space reddening in the galaxy.» In: *Contributions from the Mount Wilson Observatory / Carnegie Institution of Washington* 617, pp. 1–21 (Cited on page 11).

Sterken, Veerle J., Peter Strub, et al. (Oct. 2015). «Sixteen Years of Ulysses Interstellar Dust Measurements in the Solar System. III. Simulations and Data Unveil New Insights into Local Interstellar Dust». In: *ApJ* 812.2, 141, p. 141. DOI: 10.1088/0004-637X/812/2/141 (Cited on page 22).

Tchernyshyov, Kirill, Margaret Meixner, et al. (Oct. 2015). «Elemental Depletions in the Magellanic Clouds and the Evolution of Depletions with Metallicity». In: *ApJ* 811.2, 78, p. 78. DOI: 10.1088/0004-637X/811/2/78. arXiv: 1503.08852 [astro-ph.GA] (Cited on pages 43, 45, 56, 100, 101, 110, 152).

Timmes, F. X., J. T. Lauroesch, and J. W. Truran (Oct. 1995). «Abundance Histories for QSO Absorption-Line Systems». In: *ApJ* 451, p. 468. DOI: 10.1086/176235. arXiv: astro-ph/9504031 [astro-ph] (Cited on pages 36, 48).

Tinsley, B. M. (Jan. 1980). «Evolution of the Stars and Gas in Galaxies». In: *Fund. Cosmic Phys.* 5, pp. 287–388. DOI: 10.48550/arXiv.2203.02041. arXiv: 2203.02041 [astro-ph.GA] (Cited on page 4).

Travaglio, C., W. Hillebrandt, et al. (Oct. 2004). «Nucleosynthesis in multi-dimensional SN Ia explosions». In: *A&A* 425, pp. 1029–1040. DOI: 10.1051/0004-6361:20041108. arXiv: astro-ph/0406281 [astro-ph] (Cited on page 57).

Triani, Dian P., Manodeep Sinha, et al. (Apr. 2020). «The origin of dust in galaxies across cosmic time». In: *MNRAS* 493.2, pp. 2490–2505. DOI: 10.1093/mnras/staa446. arXiv: 2002.05343 [astro-ph.GA] (Cited on pages 12, 41).

Trumpler, Robert Julius (Jan. 1930). «Preliminary results on the distances, dimensions and space distribution of open star clusters». In: *Lick Observatory Bulletin* 420, pp. 154–188. DOI: 10.5479/ADS/bib/1930LicOB.14.154T (Cited on page 10).

Tumlinson, Jason, Molly S. Peeples, and Jessica K. Werk (Aug. 2017). «The Circumgalactic Medium». In: *ARA&A* 55.1, pp. 389–432. DOI: 10.1146/annurev-astro-091916-055240. arXiv: 1709.09180 [astro-ph.GA] (Cited on pages 4, 5, 253).

Tumlinson, Jason, J. Michael Shull, et al. (Feb. 2002). «A Far Ultraviolet Spectroscopic Explorer Survey of Interstellar Molecular Hydrogen in the Small and Large Magellanic Clouds». In: *ApJ* 566.2, pp. 857–879. DOI: 10.1086/338112. arXiv: astro-ph/0110262 [astro-ph] (Cited on page 172).

Valencic, Lynne A., Geoffrey C. Clayton, and Karl D. Gordon (Dec. 2004). «Ultraviolet Extinction Properties in the Milky Way». In: *ApJ* 616.2, pp. 912–924. DOI: 10.1086/424922. arXiv: astro-ph/0408409 [astro-ph] (Cited on pages 13, 169).

Valiante, Rosa, Raffaella Schneider, et al. (Aug. 2009). «Stellar sources of dust in the high-redshift Universe». In: *MNRAS* 397.3, pp. 1661–1671. DOI: 10.1111/j.1365-2966.2009.15076.x. arXiv: 0905.1691 [astro-ph.CO] (Cited on pages 19, 119).

Van der Swaelmen, M., V. Hill, et al. (Dec. 2013). «Chemical abundances in LMC stellar populations. II. The bar sample». In: *A&A* 560, A44, A44. DOI: 10.1051/0004-6361/201321109. arXiv: 1306.4224 [astro-ph.GA] (Cited on page 59).

Velichko, Anna, Annalisa De Cia, et al. (May 2024). «The α-element enrichment of gas in distant galaxies». In: *A&A* 685, A103, A103. DOI: 10.1051/0004-6361/202348601. arXiv: 2402.15508 [astro-ph.GA] (Cited on pages 151, 165, 174, 207).

Ventura, P., A. Karakas, et al. (Apr. 2018). «Gas and dust from solar metallicity AGB stars». In: *MNRAS* 475.2, pp. 2282–2305. DOI: 10.1093/mnras/stx3338. arXiv: 1712.08582 [astro-ph.SR] (Cited on pages 19, 21, 22).

Viegas, Sueli M. (Sept. 1995). «Abundances at high redshift: ionization correction factors». In: *MNRAS* 276.1, pp. 268–272. DOI: 10.1093/mnras/276.1.268 (Cited on pages 9, 35, 42).

Vladilo, G. (Aug. 2002). «Chemical abundances of damped Ly alpha systems:. A new method for estimating dust depletion effects». In: *A&A* 391, pp. 407–415. DOI: 10.1051/0004-6361:20020822. arXiv: astro-ph/0206048 [astro-ph] (Cited on pages 16, 27, 42, 59).

Vreeswijk, P. M., S. L. Ellison, et al. (June 2004). «The host of GRB 030323 at z=3.372: A very high column density DLA system with a low metallicity». In: *A&A* 419, pp. 927–940. DOI: 10.1051/0004-6361:20040086. arXiv: astro-ph/0403080 [astro-ph] (Cited on page 9).

Wang, Shu, Aigen Li, and B. W. Jiang (Nov. 2015). «The interstellar oxygen crisis, or where have all the oxygen atoms gone?» In: *MNRAS* 454.1, pp. 569–575. DOI: 10.1093/mnras/stv1900. arXiv: 1508.03404 [astro-ph.GA] (Cited on page 171).

Watson, D. (Sept. 2011). «The Galactic dust-to-metals ratio and metallicity using gamma-ray bursts». In: *A&A* 533, A16, A16. DOI: 10.1051/0004-6361/201117120. arXiv: 1107.6031 [astro-ph.GA] (Cited on page 116).

Watson, D., J. P. U. Fynbo, et al. (Dec. 2006). «A logN_{HI} = 22.6 Damped Lyα Absorber in a Dark Gamma-Ray Burst: The Environment of GRB 050401». In: *ApJ* 652.2, pp. 1011–1019. DOI: 10.1086/508049. arXiv: astro-ph/0510368 [astro-ph] (Cited on page 128).

Watson, Darach, Lise Christensen, et al. (Mar. 2015). «A dusty, normal galaxy in the epoch of reionization». In: *Nature* 519.7543, pp. 327–330. DOI: 10.1038/nature14164. arXiv: 1503.00002 [astro-ph.GA] (Cited on pages 19, 41).

Weingartner, Joseph C. and B. T. Draine (Feb. 2001). «Dust Grain-Size Distributions and Extinction in the Milky Way, Large Magellanic Cloud, and Small Magellanic Cloud». In: *ApJ* 548.1, pp. 296–309. DOI: 10.1086/318651. arXiv: astro-ph/0008146 [astro-ph] (Cited on page 11).

Welty, D. E., S. R. Federman, et al. (July 2006). «VLT UVES Observations of Interstellar Molecules and Diffuse Bands in the Magellanic Clouds». In: *ApJS* 165.1, pp. 138–172. DOI: 10.1086/504153. arXiv: astro-ph/0603332 [astro-ph] (Cited on page 128).

Welty, Daniel E. and Paul A. Crowther (May 2010). «Interstellar TiII in the Milky Way and Magellanic Clouds». In: *MNRAS* 404.3, pp. 1321–1348. DOI: 10.1111/j.1365-

2966.2010.16386.x. arXiv: 1001.3687 [astro-ph.GA] (Cited on pages 14, 43, 45, 54, 101, 110, 125, 128, 152).

Wendt, Martin, Nicolas F. Bouché, et al. (Apr. 2021). «MusE GAs FLOw and Wind V. The dust/metallicity-anisotropy of the circum-galactic medium». In: *MNRAS* 502.3, pp. 3733–3745. DOI: 10.1093/mnras/stab049. arXiv: 2009.08464 [astro-ph.GA] (Cited on pages 4, 209).

Werner, M. W., K. I. Uchida, et al. (Sept. 2004). «New Infrared Emission Features and Spectral Variations in NGC 7023». In: *ApJS* 154.1, pp. 309–314. DOI: 10.1086/422413. arXiv: astro-ph/0407213 [astro-ph] (Cited on page 12).

Wheeler, J. Craig, Christopher Sneden, and Jr. Truran James W. (Jan. 1989). «Abundance ratios as a function of metallicity.» In: *ARA&A* 27, pp. 279–349. DOI: 10.1146/annurev.aa.27.090189.001431 (Cited on page 49).

White, S. D. M. and M. J. Rees (May 1978). «Core condensation in heavy halos: a two-stage theory for galaxy formation and clustering.» In: *MNRAS* 183, pp. 341–358. DOI: 10.1093/mnras/183.3.341 (Cited on page 3).

Whittet, D. C. B. (Feb. 2010). «Oxygen Depletion in the Interstellar Medium: Implications for Grain Models and the Distribution of Elemental Oxygen». In: *ApJ* 710.2, pp. 1009–1016. DOI: 10.1088/0004-637X/710/2/1009. arXiv: 0912.3298 [astro-ph.GA] (Cited on page 171).

Williams, Brian J., Kazimierz J. Borkowski, et al. (June 2013). «Azimuthal Density Variations around the Rim of Tycho's Supernova Remnant». In: *ApJ* 770.2, 129, p. 129. DOI: 10.1088/0004-637X/770/2/129. arXiv: 1305.0567 [astro-ph.HE] (Cited on page 21).

Wiseman, P., P. Schady, et al. (Mar. 2017). «Evolution of the dust-to-metals ratio in high-redshift galaxies probed by GRB-DLAs». In: *A&A* 599, A24, A24. DOI: 10.1051/0004-6361/201629228. arXiv: 1607.00288 [astro-ph.GA] (Cited on pages 9, 54, 107, 110, 121, 127).

Witstok, Joris, Irene Shivaei, et al. (Sept. 2023). «Carbonaceous dust grains seen in the first billion years of cosmic time». In: *Nature* 621.7978, pp. 267–270. DOI: 10.1038/s41586-023-06413-w. arXiv: 2302.05468 [astro-ph.GA] (Cited on pages 169, 210).

Witt, Adolf N. and Karl D. Gordon (Jan. 2000). «Multiple Scattering in Clumpy Media. II. Galactic Environments». In: *ApJ* 528.2, pp. 799–816. DOI: 10.1086/308197. arXiv: astro-ph/9907342 [astro-ph] (Cited on page 109).

Wolfe, Arthur M., Eric Gawiser, and Jason X. Prochaska (Sept. 2005). «Damped Ly α Systems». In: *ARA&A* 43.1, pp. 861–918. DOI: 10.1146/annurev.astro.42.053102.133950. arXiv: astro-ph/0509481 [astro-ph] (Cited on pages 9, 41).

Wolfe, Arthur M., Kenneth M. Lanzetta, et al. (Dec. 1995). «The Large Bright QSO Survey for Damped LY alpha Absorption Systems». In: *ApJ* 454, p. 698. DOI: 10.1086/176523 (Cited on pages 7, 9).

Yang, X. J., Lijun Hua, and Aigen Li (Aug. 2024). «Where Have All the Sulfur Atoms Gone? Polycyclic Aromatic Hydrocarbon as a Possible Sink for the Missing Sulfur in the Interstellar Medium. I. The C–S Band Strengths». In: *arXiv e-prints*, arXiv:2408.04857, arXiv:2408.04857. DOI: 10.48550/arXiv.2408.04857. arXiv: 2408.04857 [astro-ph.GA] (Cited on page 171).

York, Brian A., Sara L. Ellison, et al. (Aug. 2006). «Detection of Diffuse Interstellar Bands in the z=0.5 Damped Lyα System toward AO 0235+164». In: *ApJ* 647.1, pp. L29–L32. DOI: 10.1086/505907. arXiv: astro-ph/0605471 [astro-ph] (Cited on page 169).

York, D. G., L. Spitzer, et al. (Mar. 1983). «Interstellar abundances of oxygen and nitrogen.» In: *ApJ* 266, pp. L55–L59. DOI: 10.1086/183977 (Cited on pages 25, 41).

York, Donald G., J. Adelman, et al. (Sept. 2000). «The Sloan Digital Sky Survey: Technical Summary». In: *AJ* 120.3, pp. 1579–1587. DOI: 10.1086/301513. arXiv: astro-ph/0006396 [astro-ph] (Cited on page 8).

Zabl, Johannes, Nicolas F. Bouché, et al. (May 2019). «MusE GAs FLOw and Wind (MEGAFLOW) II. A study of gas accretion around z $\approx$ 1 star-forming galaxies with background quasars». In: *MNRAS* 485.2, pp. 1961–1980. DOI: 10.1093/mnras/stz392. arXiv: 1901.11416 [astro-ph.GA] (Cited on page 4).

Zafar, T., D. Watson, et al. (Aug. 2011). «The extinction curves of star-forming regions from z = 0.1 to 6.7 using GRB afterglow spectroscopy». In: *A&A* 532, A143, A143. DOI: 10.1051/0004-6361/201116663. arXiv: 1102.1469 [astro-ph.CO] (Cited on pages 125, 169).

Zafar, Tayyaba and Palle Møller (Jan. 2019). «Metals, depletion, and dimming: decrypting dust». In: *MNRAS* 482.2, pp. 2731–2738. DOI: 10.1093/mnras/sty2856. arXiv: 1810.07843 [astro-ph.GA] (Cited on page 110).

Zafar, Tayyaba and Darach Watson (2013). «The metals-to-dust ratio to very low metallicities using GRB and QSO absorbers; extremely rapid dust formation». In: *Astronomy & Astrophysics* 560, A26 (Cited on page 128).

Zafar, Tayyaba, Darach Watson, et al. (July 2012). «The Properties of the 2175 Å Extinction Feature Discovered in GRB Afterglows». In: *ApJ* 753.1, 82, p. 82. DOI: 10.1088/0004-637X/753/1/82. arXiv: 1205.0387 [astro-ph.CO] (Cited on pages 14, 125).

Zhang, Shaohua, Jian Ge, et al. (July 2022). «The 2175 Å bump features in FeLoBAL quasars: One indicator of MW-like dust in the nuclear region of quasars». In: *A&A* 663, A63, A63. DOI: 10.1051/0004-6361/202142476. arXiv: 2203.03789 [astro-ph.GA] (Cited on page 14).

Zhukovska, S., H. P. Gail, and M. Trieloff (Feb. 2008). «Evolution of interstellar dust and stardust in the solar neighbourhood». In: *A&A* 479.2, pp. 453–480. DOI: 10.1051/0004-6361:20077789. arXiv: 0706.1155 [astro-ph] (Cited on pages 20–22, 41, 119, 253).

Zuo, Wenbo, Aigen Li, and Gang Zhao (Dec. 2021b). «Interstellar Extinction and Elemental Abundances: Individual Sight Lines». In: *ApJS* 257.2, 63, p. 63. DOI: 10.3847/1538-4365/ac2cc3. arXiv: 2111.03903 [astro-ph.GA] (Cited on page 172).

— (Feb. 2021a). «Interstellar Extinction and Elemental Abundances». In: *ApJS* 252.2, 22, p. 22. DOI: 10.3847/1538-4365/abcc6d. arXiv: 2011.09440 [astro-ph.GA] (Cited on pages 169, 170, 172).

de Boer, T. J. L., V. Belokurov, et al. (Sept. 2014). «The α-element knee of the Sagittarius stream». In: *MNRAS* 443.1, pp. 658–663. DOI: 10.1093/mnras/stu1176. arXiv: 1406.3352 [astro-ph.GA] (Cited on pages 49, 60).

van Paradijs, J., P. J. Groot, et al. (Apr. 1997). «Transient optical emission from the error box of the γ-ray burst of 28 February 1997». In: *Nature* 386.6626, pp. 686–689. DOI: 10.1038/386686a0 (Cited on page 8).